SUBJ
MNG
MB
GL01179
UNIVERSITY OF UTAH
RESEARCH INSTITUTE
EARTH SCIENCE LAB.

Minerals Beneficiation

By L. J. BECHAUD, JR.*
Director
Newmont Exploration Ltd.

Mill men continue their search for process improvements that will give lower costs and better performance

THE less than favorable economic weather prevailing in the business world has continued to hold the damper on advancements in milling and minerals research. Toward year's end came announcements of strike settlements and cuts in prices of copper, zinc and lead. Anaconda's six week shutdown at Chuquicamata was ended November 14 with the New Jersey Zinc settlement being announced a few days later. The Bunker Hill strike ended near the close of the year. Earlier, settlement of the strike at White Pine was effected.

Despite the presently retarded economic outlook, new plants were put into production, construction proceeded on schedule at other properties, and ambitious undertakings involving multi-million dollar expenditures were announced, particularly in the iron and steel industries. Mill men have not neglected improvements in milling circuits favoring automation and automatic controls in the continuing search for lower costs and optimum performance.

As usual, the greatest activity appears centered in the iron and steel industry with plant expansions announced for Reserve and Republic, a new taconite project being planned in Wyoming for Columbia-Geneva, and announcement of plans for three commercial installations based on the Strategic-Udy direct iron process, two of these in Canada and one in the U. S. Vigorous activity was also afoot in the base metal industry, notably the announcement of construction of integrated copper-lead smelting facilities at Tsumeb in South-West Africa, Asarco's 15,000-tpd Mission project near Tucson, and bringing into production Southern Peru's Toquepala mill and smelter and Inco's Thompson project in Canada.

Autogenous Grinding Under Intensive Study

Efforts to reduce grinding costs have spurred interest in the possible benefits to be derived from autogenous grinding with attendant savings for crushing circuits. Extensive theoretical and pilot plant studies of the dry-grinding Aerofall mill were made and reported on in two papers at the International Mineral Processing Congress in London in April. Results tend to indicate that metallurgical advantages, in addition to low power and wear, may also be possible due to disintegration of the ore along grain boundaries to its natural grain size. This would seem to be of particular importance for the dry processing of specular hematite or magnetite ores having a moderately coarse liberation size. Iron ore metallurgists, being well abreast of developments, have had this mill under investigation for some time.

Extensive testing is also well under way with the Hardinge Cascade mill. The Quebec-Cartier installation at Lac Jeannine, employing twelve 18-ft. diam Cascade mills and due to commence grinding in December will be watched with interest by all mill men.

Every flotation operator is well aware that his grinding mill effects changes in surface chemistry as well as performing the purely physical task of comminution. These chemical changes are often unpredictable, sometimes detrimental, and sometimes beneficial. Often deliberate attempts are made to enhance or to retard the chemical effects. As autogenous grinding finds more application in sulfide flotation plants, it will be of considerable interest to observe and compare the chemical phenomena with that of conventional methods.

Iron Ore Beneficiation

The past year has seen the active resumption of the steady technological progress in mineral preparation that has come to be expected of the iron ore industry. The increasingly keen competition from high grade foreign ores and "manufactured" blast furnace burdens is forcing domestic operators to bend every effort to prepare chemically and physically enhanced materials having improved digestibility in the blast furnace.

After many years of lying dormant, the technically sound process of magnetic reduction has been dusted off and is being carefully scrutinized for processing semitaconite such as that found on the west end of the Mesabi range. A wealth of development work has gone into this process over the years and now it appears the next step to commercial reality will be taken as illustrated by the M. A. Hanna Co. announcement of a $2,000,000 expenditure for pilot plant

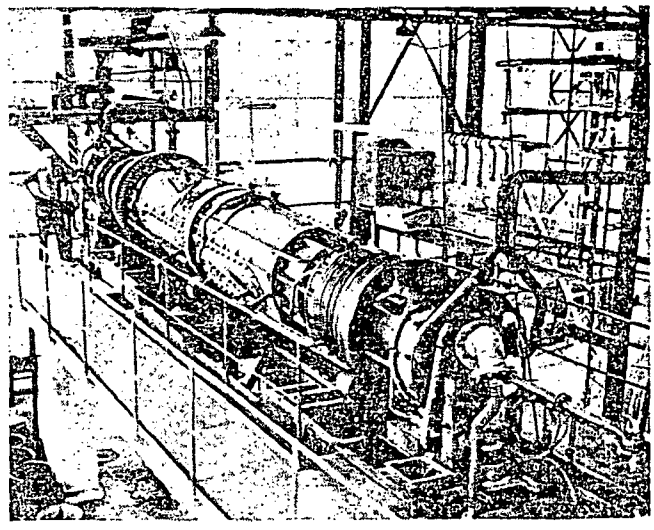

Two semitaconite processing pilot plants that will utilize Dravo-Lurgi magnetizing roasting kilns, similar to the one-half tph test model pictured, are under construction on the Mesabi Range. These plants will convert semitaconite to a synthetic magnetite which can subsequently be recovered using conventional magnetic equipment

* *The author was assisted by W. C. Hellyer and K. C. Peterson, metallurgists on the staff of Newmont Exploration Ltd., in the preparation of this article.*

facilities in the Nashwauk-Cooley area. The favorable tax structure for semitaconites created by the Minnesota legislature in 1959 is reported to have influenced the decision for this expenditure. In some cases, a break on costs might be realized in grinding due to increased friability after heat treatment. Many different types of furnaces have been investigated over the years for the magnetic roasting step and at present the Lurgi kiln appears to be finding the most favor.

Expansion in the capacity of its E. W. Davis works to 9,000,000 tons of pellets per year was announced by Reserve Mining Co. during 1960. This represents a 50 percent increase over present tonnage and reportedly would involve new crushing, concentrating and pelletizing equipment as well as rail and power facilities.

The expansion of Cleveland-Cliffs' Humboldt plant on the Marquette range to an annual capacity of 650,000 tons of pellets was completed in 1960. This plant has the first commercial Allis-Chalmers Grate-Kiln system of concentrate agglomeration and heat treatment of pellets. Plans were also announced by Cleveland-Cliffs to expand the capacity of the Republic low grade mine to 1,600,000 tons of iron ore concentrates per year. Both Republic and Humboldt employ flotation for the concentration of iron minerals from the low grade jasper, and together with M. A. Hanna Company's Groveland operation, also on low grade jasper, will provide a source of some 3,000,000 tons of highly beneficiated concentrates per year from the upper Michigan peninsula. Adding to this, Erie Mining Company's production of pellets and the new goal of Reserve gives the phenomenal total of 20,000,000 annual tons of "manufactured" high grade product from the Minnesota-Michigan ranges.

Other Developments in Iron Ore Concentration

Other processes continue to be examined closely to improve quality of product and to reduce costs. Improvement of quality of dense media through control of particle shape is a move in this direction. The rotary scrubber is also being re-examined to obtain a better understanding of the improvements to be expected by this method of removing loosely adhering silica from ore particles.

Development of dry methods of iron ore concentration continues to be of interest, spurred by the activity in the Wabush area of Labrador. Low

Pouring steel into an electric furnace during test run of the Strategic-Udy process

and high intensity magnetic separators, principally of foreign origin, appear to be attracting the most interest. But wet methods of separation have not been ignored. At least one company has experimented with a new type of gravity separation device which has produced remarkable results in the extreme fine size range; this equipment is still in the experimental stage.

Of considerable interest is the expansion of Inco's iron ore recovery plant at Copper Cliff, Ont., to triple its present capacity. This novel process, which converts nickeliferous pyrrhotite into agglomerated pellets of 68 percent Fe content and recovers by-products of nickel and sulfur, is a tribute to the determination and ingenuity of Inco personnel. The high quality pellets are reported to be finding use as open hearth lump.

Economics of Direct Reduction Still Controversial

A great deal of information on direct reduction of iron ore was published during 1960. While there is still considerable controversy over the economics of D-R in the U. S., there is little doubt but that in specialized instances a commercial operation can be mounted. The Kellogg engineered HyL process at Monterey, Mexico, has been well described in the literature and is a case in point. More recently, a 500-tpd addition to this plant was announced.

L. J. Bechaud, Jr., is one of the world's foremost authorities on extractive metallurgy of germanium and is a holder of several patents. For the past eight years he has been associated with Newmont Exploration Limited and is currently director of its Metallurgical Department. Bechaud has been in his present post for three years, prior to which he was at Newmont's Grass Valley, Calif., operations. Before that, he was chief research metallurgist for M. A. Hanna Co. on the iron ranges of Minnesota, pioneering in the development of magnetic taconites and Michigan jaspers. He came to Hanna from Pan American Mining Co. and the goldfields of California.

The well publicized Strategic-Udy process, while not yet commercialized, is being planned for installation at Anaconda, Mont. This plant will produce steel from current and stockpiled slag. Canadian projects employing the Strategic-Udy process have also been announced. One of these is for a 150,000-tpy plant for New Mylamaque Exploration at Kingston, Ont. The other is for Quebec South Shore Steel at Varennes, Que.

Other D-R processes of commercial stature include H-Iron, Krupp-Renn, Höganäs, and the classic Wiberg-Söderfors. All but H-Iron have been in operation a number of years. More recently, the H-Iron process for producing low-carbon iron powder was put into operation by Alan Wood Steel Co. at Conshohocken, Pa., and Bethlehem Pacific has engineered a second plant at its Vernon steel works. The product from the latter plant will reportedly be charged to an electric steel-making furnace.

Two newcomers on the scene during the latter part of the year were the Dwight-Lloyd McWane and the Allis-Chalmers Agglomeration-Reduction processes, both in the development stage. The D-LM process employs pre-reduction of a prepared and pelletized feed on a traveling grate followed by introduction of the pre-reduced pellets directly to an electric furnace for steel making. This process appears to have the advantages of simplicity, close control, and flexibility, and should appeal to operators who tend to shy away from the complexities of more sophisticated equipment. The Allis-Chalmers process is a unique combination of two concentrically aligned kilns, the inner kiln providing for reduction by means of catalytically cracked hydrocarbon gas, with excess gas being burned in the annular space between the kilns to provide the heat.

Interest in Automation Grows

Interest in automatic control of mill processes in the mineral industries continues to grow. Although the fully automated push-button mill, controlled by a computer, is still some-

where in the future, advances have been made in applying mechanical and electronic controls to a number of unit operations involved in milling practice.

True automation with its implication of sensing and control devices, which are integrated by means of feedback systems with a sophisticated control center, is probably closest to reality in those mineral industries where efficient materials handling contributes largely to economy of operation and process variables are reasonably uncomplicated. These areas include pimarily such operations as cement plants and coal cleaning units where great progress in automatic control has been reported recently. Among the cement manufacturers reporting such advances in automatic control are the Dundee, Mich., plant of the Dundee Cement Co., the Ada, Okla., plant of Ideal Cement Co., and Riverside Cement Co.

The Dundee operation, while not under the direct control of a computer, utilizes an IBM electronic computer set-up for extremely rapid evaluation of data to achieve optimum operating conditions. The use of automatic control of burners on the kilns, clay and limestone preparation, and closed circuit TV observation of transfer points are just a few of the devices reported to be incorporated in the Dundee plant. Other cement plants are understood to be attempting to incorporate more direct control of unit operations into the electronic computer center.

The Moss No. 3 preparation plant of Clinchfield Coal Co. has put practically all materials handling and operation of dense media separation under centralized control. Rail cars move by gravity and are controlled remotely by target and limit switches and compressed air operated retarders. Handling, storage, and charging of the magnetite heavy medium to the separators is also under remote control. Gamma ray absorption devices are used to measure, report and record the specific gravity in each of nine dense media units. Under such control, product quality is reported to be better and more consistent, and significant economy in labor costs have resulted.

In the field of metallic minerals, the iron ore processing plants continue to lead in the field of automatic control of unit processes, particularly that of sintering. In addition, the application of computers to the problem of optimizing the operation and burdening of blast furnaces has been widely reported.

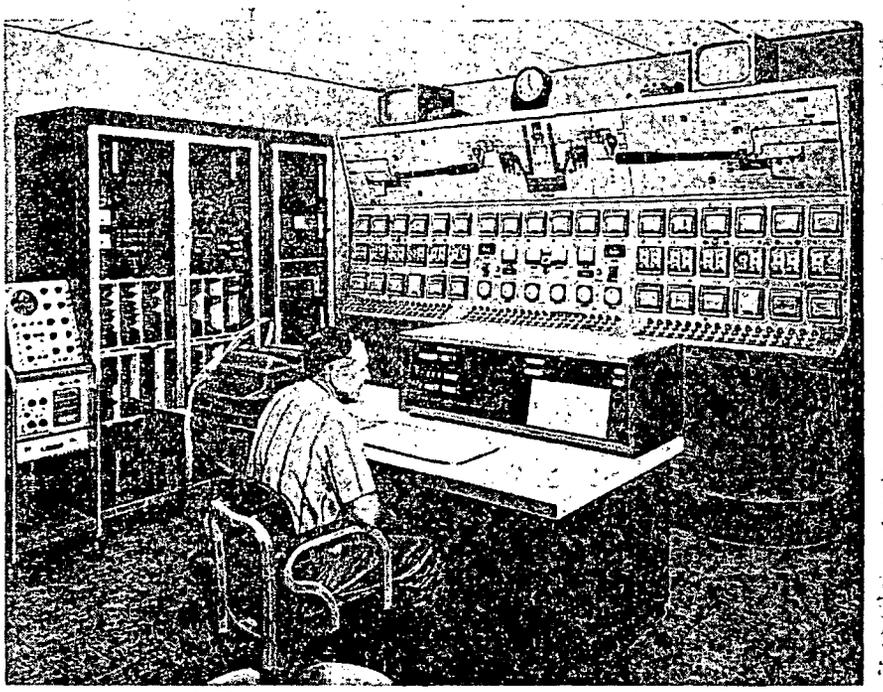

While the goal of a fully-automated push-button mill controlled by a computer is still in the future, mineral processers are making more and more use of both computers and automatic controls

Instrumentation in the Nonferrous Industry

Operators in nonferrous mills are plagued with the ancient problem of having to tailor-make control devices to fit each and every situation. A few novel approaches to the control of pulp density and grinding mills have been reported recently.

Asarco has two schemes under consideration for control of the grinding circuit for the new 15,000 tpd Mission copper concentrator. The first method is based on a determination of the difference in the temperature of the feed water and the ball mill discharge. A large temperature difference indicates the mill is underloaded and the electronic control system calls for an increase in the rate of feed.

The second system depends upon measuring and constantly controlling pulp density of the ball mill discharge at a predetermined value by automatically adjusting the rate of feed of water to the mill. The water flow rate is measured in turn and this information is used to automatically compensate for fluctuations by adjusting the rate of ore feed so that the water and ore are in balance.

The new Levack mill of Inco is reported to be extensively instrumented. Water addition to the classifiers is regulated by pulp density measuring devices based on gamma ray absorption. In the flotation circuit, pulp density, pH and temperature are measured automatically and controlled from a central point. Thickeners and filters are instrumented and operated from another centralized control point.

Much of the over-all problem associated with more complete automation of mineral beneficiating plants is involved in the lack of suitable sensing devices for measuring process variables. Considerable progress has been made recently in the application of such techniques as gamma ray absorption to determine pulp density as mentioned above. X-ray fluorescence is being employed by Anaconda to yield essentially continuous analyses for a number of elements in mill feed, concentrates and tailings. Kennecott is reported to be installing similar units at Utah Copper. While these extremely rapid assay tools are not automatic control devices, they do give the operator a more up-to-the-minute picture of the performance of his mill, and certainly these techniques represent one more advance toward automatic process control.

Hydrometallurgy Confined Largely to Uranium and Rare Earths

Significant new activity in the field of hydrometallurgy is still confined in large scale to the uranium extraction field. Several new mills went into operation or were approved for AEC contracts, principally in the Gas Hills district of Wyoming. Extraction techniques in the new mills are standard acid-leach or carbonate-leach followed by liquid-liquid extraction and stripping units.

The status of buying contracts between yellow-cake producers and

AEC for the 1962–1966 period continued to be cloudy. General policies announced by AEC are, by apparent necessity, broad and somewhat nebulous so that each operator's position during the forthcoming period must be individually established. By the end of the year, the major portion of the established uranium mills were reported to have reached new agreements with AEC regarding price for and amounts of yellow cake to be produced.

From a production standpoint, the application of hydrometallurgical techniques continued to be confined mainly to the rare-earths and nuclear products sectors of the industry. In the area of base metal production, an amine leaching process for producing high purity lead from mixed sulfide ores was developed at the University of British Columbia in cooperation with Sherritt Gordon Mines and was received with a good deal of interest.

Briefly, the process consists of a pressure oxidizing leach in acid medium to convert PbS to $PbSO_4$. The resulting lead sulfate is selectively leached at room temperature with a 15 percent solution of diethylene triamine which forms a lead complex. Lead is precipitated from the amine as a basic carbonate by the addition of CO_2. Silver free lead is produced from the carbonate by reduction. The amine leach solution is regenerated with CaO producing gypsum as a waste by-product.

In this process reagent consumption appears to be quite low. All steps, except for the initial oxidation and final reduction of lead, are conducted at room temperature and pressure. This appears to be a practical process having application to non-separable base metal bulk concentrates. Lead purity is said to be four nines.

Wet Processes for GeO_2 and Cu Recovery

At Tsumeb in South-West Africa a new wet process plant for production of germanium dioxide went on stream in the latter part of the year. Sulfide concentrates are roasted for selective oxidation of arsenic and germanium. Calcines are acid leached and pregnant solution is concentrated in a submerged combustion evaporator. Evaporator sludge and liquor is distilled with hydrochloric acid to produce germanium tetrachloride which is subsequently hydrolyzed to GeO_2.

Empressa Minera de Matos Blancos S.A., has initiated a project in Northern Peru designed to recover copper occurring predominantly in the form of basic copper chloride, atacamite. The patented process consists of percolation leaching with sulfuric acid followed by sulfur dioxide absorbtion to precipitate insoluble copper chloride. The pure chloride is then pelletized with limestone and coke and is smelted in three 4 by 3-meter Lurgi rotary furnaces. Two additional furnaces are used to produce wire bars. Plant is designed to handle 3000 tpd of ore.

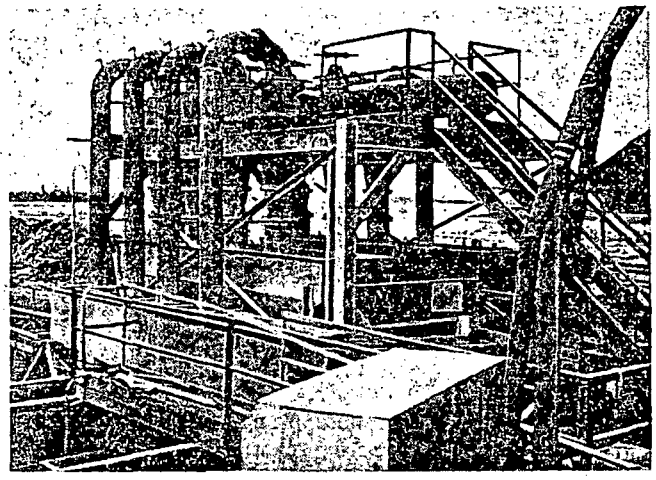

In recent years, the use of hydrocyclones in mineral processing systems has grown steadily

Although specific details are lacking, it is reported that a new technique is under investigation by the British Department of Industrial and Scientific Research involving the use of napthenic acid in liquid-liquid extractions. Priced more cheaply than alkyl-phosphoric acid, napthenic acid is reported to be equally effective.

Segregation Process Revived

The process of copper segregation is an example of an apparently dead horse which has recently shown surprising signs of life. While the exact mechanism of copper segregation has not been well defined, the over-all process consists of roasting oxidized copper ore with salt and carbonaceous material under controlled atmosphere conditions at 700–750° C. Simultaneous chloridization and reduction of the copper mineral apparently occurs such that metallic copper is produced in the form of separate well defined particles outside the ore matrix. This metallic copper is recoverable by standard flotation techniques.

Interest in the segregation process lagged after two experimental plants in the Congo and Southern Rhodesia closed in the early 1930's due to economic and mechanical difficulties. The U. S. Bureau of Mines at Tucson recently undertook a renewed evaluation of the process. Partly as a result of this work and the natural interest in a process for recovering copper from oxide and silicate minerals, pilot plants have been built in Mexico at Santa Rosalia and d'Akjoujt in Mauretania.

The first commercial segregation plant in the U. S. was recently put into operation by Trans-Arizona Resources near Tucson. The reactor in this plant is reported to be a 54-in. by 42-ft long indirect fired rotary kiln.

A pilot plant of particular interest is that of the Berenguela mine in Peru which is built to handle one tpd of ore. Here the older technique of roasting in rotary kilns under a relatively static atmosphere has been replaced by pelletizing the ground ore with coke and salt followed by roasting in a shaft furnace. Both copper and silver are segregated and recovered by flotation from a manganiferous ore containing from one to two percent copper and five to twenty oz of silver per ton. An interesting feature is the departure from the rotary or hearth type furnaces of previous plants.

New Separation and Classification Methods

A new and unique process developed at Battelle, which is used to upgrade rock salt at the Detroit mine of International Salt Co., makes use of a differential in radiant heat absorbtion to cause one fraction of "ore" to adhere to a heat sensitive belt. Other applications are possible.

Dorr Oliver, Inc., introduced a new dense-media process claimed to be capable of treating the full size range from 2½-in. to 65-mesh. The process includes DorrClone cyclones, dense media ore classification units, and DSM screens. Feed is introduced under gravity head thus eliminating pumping of ore with media. Media losses are claimed to be drastically reduced.

A double-drum, concurrent style permanent ceramic magnet, wet-drum separator has been developed by Stearns Magnetic Products, Milwaukee. The high strength ceramic material is said to provide savings in weight, operating and maintenance costs. Stainless steel is used for feed box and collection tank.

Successful application of the Buell developed Gravitational-Inertial classifier was reported on limestone and phosphate rock processing. This high efficiency dry classifier makes use of aerodynamic principles not previously utilized in classification. There are no moving parts in the separating chamber proper, hence maintenance costs should be low. Once the cut point has been set it is claimed no further attention is required. The classifier makes its separation by entraining fine dust particles in an induced eddy current which exhausts from the top of the unit. The coarser particles, which cannot make the turn into the eddy chamber, fall by gravity through an opening in the bottom. A secondary air current is directed onto the falling coarse particles and removes adhering fines.

Russians Dominate Flotation Research

Advances in flotation practice and research in the free world were at a modest level. New mills were designed but the flotation circuits reported rely mainly on the cut and dried standard techniques which have served the industry so well in the past.

Probably the most significant development in flotation was the domination of the Soviets in the fields of both basic and applied research. At the International Mineral Processing Congress held in London during April, six of thirteen papers concerned with flotation were of Russian origin among a total of seven nations whose representatives gave papers. A cursory check of published articles reveals that a large and steadily increasing amount of work in flotation research is being conducted behind the Iron Curtain.

During the past year in the Soviet Union, a large scale production plant was put into operation employing the L-P-F process on a copper ore. Sodium sulfide is used as the precipitant, it being claimed that this is simpler, cheaper, and gives better grade of concentrate than does sponge iron. One Soviet paper again emphasized the role and possible significance of gas precipitation in flotation. Indications are that losses of slimed mineral might be reduced by making more effective use of this phenomenon.

In North America, evidence of a growing interest in columbium was given by announcement from four different companies of the development of a flotation process for concentrating columbium minerals. Long chain amines, di-amines, and wetting agents is one combination; hydroxyquinoline chemicals for collector is used in another instance.

On a laboratory scale, interesting results were obtained at Washington State University on flotation of autunitic uranium ores with an aqueous emulsion of stearic acid, soap, and kerosene. The reagent also floats uraninite, uranophane, monozite, apatite, and with a soluble phosphate, chrysocolla is also reported to be floated. The only catch is that selectivity is not good.

MINING EDUCATION

(Continued from page 50)

convincingly. If adequate favorable case history does exist, one of the most useful things that can be done is to pull it together and make it available.

In the modern scene, on-the-job training is necessary unless work-study cooperative programs are developed. Few companies offer it. Both educators and industry spokesmen hold that the job of the schools is to give a broad fundamental training, leaving much of the detail and most of the practical applications to industry. To be adequate in this context, on-the-job training consists of more than just learning the jobs and psychology of labor. It involves experience in various departments of the company, reports from the trainee and from his immediate supervisor, correction, and periodic interviews with local top management.

Nothing can be accomplished by retreating into the viewpoint that the young fellows are too soft or too desirous of made-to-order careers. To the extent that they may be found wanting in these respects it is the fault of conditions created by their elders. Anyway, we have to work with people as they are, not as they might have been. Furthermore, anyone who will take the trouble to learn the viewpoints of young men will find that they lack neither intelligence, manhood or valid philosophies. Can they be blamed for taking advantage of the offers of better competitors for their services?

Mining is a necessary, useful field. For people who thrive on challenges, it is continuously fascinating in its diversity, opportunity, geographic spread and incessant change. Until it regains status as a field of unusual opportunity and a home for an elite class of humanity we have no cause to be complacent. Meanwhile, there is much to be done involving cooperation between the industry and educators.

MINING GEOLOGY

(Continued from page 57)

the ore was deposited from a concentrated brine high in Na and Cl, and lower in K, Ca, Mg, B and SO_4, containing only small amounts of the ore minerals, perhaps as little as ten ppm.

A geologic therometer, that may be of great range and precision, has tentatively been established by R. N. Clayton of the University of Chicago and H. L. James of the Geological Survey. Using the O^{18}/O^{16} ratios of iron oxides, calcite and quartz, temperatures ranging from 80° C (Iron River, Mich.) to 700° C (Iron Springs, Utah) have been estimated. Further data suggest that iron oxides of the main ore bodies in the Lake Superior region were formed from solutions isotopically similar to present-day fresh water.

The year 1960 witnessed a continuation of the debate concerning basic theories of ore genesis. Many papers presenting discussions on this subject have been carried in *Economic Geology*. The conflict between the syngenetic and epigenetic schools is sometimes heated, but these debates, spurred by papers and discussions of such men as C. L. Knight, G. M. Schwartz, J. L. Kulp, R. H. Sales, H. L. James and many others, are a valuable contribution to geological science.

Difficult Problems Ahead

In conclusion, it can be stated that the mining industry has entered a period requiring considerable adjustment, both economic and technical. There will be difficult problems to solve in the immediate years ahead. Strong leadership and decisive action are needed to cope with rising costs, increasing taxes, restrictive legislation, and competition from the Communist world. At the same time, the industry is confronted with the task of constantly replacing and even expanding diminishing reserves in order to supply the free world with its vital mineral requirements.

SUBJ
MNG
MBAB

Hydrometallurgy, 5 (1980) 295—304
© Elsevier Scientific Publishing Company, Amsterdam — Printed in The Netherlands

MATERIAL BALANCE AS THE BASIS FOR PROCESS CONTROL IN ELECTROWINNING AND ELECTROREFINING

UNIVERSITY OF UTAH
RESEARCH INSTITUTE
EARTH SCIENCE LAB.

W.W. HARVEY

EIC Corporation, 55 Chapel Street, Newton, Massachusetts 02158 (U.S.A.)

(Received July 17th, 1979; accepted October 4th, 1979)

ABSTRACT

Harvey, W.W., 1980. Material balance as the basis for process control in electrowinning and electrorefining. *Hydrometallurgy*, 5: 295—304.

Electrowinning and electrorefining, like chemical processes generally, are amenable to comprehensive material balance analysis for purposes of process control. However, current efficiency in electrowinning is insufficient to provide the requisite agreement between current and electrolyte flows on the one hand and observed concentration changes on the other. The many factors contributing to volume change and metal loss in electrowinning determine a "volume efficiency", as previously defined, which can differ significantly from 100%. Use of volume efficiency in conjuction with current efficiency is illustrated by experimental data for the case of nickel electrowinning employing a porous separator. In electrorefining, anode current efficiency is a major factor in the material balance. The chemical compositions of anodes and cathodes and their respective current efficiencies contribute the source terms for soluble impurity buildup in the electrolyte. An analysis is developed which takes into account the principal mechanisms of extraneous weight loss of anodes, including dissolution of oxide inclusions, disintegration and chemical corrosion. The considerations involved are illustrated for nickel impurity in copper anodes.

INTRODUCTION

Since publication of a previous communication [1] on material balance in electrowinning, the author has received a number of inquiries relative to (a) the applicability of the formulism to the case of electrowinning cells with separators and (b) the feasibility of precisely treating material balance in electrorefining. The answer to both questions is affirmative. Of course, in the case of electrowinning in divided cells, there is a larger number of solution compositions and volumes to be taken into account. For example, in conventional nickel electrowinning from sulfate electrolyte, a minimum of four solutions must be included in the material inventory, viz., influent electrolyte, catholyte, anolyte, and cell effluent. In electrorefining, anode composition and current efficiency dominate the material balance considerations, and an approach and frame of reference that differ from those appropriate to electrowinning are warranted. Accordingly, electrorefining and divided-cell electrowinning are treated separately below.

ELECTROWINNING WITH DIAPHRAGM CELLS

As stated above, the same conceptual framework pertains for electrowinning in cells with internal separators, or diaphragms, as for the previously illustrated case of electrowinning in diaphragm-less cells. Thus, a "volume efficiency", V.E. (%), may be defined (eqn. (1)) in terms of the mass w of metal deposited, the volumes V' and V'' of influent and effluent electrolyte, and the respective concentrations c' and c'' of the metal being electrowon:

$$w = V'c' - V''c'' - \delta w \equiv V' (c' - \text{V.E.}c''/100) \qquad (1)$$

Note that most prior formulations of material balance in electrowinning (e.g., ref. [2]) take V' and V'' to be sensibly equal and also omit consideration of a weight decrement, δw, which includes the resultant of errors in the measurement of volume and concentration as well as metal value actually lost from the electrowinning circuit. The previous communication lists a number of factors that contribute to volume change and metal loss in electrowinning.

There are other and possibly more convenient ways of defining a volume efficiency in electrowinning, but this possibility has not been fully explored. As defined above, V.E. is given by

$$\text{V.E.} = 100\left(\frac{V''}{V'} + \frac{\delta w}{V'c''}\right) \cong 100\left(\frac{V''}{V'} + \frac{\delta w}{V''c''}\right) \qquad (2)$$

i.e., by the ratio of effluent to influent electrolyte volumes plus the ratio of apparent metal loss (or gain) to metal contained in the effluent electrolyte (approximately). In electrowinning cells with separators, the estimation of δw requires a knowledge of any changes in volume as well as in concentration of the distinguishable cell solutions. A method of V.E., C.E. analysis will now be illustrated for the case of conventional nickel electrowinning from sulfate electrolyte, following approximately the Outokumpu conditions [3,4].

In a four-day nickel electrowinning campaign, analyzed cell feed was transferred daily to a holding tank, from which it was metered into the cathode compartment. The partially nickel-depleted electrolyte flowed out under a small hydrostatic head through a permeable separator (cathode bag) into the anode compartment and exited the cell via an overflow. The weight of nickel deposited was 17.46 kg, as obtained by quantitative analysis of the weighed deposits, i.e., this figure does not include the small amounts of co-deposited metals and oxide oxygen.

Pertinent items of electrolyte inventory are presented in Tables 1 and 2. The net volume change was 847.4-862.5 l = -15.1 l, or -1.8%. The volume of catholyte displaced by the nickel deposit, namely, 17.46 kg ÷ 8.90 kg/l = 1.96 l is a correction to the apparent decrease of combined catholyte + anolyte volumes: 195.8 l (end)-204.5 l (start) + 1.96 l (displaced) = -6.8 l.

TABLE 1

Nickel electrowinning, material balance: inputs to system*

Electrolyte	Weight (kg)	Density (kg/l)	Volume (l)	Ni (g/l)	Ni (kg)	H_2SO_4 (g/l)	H_2SO_4 (kg)
Initial holding tank contents			73.7	73.78	5.43_6	pH 2.86	—
Initial catholyte	43.1_8	1.2303	35.1_0	50.22	1.76_3	pH 3.48	—
Initial anolyte	209.4_7	1.2365	169.4_1	50.76	8.59_9	38.15	6.46_3
1st day cell feed	204.3_9	1.2780	159.9_3	76.00	12.15_5	pH 3.00	—
2nd day cell feed	186.5_2	1.2879	144.8_2	79.89	11.57_0	pH 2.63	—
3rd day cell feed	177.3_1	1.2862	137.8_6	78.77	10.85_9	pH 2.80	—
4th day cell feed	182.1_7	1.2851	141.7_2	78.40	11.11_1	pH 2.71	—
Totals			862.5_3		61.49_3		6.46_3

* Numbers shown as subscript are not significant; precision of liquid weight measurements ca. 0.05 kg, repeatability of nickel analyses ca. 0.1 g/l.

TABLE 2

Nickel electrowinning, material balance: outputs from system*

Electrolyte	Weight (kg)	Density (kg/l)	Volume (l)	Ni (g/l)	Ni (kg)	H_2SO_4 (g/l)	H_2SO_4 (kg)
1st day cell effluent	207.9_3	1.2373	168.0_5	50.69	8.51_9	45.04	7.56_9
2nd day cell effluent	175.8_1	1.2388	141.9_3	51.09	7.25_1	47.69	6.76_8
3rd day cell effluent	166.0_6	1.2388	134.0_5	50.75	6.80_3	50.06	6.71_0
4th day cell effluent	199.7_6	1.2394	161.1_7	50.08	8.07_2	51.79	8.34_7
Final anolyte	154.0_0	1.2410	124.0_9	50.01	6.20_6	48.60	6.03_1
Final catholyte	88.6_3	1.2365	71.6_8	51.35	3.68_1	pH 2.54	—
Final holding tank contents			46.4	78.35	3.63_3	pH 2.88	—
Totals			847.3_7		44.16_6		35.42_6

* Numbers shown as subscripts are not significant; precision of liquid weight measurements ca. 0.05 kg, repeatability of nickel analyses ca. 0.1 g/l.

Part of this measured decrease in volume of cell liquids is ascribable to inability to effect quantitative withdrawal of anolyte and catholyte from the cell, and part may be due to changes in electrolyte levels. For prolonged electrowinning campaigns, these factors would exert diminished influence on overall solution inventory. However, there would still remain those contributions to a change in electrolyte volume such as evaporation, misting, etc., as enumerated in the previous paper [1].

Nickel recovery was nearly quantitative: 17.46 kg (deposited) + 44.17 kg (effluent)-61.49 kg (feed) = + 0.14 kg. The measured apparent gain in the quantity of nickel illustrates the point that the weight decrement (in this case, δw = -0.14 kg) includes errors in the determination of volumes and concentrations. It is, therefore, an operationally significant quantity. An average effective volume efficiency can now be calculated according to eqn. (2):

$$\text{V.E.} = \frac{100}{862.5\ \text{l}}\left(847.4\ \text{l} - \frac{-140\ \text{g}}{50\ \text{g/l (approx.)}}\right) = 98.6\%$$

It is interesting and significant that, for lack of prior knowledge of V.E., the electrowinning of this example was conducted on the basis of an apparent volume efficiency of 100%. In order finally to arrive at the target nickel concentration of 50 g/l in the cell effluent (Table 2) by daily adjustment of the cell current, assumed values of cathode current efficiency were assigned as follows (successive days): C.E. (assumed) = 97.5, 97.5, 94.5, 93%. By comparison, the actual overall current efficiency of nickel deposition was 96.1%. Clearly, without accounting for $V' \neq V$ and $\delta w \neq 0$, an exact correlation will not generally be obtained between C.E. and $-\Delta c$.

It may be of interest to consider briefly the efficiency of the simultaneous anodic generation of acid, since erroneous interpretations are sometimes given to a measured deviation of $-\Delta c(\text{acid})/\Delta c(\text{metal})$ from the stoichiometric value. In the example cited, the values of $[H_2SO_4]/[Ni^{2+}]$ on successive days were (Tables 1 and 2): 1.780, 1.656, 1.787, 1.829, as compared with the stoichiometric ratio 1.670. These results suggest that, on average, the current efficiency of anodic acid generation was appreciably greater than the current efficiency of cathodic nickel deposition, i.e., greater than 96.1%.

In actual fact, anodic current efficiency was slightly less. Thus, total H_2SO_4 generation was 35.43-6.46 = 28.96 kg, yielding a real anodic current efficiency of 95.4%. As described in the previous paper [1], the same considerations relative to inclusion of volume changes and extraneous losses apply to the principal anodic reaction as to the principal cathodic reaction.

ELECTROREFINING (SOLUBLE ANODES)

The considerations presented in this section were developed largely in conjunction with a previously reported [5]experimental study of copper

electrorefining. The formulism is sufficiently general, however, that it doubtless has applicability to the electrorefining of impure metallic anodes rather broadly. The approach is to evaluate the resultant of the processes occurring at the anode and the cathode, the ratio of anode to cathode weight changes being a particularly significant characteristic.

Ratio of anode to cathode weight changes

It is assumed by reference to Fig.1 that the effect of cathode-anode shorting and stray current is to decrease the real electrorefining current, fI, where I is the total current, without affecting the ratio of anode weight loss to cathode weight gain. If the "chemical" corrosion rate of the cathodes is denoted as r_c (in compatible units), then,

$$\text{cathodic current efficiency (fractional), c.e.} = (fI - r_c)/I \qquad (3)$$

An appreciable magnitude for r_c is usually the result of dissolved oxidants in the electrolyte. However, depending upon whether c.e. is evaluated on the basis of weight gain only or weight plus assay, the concept for r_c may require modification to reflect the actual assay value.

The principal mechanisms of extraneous, i.e., superequivalent, weight loss of anodes are taken to be oxide dissolution, disintegration with the formation of finely divided elemental metal and insoluble compounds, and "chemical" corrosion. It is assumed that the sum of the first two effects is a simple function of the current and that the rate of weight loss due to chemical corrosion

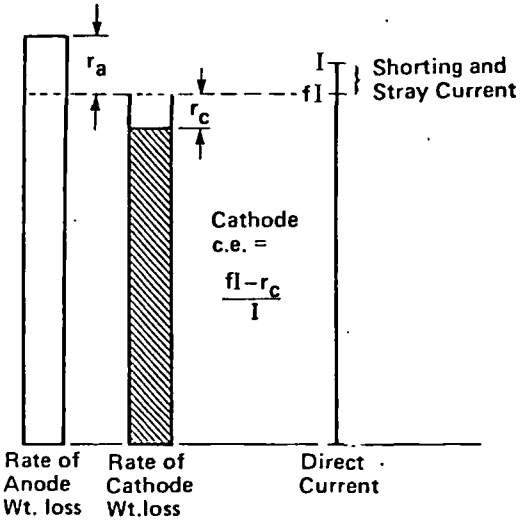

Fig.1. Graphic illustration of rates of cathode and anode weight losses in electrorefining.

of the anodes is proportional to the corresponding rate for the cathodes. The net rate of extraneous anode weight loss r_a is, then (see Fig. 2),

$$r_a = \alpha f I + \beta r_c \tag{4}$$

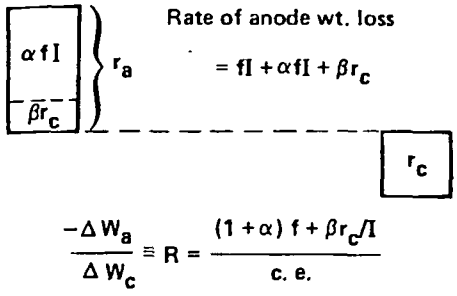

Fig.2., Detail of Fig. 1, illustrating the components of r_a, the rate of extraneous weight loss of electrorefining anodes.

If the anodic current efficiency is defined in the usual way, it may be written

$$\text{anodic ``current efficiency'' (fractional)} = \frac{fI + r_a}{I} = \frac{fI + \alpha fI + \beta r_c}{I} \tag{5}$$

The ratio, R, of the total anode weight loss to total deposit weight is substantially the same as the ratio of current efficiencies given by eqns. (3) and (5), namely,

$$\frac{-\Delta W_a}{\Delta W_c} \equiv R = \frac{fI + r_a}{fI - r_c} = \frac{(1 + \alpha)f + \beta r_c/I}{\text{c.e.}} \tag{6}$$

Consider, for example, the laboratory data plotted in Fig. 3. If f is taken to be unity (i.e., no shorting and negligible stray current) and if the current I is taken to be numerically equal to the current density (i.e., calculated on the basis of 1 ft^2 of cathode area) and if $\beta r_c = r_c$ (i.e., equal chemical corrosion rates of anodes and cathodes), Table 3 is then constructed based on r_c = 2 ASF and two assumed values of α.

The α = 0.01 column of calculated values of R was used to plot the heavier curve of Fig.3. Better agreement with the experimental data is thereby obtained than by use of α = 0.02 (lighter curve). However, an equally good fit could presumably be obtained using other sets of reasonable, assumed values of α and β; furthermore, these quantities probably vary to some degree with current density. The purpose of this illustration is mainly to systematize consideration of electrode weight changes.

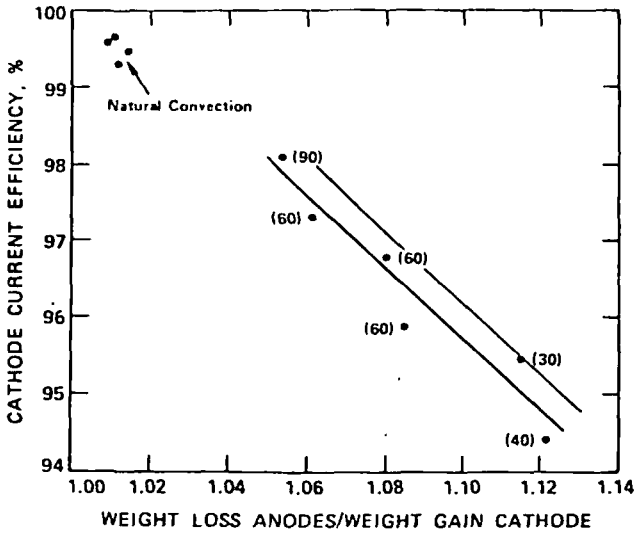

Fig.3. Anode and cathode efficiencies for air-agitation electrorefining in a small laboratory cell.

TABLE 3

Numerical example of material balance in copper electrorefining under air agitation

I (ASF)	C.E. (%)	R (kg/kg)	
		$\alpha = 0.02$	$\alpha = 0.01$
30	93.3	1.164	1.154
40	95.0	1.126	1.116
50	96.0	1.104	1.094
60	96.7	1.090	1.079
70	97.1	1.079	1.069
80	97.5	1.072	1.062
90	97.8	1.066	1.055

Assumptions: $f = \beta = 1$, $r_c = 2$ ASF.

As a hypothetical example of commercial copper electrorefining at 20 ASF, take $\alpha = 0.01$, as before, and $f = 0.90$ (i.e., 10% of the current shunted through shorts or stray paths), $r_c = 0.1$ ASF (i.e., 1/20th the cathode corrosion rate assumed above for air-agitation electrorefining), $\beta = 0.1$ (i.e., reduced chemical corrosion rate of anodes due to protective coating of anode slimes), then C.E. = 89.5% and $R = 1.016$, both being reasonable values [6].

Impurity build-up and electrolyte inventory

Whereas the rate of removal of major metal from solution by the cathodic reaction is equal to the rate of deposition, $fI - r_c$, the rate of addition of

major metal to the solution is, of course, less than the corrosion rate, $fI + r_a$, of the impure anodes. Specifically, if $y < 1$ is the "soluble" major metal assay of the anodes (Fig. 4), the net rate of addition of major metal to the solution, in units of weight per unit time, is

$$y(fI + r_a) - (fI - r_c) \approx -(1 - y)fI + (r_a + r_c) \tag{7}$$

to first-order terms. The case of anode-derived impurities that precipitate out of the electrolyte has been treated recently [7]. The electrochemistry of conventional copper anodes is such that $y(1 + \alpha) \geqslant 1$, so that even for negligible chemical corrosion, there is a net addition of copper to the electrolyte.

A comparison of the rates of build-up of soluble impurities with that of the major metal is of particular interest. Let the assay of a specific "soluble" impurity (i.e., that portion thereof not reporting to the anode slimes or incorporated in the cathodes) in the anodes be z (Fig. 4). Then the rate of addition of that impurity to the electrolyte is $z(fI + r_a)$. It is recognized that individual anodes may be grossly nonuniform with respect to the distribution and, even, mineral form of the contained impurities. It is clear, therefore, that the assay value z is the average for the entire batch of anodes to be refined in the electrolyte being monitored.

Material balance gives the manner in which the ratios of matrix metal to impurities in the electrolyte change with time. Taking as example the electrorefining of copper anodes, with no bleed-off, the total amounts of copper and nickel in the electrolyte are

$$V[\mathrm{Cu}] = V_o[\mathrm{Cu}]_o + [y(fI + r_a) - (fI - r_c]t \tag{8}$$

$$V[\mathrm{Ni}] = V_o[\mathrm{Ni}]_o + z(fI + r_a)t \tag{9}$$

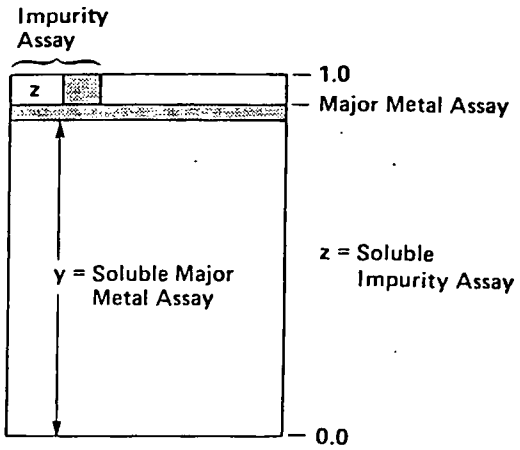

Fig.4. Anode composition showing weight fractions of the major metal and one of several impurities.

where V_o, $[Cu]_o$ and $[Ni]_o$ are the volume and concentrations at some initial time, $t = 0$. The ratio [Cu]/[Ni] will increase or decrease, respectively, depending upon whether

$$\frac{yR - 1}{zR} > \text{or} < \frac{[Cu]_o}{[Ni]_o} \tag{10}$$

That is, if no other factors are operating, the ratio of major metal concentration to soluble impurity concentration tends toward the value $(yR-1)/zR$.

In the previously-reported electrorefining pilot plant operation [5], $[Cu]_o/[Ni]_o$ was about 20 at the start, but the superequivalent solubilization of copper caused the ratio of copper to nickel to increase with time. By way of illustration, if the soluble copper and nickel assays were 98% ($y = 0.98$) and 0.1% ($z = 0.001$) and the ratio of anode weight loss to cathode weight gain were 1.06, [Cu]/[Ni] would tend toward the limiting value 30.8. Electrolyte bleed-off would then not be regulated by nickel build-up but by copper build-up. On the other hand, if for the same anodes in normal practice, y and R were 0.985 and 1.02, the ratio of copper to nickel in the electrolyte would tend toward the much lower limit, 4.65, and nickel would become a major component of the electrolyte. Some measure of indirect control of electrolyte composition in electrorefining is inherent in these considerations.

ACKNOWLEDGEMENT

The contents of this paper were summarized at the 108th AIME Annual Meeting in New Orleans, February 18—22, 1979. The contribution of N.J. Gelowtsky in developing the meeting talk outline into a manuscript for publication is gratefully acknowledged.

REFERENCES

1 W.W. Harvey, Material balance and current efficiency in electrowinning, Hydrometallurgy, 2 (1976) 35—50.
2 Anonymous, Controlling flow rate — an essential in SX-EW plants, Min. Eng., 30 (2) (1978) 154—155.
3 T. Toivanen and P.O. Grönqvist, Nickel refining in Finland, CIM Bull. 57 (1964) 653—658.,
4 J.R. Boldt, Jr. and P. Queneau, The Winning of Nickel, Van Nostrand, Princeton, N.J., 1967, pp. 370—374.
5 W.W. Harvey, M.R. Randlett and K.I. Bangerskis, Exploratory development of air-agitation copper electrorefining, J. Met., 30 (7) (1978) 32—41.
6 C.W. Eichrodt and J.H. Schloen, in A. Butts (ed.), Copper, Reinhold, New York, 1954, pp. 165—222.
7 T.B. Braun, J.R. Rawling and K.J. Richards, Factors affecting the quality of electrorefined cathode copper, in Extractive Metallurgy of Copper, The Metallurgical Society of AIME, New York, 1976, pp. 513—524.

UNIVERSITY OF UTAH
RESEARCH INSTITUTE
EARTH SCIENCE LAB.

Soo. Mining Sci. v10, N1, 1974

MECHANISM OF BACTERIAL LEACHING OF ARSENOPYRITE

V. G. Kulebakin, V. S. Meshkova,
V. K. Razlovskaya, and O. F. Purvinskii

UDC 699.8

SUBJ
MNG
MBLA

Progress in the leaching of sulfide minerals by sulfur bacteria Thiobacillus ferrooxidans (Th. f.) has led in recent years to their industrial use in the hydrometallurgy of copper and uranium and to their more extensive use for sulfide products containing gold, tin, nickel, cobalt, molybdenum, and rare elements. The conversion of ferrous metallurgical plants to processing of raw material with a high content of arsenic, compounds of which contaminate water and air, makes it necessary to find ways of extracting this element from arsenic-containing products, eliminating or reducing to a minimum its toxic effect on the surroundings. A knowledge of the chemistry of bacterial leaching of arsenic from such material might accelerate the development of an economically efficient procedure for extracting metals by means of Th. f. [1], and its commercial application.

Arsenopyrite (FeAsS), the form in which arsenic is present in ore materials, is extensively broken down by sulfur bacteria [2-5]. However, the break-down mechanism is still far from clear. According to colleagues of VNII-1, during leaching of FeAsS part of the sulfur is incorporated in the solid phase in elementary form, and the other part goes into solution after oxidation to sulfate ions [5]. As regards iron and arsenic, during bacterial decomposition they are distributed between the liquid and solid phases in a specific ratio [6]. Arsenic is deposited as insoluble iron arsenates, formed by ions of arsenic and trivalent iron. The scheme of bacterial and chemical leaching of arsenopyrite may be represented as follows:

1) $2FeAsS + 6^1/_2O_2 + 3H_2O \rightarrow 2H_3AsO_4 + 2FeSO_4$ (*Th. f.*);
2) $2FeSO_4 + H_2SO_4 + {}^1/_2O_2 \rightarrow Fe_2(SO_4)_3 + H_2O$ (*Th. f.*);
3) $Fe_2(SO_4)_3 + FeAsS \rightarrow FeAsO_4 + 2S$ (chem);
4) $2H_3AsO_4 + Fe_2(SO_4)_3 \rightarrow 2FeAsO_4 + 3H_2SO_4$ (chem);
5) $2H_3AsO_4 + 3FeSO_4 \rightarrow Fe_3(AsO_4)_2 + 3H_2SO_4$ (chem);
6) $Fe_2(SO_4)_3 + 6H_2O \rightleftharpoons Fe(OH)_3 + 3H_2SO_4$;
7) $FeAsO_4 + 3H_2O \rightleftharpoons H_3AsO_4 + Fe(OH)_3$.

It will be seen from these equations that the oxidation products of FeAsS (reaction 1) are arsenic acid H_3AsO_4 and ferrous sulfate $FeSO_4$, which is oxidized by the bacteria (reaction 2) to ferric sulfate $Fe_2(SO_4)_3$. Oxidation then takes place chemically – the $Fe_2(SO_4)_3$ regenerated by the bacteria reacts with FeAsS. Reaction in the solution between ferrous and ferric ions and H_3AsO_4 anions leads to formation of iron arsenates (reaction 4), deposited as a sediment; these undergo hydrolysis after treatment with 0.2 N hydrochloric acid (reaction 7). Thus Th. f. is involved both in direct oxidation of FeAsS and in the formation of $Fe_2(SO_4)_3$ by oxidation of the ferrous iron in arsenopyrite [6, 7].

Our aim was to study the pattern of change in the structure and composition of arsenopyrite during bacterial leaching. It was also of interest to establish the character of the crystalline system of elementary sulfur as one of the end products of bacterial decomposition of the mineral. Arsenopyrite belongs to the monoclinic system.

The sample investigated had an arsenopyrite content of 89%; the other components were sphalerite, pyrrhotite, oxidized minerals of iron and arsenic, and a few quartz grains were also present. The particle size was 0.074 mm

Institute of Soil Science and Agrochemistry, Siberian Branch, Academy of Sciences of the USSR. TsNIIolov Novosibirsk. Translated from Fiziko-Tekhnicheskie Problemy Razrabotki Poleznykh Iskopaemykh, No. 1, pp. 81-January-February, 1974. Original article submitted October 1, 1973.

© 1974 Consultants Bureau, a division of Plenum Publishing Corporation, 227 West 17th Street, New York, N. Y. 10011. No part of this publication may be reproduced, stored in a retrieval system, or transmitted, in any form or by any means, electronic, mechanical, photocopying, microfilming, recording or otherwise, without written permission of the publisher. A copy of this article is available from the publisher for $ 15.00.

TABLE 1. Results of Bacterial Leaching of Arsenic from Arsenopyrite

Sample characteristics	Content, %					
	oxidized minerals			simple sulfides and native sulfur	arsenopyrite	total
	As_{tot}	As^{3+}	As^{5+}			
Initial	0,50	0,25	0,25	0,41	40,00	40,91
After control treatment	0,72	0,25	0,47	0,15	40,36	41,23
After bacterial treatment	18,15	14,84	3,31	0,40	4,92	23,47

TABLE 2. Results of Bacterial Leaching of Iron from Arsenopyrite

Sample characteristics	Content, %		
	oxidized minerals, pyrrhotite	arsenopyrite and other complex minerals	total
Initial	0,97	31,04	32,01
After control treatment	0,97	31,12	32,09
After bacterial treatment	19,66	3,58	23,24

TABLE 3. Results of Bacterial Leaching of Sulfur from Arsenopyrite

Sample characteristics	Content, %			
	oxidzd. minerals	arsenopyrite and other minerals	elementary	total
Initial	0,09	19,75	—	19,84
After control treatment	0,09	19,87	—	19,96
After bacterial treatment	3,33	2,06	17,15	22,54

Before the investigation the samples with arsenopyrite were treated with ethyl alcohol to inactivate the natural bacteria. The experiments with FeAsS were performed on 2-g samples in Erlenmeyer flasks with continuous agitation at a frequency of 220 vibrations per minute at 27°C in a dark thermostated room for 12 days. The S:L ratio of the pulp was 1:50, the pH was 2.5. The initial bacterial concentration was 10^6 ce/ml (cells/ml). At the end of the experiments the contents of the flasks were filtered in vacuum, and the solid residues were treated in the same flasks in a shaker for 2 h with 0.2 N HCl to dissolve the precipitated iron arsenates. The filtrates and the solid residues were then analyzed to determine the changes in FeAsS during bacterial and chemical leaching.

The laboratory strain of Th. f. was grown in mineral nutrient medium 9K of the following composition: 0.1 g potassium chloride, 0.5 g monosubstituted potassium phosphate, 0.01 g calcium nitrate, 0.01 g magnesium sulfate, and 700 ml of distilled water. We then dissolved 63 g of Mohr's salt in 300 ml of distilled water acidified with 1.5 ml of 10 N sulfuric acid. After mixing the solutions the pH was 2.5. For the experiments we used 9K without Mohr's salt inocculated with a Th. f. culture (10 vol.%). In consequence, the bacteria could use only arsenopyrite as an energy source.

Results. Chemical analysis showed that when arsenopyrite was leached the arsenic concentration in the bacterial solution at the end of the experiment was 56.8%, and in the control solution 5.3%. The Th. f. concentration increased from the initial value of 10^6 to 10^5 ce/ml. The initial arsenopyrite sample and the solid residues after chemical and bacterial leaching were subjected to chemical phase analysis for the arsenic, sulfur, and iron contents [8] (Table 1).

It will be seen from Table 1 that the greatest change was exhibited by the solid residue of arsenopyrite after bacterial treatment. Of its total arsenic content, the As(III) content represented 81.8% and the As(V) content 18.2%. The incomplete disintegration of the mineral (the unleached material was 4.92%) is probably due to the inadequate length of the experiment. The arsenic content of the solid residue of arsenopyrite after chemical treatment was almost the same as that of the initial sample.

As we see from Table 2, the iron of arsenopyrite was converted to oxidized forms. This can be seen from its excess content when the balance with respect to sulfur and arsenic in the oxidized forms is calculated (see Tables 1-3). This is confirmed by the chemical analysis data for arsenic, sulfur, and iron, and by stoichiometric calculations from them.

Most of the sulfur in the solid residue after bacterial leaching of arsenopyrite (76%) was present in elementary form; a smaller amount (14.8%) was oxidized to the sulfate ion (Table 3).

TABLE 4. Interpretation of X-Ray Diffraction Patterns of Initial Sample of Arsenopyrite and Sample after Chemical and Bacterial Treatment

Line No.	Experimental data obtained from arsenopyrite samples				Literature data [9]			
	initial		after control treatment		after bacterial treatment		arsenopyrite	sulfur
	I, d/n		I, d/n		I, d/n		I, d/n	I, d/n
1								3 5,8
2					5 3,87			10 3,85
3	1	3,67	1	3,67			3 3,669	
4					2 b	3,47		5 3,45
5					10	3,22		7 3,21
6					3	3,12		6 3,10
7	2	2,94	2	2,94	2b	2,93	3 2,933	
8					1	2,85		6 2,85
9	2	2,85	2	2,85			3 2,843	
10							1 2,783	
11	10	2,67	10	2,68	7	2,68	10 2,662	
12								
13	1	2,56	2	2,56			2 2,559	4 2,63
14								4 2,50
15	10 b	2,44	10 b	2,44	5	2,44	9 2,443	
16								4 2,43
17							9 2,412	
18								3 2,39
19								3 2,30
20	2	2,20	2	2,19			5 2,206	
21								6 2,12
22	2	2,10	2	2,10			4 2,078	
23	2	2,01	2	2,00			5 2,001	1 2,00
24	3	1,945	2	1,945			6 1,943	
25					2	1,90		6 1,90
26								4 1,83
27	9	1,815	9	1,815			10 1,817	
28								6 1,78
29	2	1,753	3	1,761			7 1,758	
30					2	1,73		5 1,73
31							5 1,698	
32	3	1,630	7	1,630			8 1,629	
33	2	1,605	2	1,604			7 1,594	

Notation: I)line intensity, d/n)interplanar spacing in kX, b)broad line.

The initial sample, represented by arsenopyrite, and the solid residues obtained after control and bacteri experiments were subjected to x-ray phase analysis * (Debye method), the results of which are given in Table

A comparison of the interpretation of the x-ray diffraction patterns with the literature data (see Table 4) revealed that the solid residue underwent no structural changes after the control experiment. The x-ray diffrac pattern obtained from the solid residue after bacterial leaching exhibited the strongest characteristic lines of a pyrite. The other lines are probably due to the presence of orthorhombic elementary sulfur in the sample. Cry line compounds of arsenic and iron were not observed. It is likely that some of the material containing sulfur a arsenic was amorphous to x rays. No diffraction lines corresponding to any compounds of arsenic or iron were observed.

To refine the data of x-ray structural phase analysis and to study the processes taking place on the miner surface, the same samples were subjected to electron-diffraction analysis in an ÉG-100-A electron-diffraction camera.

Our interpretation of the electron-diffraction pattern of the initial sample confirmed that it contained onl arsenopyrite. The electron-diffraction pattern of the arsenopyrite sample after bacterial treatment exhibited we diffraction rings. It may be assumed that the orthorhombic sulfur was covered by very fine particles of arsenopy The dispersity of these particles is confirmed by the diffuseness of the diffraction rings.

*Recording conditions: RKD camera, Fe anticathode, U 30 kV, I 9mA, no filter.

TABLE 5. Interpretation of the Second Electron-Diffraction Pattern of Arsenopyrite after Control Treatment

Serial no.	Experimental data			Literature data [9]			
				scorodite		arsenopyrite	
	2r	d	I	d	I	d	I
1	17,0	4,62	w	4,44	10	—	—
2	19,2	4,08	w	4,06	5	—	—
3	21,5	3,65	m	—	—	3,669	3
4	23,0	3,56	w	3,50	5	—	—
5	26,8	2,93	v.w	2,98	6	2,993	3
6	29,5	2,66	w	2,67	5	2,662	10
7	39,0	2,01	v.w	2,00	5	2,001	5
8	40,5	1,94	v.w	—	—	1,943	6
9	43,2	1,805	v.w	1,797	—	1,817	10
10	45,8	1,71	v.w	—	—	1,758	7

Notation: d) periods in Å, I) line intensity, 2r) diameter of diffraction ring.

From the sample of mineral treated with 9K we obtained two completely different electron-diffraction patterns. The interpretation of the first one confirmed the presence of arsenopyrite in the surface layer of the sample. However, the first ring was very diffuse (it encompasses the first three to four structural rings of arsenopyrite), which indicates decomposition of the arsenopyrite structure.

According to our interpretation of the second electron-diffraction pattern (Table 5), a new structure, namely scorodite, was formed on the sample surface. However, recrystallization was not complete, as shown by the fact that strong lines of arsenopyrite were still present.

Thus the results of the investigations showed that on the surface of the arsenopyrite sample after control treatment a scorodite structure was formed, and after bacterial treatment orthorhombic elementary sulfur was formed. The As(III) and As(V) proportions of the total arsenic content in the solid residue were respectively 81.8% and 18.2%. The iron in arsenopyrite is converted to oxidized forms during bacterial leaching.

LITERATURE CITED

1. S. I. Pol'kin, G. I. Karavaiko, V. D. Dyatlov, and V. V. Panin, in: Physics of Rocks and Processes, Summaries of Conf. Reports [in Russian], Moscow (1971).
2. H. L. Ehrlich, Economic Geology, 59, 1306-1312 (1964).
3. D. W. Duncan, Canad. Mining and Metallurg. Bull., No. 653, 1070-1079 (1966).
4. N. N. Lyalikova, Oxidation of Sulfides by a Thiobacillus ferrooxidans. Biology of Autotrophic Microorganisms [in Russian], Izd. MGU (1966), pp. 211-216.
5. N. B. Korostyshevskii, G. P. Arkhipova, and I. A. Kogan, in: Tr. VNII-1, 26, Magadan (1967).
6. G. I. Karavaiko, S. I. Kuznetsov, and A. I. Golomzik, The Role of Microorganisms in the Leaching of Metals from Ores [in Russian], Nauka, Moscow (1972).
7. Z. A. Tauzhnyanskaya, "Study of the kinetics, conditions, and mechanism of bacterial leaching of arsenic in tin–copper–arsenic concentrates," Author's Abstract of Candidate's Dissertation [in Russian], Moscow (1970).
8. N. A. Filippova, Phase Analysis of Ores [in Russian], Moscow (1963).
9. V. I. Mikheev, X-Ray Determinative Table for Minerals [in Russian], Gosgeoltekhizdat, Moscow (1957).

SUBJ
MNG
MCIS

MINING COPPER IN SITU

By
D. L. MYERS, '41
Golden, Colorado

UNIVERSITY OF UTAH
RESEARCH INSTITUTE
EARTH SCIENCE LAB.

Introduction

This paper presents an old method in the light of new progress, recent research, and economic adjustments. The author does not lay claim to any new discovery. He has attempted to present all the pertinent facts relative to the consideration of an effort to produce a mine from a copper deposit by the adoption of a particular mining method.

Geologists have long noted that in abandoned copper mines the decomposition of the ore may take place indefinitely producing cupriferous water. The decomposition of iron sulphides, usually associated with copper ores, produces weak sulphuric acid and soluble ferric sulphate. Both these products are capable of dissolving various copper minerals. Attempts to imitate this natural process have been made on several continents. The deposit may be developed as in the exploration of a mine, the workings all leading to a centralized point for solution collection. After the copper is removed from the collected solution the water may be recirculated over the ore body, or, it may be simply discarded.

The science and chemistry of the method has been developed by years of experience with surface leaching plants. This long experience has added much to the literature of the process which treats profusely on the relative merits of various procedures, reagents, and operations. In this paper those particulars are presented about the methods that have come to stand highest in the estimation of the experts and practitioners.

The author expects to find disagreement among his readers. He hopes, however, to influence one reader who will carefully consider the method in conjunction with some known deposit of copper, and who may therefrom develop a copper mine.

If any part of this paper suggests a solution to the problem it will have served its purpose.

The Selection of a Stoping Method

There are many important details which must be taken into consideration when choosing a particular mining method. These details are concerned with the structural geology of the mine being considered and can be arranged under two headings.[1]

1. The character of the deposit. This includes the size, shape, dip, wall conditions, extent and consistency of the ore.
2. The character of the ore. This is the value per ton, percent extraction required for a profit, fire hazard, and the metallurgical requirements for winning the metals.

The method selected must embody the principles of SAFETY, EFFICIENCY, and ECONOMY. Safety of the men is paramount. If the method is not safe it must be ruled out at once. Efficiency comprises flexibility of output, good working conditions for the men, and the elimination of wasted efforts. Economy calls for a reasonable outlay for the original development work. It demands the lowest cost per ton mined consistent with good business principles. Fixed costs should be carefully weighed before they are established. They do not decrease when production falls off.

Labor has established itself in the past few years as a dominant item to be reckoned in any endeavor. A mining method today must be considered in the light of what injury labor may do to it. Mining methods using the forces of gravity will not wait for a labor dispute to be settled. The cost of rehabilitating a stope may exceed the worth of the ore recovered. The present wage-hour laws call for a method of mining whereby the work can be allocated and immethodically rotated among the men. Each job must be composed so that the swingman can quickly and efficiently assume the duties of the man who must lay off for the duration of the week.

The capital and time required to place a property on a paying basis should be considered. Quick development may be the aim of capital in order to realize on high, transitory, metal prices. This type of policy may require a mining method that would ultimately ruin the mine. Flexibility of output without a sacrifice of efficiency is an important point in any mining method. The goal of industry is stabilization, but supply and demand still governs in most cases. Therefore, a mining method should be flexible to meet the broad fluctuations peculiar to the marketing of metals and the idiosyncrasies of modern labor dictation.

Rock that is "non-commercial" one year may be commercial ore the next as a result of marked advance in mining and metallurgical processes. Due to the exhaustion of higher grade deposits, increasing demand for metal, and lower market values, low cost mining methods are imperative. Twenty years ago the mining of 0.7% copper ore at a profit would have been considered an impossibility. Today it is one of the world's biggest mining operation and profit maker.* This example indicates that within certain limitations tonnage is becoming increasingly more important than grade. Large scale operations, and the liberal expenditure of sufficient money at the start to insure the most economical operation, is the secret of many mining successes.[2]

The fact that a profit is being made by an enterprise does not signify that it is being managed and engineered to the best advantage. Mining methods showing a profit may be changed and consequently produce a much improved condition and a higher capital return. The same reasoning can be applied to properties showing a working loss. Methods are sometimes condemned when the fault, as a rule, is not with the method but in its wrong application. Each ore body is accompanied by a certain set of conditions which will influence the method of stoping to be adopted. Careful observation of these conditions and a knowledge of all the methods will enable a decision to be made as to the particular method which is most applicable under the existing circumstances.

The constantly decreasing grade of the deposits now being considered affords only a limited choice of mining methods. This calls for the application of engineering ability, experience, and initiative, in welding together one extremely low cost operation.

The ultimate object of mining is a profit and the method used is subordinate to this fact. Ingenuity, based on sound engineering principles, can do much towards the revivification of a method that may be able to produce a production success.

The Method

Mining "in situ," using a leach solution, is the application of a solvent to an ore body without disturbing the

[1] Mitke, C. A., "Mining Methods," p. 7, McGraw-Hill, 1930.

* Utah Copper Company, Bingham, Utah.

[2] C. A. Mitke, op. cit., page 8.

position of the ore body as it is found in the earth. The method is sometimes referred to as mining "in place." Leaching, as used here, is the dissolution of the valuable metal from its ore by means of a solvent.

Mining in situ does not entail the usual costs of developing and extracting ore from within the earth. There is no expense of breaking and moving rock for subsequent mill treatment. The ore is not crushed or ground in a mill. Consequently, there is no expense for the disposal of mill tailings. These expensive operating items are all eliminated when mining in situ.

In order that an ore may be treated by leaching it must have the following characteristics:[3]

1. The metals to be mined must be soluble in the solvent used.
2. The gangue minerals must be insoluble in the solvent.
3. The dissolved metal must be recoverable from the solution.

The method functions with relation to the porosity of an ore body as it is found within the earth. The solvent is placed above the ore body in solution form and then permitted to disperse downward, (acting under the laws of gravity), and is later collected as "pregnant solution" at drainage points underneath the ore body. This collected solution is then led to precipitation cells where the valuable metal is recovered as cement copper. The solution, now "barren," may then be discarded, or, it may be regenerated and made to repeat its cycle of flow through the ore body until all of the valuable mineral has been recovered. This, in brief, is the mechanics of mining in situ.

The capital required for the method can be summarized into the following items which will not be considered in detail:

1. Precipitation plant, usually relatively small.
2. Reagents for the dissolution and precipitation of copper.
3. Circulation of the solvent solution.
4. Regeneration of the spent solution.
5. Development work necessary to establish points for solution drainage and application.

The equipment necessary for a precipitation plant consists of series connected, water-tight cells that have receptacles for the precipitating agent. The size and number of these cells will depend upon the volume of solution being handled. Some installations have found it advantageous to provide for cell aeration during the formation of cement copper.[4] Suitable means for the ease of handling cement copper and native iron into and out of the cells should be provided as labor saving devices for this detail will materially reduce operating costs. Sufficient cells should be built so that stand-bys are available during periodic clean-ups of cement copper. It is desirable to install the precipitation plant at the point of solution recovery, possibly far underground. In this case there will be no expense for a building and attendant repairs, and there will not arise the problem of handling and transferring corrosive copper sulphate waters.

The reagents required for the dissolution of copper as a sulphate are sulphuric acid and, (if the ore requires it), ferric sulphate. The only reagent required for the precipitation of cement copper is native iron. Theoretically, the sulphuric acid and iron required to produce one pound of copper is 1.66 pounds of H_2SO_4 and 0.95 pounds of iron. At current market prices, (less freight), this is 2.651 cents per pound of copper produced.[5] Actual working conditions will change this cost figure with the possibility of one reagent compensating for the other. Water in a large amount is used. The water should not be basic because it would then increase consumption of sulphuric acid.

The solvent solution must be conducted to the upper regions of the ore body and to do so will usually require pumping. When a regenerated solution is used the solution will be pumped the entire height of the ore body being mined. The resulting pregnant solutions must be handled in other than ordinary iron pipe due to the corrosive action of copper sulphate on iron. A regenerated, (barren), solution should not be corrosive as the corrosive copper sulphate has been removed from it. Pumping costs, (for an example), at Cananea were 0.094 cents per pound of copper produced.[6]

If there is a limited quantity of water at the premises it will be necessary to re-use the barren solution as it comes away from the precipitation cells. This solution will be high in ferrous sulphate and may need to have its free acid strength increased. As the solution becomes stronger in ferrous sulphate, through re-use, there will be a tendency for the ferrous iron to form basic oxides of iron. These basic oxides will precipitate in a nearly neutral solution. If this precipitation should occur within the ore body it will clog up the natural solution channels in the ore particles and thus shut off the valuable mineral from the dissolving solution. It is therefore necessary to rid the barren solution of excess ferrous iron, increase the free acid strength, and when treating sulphide ores, to oxidize ferrous iron to ferric iron. In the presence of sulphuric acid and oxygen, ferrous sulphate can be oxidized to ferric sulphate.[7] This treatment of the barren solution is entitled "regeneration." At the higher valence the iron will not readily form basic salts, and it will materially aid in the formation of oxide copper. Another way to rid the solution of ferrous iron is to neutralize the solution and filter away the precipitated basic salts. This method, however, raises the cost of later acidifying the solvent solution. Ferrous iron is difficult and expensive to electrolyze out of solution.[8]

The development work required for any given ore body will naturally depend upon the geologic structural conditions. Access to the top of the ore may be at the surface. Under other circumstances lengthy tunnels may have to be driven to reach the point of solution application. Advantage can be taken of natural faults, bedding planes, and other geological type formations. It is essential that the solution carrying the dissolved copper be recovered with very little loss. To accomplish this the points of collection will need to be located at natural drainage channels. If natural agencies do not exist, then it will be necessary to establish artificial dams and cutoffs underneath the ore body before mining operations are begun. Good judgment and preliminary examination of structural conditions will do much to reduce the expense of developing the property for mining in situ.

In the case of mining "lost ore," stope fill, or ground that has been mined around due to its low grade, the original development work will usually be completed. It will be only necessary to set up the equipment and pipe lines for solution circulation. Under these circumstances some plants have been able to finance themselves solely from earnings and the junking of mills.[9]

Analysis of Possible Applications

Large disseminated copper zones are known where the preexistent deposits of copper have been attacked during the ages and generally carried away dissolved in the ground water.[10]

[3] Joseph Newton, "Introduction to Metallurgy," p. 267, Wiley & Sons, 1938.

[4] Lavender, H. L., Water Treatment & Underground Leaching at Bisbee, Mining Congress Journal, Sept. 1926, p. 663. Greenwood, C. C., Underground Leaching at Cananea, Engineering & Mining Jour.-Press, vol. 121, Mar. 1926, p. 518.

[5] Oil, Paint, & Drug Reporter, vol. 139, no. 1, Jan. 6, 1941.

[6] Greenwood, C. C., op. cit., p. 519.

[7] McBain, J. W., Oxidation of Ferrous Solutions by Free Oxygen, Jour. Phys. Chem., vol. 5, Dec. 1901, p. 622.

[8] Table of Standard Electrode Potentials.

[9] Anderson and Cameron, Recovery of Copper by Leaching at the Ohio Copper Co. of Utah: Trans. Am. Inst. Min. and Met. Eng., vol. 73, 1926, p. 3

[10] Clarke, F. W., Data of Geochemistry, U. S. Geol. Survey Bull. 770, 5th ed., 1924, p. 675.

Copper remaining in the leached zones, due to the mechanics of weathering, is found as some form of copper oxide. Copper carried away may sometimes be found at a lower depth re-precipitated as chalcocite, covellite, bornite, and other sulphides. An important thing to remember here is that these deposits are genetically related to penetrating solutions following preformed passages along cleavage planes, fractures, and fissures within the ore body. It is therefore contended that artificial solutions of predetermined strengths can be directed through these same passages for the purpose of removing the copper.

Low grade bodies of copper may become ore bodies provided they are of sufficient size, occur in a favorable position, and can meet the requirements of the method. The grade of the deposit is not confined to certain limits. The quantity, character, and extent of the deposit, together with the required development costs, plant outlay, operating costs and amortization will set the minimum tenor of the ore. Operating costs of actual operations have been as low as 3.84 cents per pound of copper produced.[11] Plant investments may be as low as $2500. One plant in mind was financed wholly from earnings.[11] These figures indicate a possible application of the method to copper deposits containing as little as 0.2% copper. Costs of the process are more fully covered in a later section.

Mining in situ with the use of a leach solution has two requirements. The method uses a very dilute acid solution to maintain low operating costs and thus the locality should have a copious water supply. The ore body must be susceptible to water penetration. Any mineralized copper deposit can be considered adaptable to the method if it can meet these two conditions.

The demand for water is not as heavy as first implied because the solution can be recovered, regenerated, and then recirculated. For any solution to produce a metal it must make a contact with and dissolve some form of the metal. Hence the material in question must be permeable to the solution and the valuable metal must be soluble in that solution. There are many modes of application and the usual occurrence of mineralized zones lend themselves to the method.

If a low grade deposit should contain copper that is quickly attacked by solution, the returns from the operation may be large within a comparatively short time. The oxide ores of copper are quickly soluble in weak acids and it is this type of deposit that is attractive to the method.[12] Sulphide ores of copper require a longer length of time for dissolution. See table I, for comparison. For this reason a much larger area of sulphide ore must be treated simultaneously to produce a yield commensurable with the investment.

Low grade deposits should lie in a position that will aid the work of gravity when applying and recovering the leach solution. Geological structural conditions should favor the application and control of solution as well as the chemistry of the method. These requirements may at first appear to be severe, but in actual instances they have been found to be present wherever ore bodies are present due to the inherent nature of ore deposition itself. The method, after all, is the reverse of nature's method of ore permeation. Where deposition has occurred, conditions for deposition must be present. These are the same conditions that should prevail for the leaching of ore in situ. As a rule the copper deposits do not lack suitable structural and physical features required by the method.

During the course of some mining adventures certain blocks of ore have been known to become "lost." By this term is meant ore that has come to lie in a relative position too dangerous to extract; ore that requires too much development work to recover; ore that has become contaminated with waste so that it is no longer ore when considered as a block. When such bodies of ore are of sufficient size, mining them in situ can be done at a profit.[13] [14] It is not too difficult to apply solutions to a section of ground that at the same time is too dangerous to place men within. If the ground in question is badly broken, hard to hold open, or running, it would be an expensive operation to safely place workmen and establish an extractive mining method in it. However, just such conditions are favorable for efficient solution distribution necessary for effecting metal recovery by mining in situ. Solution can be led to such blocks of ore by various means. Drill holes, subsidence cracks, and caved workings can all be utilized for mining in situ.

At some of the larger mines old stopes have been filled with mill refuse. These tailings are a possible source of copper metal. It would be easy to apply the method to these stope fillings if their copper content warranted the capital outlay. Installation

TABLE I

COMPARATIVE RATE OF DISSOLUTION OF VARIOUS COPPER MINERALS SIZED TO MINUS 100 PLUS 200 MESH; TEMPERATURE, 35° C.

Mineral	Time of Treatment	Solvents Used	Percent of Copper Dissolved
Azurite	1 hour	1% H_2SO_4	100
Malachite	1 hour	1% H_2SO_4	100
Tenorite	2 hours	1% H_2SO_4	98
Chrysocolla	1 hour	1% H_2SO_4	90
Chrysocolla	1 hour	2% H_2SO_4	98
Cuprite	1 hour	5% H_2SO_4	71
Cuprite*	12 hours	5% H_2SO_4	99
Cuprite	24 hours	5% H_2SO_4	100
Cuprite	1 hour	2% $Fe_2(SO_4)_3$ and 2% H_2SO_4	100
Chalcocite	1 hour	1% $Fe_2(SO_4)_3$ and 0.5% H_2SO_4	33
Chalcocite	1 hour	1% $Fe_2(SO_4)_3$ and 0.5% H_2SO_4	49
Chalcocite	8 days	1% $Fe_2(SO_4)_3$ and 0.5% H_2SO_4	90
Chalcocite	20 days	1% $Fe_2(SO_4)_3$ and 0.5% H_2SO_4	97
Bornite	1 hour	1% $Fe_2(SO_4)_3$ and 0.5% H_2SO_4	27
Bornite	7 days	1% $Fe_2(SO_4)_3$ and 0.5% H_2SO_4	69
Bornite	21 days	1% $Fe_2(SO_4)_3$ and 0.5% H_2SO_4	99
Covellite	1 day	1% $Fe_2(SO_4)_3$ and 0.5% H_2SO_4	8
Covellite	47 days	1% $Fe_2(SO_4)_3$ and 0.5% H_2SO_4	57
Chalcopyrite	43 days	1% $Fe_2(SO_4)_3$ and 1% H_2SO_4	2
Enargite	60 days	1% $Fe_2(SO_4)_3$ and 0.5% H_2SO_4	2
Tennantite	30 days	2% $Fe_2(SO_4)_3$ and 0.5% H_2SO_4	7
Tetrahedrite	23 days	1% $Fe_2(SO_4)_3$ and 0.5% H_2SO_4	95

* Impure samples dissolved at different speeds.

Taken from U. S. Bur. Mines Rept. Inv. No. 3228, p. 50.

[11] Anderson and Cameron, op. cit., p. 31.

[12] Sullivan, J. D., Dissolution of Various Oxidized Copper Minerals, U. S. Bur. Mines Rept. Inv. 2934, p. 9, 1929.

[13] Anderson and Cameron, op. cit., p. 30.

[14] Greenwood, C. F., op. cit., p. 519.

costs for such a venture would be low, and the copper reclaimed would represent higher extraction efficiency and a metal bonus. At some mines where the mine water is acidic, a plan may possibly be worked out whereby mill tailings would be placed into the old stopes chiefly for the purpose of further extraction of copper by circulating the acidic water through the tailings. However, the plan may need to be augmented or modified. If the ore had previously been subjected to an extractive process that placed deleterious material into the tailings then further treatment may be too costly for the method. Most copper ores are now treated by some form of flotation. A few organic reagents used in flotation will consume leaching reagents unduly. Their presence in the tailings would prohibit the installation of a stope fill leaching system.

The chemistry of the method is so simple, and the method so flexible, that copper, dissolved in solution, can be made to precipitate along a predetermined horizon provided that horizon contains the necessary precipitants. The characteristics of a particular deposit may prohibit the usual methods of exploitation. Certain lateral sections of the deposit, however, may be exploitable. Here, mining in situ can be applied, not to extract the metal, but to cause a secondary enrichment at the level of the lateral section to be mined. Descending solution will dissolve metal from gangue and reprecipitate it when contact is made with sulphides, with the water table, or when a saturated condition occurs within the solution.[15] It may therefore be possible to bring about an artificial condition of secondary enrichment, thus substantially raising the tenor of the ore that is already in line for the usual mining methods. Geologic conditions and engineering technique will determine the feasibility and efficiency of such an undertaking.

Infinitesimal reactions cannot be hurried along within the boundaries of an ore deposit, but when the reaction is extended over a large area the summation of each reaction will produce a daily product measurable in tons.

Solutions Applicable to the Method

The several known chemical processes used in copper leaching may be classified on the basis of the solvent employed. They are the following:[16]

1. Alkali Process.
2. Sulphite Method.
3. Sulphate Process.
4. Chloride Process.
5. Nitrate Methods.

[15] Emmons, W. H., Principles of Economic Geology, 2nd ed., p. 281, McGraw-Hill, 1940.
[16] Greenawalt, W. E., "Hydrometallurgy of Copper," p. 169, McGraw-Hill Book Co., 1912.

Campbell lists the following reagents: "In the order of their importance the chief solvent reagents used in copper leaching are: sulphuric acid, ammonia and ammonium carbonate, ferric sulphate, ferric chloride, sulphurous acid, chlorine, and nitric acid. Of these the first three are the most common today."[17]

Nitrate methods are frequently suggested as solvents of copper. The fixation of atmospheric nitrogen by electricity offers a cheap source of nitric acid, and nitric acid is the best known copper solvent. However, nitric acid is also an excellent solvent of almost all of the impurities found associated with copper. Their subsequent dissolution would present insurmountable difficulties in the clean precipitation of free copper and in the regeneration of the solvent. The applicability of any solvent for the extraction of copper depends on the character of the ore. All acids likely to be used in a solvent process can react with other elements in the ore, and when so consumed are unavailable for the work of dissolving the copper.

The elements most detrimental to copper leaching acid processes are these:[18] calcium, magnesium, aluminum, zinc and manganese. The quantity of these elements in the ore should be determined before installing a particular leaching method. It is important to remember, however, that a chemical analysis of the ore cannot be made the criteria upon which to determine the applicability of an acid process. Lime, for example, is detrimental only in certain combinations such as the oxide or carbonate. In many copper ores it will be found as harmless sulphate or silicate. Alumina also is usually combined in such forms as not to effect an acid leach. The Cripple Creek ores, containing as much as 20% alumina, have been successfully treated with sulphuric acid in connection with their chlorination.[19] The other elements mentioned are usually not found in sufficient amount with low grade copper ores to seriously interfere with the method.

The highly oxidized ores are in the most susceptible condition for the application of any solvent. Reagents may be introduced to produce an oxide of copper for the solvent to attack. See table I, which shows the ease with which oxides of copper are dissolved. Several of the copper sulphides have the property of reducing ferric sulphate to the ferrous salts, the copper thereby being brought directly into solution as soluble copper sulphate. This reaction is employed by the ferric sulphate and ferric chloride process.*

The alkali processes have not met with success. The solubility of copper in an alkali solution is relatively low. Because many basic salts are thrown down in alkaline solutions an alkali process would soon clog up the circulation channels in the ore body, hence it is impractical for mining in situ.

Oxides and carbonates of copper are readily soluble in an ammoniacal solution but the volatility of the gas in aqueous solution is high. The presence of sulphates will decompose the reagent. An ammoniacal solution would lose most of its strength to the atmosphere if it was applied to the surface of a broken ore body. Due to these reasons reagent costs would be excessively high when attempting to mine in situ with any ammonium solvent.

The theory of the sulphite process is attractive. The chemistry of the method requires only 32 pounds of sulphur in the form of sulphurous acid to dissolve the same amount of copper as is required of 98 pounds of sulphur when in the form of sulphuric acid.[20]

$$CuO + SO_2 \rightarrow CuSO_3$$
$$3CuSO_3 + CuO \rightarrow Cu_2SO_3 \cdot CuSO_3 + CuSO_4$$

The sulphurous acid can be dissolved in sulphuric leach solution. The dissolved cupro-cupric sulphite which forms can be precipitated by driving excess sulphurous acid from the solution. The solution is usually heated to effect this removal of sulphurous acid. The copper sulphite so produced is quite pure in content but it must be reduced to native by the usual converter process. Only sulphite copper will precipitate in this manner. All sulphate copper must be removed by electrolysis or by metallic conversion of iron. Certain features of the process, while possible to control in a well designed plant, would prevent its adaptation to mining in situ. It is difficult to saturate the solution merely by blowing the sulphur dioxide into it. The maximum amount of copper that can be held in the solution is two percent. The copper sulphite will separate very easily from the solution, and should it do so within the ore mass proper it would defeat the purpose of the method. Approximately 40 percent of the copper will go to sulphate and will have to be precipitated by other methods. Rare metals, such as silver,

[17] Campbell, T. P., Examples of Hydrometallurgical Operations, Mines Mag., vol. 21, no. 10, Oct. 1931, p. 10.
[18] Greenawalt, W. E., op. cit., p. 169.
[19] Idem, p. 170.

* See Introduction for details of this reaction.
[20] Idem, p. 176.

would not be recovered with the method.

The chloride processes have been applied to the extraction of copper from its various ores.* Hydrochloric acid, ferric and ferrous chlorides are the solvents usually employed. Hydrochloric acid has the advantage but is more expensive. The acid is less apt to form basic salts and thus the solution will hold more iron during the precipitation of the copper chloride as cement copper. It is applicable only to oxidized ores. Ferric chloride has the property of dissolving copper from its oxide, carbonate, and sulphide combinations.[21] The chloride of copper which forms is precipitated with iron which produces cement copper and iron chloride. The precipitation is slow in a cool solution. In a near-neutral solution, ferric chloride reacts with copper oxide to form a basic salt of iron that would soon interfere with the normal passage of the leach solution through the ore mass. The same objection is raised when treating $3CuO + 2FeCl_3 \rightarrow CuCl_3 + Fe_2O_3$ the sulphide of copper with ferric chloride. In this case

$CuS + FeCl_3 \rightarrow CuCl + FeCl_2 + S$

the free sulphur produced would soon choke up the natural flow of the leach solution and prevent the further dissolution of copper mineral left in the ore. These objections are sufficient to eliminate the use of any chloride processes when leaching copper in place.

Sulphate Method

It is the sulphate process that best lends itself to the mining of copper in situ. The reagents are relatively cheap. The solvent produces a high efficiency with few detrimental products. The solution is very stable and cheap to produce. Equal quantities of copper are produced for iron consumed which fact insures the economics of the method so long as iron + is cheaper than copper. The leach solution is maintained at an acid strength too weak to dissolve undesirable material but which is sufficient to dissolve any copper salts in the ore. It is possible to regenerate the barren solution at a low cost thus saving on reagent costs. Native copper, (cement copper), is produced. The percent of contained impurities in the cement copper depends upon technique and control during precipitation. The entire method is carried out at normal temperatures and pressures and requires power only for the circulation of solution. The method will function in all climates. Only extreme freezing conditions, (40 below zero underground), will stop operations.

* At Rio Tinto, Spain; Helsingborg, Sweden; Chiquicamata, in Chile.

[21] Idem, p. 216.

It is taken for granted that extraction is exceedingly slow, and that, for the venture to be successful, the extraction must be spread over a large area so that the daily recovery can be measured in terms equitable with the costs. It is also granted that the operation will usually have a fairly long life in order to make an efficient extraction from a given ore body.

The two basic chemical equations of the sulphate method are:[22]

$$CuO + H_2SO_4 \rightarrow CuSO_4 + H_2O$$
$$CuSO_4 + Fe \rightarrow Cu + FeSO_4$$

The copper minerals found in disseminated deposits are usually oxides or sulphides. The following sub-group of copper minerals are fairly easily decomposed and converted into copper oxide by weak oxidizing agents: Chalcanthite, copper sulphate; Brochantite, basic copper sulphate; Malachite and Azurite, basic copper carbonates; Atacamite, basic copper chloride; and Chrysocolla, copper silicate.[23] These sub-group minerals are often dissolved in nature by underground waters and re-deposited at lower depths on contact with iron pyrite. They do not form true primary copper sulphides and are a class of sulphides that are susceptible to a weak acid leach.

Ferrous iron has been the biggest problem in the sulphate method of leaching. Properly controlled it can be turned into an asset, if it is disregarded it will eventually ruin the operation. From the second equation above, 2.38 pounds of ferrous sulphate is formed for every pound of copper recovered. This ferrous sulphate will remain dissolved in solution up to certain solution strengths. It is very desirable that this ferrous sulphate stay dissolved. The production of copper will quickly decline if the ferrous iron should come out of solution in the small leaching channels in the ore mass. This item is covered extensively in the section on control of the solution.

The question of oxidizing sulphide copper has been given considerable attention by metallurgists. Mining in situ, of course, precludes any roasting operation. Weinig states that, "sulphide minerals promptly start to oxidize when exposed to water and air, and that the result of this oxidation, among other things, is the production of films on the mineral composed of its own salts or oxidation products. It has been found that sulphide minerals occurring in the older geological formations are more stable

[22] Idem, p. 180.

[23] Sullivan, J. D., Dissolution of Various Oxidized Copper Minerals, U. S. Bur. Mines Rept. Inv. 2934, p. 7, 1929.

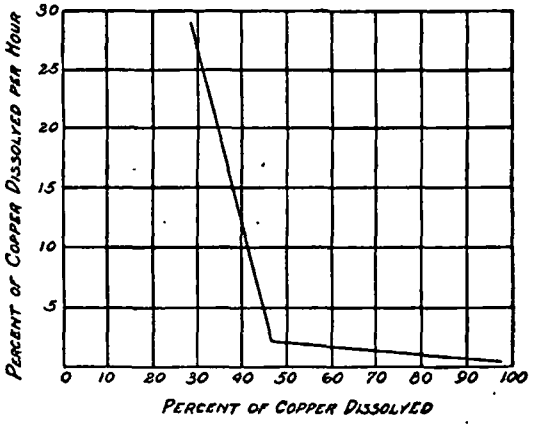

▼ Table II—Graph showing the Rapid and then Partial Dissolution of Chalcocite. Compiled from data taken from U. S. Bureau of Mines Tech. Paper No. 473.

than those of more recent date."[24] He has also found that copper sulphate acts as a catalyst during the oxidation of sulphides to oxides.

When cupriferous pyrite is treated with a solution of ferric sulphate in the presence of sulphuric acid and oxygen, copper will go into solution in proportion to the quantity of iron that has been reduced from the ferric to the ferrous condition.[25] [26] When chalcocite, (Cu_2S), is leached with ferric sulphate, one-half of the copper dissolves rapidly, and the residue has the approximate formula of covellite.

$$Cu_2S + Fe_2(SO_4)_3 \rightarrow CuS + CuSO_4 + 2FeSO_4$$

This CuS does not remain constant, but continually undergoes change as more copper is dissolved until the atomic ratio of copper to sulphur becomes 0.9 or less.

$$CuS + Fe_2(SO_4)_3 \rightarrow CuSO_4 + 2FeSO_4 + S$$

This is shown graphically by table II. Artificial covellite produced by the leaching of chalcocite, dissolves at a much faster rate than does natural covellite.[27] Table III illustrates this difference in leaching speed.

Sullivan has found that the size of the ore particle has no effect upon the rate of dissolution provided the solution was able to enter the sample. Ore samples ranging in size from plus ten to minus two hundred mesh gave practically identical rates of dissolution.[28] (Table IV.) Ores of copper are usually of the disseminated type and solid particles larger than ten mesh would be rare.

[24] Weinig & Carpenter, The Trend of Flotation, Colo. Sch. of Mines Quarterly, vol. 32, no. 4, 4th ed., Oct. 1937, p. 16.

[25] Greenawalt, W. E., op. cit., p. 193.

[26] Sullivan, J. D., Chemistry of Leaching Chalcocite, U. S. Bur. Mines Tech. Paper 473, p. 24, 1930.

[27] Sullivan, J. D., Chemistry of Leaching Covellite, U. S. Bur. Mines Tech. Paper 487, p. 16, 1930.

[28] Sullivan, J. D., Chemistry of Leaching Chalcocite, U. S. Bur. Mines Tech. Paper 473, p. 23, 1930.

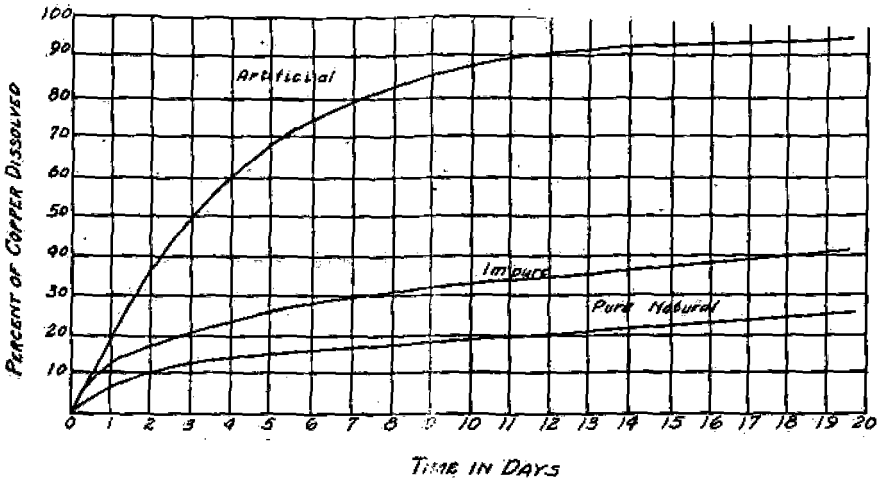

▼Table III—Comparison of the speed of dissolution of artificial covellite, impure covellite, and pure, natural covellite. Compiled from data taken from U. S. Bureau of Mines Tech. Paper No. 487.

The rate of dissolution of chalcocite has been found to be independent of the acid strength of the solution. Sullivan's experiments on chalcocite with solutions containing one percent of ferric iron plus sulphuric acid ranging in strengths from 0.25% to 10.0% showed practically identical rates of dissolution. This fact, that only a very weak concentration of sulphuric acid is required, greatly decreases the operating costs of the method and is very important to the leaching of sulphide copper ores in situ. It is a distinct advantage because a weak acidic solution will not dissolve the many impurities found associated in the disseminated ores of copper.

Oxidized copper minerals are readily dissolved by ferric sulphate. The ferric sulphate is decomposed and converted into the oxide, hydroxide, or basic sulphate. These products will precipitate from the solution unless it is acidic. When sulphuric acid is present the ferric sulphate is decomposed and converted into ferrous sulphate which is soluble in the leach solution. The presence of sulphuric acid is, therefore, desirable in leaching mixed ores of copper.

It is important to keep the concentration of ferric iron as low as possible because the ferric ion will consume native iron in the precipitation cells during the formation of cement copper. All the ferric sulphate introduced into the leach solution should be consumed within the ore body and produce soluble copper sulphate. If it is not completely consumed it will materially increase the cost of the operation by consuming raw iron intended for the copper reduction.

By repeatedly re-using the barren solutions after the precipitation of cement copper, the concentration of ferrous sulphate increases far beyond reaction concentrations and there will result a retardation in the dissolution of chalcocite. However, the formation of basic salts of iron within the ore body by the re-use of barren solutions is of more serious consequence.

Control of the Method

There are several essential factors pertaining to the successful leaching of any copper deposit "in situ." Among the factors that need to be considered these four are of particular importance in the regulation of the process.

1. An economical solution that will attack the copper minerals must penetrate the body of the ore particles and make contact with the copper mineral.
2. The copper mineral must be dissolved solely by the chemical action of that solution.
3. The solution containing the dissolved copper must find its way out of the voids of the rock and into the points of collection.
4. The copper in the leach solution must be easily recovered by an economic means of precipitation.[29]

In order to insure continued operation close watch should be maintained to prevent the introduction of deleterious constituents into the solution or into the ore mass proper. It is propitious to replenish the spent solutions with fresh water. The re-use of the barren solution will eventually lead to difficulty due to its constantly increasing iron content. Surveillance must be maintained over the free acid strength of the leach solution. A slightly higher strength will produce considerable acid loss with attending increases in reagent expense. Constant care of the precipitation cells is necessary. Neglect will result in contamination of the cement copper as well as excess losses of iron reagent and decreased efficiency of copper recovery. Once begun the operation should be constantly attended until all leach solution has passed through the precipitation cells. Labor for the work presence of one technical man would be sufficient to maintain operations once they were started.

Control of the solution can be kept at the point of application, during regeneration, and in the feeder reservoirs. The dissolved copper must be removed from the pregnant solution as it is received and in the quantity in which it arrives. Should the pregnant solution contain excesses of reagents the remedy will be applied to the feeding solution. If difficulties should arise during the extraction of the dissolved copper, due possibly to certain concentrations in the solution, it would be perfectly safe to feed the "semi" pregnant solution back over the ore body together with the correction needed for efficient extraction.

Copper is soluble, (at usual conditions of temperature and pressure), in very weak acid solution up to 0.4 pounds of copper per gallon of solution.[30] The usual copper content of leach solution coming from ore in place may be 0.04 pounds of copper per gallon of leach solution. This copper content can be increased by increasing the ferric iron concentration in the leach. Careful control, however, must be kept on the ferric iron concentration to insure its consumption solely in the ore mass. It is important that very little ferric iron enters the precipitation cells as no copper will precipitate while ferric iron is present. The presence of ferric iron in the cells is also expensive as it consumes the native iron intended for the reduction of the copper. The system should not be loaded down with ferrous iron. Ferrous iron has no useful work to perform and its elimination is beneficial. Its elimination, however, is expensive unless the entire barren solution is discarded. The iron content of the batch can be determined easily by simple titration.

An important item is the application of the solution to the ore body. The ore should be subjected to alternate cycles of wetting and drying. When soluble copper is extracted from the interior of a rock by alternate wetting and drying, evaporation draws copper salts to the surface of the rock during the drying period. These salts are subsequently removed by the next application of the leach solution. Some of the solution will penetrate into the cavities, cleavage planes, and interstices within the rock during the time that the surface salts are being removed by washing. The distance the solution penetrates into the rock is a function of the time of washing. If all of the moisture within the rock is removed

[29] Sullivan, Keck & Oldright, Factors Governing the Entry of Solutions Into Ores During Leaching, U. S. Bur. Mines Tech. Paper 441, p. 1, 1929.

[30] Greenawalt, W. E., op. cit., p. 162.

during the drying cycle, the soluble copper salts will be crystallized, partly at the surface and partly inside the rock. The amount of copper brought to the surface will depend upon the size, shape, and general character of the voids within the ore. The ore mass particles will become saturated if the washing period is long enough regardless of whether or not the moisture was completely removed in the previous drying process.[31] This scheme produces soluble copper faster than chemical diffusion. It will also aid in the oxidation of any sulphide copper present in the ore body. It can be accomplished by dividing the ore body into sections, one section can be receiving the solution during the time another is drying.

When the leach solution is applied its temperature should be the same as the ore body's. Higher temperatures will raise the vapor pressure of the solution and prevent its efficient penetration into the voids of the rock. In this connection it has been suggested that the solution be saturated with a non-acting gas having a lower vapor pressure than that of the ore body's.[32] However, the cost of processing the leach may not compensate for the increased production. Evidence has been offered to show that the solubility of the gas contained within the ore, with respect to the penetrating liquid, is the deciding factor that determines the rate of ingress of solution.[33]

It has been agreed that the solution must make contact with the ore particle. There will be questions raised as to the possibility of any solution making contact with an ore particle far inside the interior of an ore mass. It is the author's contention that an ore mass is susceptible to circulating waters and solutions, otherwise it would not contain ore particles. Tolman states that, "confined flow in fractures commonly extends to considerable depths and rises along master fractures to the discharge point of the major fractures. A tunnel, by interception, may drain an entire fracture system and its tributaries. The lowering of the water table in fractured rock by artificial excavations has been the subject of many actions at law."[34] For example, hydrothermally altered granite is generally very porous. When a specimen of such rock is dipped in dye it instantly becomes colored, and the dye will permeate deeply.[35] Many of the copper ores owe their origin to the circulation of hydrothermal solutions. It is thus logical to presume

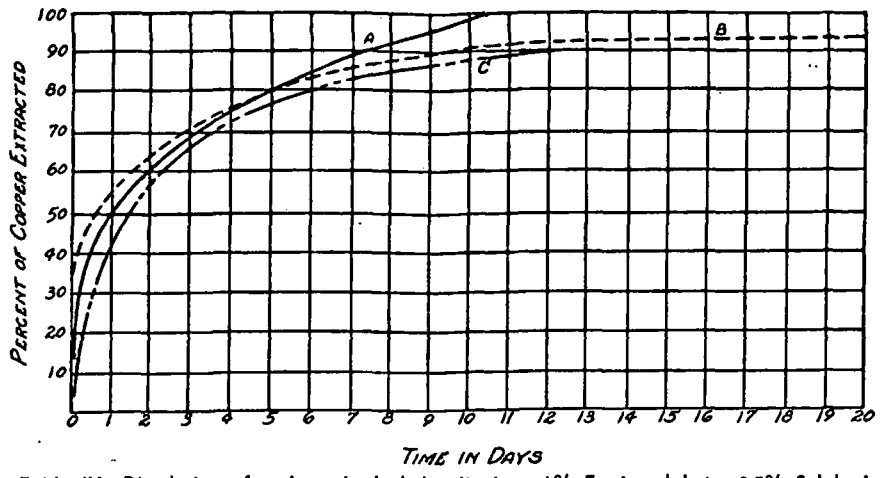

▼Table IV—Dissolution of various sized chalcocite in a 1% Ferric sulphate, 0.5% Sulphuric acid, solution. Taken from U. S. Bureau of Mines Tech. Paper No. 473.

A . . . Kennecott, —100 +200 mesh.
B . . . Bisbee, —10 +28 mesh.
C . . . Bisbee, —2 +3 mesh.

that cold solutions will penetrate altered rock as well as hydrothermal solutions because of their lower vapor pressure.

Sullivan, Keck, and Oldright found that the size of an ore particle did not determine the speed of solution ingress. Their solutions always penetrated the rocks rapidly at first, then the rate of penetration decreased and finally became nearly constant.[30] Table V shows the results of some of their work. There is an initial rapid penetration of solution into the ore along the larger fractures and openings. From these larger avenues the solution seeps into smaller fractures, crevices, and interspaces. Actually, the solution does not have to penetrate three inches of minute openings to reach the center of a six-inch piece; rather, it enters through larger arteries and travels to smaller ones. As copper is removed, more space is made for further ingress of later solutions. "With the rocks studied it has been found that the solutions enter along fractures and cleavage planes; from these larger fractures it gradually seeps into the rest of the rock. The first 50 to 75 percent of the total penetration takes place very rapidly along these crevices and fractures, and the smaller voids are then filled more slowly from these points of initial penetration. This explains why only 59 percent more time is needed to saturate a six-inch piece than a one-inch piece."[37]

[30] Sullivan, Keck, and Oldright, op. cit., p. 8.

[37] Idem, p. 38.

▼Table V—Rate of penetration of 5% copper sulphate solution into Ajo ore. Data from U. S. Bureau of Mines Tech. Paper No. 441.

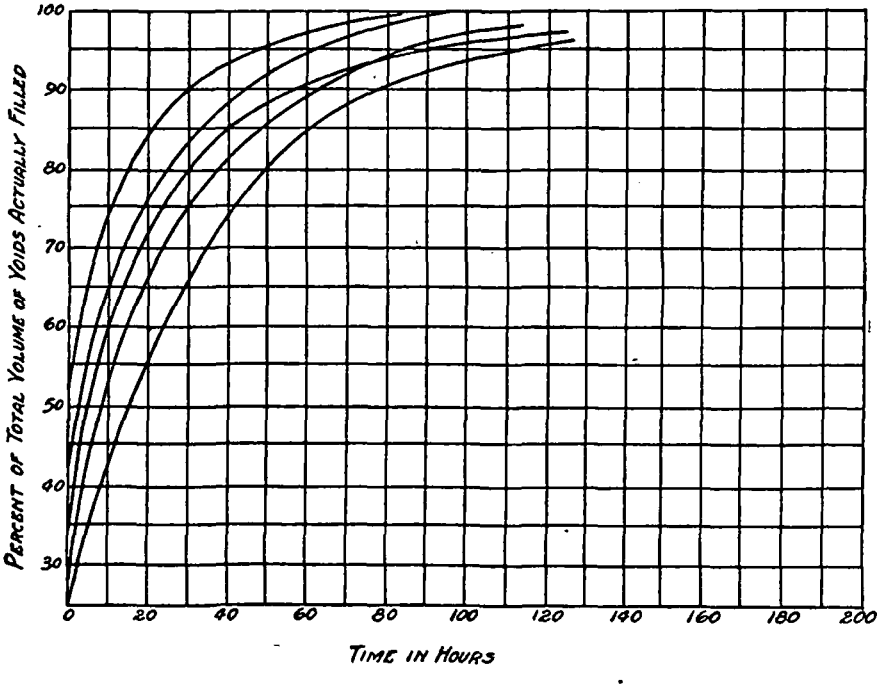

[31] Guggenheim & Sullivan, Acceleration of Extraction of Soluble Copper from Leached Ores, U. S. Bur. Mines Tech. Paper 472, p. 29, 1930.

[32] [33] Sullivan, Keck, & Oldright, op. cit., pp. 35-7.

[34] Tolman, C. F., "Ground Water," 1st ed., pp. 297-8, McGraw-Hill Book Co., 1937.

[35] Emmons, W. H., op. cit., p. 160.

The chemical action of the solvent must be strong enough to dissolve the copper mineral. Yet the dissolving action of the solvent must not be great enough to spend itself upon the worthless material present with the copper. Experience has shown that a sulphuric acid leach containing about 0.5 percent free acid is sufficient to dissolve copper oxide and at the same time not effect silicates and the other gangue minerals usually present with copper deposits. The acid strength needed must be determined before the method can be passed upon as applicable to a certain deposit. The presence of ferric sulphate, (or other ferric compounds), will speed the dissolution of copper oxide in the acid leach. Regulation is thus required to maintain a predetermined strength of ferric ion and sulphuric acid in the leach solution. It should be remembered that too high a ferric strength will result in ferric ion appearing at the precipitation cells and causing excessive raw iron losses. Control is entirely in the hands of the laws of physics and chemistry after the solution has been distributed at the points of application. Not until the solution appears at the point of recovery can the technician remedy any difficulties.

The fourth named essential is that the copper be removed economically from the pregnant solution. The amount of solution appearing at the receiving point will be equal to the amount delivered at the distributing point if the plant has been developed correctly and solution losses have been prevented. The quantity of leach solution for a good economic basis should be about 100 gallons per minute. Larger volumes are recommended. A solution volume of 1500 gallons per minute has been successfully re-circulated against a head of 1000 feet.[38] At the same installation, solution velocities of 40 feet per minute were maintained in the precipitation cells to insure a clean product of cement copper. A poor grade of cement copper will increase refining costs. Control is needed to see that the cement copper is not precipitated in a contaminated condition. Foreign material would be included in the cement copper if the solution were not quickly circulated. The plant at Britannia Beach could not produce a high grade cement copper because of difficulties in the precipitation cells.[39] Air agitation has been practiced during precipitation to produce uncontaminated cement copper. Air agitation tends to oxidize ferrous sulphate forming ferric ions and causing an increased raw iron consumption.

As copper is formed, native iron is dissolved, and a convenient method of handling both will do much to lower operating costs. A constant supply of raw iron must be kept in the precipitation cells. It is this phase of the method that requires the largest portion of man-hours. If there is a large and sufficient supply of scrap iron on the premises it may be economical to use it in the cells rather than buy raw iron. Cutting and handling costs of scrap material is high. De-tinned scrap iron makes the best precipitating reagent. It is a most efficient copper precipitant, and full value in iron content is received for its cost. This type of scrap has a large surface area, and is nearly pure iron due to the method in which it is processed. Its large surface area is objectionable to iron scrap foundries and thus de-tinned scrap does not command a market price equivalent to its iron content. When placed in a moving solution of copper sulphate, the large surface of the scrap allows the precipitation of copper to occur quickly and efficiently. The same advantages would hold for machine cuttings and shop waste provided the material is not alloyed with elements that have a retarding effect in the cells.

Due to the corrosive action of copper sulphate upon iron pipe it is advisable to precipitate all the copper at, or near, the point where the pregnant solution comes from the ore body. This can be done because the precipitation cells are not large and can be strung along both sides of a moderately sized tunnel. Copper sulphate solution can be transported through lead pipe, wooden launders, wooden pipe, and copper-alloyed materials. Pumps used for the circulation of copper sulphate solution should be made of bronze parts. The precipitation cells are usually made of wood, copper nails, and are fitted with lead connections.

Examples of Past Practices

Mining in situ is not something that is new and untried. The method has been applied in several localities and has met with varying degrees of successfulness. In Sonora, Mexico, the Cananea Consolidated Copper Company recovered 189 tons of copper from the leaching of one single stope. In British Columbia the Britannia people made a profitable extraction of 600 tons of copper per year using the method. During a four year period in Utah, the Ohio Copper Corporation extracted 8500 tons of copper from a caved section of low grade ore. The method has also met with reverses. The Bagdad people of Arizona abandoned, in 1924, an attempt to leach in situ because of excessive reagent consumption and serious losses of pregnant solution.[40] Mining in place has been successful as a rule on ore bodies that have been subjected to caving action of some kind or other which has developed the natural occurring solution channels.

An outstanding example of successful stope leaching is the record made by the Ohio Copper Corporation of Utah in the years 1922 through 1926.[41] An immense body of low grade copper ore had been developed and the usual methods of block-caving mining had met with financial losses. Much development work had been done up to 1922, and the caving stopes had been closed down because of an insufficient grade of ore and a poor metallurgical recovery. The ore was chiefly oxidized copper, disseminated in shattered quartzite. The sulphide copper in the ore oxidized fairly easily when it was exposed to the arid climate of the region. In 1922, Messrs. S. K. Kellock and F. E. Turner junked the equipment of the metallurgical mill and began the installation of an underground leaching plant.[42] The cost of the leaching plant was paid for by the sale of junk from the old mill. These men began operations by dispersing 250 gallons of sulphuric acid leach solution per minute over the top of broken rock overlying a caved stope. The solution drained through 1000 feet of vertical distance and emerged through four raises into the Mascotte tunnel. This point was two miles underground from the portal. Precipitation cells had been constructed there, and the pregnant solution was made to precipitate its copper content using scrap iron. Improvements were made until the volume of leach solution recovered from the stope was 1500 gallons per minute. This volume required the services of 15 men attending the cells, replenishing the iron, and removing the cement copper. It was found that a high speed flow of pregnant solution, through 32-inch cells containing de-tinned scrap iron held on a false bottom 17 inches high, would produce cement copper of about 85 percent purity. The recovery of copper from the pregnant solution was 98 percent of the head assay. The raw iron consumption was

[38] Anderson & Cameron, Recovery of Copper by Leaching at the Ohio Copper Co. of Utah; Trans. Am. Inst. Min. & Met. Eng., vol. 73, p. 31, 1926.

[39] Brennan, C. V., Mining Operations at the Prop. of the Britannia Min. & Smelt. Co., U. S. Bur. Mines Inf. Circ. 6815, p. 27, January 1935.

[40] Private correspondence with Gen. Mgr. J. W. Still, Dec. 1940.

[41] Anderson & Cameron, op. cit., pp. 30-33.

[42] Leaching a Copper Mine, Eng. & Min. Jour., vol. 116, p. 668, Oct. 1923.

found to average pound for pound of copper produced. This is only 14 percent above the theoretical and indicates fairly good technical control of the leach solution. The district did not furnish an unlimited supply of fresh water hence the company was forced to re-use its barren solution. Additions of fresh water were made from time to time to decrease the ferrous iron content. It is believed, however, that the ferrous iron was allowed to build up in the circuit until it began to precipitate in the ore body as basic salts of iron.[43] This resulted in a decreased copper content in the pregnant solution due to the formation of basic iron pipes leading directly through the stope and shunting the leach solution away from fresh ore.

Operations of the company had advanced in 1925 until the cost of producing copper at the mine was 3.847 cents per pound. After refining costs and freight charges on the cement copper were paid, they realized a profit on any price of copper above 6.324 cents per pound. Their production of pure copper from leaching in place had reached 17 million pounds at the end of 1925.

A copper mine in Mexico turned a curse into a profit by applying the leaching method to old, filled, shrinkage stopes. At Cananea the mine was troubled with acidic copper bearing water that attacked the pumps and pipes through which it was transferred. This mine water running through the workings ate away the rails and any other iron that it contacted. In an attempt to reduce maintenance costs, precipitation cells were placed at vantage points in the mine. These cells produced so much inexpensive copper, the idea was expanded and improvements installed to expedite results. Mine water was dispersed over the surfaces of the old filled stopes which were estimated to carry about 1.0 percent copper. Of this 1.0 percent only 0.05 percent was acid soluble. The remaining 0.95 percent was sulphide copper. This sulphide copper was held in tiny seams and veinlets as secondary chalcocite.

Their installation in 1926 was not on a large scale. The volume of solution running through the precipitation cells averaged 50 gallons per minute. They, too, re-circulated the leach solution to effect savings on fresh water. Wooden pipe and bronzed pumps were installed to prevent corrosion of the equipment. Air agitation in the precipitation cells was practiced to give a higher grade of cement copper as the slow moving solution produced slow precipitation and contamination of the cement copper with attendant coating of the raw scrap iron.

The company had a plentiful supply of scrap iron on hand which they used for precipitation. They acknowledged, however, the efficiency could have been doubled by using de-tinned scrap iron. The operating costs of a plant handling and using heavy scrap iron would be high. The iron must be cleaned and cut down in size so that it can be used inside the cells. Their production costs in 1926 were 4.69 cents per pound of copper which included the entire cost of plant and equipment of $2600. They did not have a shortage of water and were thus able to discard the barren solution when it became too highly concentrated with ferrous iron.

It was here that the leaching of "lost" ore proved to be feasible and possible. In the Veta stope they leached 42,000 tons of broken ore that had been left in an old shrinkage stope and that had subsequently been caved upon from the back and walls. This contamination resulted in a copper content of less than 0.8 percent. In ten months time, using a leach solution of 70.5 gallons per minute, they realized 142 tons of copper from the stope, a recovery of 42 percent. Leaching was still in progress on the stope when these figures were released.[44]

Ideal conditions suitable for mining in situ were found at the mine of the Britannia Mining and Smelting Company, Britannia Beach, British Columbia. A large body of low grade copper ore had caved subsequent to glory holing. This ground was connected to the lower levels by caved-in stopes and raises. A bountiful fresh water supply was available above the ore, and it had only to be led to the upper horizon of the caved zone. A volume of leach solution from 100 to 650 gallons per minute was caught in the lower workings and sent through large, five-foot, precipitation cells. As the ore contained copper oxides with sulphates and some pyrites, the solution made its own sulphuric acid of sufficient strength to dissolve the copper in the caved ore. The analysis of the pregnant solution was:

	Grams Per Litre
Free sulphuric acid	0.023
Copper	0.98
Ferrous iron	0.17
Ferric iron	1.61

Air agitation in the precipitation cells was practiced. They used low air pressures which were fed into the cells through lead pipe. Precipitation was effected with local scrap iron, tin cans, and other junk. They secured a cement copper product of 67 percent purity. This was rather low but was due to the type of precipitant used and the cell construction. As the only reagent cost was for raw iron, production costs were, of course, very low. Copper was produced at the mine for 2.14 cents per pound. The magnitude of the deposit and volume of leach solution handled was sufficient to produce 600 tons of copper per year.[45]

Conclusion

There is no doubt that a number of the copper minerals are soluble in a very weak acid leach. The technical information on this phase of the subject is profuse. It is quite possible that a particular leach solution may be developed in the near-future strictly for mining in situ. New ideas applied to leach solutions may quickly popularize the method and give it distinction. As already pointed out, the sulphate leach contains much to recommend it. However, it can stand considerable improvement in connection with the regeneration of the barren solution. So far, few attempts have been made to develop a particular leach solution for mining ore in situ.

Today the method is adaptable to certain deposits, developed in certain details, as proved by several, already mentioned, successful ventures. That the method is adaptable to deposits that have not been subjected to certain development remains to be seen.

We know the formation of ore deposits is usually an orderly process of progressive concentration through the agency of mineralizers. The circulation of these mineralizers is facilitated by fault fractures, planes of bedding or schistosity, and by porous strata. Experience has shown that most veins are formed along just such passages.[46]

Eminent geologists have shown where nature, using solutions, has deposited ore "in place." Can the technical engineer reverse this concentration through the agency of a chemical process? Can ore material be leached in place without first disturbing it? These questions remain to be proved by a full-sized, practical operation, applied to a geological structure that meets the requirements of the method.

[43] Private correspondence with A. E. Anderson, Oct. 1940.

[44] Greenwood, C. C., Underground Leaching at Cananea, Eng. & Min. Jour., vol. 121, p. 518, Mar. 1926.

[45] Brennan, C. V., op. cit., pp. 27 etc.

[46] Stephen Taber, Mechanics of Vein Formation, A. I. M. E. Transactions, vol. 161, p. 36.

SUBJ
MNG
MCLP

UCRL 77379

1975

UNIVERSITY OF UTAH
RESEARCH INSTITUTE
EARTH SCIENCE LAB.

POST 74

MINERALOGICAL CONSIDERATIONS IN LEACHING OF PRIMARY COPPER SULFIDES AT ELEVATED TEMPERATURES AND PRESSURES

By

David L. Leach

MINERALOGICAL CONSIDERATIONS IN LEACHING OF PRIMARY COPPER SULFIDES AT ELEVATED TEMPERATURES AND PRESSURES*

David L. Leach

Lawrence Livermore Laboratory, University of California
Livermore, California 94550

ABSTRACT

This report describes the leaching characteristics of four different ores in sulfuric acid systems pressurized with oxygen. The variations in the leaching characteristics between different ores can be largely attributed to differences in mineralogy. Certain gangue mineral alteration phases produced during leaching may trap copper from solution, as well as reduce the porosity of the ore. In addition, the formation of secondary copper sulfides, digenite, and covellite may limit the extraction of copper if the supply of oxygen is restricted to chalcopyrite. Apparently, the key consideration for successful leaching is maximizing the rate of oxidation of the sulfides and, at the same time, minimizing the rate of gangue mineral alteration. This can be accomplished at high oxygen pressures and moderate temperatures (70° to 90°C) and low pH ($\leq$2.0). The ideal ore mineralogy is one that is low in carbonates and easily altered Fe-Mg minerals such as biotite and hornblende, and one that has acceptable pyrite/chalcopyrite ratios.

---

*This work was performed under the auspices of the U.S. Energy Research & Development Administration, under contract No. W-7405-Eng-48.

INTRODUCTION

It is inevitable that as surface deposits are depleted, copper and related metals will have to be obtained from deeper deposits. The recovery of ore minerals at depth will probably not be economically amenable to conventional mining techniques unless the ores are of significantly high grade. Consequently, it is important that we develop some new methods, such as solution mining, that will ensure a future supply of copper and similar metals.

I will restrict my discussion to the application of solution mining to relatively low-grade copper ores below the water table at a depth of 1000 ft or more. Although this type of occurrence probably contains a rather significant amount of the potential supply of copper, geologists have not been actively exploring for deep low-grade deposits largely because a technology does not exist to exploit these deposits. Considering the significant time-lag between the research and development stage and actually applying a new technology, we must proceed rapidly toward understanding the many technical uncertainties in solution mining at depth.

A proposed deep solution mining process has been under development at the Lawrence Livermore Laboratory.[1-5] The first step in such a process is the rubblization of a region of the ore deposit by the use of nuclear explosives, or, alternatively, by undercutting and caving using conventional methods. The ore fragments are then leached in the aqueous sulfuric acid system produced by introducing oxygen into the flooded ore under hydrostatic pressure. The increase in solubility of oxygen under these conditions, together with the elevation in temperature resulting from the oxidation of the sulfide minerals, greatly accelerates the rate of copper recovery from primary copper ores.

The objective of our research program is to obtain experimental data and to develop a fundamental understanding of the leaching process that will enable extrapolation of results from laboratory experiments to field conditions. One important achievement in the LLL program was the development of a leaching model by Braun et al.[3] that successfully describes the recovery of copper from ore fragments of any given particle size distribution under limited conditions of temperature and pH. The leaching mechanism involves mixed kinetics and includes a surface reaction within a moving reaction zone plus pore diffusion of dissolved oxygen through the reacted portion of the ore fragment to the reaction zone. The application of this model over a broad range in temperature and pH is difficult because of changes in the chemistry of the leach solution, as well as mineralogical and physical changes within the ore.

In this presentation, I will emphasize the importance that ore mineralogy, particularly the gangue mineralogy, has to the leaching of chalcopyrite ores in sulfuric acid solutions at elevated temperatures. The variations in the leaching characteristics that we observe between different ores can be largely attributed to differences in mineralogy and to a lesser degree, the grain size of the mineral constituents. For a given set of experimental conditions (T, PO_2, pH), the mineralogy of the ore controls the composition of the leach solution, and the amount of alteration products yielded during leaching. These factors in turn have important controls on the recovery of copper.

EXPERIMENTAL LEACHING OF PRIMARY SULFIDE ORES

Braun et al.[3] described a series of experiments demonstrating that a porphyry copper ore can be successfully leached at 90°C and 400 psig oxygen with deionized water as the starting solution. The ore used in these

experiments is a primary porphyry copper ore from the San Manuel Mine (Magma Copper Company, Arizona). The general mineralogy of the San Manuel ore is given in Table 1.

The copper recovery for one of these experiments is shown in Fig. 1. For the experiments at 90°C, the pH of the system decreased from an initial value near neutral to a steady-state value near 2 (Fig. 2). The buffering effect observed in these experiments is an important feature of the leaching system and represents a steady-state balance of H^+-dependent reactions involving both the sulfides and gangue minerals.

The net chemical reaction of the sulfide minerals in laboratory leaching San Manuel ore is:

$$CuFeS_2 + 2FeS_2 + \frac{45}{4} O_2 + \frac{43}{6} H_2O = Cu^{+2} + Fe_3(SO_4)_2(OH)_5 \cdot 2H_2O + \frac{1}{3} S^\circ + \frac{11}{3} SO_4^{-2} + \frac{16}{3} H^+ \quad (1)$$

The hydrogen ions produced in this reaction are mostly consumed either by reaction with calcite to produce calcium sulfate or by reaction with other gangue minerals to release equivalent amounts of other cations, principally Mg^{+2} and Al^{+3}. The system is observed to buffer at a quenched pH of about 2, representing a steady-state balance of H^+-dependent reactions.

The chemical composition of the leach solution for a self-buffered experiment at 90°C is shown in Fig. 3. The high sulfate concentration is an important feature of the system. Most of the metal ions produced during leaching are combined with sulfate as metal-sulfate complexes or precipitates.

The calcium concentration shown in Fig. 3 steadily decreases because of the precipitation of anhydrite. The Na, K, Fe, and Al concentrations are

limited by the precipitation of jarosite-alunite minerals [$KFe_3(SO_4)_2(OH)_6$ - $KAl_3(SO_4)_2(OH)_6$ with Na substitution for K and limited substitution between Al and Fe].

Jarosite and alunite are the most common alteration products observed in the leached samples. They occur as fine-grained material throughout the rock and as replacements of K-feldspar and K-mica.

Leaching experiments at temperatures in the 70° to 150°C range and at pH values in the 0.25 to 2.0 range clearly show that temperature and pH have a pronounced effect on the rate and ultimate recovery of copper from San Manuel ore. These effects are predictable in part from the leaching model developed by Braun et al.[3] Their model is based upon a diffusional rate constant for oxygen and a chemical rate constant, both of which are temperature dependent. Although the leaching model does not directly account for variations in pH, several factors that are included in the model are affected by pH. For example, the porosity of the ore would be greater at a low pH because of less precipitation of iron salts.

At temperatures of 90°C or less, the effect of maintaining a pH below the self-buffered value of approximately 2.0 is to increase the rate of extraction, particularly in the early stages of leaching. The effect at 70°C is shown in Fig. 4. The increase in rate of extraction may be caused by the increased oxidation of chalcopyrite by Fe^{+3} or by the increase in porosity of the rock because of less precipitation of alteration products.

At 110°C, successful recovery can be accomplished only if the pH is between approximately 2.0 and 0.75. At temperatures in excess of 110°C, leaching is unsuccessful at any pH.

The leached ore from the experiments was studied by x-ray diffraction, optical microscopy, and electron microprobe analyses. The results show that

physical and mineralogical changes in the gangue and sulfide minerals are major limiting factors, particularly where certain mineral reactions are accelerated at elevated temperatures. Decomposition or alteration of the silicate minerals to copper-bearing phases are accelerated at elevated temperatures, particularly when high temperatures are combined with low pH. Elevated temperatures also accelerate the rate at which chalcopyrite is replaced by secondary sulfides, covelite, and digenite.

Leaching experiments were conducted on three other ores, including two ore types from the Ruth Mine (Kennecott Copper Corporation, Ruth, Nevada). One is a typical porphyritic, highly altered quartz monzonite referred to as Ruth. The other is a hornfels-type, fine-grained rock consisting largely of plagioclase and hornblende. This ore will be referred to as Ely. The third ore is from the Kelley Mine (Anaconda Company, Butte, Montana). The general mineralogy of the ores is given in Table 1.

The extraction rates for San Manuel, Ruth, and Kelley at 90°C, 400 psig O_2 (Fig. 5) are very similar, which is not surprising considering the similar mineralogy and texture of the ores. However, at 110°C the extraction curve of Kelley ore was quite different from that of San Manuel under the same conditions. At 110°C, the Kelley curve passed through a maxima of 80% extraction at 160 days, then decreased to approximately 45% extraction at the termination of the experiment at 280 days. The copper that had been successfully leached from the ore was incorporated into silicate alteration products yielded during leaching.

The Ely ore could not be successfully leached at any temperature or pH. The extraction curve for Ely at 90°C and 400 psig O_2 is shown in Fig. 6. The curve passed through a maxima of 20 to 30% extraction, then rapidly fell to less than 5% extraction at the termination of the experiment. The Ely ore was

in an advanced state of alteration to a fine-ground material consisting of disaggregated rock fragments and alteration products composed of montmorilonite, amorphous phase (largely SiO_2), hematite, and jarosite. The chalcopyrite was almost completely leached, and presumably the copper entered the alteration phases. The leaching experiments on Ely and Kelley ore clearly demonstrate that the alteration of gangue minerals is an important consideration in the leaching of ores at elevated temperatures.

GEOCHEMISTRY OF LEACHING SILICATE GANGUE MINERALS

The leaching of porphyry copper ores is very similar to the hydrothermal reactions that deposited the primary sulfides. Therefore, considerable insight into the process of leaching sulfide ores can be obtained from the extensive body of research on hydrothermal ore deposition.[6,7] For the leaching experiments, the T, PO_2, and pH are fixed. The pH is controlled by the addition of sulfuric acid or by the production of H_2SO_4 from the oxidation of the sulfides and is buffered largely by the $HSO_4^-/SO_4^=$ boundary as well as related equilibria.

The process by which the gangue mineral reacts with the acid solution may be defined as "hydrolysis" or "base leaching." This process can be viewed as a decomposition reaction with water in which H^+ is consumed and an equivalent amount of cations released to the solution. This type of reaction between the silicate minerals and the aqueous solution containing H^+ ions is perhaps best illustrated by the reaction:

$$\text{K-feldspar} \xrightarrow{(2)} \text{K-mica} \xrightarrow{(3)} \text{Kaolinite} \xrightarrow{(4)} Al^{+3} + H_4SiO_4 \ ,$$

$$\underset{\text{K-feldspar}}{3KAlSi_3O_8} + 2H^+ + 12H_2O = \underset{\text{K-mica}}{KAl_3Si_3O_{10}(OH)_2} + 2K^+ + 6H_4SiO_4 \ , \qquad (2)$$

$$\underset{\text{(K-mica)}}{2KAl_3Si_3O_{10}(OH)_2} + 2H^+ = \underset{\text{(Kaolinite)}}{3Al_2Si_2O_5(OH)_4} + 2K^+ , \qquad (3)$$

$$\underset{\text{(Kaolinite)}}{Al_2Si_2O_5(OH)_4} + 6H^+ = 2Al^{+3} + H_2O + 2H_4SiO_4 . \qquad (4)$$

Reactions to the right consumes H^+ ions and releases an equivalent amount of K^+ for Eqs. (2) and (3) and of Al^{+3} for Eq. (4). Since the activity of the solids and water may, to a first approximation, be taken as unity and the H_4SiO_4 concentration fixed by the equilibrium with amorphous silica, the equilibrium constant at a given temperature and pressure takes the simple form:

$$K = \frac{aK^+}{aH^+} \qquad \text{Eqs. (2) and (3)}$$

and

$$K = \frac{aAl^{+3}}{(aH^+)^3} \qquad \text{Eq. (4) .}$$

The lack of thermodynamic data on the chemical species in the leach solution at the temperatures of interest prevents calculation of the activities from concentrations. However, one can make an "order of magnitude" approximation of the relative stability of the gangue minerals by equating concentrations with activities. Using the analyses of the leaching solutions and the data of Helgeson,[8] it is clear that K-spar, K-mica, and kaolinite are grossly out of equilibrium with the leach solution. Similar argument can be made to show that, with the exception of quartz, all of the major gangue minerals should be decomposing. Petrographic studies on the leached ores show that the relative reactivity of the gangue minerals in acid solution is:

Hornblende > Biotite > Plagioclase > K-spar > K-mica .

The K^+ and Al^{+3} concentrations are much lower than what is expected because of precipitation of a jarosite-alunite phase. Rather than releasing K^+ to the solution as in a simple hydrolysis reaction, the K^+ along with H^+, $SO_4^=$, and Fe^{+3} may be fixed at K-rich sites (K-spar, K-mica, and biotite). The most apparent alteration of K-spar and K-mica can be shown as:

$$\overset{\text{(K-spar)}}{KAlSi_3O_8} + 2SO_4^{-2} + 2Fe^{+3} + 4H_2O = \overset{\text{(Jarosite)}}{K(Fe_2Al)(SO_4)_2(OH)_6} + 3SiO_2 + 2H^+ , \qquad (5)$$

$$\overset{\text{(K-mica)}}{KAl_3Si_3O_{10}(OH)_2} + 4H^+ + 2SO_4^{-2} + 2Fe^{+3} = \overset{\text{(Jarosite)}}{K(Fe_2Al)(SO_4)_2(OH)_6} + 3SiO_2 + 2Al^{+3}. \qquad (6)$$

Hornblende, biotite, and plagioclase alteration products generally consist of a very fine-grain brown clay together with a jarosite-alunite phase. The brown clay is believed to be a mixture of montmorillonite, jarosite-alunite, anhydrite, hematite, and a glass phase (probably amorphous clay and SiO_2).

At temperatures of 90°C or less, the rates of these reactions are rather small compared with the rate at which the sulfides are oxidized. At temperatures greater than 110°C, the rate of silicate gangue mineral decomposition is greatly accelerated. This is important because some of the alteration phases may trap copper as distinct copper phases or else by adsorption.

POSSIBLE COPPER BEARING ALTERATIVE PHASES

The abrupt loss of copper from solution observed in several leaching experiments, particularly with Ely ore, may be caused by the incorporation of copper into certain alteration products. Petrographically, the only unique feature of the leached ore in these experiments is the rather advanced state

of gangue mineral alteration. There is an appreciable amount of jarosite-alunite, montmorillonite, an amorphous phase (≈60% SiO_2), and hematite.

Montmorillonite: The formation of montmorillonite is of considerable interest, both because it is capable of trapping copper and because it is a common alteration product in the leached ore. The copper can be adsorbed on the clay mineral surfaces, occur as an interlayer cation, or occur in a lattice position substituting for Al (medmontite[9]). The activity product constant for a hypothetical Mg-Montmorillonite from Eq. (7):

$$6Mg_{0.167}Al_{2.33}Si_{3.67}O_{10}(OH)_2 + 44H^+ + 16H_2 = Mg^{+2} + 14Al^{+3} + 22H_4SiO_4 \qquad (7)$$

is

$$K_{(T)} = \frac{(Mg^{+2})\ (Al^{+3})^{14}\ (H_4SiO_4)^{22}}{(H^+)^{44}} .$$

Helgeson[8] gives us the following values for log $K_{(T)}$:

Temperature, °C	25	60	100	150
log $K_{(T)}$	36.60	16.49	-0.96	-18.25 .

At a constant pH, the significant decrease in log K with an increase in temperature shows that the formation of montmorillonite is favored at high temperatures.

Because montmorillonite is very fine grained and dispersed with other alteration products, we have not been successful in identifying a distinct copper montmorillonite. It is reasonable, however, to suspect that copper may be adsorbed onto the clay particles. Significant amounts of copper do commonly occur in the fine-grained alteration products including montmorillonite.

Amorphous Phase: An amorphous phase is a common alteration phase and is particularly abundant in the leached ore that showed significant loss of copper during the course of the experiment. X-ray analysis indicates approximately 60% of the amorphous phase is SiO_2. The remaining is probably amorphous clay material. Electron microprobe analyses did not detect any copper in the glass phase. However, if copper was adsorbed on the surface of the amorphous phase, preparation of the sample for analysis perhaps removed it from the surface.

Jarosite-Alunite: X-ray diffraction studies have shown the presence of either alunite ($KAl_3(SO_4)_2(OH)_6$), jarosite ($KFe_3(SO_4)_2(OH)_6$), and possibly natroalunite ($NaAl_3(SO_4)_2(OH)_6$). Minor amounts of copper were detected by electron microprobe analysis of a jarosite-alunite phase in ore leached at high temperatures (110°C). However, no copper was detected in the jarosite-alunite phase formed at 90°C or less. It is possible that high temperatures may lead to the formation of a phase similar to one of the alunite minerals, beaverite ($Pb(Cu,Fe,Al)_3(SO_4)_2(OH)_6$). The similar ionic size of Cu^{+2}(0.69Å) and Fe^{+3}(0.64Å) may permit substitution if valence compensation is made elsewhere in the structure.

Altered Biotite: Electron microprobe analysis has shown the presence of minor amounts of copper to be located at sites of altered biotite crystals. It is not clear whether the copper is located within the leached biotite (vermicullite phase) or in the associated montmorillonite.

Formation of Secondary Sulfides: Covellite and digenite were observed in all the leached ore; they can be found in experiments that have leached well and in those that have leached unsatisfactorily. During leaching, covellite and digenite are continually being formed in the interior of the ore fragments as copper diffuses into the rock and reacts with the chalcopyrite. As the oxidizing zone advances into the ore fragment, chalcopyrite, as well as

the previously formed secondary covellite and digenite are oxidized and release copper to the solution. As long as the rate of oxidation in the reaction zone proceeds faster than the loss of copper to form digenite and covellite, the ore will have a favorable leaching rate.

This is particularly important for the success of an in-situ leaching operation because if for some reason the supply of oxidant is restricted to part of the rubblized ore, this part of the ore will act as a "sink" for copper successfully leached elsewhere.

OTHER CONSIDERATIONS

Acid Consumption: For ores with relatively high carbonate content, it may be necessary to add sulfuric acid to the leach solution to maintain a sufficiently low pH (near 2.0). This is particularly true in the early stages of leaching where the dissolution of calcite is most rapid. For San Manuel ore, acid additions were unnecessary because the amount of sulfuric acid produced from the oxidation of the sulfides was sufficient to dissolve the calcite. However, Kelley, Ruth, and Ely ores required additions of acid to maintain the desired pH during early stages of leaching. It is desirable to have a reasonable amount of pyrite relative to the chalcopyrite content because of the increase in production of sulfuric acid. Conversely, too much pyrite leads to higher oxygen consumption. Therefore, the calcite content of the ore, as well as the pyrite/chalcopyrite ratio are important considerations in evaluating the economics of solution mining. In addition, the dissolution of calcite $CaCO_3 + 2H^+ + SO_4^= = CaSO_4 + CO_2 + H_2O$ liberates carbon dioxide causing a reduction in oxygen partial pressures either by dilution or by stripping oxygen from the leach solution.

Volume Change: Because chemical and mineralogical changes occur within the ore during leaching, there will be changes in mass and in volume (pore volume as well as fracture volume). During the course of leaching, basic cations and CO_2 are removed from the ore whereas H^+, O_2 (in the form of $SO_4^=$), and H_2O are added to the ore. The overall change in mass during leaching may be small when compared with the change in volume of the ore. The formation of the common alteration phases, alunite, jarosite, amorphous phase, montmorillonite, and hematite have significantly larger molar volumes than do the primary silicates from which they formed. The alunitization of K-mica as shown below can lead to a significant increase in volume.

$$\underset{\text{K-mica}}{KAl_3Si_3O_{10}(OH)_2} + 4H^+ + 2SO_4^= \rightarrow \underset{\text{Alunite}}{KAl_3(SO_4)_2(OH)_6} + \underset{\text{Amorphous silica}}{3SiO_2}$$

$\overline{V}$ = molar volume

$$\overline{V}\ \text{alunite}\ (146.8\ cm^3) + 3\overline{V}\ SiO_2\ (\text{amorphous})\ (27.27\ cm^3) - \overline{V}\ \text{K-mica}\ (140.71\ cm^3)$$

$\Delta\overline{V}$ reaction = $+87.9\ cm^3$

(maximum percent increase in volume = 62%)

The gangue minerals seldom are completely altered; however, they do react sufficiently to reduce the pore and fracture volume of the rock, particularly at high temperatures. The effect of reducing the porosity of the rock is to restrict the supply of oxygen to the sulfides. This in turn lowers the copper extraction rate.

SUMMARY

The experimental and theoretical work conducted at LLL demonstrated that chalcopyrite ore can be successfully leached in sulfuric acid systems pressurized with oxygen. We believe that this technology can be used successfully for the in-situ recovery of copper and that this method is particularly attractive for ore deposits that cannot be economically mined by conventional methods.

We showed that the gangue mineralogy plays an important role in the rate and ultimate recovery of copper. The temperature and pH of the leach solution control the rate at which gangue mineral decompose to certain alteration products. The formation of alteration products may in some instances trap copper from solution, as well as reduce the porosity of the ore. Apparently, the key consideration to successful leaching is maximizing the rate of oxidation of the sulfides and, at the same time, minimizing the rate of gangue mineral alteration. This can be accomplished at high oxygen pressures and moderate temperatures (70° to 90°C), and low pH (< 2.0).

For successful leaching at elevated temperatures, the ideal ore mineralogy is one that is low in carbonates and easily altered Fe-Mg minerals such as biotite and hornblende and has acceptable pyrite/chalcopyrite ratios.

ACKNOWLEDGMENTS

I gratefully acknowledge the technical contributions of R. L. Braun, J. Tewhey, and A. E. Lewis as well as the dedicated efforts of P. Bowen and W. Beiriger in the experimental work.

REFERENCES

1. A. E. Lewis, "Chemical Mining of Primary Copper Ores by Use of Nuclear Technology," in Proc. Symp. Engineering with Nuclear Explosives (Am. Nucl. Soc., 1970), CONF-700101, vol. II.

2. A. E. Lewis and R. L. Braun, "Nuclear Chemical Mining of Primary Copper Sulfides," Trans. SME-AIME, 257, 217-224 (1973).

3. R. L. Braun, A. E. Lewis, and M. E. Wadsworth, "In-Place Leaching of Primary Sulfide Ores: Laboratory Leaching Data and Kinetics Model," Trans. Metall. Soc. AIME, 5, 1717-1726 (1974).

4. A. E. Lewis, R. L. Braun, C. J. Sisemore, and R. G. Mallon, "Nuclear Solution Mining - Breaking and Leaching Considerations," in Solution Mining Symp. F. F. Aplan, W. A. McKinney, and A. D. Pernichele, Eds. (AIME, New York, 1974), pp. 56-75.

5. R. L. Braun, R. G. Mallon, and A. E. Lewis, "Distribution of Oxygen in a Large Underground Flooded Region of Broken Ore," Lawrence Livermore Laboratory, Rept. UCRL-75290 (1974).

6. C. Meyer and J. J. Hemley, "Wall Rock Alteration," in Geochemistry of Hydrothermal Ore Deposits, H. L. Barnes, Ed. (Holt, Rinehart, and Winston, 1967), p. 670.

7. J. J. Hemley and W. R. Jones, "Chemical Aspects of Hydrothermal Alteration with Emphasis on Hydrogen Metasomatism," Econ. Geol. 59, 538-569 (1964).

8. H. C. Helgeson, "Thermodynamics of Hydrothermal Systems at Elevated Temperatures and Pressures," Am. J. Sci. 267, pp. 729-800 (1969).

9. F. V. Chukhrov and F. Ia. Anosov, "On Nature of Chrysocolla," Mem. All Union Mineral. Soc. 79, (2) (1950).

Table 1. General mineralogy of the San Manuel, Kelley, Ruth, and Ely copper ores.

	Rock Type	Major Gangue Minerals	Minor Gangue Minerals	Sulfides
SAN MANUEL	Quartz-sericite rock Altered-quartz monzonite Quartz-sericite-biotite rock	Quartz K-mica Biotite	K-spar (largely altered to sericite) Plagioclase Hematite Calcite Magnetite Kaolinite Montmorillonite Hornblende	Chalcopyrite Pyrite py/cp = 2 Ore Grade: 0.7 wt.% Cu Calcite/py = 0.43
KELLEY	Altered-quartz monzonite	Quartz K-spar Biotite K-mica	Plagioclase Chlorite Kaolinite Montmorillonite Calcite Hornblende Zircon Rutile	Chalcopyrite Pyrite py/cp = 2.1 Ore Grade: 0.49 Cu Calcite/py = 1.38
RUTH	Altered-porphyritic quartz monzonite	Quartz K-feldspar Plagioclase Muscovite	Calcite Biotite Apatite	Chalcopyrite Pyrite py/cp = 0.46 Ore Grade: 1.44 wt.% Cu Calcite/py = 2.5
ELY	Altered-hornfels	Plagioclase Hornblende Quartz Biotite	Calcite Chlorite Epidote Apatite	Chalcopyrite Pyrite py/cp = 2.7 Ore Grade: 0.75 wt.% Cu Calcite/py = 0.84

FIGURE CAPTIONS

Fig. 1. Extraction of copper at 90°C and self-buffered pH. Ore size, 16 ± 3 mm.

Fig. 2. Solution pH during leaching at 90°C. Ore size, 16 ± 3 mm.

Fig. 3. Chemical composition of the leach solution at 90°C and self-buffered pH.

Fig. 4. Extraction of copper at 70°C and various pH. Ore size, 16 ± 3 mm.

Fig. 5. Extraction rates for San Manuel, Ruth, and Kelley at 90°C, 400 psig O_2. Ore size, 16 ± 3 mm.

Fig. 6. Extraction curves for Ely and San Manuel at 90°C and 400 psig O_2. Ore size, 16 ± 3 mm.

NOTICE

"This report was prepared as an account of work sponsored by the United States Government. Neither the United States nor the United States Energy Research & Development Administration, nor any of their employees, nor any of their contractors, subcontractors, or their employees, makes any warranty, express or implied, or assumes any legal liability or responsibility for the accuracy, completeness or usefulness of any information, apparatus, product or process disclosed, or represents that its use would not infringe privately-owned rights."

JRH/gw

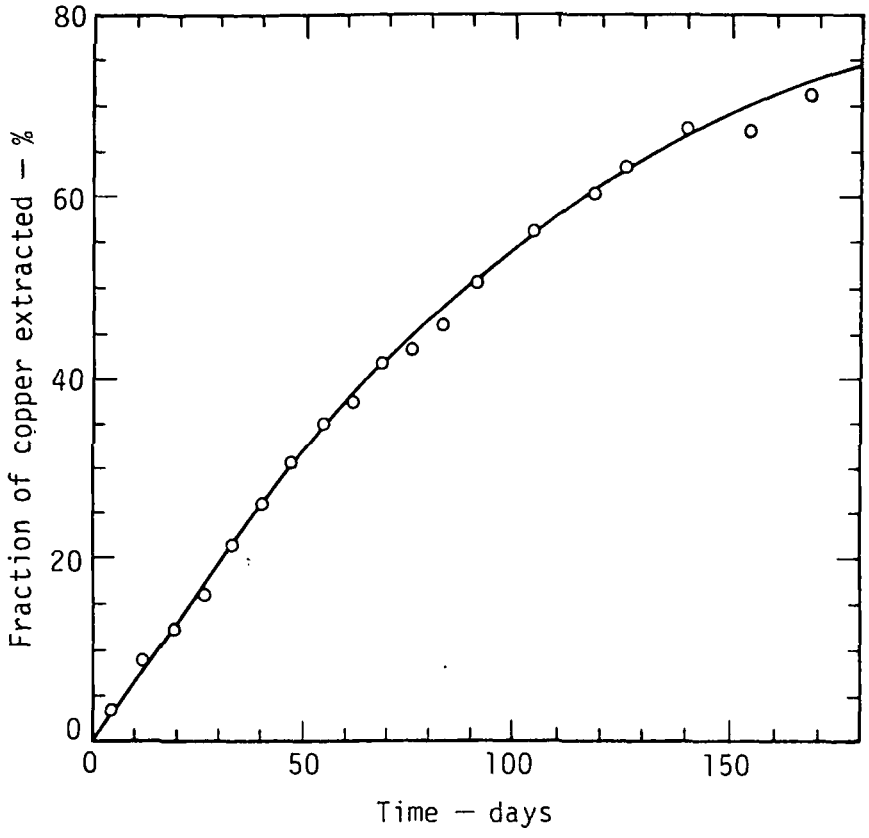
80
60
40
20
0
Fraction of copper extracted – %
0
50
100
150
Time – days

Leach - Fig. 1

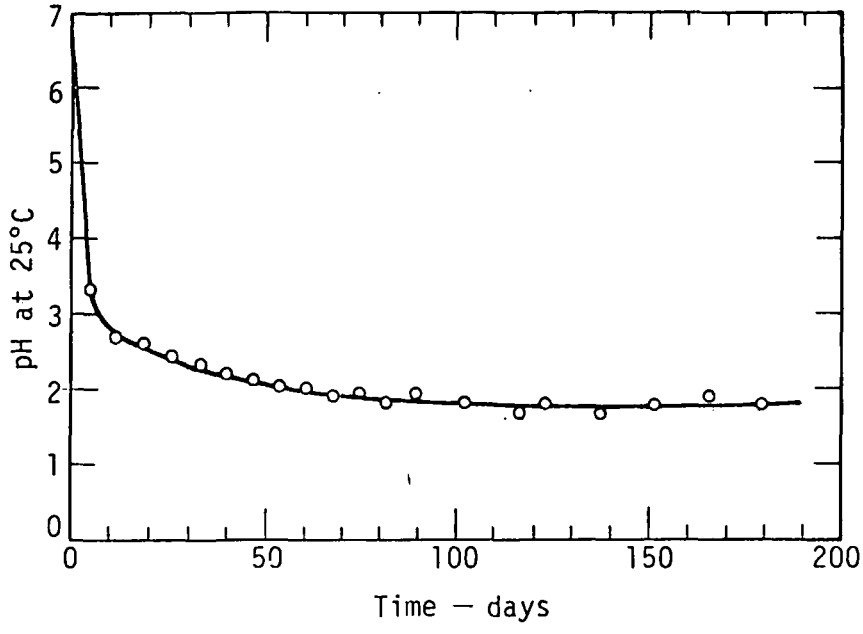

Leach - Fig. 2

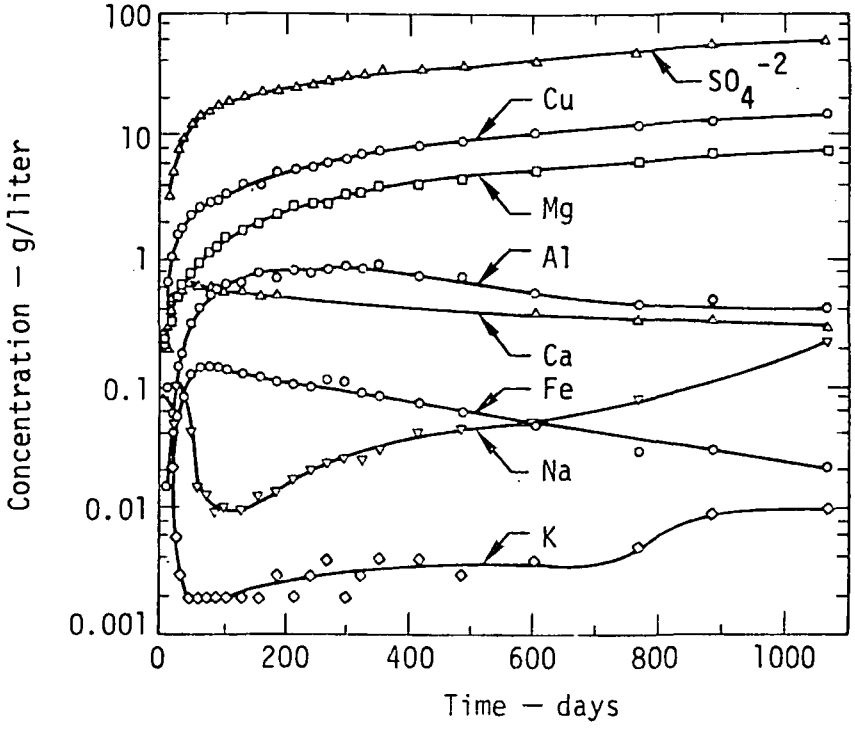
100
10
1
0.1
0.01
0.001
Concentration — g/liter
0
200
400
600
800
1000
Time — days
SO_4^{-2}
Cu
Mg
Al
Ca
Fe
Na
K

Leach - Fig. 3

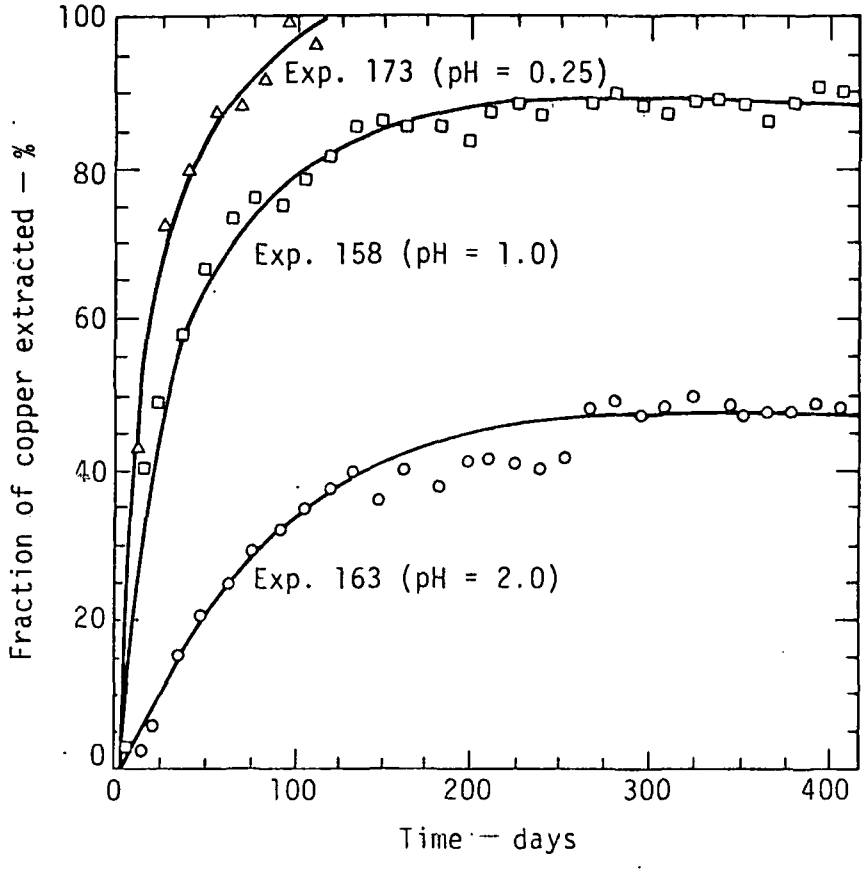
Exp. 173 (pH = 0.25)
Exp. 158 (pH = 1.0)
Exp. 163 (pH = 2.0)
Fraction of copper extracted — %
Time — days
0
20
40
60
80
100
0
100
200
300
400

Leach - Fig. 4

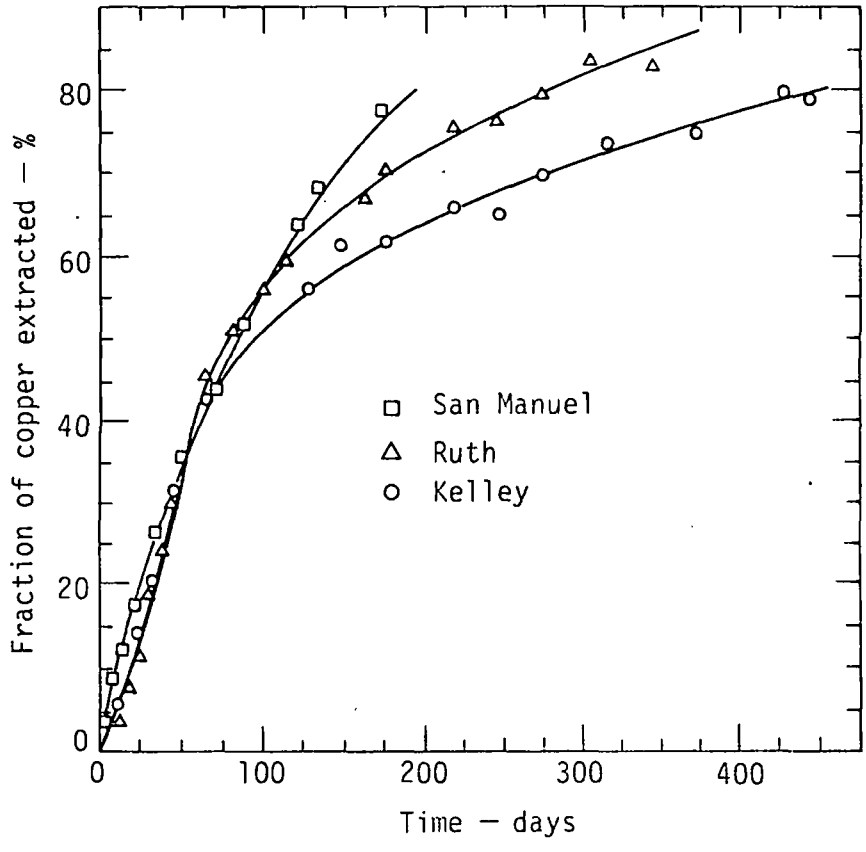
Fraction of copper extracted — %
80
60
40
20
0
0
100
200
300
400
Time — days
San Manuel
Ruth
Kelley

Leach - Fig. 5

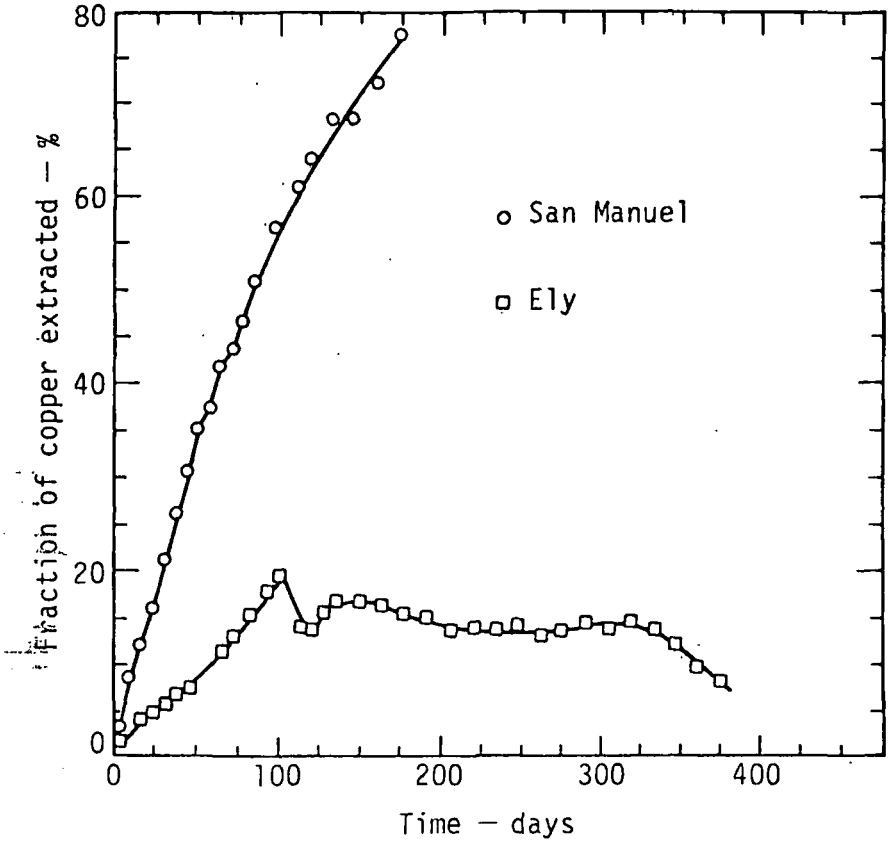
80
60
40
20
0
0
100
200
300
400
Fraction of copper extracted — %
Time — days
San Manuel
Ely

Leach - Fig. 6

UNIVERSITY OF UTAH
RESEARCH INSTITUTE
EARTH SCIENCE LAB.

MATHEMATICAL DESCRIPTION OF THE ALUMINATE SOLUTION DESILICONIZING PROCESS

UDC 669.712.1.001.57

I. Z. Pevzner, A. S. Dvorkin, M. Ya. Fiterman, N. I. Éremin, and Ya. B. Rozen

A great deal of attention has recently been given to the optimization of technological processes using mathematical descriptions. In spite of the abundance of experimental material, a sufficiently complete mathematical model of the aluminate solution desiliconizing process has not been available up to the present. The existing work [1-3] is far from complete and does not extend to all the aspects of this complex process in chemical technology.

Published findings and our own researches are used in the present work as a basis for mathematical description of the physical and chemical processes which take place in the first stage of aluminate solution desiliconizing and involve the evolution of silica from solution in the form of sodium hydroaluminosilicate.

According to [4,5], the process of aluminosilicon complex formation in the solution is in accordance with the following reaction equations:

$$SiO_2(OH)_2^{2-} + AlO_2^- \rightleftarrows [SiAlO_4(OH)_m]^{(1+m)-} + (2-m)OH^-. \quad (1)$$

With an increase in the aluminum ion concentration, new complexes are formed according to the following system:

$$[SiAlO_4(OH)_m]^{(1+m)-} + AlO_2^- \rightarrow [SiAl_2O_6(OH)_m]^{(2+m)-} + AlO_2^- \rightarrow \quad (2)$$
$$\rightarrow [SiAl_3O_8(OH)_m]^{(3+m)-} + AlO_2^- \rightarrow [SiAl_nO_{2(n+1)}(OH)_m]^{(n+m)-}$$

or in total

$$SiO_2(OH)_2^{2-} + nAlO_2^- \rightleftarrows [SiAl_nO_{2(n+1)}(OH)_m]^{(n+m)-} + (2-m)OH^-. \quad (3)$$

where n = 1, 2, 3, 4.

The formation of sodium hydroaluminosilicate from these complexes can be described by the following reaction equation:

$$2[SiAl_nO_{2(n+1)}(OH)_m]^{(n+m)-} + 2Na^+ + xAl_2O \rightleftarrows (Na_2O \cdot Al_2O_3 \cdot 2SiO_2 \cdot x\,H_2O) + 2(n-1) \times AlO_2^- + 2m(OH)^-. \quad (4)$$

The sodium hydroaluminosilicate which forms initially is amorphous in structure; it subsequently crystallizes into a structure which is thermodynamically stable in the given conditions.

We adopt the following well-known propositions and assumptions for the mathematical description of the kinetics of elementary processes in desiliconizing.

1. The kinetics of chemical reaction (4) and the diffusion of aluminosilicon complexes to the surface of the solid phase are the limiting stages in the formation of sodium hydroaluminosilicate.
2. The law of mass action written in concentrations holds good for reactions (3) and (4).
3. The concentration of aluminum and sodium in the liquid phase is much higher than the silica concentration.

The following notations were adopted for the mathematical description: C_{Al}, C_{Na}, C_{OH}, and C_{Si} are the respective concentrations of AlO_2^-, Na^+, OH^-, and $SiO_2(OH)_2^{2-}$ ions in the solution, kmole/m^3; C_{cp} is the concentration of aluminosilicon complexes $[SiAl_nO_{2(n+1)}(OH)_m]^{(n+m)-}$ in the solution, kmole/m^3; C is the solution total silica content, kmole/m^3; C^e is the equilibrium SiO_2 concentration in the $Na_2O - Al_2O_3 - SiO_2 - H_2O$ system, kmole/m^3; C_d is the total silica concentration in the diffusion layer, kmole/m^3; C_{cdp} is the concentration of aluminosilicon complexes $[SiAl_nO_{2(n+1)}(OH)_m]^{(n+m)}$ in the diffusion layer, kmole/m^3; G is the specific amount of solid phase (in a unit of solution volume), kg/m^3; β_p and β_{cp} are the chemical reaction equilibrium constants, kmole/m^3; K_1 and K_2 are the normalized constants for the speed of the sodium hydroaluminosilicate formation reaction, l/sec, m^3/(kmole.sec); K_d is the diffusion speed constant, m/sec; δ is the thickness of the diffusion layer, m; d_e is the sodium hydroaluminosilicate particle equivalent diameter, m; S is the total specific surface of the sodium hydroaluminosilicate particles, 1/m; and ρ is the density of the solid phase, kg/m^3.

The structure of the mathematical model is a system of algebraic and ordinary differential equations, based on the material balances for sodium hydroaluminosilicate, silicon, and the aluminosilicon complexes.

Let us find the relationship between the principal parameters governing formation of aluminosilicon complexes and sodium hydroaluminosilicate in the solution in accordance with the assumed process mechanism.

Formation of Aluminosilicon Complexes. Aluminosilicon complexes are formed in the liquid phase as a result of instantaneous chemical reactions (3). The equilibrium conditions for these reactions will be written in the form

$$\beta_{cp}=\frac{C_{cp}C_{OH}^{2-m}}{C_{Si}C_{Al}^{n}}. \tag{5}$$

The ionic balance can be written as follows, on the basis of the electrical neutrality conditions for the solution:

$$C_{Al}+C_{OH}+2C_{Si}+\sum_{n=1}^{4}(n+m)C_{cp}=C_{Na}.$$

Since C_{Si}, $C_{cp} \ll C_{Al}$, C_{Na} in the solution, the ionic balance will be

$$C_{Al}+C_{OH}\approx C_{Na}$$

or

$$C_{OH}\approx C_{Na}-C_{Al}. \tag{6}$$

The material balance for silica in the liquid phase is shown thus:

$$C_{Si}+\sum_{n=1}^{4}C_{cp}=C;$$

for C_{Si} we obtain

$$C_{Si}=C-\sum_{n=1}^{4}C_{cp}. \tag{7}$$

Then by substituting (7) and (6) into (5) we find

$$\beta_{cp}=\frac{C_{cp}(C_{OH}-C_{Al})^{2-m}}{\left(C-\sum_{i=1}^{4}C_{kl}\right)C_{Al}^{n}}$$

or we obtain the following by way of the caustic modulus $\alpha = C_{Na}/C_{Al}$:

$$\beta_{cp}=\frac{C_{cp}(\alpha-1)^{2-m}}{\left(C-\sum_{i=1}^{4}C_{kl}\right)C^{n-2+m}}. \tag{8}$$

To find C_{cp} (n = 1, 2, 3, 4) from the system of equations we multiply each equation (8) by C_{Al}^{n-2+m} and integrate for n:

$$\sum_{i=1}^{4}\beta_{kl}C_{Al}^{i-2+m}=\frac{(\alpha-1)^{2-m}\sum_{i=1}^{4}C_{kl}}{C-\sum_{i=1}^{4}C_{kl}}.$$

Hence we find

$$\sum_{i=1}^{4}C_{kl}=C\frac{\sum_{i=1}^{4}\beta_{kl}C_{Al}^{i-2+m}}{(\alpha-1)^{2-m}+\sum_{i=1}^{4}\beta_{kl}C_{Al}^{i-2+m}}$$

and obtain the following by substituting into (8):

$$C_{cp}=C\frac{\beta_{cp}C_{Al}^{n-2+m}}{(\alpha-1)^{2-m}+\sum_{i=1}^{4}\beta_{kl}C_{Al}^{i-2+m}}. \tag{9}$$

Formation of Crystalline Sodium Hydroaluminosilicate. Crystalline sodium hydroaluminosilicate is formed as a result of heterogeneous chemical reactions (4), the formation being accompanied by diffusion of aluminosilicon complexes to the particle reaction surfaces.

We find the expressions for the speeds of reactions (4) in accordance with the law of formal kinetics:

speeds of forward reactions ω_{fr_n}:

$$\omega_{fr_n} = K_n C_{cdp}^2 C_{Na}^2; \tag{10}$$

speeds of reverse reactions ω_{rr_n}:

$$\omega_{rr_n} = K_n' C_{Al}^{2(n-1)} C_{OH}^{2m}; \tag{11}$$

resultant reaction speeds ω_{r_n}:

$$\omega_{r_n} = \omega_{fr_n} - \omega_{rr_n} = K_n C_{Na}^2 (C_{cdp}^2 - C_{cp}^{e^2}), \tag{12}$$

where K_n and K_n' are the forward and reverse speed constants of reactions (4) and C_{cp}^e are the equilibrium aluminosilicon complex concentrations obtained from (10) and (11) for $\omega_{fr_n} = \omega_{rr_n}$ and $C_{cdp} = C_{cp}^e$:

$$C_{cp}^e = \beta_n \frac{C_{Al}^{n-1} C_{OH}^m}{C_{Na}}, \tag{13}$$

where

$$\beta_n = \sqrt{\frac{K_n'}{K_n}}.$$

Since expression (9) obviously holds good for the diffusion layer also, C_{cdp} and C_{cp}^e can be obtained from (9) by assuming $C = C_d$ and $C = C^e$ in it respectively. We then obtain the following instead of (12), taking account of ionic balance (6):

$$\omega_{rp} = K_n Z_n^2 (C_d^2 - C^{e^2}), \tag{14}$$

where

$$Z_n = \frac{\beta_{cp} C_{Al}^{n-1+m} \alpha}{(\alpha-1)^{2-m} + \sum_{i=1}^{4} \beta_{ki} C_{Al}^{i-2+m}}.$$

By equating (9) and (13) for $C = C^e$ and $C_{cp} = C_{cp}^e$ we find the expression for the equilibrium concentration of SiO_2 is the system taking account of the ionic balance (6):

$$C^e = \frac{\beta_p}{\beta_{cp}} \frac{(\alpha-1)^2}{\alpha} + \frac{\beta_p}{\beta_{cp}} \frac{(\alpha-1)^2}{\alpha} \sum_{i=1}^{4} \beta_{ki} C_{Al}^{i-2+m}.$$

It follows from this expression that

$$\frac{\beta_p}{\beta_{cp}} = \text{const} = \beta,$$

therefore

$$C^e = \beta \frac{(\alpha-1)^2}{\alpha} \left[(\alpha-1)^{2-m} + \sum_{i=1}^{4} \beta_{ki} C_{Al}^{i-2+m} \right]. \tag{15}$$

Having regard to the fact that the total speed of the reverse reactions of sodium hydroaluminosilicate solution is determined mainly by the driving force $C_d^2 - C^{e2}$ [see equation (14)], it may be regarded as independent of C_{Al} and α, i.e., it is possible to assume $\sum_{i=1}^{4} K_i Z_i^2 = \text{const} = K$; then we find the total resultant speed of sodium hydroaluminosilicate formation ω_r by integrating (14) for n = 1, 2, 3, 4:

$$\omega_r = \sum_{i=1}^{4} \omega_{pi} = K(C_d^2 - C^{e^2}). \tag{16}$$

We can now compile instantaneous material balances for SiO_2 in the body of the solution and in the diffusion layer. Assuming, as is customary, that the speed of diffusion is proportional to the drop in concentrations on the diffusion region boundaries we have:

the balance in the body of the solution

$$\frac{dC}{dt} = -K_d(C - C_d)S; \quad (17)$$

the balance in the diffusion region, taking account of the fact that the volume of the diffusion layer for all particles is $S\delta V$

$$\delta\frac{dC_d}{dt} = K_d(C - C_d) - K(C_d^2 - C^{e_2}),$$

or, after dividing by δ

$$\frac{dC_d}{dt} = K_1(C - C_d) - K_2(C_d^2 - C^{e_2}). \quad (18)$$

It is convenient to express the specific surface S of the particles in terms of the concentration G and the equivalent diameter d_e of the solid phase particles. We have

$$S = S_1N, \quad G = V_1\rho N,$$

where S_1 and V_1 are the surface and the volume of one particle and N is the concentration of the solid phase part.

The total specific surface of the sodium hydroaluminosilicate is

$$S = \frac{S_1}{V_1}\frac{G}{\rho},$$

or, expressing S_1/V_1 in terms of the equivalent particle diameter d_e

$$\frac{S_1}{V_1} = \frac{6\pi d_e^2}{\pi d_e^3} = \frac{6}{d_e},$$

we obtain

$$S = \frac{6G}{\rho d_e}. \quad (19)$$

Equations (15), (17), and (18) taking account of (19) form a complete mathematical model of the aluminate solution desiliconizing process.

Table 1
File of Experimental Values of C^e, $C_{Al_2O_3}$, and α (T = 98° C)

α	$C_{Al_2O_3}$, kg/m³				
	80	100	120	140	160
1,75	0,30	0,35	0,44	0,63	0,80
2,00	0,29	0,38	0,54	0,73	0,84
2,25	0,32	0,41	0,56	0,84	0,94
2,50	0,32	0,44	0,64	0,86	1,01

Note: The data are averaged from four series of parallel experiments.

Identification of the Mathematical Model. The unknowns in the mathematical model are the equilibrium constants β, β_n (n = 1, 2, 3, 4), the diffusion speed constant K_d and chemical reaction speed constants K_1 and K_2, and also the stoichiometric integral coefficient m in the formula for the complex aluminosilicon ions. The coefficients enumerated were found by identification of the mathematical model, the equilibrium constants β and β_n and coefficient m being found by statistical processing of the equilibrium states of the system $Na_2O - Al_2O_3 - SiO_2 - H_2O$ according to formula (15) and constants K_d, K_1, and K_2 by statistical processing of the kinetics in that system according to equations (17) and (18). The file of experimental values of C^e, C_{Al}, and α obtained in experiments with 100 - 170-hr desiliconizing of synthetic solutions is given in Table 1.

Table 2
File of Experimental Values of C(t), G, and d_e (T = 98° C, $C_{Al_2O_3}$ = 120 g/liter, α = 1.8)

t, min.	C, kg/m³.		
	G=20 kg/m³; d_e=50 μm	G=40 kg/m³; d_e=65 μm	G=60 kg/m³; d_e=55 μm
0	3,63	3,61	3,62
10	3,45	3,30	3,30
30	3,00	2,44	2,40
60	2,40	1,65	1,40
90	1,80	1,15	1,00
120	1,41	0,90	0,73
150	1,00	0,65	0,55
180	0,85	0,60	0,54
240	0,85	0,49	0,47
360	0,60	0,50	0,48
480	0,52	0,45	0,44

Note: The data are averaged from four series of parallel experiments

The total specific surface of the sodium hydroaluminosilicate is

$$S = \frac{S_1}{V_1}\frac{G}{\rho},$$

or, expressing S_1/V_1 in terms of the equivalent particle diameter d_e

$$\frac{S_1}{V_1} = \frac{6\pi d_e^2}{\pi d_e^3} = \frac{6}{d_e},$$

we obtain

$$S = \frac{6G}{\rho d_e}. \quad (19)$$

Equations (15), (17), and (18) taking account of (19) form a complete mathematical model of the aluminate solution desiliconizing process.

Identification of the Mathematical Model. The unknowns in the mathematical model are the equilibrium constants β, β_n (n = 1, 2, 3, 4), the diffusion speed constant K_d and chemical reaction speed constants K_1 and K_2, and also the stoichiometric integral coefficient m in the formula for the complex aluminosilicon ions. The coefficients enumerated were found by identification of the mathematical model, the equilibrium constants β and β_n and coefficient m being found by statistical processing of the equilibrium states of the system $Na_2O - Al_2O_3 - SiO_2 - H_2O$ according to formula (15) and constants K_d, K_1, and K_2 by statistical processing of the kinetics in that system according to equations (17) and (18). The file of experimental values of C^e, C_{Al}, and α obtained in experiments with 100 - 170-hr desiliconizing of synthetic solutions is given in Table 1.

The file of experimental values of C(t) obtained in 8-hr kinetic experiments on desiliconizing synthetic aluminate solutions with addition of solid phase in the form of slime from Turgaisk bauxite leaching is given in Table 2.

Expression (15) was equalized as follows:

$$Y = \beta + aX,$$

where

$$Y = \frac{C^e\alpha}{(\alpha-1)^2}; \quad X = (\alpha-1)^{m-2}; \quad a = \sum_{i=1}^{4}\beta_i C_{Al}^{i-2+m}.$$

The file of experimental values of C^e and α for C_{Al} = const (and consequently a = const) was then plotted in a Y-X system of coordinates for various values of m (see Fig.). It is apparent from the Figure that the optimum value of m = 1.

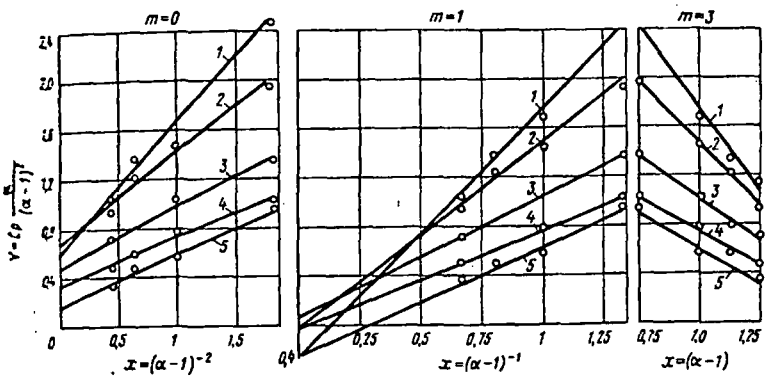

Finding coefficient m for the following Al_2O_3 contents, g/liter: 1) 160; 2) 140; 3) 120; 4) 100; 5) 80.

The values of equilibrium constants β and β_n were found in the next stage of identification in the equilibrium state. Two of the β_n constants were left in (β_1 and β_3 proved to be the most suitable for this), because the accuracy of the experiments did not permit reliable determination of all four of the β_n constants (n = 1, 2, 3, 4) in equation (15).

Expression (15) was equalized as follows:

$$Y=\beta X_1+\beta_1+\beta_3 X_2, \qquad (20)$$

where

$$Y=\frac{Ce\,\alpha}{\alpha-1};\quad X_1=\alpha-1;\quad X_2=C_{Al}^2.$$

Statistical processing of formula (20) gave the following result: β = 0; β_1 = 0.224×10^{-2} kmole/m^3; β_3 = 0.293×10^{-2} kmole/m^3; the maximum relative error in formula (15) was 7.2% and the mean-square error was 5%.

The zero value of coefficient β, which is equal to β_n/β_{cp} according to the notation, provides practical evidence of the high values of the β_{cp} equilibrium constants, i.e., of the fact that almost all of the silica in the solution is present in the form of aluminosilicon complexes. This is also confirmed by the published findings [4].

After identification, formula (15 takes the following form:

$$Ce=\frac{\alpha-1}{\alpha}(0{,}224\cdot10^{-2}+0{,}293\cdot10^{-2}C_{Al}^2). \qquad (21)$$

The kinetic constants K_d, K_1, and K_2 were found by the method of least squares by minimizing the sum of the squares of the deviations of SiO_2 concentration experimental values from the calculated values:

$$K_d = 0.251 \times 10^{-6} \text{ m/sec};\ K_1 = 0.606 \times 10^{-4} \text{ 1/sec};$$
$$K_2 = 0.166 \times 10^{-10} \text{ m}^3/(\text{kmole.sec}).$$

The mean-square error of formulas (17) and (18) is 5.4%.

Thus the mathematical model obtained may be regarded as adequate for the physical and chemical processes which take place during desiliconizing of aluminate solutions.

REFERENCES

1. S. I. Kuznetsov, V. A. Derevyankin, I. P. Kraus, and T. P. Porotnikova. In the book: Theory and Practice of Desiliconizing Aluminate Solutions. Moscow. Tsvetmetinformatsiya, 1971, pp. 42-47.
2. N. F. Balabai, A. Ashimov, and V. D. Ponomarev. Theory and Technology of Alumina Production. No. 35. Alma-Ata, IMO AN KazSSR, 1969, pp. 23-25.
3. N. F. Pecherskaya and L. P. Ni. New Processes in Alumina Production. No. 47. Alma-Ata, IMO Kaz SSR, 1972, pp. 34-37.
4. I. Z. Pevzner, N. I. Eremin, Ya. B. Rozen, et al. ZhPKh, 1974, vol. 47, No. 12, pp. 2758-2760.
5. I. Z. Pevzner, A. S. Dvorkin, M. Ya. Fiterman, and Ya. B. Rozen. Alumina Production. Collection No. 85, Leningrad, VAMI, 1974, pp. 61-65.
6. I. Z. Pevzner, A. S. Dvorkin, M. Ya. Fiterman, et al. In the book: Materials of the Vth Anniversary Scientific-Technical Session of MISiS Dedicated to the 50th Anniversary of the USSR. Moscow, MISiS, 1972, pp. 159-160.

1977 v.18 N6

SUBJ
MNG
MDFD

UNIVERSITY OF UTAH RESEARCH INSTITUTE EARTH SCIENCE LAB.

MATHEMATICAL DESCRIPTION OF A FULL DESILICONIZING PROCESS FOR ALUMINATE SOLUTIONS

UDC 669.712.034

I. Z. Pevzner, Ya. B. Rozen, M. Ya. Fiterman, and N. I. Eremin

After the first stage of desiliconization, aluminate solutions contain silica at a level close to the equilibrium concentration for SiO_2 in the $Na_2O-Al_2O_3-SiO_2-H_2O$ system. This level of SiO_2 removal from the solutions proves to be insufficient to obtain high-grade aluminum hydroxide in alumina production by the sintering method. The level of desiliconization is raised by making the silica in the solution combine to form hydrogarnet, a compound which is less soluble than sodium hydroaluminosilicate.

Hydrogarnet is formed as a result of chemical reactions between lime and aluminate solution containing silica. Its composition is expressed by the formula $3CaO \cdot Al_2O_3 \cdot xSiO_2 (6 - 2x)H_2O$. The formation of this compound can be expressed as follows.

According to [1, 2], silica is present in aluminate solutions as two compounds: the simple ion $SiO_2(OH)_2^{2-}$ and alumosilicon complexes $[SiAl_nO_{2(n+1)}(OH)_m]^{(m+n)-}$, n = = 1, 2, 3, 4, which are formed by the following reaction:

$$SiO_2(OH)_2^{2-} + nAlO_2^- \rightleftharpoons [SiAl_nO_{2(n+1)}(OH)_m]^{(m+n)-} + (2-m)OH^- \quad (1)$$

When lime reacts with the aluminate solution, tricalcium hydroaluminate forms first according to the following reaction equation:

$$3Ca^{2+} + 2AlO_2^- + 4OH^- + 4H_2O \rightleftharpoons 3CaO \cdot Al_2O_3 \cdot 6H_2O. \quad (2)$$

The latter reacts with silica in the solution, forming hydrogarnets by the following reaction:

$$3CaO \cdot Al_2O_3 \cdot 6H_2O + xSiO_2(OH)^{2-} \rightleftharpoons 3CaO \cdot Al_2O_3 \cdot xSiO_2 \cdot (6-2x)H_2O + 2xOH^- + 2xH_2O. \quad (3)$$

Formation of hydrogarnet by this reactions shifts the equilibrium of Reaction (1) toward breakdown of the alumosilicon complexes, which do not participate directly in hydrogarnet formation.

In accordance with heterogeneous reaction (3), the formation of hydrogarnets on the phase interface must be accompanied by diffusion of $SiO_2(OH)_2^{2-}$ in the liquid phase. Apart from liquid-phase diffusion there is solid-phase diffusion, causing particle saturation with silica X which decreases steadily in depth .

From the mathematical viewpoint, the formation of particles with a degree of silica saturation variable in depth is equivalent to the formation of a hydrogarnet layer of finite thickness with a constant degree of saturation with silica X around particles of tricalcium aluminate.

Thus, it may be assumed that solid-phase diffusion takes the form of growth of the hydrogarnet layer into the particles of tricalcium hydroaluminate.

According to [3], the kinetics of full desiliconization in the initial stage can be satisfactorily explained by the laws of chemical kinetics; it then apparently passes into the solid-phase diffusion region as the tricalcium hydroaluminate becomes saturated with silica. Differential equations for transfer of a substance with a discontinuous right-hand side are mathematically adequate for this physical model of the hydrogarnet formation process.

Thus, the structure of the mathematical model of physico-chemical reactions in full desiliconization takes the form of a material balance equation and differential transfer equations witha piecelike smooth right-hand side, as well as geometric relationships to describe the interface of the solid and liquid phases.

The following assumptions were made for mathematical description of the physical model formulated for full desiliconizing processes.

1. Formation of the complex alumosilicon ions (1) and tricalcium hydroaluminate (2) is instantaneous.
2. The law of mass action in concentration form is applicable to all the reactions.
3. The tricalcium hydroaluminate particles which form as a result of the chemical reaction between lime and aluminate solution are spherical in shape and with an identical diameter constant in time,
4. The diffusion layer is a thin globular layer adjacent to the particle outer surface, having an identical concentration gradient for all particle and a thickness variable in time.

The following symbols were adopted for the mathematical description:

C_{Al}, the concentration of AlO_2^- ions in the solution, kmoles/m^3;
ΔC_{Al}, losses of aluminum with tricalcium hydroaluminate, kmoles/m^3;
C_{Na}, the concentration of Na^+ ions in the solution, kmoles/m^3;
C_{Si}, the concentration of $SiO_2(OH)_2^{2-}$ ions in the solution, kmoles/m^3
C_{Si}^e, the equilibrium concentration of $SiO_2(OH)_2^{2-}$ in the $Na_2O-Al_2O_3-SiO_2-H_2O$ system kmoles/m^3;

C_c, the concentration of alumosilicon complexes $[SiAl_nO_2(n+1)(OH)m]^{(m+n)-}$ in the solution, kmoles/m³;
C, the solution total SiO_2 content, kmoles/m³;
Ce, the equilibrium SiO_2 concentration in the $Na_2O-Al_2O_3-SiO_2-H_2O$ system, kmoles/m³;
C_{Ca}, the concentration of Ca^{2+} ions in the solution, kmoles/m³;
C_{OH}, the concentration of OH^- ions in the solution, kmoles/m³;
G_{3CAl}, the specific amount (concentration) of tricalcium hydroaluminate $3CaO \cdot Al_2O_3 \cdot 6H_2O$ in a unit of solution volume, kmoles/m³;
G_h, the specific amount of hydrogarnet $3CaO \cdot Al_2O_3 \cdot xSiO_2 (6-2x)H_2O$;
D, the diffusion coefficient, m²/sec;
δ, the thickness of the diffusion layer, m;
d, the particle diameter, m;
N, the particle concentration, 1/m³;
β, the equilibrium constant of chemical reaction (3);
$\alpha = C_{Na}/C_{Al}$, the aluminate solution ratio;
μ_{3CA}, μ_h, the molecular masses of tricalcium hydroaluminate and hydrogarnet, kg/(kmole);
ρ_{3CAl}, ρ_h, the densities of tricalcium hydroaluminate and hydrogarnet, kg/m³.

Mathematical Model of Elementary Processes

In the initial stage, the process of full desiliconization is governed by the speed of chemical reaction (3), which according to [3] is of the second order:

$$w_e = K(C_{Si} - C_{Si}^e)^2,$$

where K is the chemical reaction speed constant.

According to Fick's equation, the speed of diffusion $SiO_2(OH)_2^{2+}$ ions through the layer of hydrogarnet which forms is:

$$w_d = \frac{D}{\delta}(C_{Si} - C_{Si}^e).$$

We will assume the point at which the speeds of the chemical reaction and of diffusion are equal to be the points of transition τ from the kinetic region to the diffusion region:

$$K[C_{Si}(\tau) - C_{Si}^e]^2 = \frac{D}{\delta(\tau)}[C_{Si}(\tau) - C_{Si}^e]$$

or

$$[C_{Si}(\tau) - C_{Si}^e]\delta(\tau) = \frac{D}{K}. \quad (4)$$

Having regard to what has been said, it follows from the material balance for $SiO_2(OH)_2^{2-}$ in the solution that

$$\frac{dC_{Si}}{dt} = \begin{cases} -w_e \pi d^2 N \text{ where } t < \tau; \\ -w_d \pi d^2 N \text{ where } t > \tau \end{cases}$$

or, by substituting the w_e and w_d values:

$$\frac{dC_{Si}}{dt} = \begin{cases} -K\pi d^2 N (C_{Si} - C_{Si}^e)^2 \text{ where } t < \tau; \\ -\frac{D}{\delta}\pi d^2 N (C_{Si} - C_{Si}^e) \text{ where } t > \tau. \end{cases} \quad (5)$$

According to [4], the relationship between the total concentration of silica and the concentration of silicon ions in the solution can be expressed by the following equation:

$$C_{Si} = C - \frac{\alpha - 1}{\alpha - 1 + \sum_{i=1}^{4} \beta_{ki} C_{Al}^{i-1}}. \quad (6)$$

where β_{ki} are the stability constants of the corresponding alumosilicon complexes.

In the equilibrium state ($t \to \infty$), taking the ionic balance into account

$$C_{Al} + C_{OH} \approx C_{Na}$$

we obtain, from Reaction (3)

$$\beta^z = \frac{(C_{Si}^e)^z}{(C_{Na} - C_{Al})^{2z}}. \quad (7)$$

We obtain the following from Equations (6) and (7) for the equilibrium state of the system (where $t \to \infty$):

$$C^e = (\alpha - 1) C_{Al}^2 \left[\beta(\alpha - 1) + \sum_{i=1}^{4} \beta_i C_{Al}^{i-1}\right], \quad (8)$$

where $\beta_i = \beta\beta_{ki}$.

We then find the relationship between the geometric characteristics of the particles d and δ and the concentrations of the solids formed G_{3CAl} and G_h. Taking into account (see paragraphs 3 and 4 of the assumption) that the particle volume is $1/6\pi d^3$ and the volume of the globular hydrogarnet layer is $\pi d^2 \delta$, we may write

$$\frac{1}{6}\pi d^3 N = \frac{G_{3CAl}\mu_{3CAl}}{\rho_{3CAl}}, \quad \pi d^2 \delta N = \frac{G_h \mu_h}{\rho_h}.$$

Hence,

$$N = \frac{6G_{3CAl}\mu_{3CAl}}{\pi d^3 \rho_{3CAl}},$$

$$\delta = \frac{G_h \mu_h \rho_{3CAl} d}{6 G_{3CAl} \mu_{3CAl} \rho_h}. \quad (9)$$

The concentrations G_{3CAl} and G_h of the solids can be found from the material balances. According to equation (2), we have:

$$G_{3CAl} = \frac{1}{3} C_{Ca}. \quad (10)$$

Similarly according to the equation for reaction (3) we have

$$G_h = \frac{C_{Si}(0) - C_{Si}}{x}. \quad (11)$$

Using relationships (6)-(11), we write differential equation (5) relative to the total silica concentrations in solution C in explicit form:

$$\frac{dC}{dt} = -K_1 \frac{(\alpha-1)^3 C_{Al}^2 C_{Ca}}{C^e}(C - C^e), \text{ where } t < \tau; \qquad \frac{dC}{dt} = -K_2 \frac{C^e C_{Ca}^2}{C_{Al}^2(\alpha-1)^3} \frac{C - C^e}{C(0) - C} \text{ where } t > \tau, \quad (12)$$

where

$$K_1 = \frac{2K\beta\mu_{3CAl}}{d\beta_{3CAl}}; \qquad K_2 = \frac{D\rho h x}{\beta \mu_h} \left(\frac{2\mu_{3CAl}}{d\rho_{3CAl}}\right)^2.$$

The expression for determining τ is obtained from equations (4) or (12) and is as follows, taking into account the symbols which have been introduced:

$$[C(\tau) - C^e][C(0) - C(\tau)] = \frac{K_2}{K_1} \frac{(C^e)^2 C_{Ca}}{(\alpha-1)^4 C_{Al}^4}. \quad (13)$$

Finally, the losses of aluminum ΔC_{Al} with the tricalcium hydroaluminate which forms are governed by the amount of lime added and are as follows, in accordance with the equation for reaction (2):

$$\Delta C_{Al} = \frac{2}{3} C_{Ca}. \quad (14)$$

Thus, the mathematical model for elementary processes in full desiliconizing takes the following form:

(15a)

$$\frac{dC}{dt} = -K_1 (C - C^e)^2 \frac{(\alpha-1)^2 C_{Al}^2 C_{Ca}}{C^e} \text{ where } t < \tau; \qquad \frac{dC}{dt} = -K_2 \frac{C - C^e}{C(0) - C} \frac{C^e C_{Ca}^2}{C_{Al}^2 (\alpha-1)^3} \text{ where } t > \tau;$$

$$[C(\tau) - C^e][C(0) - C(\tau)] = \frac{K_2}{K_1} \frac{(C^e)^2 C_{Ca}}{(\alpha-1)^4 C_{Al}^4};$$

$$C^e = (\alpha-1) C_{Al}^2 \times \left[\beta(\alpha-1) + \sum_{i=1}^{4} \beta_i C_{Al}^{i-1}\right];$$

$$\Delta C_{Al} = \frac{2}{3} C_{Ca}.$$

Identification of Mathematical Model

The undefined coefficients in mathematical model (15) are K_1, K_2, β, and βi. Only β and β_i affect the equilibrium state of the process; these can be found from equation (15c) by identification according to the results of experiments in the equilibrium state.

Coefficients K_1 and K_2 reflect the kinetics of the process and can be found by identification of the mathematical model according to the results of experiments on the kinetics of full desiliconizing with the β and β_i values which have been found.

The methods and results of the experiments on full desiliconizing have been set out in detail in [5].

The substantial error in measuring the SiO_2 concentration at values less than 0.1 kg/m^3 prevents reliable determination of β and β_i, which prove to be close to zero within the limits of error.

$$C^e = 0, \quad (16)$$

is therefore adopted, and $K_2 C^e$ in formula (15a) is replaced by K'_2:

$$K_2 C^e = K_2 = \text{const}. \quad (17)$$

Statistical treatment of equation (15a) then revealed that the kinetics of full desiliconizing were well described by one equation (15a) for $t > \tau$ in the entire range of time $t > 0$:

$$\frac{dC}{dt} = -\frac{K_2 C_{Ca}^2}{C_{Al}^2 (\alpha-1)^3} \frac{C}{C(0) - C}. \quad (18)$$

Consequently, the process of full desiliconzing is limited by the diffusion stage. To find K_2', equation (18) was balanced by the following replacement of variables:

$$X = \frac{1}{C}; \quad X_0 = \frac{1}{C(0)}. \tag{19}$$

In these variables, we have

$$\frac{dX}{dt} = K\frac{X^2 X_0}{X - X_0},$$

where

$$K = \frac{K_2' C_{Ca}^2}{C_{Al}^2 (\alpha - 1)^2},$$

and by integrating, we obtain:

$$\frac{1}{X_0}\ln\frac{X}{X_0} + \frac{1}{X} - \frac{1}{X_0} = Kt. \tag{20}$$

Consequently, it is necessary to take the following to balance (20):

$$Y = C(0)\ln\frac{C(0)}{C} + C - C(0). \tag{21}$$

We then have the following instead of (20):

$$Y(t) = K_2'\frac{C_{Ca}^2}{C_{Al}^2(\alpha - 1)^2}t. \tag{22}$$

Identification of equation (22) by the least-squares method gives the following value for K_2:

$$K_2' = 2{,}71 \cdot 10^{-6} \text{ kmoles/(m}^3\text{.sec)} \tag{23}$$

with a mean square error of 10%.

Thus, the identified mathematical model of full desiliconizing takes the following form:

$$\frac{dC}{dt} = -2{,}71 \cdot 10^{-6}\frac{C_{Ca}^2}{C_{Al}^2(\alpha - 1)^2}\frac{C}{C(0) - C}; \tag{24a}$$

$$\Delta C_{Al} = \frac{2}{3}C_{Ca}. \tag{24b}$$

The equations from the mathematical model of full desiliconizing have been used with equations from the mathematical model for desiliconizing stage I [4] for optimizing the standard process of two-stage desiliconizing of aluminate solutions without autoclaves [5].

REFERENCES

1. I. Z. Pevzner, N. I. Eremin, Ya. B. Rozen, et al, Zh. Prikl. Khim., 1974, 47, No. 12, 2758-2760.
2. I. Z. Pevzner, A. S. Dvorkin, M. Ya. Fiterman, and Ya. B. Rozen, Alumina Production, Collection 85, Leningrad, VAMI, 1974, 61-65.
3. I. Z. Pevzner and A. I. Lainer, Tsvetnye Metally, 1970, No. 9, 48-51.
4. I. Z. Pevzner, A. S. Dvorkin, M. Ya. Fiterman, and Ya. B. Rozen, Tsvetnye Metally, 1975, No. 7, 49-52.
5. Collected Abstracts of Research, All-Union Scientific Information Center, Series 09, No. 17, 1974, 22 (B355486).

ESL
UNIVERSITY OF UTAH
RESEARCH INSTITUTE
EARTH SCIENCE LAB.

SUBJ
MNG
MDL

A Model of the Dump Leaching Process that Incorporates Oxygen Balance, Heat Balance, and Air Convection

L. M. CATHLES AND J. A. APPS

A one dimensional, nonsteady-state model of the copper waste dump leaching process has been developed which incorporates both chemistry and physics. The model is based upon three equations relating oxygen balance, heat balance, and air convection. It assumes that the dump is composed of an aggregate of rock particles containing nonsulfide copper minerals and the sulfides, chalcopyrite and pyrite. Leaching occurs through chemical and diffusion controlled processes in which pyrite and chalcopyrite are oxidized by ferric ions in the lixiviant. Oxygen, the primary oxidant, is transported into the dump by means of air convection and oxidizes ferrous ion through bacterial catalysis. The heat generated by the oxidation of the sulfides promotes air convection. The model was used to simulate the leaching of copper from a small test dump, and excellent agreement with field measurements was obtained. The model predicts that the most important variables affecting copper recovery from the test dump are dump height, pyrite concentration, copper grade, and lixiviant application rate.

THE leaching of low-grade copper-bearing waste has been practiced either by accident or through design for several hundred years. During the last fifty years, increasing attention has been paid to the systematic leaching of low-grade waste resulting from the open pit mining of porphyry copper deposits in the western United States. By now, this activity is yielding an important secondary source of domestic copper.[1] Indeed, some mining operations have been planned and are operating exclusively from the production of copper obtained from leaching. Many of these operations are exploiting oxide copper deposits where copper is readily leached by the application of dilute sulfuric acid.

Low-grade waste discarded as a result of open pit mining of porphyry copper deposits is dumped in gullies surrounding the deposit. The disposal site is determined primarily by the convenience of the site to the mining operation, and is not usually based on considerations necessary for optimum leaching. In the western United States several billion tons of waste has accumulated in this manner.

During the last decade, many people have become conscious of the fact that this enormous resource of copper is not being exploited effectively because insufficient attention is being paid to those factors which could lead to improved design and layout of waste dumps. It is believed that if the leaching process were completely understood, then it would be possible to design and leach copper from waste dumps in a far more efficient manner than is currently being practiced. The problem is a large one. Not only must the chemistry of leaching be understood, including both kinetic and thermodynamic aspects, but the effect of heat generation, fluid flow and other transport phenomena relating to the leaching process must also be considered. A leaching system cannot be considered in a steady state, because all factors involved in the leaching process change progressively as a function of time.

In this paper we have developed a one-dimensional model of the nonsteady-state dump leaching system. We have applied this model to a small test dump constructed and leached at the Utah Copper Division of Kennecott Copper Corporation. To our knowledge only two other attempts have been made to integrate the diverse aspects of dump leaching into a coherent all-embracing model.[2,3] While we do not feel that the model presented in this paper is the final answer to a clarification of the dump leaching process, we believe that it forms a basis upon which subsequent research in this area might be coordinated.

A MODEL OF THE DUMP LEACHING PROCESS

Initial Assumptions

Sulfides must be oxidized before their metal values may be put into solution. The conceptual basis of the model of dump leaching presented here is simply that the exothermic sulfide oxidation reactions generate heat and consume oxygen from the air, and by so doing drive air convection through the dump. This air convection is the only significant source of oxidant to the dump.

A system is envisioned in which a countercurrent interlocking flow of air and water passes through an aggregate of rock fragments, as shown in Fig. 1.

The oxygen leaves the gas phase within the dump by dissolving in the liquid phase where it oxidizes ferrous to ferric iron through the agency of bacteria. The ferric iron diffuses into the ore fragments and

L. M. CATHLES is a senior geophysicist at the Ledgemont Laboratory, Kennecott Copper Corporation, Lexington, Massachusetts. J. A. APPS, formerly a scientist at the Metal Mining Division Research Center, Kennecott Copper Corporation, Salt Lake City, Utah, is now staff scientist, Energy and Environment Division, Lawrence Berkeley Laboratory, University of California, Berkeley, California.

Manuscript submitted February 5, 1975.

oxidizes the sulfide minerals:* Acid, Fe^{++} and heat are produced along with Cu^{++}.

*At 1/5 atmosphere P_{O_2} and the temperatures involved in dump leaching, oxygen is not very soluble in water ($<8.6 \times 10^{-3}$ g/l). Typical ferric iron concentrations in leach dumps run ~1 g/l. These relative concentrations ensure Fe^{+++} will be the oxidizing agent in the diffusion controlled processes envisioned above.

For the purposes of our model, we have assumed the formation of a leached rim which is separated from the unreacted core by a sharp boundary, as shown in Fig. 2. As the leached rim grows the rate of leaching drops because of longer diffusion paths and a shrinking reaction zone. Evidence for a shrinking core has been supported observationally by Braun, Lewis and Wadsworth[4] and by Madsen, Wadsworth and Groves.[5] Theoretical arguments also support the existence of a sharp boundary for the conditions of our model (see Eq. [11]). For those reasons we will later employ the mathematical formulation of the so called "shrinking core model", as developed by Braun, Lewis and Wadsworth. However, we recognize that there are many conditions in which a sharp boundary between the leached rim and the unreacted core boundary is not observed because of variable reaction rates of the sulfides, acid gangue interaction, sulfide concentration, grain size of sulfides and gangue minerals, and porosity of the rock. A generalized model, taking account of several of these factors has been developed by Bartlett.[6]

Most low-grade waste, from which copper is leached, is derived from the outer pyritic halo of porphyry copper deposits, where the copper-bearing sulfide is chalcopyrite.[7] We assume that chalcopyrite and pyrite are the principal sulfide minerals and that they oxidize in a waste dump environment in the following manner:

$$O_2^l + \tfrac{2}{5}\,CuFeS_2 + \tfrac{2}{5}\,(2H^+ + SO_4^{--}) \rightarrow \tfrac{2}{5}\,(Cu^{++} + SO_4^{--}) + \tfrac{2}{5}\,(Fe^{++} + SO_4^{--}) + \tfrac{2}{5}\,H_2O + \tfrac{2}{5}\,S \qquad [1]$$

$$O_2^l + \tfrac{2}{7}\,FeS_2 + \tfrac{2}{7}\,H_2O \rightarrow \tfrac{2}{7}\,(Fe^{++} + SO_4^{--}) + \tfrac{2}{7}\,(2H^+ + SO_4^{--}). \qquad [2]$$

Evidence that these are the oxidation mechanisms for the two sulfides comes from studies by Wadsworth.[8] Observations by Stephens[9] show that sulfur is a product of the oxidation of sulfides in waste dumps. It can be seen that for every mole (64 g) of chalcopyrite leached, 5/2 mole (5/2 · 32 g) of oxygen will be consumed. If FPY moles of pyrite are leached per mole of sulfide copper, an additional 7/2 FPY moles (7/2 · 32 · FPY g) of O_2 will be consumed. Thus for every gram of chalcopyrite copper leached, the following number of grams of O_2 will be consumed:

$$g\ O_2\ \text{consumed} = (1.25 + 1.75\,FPY)\ g\ \frac{\text{chalcopyrite}}{\text{Cu leached}} \qquad [3]$$

Actually the amount of oxygen consumed per gram of chalcopyrite copper leached is somewhat greater than this, if account is taken of the oxidant required to precipitate, as jarosite ($KFe_3(SO_4)_2(OH)_6$), the iron exchanged for copper during cementation (2.5 lb Fe/lb Cu) and the iron produced in leaching the chalcopyrite and pyrite. The precipitation of cemetation iron *within* the dump must clearly be taken into account even though the source of the iron is outside the dump.

Further, if the excess acid produced by the oxidation of pyrite is neutralized by reaction with gangue of biotite composition* additional iron is generated, oxidized, and precipitated. With these additions Eq. [3] becomes:

$$g\ O_2\ \text{consumed} = (1.75 + 1.91\,FPY)\ g\ \frac{\text{chalcopyrite}}{\text{Cu leached}} \qquad [4]$$

*Biotite has been found to be more reactive by a factor of ~100 than other gangue minerals in a porphyry copper intrusive. Calcite, the only other highly reactive mineral likely to occur, is usually present only in minor amounts.

Waste material typically contains 10 to 100 moles of pyrite for every mole of sulfide copper. Thus pyrite is by far the most important oxidant consumer if it is oxidized in proportion to its molar ratio to sulfide copper.

Because leach solutions cannot carry significant oxidant with them as they move through the dump, air is the main source of oxidant within a dump. A liter of air contains 0.28 g O_2. Fig. 3 shows that Eq. [4] requires far more air than water to flow through a waste dump if the effluent solutions are to contain the copper concentrations typically observed. For the particular dump we shall consider, at least 80 times more air passed through the dump than water. That is, for *each liter* of leaching solution leaving the dump with a net gain of 0.25 g/l (2 lb. Cu/1000 gal.) copper, 80 liters of air are required to supply the oxidant necessary for the chemical reactions involved.

Eqs. [1] and [2] not only tell us the amount of oxidant consumed per gram of copper leached, but also the heat generated per gram of copper leached. (The enthalpy of reaction, ΔH_R, of Eq. [1] is approximately

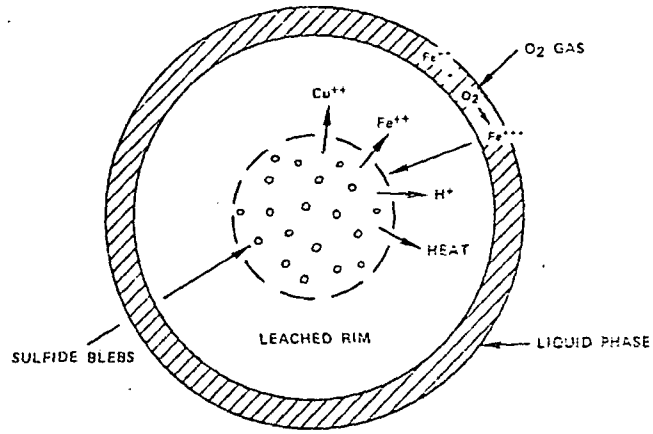

Fig. 2—Idealization of the leaching of a single waste particle.

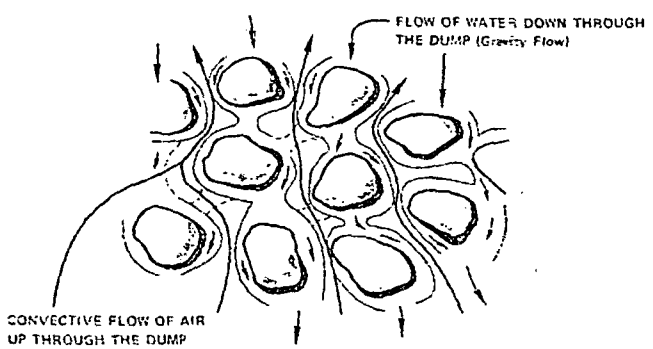

Fig. 1—Countercurrent interlocking flow of air and water through a leach dump. The flow of water is usually intermittant.

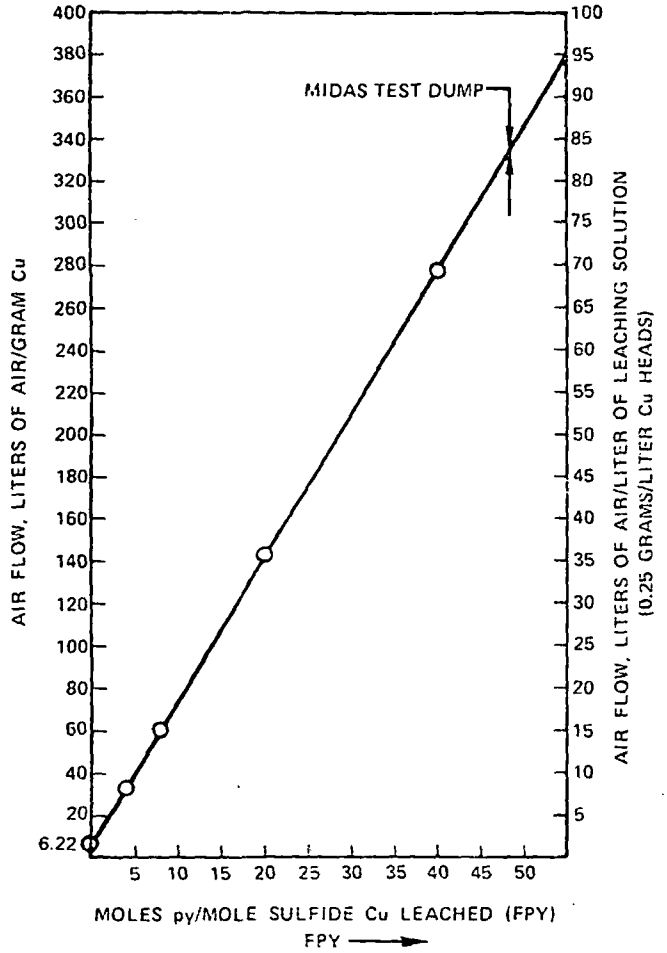

Fig. 3—Graph relating the air flow through a dump to the ratio of the moles of pyrite leached to sulfate copper leached (*FPY*), for a typical effluent copper concentration.

-108.8 kcal;* ΔH_R for Eq. [2] is -94.9 kcal). If we again take into account the heat consumed in the precipitation of jarosite, require acid and iron balance, and assume 2.5 lb. Fe are exchanged per pound of Cu at the precipitation plant:

*1 kcal = 4.1868 kJ.

$$\text{kilocalories produced} = (2.89 + 5.41\,FPY)\ \text{g chalcopyrite Cu leached} \qquad [5]$$

Again it can be seen pyrite oxidation will, in all probability, be the most significant source of heat. The rate at which a waste dump heats up is a direct measure of *FPY*.

Eqs. [4] and [5] contain the fundamentals of a model of the dump leaching process. Sulfide oxidation reactions consume oxygen from the air in a dump. Since O_2 is a heavy component in air, the oxygen depleted air is lighter. Since water vapor is a light component of air, saturation of the air inside a dump with water vapor will also produce buoyant forces. Buoyant forces tend to produce air convection. Furthermore, the oxidation reactions are exothermic, which also promotes air convection. A ΔT of 20°C produces buoyant forces two or ten times larger than complete oxygen depletion or complete water vapor saturation, respectively.

For normally observed permeabilities, air convection rather than diffusion is the principal mechanism of O_2 transport into a waste dump. In this respect our model differs from that of Harris,[2] whose pseudo-particulate leaching case assumes that O_2 transport into a dump occurs primarily by diffusion through the interstices of the particles.

In the next section we generalize Eqs. [4] and [5] slightly to take into account copper sulfides other than chalcopyrite. We then develop the rate equations relating copper extraction with oxygen uptake and heat generation. We show that these rate equations are governed by the chemical and diffusional processes occurring during the leaching of waste particles in the dump. Finally, we derive three equations describing oxygen balance, heat balance and convective air flow which are the basis for our one dimensional model.

Formulation of a One Dimensional Model

Because sulfide leaching is usually dominated by the leaching of pyrite, Eqs. [4] and [5] are quite easy to generalize. Provided *FPY* is taken as the moles of pyrite oxidized per mole of sulfide copper oxidized, and provided *FPY* is greater than ~4, Eqs. [4] and [5] will hold to good approximation even if sulfide minerals other than chalcopyrite are present.

We assume sulfide oxidation takes place in a dump only where the air filled pores of the dump contain oxygen and that the oxidation proceeds at a rate independent of the actual oxygen concentration. Unpublished studies of the bacterial oxidation of waste dump leaching solutions with air, conducted by the second author, have shown that the bacterial oxidation rate of ferrous iron is essentially independent of oxygen concentration in the air until the concentration falls below 1 pct. More recent studies by the second author involving the uptake of oxygen by wetted mine waste show that oxygen uptake is substantially independent of oxygen partial pressure for the same range of oxygen concentrations.

By contrast nonsulfide copper is leached with acid alone. Acid generated by pyrite oxidation anywhere in the dump is recirculated through the dump in normal operation. Therefore, nonsulfide copper leaching should take place everywhere in the dump at a rate independent of the presence or absence of nearby oxygen.

Suppose the fraction of sulfide copper remaining in the dump after some leaching is X_S, and the fraction of nonsulfide copper in the dump is X_{NS}. Let the original sulfide copper grade be G_S and the original nonsulfide copper grade be G_{NS}. Then the rate at which copper is leached from the dump, $\mathcal{R}_{Cu}$, may be expressed as:

$$\mathcal{R}_{Cu} = \rho_R(1-\Phi)\left(G_S\frac{dX_S}{dt} + G_{NS}\frac{dX_S}{dt}\right). \qquad [6]$$

Similarly the rate of oxygen consumption, $\mathcal{R}_{O_2}$, and the rate of heat generation $\mathcal{R}_A$, may be expressed, from Eqs. [4] and [5]:

$$\mathcal{R}_{O_2} = \rho_R(1-\Phi)G_S\frac{dX_S}{dt}(1.75 + 1.91\,FPY) \qquad [7]$$

$$\mathcal{R}_A = \rho_R(1-\Phi)G_S\frac{dX_S}{dt}(2.89 + 5.41\,FPY) \qquad [8]$$

ρ_R, the density of the rock waste, is commonly about 2.7 g/cm^3; Φ, the interblock porosity of the dump is ~25 pct; $\rho_R(1-\Phi)$, the bulk density of the dump as a whole, is equivalent to 1.7 tons/yd^3.

The rate of leaching, dX_S/dt and dX_{NS}/dt, may be described also in terms of leaching from a waste particle. Let us suppose that the leaching of a sulfide-bearing particle is governed by an equation of the form:

$$\frac{D'^{l}_{ox}\Phi_R{}^{l}}{T^{l}_{R}}\nabla^2[Ox]^{R}_{l} - k_{ox}a^{R}_{sulf}[Ox]^{R}_{l} = 0 \qquad [9a]$$

and that $[Ox]_l$ just outside the ore particle is a known function of time. The symbols given are defined in Table I.

For a simple one-dimensional case, Eq. [9a] becomes:

$$\frac{D'^{l}_{ox}\Phi_R{}^{l}}{T^{l}_{R}}\frac{\partial^2[Ox]^{R}_{l}}{\partial x^2} - k_{ox}a^{R}_{sulf}[Ox]^{R}_{l} = 0 \qquad [9b]$$

Satisfying the boundary conditions $[Ox]^{R}_{l}\big|_{x=0} = [Ox]^{l}$ and $[Ox]^{R}_{l}\ _{x\to\infty}\ 0$, the solution is

$$\frac{d[Ox]^{R}_{l}}{dx} = -\frac{[Ox]^{R}_{l}\big|_{x=0}\ e^{-x/\delta}}{\delta} \qquad [10]$$

Where δ = reaction skin depth $= \sqrt{\dfrac{D'_{ox}\Phi^{l}_{R}}{k_{ox}T^{l}_{R}a^{R}_{sulf}}}$ [11]

The reaction skin depth is the distance into the particle where the oxidant concentration has fallen to $1/e$ its initial value. Since by hypothesis the rate of oxidation reaction is proportional to oxidant concentration. δ is a measure of the distance into the ore particle that significant chemical reaction takes place.

Using values given in Table I, δ = 0.142 cm. The reaction skin depth is therefore thin, relative to the average size particle diameter. Leaching of a particle can, therefore, be described in terms of the so-called shrinking core model which is of a similar form to that developed by Braun, Lewis and Wadsworth.[4]

$$\frac{dX_S}{dt} = \frac{-3X_S^{2/3}}{6\tau_{DS}X_S^{1/3}(1-X_S^{1/3})+\tau_{CS}} \qquad [12]$$

$$\frac{dX_{NS}}{dt}\quad\frac{-3X_{NS}^{2/3}}{6\tau_{DNS}X_{NS}^{1/3}(1-X_{NS}^{1/3})+\tau_{CNS}} \qquad [13]$$

where τ_D is the time required to leach a waste particle completely when the process is solely diffusion controlled, and τ_C the time to leach a waste particle completely when the process is controlled by the decreasing surface area of the shrinking unleached core. τ_C and τ_D can be computed theoretically from the following relations:

$$\tau_{CS} = \frac{Ka}{k_{ox}a^{R}_{sulf}\delta[Ox]} \qquad [14]$$

$$\tau_{DS} = \frac{T^{l}_{R}a^{2}K}{6[Ox]D'_{ox}\Phi^{l}_{R}} \qquad [15]$$

Using the values given in Table I, τ_{CS} = 903 mo. and τ_{DS} = 1590 mo.* In addition, τ_C and τ_D may be given a temperature dependence:

*1 mo = 31 d.

Table I. Parameters Used for the Determination of τ_{DS} and τ_{CS}

Parameter	Description	Value
a	Radius of waste particle	1.5 cm
a^{R}_{sulf}	Surface area of sulfide mineralization per unit volume of waste	≈80 cm^{-1}
D'_{ox}	Diffusion constant of Fe^{+++} in water	≈2 × 10^{-5} cm^2/s
FPY	Moles of pyrite leached per mole and sulfide copper leached	47
G_S	Sulfide copper grade	0.18 wt pct
K	Oxidant required to leach a unit volume of waste particle	0.444 g/cm^3
k_{ox}	First order rate constant for the oxidation of pyrite by Fe^{+++}	≈10^{-7} cm/s
$[Ox]$	Concentration of Fe^{+++} in leaching solution	10^{-3} g/cm^3
T^{l}_{R}	Tortuosity of diffusion channels	≈5
δ	Reation skin septh (see Eq. [11])	Calculated value = 0.142 cm
Φ^{l}_{R}	Porosity of waste through which diffusion can take place	4 × 10^{-2}

$$\tau(T) = \tau(T=0°C)\ \mathrm{EXP}\left(\frac{1000\cdot E^*}{R}\frac{T}{(273)(273+T)}\right) \qquad [16]$$

This introduces activation energies E^*_{DS}, E^*_{CS}, E^*_{DNS}, E^*_{CNS}. From the literature[10] reasonable guesses for E^*_{DS} and E_{DNS} would be 5.0 kcal/mol. E^*_{CS} and E^*_{CNS} might range from 14.0 kcal/mol to 20.0 kcal/mol, the activation energies reported for the leaching of pyrite[11,12] and for chalcopyrite.[13]

Given values for τ_{DS}, τ_{CS}, τ_{DNS}, τ_{CNS}, Eqs. [12] and [13] determine the rate of leaching at any point in the dump at any stage of leaching. X_{NS} and X_S can be updated after each increment of model leaching. Model time increments may be taken as short as desired.

The most serious approximation in Eqs. [12] and [13] is probably the assumption that the dump is composed of waste particles only of one size. This may not be as serious an approximation as it might at first seem, given the tendency of small ore particles to clump together and leach as if they were a larger aggregate, and the tendency for large ore particles to have large enough cracks that they leach like somewhat smaller particles.[10]

Furthermore, recent work has also shown that copper recovery rates from operating dumps at Kennecott's Bingham mine can be correlated quite well with laboratory studies of copper recovery from similar material when the mean particle size of the waste, as found in the dump, is compared with laboratory leaching studies.

The heat balance in a waste dump may be described by:

$$\rho_T C_T\frac{\partial T}{\partial t} = -(\rho_l C_l \underline{V}_l + \rho_g C_g \underline{V}_g)\cdot\underline{\nabla}T + \mathfrak{R}_A + K_T\nabla^2 T \qquad [17a]$$

where ρ and C are the density and heat capacity of the

total dump (subscript T) and the liquid (subscript l) and gas (subscript g) phase of the dump. V_l is the Darcy liquid velocity (i.e. cm^3 water/cm^2 dump surface-s passed through the dump). V_g is the darcy air velocity through the dump (*i.e.* cm^3 air/cm^2 dump area-s). K_T, the thermal conductivity of the dump is taken to be 5×10^{-3} cal/cm·°C·s. For calculation, $\rho_T C_T = 0.6$, $\rho_l C_l = 1.0$, and $\rho_g C_g = 1.3 \times 10^{-3}$ $(0.126 + 0.0283T)$, where T is the temperature of the dump. This last expression takes into account the thermal effects of evaporation. It is assumed the air in the dump is always saturated with water; account is taken of the increase in water saturation values with increasing air temperature, T, and the effect, through the latent heat of vaporization, this would have on the heat capacity or heat carrying ability of air.

For a one dimensional dump (*i.e.* air and water flow restricted to be vertical only), Eq. [17b] simplifies to:

$$\rho_T C_T \frac{\partial T}{\partial t} = (\rho_l C_l V_l - \rho_g C_g V_g) \frac{\partial T}{\partial z} + \mathcal{R}_A + K_T \frac{\partial^2 T}{\partial z^2} \qquad [17b]$$

One dimensional convective air flow through a dump may be described:

$$V_g = \frac{k_{AVE}}{\mu_g} \frac{\Delta P}{H} \qquad [18]$$

H is the height of the dump, μ_g is the viscosity of air $= 1.9 \times 10^{-4}$ poise.* ΔP is the pressure drop across the dump. ΔP may be expressed as:

$$\Delta P = \rho_{00} g_0 H \sum_i \overline{H}_i (\alpha(T_i)\, T_i + \beta (1 - [O_2]^g)) \qquad [19]$$

Here ρ_{00} is the density of air at *STP*, g_0 is the gravitational constant, $\overline{H}_i = H_i / H$, is the normalized thickness of the ith incremental level of the dump. $\alpha(T_i)$ is the temperature dependent coefficient of thermal expansion which, like the heat capacity, includes the effects of changing water vapor saturation. β is a coefficient which describes the decrease in air density due to oxygen depletion ($\beta = 2.83 \times 10^{-2}$). $[\overline{O}_2]^g = [O_2]^g / [O_2]^g_{STP}$. k_{AVE}, the average permeability of the dump, may be expressed:

$$k_{AVE} = \frac{1}{\sum_i \overline{H}_{i/k_i}} \qquad [20]$$

Any distance, z_i, from the base of the dump, where fresh air is assumed to enter, the oxygen concentration in the dump will be:

$$[\overline{O}_2]^g = 1 - \frac{\mathcal{R}_{O_2} z_i}{V_g [O_2]^g_{STP}} \qquad [21]$$

Eqs. [17b], [18], and [21] represent a model of the dump leaching process that includes both physics (air convection) and chemistry. The equations can be solved using an implicit finite difference scheme in which the dump is considered to be broken into N layers. The method used was to start the dump leaching at some starting temperature and loop between Eqs. [18] and [21] until a steady state O_2 profile and air velocity was attained. Then Eq. [17b] was used to determine the temperature of the dump at $t + \Delta t$. Δt was generally taken to be one month. The average rate of fluid application was used, an approximation that has been shown valid so long as the leach cycle is less than three months. As will be discussed later the ambient temperature was varied seasonally in a manner appropriate to the location of the dump (temperature measurements were available from a mine station). The surface temperature of the dump was also varied seasonally but at a higher average temperature and over a more restricted range. Air convection kept the dump surface warmer than the surroundings. Snow was observed to melt more quickly on the dump than in the surrounding areas.

Given a set of parameters and operating procedures (rate of application of water), the finite difference model computes the leach history of the model dump. The dump is considered to be broken into N layers. The percent copper leached per month (or the effluent copper heads) can be computed easily:

$$\frac{\text{fraction Cu}}{\text{mo}} = \frac{dX_{TOT}}{dt}\left(2.68 \times 10^6 \frac{\text{s}}{\text{mo}}\right) = 2.68 \times 10^6 \cdot \sum_{\text{dump}} \frac{\left(G_{NS} \frac{dX^i_{NS}}{dt} + G_S \frac{dX^i_S}{dt}\right)}{N(G_S + G_{NS})} \qquad [22]$$

$$\text{HEADS [g/l Cu]} = \rho_R (1 - \Phi)\, H \cdot \sum_{\text{dump}} \frac{\left(G_{NS} \frac{dX^i_{NS}}{dt} + G_S \frac{dX^i_S}{dt}\right)}{N V_l} \cdot 1000 \qquad [23]$$

The cumulative pct leached, $1 - X_{TOT}$ is just:

$$\text{fraction Cu leached} = 1 - \frac{(G_{NS} X_{NS} + G_S X_S)}{G_{NS} + G_S} \qquad [24]$$

The next section compares the rate of leaching and the cumulative leaching of a test dump to the rate of leaching and cumulative leaching computed by the model through Eqs. [22] and [24].

CALIBRATION OF THE MODEL

Fig. 4 shows a cross section of the Midas test dump, built of mine waste with normal size distribution by the Utah Copper Division of Kennecott Copper Corporation at Bingham Canyon, Utah. The dump is about 400 ft long, 200 ft wide. The average depth is 20 ft with a

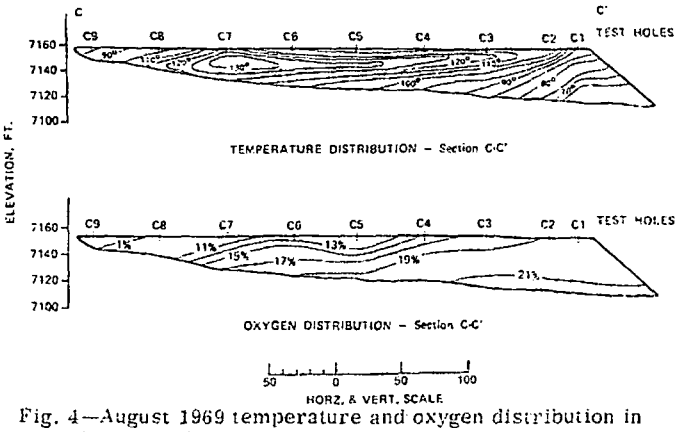

Fig. 4—August 1969 temperature and oxygen distribution in a section through the Midas test dump.

*1 poise = 0.1 Pa·S.

maximum depth of 40 ft. Fifty-eight leaching ponds cover the top of the dump. The waste tonnage beneath the ponds is about 93,000 tons (assuming 1.7 tons/yd^3). The waste itself is 60 pct quartzite and 40 pct biotite granite. The average grade of the waste is 0.145 pct copper. 80 pct of the copper was sulfide, dominantly chalcopyrite; the rest was nonsulfide copper.

Leaching of the dump began on April 9, 1969. Prior to this, there had been some runnoff through the dump but very low copper extraction. Fig. 5 shows that leaching after water application was slow at first, increased rapidly to a maximum about five months after the start of leaching, and then fell steadily, with some fluctuations that appear correlated with the season (maximum in summer). Fig. 4 shows that by August 1969 the internal dump temperature had risen to 130°F (54°C). There was substantial oxygen depletion as the air convected through the dump. It can also be seen that the air convected in along the high permeability base of the dump and then up through the dump—the one dimensional model is appropriate for this case.

As time went on the location of maximum dump temperature shifted from the far end of the dump (as shown in Fig. 4) to about the same distance from the near end.

The parameters used in the model are listed in Table II.

The following thermal boundary conditions were chosen. The base of the dump was fixed at 20°C. The top surface temperature was allowed to vary:

$$T\,(\mathrm{mo}) = 10°\mathrm{C} - 10 \cdot \cos\left((\mathrm{mo} - 1)\,\pi/6\right)$$

where mo runs from 1 to 12 and is the number of the calendar month. Thus the top surface of the dump was assumed to vary seasonally between 32°F and 68°F, (0°C and 20°C), a slightly more restricted and hotter range than the ambient temperature variation of 19°F to 63°F (−7°C to 17°C).

The temperature at the base of the test dump was observed to fluctuate somewhat. The assumption of a constant 20°C basal temperature is a matter of convenience and is probably subject to some error. Both boundary conditions are plausible. Subsequent work has shown these assumptions to be quite reasonable.

The starting temperature of the model dump was 10°C. The Midas test dump was built in winter so the dump was initially at least this cold.

Fig. 6 compares the calibrated model leaching history to the leaching history of the Midas test dump shown in Fig. 5. The match in general is quite good. In addition to the leaching history similarity, the model dump reached 51°C internal temperature by August 1969 and then decreased in temperature to about 14°C, as did the far end of the Midas test dump. In August 1969 the effluent oxygen concentration was 9 pct, in good agreement with observation (see Fig. 4). The values of τ_{CS} and τ_{DC} are quite close to the values anticipated from Eqs. [14] and [15] (compare Tables I and II).

The initial rise in extraction rate is due to the heating up of the dump. This feature is not peculiar to the Midas test dump, and can be observed in the leaching history of many dumps. The fall in leaching rate after the first seven months of leaching is due to the fact the more accessible copper has been leached and Fe^{+++} must diffuse through already leached areas to reach the remaining copper. The fall in dump temperature also contributes to the decline in leaching rate.

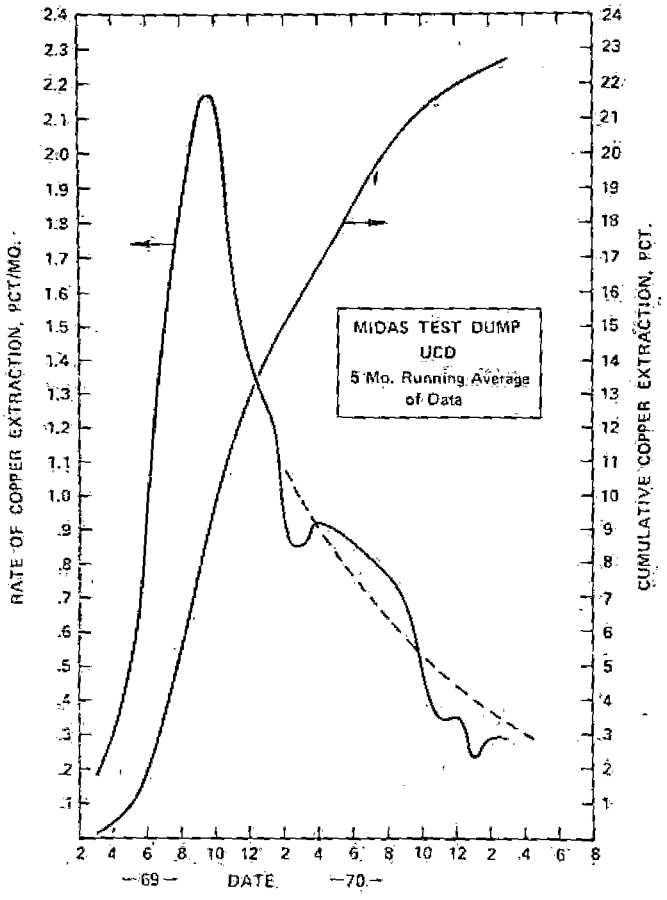

Fig. 5—The rate of extraction and cumulative extraction of copper from the Midas test dump, using a five-month running average.

VARIATIONS FROM THE BASE MODEL

It is of interest to vary the model parameters to see what effect they may have on the rate of copper extrac-

Table II. Parameters Used for the Model Shown in Fig. 6

Parameter	Description	Value
H	Height of dump	670 cm (22 ft)
FPY	Moles pyrite leached/mole Cu leached	47
k	Dump permeability k_{AVE}	10^{-5} cm^2 (1000 darcys)
V_I	Rate of water application	2.26×10^{-5} cm^3/cm^2 dump-s (0.02 gal/ft^2-h)
G_S	Dump sulfide copper grade	0.116 wt pct
G_{NS}	Dump nonsulfide copper grade	0.029 wt pct
τ_{DS}	Diffusional sulfide leach time (20°C)	1700 mo
τ_{CS}	Leach time for sulfide copper under surface area rate control (20°C)	200 mo
τ_{DNS}	Diffusional nonsulfide leach time (20°C)	500 mo
τ_{CNS}	Leach time for nonsulfide copper under surface area rate control (20°C)	300 mo
E^*_{DS}, E^*_{DNS}	Activation energies for diffusion	5.0 kcal/mol
E^*_{CS}, E^*_{CNS}	Activation energies for chemical leaching reactions	18.0 kcal/mol

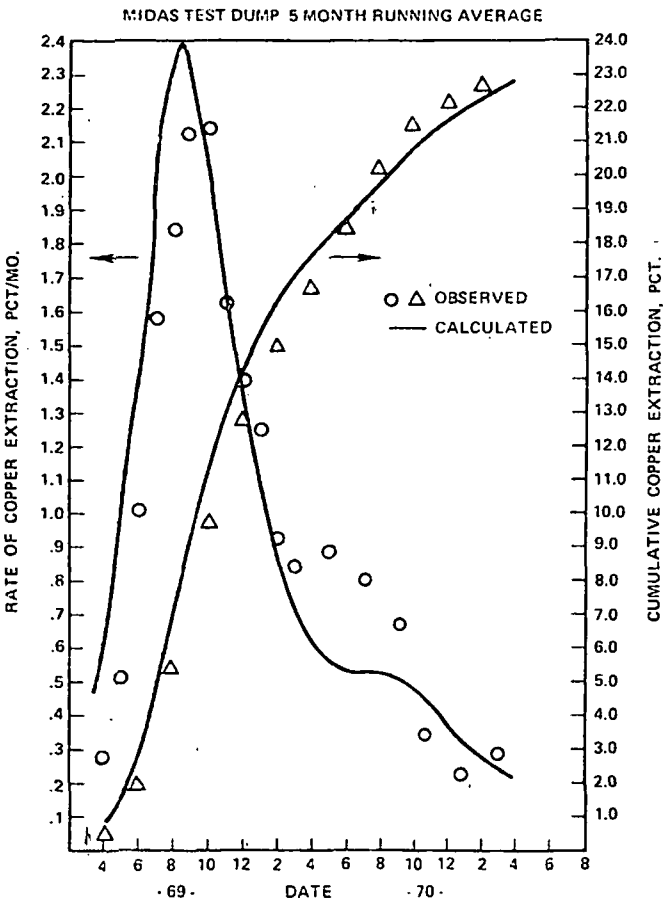

Fig. 6—Comparison of observed and calculated Midas test dump copper leaching behavior.

Table III. The Effect of Parameter Variation on Copper Recovery After 24 Months of Leaching

Parameter	Variation	Increase in Copper Recovered in 24 Months, Pct
H ✓	+10	8.9
FPY ✓	+10	6.2
τ_{DS}	−10	6.2
G_S ✓	+10	4.8
E^*_{DS}	+10	2.7
τ_{CS}	−10	1.8
V_l ✓	−10	1.3
τ_{DNS}	−10	1.3
E^*_{CS}	+10	0.9
G_{NS}	+10	0.9
τ_{CNS}	−10	0.4
E^*_{DNS}	+10	0.4
Starting Temp	+10	0.4
E^*_{CNS}	+10	0.0
k'	+10	0.0
	−10	−0.4

tion. Table III lists the parameters of Table II and shows the percent increase in copper extraction after twenty four months of leaching that results from a 10 pct alteration in the listed parameter. The parameters that are checked affect the rate of leaching primarily by allowing the dump to attain higher temperatures.

The reader is cautioned that the variations in leach rate shown in Table III are based only on what is in the model. Much may go on in a waste dump that has not been included, as yet, in the model. Secondly, not all the parameters listed in Table III are mutually independent. For example, increasing FPY at a constant sulfide copper grade will cause τ_{DS} to increase substantially. Lastly, the combination of parameters that successfully models the Midas test dump is not necessarily a unique set or the correct set. Data from more than one test dump is needed to resolve these uncertainties. The most critical uncertainties are probably the chemical activation energies and FPY (see Table II).

The lack of dependence of leach rate on permeability simply indicates the dump was shallow and permeable enough not to be oxygen starved anywhere. Had the dump been thicker (~100 ft.), a significant dependence of leach rate on permeability would be noted.

CONCLUSIONS

From the discussion presented it can be concluded:

1) Air convection is an important part of the dump leaching process and must be accounted for in any successful model of this process (Fig. 3).

2) Exothermic oxidation reactions heat up waste dumps with time (Fig. 4). Any leaching model that is to be applicable to real dumps must account for the temperature dependence of the leaching process.

3) A simple model that requires energy, mass and momentum balance, and that derives rate control from a temperature dependent shrinking core model and a single "average" waste particle diameter (Eqs. [12], [13], [16]) has proved remarkably successful in accounting for the most important observed features of the leaching history of a well studied test dump (Fig. 6).

4) Dump height, lixiviant application rate and dump permeability are the most important factors affecting the rate of copper leaching that are accessible to operational alteration. (Table III and discussion in text).

ACKNOWLEDGMENTS

The authors would like to thank Kennecott Copper Corporation for permission to publish this paper. In particular, the authors would also like to thank the Messrs. W. D. Southard, A. D. Pernichele and B. P. Ream of Utah Copper Division for permission to use the Midas test dump data as a base case for this study. Enough recognition cannot be given to the extensive, careful work of these individuals and others that was required to collect the high quality data so easily cited in this paper.

Parts of this paper were presented at the 78th National Meeting of the American Institute of Chemical Engineers in a Symposium Section on Modeling and Analysis of Dump and In-Situ Leaching Operations, August 19, 1974 in Salt Lake City, Utah.

NOMENCLATURE

a : radius of a waste particle, [cm]

a^R_{sulf} : surface area of sulfide mineralization per unit volume of waste, [cm^{-1}]

C_g : heat capacity of gas phase in dump including effects of variable water saturation, [g/cm^3]

C : heat capacity of mobile liquid phase in dump, [cal/g °C]

C_T : heat capacity of dump as a whole, [cal/g °C]

D^l_{ox} : diffusion constant of oxidant in water, [cm²/s]

E^*_{DS}, E^*_{DNS} : activation energies describing, through Eq. [16], the temperature dependence of τ_{DS}, τ_{DNS}, [kcal/mole]

E^*_{CS}, E^*_{CNS} : activation energies describing, through Eq. [16], the temperature dependence of τ_{CS}, τ_{CNS}, [kcal/mole]

FPY : moles of pyrite leached per mole of sulfide copper leached [–]

G_S : initial copper sulfide grade of dump, [wt fraction Cu]

G_{NS} : initial copper nonsulfide grade of dump, [wt fraction Cu]

g_0 : gravitational acceleration, [cm/s²]

H : height of dump, [cm]

H_i : thickness of ith layer of dump, [cm]

$\bar{H}_i$: dimensionless thickness of ith layer of dump $\bar{H}_i = H_i / H$, [–]

ΔH_R : enthalpy of reaction, [kcal]

K_{AVE} : oxidant required to leach waste particle, [g/cm³ particle]

K_T : thermal conductivity of dump as a whole (total dump), [cal/cm °C · s]

k' : intrinsic permeability of the dump, [cm²]

k : average permeability of the dump (1 Darcy ≃ 10^{-8} cm²), [cm²]

k_{ox} : chemical rate constant characterizing reaction of oxidant and sulfide minerals, [cm/s]

N : number of layers into which dump has been arbitrarily broken for sake of computation (usually 30). [–]

$[Ox]$: concentration of oxidant, [g/cm³]

$[O_2]^g_{STP}$: concentration of oxygen in air under standard conditions of temperature and pressure, [g/cm³]

$[O_2]^g$: concentration of oxygen in gas phase of dumps, [g/cm³]

$[\bar{O}_2]^g$: normalized oxygen concentration in gas phase of dump $[\bar{O}_2]^g = [O_2]^g / [O_2]^g_{STP}$, [–]

ΔP : pressure drop across (bottom to top) the dump (10^6 dynes/cm² ~ 1 atmosphere), [dyn/cm²]

R : gas constant (~2), [cal/°C-mol]

$\mathfrak{R}_A$: rate of heat generation, [kcal/cm³ dump · s]

$\mathfrak{R}_{O_2}$: rate of oxygen consumption, [g O_2/cm³ dump · s]

$\mathfrak{R}_{Cu}$: rate of copper leaching [g Cu/cm³-dump · s]

T : temperature of dump at any particular location. Temperature of water, rock, and gas phases assumed identical, [°C]

T^l_R : tortuosity of diffusion channels, [–]

V_g : darcy gas velocity through dump, [cm³ gas/cm² dump area · s]

V_l : darcy velocity of water passing through the dump. Average rate over application periods and rest cycles is used. [cm³ water/cm² dump surface · s]

X_{NS} : fraction of initial nonsulfide copper remaining in dump or given layer of dump, [–]

X_S : fraction of initial sulfide copper remaining in the dump or a given layer of the dump, [–]

z_i : distance of center of ith layer of dump from base of dump, [cm]

GREEK LETTERS

α : coefficient of thermal expansion of air including effects of changing water vapor saturation. [–]

β : coefficient describing the change in air density due to oxygen depletion. (See Eq. [19]), [–]

δ : reaction skin depth, [cm]

μ_g : viscosity of the gas phase in the dump, [p]

ρ_R : density of waste particles, [g/cm³]

ρ_T : density of the dump as a whole ("Total" dump) ($\rho_T = \rho_R[1 - \Phi]$), [g/cm³]

ρ_l : density of liquid phase of dump (water), [g/cm³]

ρ_g : density of gas phase in dump including effect of variable water vapor saturation, [g/cm³]

ρ_∞ : density of air at standard temperature and pressure, [g/cm³]

τ_{DS}, τ_{DNS} : time to leach typical waste particle completely of sulfide or nonsulfide copper assuming rate of leaching is limited by diffusion of oxidant or acid into the particle, [mo]

τ_{CS}, τ_{CNS} : time to leach typical waste particle completely of sulfide or nonsulfide copper assuming the rate of leaching is controlled by the shrinking surface area of the sulfide or non-sulfide copper ("chemical" control), [mo]

Φ : interblock porosity of dump (usually ~25 pct), [–]

Φ^l_R : porosity of waste through which diffusion can take place, [–]

REFERENCES

1. H. W. Sheffer and L. G. Evans: *Bureau of Mines I.C.*, 1968, no. 8341, 57 pp.
2. J. A. Harris: *Proc. Australian Inst. Mining Met.*, 1969, no. 230, pp. 81-92.
3. R. J. Roman, B. R. Benner, and G. W. Becker: *SME-AIME Trans.*, 1974, vol. 256, pp. 247-52.
4. R. L. Braun, A. E. Lewis, and M. E. Wadsworth: *Solution Mining Symposium*, Chapt. 21, pp. 295-323, American Institute of Mining, Metallurgical and Petroleum Engineers Inc., New York, 1974.
5. B. W. Madsen, M. E. Wadsworth, and R. D. Groves: *SME-AIME Trans.*, 1975, vol. 258, pp. 69-74.
6. R. W. Bartlett: *Proceedings of the International Symposium on Hydrometallurgy*, Chapt. 14, pp. 331-74, American Institute of Mining, Metallurgical and Petroleum Engineers Inc., New York, 1973.
7. J. D. Lowell and J. M. Guilbert: *Econ. Geol.*, 1970, vol. 65, pp. 373-408.
8. M. E. Wadsworth: University of Utah, Salt Lake City, Utah, personal communication, 1974.
9. J. D. Stephens: Kennecott Copper Corporation, Salt Lake City, Utah, personal communication, 1974.
10. Y. T. Auck and M. E. Wadsworth: *Proceedings of the International Symposium on Hydrometallurgy*, Chapt. 25, pp. 645-700, American Institute of Mining, Metallurgical and Petroleum Engineers Inc., New York, 1973.
11. C. T. Mathews and R. G. Robins: *Aust. Chem. Eng.*, 1972, pp. 21-25.
12. E. E. Smith and K. S. Shumate: Water Pollution Control Research Series 14010 FPS 02/70, U.S. Department of the Interior, Federal Water Quality Administration, 1970.
13. A. E. Lewis and R. L. Braun: UCRL-73284, preprint, Lawrence Livermore Laboratory, January 1972.

SUBJ
MNG
MEDM

Presented at
86th Northwest Mining Assoc
Conv. - Dec 6, 1980
Spokane, WA

1980 MINING AND EXPLORATION DEVELOPMENTS IN MONTANA

UNIVERSITY OF UTAH
RESEARCH INSTITUTE
EARTH SCIENCE LAB.

by
E. C. Bingler[1] and Staff[2]

Mineral exploration activity continued at a high level in Montana during 1980, extending the trend of the past few years. Major mining activity was interrupted by the 5-month copper workers' strike against The Anaconda Copper Company, but other mining activity was little affected by the national recession and continued strong throughout the state. According to statistics released by the Department of State Lands, license and permit volume increased about 20 percent overall, with the greatest increases reflected in exploration licenses and small-mine operator permits. There are currently 75 active mine-operation permits issued in Montana, and six of these were issued during 1980. Thirty-eight companies or individuals were active in exploration in the state, 12 for the first time, and these 38 firms or individuals were active in 61 projects. One thousand small-mine operator permits were issued, and of these 250 were new permits.

Increased mining and exploration activity is also reflected in increased state revenues, which have been rising dramatically during the past few years. During the last decade, net proceeds and property taxes related to mining have increased from 30 to 100 million dollars; assessed valuation of real and personal property related to patented claims, property improvements, and machinery jumped from approximately 100 to nearly 300 million dollars. Revenue from coal mining increased from less than one million in 1970 to an estimated 25 million dollars in 1980, while oil and gas income rose from 3.5 to 10 million dollars; all other sources remained about the same.

PRODUCTION

Major news items and events of interest to the mineral resource community during 1980 included:

. . .the decision by The Anaconda Copper Company, a subsidiary of ARCO, to shut down the copper smelter at Anaconda, Montana, after 80 years of operation, and the related closing of the refinery at Great Falls, due to the prohibitive cost of upgrading antiquated equipment and meeting Federal air-quality standards. Although closure represents a significant loss of U.S. smelting and refining capacity and the loss of many jobs in western Montana, the shutdown is not expected to affect mining operations at Butte.

. . .the increasing interest and favorable outlook for oil and gas potential in western Montana's overthrust belt. Several test holes were completed in western Montana during the year, and great interest continues to surround the recently completed deep test by Amoco, near Wisdom, in Beaverhead County.

. . .passage of Initiative 84 during the general election by an extremely close margin. The initiative to ban disposal of radioactive waste products in Montana was widely regarded as anti-mining, and was first reported as defeated by 2,000 votes. The final vote tally released by the Secretary of State indicated 172,909 votes were cast in support of the measure, and 172,493 votes were cast against, a margin for passage of 416 votes. Legislation for the initiative remains to be written by the 1981 Legislature.

. . .the intent of the state of Montana to finance a new High Tongue dam adjacent to the antiquated and allegedly unsafe Tongue River reservoir near Decker, by leasing

[1]Deputy Director, Montana Bureau of Mines and Geology, Butte, Montana.
[2]Willis M. Johns, Chief, Economic Geology Division; Don C. Lawson, Field Agent; R. B. Berg, H. G. McClernan, G. A. Cole, and D. E. Fine, Geologists, MBMG.

and mining coal present at the proposed reservoir site, with coal-lease revenues earmarked to partially repay bonds sold to finance the new dam construction. About $50 million in coal-lease revenues is estimated to be applicable to this project.

. . .in education, the Montana Mining and Mineral Resources Research Institute/Montana Bureau of Mines and Geology joint effort at Montana Tech to provide support to small-mine operators, continued to provide a broad range of services and advice to operators on geology, mining methods, milling and processing techniques, reclamation practices, and permitting procedures, in addition to limited metallurgical bench testing and analytical services on Montana ores. Placer mining short courses emphasizing hands-on experience have been offered in Billings, Butte, Kalispell, Great Falls, and Missoula, and consistently are oversubscribed.

. . .the National Materials and Minerals Policy, Research, and Development Act of 1980, passed by Congress and signed into law by the President on October 21, 1980, places new and heightened emphasis on the significance of non-fuel mineral policy and domestic strategic and critical mineral resources. This new legislation is expected to have a major impact on technological research and development of Montana's many strategic and critical mineral resources.

PRECIOUS METALS

Montana's precious metal mining, production, and exploration industry experienced a mixed year. Production of gold and silver was strongly curtailed because of the nationwide strike against the copper mining companies and the loss of byproduct gold and silver from Butte ore, reputed to contain an average of 0.2 oz/ton silver and 0.0028 oz/ton gold, with the announced closing of the smelter in Anaconda and the refinery in Great Falls. At the same time, Montana has been the scene of greatly revived interest in precious metal mining and recovery by small-mine operators.

Exploration and development activity continued in the Stillwater Complex by The Anaconda Copper Company and Johns-Manville/Chevron, who are exploring and developing the platinum-gold resources in the complex. During the year, Anaconda completed its development drift at the Mouat millsite. Johns-Manville began work on a new portal on Chrome Mountain—the Frog Pond project—at the west end of the complex, where ore is reputed to be 20 to 50 percent higher grade than on the east end of the complex. Drilling, sampling, and experimental stoping continue in order to develop samples for metallurgical testing and to refine grade estimates. The chrome stockpile in the Stillwater was reduced by shipments of ore from Columbus by unit train, but no exploration or production activity was recorded on chrome deposits during the year.

Gold Cup Mining Company's planned gold-silver-platinum openpit operation in the Crazy Mountains has been postponed because of delay in receiving Forest Service approval. In the Little Rockies, mining and development activities continued at Landusky and Zortman, with Newmont Mining continuing contract mining on its holdings.

Ranchers Exploration and Development Corporation announced plans to develop an openpit gold mine—the Golden Grizzley—north of Cooke City in the Lulu Pass area between Yellowstone National Park and the Absaroka-Beartooth Wilderness. Company estimates based on drilling indicate a half-million-ton orebody, averaging 0.2 ounces of gold per ton.

Western Silver Development Company, lessee of the Nancy Lee silver mine near Superior, continued to develop vein silver deposits, with vein ore reported to average more than 10 ounces

of silver per ton. Anaconda Company's Flathead mine, under lease to Condon and Kelly, was the site of considerable work this summer through an agreement with Superior Oil of Canada. Work has proceeded to the point where an application for a mill to process silver ore is being actively considered. Production from the Portal silver mine, operated by Black Pine Mining, was anticipated to increase from 9,000 to 18,000 short tons per month. Management of this modern, trackless mine is considering installation of a mill to process ore in addition to the existing optical ore sorter. Midnite Mines is also studying construction of a mill employing a combination of cyanide leaching and electrolysis at the Polaris silver mine.

Several gold heap-leaching operations were active during the year. In the Little Rocky Mountains, full-scale leaching operations were initiated by Zortman Mining Company on three-quarters of a million tons of ore near Zortman, and a similar amount of ore was successfully leached by Landusky Mining Company at its Landusky-based operations. . .leaching began at the Mammoth mine in the Tobacco Root Mountains in what appears to be a well-planned and efficient operation that recently produced the first bullion. . .favorable mill tests of stockpiled ore from the Gregory mine south of Helena indicate that most of the gold and much of the silver can be recovered by modified heap-leach techniques. . .the heap-leach operation at the Tourmaline Queen in the Elkhorn District was reported in operation this year. . .the mill in the Rochester District has been optioned, and some thought is being given to adding a cyanide circuit. No gold production was recorded from the more than 50 patented claims in the district, but Noranda is reported to have staked claims in the Rochester Basin. . .mill rebuilding is expected to begin shortly on the Goldsil-Ranchers mill at the old Drumlummon mine near Marysville. The cyanide leaching mill was damaged by fire in July.

High gold prices have stimulated considerable interest in Montana's placer gold deposits, both by major corporations and small-mine operators. International Nickel has leased the Ruby placer situated 10 miles southeast of Wisdom in Beaverhead County on Ruby Creek. Under an option to explore and lease, INCO has drilled 30 holes to bedrock and removed 1,000 yards of gravel as part of its evaluation of the placer potential of this deposit. . .Playgo Mining has proposed mining Tertiary placer deposits south of Virginia City in the Gravelly Range. Recovery of significant gold value there may be hampered by substantial clay in the gravel.

1980 saw continued production, exploration, and permitting activities at Montana mines operating on complex precious metal-base metal ores. Kootenai National Forest officials approved ASARCO's four-year mineral exploration plan for the Chicago Peak area of the Cabinet Mountains Wilderness Area. ASARCO's plan to search for copper-silver ore includes drilling 36 core holes over the 149 claims held. . .at the Argentine mine near Wickes, Mascot Silver-Lead Mines, Inc., is developing a recently discovered lead-silver-gold vein averaging 11.2 percent lead, 11.6 ounces silver, and 0.1 ounce gold. The company also plans to reopen its Meadow mine near Helena, where assays reportedly indicate over 200 ounces of silver per ton of ore. Summit Silver is exploring at the Baltimore silver mine northwest of Boulder, Montana, a major past producer of gold, lead, and copper, with a production record in present-day value of over six million dollars. Viking Exploration Company of Denver has reopened the Spotted Horse gold mine in the Judith Mountains, a major gold producer in the late 1800s and early 1900s. As part of its effort, the company has contracted with Helena Silver Mines, Inc., to rebuild its mill to process Spotted Horse ore.

BASE METALS

Major news of the year was the decision by The Anaconda Copper Company, a subsidiary of ARCO, to close the copper smelter in Anaconda and the refinery in Great Falls. The closure represents a major loss of domestic smelting and refining capacity in addition to the loss of 1,500

jobs in western Montana. According to company representatives, the closure came as a result of the prohibitive costs, estimated at $300 to $400 million, of retrofitting the smelter to meet Federal air-quality standards. Officials indicated the closure decision will not affect the mining operation at Butte, and it is reported that Butte concentrate will be shipped to Japan.

At Butte, Anaconda announced its application to the state Air Quality Bureau to build a $6 to $8 million addition to the Weed Concentrator to process molybdenum ore. The addition would include flotation and dryer sections that would extract 30 tons of concentrate daily, containing about 50 percent molybdenum.

Exploration and development activities for molybdenum remained at a high level during the year. Increased exploration activity and property acquisition by American Metals-Climax in the Neihart-Hughsville area have led to rumors of a major molybdenum discovery on the Gwen McBride property adjacent to the Block P mine. Cyprus Mines and Moly Corp are actively exploring in the East Pioneers. The U.S. Geological Survey announced discovery during the year of zones in the Pioneer Mountains likely to contain moly deposits associated with anomalous amounts of silver, copper-lead-zinc, tin, and tungsten.

Union Carbide has apparently found more tungsten in the Brown's Lake deposit near the old Minerals Engineering openpit property that operated during the fifties. No production is reported, but the company has completed considerable drilling. Homestake has been active at Jardine on property formerly leased by Anaconda. Extensive surface work and some underground activity are reported, including long hole drilling.

Uranium exploration has slowed along with the drop in price and passage of Initiative 84. Exxon is reported to have completed about a dozen drill holes in Tertiary sedimentary rocks on Parrot Bench, at the north end of the Tobacco Roots, with encouraging results. BurWest recently ceased exploration in the Helena valley in Broadwater County.

U.S. Antimony plant west of Thompson Falls continued steady production in response to a diversified market demand. The company has made application to build a second conventional mill, on Eddy Creek between Plains and Thompson Falls, to process gold-silver-lead ore.

INDUSTRIAL MINERALS

During 1980 the national economic downturn had a noticeable impact on Montana industrial mineral producers. Operators producing and selling industrial mineral products used in the construction and building industries experienced somewhat lessened demand, but major facilities such as U.S. Gypsum's Heath mine, Cominco's Warm Springs phosphate mine, and W. R. Grace's Libby vermiculite mine remained steady producers.

Barite—Montana Barite Company continued to mine barite at several deposits in western Montana, and to mill barite at its Missoula facility where the company is tripling mill capacity. Barite milling capacity will also be increased in the Missoula area by construction of a new mill at Wheeler Village. St. Regis Company, which purchased the Mullen barite mine during the year, plans to continue mining and will begin milling of barite from western Montana.

Bentonite—General softening of the domestic steel industry during the year reduced demand for bentonite in the taconite pelletizing process, which together with the manufacture of drilling mud, is a major market for Montana bentonite. Federal Bentonite Company closed its plant near Glasgow, which has not yet reopened at this writing. American Colloid continues to mine bentonite south of Malta and to operate its mill at Malta on a reduced scale, with plant production reported to be near 10,000 tons per month.

Gypsum—The U.S. Gypsum mine at Heath continued steady operation and did not appear much affected by the national recession. This mine, with substantial reserves close to the plant, is the single largest taxpayer in Fergus County. Two openpit gypsum mines are reported operating at Raynesford, and shipping gypsum to Ideal Cement at Trident, Montana, and to Kaiser Cement at Prickly Pear near Helena.

Talc—Production of Montana talc from the Beaverhead and Yellowstone mines (Cyprus Industrial Minerals) and the Treasure Chest mine (Pfizer, Inc.) is expected to decrease slightly this year because of decreased demand from paper, paint, and ceramic industries affected by the recession. Established producers and other companies not now mining talc in Montana continue to explore for new talc deposits and to develop known deposits. Some chlorite production was reported from the Golden Antler mine in Madison County during the year.

Other Commodities—Acid-grade fluorspar was mined from a pegmatite at the Snowbird mine west of Missoula in Mineral County. According to the two operators, this is the only direct-shipping, acid-grade fluorspar in the United States. Cominco's Warm Springs mine in Powell County, now in its 51st year of continuous production, remains a steady phosphate producer with no changes reported. Pacific Silica Company continued to produce metallurgical-grade silica from its mine near Basin, as in the past, and W. R. Grace continued to mine vermiculite near Libby, but Western Vermiculite, operating near Hamilton, closed until its screening plant could be modified to control dust.

FOSSIL FUELS

Production and exploration activities related to Montana's major coal, oil, and natural gas resources continued at a high level during the year.

The Fort Union Formation in southeastern Montana continues to be a major source of low-sulfur, subbituminous coal. Through September 1980, 22,101,865 tons of coal were strip mined by the 10 mines reporting production for a seasonally adjusted total of 30 million tons, which would represent a 10 percent reduction of coal produced, compared to 1979. This decrease is related to the general weakening of the economy and has resulted in some employee layoffs at the Decker mine. Despite the temporary slowdown, private companies and government agencies continue active coal exploration and resource evaluation programs to meet increasing demand for low-sulfur western coal.

Oil and gas exploration and production continued strong during the year. Major interest focused on the Disturbed Belt of western Montana, which has been the site of continuing geophysical prospecting and the completion of a deep test well by Amoco near Wisdom, Montana, in the Big Hole country.

Six hundred and one wells were completed in the state of Montana from January 1 to October 9, 1980. Of these, 321 were non-producers (including dry holes, abandoned holes, expired permits, etc.), 128 were producing oil wells, and 152 were producing gas wells. Of the producing oil and gas wells, 49 were discovery wells—26 in the Williston Basin, 19 in the Sweetgrass Arch area, and one each in the Miles City Arch, Bowdoin Dome, and the Disturbed Belt.

Most of the drilling in 1980 was in the Sweetgrass Arch area (Toole, Pondera, Liberty, Teton, and Glacier counties), and in the Williston Basin (concentrated in Richland, Roosevelt, and Sheridan counties). The majority of the oil wells (72 of 128) were drilled in the Williston Basin, and the majority of the gas wells (91 of 152) were drilled in the Sweetgrass Arch area.

Boo. Non-Fe...
1972 v.5 N5

UNIVERSITY OF UTAH
RESEARCH INSTITUTE
EARTH SCIENCE LAB.

UDC 621.762.27

Mechanism of the emergence and formation of powder particles during autoclave deposition of copper from sulphate solutions

S S Naboichenko, S E Klyain and I F Khudyakov (Urals Polytechnic Institute - Department of the Metallurgy of Heavy Non-Ferrous Metals)

SUBJ
MNG
MEF

During the treatment of sulphate solutions containing 20-80g/l of copper with hydrogen at P_{H_2} = 20-30 atm and 130-150°C the copper is deposited in the form of a powder at a rate of 0.5-0.3g/l. min. [1-2]. The autoclave deposition of copper is characterised by the following features [1, 4-6]:

a) In addition to the preferred formation of powdered copper in the volume of the pulp, part of it is deposited on the internal surface of the autoclave and on the moving parts of the mixing equipment, and this leads to blockage of the reaction volume, imbalance in the rotating components, and significantly complicates the long-term use of the equipment;

b) The degree of deposition of the powder increases with increase in the process rate (particularly at elevated temperatures) and decreases with the addition of surfactants of the polyacrylamide (PAA) type, i.e. the polymerisation products from acrylic acid;

c) The form and degree of dispersion of the particles depend on the temperature, the number of consolidation cycles, the salt composition of the solutions, and the type of surfactant;

d) The formation of monovalent copper ions in the intermediate stage.

Determination of the nature of the generation and formation of the particles of copper will make it possible not only to control the deposition of powder with specific characteristics but also to restrict the deposition of copper on the internal surfaces of the reactor. There are hardly any published data on these problems. In the present work, based on earlier [5-7] and supplementary investigations, an attempt is made to fill this gap.

In view of the determining role of Cu^+ ions the mechanism of the generation of the metallic phase [1], it is right to suppose that copper powder should not form in the presence of additions which oxidise the copper ions or combine them into insoluble compounds (e.g. the chloride $L_S = 1.02 \cdot 10^{-6}$). In experiments with oxidising agents containing ions having variable valence (Fe^{3+}, NO_3^-, CrO_4^{2-}, AsO_4^{3-}) there was an induction period, during which the content of copper in the solution hardly decreased at all. This was due to the following processes:

$$Cu^+ + Fe^{3+} \rightarrow Fe^{2+} + Cu^{2+},$$

$$Cu^+ + NO_3^- + 2H^+ \rightarrow NO + Cu^{2+} + 2OH^-,$$

$$3Cu^+ + CrO_4^{2-} + 4H^+ \rightarrow Cr^{3+} + Cu^{2+} + 4OH^-,$$

$$3Cu^+ + AsO_4^{3-} + 4H^+ \rightarrow As^{3+} + Cu^{2+} + 4OH^-.$$

In the absence of copper, with other conditions equal, the composition of the solutions did not change during the treatment of solutions of ammonium ferrisulphate, nitrate, chromate and others.

With an increasing addition of chlorides (NH_4Cl, NaCl, KCl) to the initial solution the deposition of copper on the reactor walls was reduced, while the chlorine content of the powder increased; with an equimolar (to the copper) and higher consumption of chloride ions, copper was not detected either on the reactor walls or in the metallic copper deposit. By X-ray diffraction it was established that the precipitate represented the compound CuCl. The addition of chloride ions did not affect the rate of decoppering of the solution.

Thus, experiments with oxidising agents and chloride ions confirmed convincingly that the generation of the metallic phase takes place through a stage involving the formation of cuprous ions. The subsequent discharge of the cuprous ions is more probable from energy standpoints on account of the spontaneous development of the disproportionation process.

$$2Cu^+ \rightarrow Cu^0 + Cu^{2+}; \quad \Delta G_{298} = -8.28 \text{ kcal/mole}$$

The equilibrium concentration of monovalent copper under the conditions of the investigated process is given by the equation [8]:

$$[Cu^+] = \left[\frac{[Cu^{2+}]}{4.575 \exp\left(\frac{4650}{T} - 9.14\right)} \right]^{0.5}$$

and does not depend on the concentration of hydrogen ions. Its value is small and when $C^0_{Cu^{2+}}$ = 0.5g-ion/l at 140°C, for example, amounts to only 0.06g-ion/l. To judge from the variation in the concentration of chloride ions combined with the Cu^+ ions and also from published data [8-10], the content of cuprous ions formed during the autoclave treatment of the solutions with hydrogen is considerably greater than the equilibrium content. Moreover, the properties of the powders (form, particle size, lattice constant) obtained by the autoclave deposition of copper (τ = 10 min, P_{H_2} = 38 atm, 140°C) and on account of disproportionation in the $Cu\text{-}Cu^{2+}$ system (τ = 60 min, 140°C) are quite comparable.

Thus, during the autoclave deposition of copper the metallic phase is formed as a result of disproportionation of the excess (above the equilibrium content) monovalent copper.

The unstable structure of the copper particles at the moment of generation during disproportionation, due to their excess surface energy, leads to approach of the particles to the distance characteristic of the crystal lattice and to 'condensation' of the metallic atoms in a direction perpendicular to the surface of the solid phase. As a result of the physical and chemical inhomogeneity of the solid surface, conditions are created on it for the formation of polycrystalline deposits on account of adhesion, and this increases with increase in temperature. (The formation rate of the disperse particles of copper increases). The adhesion of the copper powder to the reactor walls and to the surface of the mixing equipment, in the operating zone of which the generation of the energetically unstable crystalline particles mainly occurs, can be fully explained from these standpoints.

Table 1: Data on the specific deposition of copper (g/cm²) on certain solid materials with (I) and without (II) additions of PAA. C^0_{Cu} = 68g/l, t = 140°C, $C_{(NH_4)_2SO_4}$ = 100g/l, P_{H_2} = 28 atm, C_{PAA} = 0.4g/l.

Name of material	I	II
Titanium (VT1-0)	0.021 (0.027)	0.059 (0.073)
Steel (EI-943)	0.014 (0.019)	0.046 (0.057)
Fluoroplastic (4M)	0.022	0.023
Graphite	0.074 (0.092)	0.056 (0.129)
Copper (M00)	0.046	0.064
Molybdenum	(0.064)	(0.122)
Tungsten	0.041 (0.078)	0.058 (0.109)
Corundum	0.064 (0.068)	0.045 (0.103)
Lead	0.042 (0.053)	0.048 (0.053)
Tantalum	0.043	0.059 (0.053)

Note: The data from experiments without the addition of ammonium sulphate are given in brackets.

To determine the effect of the nature of the solid surface on the process we determined the amount of copper deposited on plates (S_y = 12cm^2) of various materials (table 1). Increased deposits of copper are brought about by contact release (Mo, W) and physical (graphite, corundum) or chemical (Ti, Pb, Ta) inhomogeneity. The copper deposits are appreciably reduced in the presence of ammonium sulphate and particularly with the addition of polyacrylamide. Without the anticoating additions powder deposits were observed even in the first 5-10 min after the beginning of the experiment.

In aqueous solutions titanium is normally coated with a film of hydrated dioxide, which has a well-developed specific surface and adsorption characteristics. The probability of solid-phase interaction in the Cu–$TiO_2 \cdot nH_2O$ system is insignificant, since the structure and lattice constants of copper (cubic, a = 3.615Å) and titanium (tetragonal, a = 4.501Å, c = 2.9Å) are different. A chemisorption mechanism of absorption of copper ions by hydrated titanium dioxide from the neutral solutions is more likely [9, 10]. Thus, with the addition of $TiO_2 \cdot nH_2O$ to the initial solution at rates of 5-50g/l the amount of copper deposited on the reactor walls was reduced in proportion to the consumption of the additive. Thus, the deposition of copper on the reactor walls was due to the physicochemical inhomogeneity of the solid surface, which increases even more in the presence of surfactant films (in the case of hydrated titanium dioxide).

To reduce the powder deposits it was necessary to inhibit the internal surface of the reactor and to create conditions for the generation of particles of copper in the volume of the solution. The addition of organic substances was most favourable for this purpose. By the use of more than 50 types of ionic and non-ionic additives it was established that soluble poly-electrolytes (polymers based on acrylic acid and its derivatives) have the greatest anticoating effect. The carboxyl groups of these substances form hydrogen bonds with the hydroxyl groups of the hydrated titanium oxide film as a result of its hydrophilicity and of the preferred adsorption of high molecular compounds [11-13]. In our opinion inhibition of the reactor walls with the addition of surfactants is possible on account of saturation of the electronic vacancies and neutralisation of the surface charge. In addition, the carboxyl groups, which possess ion-exchange characteristics, form stable associations with the cuprous ions. On account of the micellar nature of solutions of poly-electrolytes, centres with an increased concentration of copper ions, in which reduction to cuprous ions takes place under the influence of hydrogen, are generated in the volume of the solutions [14]. On the attainment of a limiting concentration the cuprous ions disproportionate to form metallic copper. The rate of the above-mentioned processes increases with increase in the Cu^{2+} concentration and temperature, and this leads to an increased yield of the fine particles of powder. The further development of the process obeys the laws of sorption kinetics and depends on the characteristics of the active groups on the additives employed.

When the solution contains cations possessing increased sorption capacity, i.e. a greater charge, a smaller ionic radius as, for example, in Fe^{3+} and H^+, the conditions for preferred sorption of Cu^{2+} ions are impaired, and this leads to an increase in the amount of deposited copper on the internal surface of the reactor. The decrease in the deposition rate of copper when the solution contains oxidising agents is due to a decrease in the concentration of cuprous ions subject to disproportionation. The accumulation of acid in the solution, particularly at temperatures above 150°C, leads to disruption in the action of the organic additive. This is why the deposition of copper becomes more appreciable towards the end of the operation. The 'sorption' mechanism for the reduction of cuprous ions is also valid for inorganic sorbents. On account of their lower capacity, however, their role is of secondary significance and only shows up when the organic functional groups are destroyed.

With an identical concentration of cuprous ions in the volume of the solution the conditions for their delivery to the various sections of the surface of the growing metallic copper, formed during disproportionation, should be identical, and this should predetermine the formation of equiaxial particles. However, the degree of dispersion and the shape of the particles of the obtained powders depend significantly on the nature of the surfactant [6] and the salt background of the solution [5].

By being adsorbed on the surface of the growing copper, additions of surfactants reduce the surface tension, and this according to Wulff's law alters the growth rate of the faces in proportion to their surface tension. The subsequent growth of the particles depends on the strength and uniformity of the adsorbed layer of surfactant, and this is determined by the chain length and the nature and orientation of the radical in the surfactant. Adsorption of uniform character assists the formation of particles with rounded form; with selective adsorption on individual faces of the growing crystal stronger development is observed in the free (unblocked by surfactant) faces, and this leads to a change in the shape of the powder particles. Fig. 1 shows the effect of certain surfactants on the shape of the powder particles. In addition, the adsorption of the surfactant leads to neutralisation of the surface energy of the particles (their screening and limitation in the number of contacts between them). The development of these processes, determined by the nature of the surfactant and the medium, limits the probability of adhesion of the particles to the solid surface, and this increases the degree of dispersion of the powder and further reduces the probability of its deposition on the reactor walls. When additives with clearly defined blocking characteristics are employed, aggregation of the individual particles of powder is possible as a result of the formation of polymeric bridges of adsorbed surfactant molecules. A similar effect is observed (fig. 2) in experiments with polyacrylamide and 'Magnoflok 140'. This effect becomes stronger as the copper is deposited (table 2) particularly in many-cycle experiments [4, 5], and this leads to an increase in the yield of the coarse fractions of powder.

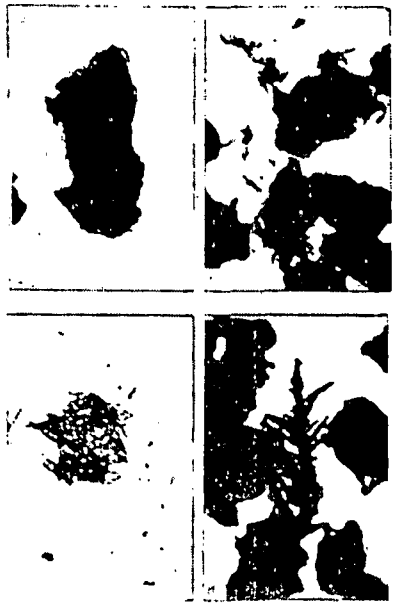

Fig.1 The large-size fractions of the powders (+100 μ) obtained from solutions containing, g/l: a) 5.0 polyacrylamide; b) and c) 0.4 granular, suspension polyacrylamide.

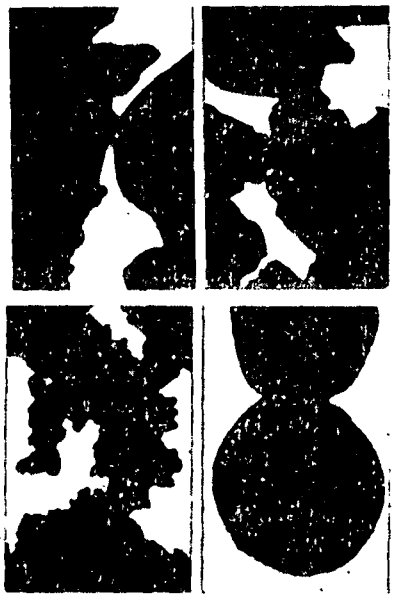

Fig.2 Electron photomicrographs of the powders obtained with polyacrylamide (0.4 g/l).

Table 2: The properties of the power as a function of the length of deposition. t = 150°C, P_{H_2} = 28 atm, C_{Cu} = 60g/l, C_{PAA} = 0.6g/l, $C_{(NH_4)_2SO_4}$ = 150g/l

Deposition time min	Content (%) of fraction μ				Specific surface area m^2/g
	+100	-100-+74	-74-+44	-44	
10	3.4	5.8	26.6	64.2	0.072
20	10.1	11.0	29.6	49.3	0.084
30	24.3	21.7	25.0	30.0	0.099

The character of the adsorption of the surfactant depends on the salt concentration of the solution. The cations of inert salts having a charge opposite to the charge of the functional group of the surfactant supresses the dissociation of the surfactant and leads to closer packing in the adsorption layer. While also possessing increased hydration, the cations give rise to partial dehydration of the surfactant. As a result the ions of the surfactant become more hydrophobic and are adsorbed on the particles of the powder. This effect becomes stronger with increase in the polarisability and with decrease in the hydration of the cations.

According to these characteristics the monovalent cations can be arranged in the order Na, K, NH_4 and divalent cations in the order Ni, Zn, Fe[14]. In these series a decrease in the degree of dispersion of the powder[6]) for a surfactant concentration of 0.4g/l was observed.

The orientation of the nuclei changes and their aggregation decreases under the influence of the electrostatic field of the cations[15]. Here, the higher the strength of the field, the more likely the formation of dispersed particles. Thus, added inert metal sulphates affect the shape and degree of dispersion of the particles of powder both directly and on account of change in the adsorption of the surfactant.

The investigations demonstrate the considerable effect of organic additives on the mechanism of the deposition of powder on the walls of the reactor and also on the formation and growth of the particles of copper.

References

1) D I Evans: Advance extractive in hydrometallurgy: London 1967, p. 831.
2) S S Naboichenko: Tsvetnye Metally 1971, (1), 26.
3) S S Naboichenko: TsIIN Tsvetnaya Metallurgiya 1971, (13), 27.
4) S S Naboichenko: Poroshkovaya Metallurgiya 1972, (4), 1.
5) S E Klyain et alia: Poroshkovaya Metallurgiya 1973, (7), 27.
6) S S Naboichenko et alia: Poroshkovaya Metallurgiya 1975, (10), 8.
7) E A von Hahn and E Peters: J. Phys. Chem. 1965, 69, (2), 547.
8) S E Klyain et alia: Izv VUZ Tsvetnaya Metallurgiya 1974, (4), 27.
9) G M Zhabrova and Yu V Egorov: Uspekhi Khimii 1961, 30, (6), 764.
10) I Riskin and T Velikoslavinskaya: Zh. Prikl. Khim. 1969, 42, (6), 1400.
11) I D Kulikova et alia: in Macromolecules at the phase boundary: (editor Yu S Lipatov), Naukova Dumka, Kiev 1971, p. 86.
12) I Callum and C T Rankin: J. Polymer. Sci. 1971, 9, (10), 751.
13) A A Berlin and V E Basin: Principles of the adhesion of polymers: Khimiya, Moscow 1974.
14) V P Vasil'ev et alia: Zh. Fiz. Khim. 1960, 34, 1763.
15) Yu A Til'mans: Crystallisation of salts from aqueous solutions in the presence of various ions as impurities: Frunze, Akad. Nauk KirgSSR 1957.

UDC 546. 722'74'683.1'267:661.183.9

Electron ion exchange properties of mixed nickel and thallium ferrocyanide

A V Kalyuzhnyi, V V Vol'khin and M V Zil'berman (Perm Polytechnic Institute - Department of General and Inorganic Chemistry)

The separation of thallium from solutions with complex compositions in the form of mixed ferrocyanides of thallium and transition metals is characterised by its high selectivity[1]). However, there is significant disadvantage in this process: the ferrocyanide only serves for one cycle and is thermally destroyed after saturation with thallium (the thallium is leached from the cake with water). The aim of the present work was to investigate the possibility of the desorption of thallium from the ferrocyanide without decomposition and to outline ways of regenerating the ferrocyanide sorbent. The search was based on the oxidation-reduction reactions involving ferrocyanides, which have already made it possible to obtain favourable results in the desorption of rubidium from analogous sorbents[2]).

The investigation was carried out with samples of ferrocyanides having the following compositions: $Tl_{1.10}Ni_{1.45}Fe(CN)_6$ (sample A): $Tl_{1.10}Ni_{1.45}Fe(CN)_6 \cdot 0.25Tl_2SO_4$ (sample B). The first of them was obtained by ion-exchange saturation of the ferrocyanide $K_{1.00}Ni_{1.50}Fe(CN)_6$ with thallium from a 0.02N solution of $TlNO_3$. To prepare the second sample the same ferrocyanide was used as the starting material, but it was saturated with thallium from a 0.02N solution of Tl_2SO_4; this led not only to ion exchange but also to molecular sorption of thallium sulphate. Solutions with the following compositions were used as oxidising agents: 0.1N $Ce(SO_4)_2$ + 1N H_2SO_4; 0.1N $KMnO_4$ + 1N H_2SO_4 (in individual experiments H_2SO_4 was replaced by HCl); 0.1M NaClO + CH_3COOH (pH ≈ 4). The oxidation was performed in airtight vessels.

The results showed that a considerable part of the thallium ions and a small amount of nickel ions pass from the

UNIVERSITY OF UTAH
RESEARCH INSTITUTE
EARTH SCIENCE LAB.

SUBJ
MNG
MISM

United States Patent [19]

Morrell et al.

[11] **4,249,777**

[45] **Feb. 10, 1981**

[54] METHOD OF IN SITU MINING

[75] Inventors: **Roger J. Morrell; William C. Larson,** both of Bloomington; **Robert D. Schmidt,** Isanti, all of Minn.

[73] Assignee: **The United States of America as represented by the Secretary of the Interior,** Washington, D.C.

[21] Appl. No.: **60,101**

[22] Filed: **Jul. 24, 1979**

[51] **Int. Cl.**[3] **E21B 43/28**

[52] **U.S. Cl.** **299/4;** 166/50; 166/245

[58] **Field of Search** 299/2, 4, 5; 166/50, 166/245

[56] **References Cited**

U.S. PATENT DOCUMENTS

1,816,260	7/1931	Lee	166/50 X
2,966,346	12/1960	Huitt et al.	299/4
3,563,606	2/1971	Sears	299/2
4,160,481	7/1979	Turk et al.	166/50 X

Primary Examiner—Ernest R. Purser
Attorney, Agent, or Firm—Thomas Zack; Donald A. Gardiner

[57] **ABSTRACT**

An improved method of in situ mining of a mineral bearing stratum. The method comprises drilling alternating rows of vertical injection and recovery wells to the depth of an aquiferrous mineral bearing stratum. Two horizontal branches are drilled at the bottom of each injection and recovery well. The horizontal branches are substantially parallel to one another and lie within the mineral bearing stratum. Leachant fluid is pumped under pressure into the injection wells to dissolve the minerals contained in the stratum. Leachant fluid containing the dissolved minerals is pumped out through the recovery wells. The method of the present invention requires substantially less drilling and pipe for extracting minerals from a given volume of a mineral bearing stratum and results in more constant mineral extraction rates than conventional techniques.

4 Claims, 2 Drawing Figures

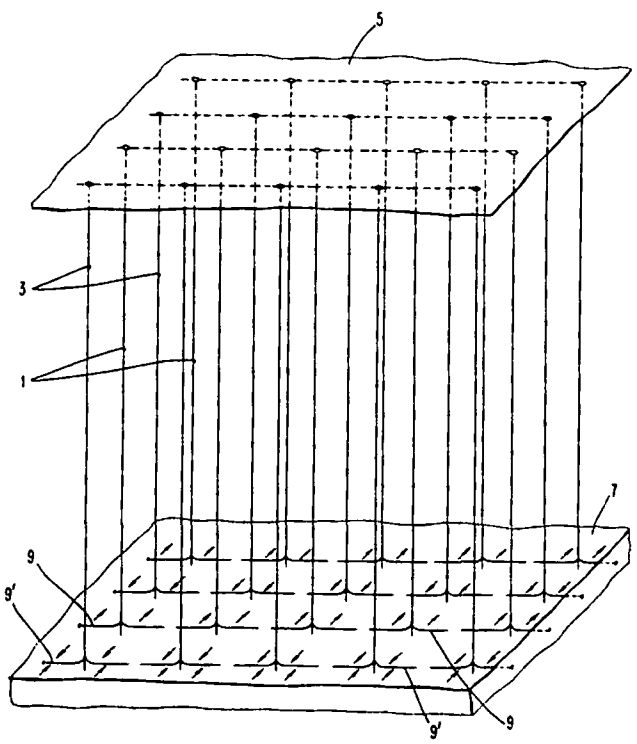

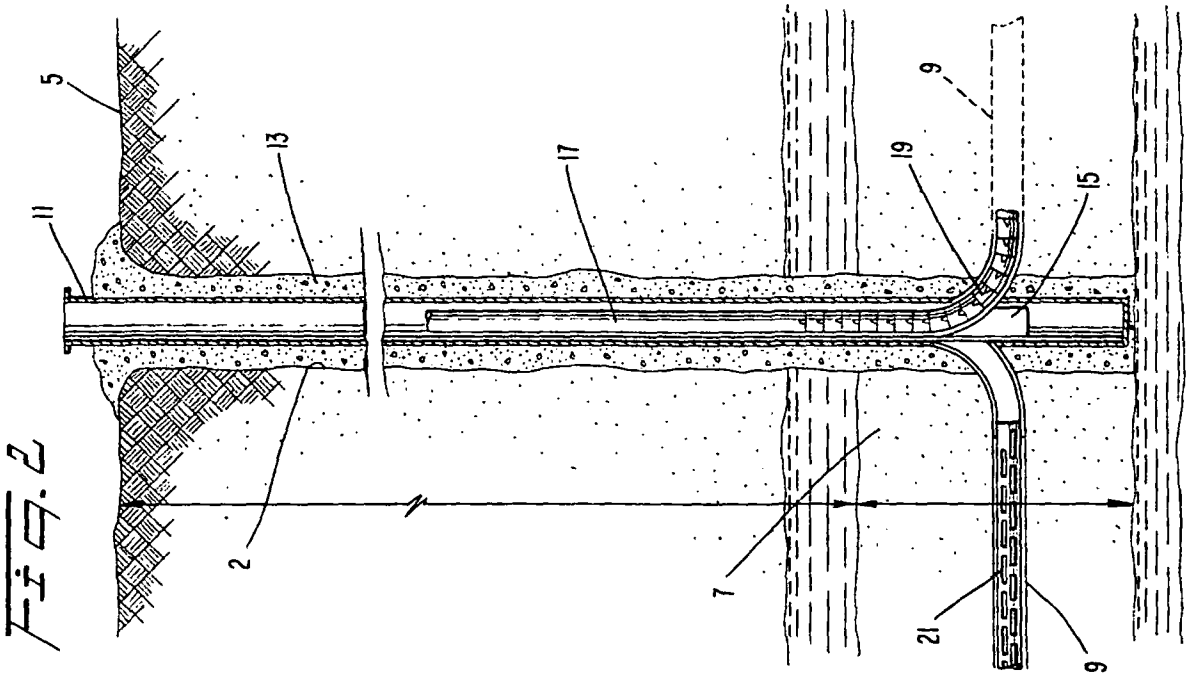

Fig. 2

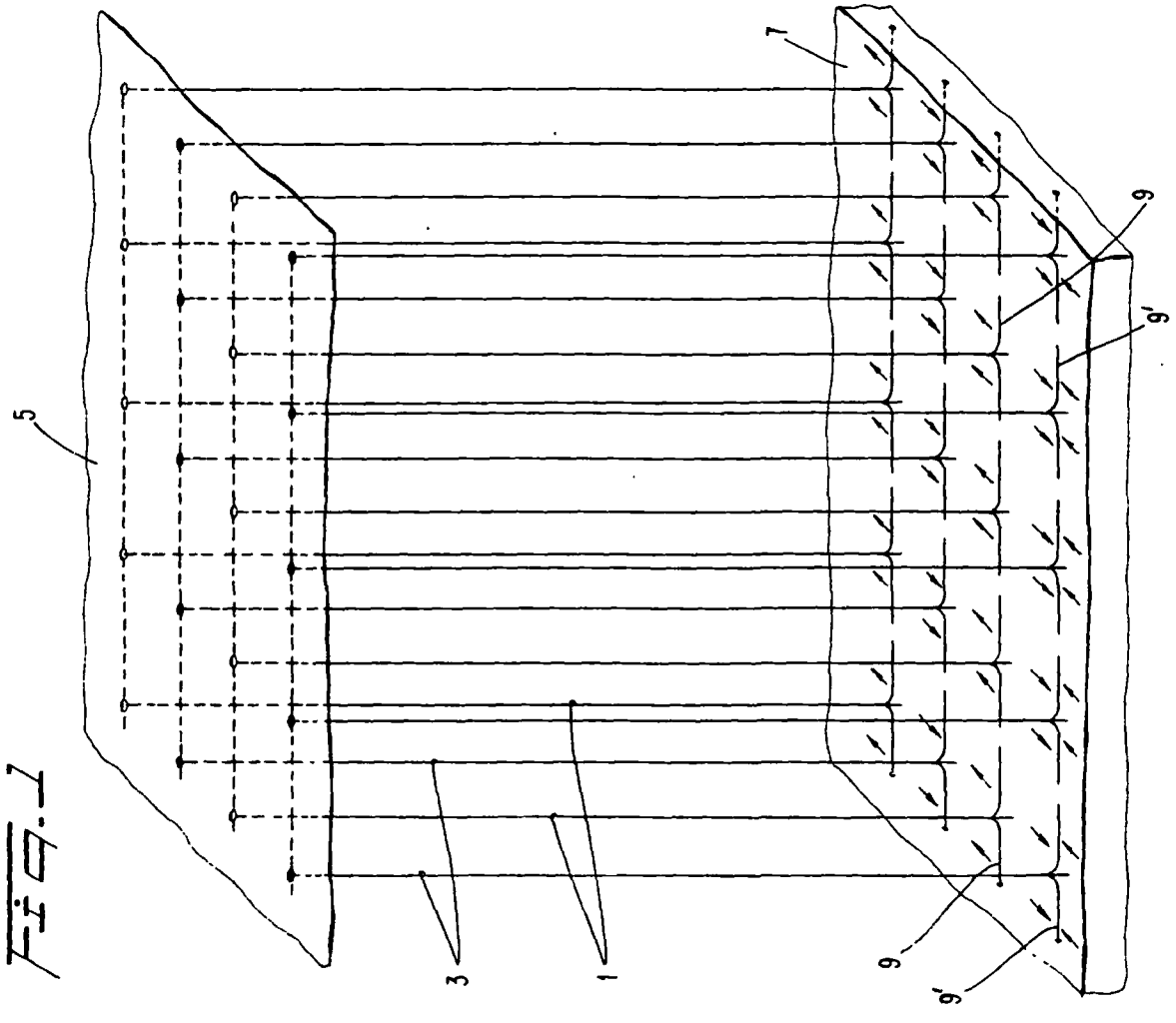

Fig. 1

METHOD OF IN SITU MINING

BACKGROUND OF THE INVENTION

The invention relates to the field of in situ mining, and more particularly to a method of in situ mining using plural alternating rows of injection and recovery wells.

In situ mining has been recognized as an effective technique for recovery of minerals contained in an ore or mineral bearing stratum. Prior techniques for in situ mining have utilized one or more vertical injection wells drilled to the depth of an aquiferrous mineral bearing stratum for injecting a chemical leachant into the stratum to dissolve the desired minerals. In the prior art, a plurality of vertical injection wells, generally greater in number than the number of recovery wells, are arranged about each recovery well to pump out the leachant containing the dissolved minerals. The wells are arranged in what are known as "five-spot," "seven-spot," and "hexagonal" patterns with one recovery well surrounded by a number of injection wells.

Each vertical injection and recovery well generally includes a vertical screen disposed at the depth of the mineral bearing stratum to allow ready flow of the leachant fluid into and out of the recovery and injection wells.

A chief disadvantage of such conventional in situ mining techniques is that a large number of wells must be drilled to adequately cover a given volume of an aquiferrous mineral bearing stratum because each recovery well requires a plurality of associated injection wells. The cost of drilling, pipes, and pumping devices is proportionally multiplied when larger ore fields are mined. The high cost of drilling and mining marginal ore fields makes such mining economically impractical.

Conventional injection/recovery well patterns characteristically produce a declining volume of dissolved minerals recovered over the lifetime of the mining operation because toward the end of the operation, most of the minerals in the area directly between the recovery well and surrounding injection wells have already been leached. Pumping speed, and hence recovery volume, using conventional well patterns is low since one recovery well receives leachant under pressure from several injection wells.

Vertically oriented injection/recovery screens, as used in conventional in situ mining techniques, must be precisely placed within the ore-bearing stratum in order to insure maximum extraction of the ore-bearing layer (i.e., greatest injection/recovery well efficiency). However, placement of vertical well holes, especially in shallow formations at great depths (approximately 1,000 feet or more), can be difficult and time-consuming. In addition, vertically oriented injection/recovery screens do not "sweep out" a large area of the ore-bearing stratum since the stratum is generally horizontally aligned, whereas the screens are vertically aligned.

It is known to use horizontally well-branches or "drain-holes" to drain off undesirable aquifer (water-containing) regions which interfere with oil well drilling and oil recovery. However, heretofore such horizontal well branches have not been used for in situ mining of a mineral bearing stratum using a leachant fluid and plural injection and recovery wells.

It is therefore a primary object of the invention to provide an improved method of in situ mining of a mineral bearing stratum.

It is an additional object to provide an improved method of in situ mining utilizing horizontal branches which method requires substantially less drilling and pipe to recover a given volume of ore-bearing material than conventional in situ mining techniques.

It is a further object to provide a method of in situ mining having a substantially constant rate of mineral recovery over the lifetime of the mining operation.

SUMMARY OF THE INVENTION

These and other objects of the invention are achieved by the present invention wherein there is provided an improved method of in situ mining of a mineral bearing stratum. The method comprises the steps of drilling alternating rows of vertical injection and recovery wells, each such row containing a plurality of wells. The injection and recovery wells are drilled to the depth of an aquiferrous mineral bearing stratum. At least two horizontal branches are drilled out from the bottom of each vertical well in approximately the middle of the ore-bearing stratum. The horizontal branches of each well are aligned substantially parallel to one another. Each branch includes an aquifer oriented screen to allow ready injection or recovery of leachant fluid.

Leachant fluid is pumped under pressure into the injection wells to dissolve the minerals contained in the stratum. Leachant fluid containing the dissolved minerals is pumped out through the recovery wells.

Preferably, the number of injection well rows is equal to the number of recovery well rows, and the number of injection wells in a single row is equal to the number of recovery wells in an adjacent row.

The method of the present invention requires substantially fewer wells and much less pipe (up to one-tenth to extract minerals from a given volume of a mineral bearing stratum than conventional single recovery well-plural injection well arrangements. The costs of mining are reduced, thus allowing formerly uneconomic or marginal ore deposits to be recovered.

The use of horizontal well branches having aquifer oriented screens results in a larger volume of the ore-bearing stratum being swept out for each injection/recovery well pair. As mentioned above, the total number of injection wells is equal to the total number of recovery wells. This, in combination with the alternating row arrangement of injection recovery wells, results in a desirably high volume flow of leachant fluid throughout the ore-bearing layer since there is a one-to-one correspondence between injection and recovery wells. Thus, the rate of mineral extraction is high and is accomplished at a constant rate.

The use of horizontal branch wells also results in wider tolerance for vertical well drilling depth errors since the depth of the horizontal branches can be adjusted if it is found that the bottom of the verical portion of the well has not been precisely placed in the middle of the ore-bearing stratum.

BRIEF DESCRIPTION OF THE DRAWING FIGURES

These and other features, objects, and advantages of the present invention are presented in the following description of the preferred embodiment, taken in con-

junction with the accompanying drawing figures, wherein:

FIG. 1 is a schematic perspective view showing an arrangement of injection and recovery wells as taught by the method of the present invention; and

FIG. 2 is a cross-sectional view of a single injection or recovery well of FIG. 1.

DETAILED DESCRIPTION OF THE PREFERRED EMBODIMENT

The method of the present invention is described in conjunction with drawing FIGS. 1 and 2. Alternating rows of vertical injection wells 1 and vertical recovery wells 3 are drilled or otherwise formed from surface 5 to the depth of a mineral bearing ore zone or stratum 7. The alternating rows of injection and recovery wells are arranged in a matrix or grid-like pattern as shown in FIG. 1.

Each injection well row and recovery well row contains a plurality of individual wells, with the number of wells of an injection row preferably equal in number to the number of recovery wells in an adjacent row. In other words, at least one injection well and at least one recovery well are contained in each row. Therefore, in its simplest preferred form a recovery field may be a single line of alternating injection and recovery wells.

At substantially the lowest portion of each injection and recovery well at least one substantially horizontal well branch 9 and 9', respectively, is formed. Preferably two such horizontal branches 9 and 9' are formed from each respective injection and recovery well. Horizontal well branches 9 and 9' are disposed substantially parallel to one another and lie within a plane defined by aquiferrous mineral bearing stratum 7.

Horizontal well branches 9 are formed as shown in FIG. 2. The well branch drilling operation is described with respect to the formation of an injection well 1. It is understood that an identical technique is used to form horizontal branches 9' for recovery wells 3.

The vertical injection well is first drilled or formed by techniques well-known in the art. Injection well bore 2 is drilled to the depth of mineral bearing stratum 7. A well casing 11 is inserted into well bore 2 to the depth of stratum 7 and cement 13 poured around casing 11 to secure the casing within well bore 2.

A removable whipstock 15 is inserted near the base of well bore 2 and locked into a position approximately mid-way in depth within mineral bearing stratum 7.

Horizontal well branches 9 are formed using what is known as a "drain-hole" drilling technique. A drill pipe string 17, having a flexible U-joint spiral reamer 19 attached to the lower end thereof, is lowered into well bore 2 until reamer 19 contacts whipstock 15. Whipstock 15 causes reamer 19 to bend outwardly at approximately right angles to well bore 2. As reamer 19 advances, it forms a horizontal well branch 9.

Reamer 19 includes a conventional spiral stablizer having a tri-cone bit mounted on the end thereof. The exact design of the stabilizer and flexible drill pipe can vary.

When a first well branch 9 is drilled to the desired horizontal length, drill pipe 17 and reamer 19 are withdrawn and whipstock 15 rotated, so that a second horizontal well branch can be drilled. Up to three such horizontal well branches can efficiently be formed from a single vertical well bore.

Branches 9 can be cased or left uncased after drilling, as desired. Aquifer oriented (horizontal) screens 21 are placed in horizontal branches 9 to prevent sediment and unwanted particulate matter from flowing into the horizontal branches.

After completion of all vertical well and horizontal branch drilling operations, a leachant fluid 23, shown as flow lines in FIG. 1, is pumped under pressure into each injection well. The particular leachant fluid employed varies depending on the minerals to be dissolved and recovered from mineral-bearing stratum 7.

Leachant fluid 23 flows under pressure from injection well horizontal branches 9 toward adjacent recovery well horizontal branches 9' (FIG. 1). The leachant fluid dissolves selected minerals contained in stratum 7. The flow of leachant fluid 23 from injection wells 1 to recovery wells 3 is generally within the plane defined by stratum 7.

Dissolved minerals from stratum 7 and leachant fluid are extracted through horizontal recovery well branches 9'. The leachant fluid containing the dissolved minerals is pumped out or otherwise extracted from recovery wells 3 to the surface. The dissolved minerals are separated from the leachant fluid in subsequent recovery steps.

The spacing between wells in a row is dependent on the length of the well branches. For conventional drilling techniques, a maximum well branch length of approximately 150 feet (of 2" to 6" diameter pipe) is possible, thus giving an appropriate spacing between wells in a row of more than 300 feet. The distance between rows is determined by the flow characteristics of the leachant fluid.

In an alternate arrangement, vertical injection and recovery wells 1 and 3 are respectively drilled to the depth of the upper and lower boundaries of mineral bearing stratum 7. Horizontal branches 9 and 9' are formed as described above. Leachant fluid is pumped into the stratum through injection wells 1 and flows substantially vertically through stratum 7 to recovery wells 3. This arrangement is advantageous for in situ mining where the mineral bearing stratum is narrow in the horizontal dimension but is vertically deep.

In the present invention, the horizontal orientation of the injection and recovery well branch screens 21 parallel to the plane of the aquiferrous mineral-bearing stratum provides several advantages over conventional in situ mining methods which use vertical screen injection and recovery. Sweep efficiency is improved since leachant fluid flows through substantially all the volume of the mineral bearing stratum which lies between the horizontal branches of an injection well and the horizontal branches of a recovery well. Fluid injection recovery capacity is increased because there is generally a one-to-one correspondence between the number of injection wells and adjacent recovery wells. This reduces the time required to leach minerals from a given volume of a mineral bearing stratum. Leachant dispersion is more uniform because of the adjacent nature of parallel injection well rows and recovery well rows. This results in a more uniform recovery rate over the lifetime of the mining operation. The in situ mining method of the present invention also gives greater control over the movement of the leachant fluid, thus reducing the possibility of leachant escape and environmental pollution.

In simulated tests, the method of the present invention may be compared to conventional "five-spot" in situ mining techniques. In the "five-spot" in situ mining technique, and analogous arrangements, a single recov-

ery well is placed at the center of a number of leachant injection wells. In the case of the "five-spot" arrangement, four vertical injection wells are drilled in an equal spaced arrangement about a central vertical recovery well. Each vertical injection and recovery well is drilled to the depth of a mineral bearing stratum. The injection and recovery wells each include vertically oriented screens disposed within the well bores with the length of the screens approximately equal to the thickness of the mineral bearing stratum.

Sweep efficienty of a particular in situ mining technique is determined by taking the ratio of the actual volume of a mineral bearing stratum through which injected leachant fluid flows to the total volume of the mineral bearing stratum to be mined.

In a standard volume of 100×100 horizontal feet by 20 vertical feet (200,000 cubic feet), a "five-spot" injection/recovery arrangement in which the mineral bearing stratum is bounded at the four corners by the injection wells, simulated tests show that the two-dimensional area swept out by leachant fluid is approximately 6.000 square feet. With a stratum thickness of 20 feet, this gives a volume swept out of 120,000 cubic feet. The sweep efficiency therefore is 120,000/200,000 or 60%.

For the same volume of an ore-bearing stratum (200,000 cubic feet), the horizontal injection/recovery technique of the present invention results in a higher sweep efficiency. Rows of vertical injection and recovery wells are spaced approximately 50 feet apart. Each vertical well includes horizontal branches approximately 100 feet long (total for both branches) disposed parallel to one another in the plane of the mineral-bearing stratum. The area swept out by leachant fluid between the horizontal injection and recovery well branches in simulated tests, as defined by the 20 foot difference between the upper and lower boundaries of the mineral bearing stratum, is approximately 1418 square feet. Multiplying this figure by the 100 feet of horizontal screen results in a figure for the volume swept of 141,800 cubic feet. Thus, the sweep efficiency for the method of the present invention is 71%. In both test simulations, the porosity and permeability of the aquiferrous stratum are assumed to be the same.

The greater efficiency of the method of the present invention over conventional "five-spot" and analogous arrangements results from the more complete saturation of the volume of the ore tone between adjacent rows of injection and recovery well horizontal branches. Unlike the "five-spot" pattern, in which leachant fluid flow lines are concentrated mainly within the areas directly between the outer injection wells and the central recovery well, the present invention provides for leachant fluid injection and recovery across substantially the entire width of a volume of mineral bearing stratum to be mined.

It is essential in in situ mining operations that the rate of leachant fluid injection and recovery be equal, to prevent leachant from escaping into and polluting the surrounding mineral bearing stratum. Fluid flow rates are limited in the "five-spot" arrangement by the fact that the ratio of vertical recovery screen to vertical injection screen length is always 1:4. Thus, the injection capacity of a typical "five-spot" or analogous well arrangement is limited by its recovery capacity. Typical fluid flow rates for recovery wells are approximately one gallon per minute per screen foot (one gal./min/ft. screen). This implies that the injection well fluid flow capacity for such prior art arrangement is limited to approximately one-quarter gallon per minute per screen foot (¼ gal./min/ft. screen).

In contrast, with horizontally oriented aquifer screens as used in the present invention, the ratio of recovery screen length to injection screen length can be up to 1:1. Thus, for a recovery of one gallon per minute per screen foot, the injection rate is as high as one gallon per minute per screen foot using the methods of the present invention.

The higher injection rates of the present invention, coupled with the greater sweep efficiency, result in overall increased fluid injection and recovery capacity over prior art in situ mining techniques.

Fluid injection/recovery capacity is measured in terms of pore volumes, where one pore volume is equal to that portion of a fixed volume of aquiferrous mineral bearing stratum which constitutes open space. For the examples given above, the fixed volume is a 100′×100′×20′ block of material. Assuming a porosity of approximately 35%, this results in one pore volume being equal to approximately 70,000 cubic feet.

In the simulated tests mentioned above, assuming 30 days of simulated pumping with the conventional "five-spot" pattern, 6.1 pore volumes of leachant are injected at the four corner wells with 0.77 pore volume (approximately 12%) of leachant recovered at the center recovery well. Therefore, approximately 88% of the leachant remained in the mineral bearing stratum after 30 days.

Using the methods of the present invention, approximately 36 pore volumes of leachant are injected into an identical 100′×100′×20′ volume of mineral bearing materials during 30 days of pumping, and 17.7 pore volumes (aproximately 49.7%) of the leachant fluid are recovered through the recovery wells after 30 days.

An important advantage of the horizontally aligned injection and recovery well screens of the present invention over conventional vertically oriented injection and recovery well screens is that a more uniform dispersion of leachant fluid is produced within the volume swept out by the leachant. This results in a more uniform mineral recovery rate over the lifetime of the mining operation. Fluid flow from all portions of the horizontal screens placed in the horizontal branches formed according to the present invention is substantially uniform. Leachant also tends to be most concentrated in the volume swept out between adjacent injection and recovery well rows. The higher concentration of leachant results in a more effective leaching process.

Leachant fluid flow and leachant pollution of surrounding areas of the mineral bearing stratum are also readily controlled by the method of the present invention.

In conventional "five-spot" arrangements having vertically oriented injection and recovery screens, leachant fluid stream lines radiate in all directions from each injection well. Since the injection wells are disposed about the central recovery well, some of the radial injection well stream lines escape the influence of the center recovery well. Thus, recovery of all the escaping leachant fluid is a difficult process. At least four intercept or "guard" wells are required around a conventional "five-spot" pattern to prevent leachant fluid escape.

In contrast, leachant flow between the parallel, horizontally aligned well branches of the present invention is concentrated in a substantially narrow area between the injection well branches and the recovery well branches. The injection and recovery wells can be ar-

ranged so that the outermost row of an array of such wells is a recovery well row. Thus, the outer recovery well rows intercept all of the leachant fluid not captured by the recovery wells disposed near the center of the well pattern. Another advantage of this arrangement is that if further areas of a mineral bearing stratum are to be mined, these outermost recovery well rows can later be used to leach adjacent blocks of the mineral bearing stratum.

Another advantage of the method of the present invention is that it requires only approximately one-tenth the total amount of drilling, pipe, and casing compared to conventional drilling patterns, for the same volume coverage. In extending a mining area by 2,500 square feet, a conventional "five-spot" pattern requires three new wells, assuming a normal well spacing of approximately 50 feet. If the depth to the mineral bearing stratum is approximately 500 feet deep, this extended drilling requires $3 \times 500' = 1{,}500$ feet of new drilling, pipe and casing. This conventional setup also requires three additional drilling rigs and the shutting down of three injection wells on the side of the well field opposite the side which is being extended.

Using the techniques of the method of the present invention, only one vertical well and associated pair of horizontal branch wells are needed to extend the leaching area of the mineral bearing stratum by 15,000 square feet. Assuming a length for each horizontal branch of 150 feet and a normal spacing between rows of wells of 50 feet, the total footage required for drilling is 500 vertical feet plus 300 horizontal feet for a total of 800 feet.

Using the figures given above, extending the conventional "five-spot" pattern 15,000 square feet requires 15,000/2,500 or six sets of three wells each (i.e., 18 new wells). For a drilling depth of 500 feet, this means a total footage of $18 \times 500'$ or 9,000 total feet is required. This amount of drilling footage is approximately 11 times greater than that required by the method of the present invention to extend the leaching area by the same amount. In addition, since every third well in the conventional "five-spot" pattern must be a recovery well, each such recovery well requires a pump. Thus, six out of the eighteen additional wells which are drilled in the "five-spot" pattern example given above would require pumps versus only one additional pump needed by the method of the present invention.

Thus, the present invention provides improved sweep efficiencies and desirable high volume flow of leachant fluid throughout a mineral bearing stratum. The rate of mineral extraction is high and is accomplished at a constant rate. The use of horizontal branch wells results in a wider tolerance for vertical well drilling depth errors since the depth of the horizontal branches can be adjusted. Leachant fluid flow is precisely controlled using the techniques of the present invention to prevent leachant escape and environmental pollution of areas surrounding a mineral bearing stratum.

While the in situ mining method of the present invention has been described in considerable detail, it is understood that various changes and modifications would occur to persons of ordinary skill in the art without departing from the spirit and scope of the appended claims.

What is claimed is:

1. A method of in situ leach mining of a mineral bearing stratum comprising the steps of:

surface drilling a plurality of generally vertical leachant injection wells, said injection wells being horizontally spaced apart and aligned in a row;

surface drilling a plurality of generally vertical recovery wells, said recovery wells being horizontally spaced apart and aligned in a row substantially parallel to said injection wells, said injection and recovery wells each being drilled to a depth substantially equal to the depth of an aquiferrous mineral bearing stratum;

surface drilling at least two generally horizontal branch wells from substantially the lowest point of each of said injection and recovery wells, said horizontal branches being parallel to one another and lying within a plane containing said stratum of minerals to be recovered each said branch including a screened section;

pumping a leachant fluid under pressure into said injection wells to dissolve minerals contained in said mineral stratum; and

pumping said leachant containing said dissolved minerals out through said recovery wells, whereby said leached minerals are withdrawn from said mineral bearing stratum at a substantially constant rate over the lifetime of the mining operation.

2. The method of claim 1 wherein there are a plurality of alternating rows of said injection and recovery wells, with the number of parallel disposed injection and recovery well rows being equal in number.

3. The method of claim 2 wherein the number of injection wells in a row is equal to the number of recovery wells in an adjacent row.

4. The method of claim 1 wherein said injection and recovery wells are drilled to a depth substantially equal to the upper and lower boundaries of the mineral bearing stratum.

* * * * *

UNIVERSITY OF UTAH
RESEARCH INSTITUTE
EARTH SCIENCE LAB.

SUBJ
,MNG
MKH

To regenerate the oxidised electron ion exchanger (sample C) we used its reduction in the presence of K^+ ions:

$$Tl_{0.20}Ni_{1.40}Fe(CN)_6 + K^+ + e \rightarrow K_{1.00}Tl_{0.20}Ni_{1.40}Fe(CN)_6 \quad (5)$$

As reducing agent we used a 0.093N solution of ascorbic acid. The amount of the potassium salt in the solution represented a fourfold excess over the stoichiometric amount according to equation (3). The dependence of φ on m_{red}, where m_{red} is the amount of reducing agent consumed [mg-eq/mg-mole $Fe(CN)_6$], is shown in fig. 1. As seen, complete reduction of Fe(III) to Fe(II) occurs in the ferrocyanide. The potential φ at the endpoint of the reduction amounts to 0.57V. According to this potential, solutions of K^+, $S_2O_8^{2-}$, $K^+ + SO_3^{2-}$, and others can be used as reducing agents. The amount of K^+ ions entering into the composition of the electron ion exchanger during the reduction x, [mg-eq K^+/mg-mole $Fe(CN)_6$] corresponds strictly to the fraction of reduced $Fe(CN)_6$ groups (fig. 3). The reduction results in the formation of a ferrocyanide with the composition $K_{1.00}Tl_{0.20}Ni_{1.40}Fe(CN)_6$, which is ready for the next cycle of sorption of Tl^+ ions.

Conclusions

The desorption of thallium from the mixed nickel thallium ferrocyanide can be realised by oxidation the ferrocyanide to ferricyanide. The sorbent can b generated by reduction.

References

1) I V Tanaev and M A Glushkova: Zh. Prikl. Khim. 1 32, 1959, 1899.
2) V V Vol'khin et alia: Zh. Prikl. Khim. 1976, 49, 172
3) A V Ragimov et alia: Izv Akad. Nauk. SSSR, Ser. K 1964, 4, 593.
4) N E Denisova: Author's Abstract of thesis: Leningr LTI 1967.
5) F Ya Kul'ba and V E Mironov: Chemistry of thall Goskhimizdat, Moscow 1963.

Soviet Non-ferrous metal Research
05, N5, 1977

UDC 669.535:546.723.66.06

The mechanism and kinetics of the hydrolytic precipitation of Fe(III) from zinc sulphate solution

E V Margulis, L S Getskin, N A Zapuskalova and M V Kravets (North-Caucasian Mining-Metallurgical Institute, All-Union Scientific-Research Institute of Nonferrous Metals)

The hydrolytic precipitation of iron plays a deciding role in the leaching of zinc calcines. However, there are no reliable data on its mechanism, and its kinetics have been insufficiently investigated. Data on the phases precipitated from solutions in the Fe_2O_3-SO_3-H_2O system[1)2)] cannot be transferred a priori to zinc solutions. Indications of the formation of basic sulphates and iron hydroxide during hydrolysis of iron in the hydrometallurgy of zinc are non-specific[3)], since a series of compounds are formed. In[4-9)] almost all the known solid products from the hydrolysis of $Fe_2(SO_4)_3$ were synthesized and their individualities were confirmed by IR spectroscopy and thermal analysis, but only a few of them are formed during the precipitation of Fe(III) from sulphate solutions with alkalis[9-11)]: Jarosite $(R, H_3O)Fe_3(OH)_6(SO_4)_2$ and the amorphous basic sulphate $2Fe_2O_3 \cdot SO_3 \cdot xH_2O$ as primary precipitation products, and goethite α-FeOOH as secondary product.

The purpose of the present work was to study the mechanism and kinetics of the hydrolytic precipitation of iron in the $Fe_2(SO_4)_3$-$ZnSO_4$-ZnO-H_2O system at 50-90°C under various concentration conditions (initial concentrations $C_{0\ Fe}$ = 0.05-15 and $C_{0\ Zn}$ = 0 and 100 g/l).

Table 1: The phase composition of the precipitates as a function of the temperature, the molar ratio m = ZnO/$Fe_2(SO_4)_3$, and time with initial $C_{0\ Fe}$ = 12 g/l and pH_0 = 1.2 in the $Fe_2(SO_4)_3$-$ZnSO_4$-ZnO-H_2O system, where $C_{0\ Zn}$ = 100 g/l

t, °C	m	Phase composition of precipitates (holding time, h)
90	1.0	A/G/(0.5); G(2-24)
	2.0 - 3.0	A(1/12); G(2-24)
	3.5	A/G/(2)
70	1.0	A(2); A/G/(7); G(24-120)
	2.0	A, G(1/12); G/A/(7); G(24-120)
	3.0	G(2-120)

Note: A = amorphous basic sulphate; G = goethite. Semi-quantitative ratios of the phases: A, G-phase G less than phase A; A/G/- phase A is the main phase, and phase G the impurity phase.

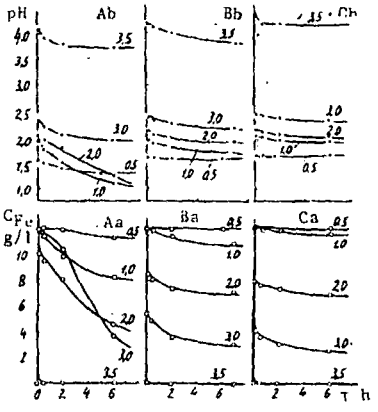

Fig.1 The variation of the concentration of iron (g/l, a) and pH (b) in solutions of the $Fe_2(SO_4)_3$-$ZnSO_4$-ZnO-H_2O system with time (h) at 90 (A), 70 (B), and 50 (C) °C. $C_{0\ Zn}$ = 100 g/l. The numbers of the curves correspond to the values of the molar ratios m = ZnO/$Fe_2(SO_4)_3$.

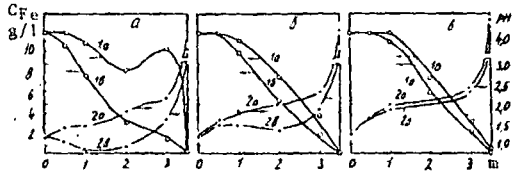

Fig.2 The concentrations of iron (g/l,1) and the pH values (2) in solutions of the $Fe_2(SO_4)_3$-$ZnSO_4$-ZnO-H_2O system as a function of m at 90 (a), 70 (b), and 50 (c) °C. $C_{0\ Zn}$ = 100 g/l. Curves 1 and 2 with letters a and b relate to holding times of 2 and 24 h respectively.

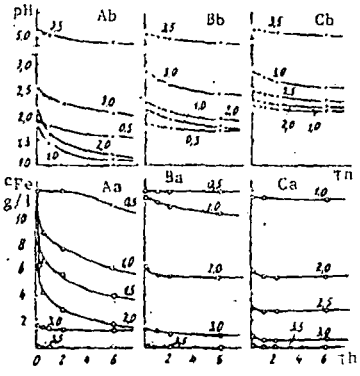

Fig.3 The variation of C_{Fe} (g/l, a) and (b) in solutions of the $Fe_2(SO_4)_3$-ZnO-H_2O system with time at 90 (A), 70 (B), and 50 (C) °C.

The procedure was similar to that described in[9]). The kinetics of the hydrolytic precipitation of Fe(III) are characterised by data on the variation of the pH and c_{Fe} with time (e.g., for $c_{0\ Fe}$ = 12 g/l in figs.1-3). The phase composition of the precipitates (table 1), established by IR spectroscopy, characterises the mechanism of the process. We note that the semi-quantitative estimates of the contents of the phases are relative, i.e., they only indicate an increase or decrease in the amounts of the given phase in relation to the others. For example, the secondary crystalline phase can be masked by the primary amorphous phase. The data in table 2 characterise the phase transitions in the precipitates.

Table 2: The degree of conversion (α, %) of the amorphous basic sulphates to goethite at 90°C as a function of the conditions

Conditions	Time, h	α, %	pH
Aqueous solution of NaOH, pH_0 = 4.5; solid:liquid 1:100	1	5.8	4.21
	3	8.0	3.72
	24	18.3	2.64
	120	68.2	-
Aqueous suspension of ZnO in stoichiometric amount, solid:liquid = 1:4	1 12	5.4	6.15
	2	22	6.05
	6	24.3	6.10
	24	32	6.05

The reasons for the observed changes in c_{Fe} and pH with time can be explained on the basis of theories about the mechanism of the hydrolytic precipitation of Fe(III)[12,13]). The addition of ZnO converted to $Zn(OH)_2$ to the solution gives rise to partial neutralisation of the acid (a sharp rise of pH from 1.2 to 1.5-4.4, as seen from fig. 1) and rapid exchange hydrolytic transformations of the aqua, hydroxo, and sulpho complexes of Fe(III) to more basic complexes with the conversion of $Zn(OH)_2$ into $ZnSO_4$. The initial rise of ΔpH_{in} shifts the hydrolysis state of Fe(III) in the solution from the equilibrium value and stimulates the hydrolysis reaction itself of the iron ions (slow decrease of pH, see figs.1 and 2).

Increase in the pH and the concentration of the hydroxo complexes of Fe(III) in the solution assists the formation of polynuclear complexes of iron, and as a result of the tendency of the latter to oxidise their polymerisation of the polycondensation type develops with the formation of colloidally disperse particles. Further consolidation of these particles leads to the formation of the amorphous hydrated oxosulphate $2Fe_2O_3 \cdot SO_3 \cdot xH_2O$[9]). The indicated composition of this compound was established in[9]) during its precipitation from a dilute solution of $Fe_2(SO_4)_3$. It is not impossible that during the precipitation from solutions more concentrated in SO_4^{2-} the basic sulphate acquires a variable composition, which changes towards a decrease in the basicity of the compound. However, it is difficult to establish this on account of the absence of reliable methods for determination or calculation of the amount of solution trapped by the amorphous precipitate without destroying the composition of the latter.

The amorphous basic sulphate is the primary product from the hydrolytic precipitation of Fe(III) from zinc sulphate solutions and changes into goethite with time (table 1). This phase transition is observed over the whole investigated range of Fe(III) concentrations in the solution and is accelerated with increase of the pH and temperature (table 1), but this transition takes place fairly slowly even at the initial pH_0 = 4.5 at 90°C, is retarded with time, and is accompanied by a decrease in the pH value (table 2), which is due to release of acid during the reaction.

$$2Fe_2O_3 \cdot SO_3 \cdot xH_2O = 4FeOOH + H_2SO_4 + (x-3)\,H_2O \qquad (1)$$

The retardation of the transformation with time is due not to the accumulation of acid in the solution but to diffusion retardation of the removal of the acid into the solution, which is created by the goethite crust on the particles of amorphous sulphate. This can be seen from the fact that the rate of reaction[1]) decreases considerably at a relatively small degree of conversion of the initial compound even with a high and practically constant pH value of 6 (table 2, neutraliser ZnO).

The secondary character of the α-FeOOH is due to the fact that the polycondensation of the hydroxo complexes of iron (III) which rapidly develops in the solution, leading to the formation of the amorphous precipitate, excludes the formation of centres for the crystallisation of goethite in the solution. As a more stable phase, the goethite is therefore formed during ageing of the amorphous precipitate of basic sulphate on account of the occurrence of reaction[1]). The mechanism of this transition was described in[14]).

It was established that with a concentration $c_{Fe} > 0.1$ g/l the initial product from precipitation of Fe(III) is the amorphous basic sulphate, while when $c_{Fe} \leq 0.1$ it is the amorphous hydrated iron(III) oxide[9]), which also changes into goethite during ageing.

On the basis of the data obtained in the work it is possible to make the following judgements about the kinetics of the process.

From the variation of the pH of the solutions with time it is seen (figs.1 and 2) that in the $Fe_2(SO_4)_3$-$ZnSO_4$-ZnO-H_2O system the hydrolysis rate of Fe(III) decreases with decrease of c_{Fe} and of the initial shift of ΔpH_{in} in the solution. For example (fig.1, at 90°C with a small ΔpH_{in} (specific consumption of neutraliser m = $ZnO/Fe_2(SO_4)_3$ = 0.5 the hydrolysis rate is low with a high value for c_{Fe}. With increase in m, ΔpH_{in} increases, but c_{Fe} decreases (on account of exchange reactions). The hydrolysis rate passes through a maximum with increase in m but decreases regularly with time on account of decrease in c_{Fe} and of the accumulation of hydrolysis acid, i.e., approach to hydrolysis equilibrium in the solution. We note the slow decrease of the pH value with time under the conditions of practically complete precipitation of iron (e.g., see fig.1 Ab, curve 3.5 or fig.2, curves 2a, c for m = 3.5), which is due to the occurrence of reaction[1]).

With other conditions equal the ΔpH_{in} value, which plays an important role in the kinetics of the process, increases with decrease in temperature (fig.1), and this is explained by the superimposition of three processes, i.e., neutralisation of the acid in the solution, exchange hydrolytic reactions, and the true hydrolysis reactions of iron. The first two processes are practically independent of temperature, but the hydrolysis of iron (it reduces the ΔpH_{in} value) is retarded with decrease in temperature (figs.1 Ab, Bb, Cb), and the contribution from hydrolysis to ΔpH_{in} increases with increase in the initial neutralisation of the acid, i.e., with increase in the departure from hydrolysis equilibrium. On account of this, ΔpH_{in} increases with decrease in temperature and the more so, the greater the m value.

The kinetics of the precipitation of iron have two clearly defined stages, i.e., rapid precipitation in the initial period and then slow precipitation. The rapid precipitation results from the sharp increase in the concentration of the hydroxo complexes on account of exchange reactions with the $Zn(OH)_2$ base and their rapid oxidation with the formation of a precipitate of amorphous basic sulphate. When the sharp initial supersaturation of the solution by the hydroxo complexes is removed by the passage of the iron into the precipitate, the subsequent formation of the precipitate is retarded and is maintained by the formation of hydroxo complexes on account of the true hydrolysis reactions. If the initial rise ΔpH_{in} is small, the formation rate of the precipitate depends on the hydrolysis rate, and there is an induction period for the formation of the precipitate of amorphous basic sulphate (fig.1 Aa and 1 Ba, curves 0.5).

The rate of precipitation of the iron is affected by ΔpH_{in}, C_{Fe}, and C_{ZnSO_4} and also by temperature. The presence of considerable amounts of $ZnSO_4$ in the solution substantially distorts the effect of the other factors on the iron precipitation rate. It is therefore expedient to compare the kinetics of the process for $c_{0\ Zn}$ = 100 g/l (fig.1) and $c_{0\ Zn}$ = 0 (fig.3).

From fig.3 it is seen that the precipitation rate of Fe(III) in the fast stage is proportional to the initial shift ΔpH_{in}

with other conditions equal (compare the curves for the various m values in fig.3 Aa or 3 Ba or 3 Ca), while, at the stage of slow precipitation it is proportional to the rate of the true hydrolysis of Fe(I) and consequently (like the hydrolysis rate) varies extremal with increase in m, i.e., the consumption of the neutraliser. Decrease in temperature reduces the precipitation rate at the stage of slow precipitation, and at the stage of fast precipitation it retards it for small m values and hardly changes it at all for large m values. (The latter probably results from compensation for the decrease in the temperature factor by the increase in the concentration factor, i.e., ΔpH_{in}).

With other conditions equal (figs.1 and 3) the content of $ZnSO_4$ in the solution reduces ΔpH_{in} (particularly with a large consumption of ZnO, e.g., for m = 3.5, which is due to partial consumption of the ZnO neutraliser on hydrolytic reaction with $ZnSO_4$[16]) instead of neutralisation of the acid), retards the hydrolysis of Fe(III) (due to the buffer action of $ZnSO_4$)[16]), and retards the precipitation of iron. The precipitation rate of Fe(III) at the fast precipitation stage decreases with increase in temperature (figs.1 Aa, Ba, and Ca), and at 90°C this stage only appears when m≥3.5. The retardation of the precipitation of Fe(III) becomes stronger with increase in the $ZnSO_4$ content of the solution; after 24h with m = 2 for $c_{0\ Fe}$ = 5 g/l the increasing $c_{0\ Zn}$ values of 0, 50, and 150 g/l correspond to Δc_{Fe} values of 3.49, 2.94, and 2.32 g/l respectively, and for $c_{0\ Fe}$ = 12 g/l the increasing $c_{0\ Zn}$ values of 0 and 100 g/l correspond to Δc_{Fe} values of 9.00 and 6.88 g/l.

The retarding effect of $ZnSO_4$ on the hydrolytic precipitation of Fe(III) becomes stronger with increase in temperature and is explained by the stabilising action of the electrolyte ($ZnSO_4$) on the colloidally disperse state of Fe(III) in the solution. At 90°C with $c_{0\ Zn}$ = 100 g/l and c_{Fe} ≥ 7.5 g/l in the pH region of 2 - 3.5 this converts the iron to the state of a hydrogel, which represents a transparent red-brown viscous solution (a structured liquid). Here the formation of the precipitate (coagel) of the amorphous basic sulphate is greatly retarded; when m = 3, the precipitation rate of Fe(III) is considerably lower than with small values of m (fig.1 Aa, curve 3.0, or fig.2a, curve 1a). This retardation of the passage of Fe(III) into the precipitate becomes stronger with increase of c_{Fe} in the solution (fig.4). The sharp increase of the light scattering (by several times) in high-iron zinc solutions at pH 2 - 3.5 compared with pure-iron solutions with equal c_{Fe} values confirms that the Fe(III) is converted into the state of a hydrogel in the zinc solutions.

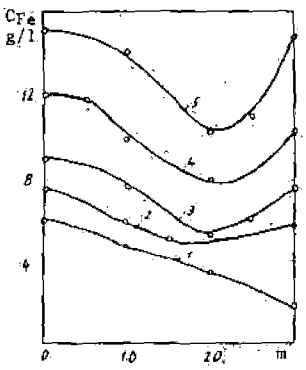

Fig.4. The c_{Fe} values (g/l) after holding for 2h in solutions of the $Fe_2(SO_4)_3$-$ZnSO_4$-ZnO-H_2O system as a function of m at 90°C with various $c_{0\ Fe}$ values, g/l: 1 - 6; 2 - 7.5; 3 - 9; 4 - 12; 5 - 15. $c_{0\ Zn}$ = 100 g/l.*

The obtained results reveal the character of the effect of various factors on the composition and state of the hydrolytic precipitates of iron and on the rate of hydrolytic precipitation of Fe(III) from zinc sulphate solutions, and this is essential as preliminary information for the construction of a mathematical model and in the search for optimum process conditions.

Conclusions

1. The primary products from hydrolytic precipitation of Fe(III) from zinc sulphate solutions are an amorphous basic sulphate $2Fe_2O_3 \cdot SO_3 \cdot xH_2O$ when $c_{Fe} \geq 0.1$ g/l and an amorphous hydrated iron oxide when $c_{Fe} \leq 0.1$ g/l. With time the amorphous phases change into crystalline goethite α-FeOOH with retardation.
2. The hydrolytic precipitation of Fe(III) takes place in two stages, i.e., a fast and then a slow stage. The precipitation rate (v_{Fe}) increases with increase in the initial neutralisation of the solution (pH_0 = 1.5 - 5.2) and with increase in the concentration of iron in the solution ($c_{Fe} \leq$ g/l) during the fast precipitation stage; during the slow precipitation stage v_{Fe} depends extremal on the initial neutralisation of the solution (passes through a maximum). With increase in the $ZnSO_4$ content of the solution ($c_{0\ Zn}$ = 0-150 g/l) v_{Fe} decreases. With increase in temperature (50-90°C) v_{Fe} decreases in the fast precipitation stage and increases slightly in the slow precipitation stage (as a result of intensification of the retarding action of $ZnSO_4$ with increase in temperature).
3. For a high-iron (c_{Fe} > 7 g/l) zinc sulphate solution with pH 2-3.5 a rise in temperature to 90°C is risky, since it leads to the formation of a viscous hydrogel of iron, which greatly retards the formation of the hydrolytic precipitate. Increase in c_{Fe} stabilises the hydrogel.

References

1) E Posnjak et alia: J. Amer. Chem. Soc., 1922, **44**, 1965.
2) L Walter-Levy et alia: Bull. Soc. Chim. France 1966, (6), 1947.
3) Principles of Metallurgy (in Russian), Moscow, Metallurgizdat, **2**, p.345.
4) M M Shokarev et alia: Zh. Neorgan. Khim., 1972, **17**, 2474.
5) E V Margulis et alia: Zh. Neorgan. Khim., 1973, **18**, 2133.
6) E V Margulis et alia: Zh. Neorgan. Khim., 1973, **18**, 2133.
7) E V Margulis et alia: Zh. Neorgan. Khim., 1975, **20**, 972.
8) E V Margulis et alia: Zh. Neorgan. Khim., 1975, **20**, 1872.
9) E V Margulis et alia: Zh. Neorgan. Khim., 1976, **21**, 1818.
10) E V Margulis et alia: Zh. Neorgan. Khim., 1977, **22**, (4), 1012.
11) E V Margulis et alia: Zh. Neorgan. Khim., 1977, **22**, (5).
12) R N Sylva: Rev. Pure Appl. Chem., 1972, **22**, (12), 115.
13) E V Margulis et alia: Zh. Prikl. Khim., 1976, **49**, 2382.
14) R A Buyanov et alia: Kinet. i Katal., 1976, **17**, 765.
15) E V Margulis et alia: Zh. Neorgan. Khim., 1965, **10**, 906.
16) A S Yaroslvtsev: Tsvetnye Metally 1976, (4), 20.

UDC 541.124/128:669.712

Determination of the accuracy and improvement of the method for determination of the diffusion coefficient by means of capillaries in the solid-liquid system

V Ya Abramov and L P Narushevich (All-Union Aluminium and Magnesium Institute)

Summary

A new method was developed for the determination of the position of the boundary between the solid and liquid phases in the capillary. The method extends the possibilities for the use of capillary models during investigation of diffusion

SUBJ
MNG
MLCM

UNIVERSITY OF UTAH
RESEARCH INSTITUTE
EARTH SCIENCE LAB.

MICROBIAL LEACHING OF COPPER MINERALS

by JOSEPH A. SUTTON and JOHN D. CORRICK

The continuing depletion of high-grade ore deposits in this country has created a need to develop more effective methods for recovering valuable metals from low-grade ores. The use of microorganisms for their biochemical reactions is one possible way to solve certain phases of this problem.[1,2,3] Bacteria have been used successfully by many diversified industries. Until recently, however, little attention has been focused on the use of bacteria in mining and metallurgical processes.

This report summarizes one phase of the microbial studies being conducted at the U.S. Bureau of Mines, College Park Metallurgy Research Center. The two-fold objective of this study was, first, to determine if pure strains of the bacteria *Ferrobacillus ferrooxidans, Thiobacillus concretivorus* and *Thiobacillus ferrooxidans* could utilize the iron and sulfur occurring in sulfide minerals to produce appreciable quantities of ferric sulfate and sulfuric acid for dissolving copper and, second, to develop the chemistry involved in the microbial oxidation of sulfide minerals. These are of particular interest as they relate directly to the feasibility of employing microorganisms in leaching operations.

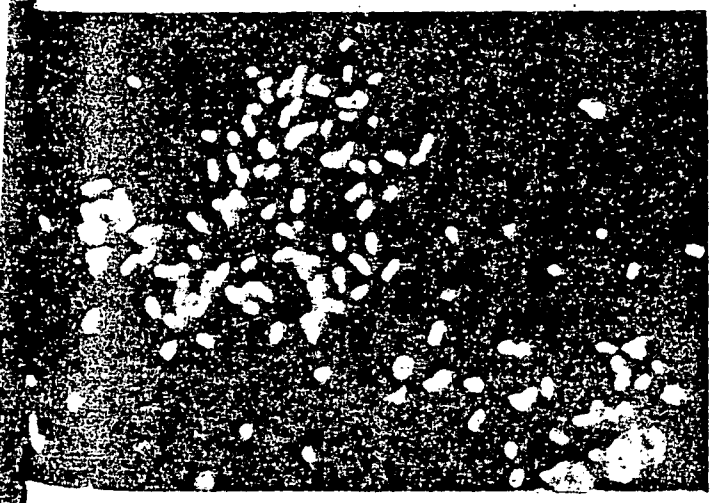

Fig. 1—Dark field photomicrograph of Thiobacillus sp. (X728).

The three strains of bacteria investigated are known to be present in the effluent waters of several copper mines in southwestern United States.[4] The presence of these bacteria in ore deposits testifies to their ability to withstand highly acidic environments and to derive necessary food for survival from their immediate surroundings.

Acid-ferric-sulfate, a solvent for extracting copper from low-grade ores, is formed within leaching areas by what has previously been considered atmospheric oxidation of sulfuritic materials associated with the copper deposits. Recent discoveries, however, provide conclusive evidence that certain

J. A. SUTTON is Physical Chemist and J. D. CORRICK is Research Biochemist, U. S. Bureau of Mines, College Park Metallurgy Research Center, College Park, Md.

oxygen consumed in chemical and microbial reactions.

Chalcopyrite	5.8	29.1
Chalcocite	10.4	26.7

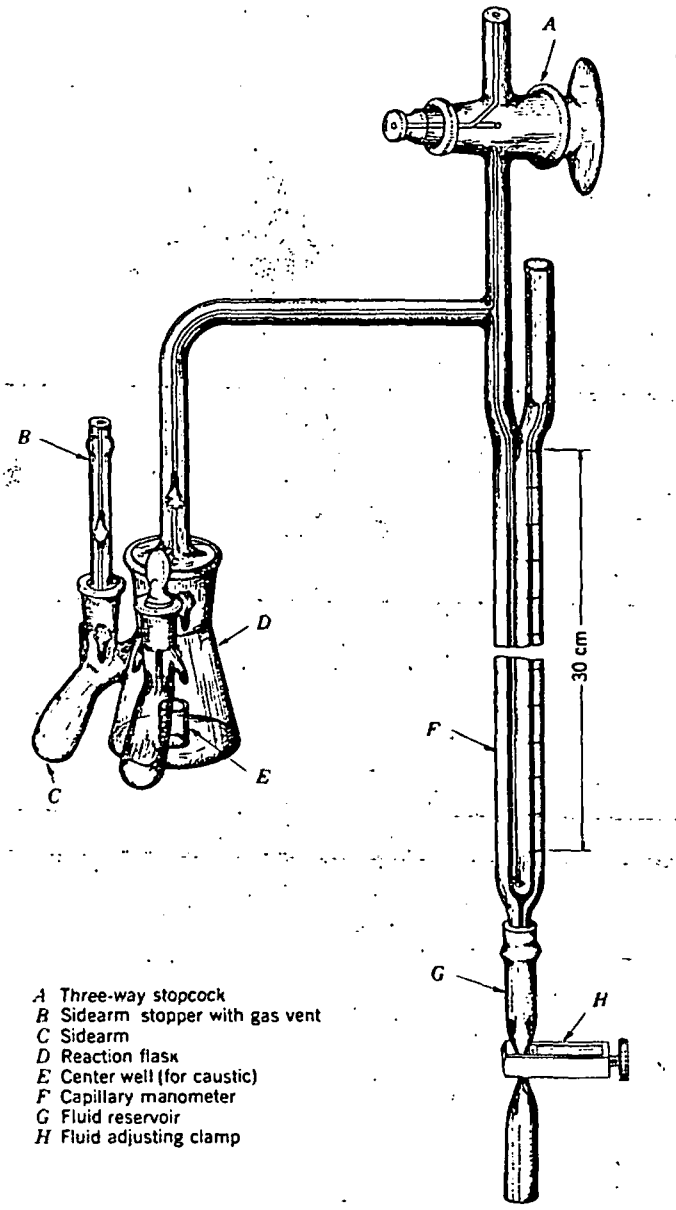

A Three-way stopcock
B Sidearm stopper with gas vent
C Sidearm
D Reaction flask
E Center well (for caustic)
F Capillary manometer
G Fluid reservoir
H Fluid adjusting clamp

Fig. 3—Warburg constant volume respirometer.

brought about the oxidation of substantial quantities of ferrous iron.

However, it was not known how the bacteria accomplished the dissolution of iron-bearing minerals. The basic question underlying the microbial oxidation of iron sulfide minerals has been whether the organisms directly attack the iron compounded with iron sulfide minerals or if they attack the ferrous sulfate released into solution as a result of the atmospheric oxidation of the iron sulfide minerals. Volger[9] has reported that the sulfur-oxidizing bacterium *T. thiooxidans* must make physical contact with sulfur in order to oxidize it. Our manometric tests with *T. thiooxidans* supported Volger's conclusions. The results of these tests (Table I) show that an increased oscillation rate which caused shorter contact time between the sulfur particles and the organisms, resulted in a drop in the $Q_{O_2}(N)$. This expression is a means of indicating the oxygen uptake by the organisms. Results of parallel tests with *F. ferrooxidans* and pyrite show that increased oscillation rate increased the up-take of oxygen. Apparently, microbial oxidation of the pyrite can be enhanced by the same mechanisms that effect reaction rates in all ordinary agitated chemical reactors. These data support the conclusion that this bacterium does not require contact with pyrite in order to oxidize it; instead, it oxidizes the ferrous iron released into solution as a result of chemical oxidation.

The acid-ferric-sulfate solutions formed as a result of microbial oxidation of iron-bearing minerals should serve as effective metal solvents and bring about the dissolution of copper from copper minerals. Although a majority of copper minerals do not contain ferrous iron, they are commonly associated in their natural environments with the minerals pyrite and chalcopyrite. The data from a series of percolator tests involving *F. ferrooxidans* reacting on ferrous sulfate show that, after 56 days of percolation, 23.7% of the copper was extracted from chalcocite, 56.3% from covellite and 29.8% from bornite. The organisms extracted 3.4 times more copper from the chalcocite than was extracted in the uninoculated control (Fig. 7).

Results from a similar series of percolator tests indicate that the sulfur-oxidizing bacterium *T. concretivorus* was not able to utilize the sulfide sulfur occurring in the minerals chalcopyrite, chalcocite, covellite and bornite. Manometric studies show that this bacterium registered a mild response to the minerals chalcopyrite, chalcocite and pyrite (Table II). However, because these minerals contained minor quantities of elemental sulfur, it was concluded that bacterial activity was governed by the availability of this sulfur and that the organisms ceased to function after the sulfur was consumed.

The chemical reactions involved in the microbial dissolution of iron and copper from sulfide minerals can be described by reference to a series of chemical equations. Pyrite in the presence of oxygen and water is slowly oxidized to ferrous sulfate and sulfuric acid according to Equation 1,

$$2FeS_2 + 7O_2 + 2H_2O \rightarrow 2FeSO_4 + 2H_2SO_4. \quad [1]$$

The iron-oxidizing bacteria in the presence of oxy-

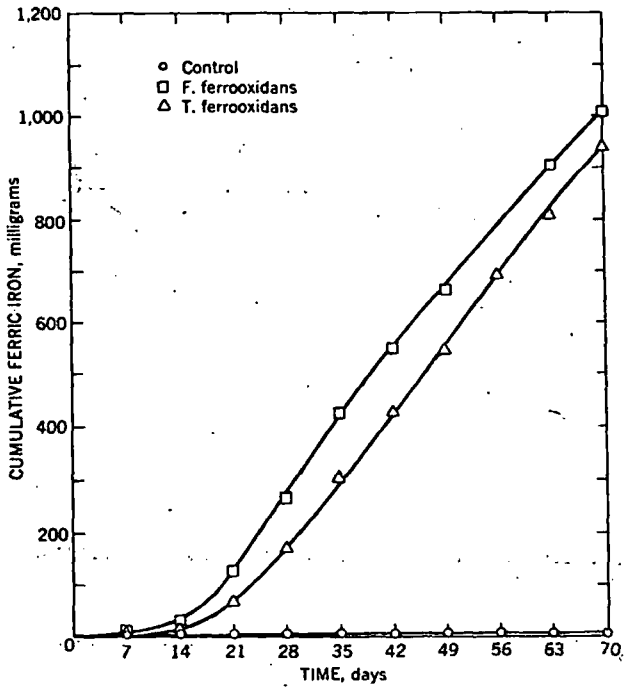

Fig. 4—Ferric iron from pyrite produced by iron-oxidizing bacteria.

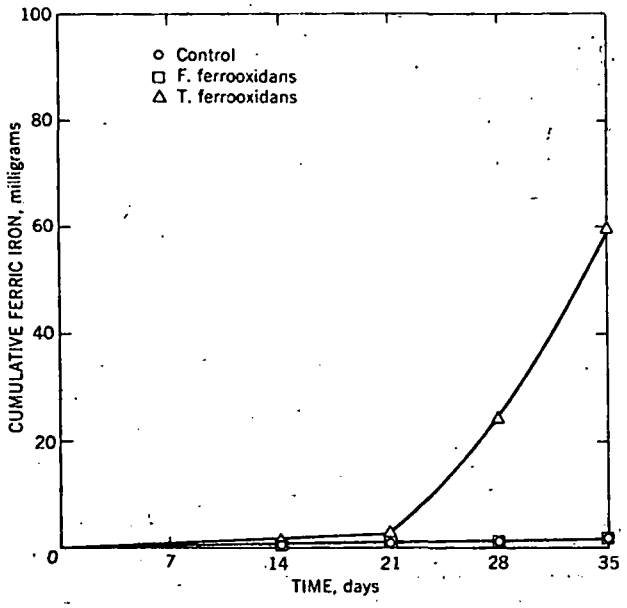

Fig. 5—Effect of F. ferrooxidans and T. ferroxidans on the oxidation of iron in chalcopyrite.

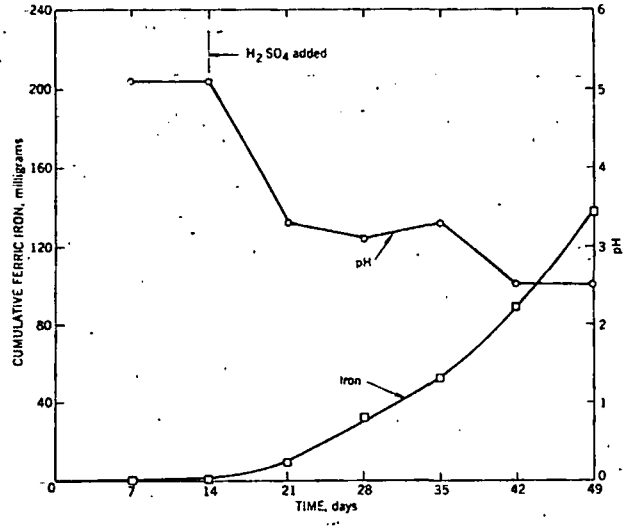

Fig. 6—Effect of pH upon the ability of F. ferrooxidans to oxidize iron in chalcopyrite.

gen and sulfuric acid then oxidizes the available ferrous sulfate and, acting as a catalytic agent, accelerates the formation of ferric sulfate as shown in Equation 2,

$$4FeSO_4 + 2H_2SO_4 + O_2 \xrightarrow{\text{Bacteria}} 2Fe_2(SO_4)_3 + 2H_2O. \quad [2]$$

The ferric sulfate that is formed can react with pyrite to form H_2SO_4 and ferrous sulfate according to Equation 3,

$$7Fe_2(SO_4)_3 + FeS_2 + 8H_2O \rightarrow 15FeSO_4 + 8H_2SO_4 \quad [3]$$

or it can react with a copper sulfide mineral, such as chalcocite, to form copper sulfate, ferrous sulfate and elemental sulfur as shown in Equation 4,

$$Cu_2S + 2Fe_2(SO_4)_3 \rightarrow 2CuSO_4 + 4FeSO_4 + S. \quad [4]$$

The ferrous sulfate is then re-oxidized by the iron-oxidizing bacteria to form more ferric sulfate and the cycle is repeated. The elemental sulfur set free (Equation 4) is oxidized by the sulfur-oxidizing

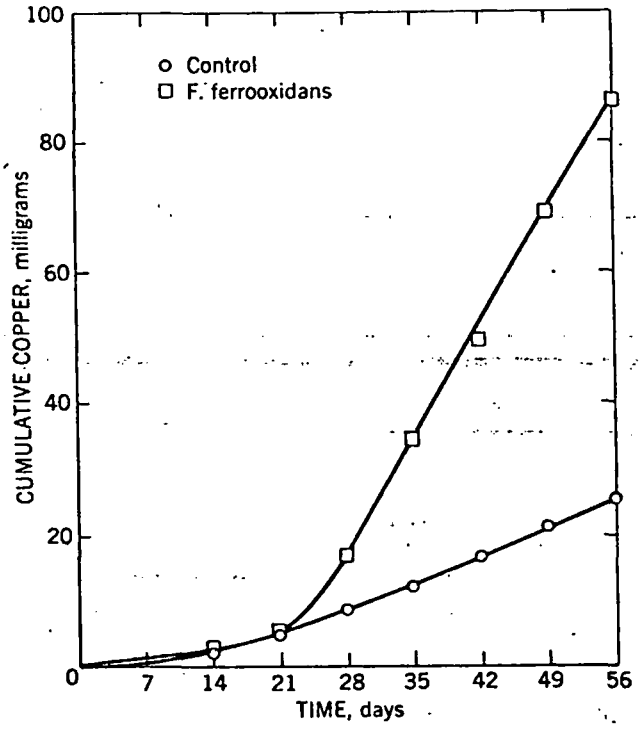

Fig. 7—Copper extracted from chalcocite by F. ferrooxidans.

bacterium *T. concretivorus* in the presence of oxygen and water to sulfuric acid, as shown in Equation 5,

$$2S + 3O_2 + 2H_2O \xrightarrow{\text{Bacteria}} 2H_2SO_4. \quad [5]$$

CONCLUSIONS

The conclusions drawn from this study are as follows:

1) The iron-oxidizing bacteria *F. ferrooxidans* and *T. ferrooxidans* are able to greatly accelerate the dissolution of the iron compounded with the minerals pyrite and chalcopyrite.

2) The bacterium *F. ferrooxidans* is capable of producing sufficient quantities of acid-ferric-sulfate from ferrous iron to bring about the dissolution of significant quantities of copper from chalcocite, covellite and bornite.

3) The bacterium *F. ferrooxidans* acts as a catalyst to the chemical oxidation of pyrite. The organism does not directly attack the iron in the mineral but rather oxidizes the ferrous iron released into solution as a result of atmospheric oxidation.

4) The sulfur-oxidizing bacterium *T. concretivorus* is not able to oxidize the sulfide sulfur occurring in the minerals pyrite, chalcopyrite, chalcocite, covellite and bornite.

REFERENCES

[1] L. C. Bryner and R. Anderson: Microorganisms in Leaching Sulfide Minerals. *Ind. & Eng. Chem.*, vol. 49, No. 10, October 1957, pp. 1721-1724.

[2] L. C. Bryner, J. V. Beck, D. B. Davis and D. G. Wilson: Microorganisms in Leaching Sulfide Minerals. *Ind. & Eng. Chem.*, vol. 46, No. 12, December 1954, pp. 2587-2592.

[3] L. C. Bryner and A. K. Jameson: Microorganisms in Leaching Sulfide Minerals. *Appl. Microbiol.*, vol. 6, 1958, pp. 280-287.

[4] J. D. Corrick and J. A. Sutton: Three Chemosynthetic Autotrophic Bacteria Important to Leaching Operations at Arizona Copper Mines. USBM *Rept. of Inv. 5718*, 1961, 8 pp.

[5] R. S. Breed, E. G. D. Murray and N. R. Smith: *Bergey's Manual of Determinative Bacteriology*. The Williams and Wilkins Co., Baltimore, Md., 1957, 7th ed., pp. 84-85.

[6] K. G. Vogler and W. W. Umbreit: The Necessity of Direct Contact in Sulfur Oxidation by *Thiobacillus thiooxidans*. *Soil Science*, vol. 51, 1941, pp. 331-337.

SUBJ
MNG
MMIS

UNIVERSITY OF UTAH
RESEARCH INSTITUTE
EARTH SCIENCE LAB.

Mathematical Modeling of In-Situ Uranium Leaching

Soc. Pet. Eng. Jour.
V. 19 No. 7
Dec. 1979

Paul M. Bommer,* SPE-AIME, U. of Texas
Robert S. Schechter, SPE-AIME, U. of Texas

Abstract

This paper presents the development and results of a computer model of in-situ uranium leaching. This model uses a streamline-concentration balance approach and is useful with a wide range of reservoirs. It can be used with any type of well system, in a reservoir with or without boundaries, and with any form of descriptive kinetics. The model also includes the effects of dispersion and consumption of oxidant by minerals other than uranium. The effects of well pattern, variable uranium concentrations, and the presence of oxidant consumers on uranium production are discussed.

Introduction

The sandstone uranium deposits of south Texas represent a possible major energy source. These deposits consist mainly of widely scattered roll fronts (pods) of unoxidized uranium minerals in loosely packed sands.[1] It is thought that these deposits were formed by the downdip migration of groundwater carrying oxidized uranium leached from the host rock, Catahoula Tuff. When the uranium-bearing waters reached a reducing zone, the uranium was precipitated, forming mainly the mineral uraninite, UO_2.[2] Much of the uranium ore in the area is low grade ($< 0.05\%$ U_3O_8) and is at depths of 100 to 1,500 ft.

Since 1960, various companies have been mining some of the higher-grade deposits to depths of up to 200 ft, using conventional strip-mining techniques. The concomitant surface disruption is extensive, and the costs of mining and transporting to a mill such large amounts of material prohibit the utilization of low-grade ore.

A mining technique that may overcome these difficulties to some extent and ultimately make more of the south Texas uranium deposits amenable to recovery is in-situ solution mining. This technique consists of pumping through the ore body a chemical solution that will dissolve the uranium minerals so that they may be leached from the ore and recovered from the solution. For this process to be economically feasible, a low-cost solution must be available that will dissolve a large portion of the uranium present, the uranium must be easily recoverable from the leach solution, the physical attributes of the ore body must be such that the leach solution can be pumped through the ore without great loss to the surroundings, and environmental hazards must be avoided.

The leaching process and its chemistry are basically simple. Uranium is generally found to have one of two oxidation states – oxidized, U^{+6}, or unoxidized, U^{+4}. In the oxidized +6 state, uranium forms many soluble ions, among them the uranyl ion UO_2^{+2}, the uranyl dicarbonate ion $UO_2(CO_3)^{-2}$, and the uranyl tricarbonate ion $UO_2(CO_3)_3^{-4}$. Hostetler and Garrels[3] have investigated the equilibria of uranium minerals with natural solutions and found that under oxidizing conditions, stable soluble ions exist over a wide range of pH. The results suggest that to dissolve uranium minerals, one must provide an oxidizing agent to oxidize reduced uranium to the +6 state and a complexing agent that will form stable complex ions with U^{+6}. A typical set of reactions is as follows:

$$UO_2 + H_2O_2 \rightarrow UO_3 + H_2O \text{ (oxidation)}. \quad \ldots . (1)$$

$$2H^+ + UO_3 + 3CO_3^{-2} \rightarrow UO_2(CO)_3^{-4} + H_2O \text{ (dissolution)}. \quad \ldots . (2)$$

The oxidation step represented by Eq. 1 uses

*Now with Bommer Engineering, San Antonio.

0037-9999/79/0012-7533$00.25
© 1979 Society of Petroleum Engineers of AIME

Jour Pet Tech

hydrogen peroxide as the oxidant. It is also possible to oxidize the uranium using air, pure oxygen, or sodium chlorate. Hydrogen peroxide is being used in most present operations, though evidence[4] suggests that it dissociates rapidly to water and oxygen at reservoir conditions. If this is the case, pure oxygen may be the preferred oxidant because it is less expensive than hydrogen peroxide.

The physical operation of an in-situ uranium solution mine is similar in many respects to conventional oilfield operations. After a suitable ore body has been located and mapped by exploratory drilling, a pattern of wells must be placed to recover a large fraction of the value in a reasonable time. A second factor concerns confining the leach solution to the region of interest to avoid environmental problems. Often, this can be achieved by the efficient placement of production and injection wells; in other cases, guard wells may be required. This paper considers the problem of well placement, the use of guard wells, uranium production rates, the effect of oxidant concentration, and many other questions concerning the in-situ leaching of uranium. The approach used here is to develop a computer model that can be used to simulate a variety of production situations. The results can then be compared and reasonable operations parameters identified.

The Flow Model

In this model, the flow is assumed to be single phase and two-dimensional so that the fluid velocity at a point can be calculated using the well-known source and sink equations that describe the flow of an incompressible fluid through a porous medium as a function of the location and volume rates of production and injection wells (see Appendix A). Given the fluid velocities, streamlines can be traced. A typical example is shown in Fig. 1.

Once streamlines have been defined, pressure drop along them can be calculated. In the approach used here, the streamlines are divided into equal pressure increments or nodes that are used later in developing a finite-difference analog of the concentration balance. The fluid velocity at each node is recorded for future use in finite-difference equations.

The streamline model can be modified to approximately account for variations in reservoir thickness, provided they can be assumed to change linearly between wells.[5] The calculation requires that the formation thickness be known at each point along a streamline. These values of thickness are entered using a grid system over the area of the pod, as shown in Fig. 2. This information is used to adjust the fluid velocities at each node. In the subsequent calculation of both uranium and oxidant concentrations, the modified velocities will be used. In this way, thickness variations are considered.

Most uranium pods are small in area compared with the aquifers in which they occur, and these are effectively unbounded systems as represented by Fig. 1. In many cases, it would be advantageous to minimize lixiviant escape from uranium-rich zones, because it is not then wasted on nonproductive areas, recovery rates are increased, and aquifer contamination is minimized. This last consideration is by far the most important one. To bound the system of production and injection wells, it is possible to drill additional wells (guard wells) outside the pod area. By properly adjusting the location and injection rates of groundwater into them, guard wells can be used to create a no-flow boundary around the periphery of the pod. The model uses a method of image wells developed by Lin[6] to simulate the bounding that can be achieved by the proper injection rates through a given system of guard wells. Therefore, the program can be used to estimate how many guard wells are required to achieve effective bounding by varying their number and spacing until a satisfactory result is obtained. Of course, there are an infinite number of combinations that will provide adequate bounding.

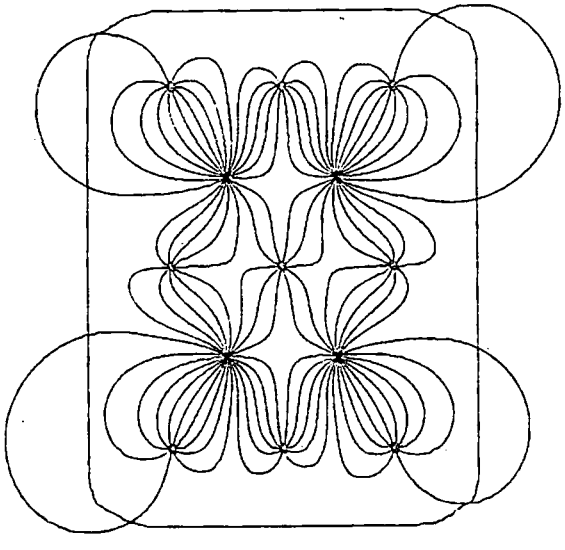

Fig. 1 – Streamline pattern for a regular, inverted five-spot in an unbounded aquifer. Rectangular region represents boundaries of the mineralized zone.

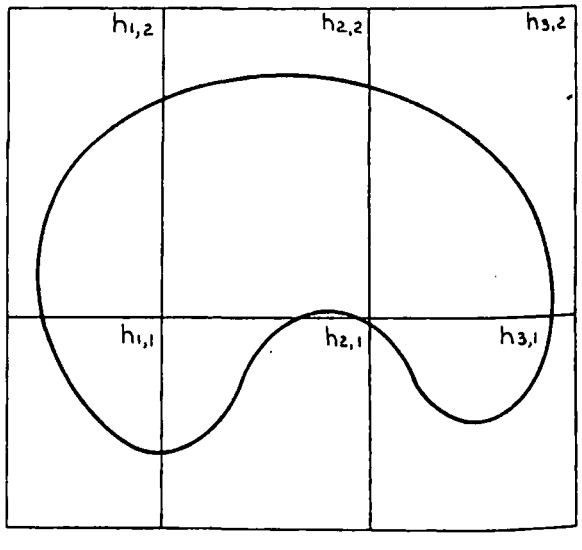

Fig. 2 – Typical thickness grid superimposed on the mineralized zone. It is used for calculating fluid velocities.

To determine the "best set," economic considerations are required. Such considerations are beyond the scope of this work.

The streamlines for a bounded system are shown in Fig. 3; if these results are compared with those of Fig. 1, the effect of confining the streamlines is evident. The guard wells distort both the streamlines and the fluid velocities from those of the unbounded system. Both these changes are taken into account when calculating uranium production.

Uranium Balance

Once the flow system has been defined, bounding has been completed if desired, and each streamline has been divided into nodes at which velocities are stored, the next step is to calculate the uranium concentration at each of the nodes as a function of time. This is done using a component balance that allows for chemical reactions and dispersion. The balance equation is first written in a rectangular coordinate system that includes the effect of dispersion and then is converted into one in which the streamlines and potential lines form the coordinates (see Appendix B). Assuming that dispersion along a line of constant potential (perpendicular to flow) can be neglected, the component balance can be written along a streamline as

$$\alpha(\Phi,\psi)\,\frac{\partial c}{\partial \Phi} + \beta(\Phi,\psi)\,\frac{\partial^2 c}{\partial \Phi^2} - R = \phi\,\frac{\partial c}{\partial t}, \quad \ldots\ldots (3)$$

where α and β depend on the velocities, which are known but are independent of the concentration, c. R is the reaction term that describes the rate at which uranium is oxidized and leached from the solid surface, and Φ is the potential function that, for a horizontal system, is the pressure measured along a streamline. The form of the reaction rate used in this paper is

$$R_{Ur} = \epsilon(W_{Ur} - W_{RUr})(1-\phi)\rho. \quad \ldots\ldots\ldots (4)$$

This rate expression was found to adequately describe the flow results reported by Galichon *et al.*[4] The results presented here are not general in that the constants used in the rate expression are expected to vary from site to site. It is necessary then to develop the appropriate rate expression using ore samples from the deposit of interest and using the leach solution to be employed in the field.

It should be noted that ϵ depends on number of factors, including the oxidant concentration. The calculations reported here use an experimentally determined relationship between the rate constant (ϵ) and the peroxide concentration (the equivalent oxygen partial pressure would serve equally well). Grandstaff[7] finds that the rate is proportional to the partial pressure when pure uraninite is dissolved in carbonate solutions at temperatures ranging from 2° to 23°C. Pearson and Wadsworth[8] found the rate constant depends on the square root of the partial pressure at higher temperatures. The experimentally determined ϵ used here is shown in Fig. 4. The other factors given in Eq. 4 have been discussed previously.[4] Eq. 3 is solved for each streamline at selected times. It is solved using a fully discrete, finite-difference approximation with an unconditionally stable Gaussian row reduction

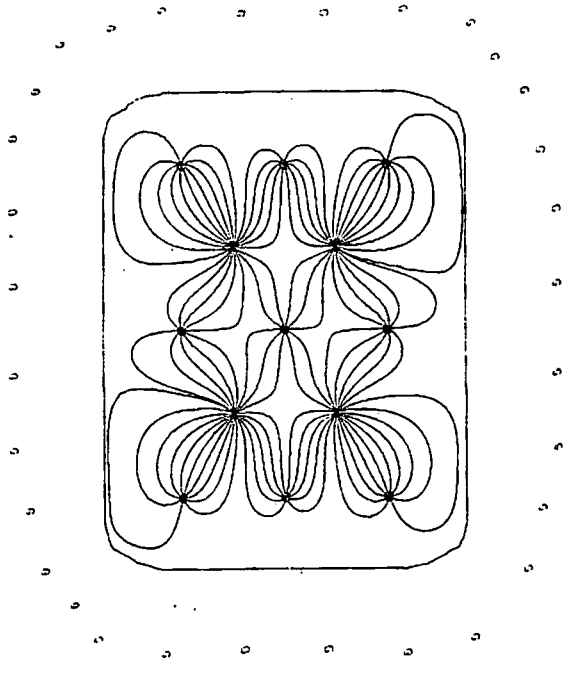

Fig. 3 – Streamline pattern for a regular, inverted five-spot bounded by guard wells around the mineralized zone.

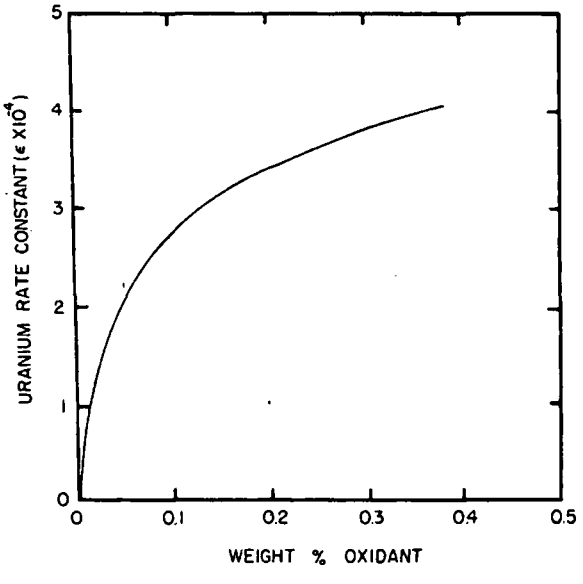

Fig. 4 – The uranium rate constant shown as a function of oxidant concentration (from Galichon's data.[12])

technique.[9] The finite-difference analogy to Eq. 3 uses an implicit technique with a two-point backward difference for the derivative of concentration with respect to time. The derivatives of concentration with respect to pressure are expressed using five-point centered differences at nodes between wells and three-point centered differences at the nodes next to wells. The three-point forms must be used near wells to maintain the pentadiagonal form of the coefficient matrix that is solved by the Gaussian technique. This finite-difference analogy has been shown to generate good results. Details of the computer program and the testing of the numerical procedure are available elsewhere.[10] The output from the balance is the uranium concentration at each node of each streamline at every time step. The uranium concentration at each wellbore can then be calculated.

Other Modeling Considerations

Most aquifers contain varying concentrations of minerals, such as pyrite, that will compete with uranium for oxidant. These minerals consume some of the injected oxygen. Therefore, the presence of these minerals has the effect of delaying uranium production. Again, a laboratory study must be conducted using samples from the ore body of interest to determine the reaction expressions required to describe the minerals' effects.

To demonstrate the impact of these oxidant-consuming minerals, a reaction-rate expression is used in an oxidant-balance equation (having the same form as Eq. 3) to calculate the oxidant concentration at each node as a function of time. This rate expression is

$$R_o = \zeta M C_o/\delta \qquad (5)$$

This expression has not been tested yet, but clearly ζ and δ will vary from formation to formation. The initial values of the oxidant-consuming mineral concentrations are stored and used in the rate expression and as the reaction proceeds:

$$\frac{dM}{dt} = -\delta R_o. \qquad (6)$$

This equation is integrated and the mineral concentration is allowed to decrease with time. Thus, given the amount of oxidant left at a node after reaction with the oxidant-consuming minerals, the appropriate uranium reaction-rate constant, ϵ, can be located from Fig. 4 and used in Eq. 4. Even if there are no oxidant-consuming minerals (save uranium) present in the pod, the oxidant balance must be solved together with the uranium balance to determine the oxidant concentration present at a particular node at a particular time and hence obtain the proper uranium reaction-rate constant.

Because most reservoirs are not homogeneous chemical systems, the model has been built to consider these differences. The same grid system used to store differences in reservoir thickness for the velocity approximation can be used to provide concentration variances. The uranium and pyrite concentrations over the entire reservoir are stored along with the thickness changes in the grid system. They now can be located by the position of each node on each streamline and used in the oxygen and uranium concentration calculations.

In unbounded or partially bounded systems, some of the streamlines escape beyond the uranium-bearing zone, as shown in Fig. 1. The portions of a streamline that lie outside the uranium-bearing area do not contribute any new uranium production to the system. They may, however, contain pyrite since the process that deposited pyrite probably was not the same one that deposited uranium. Thus, along these portions of a streamline outside the uranium-bearing area, the oxidant may continue to be consumed. To consider this phenomenon, each node along a streamline is tested to determine if it is inside or outside the uranium-bearing area. This test is performed by taking the cross-product of two vectors. The first vector passes through the node and the closest boundary point to that node. The boundary points are a finite set of discrete points used to define the uranium-bearing area. The second vector passes through the closest boundary point and the next point taken in a clockwise direction, as shown in Fig. 5. If the cross-product is positive, then the node is inside the pod. If it is negative then the node is outside the pod and no uranium production is calculated. The only instability in this method occurs when the node, closest boundary point, and second boundary point are all on line, thus forming an angle of 180°. When this occurs, the cross-product is zero and no distinction can be made. Therefore, in the event that this happens, the model uses the boundary point behind the closest boundary point to form the first vector and that point and the closest boundary point to form the second vector.

Results

The economic viability of a particular leaching

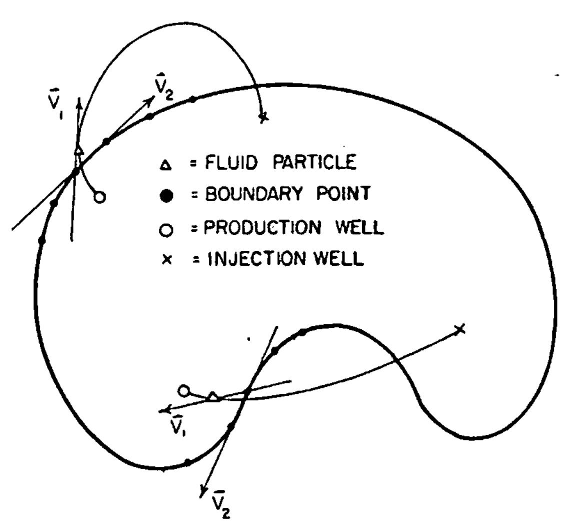

Fig. 5 – Sketch showing the vector relationships used to determine whether a point is within the mineralized zone.

project is related to both the concentration of the uranium in the produced leach solution and the time required to produce a significant portion of the mineral values. It is, therefore, critical to design a well pattern that will leach as much uranium-bearing rock as possible over a particular time period, while also minimizing the number of guard wells required to prevent the leaching solution from escaping into the aquifer. Theoretically, any well pattern will eventually sweep a pod given enough time. Thus, for a given time frame, the well pattern that recovers the most uranium would be judged the most efficient and probably the most desirable.

The importance of areal sweep has been demonstrated using the unbounded, inverted five-spot pattern of Fig. 1, the unbounded line-drive pattern of Fig. 6, and the unbounded, expanded, inverted five-spot pattern of Fig. 7. The production histories of these patterns after 6 months of production are presented in Fig. 8. It can be seen from this figure that even though the line drive has more wells than either of the other two patterns, it does not produce more uranium than the regular five-spot pattern. However, due to its greater areal sweep, the expanded inverted five-spot pattern produces in the given time roughly 1.4 times the uranium of the other two patterns. There is, however, a longer delay initially with the expanded, inverted five-spot because of the increased distance between wells.

As outlined earlier, if any oxidizable minerals such as pyrite are present in a pod, the uranium production should be delayed. To illustrate this, the system shown in Fig. 1 was modeled for 6 months, first with and then without pyrite. The production profiles are contrasted in Fig. 9. The presence of pyrite causes a marked delay in uranium production.

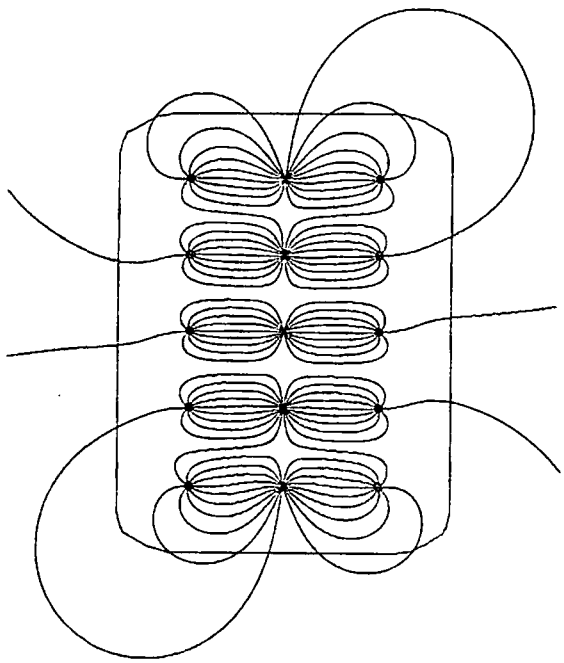

Fig. 6 – Streamline pattern for a line drive in an unbounded aquifer.

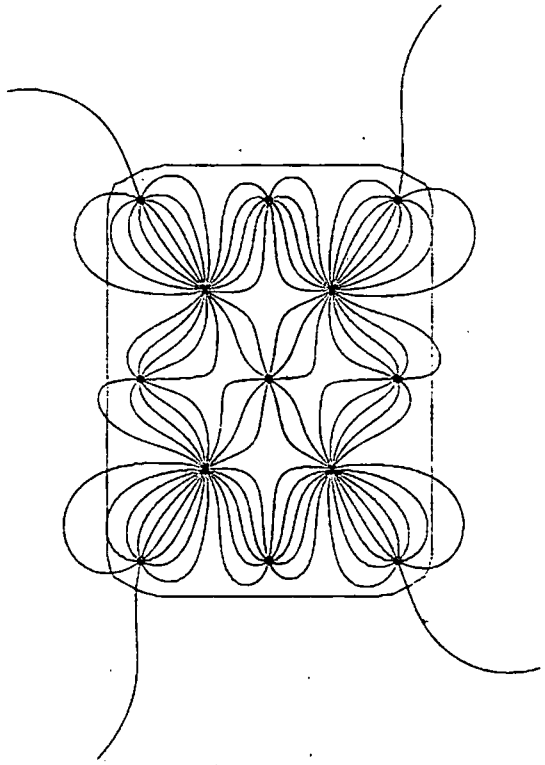

Fig. 7 – Streamline pattern for an expanded, inverted five-spot in an unbounded aquifer.

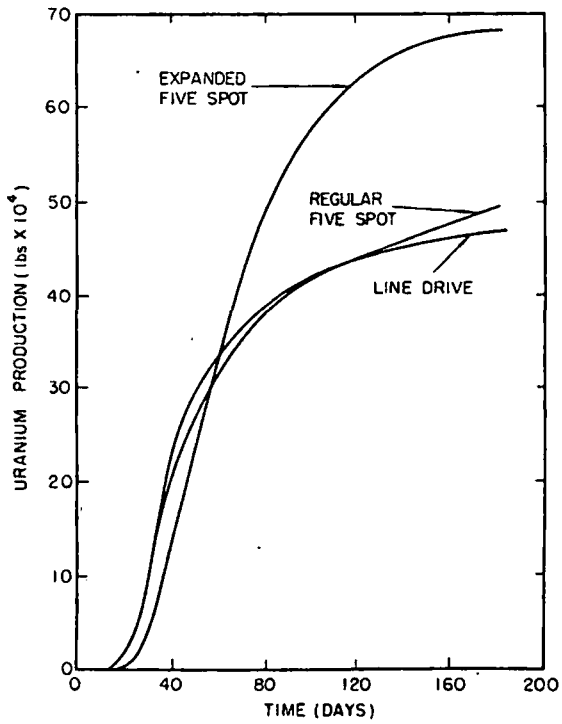

Fig. 8 – Cumulative uranium production with time as it depends on areal sweep, with all other variables held constant.

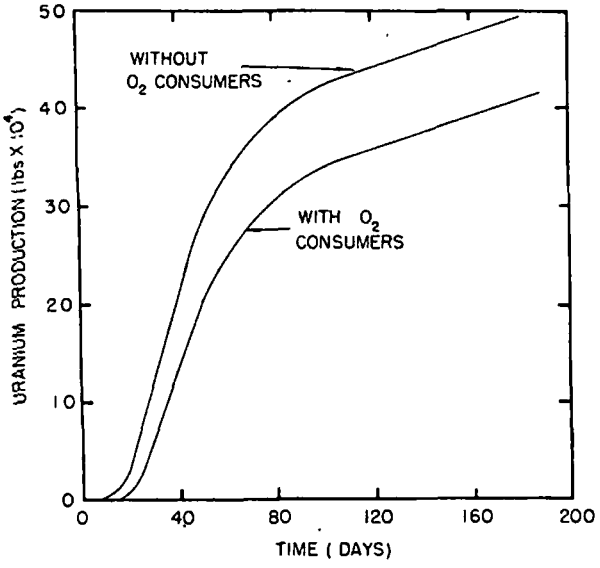

Fig. 9 – The effect of oxygen-consuming minerals in delaying uranium production.

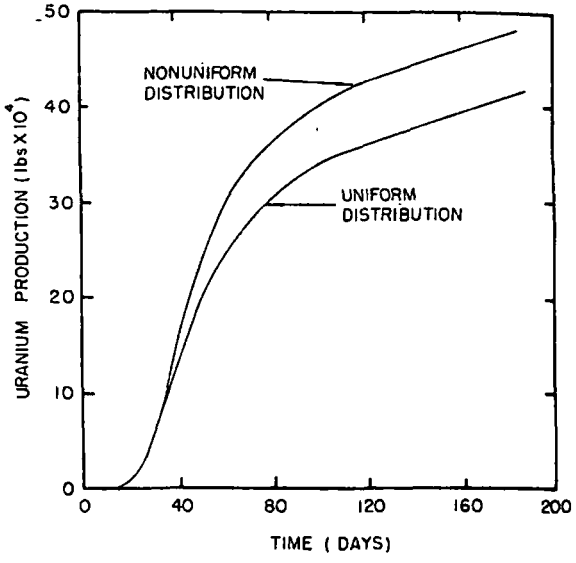

Fig. 10 – The effect of varying uranium concentrations within the mineralized zone.

With enough time, the uranium production will tend to that of the pod without any pyrite. Here again, the extent of the delay depends on the amount of oxidizable minerals present and their rate of reaction with oxygen.

Variable uranium content can have a dramatic effect on production. The pod represented in Fig. 1 was modeled first with a uniform initial uranium concentration of 0.003 g uranium per gram of rock and a second time with one-half the pod having negligible uranium concentrations, one-quarter having 0.002 g uranium per gram of rock, and one-quarter having 0.0093 g uranium per gram of rock. The average concentration for the second case was 0.003 g uranium per gram of rock. The production profiles shown in Fig. 10 show that the pod with the one high concentration quarter produced more uranium in the given time than the pod with the uniform concentration. This result is dependent on the rate expression used for the uranium reaction, and in actual situations will vary from site to site. The rate expression used for these examples, as seen in Eq. 4, contains the difference between the uranium present and unleachable or residual uranium, $W_{Ur} - W_{RUr}$. For the uniform pod this term has a value of 0.002 g uranium per gram of rock. In the nonuniform pod it has a value of 0.0083 g uranium per gram of rock, which is 4.15 times greater than in the uniform pod. So, if the effects of the other terms in the rate expression are neglected, the nonuniform pod should produce 4.15/4 or 1.04 times faster than the uniform pod. This figure is a bit lower than what actually occurred, but it points out that the rate expression controls how much uranium is produced from a pod in a given time, and the effects of high concentrations of uranium in a pod.

Summary

An in-situ uranium leaching model to predict the movement of reservoir fluid and to predict the production and accumulation of fluid volumes and leachate concentrations has been described. It can be used to optimize well patterns and guard-well systems. The model can be used with any size and shape reservoir with variable thickness, with or without boundaries, with any configuration of wells, with or without guard wells, with areal differences in reservoir makeup, and with any form of descriptive kinetics. The model also considers dispersion and the consumption of injected oxygen.

The results indicate the importance of proper well-pattern selection and the possible benefits of guard wells. Economics determine their use.

Also, it has been found that significant variations in uranium concentrations in the produced fluids may be observed in most situations. These can result from any one or more of a number of factors, including variations in reservoir thickness or permeability, nonhomogeneous distribution of uranium values, or variations in concentration of oxidant-consuming minerals.

Nomenclature

c = concentration
D_o = molecular diffusion coefficient
F = formation resistance factor
h = formation thickness
k = permeability
K = dispersion coefficient
M = pyrite concentration
P = average formation particle diameter
q = production or injection rate
R = reaction rate
RI = 2% of the average distance between wells
t = time
u = flux
v = fluid velocity
W = uranium concentration

x,y = rectangular Cartesian coordinates
α = a complex function of velocity appearing in the concentration balance
β = a complex function of velocity appearing in the concentration balance
δ = stoichiometric coefficient
Δ = increment
ϵ = uranium reaction-rate constant, time^{-1}
ζ = oxidant reaction-rate constant
μ = fluid viscosity
ρ = density
σ = formation factor
ϕ = porosity
Φ = potential

Subscripts

L = longitudinal
m = mean
n = number of wells
o = oxygen or oxidant
R = residual
t = time
Ur = uranium
x,y = rectangular coordinate direction

References

1. Galloway, William E.: *Catahoula Formation of the Texas Coastal Plain: Depositional Systems, Composition, Structural Development, Groundwater Flow History, and Uranium Distribution*, RI No. 87, Bureau of Economic Geology, U. of Texas, Austin (1977).
2. Eargle, D. Hoyle, Dickinson, K. A., and Davis, B. O.: "South Texas Uranium Deposits," *Bull.*, AAPG (May 1975) 766-779.
3. Hostetler, P. B. and Garrels, R. M.: "Transportation and Precipitation of Uranium and Vanadium at Low Temperatures with Special References to Sandstone-Type Uranium Deposits," *Economic Geol.* (1962) **57**, 138-167.
4. Galichon, Phillippe, Schechter, R. S., Cowley, Alan, and Breland, W. M.: "Chemical Factors in In-Situ Uranium Leach Mining," *In Situ* (1977) **1**, 125-146.
5. Wessels, J. W.: "Application of the Streamline Reservoir Model to Reservoirs Having Variations in Formation Thickness," MS thesis, U. of Texas, Austin (May 1973).
6. Lin, J. K.: "An Image Well Method for Bounding Arbitrary Reservoir Shapes in the Streamline Model," PhD dissertation, U. of Texas, Austin (Dec. 1972).
7. Grandstaff, D. E.: "A Kinetic Study of the Dissolution of Uraninite," *Economic Geol.* and *Bull.*, Soc. of Economic Geologists (Dec. 1976) 1493-1506.
8. Pearson, R. L. and Wadsworth, M. E.: "A Kinetic Study of the Dissolution of UO_2 in Carbonate Solution," *Trans.*, TMS-AIME, (1958) **21**, 294.
9. *Digital Computation for Chemical Engineers*, Leon Lapidus (ed.), McGraw-Hill Book Co. Inc., New York City (1962).
10. Bommer, Paul M.: "A Streamline-Concentration Balance Model for In-Situ Restoration," PhD dissertation, U. of Texas, Austin (Aug. 1979).
11. Perkins, T. C. and Johnston, O. C.: "A Review of Diffusion and Dispersion in Porous Media," *Soc. Pet. Eng. J.* (March 1963) 70-84.
12. Galichon, Philippe: "In-Situ Leaching of Uranium Ore," MS thesis, U. of Texas, Austin, (Dec. 1976).

APPENDIX A
Streamline Generation

Starting with the Laplace line-source and sink equation

$$p(x,y) = p_m - \frac{\mu}{4\pi kh} \sum_{i=1}^{n} q_i \ln[(x-x_i)^2 + (y-y_i)^2]. \quad \text{(A-1)}$$

Eq. A-1 can be differentiated with respect to x and y to obtain expressions for the vectorial components of velocity

$$v_x(x,y) = \frac{1}{2\pi\phi h} \sum_{i=1}^{n} q_i \frac{(x-x_i)}{(x-x_i)^2+(y-y_i)^2}. \quad \text{(A-2)}$$

$$v_y(x,y) = \frac{1}{2\pi\phi h} \sum_{i=1}^{n} q_i \frac{(y-y_i)}{(x-x_i)^2+(y-y_i)^2}. \quad \text{(A-3)}$$

Define RI as 2% of the average distance between wells and assume that the velocity remains constant over this small distance. Sum the vectorial components of velocity to obtain the total velocity:

$$v(x,y) = (v_x^2+v_y^2)^{1/2}. \quad \text{(A-4)}$$

The time required for a fluid particle to move the distance RI is

$$\Delta t = RI/v(x,y). \quad \text{(A-5)}$$

The new location of the fluid particle along a streamline can be calculated by

$$x_{i+1} = x_i + v_x(x,y)\Delta t, \quad \text{(A-6)}$$

$$y_{i+1} = y_i + v_y(x,y)\Delta t. \quad \text{(A-7)}$$

This procedure is repeated for each streamline of each production well. Thus, the streamlines are traced between production and injection wells.

APPENDIX B
Concentration Balance

A concentration balance, which includes dispersion that varies in the axial as compared with the radial direction, can be written as

$$-u_x\frac{\partial c}{\partial x} - u_y\frac{\partial c}{\partial y} + \frac{\partial}{\partial x}\left(K_{xx}\frac{\partial c}{\partial x}\right) + \frac{\partial}{\partial x}\left(K_{xy}\frac{\partial c}{\partial y}\right) + \frac{\partial}{\partial y}\left(K_{yx}\frac{\partial c}{\partial x}\right) + \frac{\partial}{\partial y}\left(K_{yy}\frac{\partial c}{\partial y}\right) - R = \phi\frac{\partial c}{\partial t}. \quad \text{(B-1)}$$

At this point, it is necessary to convert Eq. B-1 from rectangular coordinates to stream-function and potential coordinates. Eq. B-1 can be written as follows, provided it is assumed that dispersion perpendicular to flow can be neglected.

$$\frac{\mu}{k}\left\{u^2-K_L\left(1+\frac{u_x^2}{u^2}\right)\frac{\partial u_x}{\partial x}-K_L\left(\frac{2u_xu_y}{u^2}\right)\frac{\partial u_x}{\partial y}\right.$$

$$\left.-K_L\left(1+\frac{u_y^2}{u^2}\right)\frac{\partial u_y}{\partial y}\right\}\frac{\partial c}{\partial \Phi}+\left(\frac{\mu}{k}\right)^2\left\{\left(\frac{u_x^2+u_y^2}{u}\right)^2\right.$$

$$\left.\cdot K_L\right\}\frac{\partial^2 c}{\partial \Phi^2}-R=\phi\frac{\partial c}{\partial t}. \quad \ldots\ldots\ldots\ldots\ldots \text{(B-2)}$$

Define

$$\alpha=\frac{\mu}{k}\left\{u^2-K_L\left(1+\frac{u_x^2}{u^2}\right)\frac{\partial u_x}{\partial x}-K_L\left(\frac{2u_xu_y}{u^2}\right)\frac{\partial u_x}{\partial y}\right.$$

$$\left.-K_L\left(1+\frac{u_y^2}{u^2}\right)\frac{\partial u_y}{\partial y}\right\} \quad \ldots\ldots\ldots\ldots\ldots \text{(B-3)}$$

$$\beta=\left(\frac{\mu}{k}\right)^2\left\{\left(\frac{u_x^2+u_y^2}{u}\right)^2K_L\right\}, \quad \ldots\ldots\ldots\ldots\ldots \text{(B-4)}$$

where

$$K_L=D_o/F\phi+0.5v\sigma P,$$

which is the expression for longitudinal dispersion described by Perkins and Johnston.[11]

All the terms in α and β are either known from the streamline generator or can be calculated. So, the concentration balance, Eq. B-2, can be reduced to

$$\alpha(\Phi,\psi)\frac{\partial c}{\partial \Phi}+\beta(\Phi,\psi)\frac{\partial^2 c}{\partial \Phi^2}-R=\phi\frac{\partial c}{\partial t}. \quad \ldots\ldots\ldots\ldots\ldots\ldots\ldots \text{(B-5)}$$

The R term is the rate expression for either uranium or mineral oxidation. **SPEJ**

Original manuscript received in Society of Petroleum Engineers office Aug. 28, 1978. Paper accepted for publication April 6, 1979. Revised manuscript received Aug. 10, 1979. Paper (SPE 7533) first presented at the SPE 53rd Annual Fall Technical Conference and Exhibition, held in Houston, Oct. 1-3, 1978.

UNIVERSITY OF UTAH
RESEARCH INSTITUTE
EARTH SCIENCE LAB.

SUBJ
MNG
MMLO

Table: Metal content of the concentration products in the operations, %

No.	Feed	1st roughing		2nd roughing		Control		1st reclean		2nd reclean		3rd reclean	
		c	t	c	t	c	t	c	t	c	t	c	t
	X_f	X_1	X_7	X_9	X_8	X_{10}	y_t	X_2	X_6	X_3	X_4	y_c	X_5
1	3.0	36.10	0.52	2.62	0.052	0.63	0.025	51.94	13.43	53.90	9.07	56.60	11.48
2	3.3	38.22	0.58	12.55	0.27	3.63	0.08	45.97	11.77	52.45	11.21	54.73	15.89

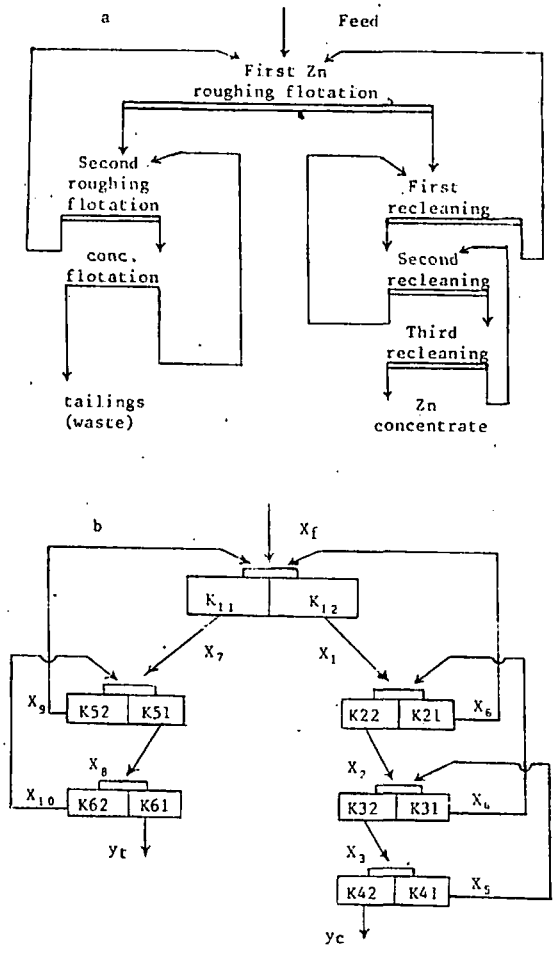

Fig.2 Qualitative (a) and structural (b) schemes of the zinc flotation process.

only to obtain the respective transfer coefficients. By the use of the static model it is possible to modify the methods for calculation of the qualitative and quantitative and water-slime schemes of flotation traditional for concentration plants and to simplify them to a considerable degree without reducing their accuracy. This is extremely important for operational-control of the process. However, most important in our view is the possibility of improving the characteristics of the flotation process by optimisation of its static model. Optimisation of the zinc flotation process by its mathematical model was realised by the simplex planning method[1]) on an MN-18 analogue computer.

The initial matrix, corresponding to twice the number of technological flotation operations, comprised 12 transfer coefficients, the values of which were varied in 13 trials in order to attain a higher quality in the zinc concentrate and to reduce the losses of metal in the tailings. Values of the coefficients taken as optimum were obtained as a result of 22 trials. The table gives comparative data corresponding to the obtained regime (1) and to the best result (2) obtained during the testing of zinc flotation.

Here it must be emphasised that the optimum values of the transfer coefficients (K_i) and the zinc content (X_i) obtained in the concentration products from the corresponding operations lie within the limits of the variation intervals of these parameters established from the results of a test of the process. Comparison of the results obtained showed that an improvement in the quality characteristics of the process can be obtained as a result of purposeful redistribution of the loads between the individual operations of the process. Thus, for example, the yield of the concentrate of the second roughing flotation is increased considerably under the optimum conditions, as a result of which the zinc content of the tailings in this operation and of the tailings of the control flotation, which are waste products, is greatly reduced. At the same time the yield of the froth product in the second recleaning operation is reduced, and its zinc content increases. The improved quality of the froth product of the first recleaning operation makes it possible to obtain a concentrate of higher quality in the second and third recleaning operations.

It is interesting to note that only under the optimum conditions was it possible to obtain recycled products ($X_9 X_{10}$) close in content to the feed of the operations ($X_7 X_f$), to which they are accordingly directed. In this case it is in our opinion possible to eliminate the control flotation without actually altering the values of the transfer coefficients ($K_{62} K_{51}$), since the extraction into the froth products amounts to less than 1%. Trends similar to those described for the optimum conditions are also traced in some of the operations of the best trial. The approach described above may be of use to investigators in the solution of problems associated with the analysis and perfection of technological concentration schemes.

Reference

1) P V Ermuratskii: Tr. MZI No. LXVII, Moscow 1966.

Sov. Non-F
1976 v. 4 N6

UDC 65.011.56

Mathematical model of the leaching of the cobalt matte in ferric chloride solutions

A I Orlov, Yu D Matyskin, N P Kashpurova, S B Polonskii and V I Beloborodov (Irkutsk Polytechnical Institute)

At the present time statistical methods are widely used to obtain a mathematical description of processes in the optimum region, including experimental design methods, since the control of technical processes is possible if there is a mathematical relationship between the parameters[1-3]).

In the present work investigations were carried out into the optimum conditions for the leaching of cobalt matte in solutions of ferric chloride. This is one of the most effective solvents for complex sulphide-containing raw material [4,5]).

The cobalt in the matte is mainly combined with the metallic phase (an alloy of iron with nickel) which contains up to 90% of the total amount in the matte. A cobalt matte containing 1.08 wt.% Co, 1.4 wt.% Ni, 49.1 wt.% Fe, and 25 wt.% S was treated with ferric chloride solution at a temperature close to its boiling point (~105°C). The cobalt content of the solutions and precipitates was determined by a photocolorimetric method[6]). The optimum particle sizes of the cobalt matte and the amounts of hydrochloric acid added to the solution for acidification purposes were first determined.

On this basis investigations were carried out in order to obtain a mathematical relationship between the degree of transfer of cobalt into solution, the leaching time, and the concentration of the solvent, and the results were treated by the experimental design method[2,3]). The factors and variation levels are given in the table.

Table

Factors	Zero level X=0	Variation interval	Upper level X = +1	Lower level X = -1
Fe^{3+} concentration g/l X_1	175	25	200	150
Leaching time h X_2	3	1	4	5

The statistical treatment of the data was realised on a Minsk-32 computer by the programme for the matrices of a multi-factorial experiment. For the degree of transfer of cobalt into solution we obtained the following equation, which adequately describes the experimental data with a 5% significance level:

$$y = 100.975 - 1.0917X_1 - 0.675X_2 + 1.625X_1X_2 - 1.9063X_1^2 - 0.9438X_2^2$$

The variance of the trial was $S^2\{y\} = 0.97583$; the variance of the reproducibility was $S^2(y) = 9.11$. $F_{calc.} = 3.42$; $F_{tab}\ (0.05; 3; 3) = 9.28$. The variance of the coefficients was: $S\{b\} = 0.1068$; $S\{b_i\} = 0.34926$, $S\{b_{ic}\} = 0.42249$, $S\{b_{ii}\} = 0.3858$.

On further treatment of the mathematical model on a computer in order to obtain a relationship for the extraction of cobalt it was found that the transfer of cobalt into solution from the cobalt matte amounts to ~100% with a ferric chloride concentration of 150g/l and with a leaching time of 1 hour. The extraction of cobalt into solution obtained experimentally was 99.5%. These conditions must be considered optimum.

References

1) V V Nalimov and I A Chernova: Statistical methods of extremal experiment design: Moscow Nauka 1965.
2) L P Ruzinov: Statistical methods of optimisation of chemical processes: Khimiya Moscow 1972.
3) S N Sautin, Experimental design in chemistry and chemical technology: Khimiya 1975.
4) I E Dutrizas and R I MacDonald: Min. Sci. and Eng., 1974, 6, (2).
5) V E Klets et alia: Leaching of sulphide concentrates and intermediates in iron salts: Tr. Irkutskogo Politekhn. In-ta (18) 1963.
6) S Yu Fainberg: Analysis of non-ferrous metal ores: Moscow 1953.

REVIEW OF BOOK BY A N Zelikman, G M Vol'dman and L V Belyaevskaya entitled "The theory of hydrometallurgical processes" (a text book for Universities), Metallurgiya, Moscow 1975

A A Zhukhovitskii

At the present time hydrometallurgy is developing very fast. It has always been characterised by a variety of processes. Their correct application and the optimum choice of parameters require the use of physicochemical theory. This determines the need for a text book devoted to the theory of hydrometallurgical processes. It should perhaps be mentioned that there are no such books in the world literature. The interest with which the book under review was received can thus be understood.

Serious difficulties are encountered in the writing of such a book both in respect of the choice of material and in the attainment of a sufficient degree of rigour and comprehensibility. The book under review covers all the main processes of hydrometallurgy (leaching, ion exchange, extraction, precipitation, crystallisation, autoclave reduction, cementation, settling, filtration and washing). Thus, in spite of the comparatively small size of the book (25 quires), it contains a very large amount of material. In the exposition of all these topics essential data are given on the thermodynamics, kinetics and mass transfer; examples of calculations are presented, and specific problems of practical importance are discussed. The scientific level of exposition satisfies the essential needs. The presentation is clear and intelligible. The wide teaching experience of the authors, who have worked on this course for many years, makes itself felt.

It is only possible to mention isolated faults in the book. Perhaps insufficient attention has been paid to the problems of the dynamics, macrokinetics, and modelling of the processes. In the meantime these aspects are important for calculation of the equipment and for discussing the problems of productivity. There is some non-uniformity of exposition, which is difficult to avoid in the collective writing of a book. Thus, the last chapters of the book differ somewhat from the remainder in the level and character of exposition. The detailed presentation of the material in them did not make it possible to pay sufficient attention to the principles and mechanisms of the processes. There are of course isolated unfortunate formulations and points. This applies, for example, to the definition of an ideal solution, in which, in the opinion of the authors "there is no interaction between the components and also between the molecules (atoms, ions) of one and the same component" (page 25). As a whole the book will undoubtedly be of great use both to teachers and students and to workers in industry and scientific institutes. In conclusion it is possible to express the desire that, on the basis of this book (intended as a text book for university students), the authors will write a text book for the corresponding special courses in the physicochemical departments of metallurgical institutes.

UNIVERSITY OF UTAH
RESEARCH INSTITUTE
EARTH SCIENCE LAB.

Ann. Rev. Earth Planet. Sci. 1981. 9:81–111

SUBJ
MNG
MMMF

MECHANICS OF MOTION ON MAJOR FAULTS[1]

x 10145

Gerald M. Mavko
US Geological Survey, Menlo Park, California 94025

INTRODUCTION

Major faults are most simply viewed as the boundaries between lithospheric plates, across which relative plate motion is accommodated. On a global scale, these plate boundaries appear as simple zones of infinitesimal width; when averaged over thousands of years, the displacement rates are approximately steady. The simplicity disappears, however, when one looks in more detail. The surface fault trace is never a smooth break. The zone of concentrated strain may vary from a few meters to tens of kilometers wide. Furthermore, fault motion during the time scale of scientific observation is seldom simple. A section of a fault may exhibit a combination of nearly steady fault slip, episodic slip, minor seismicity, and large damaging earthquakes.

In spite of the complexity, a great deal of progress has been made toward understanding the mechanics of fault motion, primarily because of many careful field and laboratory observations and a few clever models. This paper reviews some of our current understanding of major earthquake cycles in terms of large scale fault models. The emphasis is on observable quasi-static deformation including the process of strain accumulation and the coseismic changes in static stress and strain. Several other reviews have recently been published on related topics, including mechanisms of earthquake instability and rupture (Dieterich 1974, Stuart 1978, 1979, Freund 1979), fracture mechanics applied to the crust (Rudnicki 1980), earthquake-related crustal deformation (Thatcher 1979), and rock properties (Kirby 1977, Tullis 1979, Logan 1979).

[1] The US Government has the right to retain a nonexclusive, royalty-free license in and to any copyright covering this paper.

ELASTIC REBOUND

Most theories concerning earthquakes are based on elastic rebound—the idea that elastic strain energy is gradually stored in the earth and is abruptly released during episodes of failure known as earthquakes. Comparisons of the accumulation of deformation at the earth's surface before large earthquakes with the rapid deformation during earthquakes show that they often approximately cancel except for a net rigid block translation of one side of the fault past the other. This led to the idea of a rebound (Reid 1910).

In the context of plate tectonics, the process of strain buildup and release at major plate boundaries repeats itself in a roughly cyclic fashion. The driving mechanism for the earthquake cycle is the relative plate motion across the common boundary (Andrews 1978). Whether or not strain accumulates, and the way it is released, depends on the nature of slip on the boundary.

We can describe a major cycle in terms of four time phases relative to the earthquake (Mescherikov 1968, Lensen 1970, Scholz 1972). In the *interseismic* or *strain accumulation* phase, the average fault slip on the plate boundary is slower than the long term average plate rate far from the fault. A simple geometric deficiency of slip accumulates causing strain energy to be stored in the plates on both sides of the fault. The *coseismic* phase is the period of several seconds to minutes during which rapid fault slip occurs, generating seismic waves. Most of the slip deficiency is recovered; stored elastic strain energy is converted into heat and waves (kinetic energy). The coseismic phase may or may not be preceded by a *preseismic* phase. This is a period of incipient strain release characterized by higher strain rates than occur during the strain accumulation phase. Rapid changes of any sort during this period might be interpreted as precursors. Finally the *postseismic* phase is a period of transient adjustment following the rapid earthquake movement. This adjustment may take place through aseismic creep, aftershocks, or viscoelastic relaxation.

Elastic rebound is also involved in the phenomenon known as fault creep. At several sites on the San Andreas and Calaveras faults in California, creep occurs in discrete aseismic events lasting up to several hours and separated by periods of little or no slip (Nason 1973). Creep events, like earthquakes, are episodes of strain release (C.-Y. King et al 1973, Goulty & Gilman 1978), although the amount and rate of slip are at least an order of magnitude less for a creep event than the amount and rate of slip for an earthquake with the same rupture length.

The short term unsteady slip associated with earthquakes and creep events is only a small perturbation superimposed on long term plate mo-

tion. In fact most strike-slip earthquakes are confined to only the uppermost 10–15% of a typical continental lithospheric thickness (although major thrusts include a larger fraction). Nevertheless, the unsteady slip excites transient deformation over a broad range of time scales, which forms the basis for most geophysical study of faulting.

COSEISMIC ELASTIC FIELDS

The best constrained portion of a rebound cycle is the rapid coseismic or strain release part. In general, we can determine from seismic and geodetic data the approximate area and orientation of the fault plane, the average slip, and the average stress change. This is possible primarily because the short term response of the earth to rapid fault slip is elastic. Therefore abrupt changes in strain due to earthquakes are insensitive to uncertainties in plate thickness and the inelastic rheologies responsible for long term plate motion. In this section we review some first order features of coseismic fault slip that are inferred from analysis of these elastic fields.

Dislocation and Crack Models of Faulting

Theoretical approaches to computing the static elastic fields due to faulting generally fall into two types: crack models and dislocation models. Crack models are based on a prescribed stress change on the fault plane (e.g. Starr 1928, Muskhelishvili 1953, Eshelby 1957, Knopoff 1958, Sneddon & Lowengrub 1969, Segall & Pollard 1980); dislocation models are based on a prescribed fault slip (Steketee 1958a,b). An advantage of the dislocation approach is the ability to compute the stress and displacement fields due to well-defined, arbitrarily shaped faults with arbitrary slip distributions. The deformation from complex slip distributions is constructed by linear superposition of simple slip solutions. The crack problem, on the other hand, involves mixed stress and slip boundary conditions in the plane of the fault and is generally more difficult to treat mathematically. Of course, both stress and slip changes accompany faulting, and the two descriptions are equivalent. Applications of this work to faulting have also been reviewed by Chinnery (1967) and Mavko (1978).

The most useful approach to modeling the displacement fields associated with three-dimensional faults is the dislocation formalism developed by Steketee (1958a,b). Steketee showed that if we approximate a fault as a discrete surface S of discontinuity (or dislocation) in an otherwise elastic half space, the resulting vector displacement U_k everywhere in the medium is given by an integral over the fault surface of point nuclei of strain τ_{ij}^k (Love 1944) multiplied by the local value of slip ΔU_i.

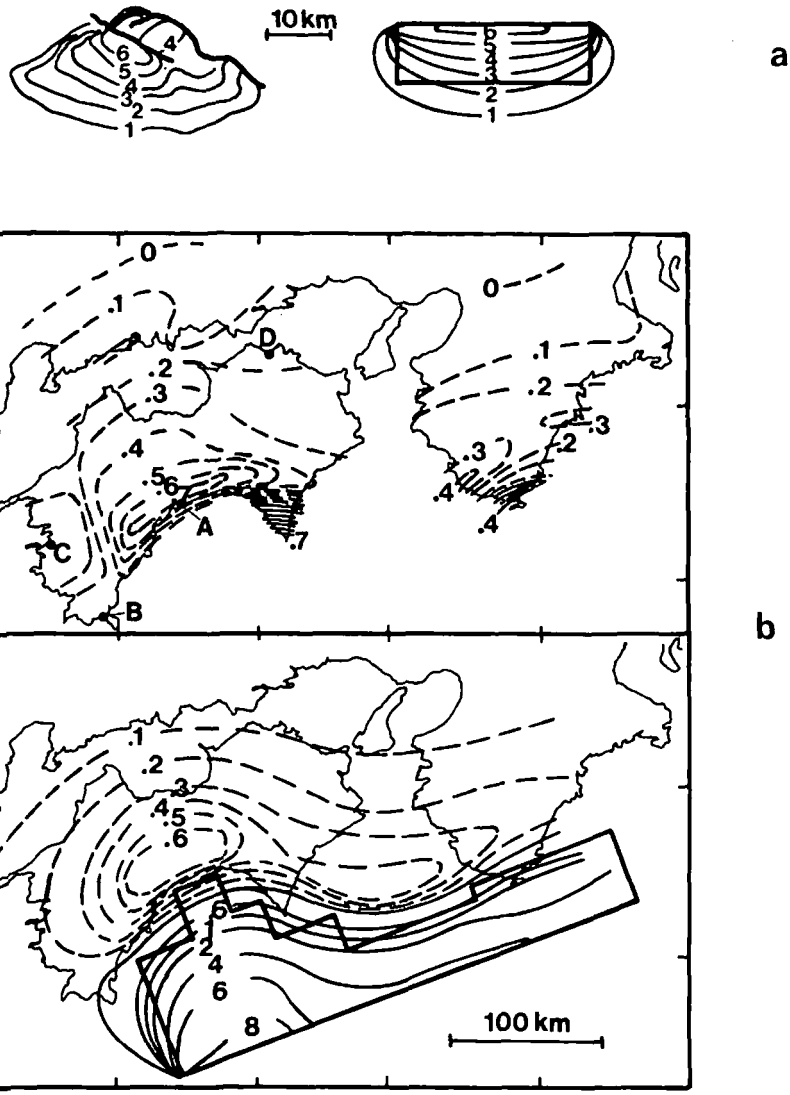

Figure 1 Contour maps comparing computed and observed surface displacement using rectangular fault models. (*a*) Observed (left) and computed (right) subsidence, in meters, associated with 1959 Hebgen Lake, Montana, earthquake (after Savage & Hastie 1966). Heavy rectangle shows the surface projection of the (normal) fault, which dips 54° S. (*b*) Observed (top) and computed (bottom) vertical displacement, in meters, associated with 1946 Nankaido, Japan, earthquake (after Fitch & Scholz 1971). Uplift is shown by solid contours; subsidence, dashed. Heavy polygon shows the surface projection of the (thrust) fault model, composed of six rectangular surfaces.

$$U_k = \frac{1}{8\pi\mu} \iint_S \Delta U_i \tau_{ij}^k \nu_j \, dS. \tag{1}$$

In Equation (1), μ is the elastic shear modulus and ν_j are the direction cosines of the normals to dS. The τ_{ij}^k are the displacements from a nucleus of strain in a half space and have been given in analytical form by Mindlin & Cheng (1950) and Maruyama (1964). Steketee's expression (1) is based on the concept of a dislocation surface composed of infinitesimal elements dS. Strains and stresses in the medium are obtained from the derivatives of (1) and Hooke's law.

A simple application of the formula (1) is the evaluation of displacements associated with uniform slip over a rectangular slip plane. The integral has been evaluated analytically and compared with observations for vertical strike-slip faults by Chinnery (1961, 1963, 1964, 1965) and for a variety of fault models, including dip-slip faults, by Maruyama (1964), Press (1965), and Savage & Hastie (1966). In fact, a rectangular fault with uniform slip is the most commonly used geodetic model of faulting. Examples of computed surface displacement for rectangular strike-slip and dip-slip faults are illustrated in Figures 1, 3, and 4.

A problem with uniform slip models is that they predict stress singularities around the edges of the fault. Furthermore, uniform slip is sometimes not sufficient to explain complicated surface deformation. Nonuniform slip on a three-dimensional fault requires numerical integration of Equation (1). Chinnery & Petrak (1967), for example, have evaluated the stress and displacements for a Gaussian distribution of slip over a roughly rectangular surface. However, in practice, strain fields from nonuniform slip are most often calculated by piecing together a finite number of rectangular fault patches, each with uniform slip (Fitch & Scholz 1971, Thatcher 1975, Dunbar 1977, Savage et al 1979).

Effects of variable slip and stress drop can be studied more easily in two dimensions. In two dimensions a very long fault (length $\gg$ depth) can be modeled as a distribution of elastic dislocation lines, screw dislocations when slip is parallel to the long fault dimension and edge dislocations when perpendicular (Weertman 1964, Bilby & Eshelby 1968, Mavko & Nur 1978). In contrast to Steketee's formalism, constructed from infinitesimal dislocation surfaces, each dislocation line marks the edge of a semi-infinite plane of slip. Variable slip $U(x)$, where x is the in-plane coordinate parallel to the fault (perpendicular to the dislocation line), is described by the dislocation density function $B(x) = -\partial U/\partial x$ where $B(x)\,dx$ represents the total length of Burgers vectors of the infinitesimal dislocations lying between x and $x + dx$.

The displacement field from a single dislocation in an infinite medium has a simple form (Weertman & Weertman 1964). For a screw dislocation lying along the z-axis with slip b parallel to the z direction, the only nonzero displacements are in the z direction:

$$U_z = \frac{b}{2\pi}\tan^{-1}(y/x). \tag{2}$$

For an edge dislocation lying along the z axis with slip b parallel to the x direction, the displacements are as follows:

$$\begin{aligned} U_x &= \frac{-b}{2\pi}\left[\tan^{-1}(y/x) + \frac{\lambda+\mu}{\lambda+2\mu}\frac{xy}{x^2+y^2}\right], \\ U_y &= \frac{-b}{2\pi}\left[\frac{-\mu}{2(\lambda+2\mu)}\log\left(\frac{x^2+y^2}{c}\right) + \frac{\lambda+\mu}{\lambda+2\mu}\frac{y^2}{x^2+y^2}\right], \\ U_z &= 0. \end{aligned} \tag{3}$$

Here λ is Lamé's coefficient and c is an arbitrary constant. The slip due to both types of dislocation is uniform over the half plane $y = 0$, $x > 0$. Because the material is linear and the elementary solutions (2) and (3) are invariant under spatial translation in an infinite medium the displacements due to variable slip are given by the convolution (Bracewell 1965) of (2) or (3) (with $b = 1$) with the distribution $B(x)$ (Canales 1975, Mavko & Nur 1978, Stuart & Mavko 1979).

The stress change in the plane of the fault is related to the slip through the Hilbert transform:

$$\sigma = \frac{\mu}{2\pi\alpha}\int_{-\infty}^{\infty}\frac{B(x')\mathrm{d}x'}{x-x'}. \tag{4}$$

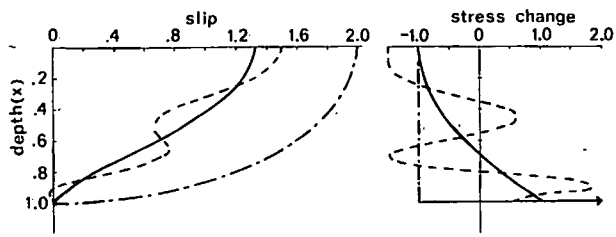

Figure 2 Three different stress-slip pairs for two-dimensional faults computed from Equation (4). Depth (x) can be interpreted as either distance from the center of a deeply buried fault, normalized by fault half width W, or actual depth, normalized by W, for vertical strike-slip faults breaking the surface. Stress is in arbitrary units τ. Displacement is in units of $\tau W\alpha/\mu$. Dashed and solid curves represent two heterogeneous fault models, both having the same moment. Dot-dashed curves represent the more familiar uniform stress drop model.

Here $\alpha = 1$ for screw dislocations, $\alpha = (1 - \nu)$ for edge dislocations, and σ is the component of shear stress in the direction of slip. The transform (4) can be evaluated numerically using the fast Fourier transform (Claerbout 1976, Mavko & Nur 1978, Stuart & Mavko 1979). Also, a large number of analytic transform pairs are given by Erdelyi et al (1954). Mavko & Nur (1978) outline a simple analytic procedure for inverting (4) for slip, given an arbitrary stress change σ expanded as a polynomial. Several stress-slip pairs for two-dimensional faults are shown in Figure 2.

A convenient feature of solutions constructed with screw dislocations is that a plane perpendicular to the fault (parallel to the dislocation lines) is traction-free whenever the slip is symmetric about the plane. Hence, the solution for a vertical strike-slip fault intersecting the free surface is just half of a full space solution constructed by mirroring the problem across the free surface (the method of images).

Geodetic Depth

A common feature of all static coseismic strain fields is that they rapidly decrease with distance from the fault, within several 10's of kilometers for strike-slip earthquakes and 100 km or so for major thrusts. Data showing the falloff of displacement with distance from the Nankai Trough (1946 Nankaido, Japan, thrust earthquake) and the Gomura Fault, Japan, (1927 Tango earthquake) are illustrated in Figures 1*b* and 3. The spatial scale of the strain release is a measure of the fault depth and can be understood in terms of the elastic models (Kasahara 1957, Chinnery & Petrak 1967).

Consider a very long (two-dimensional) vertical strike-slip fault in a half space with uniform slip D extending from the free surface to a depth W. The horizontal displacement $U(y)$ at the free surface is constructed from (2) using a buried screw dislocation and an image:

$$U(y) = \frac{D}{\pi}\tan^{-1}(y/W) \mp D/2. \tag{5}$$

(The sign $\mp$ is chosen: $-$ for $y > 0$ and $+$ for $y < 0$.)

The strain ε is the derivative $\delta U/\delta y$:

$$\varepsilon = \frac{D}{\pi W}\frac{1}{1 + (y/W)^2}. \tag{6}$$

The maximum surface strain and displacement occur at the fault trace, $y = 0$. The falloff of strain and displacement is scaled by the depth W, as illustrated in Figure 4*a*. Both U and ε drop to half their trace values at a distance $y = \pm W$, which gives a convenient surface measure of the depth

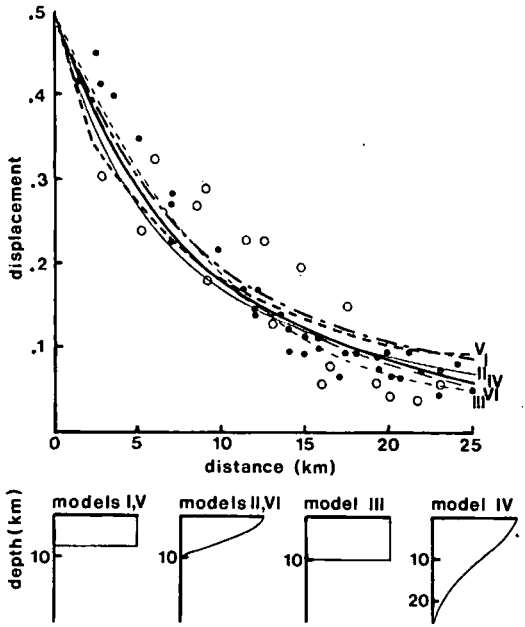

Figure 3 (*Top*) Computed and observed horizontal surface displacements associated with 1927 Tango earthquake. Closed circles—southwest side of the fault; open circles—northeast side (after Chinnery & Petrak 1967). Displacement is normalized by the trace offset; distance is perpendicular to the fault. (*Bottom*) Slip vs depth for six different fault models (see text).

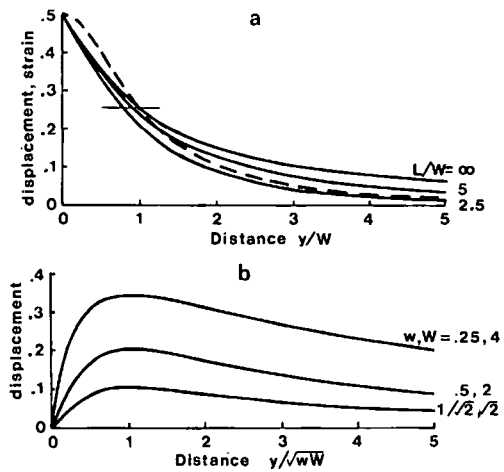

Figure 4 Falloff of surface displacement and strain with distance perpendicular to vertical strike-slip fault models. (*a*) Solid curves show displacement, normalized by the maximum trace offset, for rectangular faults with depth W and length L along the strike. Dashed curve shows shear strain for the two-dimensional case ($L/W = \infty$), arbitrarily normalized by twice the strain at the trace. (*b*) Surface displacement for three buried two-dimensional faults, all having the same mean depth, $\sqrt{wW} = 1$ and unit slip.

for this model. For faults with finite length L along strike, the displacement drops to half its trace value at a distance less than the depth.

Displacements computed for a variety of strike-slip models are compared with the observations from the 1927 Tango earthquake in Figure 3. In the figure, model I is the two-dimensional uniform slip model in Equation (5); model II is a two-dimensional model with slip smoothly tapering to zero with depth (Mahrer & Nur 1979); model III assumes uniform slip over a finite length rectangular fault (Chinnery & Petrak 1967); model IV assumes a rectangular fault with slip smoothly tapering toward zero near the edges (Chinnery & Petrak 1967). Clearly, a variety of uniform half-space models fits the data (the three-dimensional models fit a bit better than the two-dimensional ones) even though the scatter in the data is small. All of the models have a similar slip distribution of about 3 m in the uppermost 7 km, comparable to that predicted by the simplest two-dimensional model. Below 7 km, the models are quite different. This illustrates the general result that geodetic data can define the approximate depth range of greatest slip, but cannot constrain the details of slip (Weertman 1965, Chinnery & Petrak 1967). Details on a spatial scale d cannot be resolved at distances larger than d. Also the sensitivity of surface deformation to small amounts of slip decreases with depth (Thatcher 1978, Savage 1978), so that the estimated depth of faulting can be uncertain by a factor of two or more.

A more precise statement can be made about the models in Figure 3 by defining the geodetic depth as the depth of maximum slip gradient or the depth at which the slip falls to half the maximum value. In this sense the geodetic depths of the two-dimensional models I and II are within 2 km of each other and the depths of the three-dimensional models III and IV are within 4 km.

The simplest model for slip not breaking the surface is also two dimensional. The surface displacement and strain for a fault with uniform slip between depths w and W, not reaching the surface, is modeled with two dislocations and two images (Chinnery 1970):

$$U(y) = \frac{D}{\pi}[\tan^{-1}(y/W) - \tan^{-1}(y/w)], \tag{7}$$

$$\varepsilon = \frac{D}{\pi}\left[\frac{1}{W}\frac{1}{1+(y/W)^2} - \frac{1}{w}\frac{1}{1+(y/w)^2}\right]. \tag{8}$$

The displacement is shown in Figure 4*b* for several values of w and W. The position of maximum surface displacement, $y = \sqrt{wW}$ indicates the geometric mean of the upper and lower depths. The strain at the trace

Table 1 Geodetic depth and stress drop for strike-slip faults[a]

Earthquake	Magnitude	Depth (km)	Slip (m)	Reference	Stress drop (bars)
San Francisco (1906)	8.3	3.2	4.0	Knopoff (1958)	188
		6	5.0	Kasahara (1958)	125
		5	5.0	Chinnery (1961)	96
		12	4.9	Petrak (1965)	122
Tango (1927)	7.5	15	3.0	Kasahara (1958)	30
		15	3.4	Chinnery (1961)	37
		10	3.4	Chinnery (1961)	39
		25	3.4	Petrak (1965)	27
		20	3.4	Petrak (1965)	55
North Izu (1930)	7.0	8	4.0	Kasahara (1958)	75
		12	3.8	Chinnery (1961)	51
		26	3.8	Petrak (1965)	46
Imperial Valley (1940)	7.1	8	4.2	Kasahara (1958)	79
		6	4.2	Chinnery (1961)	69
		13	4.2	Petrak (1965)	96
		12	4.2	Petrak (1965)	106

[a] From a more complete table by Chinnery (1967).

and the far field displacement ($y \gg \sqrt{wW}, w - W$) are both proportional to the product $D(w - W)$. The depth range ($W - w$) can therefore be determined only if D is found independently. In practice, the fault area is often found independently from aftershock locations and slip is determined from the moment $\mu D(w - W)$.

Depths of faulting determined geodetically are shown for several strike-slip earthquakes in Table 1 (from a longer list by Chinnery 1967). The range of depths for each event results primarily from the range of models used to fit the data. An important result is that most strike-slip earthquakes are shallower than 10–20 km (Chinnery 1967, Eaton et al 1970a). The lack of deeper earthquakes has been attributed to a transition from stick-slip to stable sliding in the fault zone as the temperature increases with depth (Brace & Byerlee 1970) or to a general increase in ductility of the crust with depth (Lachenbruch & Sass 1973). Thrust faults show a larger scatter in rupture depths but are generally much deeper, particularly at subduction zones.

A complication in determining geodetic depth results from heterogeneity in crustal stiffness, which can distort surface strain fields. Rybicki & Kasahara (1977) and Mahrer (1978), for example, have found from theoretical studies that a relatively soft fault zone embedded in a stiff half

space will concentrate strain release closer to the fault than a uniform half space. This is illustrated as model V in Figure 3. Note the prominant knee in the curve illustrating the effect of the soft fault zone. Similarly Rybicki (1971) finds that a soft surface layer over a stiffer half space tends to concentrate strain closer to the fault for both surface and buried fault slip. Because fault zones and surface layers are usually less rigid than the surroundings, it appears that most geodetic determinations of fault depth, based on the falloff of surface displacements in a homogeneous half space, will be underestimated by as much as 50%.

As a counterexample, Mahrer & Nur (1979) have considered a half space with rigidity continuously increasing with depth (as opposed to a discrete soft layer over a half space) and find that the scale of surface displacements from strike-slip faulting is fairly accurately modeled by the homogeneous case (model VI, Figure 3). Chinnery & Jovanovich (1972) model faulting in a surface layer underlain by a shallow soft layer. This is one of the few plausible situations that would cause the geodetic depth, based on a uniform half-space model, to be an overestimate.

Seismic Moment and Stress Drop

An important static parameter of faulting that can be obtained directly from seismic observations is the seismic moment. In the far field at long periods a fault appears as a double couple point source. The scalar value of the moment of one of these couples is the seismic moment (Aki 1966). The seismic moment M_0 is a measure of the total final static slip ΔU on the fault surface S (Burridge & Knopoff 1964).

$$M_0 = \mu \iint_S \Delta U \, dS. \tag{9}$$

This is frequently rewritten in the form

$$M_0 = \mu \overline{\Delta U} S \tag{10}$$

where $\overline{\Delta U}$ is the average fault slip and S is the area of the slip patch. The average slip can be solved given an estimate of the rupture area S, for example, from the locations of aftershocks.

Brune (1968) showed that the contribution of seismic slip from many events to overall slip on a fault zone can be obtained from the sum of seismic moments. The average cumulative seismic slip from N events with individual moments M_{0i} distributed over fault area A_0 is

$$\overline{\Delta U}_0 = \frac{1}{\mu A_0} \sum_{i=1}^{N} M_{0i}. \tag{11}$$

Comparisons of seismic moments, Equation (10), with geodetic moments for individual earthquakes (N. King et al 1980) and cumulative slip, Equation (11), with long term geodetic slip rates (Brune 1968, Wyss & Brune 1968, Scholz et al 1969, Chinnery 1970, Langbein 1980) show that seismic slip is often much less than the total slip. Although there are uncertainties in computing moment and estimating rupture area, the differences are probably real and most likely indicate large amounts of aseismic slip.

In principle, the seismic stress drop can be computed from slip, using one of the dislocation theories, if the slip distribution is known in detail. However, the seismic moment and even geodetic data yield only the average slip from which only a certain weighted average of the stress change $\langle \Delta\sigma \rangle$ can be obtained. Seismologists usually assume the simple areal average of stress drop $\overline{\Delta\sigma}$ to be proportional to the average slip $\overline{\Delta U}$:

$$\overline{\Delta\sigma} = \frac{C\mu\overline{\Delta U}}{l}. \tag{12}$$

Here μ is the shear modulus, C is a numerical factor related to the shape of the fault, and l is a measure of the minimum fault dimension. Combining (10) and (12) yields a relation between stress drop and moment,

$$\overline{\Delta\sigma} = \frac{CM_0}{Sl}. \tag{13}$$

Values of C can be found from the ratio of average stress and slip predicted by the various crack and dislocation models. Using this method gives C of order unity for simple shapes and smooth distributions of stress and slip, although estimates will vary by a factor of 2 or 3 depending on the fault model used. For example, the value of C for the models in Figure 2 vary between .42 and .64 if $l = W$.

The uncertainty in inferring stress drop from moment is actually much worse when one considers realistic earthquakes having highly heterogeneous stress and slip distributions. Madariaga (1979) has shown that if the fault surface is planar and slip is everywhere parallel the scalar seismic moment in terms of variable stress drop is

$$M_0 = \iint_S \Delta\sigma E \, dS, \tag{14}$$

where the weighting function E is the slip calculated for a crack of the same shape but with a uniform stress drop $\Delta\sigma = \mu$. The expression (14) is valid for faults of any geometry, including multiple faults and heterogeneous stress drop. In the case of an elliptical fault, for example, with

semimajor and semiminor axes L and W

$$M_0 = \frac{3}{2} CW \iint \Delta\sigma \left(1 - \frac{x^2}{L^2} - \frac{y^2}{W^2}\right)^{1/2} dS,$$

$$= CWS\langle\Delta\sigma\rangle \tag{15}$$

where C is now a dimensionless constant that depends on the direction of slip and the ellipticity, $\varepsilon = W/L$, but not on the distribution of slip. The estimated stress drop $\langle\Delta\sigma\rangle$ is an average of the stress drop weighted with a function that emphasizes the stress near the center of the fault:

$$\langle\Delta\sigma\rangle = \frac{3}{2S} \iint \Delta\sigma(x, y) \left(1 - \frac{x^2}{L^2} - \frac{y^2}{W^2}\right)^{1/2} dS. \tag{16}$$

[Mavko & Nur (1979) independently derived the two-dimensional equivalent of (16) for the analogous problem of crack-opening under a heterogeneous pressure distribution.]

For heterogeneous stress drops $\langle\Delta\sigma\rangle$ will usually differ from the simple areal average $\overline{\Delta\sigma}$, though not by much (Madariaga 1979). Both $\langle\Delta\sigma\rangle$ and $\overline{\Delta\sigma}$, however, might be quite different from the actual stress drop. Madariaga considers the example of stress drop $\Delta\sigma_a$ at asperities covering a portion S_a of the total source area S. Assuming negligible stress drop in the rest of the plane the average stress drop is only a fraction of $\Delta\sigma_a$,

$$\langle\Delta\sigma\rangle \simeq \overline{\Delta\sigma} = \Delta\sigma_a S_a / S. \tag{17}$$

The localized or maximum stress drop at complex heterogeneous sources is usually underestimated by the average stress drop. Consider the stress drop on a two-dimensional fault expanded as a polynomial (Mavko & Nur 1978),

$$\Delta\sigma = \sum_{i=0}^{N} a_i T_i(x), \tag{18}$$

where T_i are Chebychev polynomials of the first kind (Abramowitz & Stegun 1964). The weighted stress drop $\langle\Delta\sigma\rangle$ obtained from the seismic moment is obtained from (18) substituted into (14). Because of the orthogonality of the polynomials only T_0 and T_2 contribute to the moment:

$$\langle\Delta\sigma\rangle = a_0 - a_2/2. \tag{19}$$

Wildly fluctuating stresses expressed in the form of T_i, $i \neq 0, 2$, contribute nothing to the moment, regardless of their amplitude. Simple examples are shown in Figure 2. The solid and dashed stress-drop curves correspond to the functions $\Delta\sigma = T_2$ and $\Delta\sigma = T_2 - T_8 + T_{12}/2$ respectively. Both have the same moment and the same average stress $\langle\Delta\sigma\rangle$ even though the

maximum stress drop is 50% greater and the maximum stress increase is 100% greater for the dashed function.

POSTSEISMIC, INTERSEISMIC, AND PRESEISMIC DEFORMATION

Observations of Transient Deformation

In a strictly elastic earth, complete elastic rebound would take place in a few seconds, with the characteristic time of strain release determined by the earthquake source rise time, fault dimensions, and rupture velocity. The only slow deformation would be the accumulation of tectonic strain. It appears, however, that an earthquake is often just a fraction of a larger episode of strain release. Pre- and postseismic transients are observed, which indicate a broad relaxation spectrum. For example, during the three years following the 1966 Parkfield, California, earthquake ($M = 5.5$; right-lateral strike-slip) as much as 25 cm of fault creep occurred at a decaying rate, although little or no surface breakage occurred during the main event (Smith & Wyss 1968, Scholz et al 1969). In addition, road damage occurring within several years before, and en-echelon cracks formed within a month before the earthquake (Allen & Smith 1966), suggest a preseismic transient. Rapid surface fault slip of more than 10 cm has occurred within several months following both the August 6, 1979, Coyote Lake, California, and October 15, 1979, Imperial Valley, California, earthquakes (J. Savage, personal communication, USGS 1980).

Even the great 1906 San Francisco earthquake, which led H. F. Reid to propose the elastic rebound mechanism, was followed by transient deformation. Thatcher (1975) suggests that substantial postseismic crustal strains, continuing for at least 30 years following the earthquake, can be inferred from geodetic surveys since 1906. These strains can be explained (though not uniquely) by $\sim$4 m of aseismic fault slip from 10 to 30 km depth, without additional surface slip. Thatcher (1975) also suggests anomalously rapid strain accumulation during the 50 years prior to 1906, although the evidence is weak (Savage 1978, Thatcher 1978).

Perhaps the most spectacular example of postseismic deformation was observed following the 1946 Nankaido, Japan, earthquake ($M = 8.2$; thrust type) where upheavals of as much as 2 m occurred over a 1 to 3 year period. Figure 5*a* (Matuzawa 1964, Kanamori 1973) shows the rather complicated nature, in space and time, of the vertical displacement. Similar deformations occurred during the 10 years following the 1964 Alaskan ($M = 8.4$; thrust type) earthquake (Brown et al 1977, Prescott & Lisowski 1977, 1980).

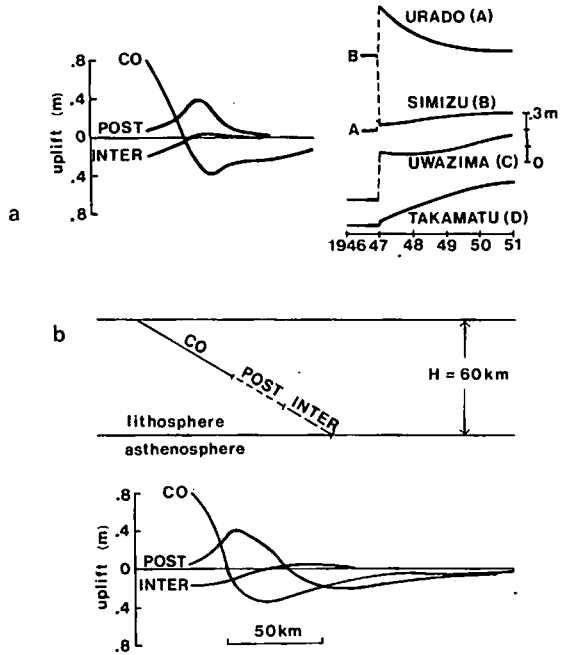

Figure 5 Observed and computed coseismic, postseismic, and interseismic vertical deformation associated with the 1946 Nankaido, Japan, thrust earthquake (after Fitch & Scholz 1971, Thatcher & Rundle 1979). (*a*) Observed profiles perpendicular to the Nankai Trough (*left*) and smoothed tide gage records (*right*) at locations labeled *A–D* in Figure 1*b*. (*b*) Two-dimensional model (see text) and computed profiles, both drawn to the same scale as the profiles, in (*a*).

Particularly short-lived transients have also been observed. Rapid fault slip lasting only several hours was recorded after a Matsushiro shock on September 6, 1966 (Nakamura & Tsuneishi 1967, Scholz 1972). A precursory aseismic slip with time constant of 300 to 600 s, starting about 1000 s before the main shock of the 1960 Chilean earthquake, has been inferred from long-period surface waves and body waves (Kanamori & Cipar 1974) and from free oscillations (Kanamori & Anderson 1975). Ando (1975), Sacks et al (1977), and Pfluke (1978) give evidence of earthquakes with geodetic moments several times that determined from seismic methods. Because large tsunamis were generated, the duration of the aseismic component of slip is apparently minutes to hours, long compared to the response band of seismographs but short compared to the response of the sea. Further examples of transient deformation are reviewed by Scholz (1972), Kanamori (1973), Dunbar (1977), Pfluke (1978), and Thatcher (1979).

Relaxation Mechanisms

An earthquake rupture superimposes a stress perturbation onto the preseismic state—decreasing the stress over much of the rupture area and increasing it elsewhere. As discussed earlier, these coseismic fields are now well understood, and numerous studies have shown that the associated abrupt displacements can be explained in terms of fault slip in an elastic medium. Postseismic observations suggest a subsequent viscoelastic response. A material is viscoelastic when its initial response to abrupt changes of stress or strain is elastic, while its longer term response is a viscous relaxation or flow (Fung 1965, Christensen 1971). Most rocks flow to relax shear stresses, as though the rigidity gradually decreases with time. Bulk relaxation is much less common.

What are the viscous elements? A simple mechanical model for the earth's crust and upper mantle, suggested by plate tectonics, consists of a relatively elastic, brittle lithosphere overlying a ductile asthenosphere. Within this framework we can distinguish geometrically three general sources of relaxation.

RELAXATION IN THE ASTHENOSPHERE The asthenosphere is characterized by high temperature relaxation mechanisms (Ashby & Verrall 1977, Weertman 1978, Tullis 1979). Solid mineral grains can flow plastically by atomic diffusion and the motion of lattice dislocations (Gordon 1965, Weertman & Weertman 1975, Heard 1976, Carter 1976). This makes the polycrystalline composite fluidlike over long time scales and can account for the large-scale, finite deformation implied by plate motion and the low strength implied by isostatic equilibrium. In addition, enhanced deformation at grain boundaries can occur resulting from dislocation motion and diffusion (Ke 1947, Zener 1948, Anderson 1967) or the viscous flow of melt (Walsh 1969, Mavko & Nur 1975, O'Connell & Budiansky 1977). Other loss mechanisms which are relevant at seismic frequencies include thermoelasticity, dislocation damping, point defect diffusion, and grain boundary effects (Anderson 1967, Jackson & Anderson 1970).

RELAXATION IN THE LITHOSPHERE The lithosphere, by definition, is a relatively strong, rigid layer that can resist permanent deformation or plastic flow for long periods of time, whereas the asthenosphere cannot (Le Pichon et al 1973). This is consistent with analyses of glacial rebound and lithospheric flexure (McConnell 1968, Walcott 1973, Forsyth 1979), as well as our concept of continental drift.

The important question becomes: How thick is the lithosphere? Or, at least, if we are to construct simple mechanical models for an earthquake cycle, what thickness is appropriate for the elastic layer?

Many investigators agree on a stratified model in which the effective mechanical thickness of the lithosphere depends on time, temperature, strain rate, and deviatoric stress (Melosh 1978b, Forsyth 1979). The upper lithosphere, above approximately the 450° ± 150°C isotherm (Watts 1978), remains essentially elastic and can support loads for 10^8 to 10^9 years; the lower part is elastic-plastic or viscoelastic and relaxes under stresses with durations a few million years. The mechanisms of relaxation in the lower part are similar to those discussed for the asthenosphere (Kirby 1977) but relaxation times are longer for the lithosphere because of lower temperatures. The effective viscosity at the base of the elastic part of the lithosphere is about 10^{26} Poise and in the asthenosphere 10^{21} Poise or less (Melosh 1977, 1978b). At an ocean trench, for example, the long term flexural thickness of the lithosphere may be only 20–40 km (Hanks 1971, Watts & Talwani 1974) because the strain rate associated with the steady component of subduction is low enough and the temperature below 40 km is high enough for the deviatoric stress to stay relaxed. In contrast, at the same trench the nonsteady strain accumulation and release during a rebound cycle lasting tens or hundreds of years occurs in a lithosphere effectively 70 km thick, which is approximately the seismically determined thickness (Kanamori & Press 1970, Le Pichon et al 1973). Similarly, in continental lithosphere the plate thickness for rebound might be the seismic thickness of 110–130 km. Anderson (1971) and Hadley & Kanamori (1977) suggest, however, that in parts of southern California the shallow crust is mechanically decoupled from the lower crust, so that the moving surface plate is much thinner than is commonly inferred from surface waves. Lachenbruch & Sass (1973) suggest a similar decoupling between the shallow crust (15–20 km) around the San Andreas Fault and the more ductile material below in order to explain a low broad heat flow anomaly. However, in this case, the crustal plate is also undergoing permanent shear flow, generating heat. This uncertainty in plate thickness can affect interpretation of surface strain.

Aside from large scale fluidlike flow, which distinguishes the asthenosphere from the lithosphere, a limited viscoelastic relaxation to changes in the stress field can occur within even the shallow lithosphere. In the shallow lithosphere the relaxed configuration is also essentially elastic, distinguished from the unrelaxed state only by a smaller effective rigidity. Hence, a viscoelastic lithosphere exhibiting transient relaxation times on the order of several years would look elastic at seismic frequencies as well as over the longer periods of flexure and isostatic rebound.

A number of relaxation mechanisms can be considered to account for the viscoelastic response. Concentrated plastic flow at grain boundaries is reasonable in much of the lithosphere (below, say, 20–30 km) where

the ratio of absolute temperature T to the melting temperature T_m is greater than one half ($T/T_m > 1/2$). Presumably, motion at grain boundaries could occur while the grains themselves remained essentially elastic, giving to the polycrystalline composite a long term finite strength, yet a short term viscoelastic strain. Pressure solution, a low temperature form of grain boundary diffusion enhanced by water (Tullis 1979), can also relax stresses.

In the shallow crust stress-induced viscous shearing and local squirt of pore fluids (Mavko & Nur 1975, 1979, O'Connell & Budiansky 1977) as well as large scale, regional diffusion (Biot 1941, Nur & Booker 1972) can give a time-dependent deformation qualitatively similar to a viscoelastic response. The regional diffusion might also be enhanced by dilatancy (Nur 1973, Scholz et al 1973).

FAULT CREEP In addition to direct observations of surface fault creep, aseismic fault slip has been invoked at depth in the lithosphere to explain pre- and postseismic surface deformation (Fitch & Scholz 1971, Smith 1974, Thatcher 1975, Brown et al 1977, Thatcher & Rundle 1979). However, very little is known about the detailed stress-strain behavior of the fault zone at any depth. Nason & Weertman (1973) conclude little more than the existence of an upper yield point phenomenon from observations of shallow creep events. In the laboratory transient stable sliding sometimes precedes stick slip on frictional surfaces (Scholz et al 1969, Dieterich 1979a,b) at conditions corresponding to several kilometers depth. At higher temperatures and pressures Stesky (1974) observes a nonlinear stress-strain rate sliding law similar to that expected for solid-state creep. Laboratory measurements on fault gouge and clay have also been made (Engelder et al 1975, Logan & Shimamoto 1976, Summers & Byerlee 1977). The main problem lies in determining what kind of material is representative of a fault zone at depth.

In addition to creep on the primary fault, creep on nearby faults can have an effect on relaxation. Even though the bulk of the crustal material is elastic, slip on secondary faults and fractures makes the crust effectively more compliant. If the slip is creep-like, the change in compliance is gradual, and the overall effect may not be distinguishable from viscoelastic relaxation.

Models

Many features of observed aseismic deformation can be explained by purely elastic models, much like the coseismic models, in which both steady and episodic aseismic slip occur around edges of the rupture surface (Savage & Burford 1970, Thatcher 1975, Shimazaki 1974). In contrast, a

number of authors have attributed the deformation to viscoelastic adjustments, primarily in the asthenosphere (Nur & Mavko 1974, Smith 1974, Rundle & Jackson 1977, Spence & Turcotte 1979, Savage & Prescott 1978a, Thatcher & Rundle 1979). It now appears that the largest postseismic and interseismic strains are dominated by a combination of these two mechanisms although their relative contributions are difficult to resolve and probably vary from region to region. Other mechanisms, for example the diffusion of pore fluids (Nur & Booker 1972), probably affect deformation much less.

STRIKE-SLIP EARTHQUAKES A commonly accepted model for a major earthquake cycle on a strike-slip fault like the San Andreas Fault in California is shown in Figure 6*a*. Two elastic lithospheric plates with thickness H slide past each other with their relative motion occurring across a narrow vertical fault zone. Seismic and geodetic data indicate that seismic slip seldom occurs deeper than ~ 15 km. Therefore, if the concept of strong plates significantly thicker than 15 km is correct, there

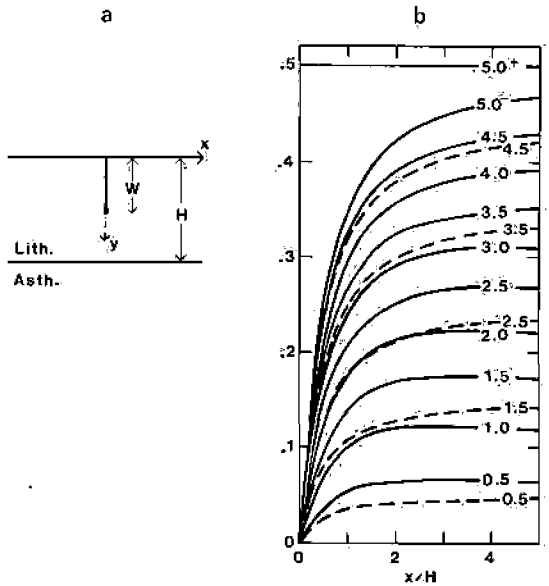

Figure 6 (*a*) Two-dimensional model for a strike-slip earthquake cycle with an elastic lithosphere over a (Maxwell) viscoelastic asthenosphere. (*b*) Surface displacement (solid curves) as a function of distance from the fault, x, for one cycle of periodically occurring earthquake sequences, with $W/H = 0.5$ (after Savage & Prescott 1978a). Displacement is normalized by the seismic slip and is shown relative to the configuration immediately following an earthquake. Curves are labeled with time in increments of $2\eta/\mu$. Dashed curves show the response of an elastic half space to the same earthquake cycle.

can be little doubt that a large amount of aseismic slip at depth is required to accomodate the relative plate offset.

Some of the earliest studies of strain accumulation considered models of deep aseismic slip in an elastic half space (Thatcher 1975, Chinnery 1970, Scholz 1972). Thatcher (1975), for example, explained a rapid episode of postseismic strain ($\sim 1.2\ 10^{-6}$ yr^{-1}) during the 30 years following the 1906 San Francisco earthquake with 3–4 m of slip between depths of 10–30 km. In effect, the rupture, which extended coseismically from the surface to ~ 10 km, gradually deepened by a factor of 2 or 3 during the postseismic period. The resulting postseismic displacement fields would have the form shown in Figure 4*b*, with maximum displacement occurring at a distance of $(10 \cdot 30)^{1/2} = 17.3$ km from the fault, and the far field displacement going to zero. The additional steady component of strain accumulation is simulated with the half space model by uniform slip extending downward to infinity (Savage & Prescott 1978a, Savage et al 1979).

A second series of models attempted to include the effect of a weak fluidlike asthenosphere by considering a plate model with stress-free upper and lower boundaries (Turcotte & Spence 1975, Savage 1975, Spence & Turcotte 1976, Turcotte 1977, Mavko 1977). These models have been criticized (Savage & Prescott 1978a, Spence & Turcotte 1979) for explicitly ignoring the viscous asthenospheric tractions at the base of the plate. It has generally not been recognized, however, that strain rates predicted by plate models with arbitrary nonzero basal tractions under steady motion (if steady motion ever occurs) are exactly the same as for the free plate model (Mavko 1977).

Later studies (Nur & Mavko 1974, Mavko 1977, Rundle & Jackson 1977, Savage & Prescott 1978a, Spence & Turcotte 1979) have included the complete viscoelastic response of the asthenosphere (assuming a Maxwell solid). An example, from Savage & Prescott (1978a), is illustrated in Figure 6*b*, comparing viscoelastic calculations with half-space results. The viscoelastic model assumes steady uniform slip below a depth $W = 0.5\ H$ (where H is the plate thickness) at a rate v equal to the far field plate velocity. In the half-space model the same uniform slip rate extends infinitely deep. Shallower than $W = 0.5\ H$ the fault is usually locked but slips abruptly a uniform amount vT at equally spaced time intervals T. In the example, $T = 5\bar{\tau}_0$ where $\tau_0 = 2\eta/\mu$, η is the asthenospheric viscosity, and μ is the elastic rigidity of the lithosphere and asthenosphere. The unique feature of the viscoelastic model is the rapid postseismic relaxation that causes the displacement rate at a distance $y/H \simeq 2$ to exceed the far field rate early in the cycle. The viscoelasticity tends to concentrate strain accumulation closer to the fault than it is in the half-space model.

Although it is commonly accepted that both slip and asthenospheric effects are important, there is little consensus on their relative contributions. One reason is the uncertainty in plate thickness. Nur & Mavko (1974) and Thatcher (1975) suggested that postseismic viscoelastic effects were not important for earthquakes on the San Andreas Fault, based on an assumed lithospheric thickness of 75–100 km compared to the 15 km coseismic depth. On the other hand, if the thickness of the elastic layer is as small as 20 km (Anderson 1971, Hadley & Kanamori 1977, Lachenbruch & Sass 1973) then the effect may be quite large. A basic problem is our inability to resolve from geodetic observations the difference between deep aseismic slip and distributed viscoelastic relaxation in a layer or half space (Rundle & Jackson 1977, Barker 1976, Savage & Prescott 1978a). In fact, for two-dimensional problems in horizontally layered media, the viscoelastic solution can always be solved using the method of images; that is, a distribution of slip in a uniform half-space model can always be found that precisely duplicates the surface displacement produced by viscoelastic relaxation in one of the buried layers (Savage & Prescott 1978a).

DIP-SLIP EARTHQUAKES Major thrust-type earthquakes at subducting plate margins often rupture through a substantial fraction of the lithosphere, so it is reasonable to expect a large asthenospheric viscoelastic response.

One of the earliest quantitative models for postseismic relaxation in the asthenosphere was the stress guide model introduced by Elsasser (1969, 1971). Patterned after plate tectonics, the model consists of a strong elastic lithospheric plate over a linear viscous fluid asthenosphere. Horizontal displacements, U, in the lithosphere, resulting from long wavelength perturbations in stress, take the form of the diffusion equation,

$$\frac{\delta U}{\delta t} = \frac{h_1 h_2 E}{\eta} \nabla^2 U, \tag{20}$$

Here h_1 and E are the thickness and Young's modulus of the lithosphere and h_2 and η are the thickness and linear viscosity of the asthenosphere, and it is assumed that the scale of lateral variations is large compared to h_1 and h_2. The obvious interpretation (Bott & Dean 1973, Anderson 1975, Savage & Prescott 1978a, Spence & Turcotte 1979) is that localized disturbances (stress drops) associated with earthquakes will diffuse away, qualitatively explaining the transient deformation following some large earthquakes. Anderson (1975) has speculated that this diffusion results in the migration of earthquakes along plate margins. The most important

result is that stress suddenly released at a plate boundary cannot instantaneously affect the whole plate. Disturbances with period T are damped to e^{-1} of their maximum value at a penetration distance δ (skin depth) from the fault:

$$\delta = \left(\frac{Eh_1h_2T}{\pi\eta}\right)^{1/2}. \tag{21}$$

For example, disturbances with period $T = 100$ years (the approximate recurrence time for great earthquakes) are restricted to within a few hundred kilometers of the plate margin, while the interior of a plate is affected only by stresses persisting for a million years or more. This result applies to both strike-slip and dip-slip earthquakes.

The stress guide model has been modified by Melosh (1976) to include a nonlinear fluid asthenosphere, appropriate for long term steady plate motion (Weertman & Weertman 1975, Post & Griggs 1973). The nonlinearity introduces a damped, yet somewhat wavelike, propagation of disturbances which Melosh argues resembles the migration of aftershocks of the 1965 Rat Island, Alaska, earthquake, therefore proving that the asthenosphere is nonlinear. While the asthenosphere is generally considered to be nonlinear, Savage & Prescott (1978b) show that Melosh's (1976) model does not prove it. The short term response of the stress guide model, either linear or nonlinear, is that of an elastic layer over an infinitely rigid half space. Initially, strains are confined to within a layer thickness or so of the fault, and these propagate outward only when the half space begins to relax. A more realistic model, incorporating the initial elastic response of the asthenosphere, results in a larger scale coseismic strain field that subsequently relaxes with less pronounced wavelike propagation. On the other hand, Melosh (1978a) emphasizes that even if the instantaneous elasticity is included, migration effects may still be significant if the asthenosphere is nonlinear. It appears that nonlinear effects on an earthquake cycle have yet to be resolved.

The most successful models of postseismic and interseismic deformation are actually extensions of the purely elastic models developed for coseismic studies. For example, using the solution for a rectangular fault in an elastic half space, Equation (1), Fitch & Scholz (1971) modeled the postseismic deformation following the 1946 Nankaido, Japan, earthquake (Figure 5) with additional forward slip on the down-dip extension of the fault plane and backslip on portions of the coseismic fault plane. A similar model incorporating forward and backslip in an elastic medium was suggested by Scholz & Kato (1978) for deformation following the 1923 Kanto, Japan, earthquake. Brown et al (1977) and Prescott & Lisowski (1977, 1980) used elastic postseismic slip to model deformation following

the 1964 Alaskan earthquake. The requirement of backslip following the Nankaido earthquake was criticized by Nur & Mavko (1974), who suggested instead that the postseismic deformation was dominated by viscoelastic relaxation in the asthenosphere without additional slip. Their model of coseismic slip in an elastic lithosphere (the free surface only crudely approximated) over a linear viscoelastic asthenosphere was the first relaxation model to include both the near field effects of fault dip angle and the initial elastic response of the asthenosphere. Again, the calculation was based on faulting in an elastic medium, with the subsequent viscoelastic response obtained using the correspondence principle (Fung 1965). A similar model, incorporating both slip and asthenospheric relaxation, was developed independently by Smith (1974, 1980).

Recently, a number of numerical models of movements landward of subduction zones, principally in Japan (Bischke 1974, Thatcher & Rundle 1979, Thatcher et al 1980, Smith 1980) and Alaska (Brown et al 1977, Prescott & Lisowski 1977, 1980), have revealed a fairly consistent pattern: rapid episodic slip, both down-dip and up-dip of the coseismic rupture, during the several year postseismic interval and subsidence due to asthenosphere relaxation during the longer interseismic phase. These are illustrated in Figure 5, patterned after the work of Thatcher & Rundle (1979) using an elastic lithosphere over a linear viscoelastic (Maxwell) half space. The curve labeled *CO* shows the vertical coseismic displacement, the elastic half-space response to abrupt slip in the upper portion of the lithosphere. This shallow stress release transfers shear stress to the deeper part of the plate and the asthenosphere. Subsequent aseismic slip down-dip of the rupture and the beginnings of viscoelastic response to both the coseismic and postseismic slip cause the postseismic deformation labeled *POST*. Finally the rapid postseismic deformation merges with the more steady interseismic deformation composed of approximately steady aseismic slip near the bottom of the plate plus viscoelastic subsidence in the asthenosphere, somewhat equivalent to the downward gravitational pull of the slab. Reasonable model parameters for deformation in Japan are a 60 km thick lithosphere and an asthenospheric viscosity of 10^{20}–10^{21} P (Thatcher & Rundle 1979, Thatcher et al 1980).

Disagreements in models are usually in detail only, reflecting our inability to resolve fine details of relaxation. While Thatcher & Rundle (1979) model the asthenosphere under Japan with a viscoelastic half space, Smith (1980) chooses a layered upper mantle with a low viscosity asthenosphere with finite thickness. Thatcher & Rundle prefer postseismic and interseismic slip on a discrete fault plane down-dip of the coseismic rupture; Smith chooses instead distributed viscoelastic relaxation in a low viscosity (10^{19} P) pocket down-dip of the fault plane. The least-understood

effects on deformation are the downward gravitational pull of the slab, buoyancy, and horizontal convergence of the plates during the interseismic period (Thatcher 1979).

HETEROGENEITY IN THE FAULT ZONE

While the emphasis of this review has been on simple quasi-static models, it is important to at least point out the possible role of heterogeneity in stress, material properties, and fault geometry on fault mechanics. Fault models having simple geometries and uniform material properties, like those already discussed, are valuable for understanding large scale low frequency deformation fields associated with an earthquake cycle. However, some heterogeneity is necessary to explain the following fundamental observations: multiple seismic events; high frequency near field ground accelerations; the frequency-magnitude distribution of earthquakes; the termination of rupture (Nur 1978, Andrews 1980, Segall & Pollard 1980).

As discussed by Andrews (1980), rupture termination requires that the difference between the initial shear stress and sliding friction stress vary on the length scale of the rupture, allowing the stress to decrease on much of the slip patch and increase around the borders to stop the rupture (Burridge & Halliday 1971, Andrews 1975). For the same rupture patch, heterogeneity is required on length scales smaller than the rupture length to explain the high frequency ground motion and subsequent smaller earthquakes (Andrews 1978, Nur 1978, Aki 1979). A problem with these frictional models is that the difference between stress and sliding friction becomes smoother with each event until eventually all earthquakes rupture the entire fault. A mechanism is needed to maintain the heterogeneity between stress and friction.

One of the most obvious sources of heterogeneity is fault geometry. The mapped trace of a fault is never a straight cut or break, but often a collection of bent, offset, and sometimes braided strands. Wallace (1973), for example, found that the longest individual fault strands along active portions of the San Andreas fault are about 10 to 18 km long, comparable to the depth of deepest earthquakes. A frequency count of segments by length suggested a distribution of the form $\log N = a + bL$ where N is the number of strands, L is the length, and a and b are constants. Irregular and discontinuous fault traces occur on all scales in nature, for both strike-slip and dip-slip faults, in a variety of rock types and tectonic settings (for a review see Segall & Pollard 1980).

While certain features of the mapped trace geometry may develop as slip propagates upward through unconsolidated sediments, there is some

evidence that faults are discontinuous at appreciable depths (Segall & Pollard 1980). For example, normal faults observed in a South African gold mine are composed of en-echelon segments centimeters to meters in length (McGarr et al 1979). In addition, seismicity patterns often correlate with the surface trace. Aftershocks, at depths of 3–15 km, following the 1966 Parkfield, California, earthquake reflect a 1 km offset in the mapped surface fault trace (Eaton et al 1970b). Bakun et al (1980) and Bakun (1980) report good correlation between the fault trace geometry and epicenter locations (depths 5–8 km), rupture directivity, and aftershock locations on both the San Andreas and Calaveras faults in central California. Hill (1977) and Segall & Pollard (1980) find that earthquake swarms are sometimes localized within fault offsets.

Segall & Pollard (1980) have studied the mechanics of pairs of interacting en-echelon cracks in considerable detail. They suggest that left-stepping offsets on a right lateral fault are sites of increased normal compressive stress that inhibits slip, while right-stepping offsets on right lateral faults have decreased compressive stress, which facilitates slip. Areas of inhibited slip (right lateral, left step) might be sites of strain accumulation and large damaging earthquakes, while areas of enhanced slip (right lateral, right step) might have high seismicity. On a larger scale Mavko (1980) has modeled the interaction of four major faults near Hollister, California, each composed of many individual short segments. Complications in geometry, like large bends, seem to be capable of locking or unlocking sections of the fault which may be important for initiating instability.

SUMMARY

Nearly all fault models are consistent with the concepts of plate tectonics and elastic rebound. Through a combination of remotely applied forces the elastic plates move relative to each other. Whether or not strain accumulates and the way it is released depends on the slip at the common plate boundaries. In terms of the data, the best constrained portion of an earthquake rebound cycle is the rapid coseismic part. Although inelastic deformation in the upper mantle is necessary for long term plate motion and strain accumulation between earthquakes, the short term response of the crust and mantle due to rapid fault slip is essentially elastic. The area, orientation, average slip, and stress drop of the earthquake source can be determined from these coseismic elastic fields using dislocation theory.

A more difficult problem is resolving the sources of aseismic strain. The largest postseismic and interseismic strains appear to be dominated

by a combination of aseismic fault slip and viscoelastic adjustments, primarily in the asthenosphere, while crustal effects, like the diffusion of pore fluids, contribute to a lesser extent.

One of the most promising lines of current research concerns the role of heterogeneity. Although much of our understanding of faulting has resulted from the success of greatly simplified models, heterogeneity in stress, material properties, and geometry is ubiquitous in nature. To some extent, these are a source of noise. For example, variations in crustal stiffness distort strain fields and complicate their interpretation. However, heterogeneity offers perhaps the only explanation for the following fundamental observations: the frequency-magnitude distribution of earthquakes; the termination of rupture; high frequency near field ground accelerations; multiple seismic events.

ACKNOWLEDGMENTS

Frequent discussions with Wayne Thatcher and Jim Savage during the preparation of this paper were extremely helpful. Barbara Mavko, John Langbein, Bill Stuart, and Wayne Thatcher provided useful comments on the manuscript.

Literature Cited

Abramowitz, M., Stegun, I. A. 1964. *Handbook of Mathematical Functions*. Washington, DC: Natl. Bur. Stand. 1046 pp.

Aki, K. 1966. Generation and propagation of G waves from the Niigata earthquake of June 16, 1964, 2, estimation of earthquake moment, released energy, and stress-strain drop from G-waves spectrum. *Bull. Earthquake Res. Inst. Tokyo Univ.* 44:73–88

Aki, K. 1979. Characterization of barriers on an earthquake fault. *J. Geophys. Res.* 84:6140–48

Allen, C. R., Smith, S. W. 1966. Parkfield earthquakes of June 27–29, Monterey and San Luis Obispo Counties, California. Pre-earthquake and post-earthquake surficial displacements. *Bull. Seismol. Soc. Am.* 56:966–67

Anderson, D. L. 1967. The anelasticity of the mantle. *Geophys. J.R. Astron. Soc.* 14:135–64

Anderson, D. L. 1971. The San Andreas fault. *Sci. Am.* 225:52–66

Anderson, D. L. 1975. Accelerated plate tectonics. *Science* 187:1077–79

Ando, M. 1975. Source mechanisms and tectonic significance of historical earthquakes along the Nankai Trough, Japan. *Tectonophysics* 27:119–40

Andrews, D. J. 1975. From antimoment to moment: plain strain models of earthquakes that stop. *Bull. Seismol. Soc. Am.* 65:163–82

Andrews, D. J. 1978. Coupling of energy between tectonic processes and earthquakes. *J. Geophys. Res.* 83:2259–64

Andrews, D. J. 1980. A stochastic fault model—I. static case. *J. Geophys. Res.* 85:3867–77

Ashby, M. F., Verrall, R. A. 1977. Micromechanisms of flow and fracture, and their relevance to the rheology of the upper mantle. *Philos. Trans. R. Soc. London Ser. A* 288:59–95

Bakun, W. H. 1980. Seismic activity (1969 to August 1979) on the southern part of the Calaveras fault in central California. *Bull. Seismol. Soc. Am.* 70:1181–98

Bakun, W. H., Stewart, R. M., Bufe, C. G., Marks, S. M. 1980. Implication of seismicity for failure of a portion of the San Andreas fault. *Bull. Seismol. Soc. Am.* 70:185–202

Barker, T. 1976. Quasi-static motions near the San Andreas fault zone. *Geophys. J.R. Astron. Soc.* 45:689–706

Bilby, B. A., Eshelby, J. D. 1968. Dislocations and the theory of fracture. In *Fracture, An Advanced Treatise*, ed. H.

Liebowitz, pp. 99–182. New York: Academic. 597 pp.
Biot, M. A. 1941. General theory of three dimensional consolidation. *J. Appl. Phys.* 12:155–64
Bischke, R. E. 1974. A model of convergent plate margins based on the recent tectonics of Shikoku, Japan. *J. Geophys. Res.* 79:4845–58
Bott, M. H. P., Dean, D. S. 1973. Stress diffusion from plate boundaries. *Nature* 243:339–41
Brace, W., Byerlee, J. 1970. California earthquakes: why only shallow focus? *Science* 168:1573–75
Bracewell, R. 1965. *The Fourier Transform and its Applications*. New York: McGraw-Hill. 381 pp.
Brown, L. D., Reilinger, R. E., Holdahl, S. R., Balazs, E. I. 1977. Post seismic crustal uplift near Anchorage Alaska. *J. Geophys. Res.* 82:3369–78
Brune, J. N. 1968. Seismic moment, seismicity, and rate of slip along major fault zones. *J. Geophys. Res.* 73:777–84
Burridge, R., Halliday, G. S. 1971. Dynamic shear cracks with friction as models for shallow focus earthquakes. *Geophys. J.* 25:261–83
Burridge, R., Knopoff, L. 1964. Body force equivalents for seismic dislocations. *Bull. Seismol. Soc. Am.* 54:1875–88
Canales, L. 1975. *Inversion of realistic fault models*. PhD thesis. Stanford Univ., Stanford, Calif.
Carter, N. L. 1976. Steady state flow of rocks. *Rev. Geophys. Space Phys.* 14:301–60
Chinnery, M. A. 1961. The deformation of the ground around surface faults. *Bull. Seismol. Soc. Am.* 51:355–72
Chinnery, M. A. 1963. The stress changes that accompany strike slip faulting. *Bull. Seismol. Soc. Am.* 53:921–32
Chinnery, M. A. 1964. The strength of the earth's crust under horizontal shear stress. *J. Geophys. Res.* 69:2085–89
Chinnery, M. A. 1965. The vertical displacements associated with transcurrent faulting. *J. Geophys. Res.* 70:4627–32
Chinnery, M. A. 1967. Theoretical fault models. In *A Symposium on Processes in the Focal Region*, ed. K. Kasahara, A. E. Stevens, pp. 211–23. Ottawa: Dominion Astrophys. Obs.
Chinnery, M. A. 1970. Earthquake displacement fields. In *Earthquake Displacement Fields and the Rotation of the Earth*, ed. L. Mansinha et al, pp. 17–38. Dordrecht: Reidel. 308 pp.
Chinnery, M. A., Jovanovich, D. B. 1972. Effect of earth layering on earthquake displacement fields. *Bull. Seismol. Soc. Am.* 62:1629–39
Chinnery, M. A., Petrak, J. A. 1967. The dislocation fault model with a variable discontinuity. *Tectonophysics* 5:513–29
Christensen, R. M. 1971. *Theory of Viscoelasticity*. New York: Academic. 245 pp.
Claerbout, J. F. 1976. *Fundamentals of Geophysical Data Processing*. New York: McGraw-Hill. 274 pp.
Dieterich, J. H. 1974. Earthquake mechanisms and modeling. *Ann. Rev. Earth Planet. Sci.* 2:275–301
Dieterich, J. H. 1979a. Modeling of rock friction, 1, experimental results and constitutive equations. *J. Geophys. Res.* 84:2161–68
Dieterich, J. H. 1979b. Modeling of rock friction, 2, simulation of preseismic slip. *J. Geophys. Res.* 84:2169–76
Dunbar, W. S. 1977. *The determination of fault models from geodetic data*. PhD thesis. Stanford Univ., Stanford, Calif.
Eaton, J. P., Lee, W. H. K., Pakiser, L. C. 1970a. Use of microearthquakes in the study of the mechanics of earthquake generation along the San Andreas fault in central California. *Tectonophysics* 9:259–82
Eaton, J. P., O'Neill, M. E., Murdock, J. N. 1970b. Aftershocks of the 1966 Parkfield-Cholame, California, earthquake: a detailed study. *Bull. Seismol. Soc. Am.* 60:1151–97
Elsasser, W. M. 1969. Convection and stress propagation in the upper mantle. In *The Application of Modern Physics to the Earth and Planetary Interiors*, ed. S. K. Runcorn, pp. 223–45. New York: Wiley
Elsasser, W. M. 1971. Two-layer model of upper-mantle circulation. *J. Geophys. Res.* 76:4744–53
Engelder, J. T., Logan, J. M., Handin, J. 1975. The sliding characteristics of sandstone on quartz fault-gouge. *Pure Appl. Geophys.* 113:69–86
Erdelyi, A., Magnus, W., Oberhettinger, F., Tricomi, F. G. 1954. *Tables of Integral Transforms, vol. 2*. New York: McGraw-Hill. 451 pp.
Eshelby, J. D. 1957. The determination of the elastic field of an ellipsoidal inclusion and related problems. *Proc. R. Soc. London Ser. A* 241:376–96
Fitch, T., Scholz, C. H. 1971. Mechanism of underthrusting in southwest Japan: a model of convergent plate interactions. *J. Geophys. Res.* 80:1444–47
Forsyth, D. W. 1979. Lithospheric flexure. *Rev. Geophys. Space Phys.* 17:1109–14

Freund, L. B. 1979. The mechanics of dynamic shear crack propagation. *J. Geophys. Res.* 84:2199–2209
Fung, Y. C. 1965. *Foundations of Solid Mechanics*. Englewood Cliffs, NJ: Prentice-Hall. 525 pp.
Gordon, R. B. 1965. Diffusion creep in the earth's mantle. *J. Geophys. Res.* 70:2413–18
Goulty, N. R., Gilman, R. 1978. Repeated creep events on the San Andreas fault near Parkfield, California, recorded by a strainmeter array. *J. Geophys. Res.* 83:5415–19
Hadley, D., Kanamori, H. 1977. Seismic structures of the Transverse Ranges, California. *GSA Bull.* 88:1469–78
Hanks, T. C. 1971. The Kuril trench-Hokkaido rise system: Large shallow earthquakes and simple models of deformation. *Geophys. J. R. Astron. Soc.* 23:173–89
Heard, H. C. 1976. Comparison of the flow properties of rocks at crustal condition. *Philos. Trans. R. Soc. London Ser. A* 283:173–89
Hill, D. P. 1977. A model for earthquake swarms. *J. Geophys. Res.* 82:1347–52
Jackson, D. D., Anderson, D. L. 1970. Physical mechanisms of seismic wave attenuation. *Rev. Geophys. Space Phys.* 8:1–63
Kanamori, H. 1973. Mode of strain release associated with major earthquakes in Japan. *Ann. Rev. Earth Planet. Sci.* 1:213–39
Kanamori, H., Anderson, D. L. 1975. Amplitude of the earth's free oscillations and long period characteristics of the earthquake source. *J. Geophys. Res.* 80:1075–78
Kanamori, H., Cipar, J. 1974. Focal processes of the great Chilean earthquake. *Phys. Earth Planet. Inter.* 9:128–36
Kanamori, H., Press, F. 1970. How thick is the lithosphere? *Nature* 226:330–31
Kasahara, K. 1957. The nature of seismic origins as inferred from seismological and geodetic observations (1). *Bull. Earthquake Res. Inst. Tokyo Univ.* 35:473–532
Kasahara, K. 1958. Physical conditions of earthquake faults as deduced from geodetic data. *Bull. Earthquake Res. Inst. Tokyo Univ.* 36:455–64
Ke, T. S. 1947. Experimental evidence of the viscous behavior of grain boundaries in metals. *Phys. Rev.* 71:533
King, C.-Y., Nason, R. D., Tocher, D. 1973. Kinematics of fault creep. *Philos. Trans. R. Soc. London Ser. A* 274:355–60
King, N. E., Savage, J. C., Lisowski, M., Prescott, W. H. 1980. Preseismic and coseismic deformation associated with the Coyote Lake, California, earthquake. *J. Geophys. Res.* In press
Kirby, S. H. 1977. State of stress in the lithosphere: inferences from the flow laws of olivine. *Pure Appl. Geophys.* 115:245–58
Knopoff, L. 1958. The energy release in earthquakes. *Geophys. J.* 1:44–52
Lachenbruch, A. H., Sass, J. H. 1973. Thermo-mechanical aspects of the San Andreas Fault system. In *Proc. Conf. Tectonic Problems of the San Andreas Fault System*, ed. R. L. Kovach, A. Nur, pp. 192–205. Stanford, Calif: Stanford Univ. Publications
Langbein, J. O. 1980. An interpretation of episodic slip on the Calaveras fault near Hollister, California. *J. Geophys. Res.* In press
Lensen, G. 1970. Elastic and non-elastic surface deformation in New Zealand. *Bull. N.Z. Soc. Earthquake Eng.* 3:131–43
Le Pichon, X., Francheteau, J., Bonnin, J. 1973. *Plate Tectonics*. New York: Elsevier. 300 pp.
Logan, J. M. 1979. Brittle phenomena. *Rev. Geophys. Space Phys.* 17:1121–31
Logan, J. M., Shimamoto, T. 1976. The influence of calcite gouge on the frictional sliding of Tennessee sandstone (abstract). *EOS, Trans. Am. Geophys. Union* 57:1011
Love, A. E. H. 1944. *A Treatise on the Mathematical Theory of Elasticity*. New York: Dover. 643 pp.
Madariaga, R. 1979. On the relation between seismic moment and stress drop in the presence of stress and strength heterogeneity. *J. Geophys. Res.* 84:2243–50
Mahrer, K. 1978. *Strike slip faulting, models for deformation in a nonuniform crust*. PhD thesis. Stanford Univ., Stanford, Calif. 190 pp.
Mahrer, K. D., Nur, A. 1979. Strike slip faulting in a downward varying crust. *J. Geophys. Res.* 84:2296–2302
Maruyama, T. 1964. Statical elastic dislocations in an infinite and semi-infinite medium. *Bull. Earthquake Res. Inst. Tokyo Univ.* 42:289–368
Matuzawa, T. 1964. *Study of Earthquakes*. Tokyo: Uno Shoten
Mavko, G. 1977. *Time dependent fault mechanics and wave propagation in rocks*. PhD thesis. Stanford Univ., Stanford, Calif.
Mavko, G. 1978. Large scale quasi-static fault models. In *Proc. Conf. III Fault Mechanics and Its Relation to Earthquake Prediction*, ed. J. F. Evernden, pp. 339–412. Menlo Park, Calif: US Geol. Surv.
Mavko, G. M. 1980. The influence of

local moderate earthquakes on creep rate near Hollister, California, *Earthquake Notes* 50:71

Mavko, G., Nur, A. 1975. Melt squirt in the asthenosphere. *J. Geophys. Res.* 80:1444–47

Mavko, G., Nur, A. 1978. The effect of non-elliptical cracks on the compressibility of rocks. *J. Geophys. Res.* 83: 4459–68

Mavko, G. M., Nur, A. 1979. Wave attenuation in partially saturated rocks. *Geophysics* 44:161–78

McConnell, R. K. 1968. Viscosity of the mantle from relaxation time spectra of isostatic adjustment. *J. Geophys. Res.* 73:7089–7105

McGarr, A., Pollard, D., Gay, N. C., Ortlepp, W. D. 1979. Observations and analysis of structures in exhumed mines. In *Proc. Conf. VIII Analysis of Actual Fault Zones in Bedrock*, ed. J. F. Evernden, pp. 101–20. Menlo Park, Calif.: US Geol. Surv. 594 pp.

Melosh, H. J. 1976. Nonlinear stress propagation in the earth's upper mantle. *J. Geophys. Res.* 81:5621–32

Melosh, H. J. 1977. Shear stress on the base of a lithospheric plate. *Pure Appl. Geophys.* 115:429–39

Melosh, H. J. 1978a. Reply. *J. Geophys. Res.* 83:5009–10

Melosh, H. J. 1978b. Dynamic support of the outer rise. *Geophys. Res. Lett.* 5:321–24

Mescherikov, J. A. 1968. Recent crustal movements in seismic regions: geodetic and geomorphic data. *Tectonophysics* 6:29–39

Mindlin, R. D., Cheng, D. H. 1950. Nuclei of strain in the semi-infinite solid. *J. Applied Phys.* 21:926–30

Muskhelishvili, N. I. 1953. *Some Basic Problems of the Mathematical Theory of Elasticity*. Groningen, Holland: Noordhoff. 704 pp.

Nakamura, K., Tsuneishi, Y. 1967. Ground cracks at Matsushiro probably of strike-slip fault origin. *Bull. Earthquake Res. Inst. Univ. Tokyo.* 45:417–72

Nason, R. D. 1973. Fault creep and earthquakes on the San Andreas Fault. In *Proc. Conf. Tectonic Problems of the San Andreas Fault System*, ed. R. L. Kovach, A. Nur, pp. 275–3895. Stanford, Calif.: Stanford Univ. Publications

Nason, R., Weertman, J. 1973. A dislocation theory analysis of fault creep events. *J. Geophys. Res.* 78:7745–51

Nur, A. 1973. Role of pore fluids in faulting. *Philos. Trans. R. Soc. London Ser. A.* 274:297–304

Nur, A. 1978. Nonuniform friction as a basis for earthquake mechanics. *Pure Appl. Geophys.* 116:964–91

Nur, A., Booker, J. R. 1972. Aftershocks caused by pore fluid flow? *Science* 175:885–87

Nur, A., Mavko, G. 1974. Postseismic viscoelastic rebound. *Science* 183:204–6

O'Connell, R. J., Budiansky, B. 1977. Viscoelastic properties of fluid-saturated cracked solids. *J. Geophys. Res.* 82:5719–35

Petrak, J. A. 1965. *Some theoretical implications of strike-slip faulting*. M.A. thesis. Univ. British Columbia, Vancouver, B.C.

Pfluke, J. H. 1978. Slow earthquakes and very slow earthquakes. In *Proc. Conf. III Fault Mechanics and Its Relation to Earthquake Prediction*, ed. J. F. Evernden, pp. 447–468. Menlo Park, Calif: US Geol. Surv.

Post, R., Griggs, D. 1973. The earth's mantle: evidence of non-Newtonian flow. *Science* 181:1242–44

Prescott, W. H., Lisowski, M. 1977. Deformation at Middleton Island, Alaska, during the decade after the Alaska earthquake of 1964. *Bull. Seismol. Soc. Am.* 66:1013–16

Prescott, W. J., Lisowski, M. 1980. Vertical deformation at Middleton Island *Earthquake Notes* 50:72 (Abstr.)

Press, F. 1965. Displacements, strains, and tilts at teleseismic distances. *J. Geophys. Res.* 70:2395–2412

Reid, H. F. 1910. The mechanics of the earthquake. In *The California Earthquake of April 18, 1906. Rep. State Earthquake Invest. Comm.* Washington, DC: Carnegie Inst.

Rudnicki, J. W. 1980. Fracture mechanics applied to the earth's crust. *Ann. Rev. Earth Planet. Sci.* 8:489–525

Rundle, J. B., Jackson, D. D. 1977. A viscoelastic relaxation model for post-seismic deformation from the San Francisco earthquake of 1960. *Pure Appl. Geophys.* 115:401–11

Rybicki, K. 1971. The elastic residual field of a very long strike-slip fault in the presence of a discontinuity. *Bull. Seismol. Soc. Am.* 61:79–92

Rybicki, K., Kasahara, K. 1977. A strike-slip fault in a laterally inhomogeneous medium. *Tectonophysics* 42:127–38

Sacks, I. S., Suyehiro, S., Linde, A. T., Snoke, J. A. 1977. The existence of slow earthquakes and the redistribution of stress in seismically active regions. *EOS, Trans. Am. Geophys. Union.* 58:437

Savage, J. C. 1975. Comment on "An analysis of strain accumulation on a strike

slip fault" by D. L. Turcotte and D. A. Spence. *J. Geophys. Res.* 80:4111–14
Savage, J. C. 1978. Comment on "Strain accumulation and release mechanism of the 1906 San Francisco earthquake" by W. Thatcher. *J. Geophys. Res.* 83:5487–89
Savage, J. C., Burford, R. O. 1970. Accumulation of tectonic strain in California. *Bull. Seismol. Soc. Am.* 60:1877–96
Savage, J. C., Hastie, L. M. 1966. Surface deformation associated with dip-slip faulting. *J. Geophys. Res.* 71:4897–4904
Savage, J. C., Prescott, W. H. 1978a. Asthenospheric readjustment and the earthquake cycle. *J. Geophys. Res.* 83:3369–76
Savage, J. C., Prescott, W. H. 1978b. Comment on "Nonlinear stress propagation in the earth's upper mantle" by H. J. Melosh. *J. Geophys. Res.* 83:5005–8
Savage, J. C., Prescott, W. H., Lisowski, M., King, N. 1979. Geodolite measurements of deformation near Hollister, California, 1971–1978. *J. Geophys. Res.* 84:7599–7615
Scholz, C. H. 1972. Crustal movements in tectonic areas. *Tectonophysics* 14:201–17
Scholz, C. H., Kato, T. 1978. The behavior of a convergent plate boundary: crustal deformation in the South Kanto district, Japan. *J. Geophys. Res.* 83:783–97
Scholz, C. H., Sykes, L. R., Aggarwal, Y. P. 1973. Earthquake prediction: a physical basis. *Science* 181:803–10
Scholz, C. H., Wyss, M., Smith, S. W. 1969. Seismic and aseismic slip on the San Andreas fault. *J. Geophys. Res.* 74:2049–69
Segall, P., Pollard, D. D. 1980. Mechanics of discontinuous faults. *J. Geophys. Res.* 85:4337–50
Shimazaki, K. 1974. Preseismic crustal deformation caused by an underthrusting oceanic plate, in eastern Hokkaido, Japan. *Phys. Earth Planet. Inter.* 8:148–57
Smith, A. T. 1974. Time-dependent strain accumulation and release at island arcs. *EOS, Trans. Am. Geophys. Union* 55:427
Smith, A. T. 1980. *Final Technical Report: Earthquake risk analysis using numerical and stochastic models of time-dependent strain fields.* Santa Cruz, Calif: Univ. Calif.
Smith, S. W., Wyss, M. 1968. Displacement on the San Andreas fault initiated by the 1966 Parkfield earthquake. *Bull. Seismol. Soc. Am.* 58:1955–74
Sneddon, I. N., Lowengrub, M. 1969. *Crack Problems in the Classical Theory of Elasticity.* New York: Wiley. 221 pp.
Spence, D. A., Turcotte, D. L. 1976. An elastostatic model of stress accumulation on the San Andreas fault. *Proc. R. Soc. London Ser. A* 349:319–41
Spence, D. A., Turcotte, D. L. 1979. Viscoelastic relaxation of cyclic displacements on the San Andreas fault. *Proc. R. Soc. London Ser. A* 365:121–44
Starr, A. T. 1928. Slip in a crystal and rupture in a solid due to shear. *Proc. Camb. Philos. Soc.* 24:489–500
Steketee, J. A. 1958a. On Volterra's dislocations in a semi-infinite medium. *Can. J. Phys.* 36:192–204
Steketee, J. A. 1958b. Some geophysical applications of the elasticity theory of dislocations. *Can. J. Phys.* 36:1168–97
Stesky, R. M. 1974. Steady-state creep law for frictional sliding at high temperature and pressure. *EOS, Trans. Am. Geophys. Union* 55:428
Stuart, W. D. 1978. Review of theories for earthquake instabilities. In *Proc. Conf. III Fault Mechanics and Its Relation to Earthquake Prediction*, ed. J. F. Evernden, pp. 541–88. Menlo Park, Calif: US Geol. Surv.
Stuart, W. D. 1979. Quasi-static earthquake mechanics. *Rev. Geophys. Space Phys.* 17:1115–20
Stuart, W. D., Mavko, G. M. 1979. Earthquake instability on a strike-slip fault. *J. Geophys. Res.* 84:2153–60
Summers, R., Byerlee, J. D. 1977. A note on the effect of fault gouge composition on the stability of frictional sliding. *Int. J. Rock Mech. Min. Sci.* 14:155–60
Thatcher, W. 1975. Strain accumulation and release mechanism of the 1906 San Francisco earthquake. *J. Geophys. Res.* 80:4862–72
Thatcher, W. 1978. Reply. *J. Geophys. Res.* 83:5490–92
Thatcher, W. 1979. Crustal movements and earthquake-related deformation. *Rev. Geophys. Space Phys.* 17:1403–10
Thatcher, W., Matsuda, T., Kato, T., Rundle, J. B. 1980. Lithospheric loading by the 1896 Riku-U earthquake, northern Japan: implications for plate flexure and asthenospheric rheology. *J. Geophys. Res.* In press
Thatcher, W., Rundle, J. B. 1979. A model for the earthquake cycle in the underthrust zones. *J. Geophys. Res.* 84:5540–56
Tullis, J. A. 1979. High temperature deformation of rocks and minerals. *Rev. Geophys. Space Phys.* 17:1137–54
Turcotte, D. L. 1977. Stress accumulation and release on the San Andreas fault. *Pure Appl. Geophys.* 115:413–25
Turcotte, D. L., Spence, D. A. 1975. Reply to comments by J. C. Savage, *J. Geophys. Res.* 80:4115

US Geological Survey. 1980. *Professional Paper, The Imperial Valley Earthquake of October 15, 1979*. Menlo Park, Calif: US Geol. Surv.

Walcott, R. I. 1973. Structure of the earth from glacio-isostatic rebound. *Ann. Rev. Earth Planet. Sci.* 1:15–37

Wallace, R. E. 1973. Surface fracture patterns along the San Andreas fault. In *Proc. Conf. Tectonic Problems of the San Andreas Fault System*, ed. R. L. Kovach, A. Nur. Stanford Univ. Publications

Walsh, J. B. 1969. A new analysis of attenuation in partially melted rock. *J. Geophys. Res.* 74:4333

Watts, A. B. 1978. An analysis of isostasy in the world's oceans, 1, Hawaiian-Emperor seamount chain. *J. Geophys. Res.* 83: 5989–6004

Watts, A. B., Talwani, M. 1974. Gravity anomalies seaward of deep sea trenches and their tectonic implications. *Geophys. J.R. Astron. Soc.* 36:57–90

Weertman, J. 1964. Continuum distribution of dislocations on faults with finite friction. *Bull. Seismol. Soc. Am.* 54:1035–58

Weertman, J. 1965. Relationship between displacements on a free surface and the stress on a fault. *Bull. Seismol. Soc. Am.* 55:945–53

Weertman, J. 1978. Creep laws for the mantle of the earth. *Philos. Trans. R. Soc. London Ser. A* 288:9–26

Weertman, J., Weertman, J. R. 1964. *Elementary Dislocation Theory*. London: Macmillan. 213 pp.

Weertman, J., Weertman, J. R. 1975. High temperature creep of rock and mantle viscosity. *Ann. Rev. Earth Planet. Sci.* 3:293–315

Wyss, M., Brune, J. N. 1968. Seismic moment, stress, and source dimensions in the California-Nevada region. *J. Geophys. Res.* 73:4681–94

Zener, C. 1948. *Elasticity and Anelasticity of Metals*. Chicago: Univ. of Chicago Press. 170 pp.

SUBJ
MNG
MPSD

THE MECHANICS OF PRE-SPLITTING

P.N. WORSEY, I.W. FARMER,

Department of Mining Engineering, N

Proceedings of the 22nd U.S. Symposium on Rock Mechanics: Rock Mechanics from Research to Application held at Mass. Inst. of Tech., June 28-July 2, 1981 compiled by H.H. Einstein

INTRODUCTION

Pre-split blasting is a technique used to reduce damage to excavation profiles during blasting by pre-forming a continuous fracture between parallel boreholes lightly charged with decoupled explosives along the line of the required surface. Various theories and hypotheses have been presented to explain the phenomenom of pre-split blasting (see for instance Aso, 1966; Carrasco and Saperstein, 1977; Griffin, 1973 and Kutter, 1967) but no totally satisfactory explanation of the mechanics of fracture formation and extension has been provided.

Most previous approaches (Aso, 1966; Griffin, 1973 and Paine, 1961) have tended to concentrate on the mathematics of interaction between stress waves from adjacent sources. Interaction of stresses induced by expanding gases following detonation has been considered of minor importance. However, decoupling introduced during pre-splitting is specifically designed to reduce dynamic effects and to emphasize rock stresses resulting from expansion of detonation products. It could indeed be argued that the phenomenom has more in common with hydrofracture than with the conventional use of high explosives.

MECHANICS OF PRE-SPLITTING

Energy release and transfer to the rock body from an explosive detonating in a borehole in rock is a complex process, being affected partly by the relative impedances of the explosive and rock and the efficiency of the coupling, and partly by the pressures exerted by expanding gases in the borehole. It is useful to differentiate between these two aspects of the process by describing them as the dynamic and quasi-static components of energy release.

The dynamic component comprises initially a plastic headwave, decaying rapidly to form a radially expanding compression wave. The energy in the wave, its shape and velocity are related to the explosive energy and the degree of coupling of the explosive and rock and their relative impedances. The initial high energy in the wave is dissipated by local crushing at the borehole periphery and/or limited radial cracking parallel to the direction of maximum compression. According to Carrasco and Saperstein (1977) these cracks are initiated near to but not at the hole surface. Since the wave velocity is approximately three times the maximum crack propagation velocity (Edgeston and Barstow, 1941), extension of cracks by wave action is minimal and intact rocks generally have a high resistance to transient compression. The main effect of the wave is in loosening discontinuities in the rock through tensile reflection at interfaces which cross the wave path.

As the headwave leaves the zone of the borehole, the borehole itself is pressurised by the build up of the gases which are a byproduct of the rapid combustion characterised by detonation. These exert a high quasi-static pressure on the borehole sidewall. The effect of this pressure is to induce compressive radial and, more important, tensile tangential stresses around the borehole which effectively open the existing limited length cracks produced by the dynamic wave. This results in two effects:

(a) The opening of the crack surfaces on/or near the borehole circumference will induce tensile stresses at the tips of the cracks, creating conditions for crack extension.

(b) Gases of detonation migrating into the opened cracks will cause further crack extension.

Various explanations of the processes involved in crack propagation are available in the literature on hydrofracturing, (see for instance Perkins and Krech, 1966; 1968; Sneddon, 1946; Wong and Farmer, 1973). The principal conclusion is that very high pressures are required to propagate cracks. In the case of detonation gases however, these pressures exist. Initially, the increasing pressure within a crack will result in an increase in the extent of the stress altered region around the crack, maintaining it in a state of elastic stability. However, beyond a critical pressure the system will become unstable and the crack will extend radially until further extension of the stress altered region leads to a return to stability, thus limiting further extension. The differential work in extending cracks is the product of the volume of the cracks created and the pressure increment. This energy is partly stored as reversible strain energy and partly absorbed in creating new crack surfaces.

The preferred direction of crack propagation if a line of boreholes exists will be that in which cracks can be most easily opened and into which the high pressure detonation gases can most easily penetrate. It is evident that the greatest tendency for crack opening will occur where tangential tensile stress zones overlap between neighbouring pressurised boreholes. It is equally evident that less favourable conditions will exist for opening of cracks normal to the borehole line. Where cracks from neighbouring boreholes intersect, a continuous fracture will be formed and subsequently opened, releasing pressure and inhibiting further crack extension except at its extremities.

The interaction of the individual stress fields around boreholes within a pre-split panel will cause the radial crack zones to expand in a slightly elliptical shape with the major axes orientated along the pre-split line. If a discontinuity is present between the holes then the first crack to reach the discontinuity will tend to create a path for further reduction of gas pressure, inhibiting further crack extension. Due to the geometry involved the crack should intersect the discontinuity at approximately 90°. If the discontinuity is closed a stress 'bulb' will be formed on the opposite side, cracks from the adjacent borehole will be induced to extend and curve to that point. If the discontinuity is open the crack will terminate.

UNIVERSITY OF UTAH
RESEARCH INSTITUTE
EARTH SCIENCE LAB.

where R = radial depth of crack zone

d = borehole diameter

For series (a) A = 45.7, B = +0.589

and for series (b) A = 26.9, B = +0.702

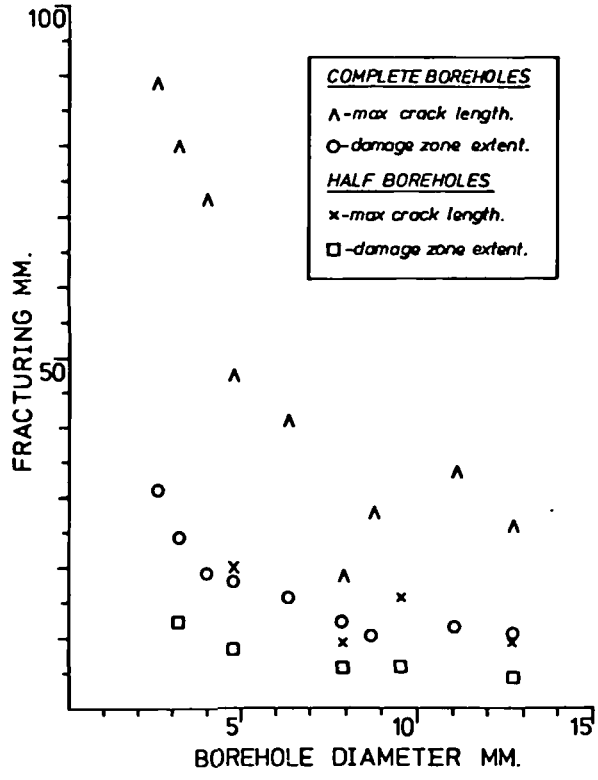

FIGURE 2. Graph of maximum crack length and damage zone extent for single normal series (a), and vented series (b), hole tests.

Since the value of B for series (b) tests is of a greater magnitude than for series (a) tests it is evident that increasing decoupling has a greater reduction on the dynamic component than the quasi-static component. Together the tests in series (a) and (b) demonstrate that for single holes, whilst the dynamic component may be responsible for crack initiation, the quasi-static gas component is the dominant mechanism in crack extension.

The main results of series (c) testing are summarised in Figure 3, which illustrates the maximum successful pre-split borehole separation obtained for various degrees of decoupling, expressed as borehole diameter, for single explosive cord. The relationship obtained was again exponential and was calculated as:

$$d = 372b^{-0.9}$$

where: d = borehole diameter (mm)

and b = maximum borehole separation (mm)

Generally the maximum successful pre-split borehole separation in series (c) was found to be approximately double the maximum crack length from series (a) tests on corresponding borehole diameters.

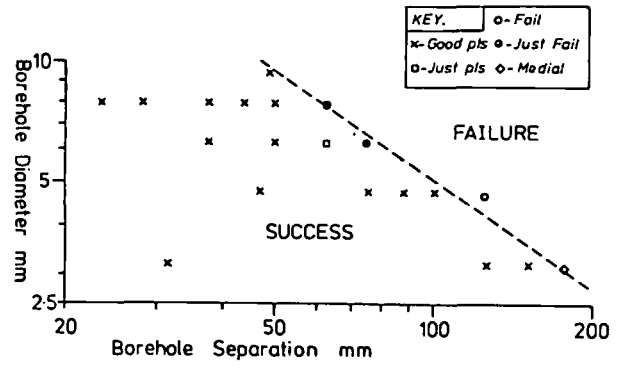

FIGURE 3. Graph of the relationship obtained in series (c) testing between borehole diameter and maximum borehole separation for pre-split (p/s) success.

FIGURE 4. A comparison of the maximum pre-split borehole separations for dynamic component (left) and dynamic plus gas pressure component of explosive energy (right) for 3.2 mm (0.125 in) holes.

The crack geometry dictates that during pre-split blasting the degree of irregularity of the final face is dependant on the discontinuity set orientation. The results show that at a discontinuity intersection angle of less than 60°, irregularities in the pre-split line become marked and if decreased to 15°, a high degree of overbreak will be sustained behind the line of boreholes (see Figure 6). Similar results were obtained for the tests in sandstone but only open cracks were visible.

From series (f) results it was found that dominant cracks are able to cross successive parallel discontinuities, as in Figure 7, but were observed to terminate at the discontinuity located immediately before the next borehole (except for discontinuity intersection angles below 20°). With increasing crack frequency, secondary cracking became less pronounced. Overbreak volume increased with the change from single to multiple discontinuities and with increasing discontinuity frequency up to four discontinuities per borehole spacing where tailing off occurred.

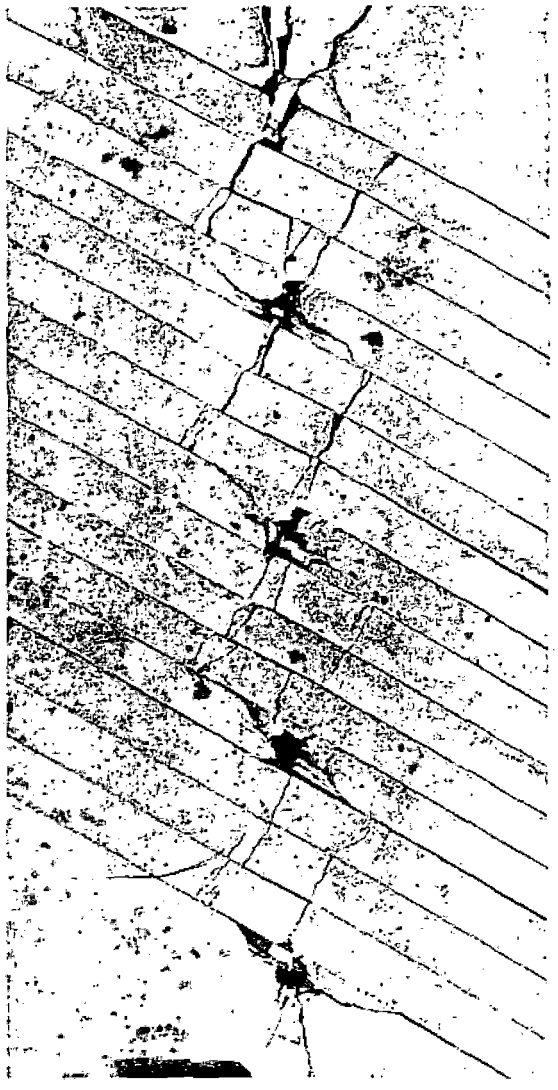

FIGURE 7. Pre-split in sandstone with multiple parallel discontinuities. Illustrating the propagation of dominant fracturing across and perpendicular to successive discontinuities.

FIELD OBSERVATIONS

Early field observations confirmed the trends from Phase I tests but the majority of field work was aimed at examining the effect of geotechnical factors on pre-splitting.

Pre-splitting at various highway construction sites in Scotland (both successful and unsuccessful) in dolerites, basalts, gneisses and schists was visited over the complete spectrum of constructional stages. In addition, various quarries in limestone and sandstone, utilising the technique for the stabilisation of production faces and protection of haul roads, were visited.

Initial discontinuity surveys were made to assess the overall 'intrinsic' stability of the rock mass at the various sites, particularly as affected by major faults and shears. This was followed by an assessment of how individual jointing affected the pre-split face by recording orientations of natural and imposed discontinuities.

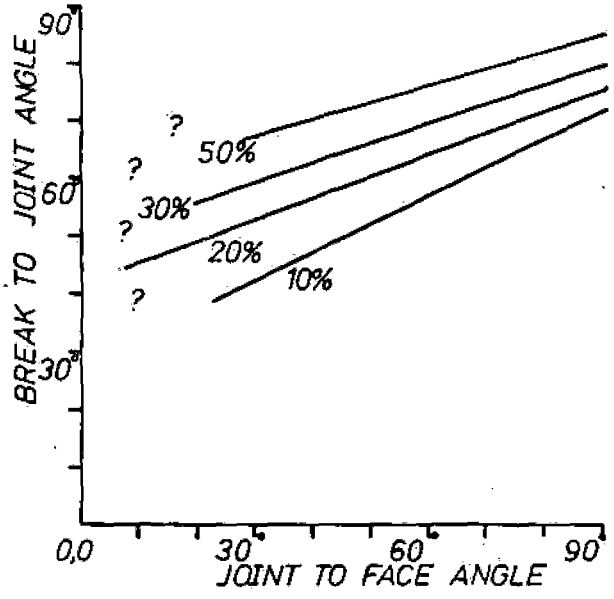

FIGURE 8. Graph of percentage occurrence of a total of 453 sets of fracturing to discontinuity field readings. Illustrating that the majority of fracturing is (sub)perpendicular to jointing. The fanning out of data for lower joint to face angles is attributed to secondary fracturing, and the absence of data below 20° to failure of pre-split.

From field observations it was concluded that if the face was intrinsically unstable either through a tendency to plane or wedge failure or toppling, pre-splitting did not lead to any improvement. Of more fundamental importance, it was shown that the tendency noted in the laboratory for fractures to spread in a direction normal to the direction of discontinuities was repeated. This is illustrated in Figure 8. Curved secondary fractures were also found to be present. This dictated that where continuous discontinuity planes and the pre-split line met at an angle of less than 60° irregularities in the pre-split line became marked. When this angle was decreased to

15°, pre-split blasting was observed to have had no beneficial effect on the resulting slope profile. Field examples of a failure to pre-split due to the presence of medium and large scale near vertical discontinuities at less than 15° to the intended face and a particularly successful pre-split are illustrated in Figure 9.

FIGURE 9. Top: successful pre-splitting with the predominant discontinuity set orientated perpendicular to the face.

Bottom: unsuccessful pre-splitting and high overbreak due to the major joint set being within 15° of the face.

CONCLUSIONS

(a) Although the initiation of cracking around a borehole is generally caused by the dynamic headwave, the majority of cracking is caused exclusively by the quasi-static gas pressure component of explosive energy.

(b) Pre-splitting is primarily caused by the interaction of the tangential tensile stresses induced in the rock by quasi-static gas pressure components from neighbouring boreholes.

(c) A pre-split may be obtained by using the dynamic component only of explosive energy, but the maximum borehole separation for this is less than 1/5th of maximum separation utilising gas pressures.

(d) Pre-split fractures intersect discontinuities in the rock at right angles.

(e) The first crack to reach a discontinuity tends to become dominant, inhibiting further crack propagation.

(f) Dominant cracks may cross successive discontinuities at right angles forming irregular breaks between neighbouring boreholes.

(g) The presence of discontinuities at less than 60° to the proposed pre-split line tends to cause poor line definition. If the angle is less than 15°, pre-split blasting has no effect on slope profiles.

REFERENCES

ASO, K., 1966, Phenomena involved in Pre-splitting by Blasting, PhD. Thesis, Stanford University.

CARRASCO, L.G., and SAPERSTEIN, L.W., 1977 Surface Morphology of Pre-split Fractures in Plexiglass Models, International Journal of Rock Mechanics, Vol 14, pp 261-275.

EDGESTON, H.E., and BARSTOW, F.E., 1941, Further studies of Glass Fracture with high speed photography, Journal of the American Ceramic Society, Vol.24 pp 131-137.

GRIFFIN, K.G., 1973 Mathematical theory to Pre-solit Blasting, Proceedings of the 11th Engineering Geology and Soils Engineering Symposium, Idaho, pp 217-225.

KUTTER, H., 1967, The interaction between Stress Wave and Gas Pressure .. with particular application to Pre-splitting, PhD. Thesis, University of Minnesota.

PAINE, R.S., et al, 1961, Controlling overbreak by Pre-splitting. International Symposium on Mining Research, Missouri School of Mining and Metallurgy, Chap. 13, pp 1-9.

PERKINS, T.K., and KRETCH, W.W., 1968, The energy balance concept of Hydraulic Fracturing, Journal of the Society of Petroleum Engineers, Vol 8, pp 1-12.

SNEDDON, I.N., 1946, The distribution of Stress in the neighbourhood of a crack in an Elastic Solid, Proceedings of the Royal Society A, Vol 187, 229.

WONG, H.Y., and FARMER, I.W., 1973, Hydrofracture mechanisms in rock during pressure grouting. Rock Mechanics, Vol 5, pp 21-41.

ACKNOWLEDGEMENTS

This work was carried out under a joint SRC/TRRL CASE studentship held by Paul N. Worsey. It is published with the permission of the Director, Transport & Road Research Laboratory (TRRL), United Kingdom.

SUBJ-
MNG
MRAI

UNIVERSITY OF UTAH
RESEARCH INSTITUTE
EARTH SCIENCE LAB.

A Method for Removing Ammonium Ions From a Subterranean Formation After In-Situ Uranium Leaching

T.Y. Yan, Mobil Research and Development Corp.

Summary

Ammonium carbonate and bicarbonate are the preferred carbonate sources in alkaline in-situ leaching of uranium. The ammonium ion exchanges into the clay in the formation and is difficult to remove during restoration operations. A new process is proposed which holds the potential for rapid and effective reduction of ammonia in the formation and groundwater to acceptably low levels. The process employs pH-adjusted, chlorinated water to decompose the ammonia quantitatively. The operation involves flushing the formation with connate water or brine, injecting chlorinated water, and finally flushing with connate water. This process is effective in laboratory tests.

Introduction

In-situ leaching, or solution mining, is now emerging as a viable technique for recovering uranium from some low-grade ore bodies.[1,2] As a result, several pilot and commercial in-situ leaching plants are in operation in south Texas – e.g., Mobil Oil Corp., Intercontinental Energy Corp., Wyoming Minerals Corp., Union Carbide Corp., and U.S. Steel Corp.

Leaching systems are classified conveniently as either acidic or alkaline. For sandstone ores containing substantial quantities of carbonates, alkaline leaching is preferred. The alkaline leach solutions contain an oxidant (H_2O_2, $NaClO_3$, or O_2) and a mixture of carbonates. Ammonium carbonates have been the most popular source of carbonates. This type of leaching formulation has been used sucessfully in south Texas.

Since the ore bodies generally contain up to 20% or more of cationic exchangeable clays, the NH_4^+ in the leach solution exchanges with the cations in the clay according to the following equations.

$$Na \cdot clay + NH_4^+ \rightleftharpoons NH_4 \cdot clay + Na^+ .$$

$$Ca \cdot clay + 2NH_4^+ \rightleftharpoons (NH_4)_2 clay + Ca^{++} .$$

The selectivity of clays for NH_4^+ is high, and the NH_4^+ ion exchange capacity of the ore may become quite high depending on the overall clay content. A typical NH_4^+ ion exchange isotherm is presented in Fig. 1, which shows, for example, that for a leach solution containing 10g/L of NH_4HCO_3, the equilibrium concentration of NH_4^+ on the ore is 0.14 meq/g, equivalent to an NH_3 concentration of 0.24% of NH_3 in the ore body. At the conclusion of the leach operation, the formation is contaminated with this great quantity of NH_4^+ ion. If not removed, the NH_4^+ ion will release slowly by exchanging with the incoming cations in the aquifer, resulting in pollution of the groundwater.

Government regulations require that water in the leached formation be restored substantially to its original quality. Furthermore, the current Texas Dept. of Water Resources permit procedures require groundwater restoration be completed immediately upon completion of mining of the site.[3] Although baseline levels for NH_3 are not set yet, levels in the 10-ppm range have been suggested. Since the ammonia is exchanged into the clays chemically, it cannot be flushed out readily and requires counter ions, such as Na^+ or Ca^{++}, for removal by ion exchange. Furthermore, the ion exchange equilibrium limitation makes the restoration of the desired low level difficult and time consuming.

To speed up the restoration process, a restoration fluid with high salt content of NaCl or $CaCl_2$ can be used. To speed up the restoration process further, a

0149-2136/0005-9491$00.25
Copyright 1981 Society of Petroleum Engineers of AIME

restoration fluid comprising an aqueous solution of a strong soluble alkaline compound, such as NaOH, can be used.[4] However, while these approaches work well for some ore bodies, they require a substantial quantity of chemicals and produce a large quantity of waste water containing ammonia which has to be disposed of properly at the surface. Furthermore, in some instances the use of caustic solution as the restoration fluid may require the addition of a salt such as sodium chloride[5] to prevent clay swelling and, hence, resultant loss in formation permeability.

In this paper, a technique is presented which holds the potential for rapid and effective removal of ammonium ion from the formation during groundwater restoration.

Technique

The proposed technique for removing ammonium ions comprises the following three steps.[6]

1. Flush the leached formation with connate water to remove ammonia and other dissolved solids from the pores.
2. Inject the required amount of chlorine water or hypochlorite solution at pH of 8 to 10. The produced water is made up with chlorine or hypochlorite for recycle.
3. Flush the formation to lower the total dissolved solids to the desired level.

In the following sections, the theoretical basis of the process, the reactions involved, and the mechanism of ammonium ion removal are discussed and confirming laboratory experiments are described.

Reactions of Ammonia With Chlorine and Hypochlorite

The equilibria between NH_4^+ in the clay and other cations such as Na^+ in the formation or restoration fluid are represented by

$$NH_4 \cdot clay + Na^+ \rightleftharpoons Na \cdot clay + NH_4^+, \quad \ldots\ldots (1)$$

or

$$(NH_4)_2 \cdot clay + Ca^{++} \rightleftharpoons Ca \cdot clay + 2NH_4^+ \ldots (2)$$

In turn, the NH_4^+ ion is in equilibrium with NH_3:

$$NH_4^+ + OH^- \rightleftharpoons NH_3 + H_2O. \quad \ldots\ldots\ldots\ldots (3)$$

As the pH of the system is increased, Eq. 3 is shifted toward the right to form more NH_3 and decrease NH_4^+. This, in turn, shifts Eqs. 1 and 2 toward the right to facilitate NH_4^+ removal from the clay. The NH_3 in the formation then is reacted with chlorine or hypochlorite.

These reactions are of great importance in water treatment. Chlorination of drinking water for disinfection is used widely by many municipalities. However, the reactions are not well understood. The reactions are presumed to proceed in the following sequence.[7,8]

$$Cl_2 + H_2O \rightleftharpoons H^+ + Cl^- + HOCl. \quad \ldots\ldots\ldots (4)$$

$$NH_3 + HOCl \rightleftharpoons NH_2Cl + H_2O. \quad \ldots\ldots\ldots\ldots (5)$$

$$NH_2CL + HOCl \rightleftharpoons NHCl_2 + H_2O. \quad \ldots\ldots\ldots (6)$$

$$NHCl_2 + HOCl \rightleftharpoons NCl_3 + H_2O. \quad \ldots\ldots\ldots\ldots (7)$$

$$2NCl_3 - 3Cl_2 + N_2. \quad \ldots\ldots\ldots\ldots\ldots\ldots (8)$$

The Cl_2 reacts with water to form hypochlorite, with which NH_3 starts to react. The overall reaction between NH_3 and chlorine can be written as follows.

$$2NH_3 + 3Cl_2 - 6H^+ + 6Cl^- + N_2\uparrow. \quad \ldots\ldots\ldots (9)$$

Note that Eqs. 4 through 7 are reversible, while the decomposition reaction (Eq. 8) is irreversible, leading to the possibility of complete removal of NH_3 without equilibrium limitation. The approximate equilibrium constants for the preceding reactions have been presented by Drago.[9]

Studies of the rates of decomposition of the chloramines have shown that, depending on the pH and the reaction step, the second-order rate constants at 25°C are high and in the range of 10 to 10^4 $L \cdot mol^{-1} \cdot s^{-1}$.[10,11] Preliminary results from this laboratory showed that the reaction between hypochlorite and ammonia and ammonium ions in both aqueous solution or on clay can be completed in less than 10 minutes. The contact time between the restoration fluid and ammonium-containing formation (or number of days to pump through 1 PV of fluid) is typically 2 to 4 weeks. Therefore, reaction between hypochlorite and ammonia and the decomposition reaction of chloramines can be considered instantaneous in the time scale for groundwater restoration operations.

Alternatively, the NH_4^+ may react directly with hypochlorite to form nitrogen and chloride ion.

As pointed out, the last reaction in the sequence involving ammonia and chlorine or hypochlorite is irreversible, making it possible to carry the overall reaction to completion. This is one of the most important features of this process. When caustic or lime water is used to remove ammonia, the process is limited by the equilibrium described and by the law of mass action. This makes restoration of groundwater to acceptable ammonia levels extremely difficult. Based on the ion exchange isotherm in Fig. 1, we have estimated that 99.5% of the NH_4^+ ion in the clay has to be exchanged with other cations such as Ca^{++} or Na^+ to restore the ammonia in the groundwater to a stable level of 3 ppm or lower.

In summary, chlorine water or hypochlorite injected into the formation would react with ammonia in equilibrium with the ammonium clay through a series of reactions to form harmless nitrogen gas. The reactions are fast enough to be considered instantaneous. The overall reaction is irreversible and makes complete removal of ammonium ion possible.

Experimental

The efficiency of chlorinated water as a restoration fluid was studied in laboratory column tests using 1-cm-ID, 30-cm-long glass columns packed uniformly with 18 cm^3 (23.4 g) of the uranium ore. The top and the bottom of the columns were filled with 3 cm^3 each of 100-200 mesh fine quartz to ensure uniform flow of the liquid through the bed. The uranium ore

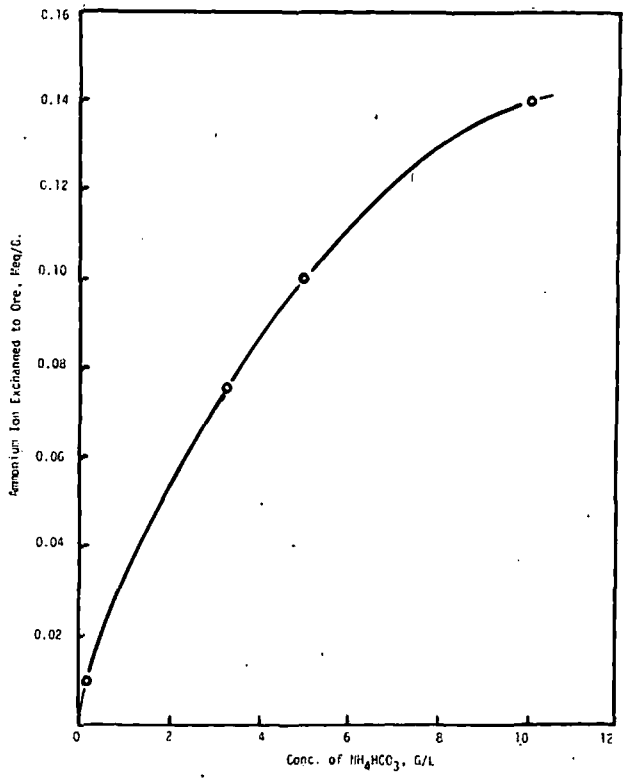

Fig. 1 – Exchange isotherm of ammonium ion on ore.

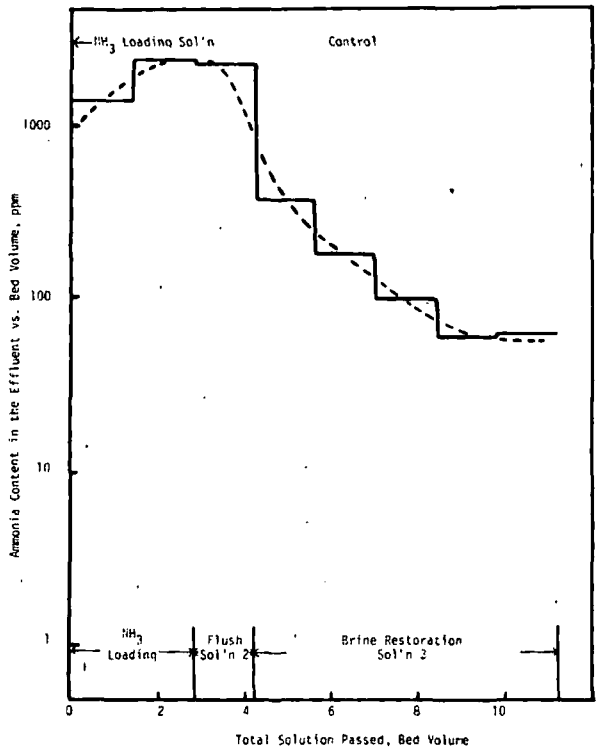

Fig. 2 – Ammonia content in the effluent vs. bed volume.

was obtained from the Catahoula formation of the Texas coastal plain. The clay content was about 20 wt%, mainly in the form of smectite (montmorillonite). Its ion exchange capacity for NH_4^+ was 0.15 meq/g.

The solutions used were prepared by adding CP-grade chemicals to distilled water. Chlorinated water was prepared by saturating the solutions with chlorine gas at 1 atm. The composition of the various solutions used are shown in Table 1. The final pH of the solution was adjusted to the level indicated.

The packed columns first were loaded with NH_4^+ ion by pumping 2.8 bed volumes of Solution 1 (Table 1) to simulate the leaching operation. In this experiment, 1 bed volume of solution is.18 cm^3. At the end of this loading step, the ore was saturated with ammonia as indicated by the ammonia concentration of the effluent, which was equal to that of the feed, Solution 1 (Fig. 1). The loaded columns then were flushed with 1.4 bed volumes of flushing Solution 2 (Table 1), which simulates the connate water normally present in the natural formation.

The columns thus prepared were restored as follows.

Col. 1. The control column was flushed with 7 bed volumes of restoration fluid, Solution 3 (Table 1).

Col. 2. The column was flushed continuously with 5.6 bed volumes of chlorinated water, Solution 4.

Col. 3. To simulate slug injection, 2.8 bed volumes of the chlorinated water, Solution 4, were injected. This was followed by injection of 2.8 bed volumes of chlorine-free restoration fluid, Solution 3.

To facilitate direct comparison of its efficacy for ammonia removal with the conventional high-brine flushing, the chlorinated water (Solution 4) was prepared by adding chlorine to the high-brine restoration fluid (Solution 3). In the proposed scheme the formation water, rather than the high-brine solution, will be used in preparing chlorinated water.

The process of NH_4^+ removal was followed by collecting samples of the effluent every 1.4 bed

TABLE 1 – COMPOSITION OF SOLUTIONS USED

Component	Solution 1,* Ore Pretreating	Solution 2, Flushing	Solution 3, Restoration	Solution 4, Chlorination
NaCl, g/L	5.0	5.0	20	20
NH_4HCO_3, g/L	3.0	–	–	–
NH_4OH, g/L	5.8	–	–	–
Cl_2, g/L	–	–	–	6.3**
pH†	9.4	8.0	10.0	10.0

*NH_3 content was 2,670 ppm by analysis.
**Based on chlorine solubility.[12]
†pH adjusted.

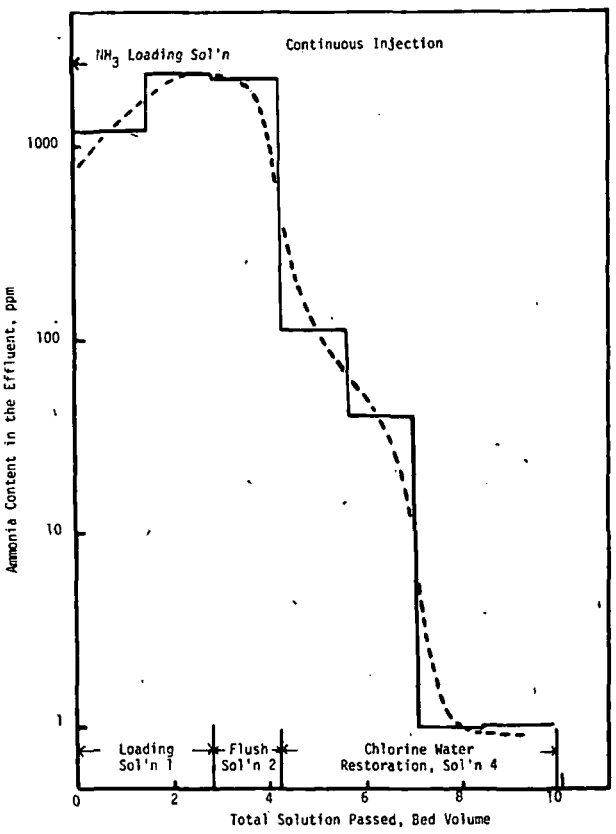

Fig. 3 – Ammonia content in the effluent vs. bed volume.

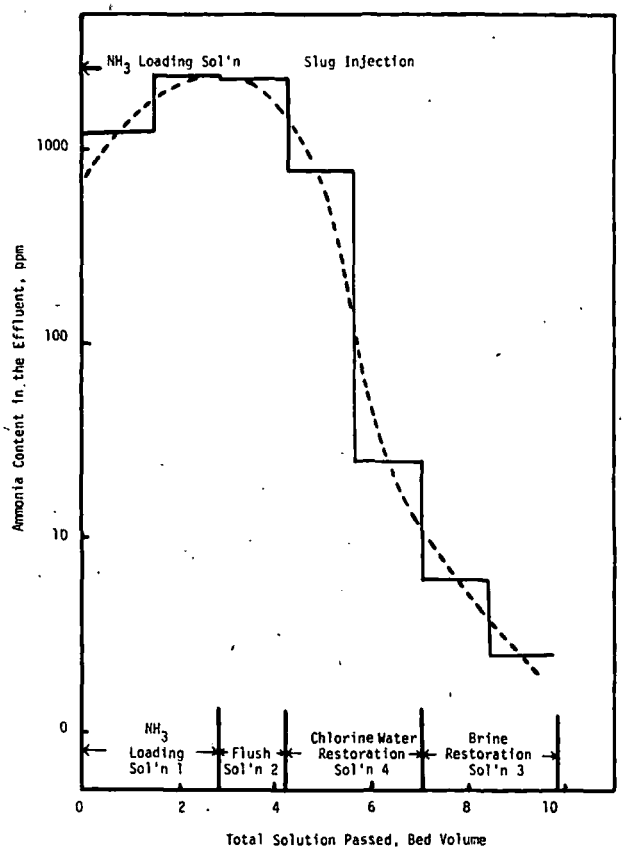

Fig. 4 – Ammonia content in the effluent vs. bed volume.

volumes and analyzing for NH_3. Ammonia was determined using an ammonia electrode. This method is acceptable to U.S. federal and state agencies for analysis of ammonia in water. Note that in this test, both free NH_3 and NH_4^+ ion in the solution are included in the determination.

Results and Discussion

The results are shown in Figs. 2, 3, and 4 by plotting the ammonia content of the effluents against the total bed volumes of restoration fluid passed through a respective column.

Efficacy of Chlorine Water for Removing Ammonia

A comparison of Figs. 3 and 4 with Fig. 2 shows that chlorine was effective in lowering ammonia. In addition, it takes small quantities (in terms of bed volumes) of chlorine water to achieve levels of ammonia removal. In the continuous mode, 3 bed volumes of chlorinated water brought the ammonia level in Col. 2 from 2,600 ppm down to the target level of 3 ppm, while the ammonia content of the effluent from the control run was still 130 ppm after 3 bed volumes. Furthermore, the rate of ammonia removal fell off rapidly in the control run, suggesting the difficulty of ammonia removal to a low level in accord with the rationale described previously.

Mode of Chlorine Water Injection

In Col. 3, the chlorine water was injected as a slug. After 1.4 bed volumes of flushing fluid, 2.8 bed volumes of the chlorinated water were injected, followed by 2.8 bed volumes of chlorine-free restoration fluid (Solution 3). The ammonia content of the effluent was down to the target value of 3 ppm after a total 4.6 bed volumes were passed. Thus, it may be feasible to inject chlorine water in the form of a slug to reduce operation costs.

Mechanism of Ammonia Removal

To remove ammonium ions from the clay and to reduce the ammonia in the produced water, there are two mechanisms: (1) cationic exchange between ammonium ion in the clay and cations (e.g., Na^+) in the groundwater and (2) decomposition of ammonia with chlorine or hypochlorite. In a column test or field operation, both of these mechanisms are operative. During the early stages of restoration, the injected chlorine reacts rapidly with the ammonia. The chlorine-depleted restoration fluid continues to move downstream and continues to remove ammonium ion by cationic exchange. The ammonia released from the clay is produced in the effluent. However, as more chlorinated water is injected, there is more chlorine to react with ammonia, resulting in very low levels of ammonia in the effluent. In the early stage of restoration when ammonia level is high, a large quantity of ammonia can be removed by flushing with connate water and ion exchange with chlorine-free brine solution. To minimize con-

sumption of chlorine, the formation can be flushed with connate water and ion exchanged with brine solution before injecting chlorinated water.

The reaction rate between ammonia and hypochlorite is high, as suggested by the preliminary results mentioned. There was no breakthrough of hypochlorite while there was any detectable ammonia in the effluent.

Chlorine Requirement

The chlorine requirement for this restoration process depends on three factors: the amount of ammonium ion in the formation when the chlorine water injection is started, the stoichiometry of the reaction between ammonia and chlorine, and the selectivity of chlorine for ammonia. As a result, the chlorine requirement is rather ore specific.

If the reaction sequence shown is correct and the selectivity for NH_3 is unity, it takes 1.5 mol of Cl_2 to decompose 1 mol of NH_3 (Eq. 9) corresponding to 6.3 lbm of Cl_2 per 1 lbm of NH_3. In actual field operation, it may take somewhat more chlorine to compensate for side reactions.

Although the column data in this study are not exact enough to determine the chlorine consumption, an estimate was made by means of ammonia and chlorine balances. For this estimation, the following assumptions were made.

1. The ammonium ion content in the formation after connate water flushing is 0.14 meq/g, as expected from the ion exchange isotherm.
2. The ammonium ion either is produced in the effluent or is decomposed by chlorine.
3. Chlorine content in the formation up to 2.8 bed volumes of injection is nil.

The results are 6.0 and 8.4 lbm of chlorine per 1 lbm of NH_3 for the continuous and slug injection model, respectively (Table 2). The difference in the chlorine consumption between these two runs is relatively large, but this is believed to be within the expected limits of experimental accuracy.

Note that the crude chlorine consumptions are not too far from the theoretical value of 6.3 lbm per 1 lbm of NH_3. Therefore, it is most likely that the chlorine would react selectively and quantitatively with ammonia underground, and the stoichiometry based on the reaction sequence described is a good guide to estimate chlorine consumption.

There are compounds in the ore body which can be oxidized by hypochlorite, such as pyrite, molybdenum, and organic carbon. These reducing compounds can compete with NH_3 for hypochlorite to increase the chlorine requirement. Fortunately, the selectivity of dilute chlorine water for NH_3 is very high, as indicated by the results shown. Furthermore, when this process is applied to leached ore bodies, most of easily oxidizable compounds such as molybdenun and pyrite in the flowing channels already will have been oxidized.

In a series of separate experiments, it was found that after flushing the columns for 10 days with 5 PV of dilute chlorinated water, the NH_3 content of the effluent was reaching very low levels but no sulfate ion could be detected. Complete oxidation of pyrite would have led to sulfate ion. Sulfate ion did break through after 7 PV when the NH_3 essentially was exhausted. These results suggest that much of the chlorine injected to the formation could travel through the formation to react with NH_3.

TABLE 2 – CHLORINE CONSUMPTION

	Col. 2, Continuous Injection	Col. 3, Slug Injection
Initial NH_4^+ in formation as NH_3, 10^{-2} g	5.69	5.69
NH_3 produced,* 10^{-2} g	0.46	1.94
NH_3 decomposed, 10^{-2} g	5.23	3.75
Chlorine injected, 10^{-2} g	31.5	31.5
Chlorine consumption, g/g	6.0	8.4

*During the 2.8 bed volumes of chlorine water injection.

Conclusions

Ammonium carbonate and bicarbonate are favored as the source of carbonate for alkaline in-situ leaching of uranium. Upon completion of the leaching operation, the formation and groundwater have to be restored to near the baseline quality levels. Ammonia is difficult to remove in this restoration process, and current restoration procedures are either difficult to employ due to formation permeability loss or require many pore volumes of restoration fluid. A process is proposed which has the potential for rapid and effective reduction of ammonia in the groundwater to very low levels,

The restoration process involves three steps: (1) flushing the formation with formation water or brine, (2) injecting pH-adjusted chlorinated water or hypochlorite and producing an equal amount of water at the production well, and (3) again flushing the formation with connate water.

The process is effective in laboratory column tests, where less than 3 bed volumes are required to lower the ammonia level from 2,700 to 3 ppm, but has not been tested in the field. The chlorinated water can be injected continuously or in the form of slug, as long as sufficient chlorine is injected. In the absence of other reducing compounds in the formation, the chlorine consumption is estimated to be about 6 lbm per 1 lbm of NH_3. To minimize chlorine consumption, restoration can be started with connate water flushing and brine ion exchange to remove the initial, easily removed ammonia.

References

1. Borkert, J.J. and Gerity, C.E.: "The Economics of In Situ Mining Versus Open Pit Mining," paper presented at the South Texas Uranium Seminar, Corpus Christi, TX, Sept. 10-13, 1978.
2. Phillips, P.E.: "A Comparison of Open Pit and In Situ Leach Economics," *Proc.*, First Conference on Uranium Mining Technology, Y.S. Kim (ed.), U. of Nevada, Reno (1977).
3. Whitlington, D. and Taylor, W.R.: "Regulations and Restoration of In Situ Uranium Mining in Texas," paper presented at the South Texas Uranium Seminar, Corpus Christi, TX, Sept. 10-13, 1978.

4. Snavely, E.S. and Singleton, H.P.: "Method of Treating to Remove Ammonium Ions," U.S. Patent No. 4,079,783 (March 21, 1978).
5. Foster, W.R. and Snavely, E.S.: "Method of Treating Formation to Remove Ammonium Ions Without Decreasing Permeability," U.S. Patent No. 4,114,963 (Sept. 19, 1978).
6. Yan, T.Y.: "Method of Treating Formation to Remove Ammonium Ions," U.S. Patent No. 4,162,707 (July 31, 1979).
7. Weil, I. and Morris, J.C.: "Kinetic Studies of Chloramines. I. The Rates of Formation of Monochloramine, N-Chlormethylamine and N-Chlordimethylamine," *J. Am. Chem. Soc.* (May 1949) 71, 1664-1671.
8. Morris, J.C.: "Application: Kinetics of Reactions Between Chlorine and Phenolic Compounds," *Principles and Applications of Water Chemistry*, S.D. Faust and J.V. Hunter (eds.), John Wiley and Sons Inc., New York City (1967) 23-51.
9. Drago, R.S.: "Chloramine," *J. Chem. Ed.* (Nov. 1957) **34**, 541-544.
10. Patton, C.J. and Croch, S.R.: "Spectrophotometric and Kinetics Investigation of the Berthelot Reaction for the Determination of Ammonia," *Anal. Chem.* (March 1977) **49**, 464-469.
11. Kleinberg, J., Tecotzky, M., and Audrieth, L.F.: "Absorption Spectrum of Aqueous Monochloramine Solutions," *Anal. Chem.* (Aug. 1954) **26**, 1388-1389.
12. Seidel, A.: *Solubilities of Inorganic and Metal Organic Compounds*, W.F. Linke (ed.), D. Van Nostrand Co., New York City (1958).

SI Metric Conversion Factors

atm	×	1.013 250*	E+02	= kPa
°F		(°F−32)/1.8		= °C
L	×	1		= dm^3
lbm	×	4.535 924	E−01	= kg

*Conversion factor is exact.

JPT

Original manuscript received in Society of Petroleum Engineers office May 20, 1980. Paper accepted for publication Feb. 18, 1981. Revised manuscript received March 23, 1981. Paper (SPE 9491) first presented at the SPE 55th Annual Technical Conference and Exhibition, held in Dallas, Sept. 23-26, 1980.

SUBJ
MNG
MSDP

Minerals Separation Devises Process for Mixed Copper Ores

UNIVERSITY OF UTAH
RESEARCH INSTITUTE
EARTH SCIENCE LAB.

Tests in London Demonstrate Success of Preheating With Carbon and Salt, Followed by Flotation, With Prospect of Commercial Application to Northern Rhodesian Practice

OWEN LETCHER

SULPHIDE copper ores predominate in Northern Rhodesia, but large quantities of malachite and of chrysocolla exist, as well as admixtures of these ores with sulphide ores, the treatment of which was expected to entail considerable difficulty. All the copper mines in Northern Rhodesia have such mixed ores. N'Changa, for example, possesses large tonnages of carbonates, silicates, and mixed ores. To solve the problem of the economic and efficient treatment of the mixed ores, Minerals Separation has been engaged for three years in the development of a treatment process. It is known as the "Segregation Process." It consists of a heat-treatment of the ore at 600 to 700 deg. C. with 1 to 2 per cent carbon (charcoal, coal, or coke) and less than 0.5 per cent common salt. Instead of the usual chloridizing effect, an alternative reaction occurs. The copper leaves the gangue almost entirely, even particles of copper silicate ore up to 2 mm., and deposits as metal on the carbon, with which it forms segregations of varying size that are readily amenable to flotation.

At the experimental plant of Minerals Separation in London, tests have been made on ore from Northern Rhodesia and elsewhere, indicating an extraction of 95 per cent from oxidized ores and of 92 per cent from mixed ores. The installation consists of an ore feeder and two revolving cylinders, the preheaters, the reaction furnace, and a cooling cylinder, revolving at 1 r.p.m. Treatment comprises dry crushing to about 2 mm., segregation, and flotation of the segregated ore. Smelting and refining of the metallic copper obtained would follow in the normal course.

Crushed ore is fed into the preheater and then passes into the reaction cylinder, where it is mixed with the salt and carbon. The temperature of the furnaces is maintained at about 650 deg. C. The product from the reaction chamber is passed through the cooling cylinder, and then goes to flotation machines for treatment by ordinary methods. Copper separates out as finely divided particles of metal. The concentrate from the flotation machines, when examined under the microscope, revealed the presence of the fine metallic grains in association with small quantities of carbon and a negligible amount of quartz gangue. A pilot plant, in accordance with these principles of treatment, will probably be designed and sent to N'Changa Copper in the near future.

Other News of the Week

THE United States Senate, on Nov. 7, put manganese back on the tariff bill with a duty of 1c. a pound on metallic manganese ores and concentrates containing more than 10 per cent manganese. On this page.

* * *

Inspiration Consolidated has completed important changes in its power plant, near Miami, Ariz., giving it a total capacity of 30,000 kw. Page 787.

* * *

Broken Hill South will be able to dismantle the old wooden structures at its concentrator in the Broken Hill district, New South Wales, by the end of the month, as the new steel building is almost complete. Page 787.

* * *

With higher copper prices prevailing, the Bingham district of Utah is enjoying its most prosperous and productive year. Notes on progress at this important Western camp. Page 788.

* * *

Grootvlei, adjoining East Geduld on the Far East section of the Witwatersrand, Transvaal, will probably be developed through the latter's workings. Page 791.

* * *

Between the 2,000 and 3,000 levels of Teck-Hughes, at Kirkland Lake, Ont., development has disclosed a continuation of its rich gold orebodies as favorable as in the levels above, according to the company's annual report. Page 790.

Senate Puts Manganese Back on Tariff Bill

AFTER more than five hours of debate, during which the net profits of eight steel companies in six years of operation under the Fordney-McCumber tariff were disclosed, the United States Senate voted 60 to 18, on Nov. 7, to restore a duty of 1c. a pound on the metallic manganese content of manganese ores and concentrates.

The Senate not only rejected the Finance Committee amendment placing manganese ores on the free list, but it extended the duty to low-grade ores containing between 10 and 30 per cent of metallic manganese. Under the House bill and existing law, manganese ores containing less than 30 per cent of metallic manganese were entered free.

The Senate's action on manganese corresponded to that first taken by the Finance Committee majority before this group, in writing the tariff bill (H. R. 2667), reversed itself and placed manganese on the free list.

In the course of debates on manganese, Senator Ashurst, of Arizona, read into the record the profits of eight steel companies in the years since enactment of the 1922 tariff law through 1928. These net profits, he said, aggregated $930,181,054.

The manganese amendment adopted by the Senate was presented by Senator Oddie, of Nevada, chairman of the Committee on Mines and Mining. As originally introduced, Mr. Oddie's proposal would have put a graduated rate on manganese ores dependent upon the metallic manganese content. All manganese ores containing 25 per cent of metallic manganese or more, the bulk of the imported product, would have been taxed at 1½c. a pound. Senator Oddie later modified his amendment to the form in which it was adopted.

On Nov. 2, the Senate rejected a committee amendment making the duty 5 per cent ad valorem on amorphous graphite. It is now 10 per cent and was unchanged by the House. It also adopted an amendment offered by Senator Black, of Alabama, to make the duty on crystalline graphite 2c. a pound. The Finance Committee recommended that the duty be 20 per cent ad valorem, as at present. The House bill increased the rate to 25 per cent.

Barry Hollinger Must Alter Tailing Disposal

Justice T. E. Godson, judge of the Ontario Mining Court, has allowed Barry Hollinger Gold, operating near Kirkland Lake, Ont., ten days within which to submit plans for a new method of handling tailing. The order follows a hearing on the company's application for permission to deposit tailing from its 100-ton plant in a small creek near the mill, which later flows through farming lands.

SUBJ
MNG
MSRF

UNIVERSITY OF UTAH
RESEARCH INSTITUTE
EARTH SCIENCE LAB.

United States Patent [11] 3,630,278

[72] Inventor Harry W. Parker
Bartlesville, Okla.

[21] Appl. No. 773,989
[22] Filed Nov. 7, 1968
[45] Patented Dec. 28, 1971
[73] Assignee Phillips Petroleum Company

[54] METHOD FOR STRENGTHENING RESERVOIR FRACTURES

9 Claims, 1 Drawing Fig.

[52] U.S. Cl. 166/259, 166/247
[51] Int. Cl. E21b 43/24, E21b 43/26
[50] Field of Search 166/247, 256, 259, 261, 271, 302

[56] References Cited
UNITED STATES PATENTS

1,361,282	12/1920	Nolan	166/288
2,771,952	11/1956	Simm	166/288 X
2,780,449	2/1957	Fisher et al.	166/259
2,796,935	6/1957	Bond	166/260
3,072,188	1/1963	Morse	166/288
3,342,257	9/1967	Jacobs et al.	166/247
3,346,044	10/1967	Slusser	166/259 X
3,460,620	8/1969	Parker	166/257
3,468,376	9/1969	Slusser et al.	166/259 X

Primary Examiner—Stephen J. Novosad
Attorney—Young and Quigg

ABSTRACT: Hydrocarbons are produced from hydrocarbon bearing formations, including oil shale, in situ through fractures communicating with production wells by injecting combustion supporting materials such as an oxygen-containing gas substantially completely throughout the fractures and then initiating in situ combustion (supported by the injected gas) at an extremity of the fractures prescribed by either injection or production wells or a subterranean detonation zone or cavity and directing the resultant in situ combustion front along the axis of the fractures and maintaining combustion at a level sufficient to fuse the formation adjacent the fractures whereby the resistance of the fractures to collapse under compressive stress is increased. Collapse of fractures treated in this manner under the influence of formation expansion promoted by subsequent temperature elevation accompanying retorting is substantially retarded. Therefore the strengthened fractures can be employed to facilitate heat transfer throughout the formation.

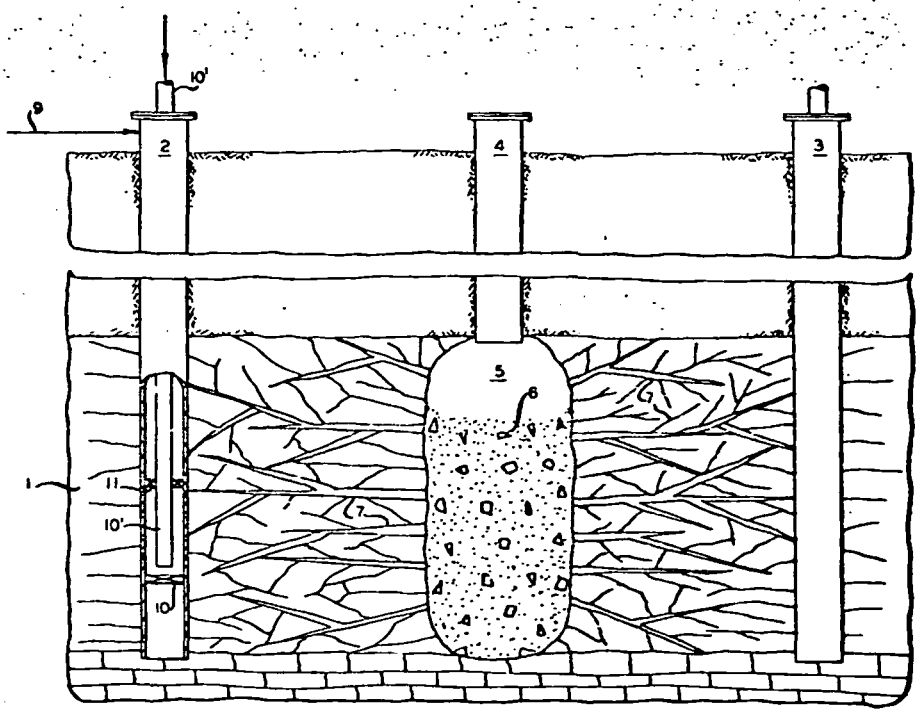

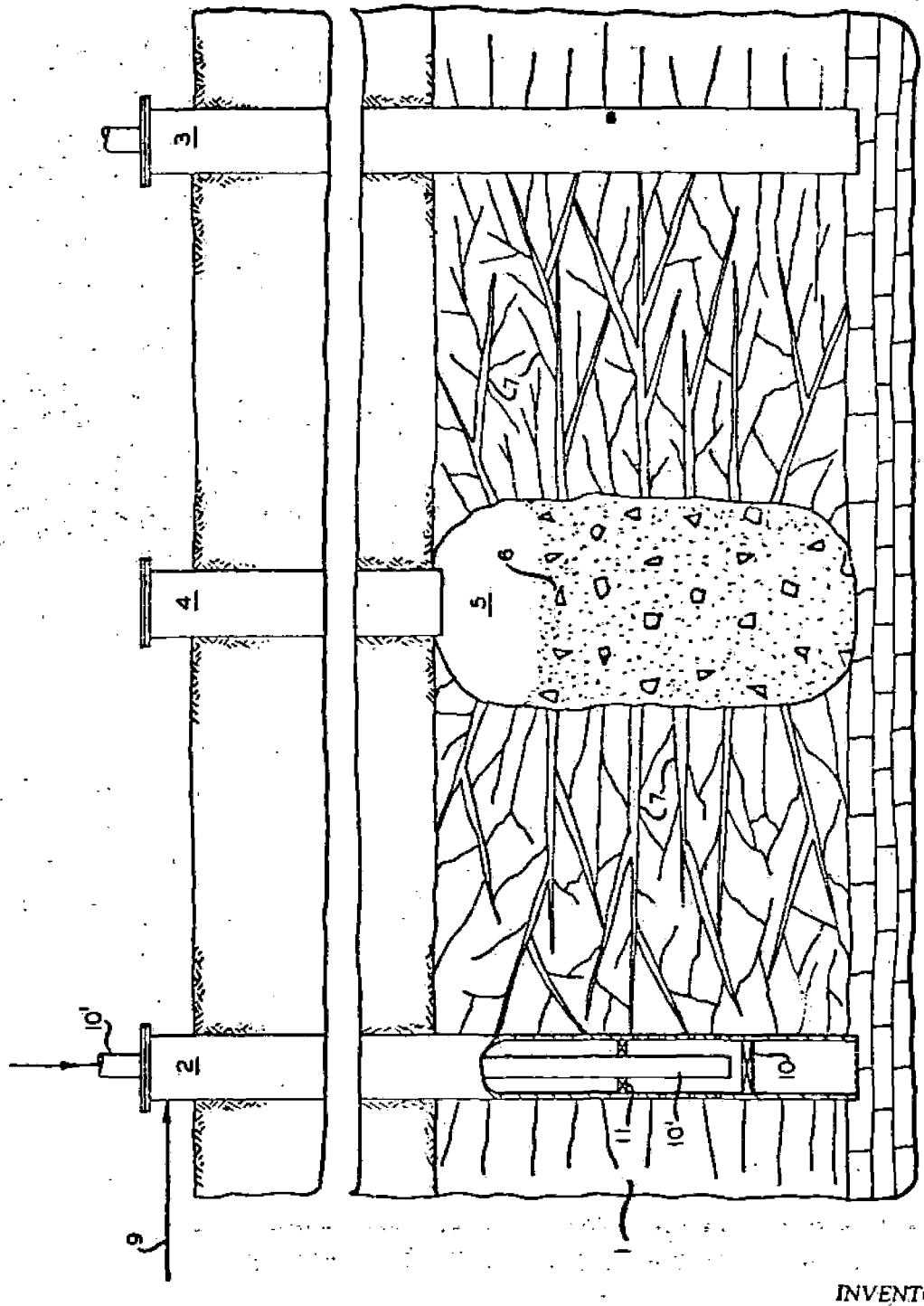

INVENTOR.
H. W. PARKER
BY Young & Quigg
ATTORNEYS

METHOD FOR STRENGTHENING RESERVOIR FRACTURES

BACKGROUND OF THE INVENTION

This invention relates to a process for the in situ production of oil from oil shale by pyrolysis with hot gases. In accordance with another aspect, this invention relates to an improved method of obtaining oil from oil shale around a nuclear produced chimney by burning the fractures therethrough in an oxygen-enriched atmosphere, and thereafter producing the formation by the use of hot inert gases.

Tremendous deposits of oil shales occur in Colorado, Utah, and Wyoming, and various petroleum companies and the federal government are doing research on methods of producing oil from these deposits. Numerous proposals have been made, including mining the shale and retorting the mined shale above ground and applying heat to the shale in situ with hot gases including oxygen and excluding oxygen. Steam, hot combustion gas, hot air, etc. have been proposed as heating media for the pyrolysis operation.

In situ combustion and in situ retorting by either in situ combustion or injection of heat exchange fluid has been the subject of considerable experimental investigation as means for expediting the secondary recovery and have found commercial application in numerous instances. It is recognized that during the course of these secondary recovery procedures the formation strata is subjected to considerable expansion due to temperature elevation. This expansion generally results in the collapse and termination of relatively unstable communication networks, e.g., fractures, throughout the formation with the result that fluid flow to recovery wells and from injection wells is diminished or deterred by an extent necessitating increased driving forces, i.e., differential pressure between input and production wells. It is quite understandable that this collapse also deters natural drainage of hydrocarbons from retorted formation where the hydrocarbon fluids are not subjected to artificial driving forces.

The utilization of such fluid communication channels is particularly attractive in highly fragmented or fractured formations such as those which result from the subterranean detonation of explosive charges. Although the formation rock in the immediate vicinity of the detonation zone or chimney is fragmented sufficiently to enable ready access or egress of fluids, the adjacent formation is fractured to a lesser extent and generally comprises a relatively unstable network of intercommunicating fractures which are either substantially restricted or completely closed by thermal expansion of the adjacent formation under the influence of elevated temperatures necessary to retort those portions of the hydrocarbon bearing strata. Throughout the specification and claims the term hydrocarbon is intended to include not only compounds of carbon and hydrogen, but also other formation organic matter such as the kerogen contained in oil shale from which hydrocarbons and other substances are formed by heat.

The use of nuclear explosives to fragment underground formations has gained considerable acceptance as an economically feasible method of producing oil and gas from reservoirs having such low original permeability as to be incapable of economic production in the original state. The utilization of nuclear explosives in this regard is described briefly by D. B. Lombard in his article "Recovering Oil from Shale with Nuclear Explosives" published in Aug. 1965, issue of *Journal of Petroleum Technology*, pages 877–882.

By this method a nuclear charge is placed at the desired elevation in a suitable reservoir strata and detonated to produce a cavity containing fragmented reservoir rock, the dimensions of the cavity and the extent of fragmentation depending, of course, upon the magnitude of the detonation and the characteristics of the surrounding formations. For example, Lombard refers to the effects of detonating nuclear charges having energies of from 20 to about 100 kilotons in "hard rock" and indicates that the resulting fragmentation zone, i.e., nuclear chimney, has a diameter of from 100 to several hundred feet and a vertical extent of about 2¼ cavity diameters measured from the point of detonation to the chimney top.

It is further pointed out by Lombard that although the fragmentation zone or nuclear chimney is fairly well defined, that the sidewalls, i.e., the remaining unfragmented formation defining the nuclear chimney, possess numerous fractures extending outwardly in all directions from the sidewalls for a distance of approximately one-half of the diameter of the fragmentation zone. These fractures result in a substantial increase in the permeability of the formation surrounding the fragmentation zone which enable the egress of formation fluids from the fragmentation zone and the strata immediately surrounding the nuclear chimney during subsequent retorting operations and correlary procedures involving the use of elevated temperatures and pressures within the fragmented area.

The degree of fracturing and consequently the degree of permeability which results in those strata defining the outer periphery of the fragmentation zone depends primarily on certain characteristics of the formations, per se, and to some extent on the intensity of the detonation.

It is therefore one object of this invention to provide a method for treating fragmentation zones produced by subterranean detonation.

It is another object of this invention to improve the production of reservoir fluids from fragmentation zones resulting from subterranean detonations.

It is yet another object of this invention to provide a method for treating subterranean nuclear chimneys and fractures resulting therefrom.

It is another object of this invention to provide a method for decreasing the permeability of fractures extending and surrounding nuclear chimneys.

It is yet another object of this invention to improve the ultimate recovery of reservoir fluid from strata fragmented by subterranean detonation.

It is another object of this invention to provide a method for utilizing the heat retained in retorted subterranean fragmentation zones.

SUMMARY OF THE INVENTION

In accordance with the invention, the fractures or channels extending outwardly from the periphery of a fragmentation zone are contacted with an oxygen-containing gas under combustion conditions to form slag channels between the fragmentation zone and input and output wells spaced around the periphery of the fractures extending out from the fragmentation zone.

In accordance with one embodiment of this invention, the fractures extending outwardly from a fragmentation zone are contacted by an oxygen-enriched gas injected through wells drilled into the fractures extending outwardly from the fragmentation zone whereby the fractures are burned outwardly by counterflow combustion to form slag channels. Oil is produced from the formation by passing gases through the fragmentation zone to be heated and then through the channels and up the surrounding wells positioned near the periphery of the fractures.

In accordance with a further embodiment of the invention, to prevent bypassing of some of the fractured channels an inert gas can be injected through some of the fracture channels while others are being burned by an oxygen-enriched gas.

More specifically, in the production of oil shale, a nuclear device is detonated at a sufficient depth to produce an upwardly extending chimney containing Kerogen, which can be retorted under known conditions to produce shale oil. This nuclear detonation also produces fractures in the adjacent strata. This strata normally contain as much shale oil as the chimney, but cannot be produced since normal retorting procedures cause the collapse of the strata adjacent the chim-

ney. Thus, according to this invention, a plurality of peripheral wells are placed at the furtherest extremities of the fractures produced by the nuclear explosion, and then an oxygen-enriched gas is injected into the fractures from the injection wells, producing the combustion of the Kerogen contained within the fractures, commencing adjacent the chimney and proceeding back toward the injection wells, and the molten Kerogen produces a slag that, when cooled, forms a fused lining on the interior of the fractures. The strata in between the nuclear chimney and the peripheral injection wells can now be retorted employing normal techniques and the slag-lined fractures form channels for the production of the oil shale, which will not collapse under the retorting conditions.

The cost of breaking oil shale via nuclear explosives can be cut by a factor of 5 to 10 if the shale which is only fractured can be retorted as well as the shale which is reduced to broken rubble in the detonation zones. The present invention provides a method for preparing flow channels in fractured oil shale which will not heal by thermal expansion and thus allow for more efficient production of oil from the use of a single nuclear device.

Although the method herein described affords advantages when applied to all types of hydrocarbon bearing formations in which it is desired to substantially preserve the integrity of fractures and/or channels within the formation strata, it is particularly advantageous when applied to formations which have been extensively fractured by the detonation of explosive charges. For this reason the method is described with relation to the recovery of oil from strata fractured by such a subterranean detonation.

BRIEF DESCRIPTION OF THE DRAWING

The drawing shows a cross section of a hydrocarbon-bearing formation having a nuclear detonation chimney and accompanying injection and production wells.

DESCRIPTION OF THE PREFERRED EMBODIMENTS

Such a formation and accompanying injection and production of wells are illustrated schematically in the drawing wherein hydrocarbon bearing strata 1 is penetrated by wells 2, 3, and 4 is occupied by detonation zone or chimney 5 and outwardly extending fractures 7. Wells 2 and 3 are placed so as to communicate with fractures 7 and thereby indirectly communicate with the nuclear chimney 5 and the intervening strata.

Prior to the treatment of this intervening strata the highly fragmented reservoir rock 6 in nuclear chimney 5 can be retorted by any one of several methods, some of which have already been discussed. For example, the fragmented shale in such chimneys can be retorted by the passage of a flame front from the uppermost portion of the fragmented oil shale downwardly through the entire mass of fragmented rock whereby liberated hydrocarbons flow downwardly through the fragmentation zone and accumulate in the lower extremities thereof. The temperature of the combustion zone is controlled by recycling, for example, 3 to 5 volumes of gas for each volume of air injected. These accumulated hydrocarbons are then preferably produced by means of a production well drilled directionally downwardly and laterally into the lower extremities of the fragmented area. Such production of the accumulated fluids can be accomplished by any conventional means. These methods can be made more efficient by operating at a positive pressure over the accumulated fluid in order to prevent the vaporization thereof by the elevated temperature encountered during shale retorting.

Elevated operating pressures, e.g., 100 to 1,000 p.s.i.a., are desirable in some processes to retort nuclear chimneys such as when hot shale gas is recycled to retort the nuclear chimney to reduce the cost of compressors and wells. One embodiment of the hot shale gas recycle process is described in copending application Ser. No. 641,815. The process of this invention has several advantages when employed in combination with the retorting process described in copending application Ser. No. 639,490 now U.S. Pat. No. 3,490,202: the shale would be preheated and the amount of air necessary to retort the chimney would be reduced.

Following this procedure whereby the fragmented rock 6 within the nuclear chimney is retorted, it is desirable to retort the shale disposed between the outer periphery of the fragmentation zone and the adjacent wells 2 and 3 taking advantage of the fluid communication network defined by the series of fractures 7. However, if the temperature of this adjoining formation is elevated to a point sufficient to retort the formation rock that strata expands due to its thermal coefficient of expansion and plastic deformation characteristics by an amount sufficient to compress and collapse the fractures, thereby destroying the network of fractures from which fluids could otherwise be injected into the formation and through which exuded hydrocarbons could be directed to the production wells 2 and 3. The method of this invention reduces the extent of collapse associated with the elevation of formation temperature by fusing and cooling the fracture sidewalls thereby greatly increasing their resistance to collapse under the influence of compressional forces.

By this procedure an oxidizing material such as air is injected into the fractures through either of the wells 2 or 3 and combustion or formation hydrocarbon is instituted in the formation immediately adjacent the fractures and propagated by the addition of the oxidizing material thereto with the result that the temperature of the formation rock defining the fractures, i.e., the fracture sidewalls, is elevated sufficiently to fuse the same. Following a sufficient degree of burning to accomplish the extent of fusion desired the combustion is terminated by discontinuing the injection of oxidizing gas and the formation sidewalls are allowed to cool to a point below their fusion temperature. It is also preferably to restrict the high temperature fusion zone to the vicinity of the fracture sidewalls. This can be accomplished by judiciously controlling the pressure on the combustion supporting medium at a level sufficient only to force the gas into the fractures and preferably not more than 150 p.s.i. above formation pressure.

In initiating combustion in the strata adjoining the nuclear chimney and in the subsequent retorting of that strata it is desirable to take advantage of the heat stored in the detonation zone by virtue of the previous retorting of that area of the formation. As a result, it is presently preferred to inject the oxidizing material, i.e., air, into injection wells 2 and/or 3 and to force the gas outwardly through the series of fractures 7 to the periphery of the chimney at which point the reservoir is at a temperature sufficient to autoignite the hydrocarbon retained in the strata adjacent the chimney. This temperature should be at least about 600° F. and is usually in the range of from about 750° F. to about 1,000° F. shortly after the termination of retorting procedures employed to produce the hydrocarbon in the chimney 5. Injection of oxidizing gas is continued at a rate sufficient to maintain the in situ combustion of hydrocarbons radially outwardly from the chimney toward the injection well until the burning has progressed to the immediate vicinity of the injection well bore or until the desired degree of fusion along the fracture walls has been achieved.

Air injection rates will, of course, vary considerably depending upon the extent of fracturing and the extent of burning maintained at any given time. However, exemplary of the injection rates that can be employed in such operations are those within the range of about 50,000 to about 100,000 standard cubic feet per hour of atmospheric air. These injection rates are sufficient to maintain a degree of combustion along the fracture of the sidewalls such that the temperature of the sidewalls is elevated to a point above the fusion point of the hydrocarbon-bearing formation. For example, when the formation is oil shale the fracture sidewalls should be elevated to a temperature of at least about 1,400°–2,000° F. to accomplish this purpose. It is also possible by this method to treat selected portions of the fractured strata by sealing off the injection well bore as illustrated in the drawing by means of packers 10 and 11. The oxidizing fluid is then injected by way of pipe 10' to

the space intermediate the packers and consequently enters those fractures which communicate with the well bore in the region defined by the packers. During such selective treatment procedures an inert gas can be injected through pipe 9 to prevent airflow and undesired combustion in these areas. Fluids are produced from well bore 4 as desired to control the pressure in the nuclear chimney.

Following this method of preparation the fractured formation can be retorted to recover hydrocarbons by any one of the numerous retorting procedures known to the art several of which have already been discussed. Retorting temperatures are generally within the range of from about 750° to about 1,000° F. and should, of course, be maintained below the fusion point of the formation strata in order that the structural integrity of the formation and the fluid communication network defined by fractures 7 is not destroyed. Steam or nonoxidizing gas injected for this purpose can be passed into the formation as already described by way of the fractures 7 and is preferably introduced through retorted chimney 5, and through the sidewalls of the detonation zone into the adjoining formation to take advantage of the heat stored in the chimney 5. For example, in one embodiment steam or water can be injected by way of well bore 4 into chimney 5 wherein the heat stored in the chimney is transferred to the injected water after which it is passed to the sidewalls of the chimney into fractures 7 for the purpose of elevating the temperature of the intermediate strata.

It is also possible to retort intermediate strata selectively in a manner analogous to that already described in relation to the preparation of the network of fractures. For example, the heating medium can be injected by well bore 4 through chimney 5 into the adjoining fracture network and passed selectively through the lower portion thereof prescribed by the blocked zone in the well bore 2 defined by the position of packers 10 and 11 by blocking outlet 9. For example, the upper portions of the hydrocarbon bearing strata can be retorted in a first stage by blocking exit 10', whereby the heat exchange medium passes through the upper portions of the reservoir.

After this retorting has been terminated the heat contained in that portion of the reservoir can be employed along with the heat contained in the chimney 5 by injecting steam or water both through well bore 4 and opening pipe 10' and/or whereby the steam from the chimney enters the lower portion of the formation through the nuclear chimney wall, passes through the formation by virtue of the intercommunicating network of fractures 7 and into the area of the well bore 2.

SPECIFIC EXAMPLE

A nuclear chimney is formed by a 200 kiloton bomb at a depth of 3,000 feet in an oil shale formation. The resulting nuclear chimney is 420 feet in diameter and 1,000 feet high. Fractures induced by preparation of the nuclear chimney extend outwardly from the center of the nuclear chimney for a distance of 500 to 600 feet.

The ring of 15 wells is drilled concentric to the nuclear chimney with a radius of 500 feet. The wells are cased and cemented. At intervals of 40 feet starting from a position adjacent the top of the nuclear chimney the casing is perforated or cut and packers set so oxygen can be injected. Oxygen is injected at a rate of 80,000 standard cubic feet per hour. When the oxygen injected into the fractures reaches the hot previously retorted nuclear chimney the adjacent oil shale is ignited and burns very intensely, melting the adjacent shale matrix and enlarging the fracture. The combustion zone burns back to the injection well in 5 to 8 hours, resulting in a flow channel propped with molten shale which has solidified. The flow channels are about 2 inches wide and 5 to 10 feet across. This process of forming flow channels is repeated at each 40-foot interval in each of the 15 wells. As a safety precaution, inert gas is injected into the previously formed flow channels. After the flow channels are formed, the shale adjacent the channels is retorted by injection of hot produced shale gases through the chimney which flow through the propped fractures to the surrounding wells to cause heating of the shale around the propped fractures to produce hydrocarbons. The bottom hole temperature of the surrounding wells is maintained at a temperature in the 300°–400° F. range by regulating the flow of gases therefrom at the surface.

I claim:

1. A method of producing a hydrocarbon-bearing shale formation in situ which comprises fracturing said formation, injecting a combustion supporting material into said fractures and burning at least a portion of said hydrocarbon contained in said formation immediately adjacent said fractures at a rate and for a period of time sufficient to elevate the temperature of said formation adjacent said fractures to at least about 1,400° F. to fuse the sidewalls of said fractures thereby increasing the structural resistance of said fractures to compressive forces, retorting said formation to liberate hydrocarbon therefrom and producing the thus liberated hydrocarbon at least partially through said fractures.

2. The method of claim 1 wherein said combustion-supporting material is an oxygen-containing gas.

3. The method of claim 2 wherein said formation further comprises a subterranean nuclear chimney and accompanying radially outwardly extending fractures in communication with at least one injection well bore, and said oxygen containing gas is injected into said fractures through said injection well and passed through said fractures at least to the periphery of said chimney, igniting said hydrocarbon in said sidewalls of said fractures adjacent said chimney and continuing the passage of said oxygen-containing gas into said fractures to direct said combustion radially outwardly from said chimney and axially along said fractures to said injection well and thereby fusing the walls of said fractures.

4. The method of claim 3 wherein the temperature of said chimney is at least about 600° F. and said hydrocarbons are autoignited by contact with said oxygen-containing gas at said temperature.

5. The method of claim 3 wherein the injection pressure of said gas is up to about 150 p.s.i. above the formation pressure adjacent said fractures.

6. The method of claim 3 wherein said chimney is retorted prior to the injection of said oxygen-containing gas via said injection wells and is at a temperature of from about 750° to about 1,000° F.

7. The method of claim 6 further comprising retorting said formation following said fusing of said fractures.

8. The method of claim 7 wherein said formation is retorted by injecting a heating medium into said formation via said chimney and said fractures.

9. The method of claim 8 wherein said heating medium is steam produced at a temperature of from about 750° to about 1,000° F. by injecting one of steam and water into said detonation zone to heat the same via an injection well communicating with said chimney.

* * * * *

SUBJ
MNG
MSS

MISCELLANEOUS PAPER N-69-2

MINE SHAFT SERIES
EVENTS MINE UNDER AND MINE ORE
EJECTA STUDIES

by

J. W. Meyer
A. D. Rooke, Jr.

UNIVERSITY OF UTAH
RESEARCH INSTITUTE
EARTH SCIENCE LAB.

September 1969

Sponsored by

Defense Atomic Support Agency

Conducted by

U. S. Army Engineer Waterways Experiment Station
CORPS OF ENGINEERS
Vicksburg, Mississippi

ARMY-MRC VICKSBURG, MISS.

Eac
pric

Approved for Public Release; Distribution Unlimited

ave

ABSTRACT

The MINE SHAFT Series is a program of high-explosive tests primarily concerned with ground-shock and cratering effects from explosions at or near the surface of a rock medium. The series is sponsored by the Defense Atomic Support Agency (DASA) as a follow-on to similar tests in soil (SNOW BALL, DISTANT PLAIN, PRAIRIE FLAT). The two major events of MINE SHAFT during 1968 were MINE UNDER and MINE ORE; both were explosions of 100-ton TNT spheres detonated in near-surface geometries and in/over a granite medium.

Studies of the crater ejecta were conducted on MINE ORE (buried one-tenth of the charge radius) with the objectives of determining the spoil density and distribution from this event, examining the role of the ejection mechanism in crater formation for this medium, and obtaining additional information on natural missile trajectories. MINE UNDER, an above-surface event, produced a spalled rubble mound and a small field of debris; this was also recorded as part of the study.

MINE ORE produced a low, irregular crater lip which extended to an average range of 47 feet from ground zero (GZ) with a maximum of roughly 90 feet. Beyond this, discrete ejecta particle size and distribution frequency decreased with increasing distance from GZ. The maximum observed range was 2,120 feet for a 1-pound natural missile

with smaller fragments found out to about 2,300 feet from GZ. Maximum ejecta ranges were observed downhill from and parallel to the main joints.

Missile ranges scaled approximately as $W^{0.3}$. The jointing system of the rock appeared to be the single most influential element in concentrating debris along certain radials, as well as in the overall distribution of debris.

PREFACE

The MINE SHAFT Series includes participation by a number of agencies under the technical direction and support of the U. S. Army Engineer Waterways Experiment Station (WES). Details of the organization for Events MINE UNDER and MINE ORE are contained in a Technical, Administrative, and Operational Plan.[1] Mr. L. F. Ingram of the Nuclear Weapons Effects Division (NWED), WES, is serving as Technical Director for the MINE SHAFT Series. The Director of Program 1 (Cratering and Ejecta Studies) is Mr. J. N. Strange, also of NWED.

Subtask N122, General Ejecta Studies, was prepared and executed during the period August-November 1968 as a part of Program 1 by Messrs. A. D. Rooke, Jr., Project Officer, and J. W. Meyer, the authors of this report. Assistance in the field was provided by Messrs. J. W. Scanlan of the WES and D. E. Stroberger of the Boeing Company. During this time Mr. G. L. Arbuthnot, Jr., was Chief of the NWED, COL Levi A. Brown was Director of the WES, and Messrs. J. B. Tiffany and F. R. Brown were Technical Directors of the WES.

---

[1] DASIAC Special Report 77-1, 1 October 1968, DASA Information and Analysis Center, General Electric Co., TEMPO, 816 State Street, Santa Barbara, California.

CONTENTS

TABLES

FIGURES

CONVERSION FACTORS, BRITISH TO METRIC UNITS OF MEASUREMENT

British units of measurement used in this report can be converted to metric units as follows.

Multiply	By	To Obtain
inches	2.54	centimeters
feet	0.3048	meters
miles	1.609344	kilometers
feet per second	0.3048	meters per second
miles per hour	1.609344	kilometers per hour
square feet	0.092903	square meters
cubic yards	0.764555	cubic meters
pounds	0.45359237	kilograms
tons (2,000 pounds)	907.185	kilograms
pounds per square inch	0.070307	kilograms per square centimeter
pounds per square foot	4.88243	kilograms per square meter
pounds per cubic foot	16.0185	kilograms per cubic meter
Fahrenheit degrees	-[a]	Centigrade or Kelvin degrees

[a] To obtain Centigrade (C) temperature readings from Fahrenheit (F) readings, use the following formula: $C = (5/9)(F - 32)$. To obtain Kelvin (K) readings, use: $K = (5/9)(F - 32) + 273.15$.

CHAPTER 1

INTRODUCTION

1.1 BACKGROUND

The past 15 years or so have seen a great increase in interest and research effort on the subject of cratering. The military importance of cratering, particularly by nuclear energy, stems from its damaging capability against hardened underground facilities, from damage associated with ejected material (either in the form of impact damage or from the depth of deposition), and from the creation of tactical obstacles. Proper usage of cratering as a military tool and appreciation of its hazards require detailed knowledge of the mechanics of crater formation.

An obvious mechanism is that of ejection of material from the crater void. The early cratering tests, largely buried explosions in the arid soil of the western U. S. A., indicated that this ejection (or throwout) manifested itself primarily as an overburden problem, with areal density decreasing exponentially with increasing distance from ground zero (GZ). The small-grain material of the cratered medium posed no particular threat to nearby structures other than to render them ineffective by covering them with a blanket of soil; further, the average particle reached terminal velocity early in the ejection process, and therefore had a relatively short range.

In recent years, interest in hardened military facilities built in rock has required that additional emphasis be placed upon the study of crater ejecta in this medium. Here the possibility of long-range damage by discrete ejecta particles is as much a concern as depth-of-ejecta considerations. Further, important changes have occurred in research concepts relating to the shot geometry itself. The surface or near-surface burst, such as might be expected from an incoming warhead, has received special attention. The hemispherical charge, which sought to model the blast effects of a true surface shot (half above, half below ground) twice its actual size, has given way to the spherical charge, which more realistically represents the "point source" of energy that a nuclear burst would provide. The use of chemical explosives has, of course, been made necessary by the requirement to substitute high explosives (HE) for nuclear devices, in keeping with requirements of the Nuclear Test-Ban Treaty.[1] In addition, means have been sought to more closely reproduce the crater of a nuclear weapon, recognizing that unless this aspect of energy expenditure can be modeled it is unlikely that other aspects will be properly modeled. This has been attempted by offsetting the charge

---

[1] Entered into by the USSR, Great Britain, and the U. S. A. in 1963. Radioactive contamination of the atmosphere beyond national borders is prohibited.

center of gravity above that of the nuclear burst which is being modeled. Thus, in earlier tests in soil, it appeared that a spherical HE charge resting on (tangent to) the ground surface might provide a better representation of a nuclear surface-burst crater than one in which the center of gravity was actually at the ground surface.

It was this last consideration that dictated the choice of charge geometry for Event MINE ORE. This shot, together with the above-surface shot MINE UNDER, was a major event of the MINE SHAFT Series, a program of HE tests in rock sponsored by the Defense Atomic Support Agency. A small-scale (calibration) series of shots pointed to a burial depth of one-tenth the charge radius as most representative of a nuclear surface burst. This was generally in keeping with theoretical considerations and small-scale laboratory experiments conducted by Physics International, Incorporated.

1.2 OBJECTIVES

The primary objective of the study reported herein was to determine the ejecta mass density and azimuthal distribution associated with the MINE ORE Event. Secondary objectives were to:

1. Obtain information on the mechanics of crater formation for the MINE ORE test geometry by locating the original and final positions of ejected material.

2. Obtain information from which quantitative estimates of ejecta trajectories might be made.

3. Evaluate the hazards of natural missiles resulting from such explosions.

1.3 THEORY

The crater, lip, and surrounding regions of deformation or damage resulting from a surface or near-surface explosion are illustrated in Figure 1.1.

Preshot predictions of ejecta parameters (e.g., maximum missile range) followed two general approaches, viz, a consideration of initial particle velocities based upon shock conditions, and scaling of other experimental results to the yield for MINE ORE. The limitations on both approaches are well recognized. In the case of the former, the behavior of the shock front in the region where ejection originates is argumentative and to some extent a matter for conjecture. On the other hand, scaling of any phenomenon requires a knowledge of the mechanics involved, and these, too, are not completely understood. Thus, it is not known whether refraction of the compressive stress wave in the rock or stress relief (rebound) following the passage of the compressive stress wave predominates in the ejection mechanism. Equally uncertain is the degree to which scouring action by the explosion gases influences debris ejection. It is

likely that all of these mechanisms, among others perhaps, play a part.

Observations of near-surface explosions show an early, fast-moving "ring" of material ejected from a position near the charge and at an angle nearly normal to the ground surface, perhaps the result of a spalling action. The ejection process is, however, known to take place over a longer period of time and to include lower exit angles. This suggests that material fractured by the compressive stress wave may be dislodged and ejected by the explosion gases. In order to obtain some appreciation of the probable hazard from ejected rock, both shock conditions and scaling parameters were examined.

For the former approach, an expression for particle velocity just behind the shock front may be obtained from

$$p = \rho c u \tag{1.1}$$

where

p = shock front pressure in terms of force per unit area

ρ = medium mass density (MT^2L^{-4} in units of mass-length-time)

c = sonic velocity in the medium

u = particle velocity of the medium

Certain assumptions are immediately necessary, the major one being the value to be assigned to p. A thorough study of ejecta from a 20-ton[2] surface burst in soil (Reference 1) has shown that the

longest range particles originate near the ground surface and within a distance equal to about one charge radius from the surface of the explosive. The rock in intimate contact with the charge is probably pulverized. Material adjacent to the charge achieves large initial velocities; however, the material ejected from this region is thought to reach an early terminal velocity and experience a short trajectory, due to its highly comminuted condition. Photographic analysis indicates that this is the case (Reference 2). At a distance of around two charge radii from GZ, larger particles should remain intact. At this range, the shock wave in rock, assuming the pressure at the charge-medium interface is between 100 to 150 kilobars and decreases inversely as the square of radial distance, should be on the order of 25 to 38 kilobars. As would be expected, this is appreciably higher than comparable shock-wave pressures of about 20 kilobars observed in soil (Reference 3). Although the ground may be moving downward due to airblast loading, it is assumed that this has no significant effect on the directly coupled shock in the region of interest.

Rounding off all values to the greatest accuracy justified and solving for u,

---

[2] A table of factors for converting British units of measurement to metric units is presented on page 9.

$$u \approx \frac{(5.4 \times 10^7 \text{ lb/ft}^2)}{\left(5.0 \frac{\text{lb-sec}^2}{\text{ft}^4}\right)(1.2 \times 10^4 \text{ ft/sec})}$$

$$\approx 900 \text{ ft/sec}$$

based upon a charge-medium interface pressure of 100 kilobars. Since there is some inertia associated with all fragments, this value is actually too high. It provides, however, a point of departure for calculations of ballistic trajectory, and, further, agrees fairly well with values calculated in Reference 1 for an explosion in soil.

The equation for ballistic trajectory is well known. It states

$$R = C\left(\frac{V_o^2 \sin 2\alpha}{g}\right) \qquad (1.2)$$

where

R = range

V_o = initial velocity (speed and direction) of a projectile (or particle)

α = initial angle (with a horizontal plane) of the particle

g = gravitational acceleration

C = a constant which compensates for the effects of air drag. Reference 4, which includes some observations of ejecta particles, expresses this constant as a ratio of the observed range to the range in a vacuum.

The concept of the retarding force on an ejected particle being constant is a rather gross simplification of the actual problem, which includes such variables as particle size, shape, and velocity,

as well as density and viscosity of the air (References 4 and 5). The airblast also influences ejecta motion (Reference 6).

Substituting the calculated particle velocity for V_o in Equation 1.2, and applying certain data from Reference 1,

$$R \approx 0.05 \left[\frac{(900 \text{ ft/sec})^2 \sin 2 (25 \text{ degrees})}{32.2 \text{ ft/sec}^2} \right]$$

$$\approx 960 \text{ ft}$$

If spall is considered the predominant means of particle ejection, it may be noted that the spall velocity is twice that of the particle velocity given in Equation 1.1, or approximately 1,800 ft/sec. Substituting this value in the ballistic trajectory equation provides a range of approximately 3,860 feet. Greater ranges would result from an increase in the angle of ejection (up to 45 degrees), as might be expected for a spalled particle.

Since the results of a 1,000-pound calibration series[3] (Reference 7) were available, the selection of a suitable scaling exponent was required in order to predict certain debris parameters

---

[3] Conducted to assist in selection of a shot geometry, and also to permit the trial of certain instrumentation techniques. Charges were fired which modeled both MINE ORE and MINE UNDER, as well as other geometries in the near-surface regime.

by scaling the observed data to the yield of the MINE ORE Event. The most logical exponent appeared to be that derived from the expression for particle velocity for a buried explosion (Reference 8). With this selection, it remained to be determined which scaling rule is most applicable. Clearly, gravity must be included, which narrows the choice to mass-gravity or energy-gravity rules, as defined and developed in Reference 8. Since the former does not permit realistic scaling of linear dimensions of the charge and crater, mass-gravity scaling was tentatively chosen.

From the dimensional analysis of Reference 8, the following mass-gravity relation can readily be obtained:

$$\frac{\rho_1 u_1^2}{\rho_2 u_2^2} = \frac{g_1}{g_2}\left(\frac{\rho_1}{\rho_2}\right)^{2/3}\left(\frac{W_1}{W_2}\right)^{1/3} \tag{1.3}$$

where W is the charge weight and the subscripts 1 and 2 refer to different experiments. When ρ and g are held constant between two experiments, Equation 1.3 becomes

$$\frac{u_1}{u_2} = \left(\frac{W_1}{W_2}\right)^{1/6} \tag{1.4}$$

provided all other conditions for similarity are met. This, of course, was not the case. Yield strength, viscosity, and sonic velocity of the medium were also constant (or approximately so) in the MINE SHAFT experiments, as was hydrostatic (atmospheric) pressure. Scaling of these variables is necessary for similarity, and

failure to meet this requirement can be expected to cause deviations in what might otherwise appear to be theoretically correct scaling relations. As is pointed out in Reference 8, the cumulative result of these dissimilarities is to enlarge the scaled dimension of the larger explosion. Thus,

$$\frac{R_1}{R_2} = \left(\frac{W_1}{W_2}\right)^{1/6(+)} \qquad (1.5)$$

for the MINE SHAFT Series. If the maximum observed missile range (450 feet) for the calibration test which modeled MINE ORE is substituted in Equation 1.5, the maximum range for ejecta on MINE ORE is found to be equal to or greater than 1,200 feet.

Some experimental corroboration of the $(W)^{1/6}$ scaling rule is desirable, and this is found in Reference 9, in which it was concluded that the available maximum-range data for buried charges did indeed scale most closely to the sixth root of the charge yield. However, special attention was given to surface-burst data (taken to include hemispherical shots), for which four-tenths scaling was indicated. The latter rule provides an ejecta-range prediction on the order of 3,700 feet when applied to MINE ORE, using the calibration data as a model.

Summarizing the theoretical approaches to the determination of debris range, it appears that predictions which assume a scouring action by the shock wave are unreasonably low. Similarly,

predictions based upon sixth-root scaling are lower than would be dictated by experience. Empirically derived scaling exponents indicate a radical change in scaling associated with a surface-burst geometry. This, in turn, indicates that the sixth-root rule may become invalid as the charge position is moved upward through the earth-air interface. Why this should be is not immediately clear, since the parameters included in the dimensional analysis of Reference 8 appear equally valid for the near-surface case. Obviously, more information is needed to correlate theoretical calculations with observed results. It is particularly important that ejecta origins be determined, along with the trajectory time-histories resulting from use of various missile shapes and sizes.

1.4 PRESHOT PREDICTIONS

Based on the preceding discussion, the following preshot estimates of natural missile ranges were made for Event MINE ORE (Reference 10):

Maximum range = 3,000 feet

Range within which 90 percent of the ejecta will fall = 1,300 feet

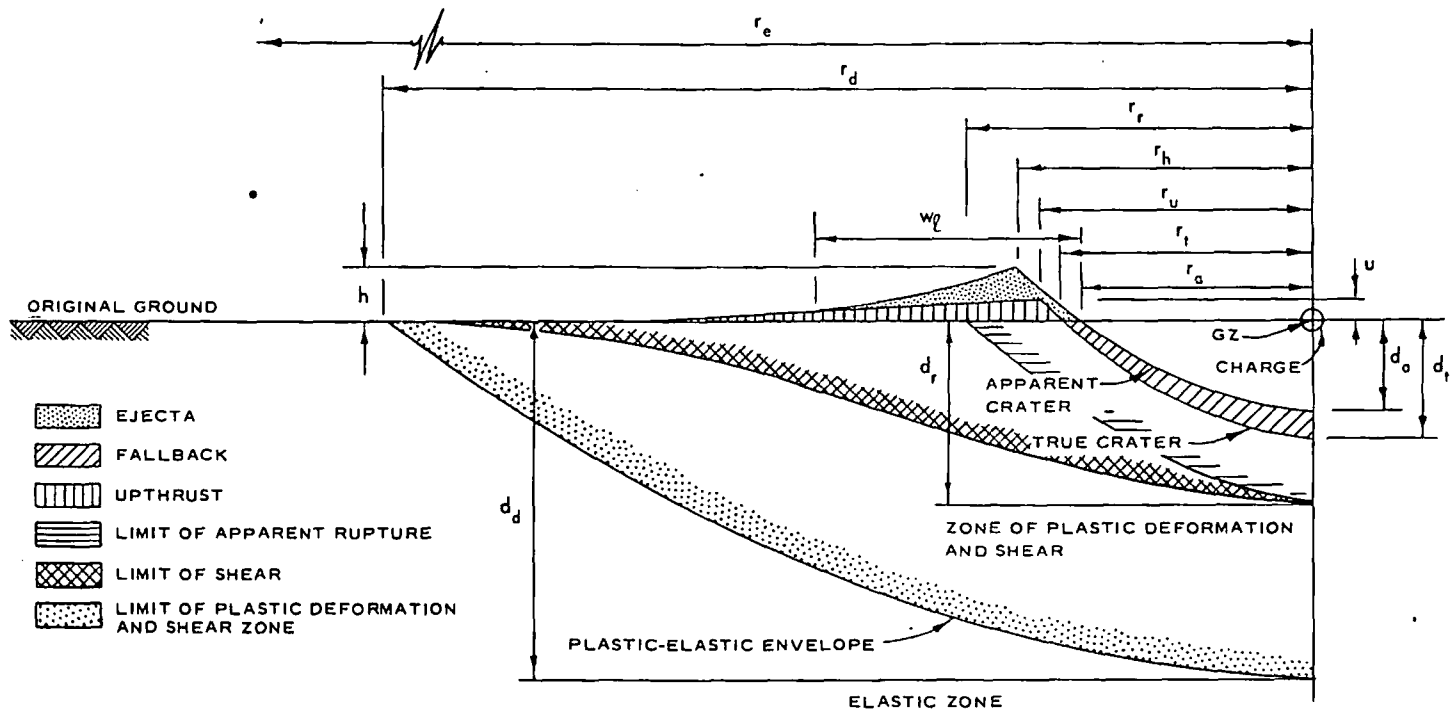

Figure 1.1 Typical half-crater profile and nomenclature for surface or near-surface burst. Profiles and dimensions are symmetrical about the centerline. Various radial and depth dimensions are indicated by r and d, respectively. Crater lip and upthrust heights are shown by h and u, while the width of the lip is noted as w_ℓ. The radius of ejected debris is indicated by r_e.

CHAPTER 2

EXPERIMENTAL PROCEDURES

2.1 TEST SITE

The MINE SHAFT test site was located on a granite laccolith in the Iron Mountains of southwest Utah, about 8 miles northwest of Cedar City, Utah. Figure 2.1 is a map of the test area. The site has a semidesert environment with juniper trees, sage, and cactus as the predominant vegetation. It is characterized by a thin layer of sandy silt soil (desert alluvium) with intermittent, smoothly rounded rock outcrops. The elevation of the site is approximately 5,900 feet msl, and the area slopes gently toward the east at about two degrees. A steep-sided, 500-foot peak is located 1,800 feet southwest of the site. The area within approximately 100 feet of both GZ's was cleared of soil and weathered rock. The trees and brush on the south and southwest sides of the area were removed for a distance of 1,000 feet from MINE ORE GZ.

The events reported herein were fired at the following geographical coordinates:

Event	Latitude	Longitude
MINE UNDER	37°46'10.050"	113°10'48.494"
MINE ORE	37°46'10.247"	113°10'49.976"

2.2 TEST SCHEDULE AND GEOMETRY

This phase of the MINE SHAFT Series consisted of two 100-ton HE charges: MINE UNDER, detonated on 22 October 1968, and MINE ORE, detonated on 13 November 1968. Each charge was formed of 32.6-pound blocks of trinitrotoluene (TNT) stacked to approximate a sphere. The charge radius was approximately 8 feet. MINE UNDER was designed as an above-surface burst with a height of burst (HOB) of 2.0 charge radii (15.70 feet). MINE ORE was a near-surface burst with an HOB of 0.9 charge radius (7.07 feet). Figure 2.2 shows the charge geometries for MINE UNDER and MINE ORE.

2.3 WEATHER CONDITIONS

Pertinent surface-weather data for MINE UNDER and MINE ORE shot days are given below:

	MINE UNDER	MINE ORE
Temperature	65.4 F	38.5 F
Barometric pressure	820 mb	808 mb
Relative humidity	18 pct	50 pct
Wind direction/velocity	300 degrees/2.3 mph	10 degrees/13.8 mph

These data were furnished by Program 5, Airblast.

2.4 EJECTA MASS DENSITY AND DISTRIBUTION SAMPLING

This section deals with the procedures for sampling the ejecta from Event MINE ORE. Since no ejecta was expected from Event MINE UNDER, the procedures discussed in the remainder of this chapter were prepared only for MINE ORE.

Measurements of ejecta mass density (pounds per square foot) were divided into three categories: (1) ejecta within the crater lip, (2) natural missiles falling beyond the crater lip, and (3) fine-grain ejecta dust falling beyond the crater lip. Primary sampling sectors extended south and west, or approximately parallel and perpendicular to what appeared to be the main jointing system of the rock.

2.4.1 Ejecta Within the Crater Lip. The mass density of the ejected material in the crater lip was determined by excavation, sieving, and weighing. Excavation was carried out in coordination with Subtask N121, Crater Investigations. Five trenches were excavated through the crater lip as shown in Figure 2.3. The trenches to the south, west, and northwest were 20-degree sectors, while those to the east and north were 6-foot-wide corridors. Each trench was divided into three sections so that mass density as a function of radial distance could be determined. The limits of these sections were spaced at one, two, and three apparent crater radii. The ejected material from each section was picked up with a front-end

loader and placed in a dump truck. The total sample was weighed, then hauled to a rock-crushing plant for sieving (Figure 2.4). There it was separated into four size groups: 12-inch plus, 6 to 12 inches, 3 to 6 inches, and 3-inch minus. Each size group was then weighed in order to provide a size-distribution curve for the specified area.

2.4.2 Missiles Beyond the Crater Lip. The number of natural rock missiles that fell beyond the crater lip were sampled three ways: (1) by photography, (2) by counting and weighing in surveyed sectors, and (3) by plane-table survey. Each method was used in a different region as shown in Figure 2.5. The objectives of this sampling were to determine mass density and a particle count per unit area of the ejecta as functions of radial distance and to examine the relation between missile size and range.

Photography was used in the region extending from 100 feet, assumed as the approximate edge of the crater lip, to 1,000 feet from GZ. Twenty photography stations, spaced to match a geometric progression, were used along both the south and west radials. The camera grid and mount used are shown in Figure 2.6. A Kodak 35-mm Reflex camera was used with Kodak Panatomic X film. The grid area covered by a single photograph was 25 ft^2. The grid pattern consisted of 6-inch squares. For those stations between 100 and 250 feet from GZ, a single photograph was taken. Between 250 and

500 feet, four photographs were taken, giving a sample area of 100 ft^2. Sixteen photographs for a sample area of 400 ft^2 were taken between 500 and 1,000 feet from GZ.

Beyond 1,000 feet from GZ, the missile population was so sparse that photography was no longer effective. Here, 20-degree counting and weighing sectors were laid out on the south and west radials as shown in Figure 2.5. Each sector was 100 feet deep. All missiles greater than 1 pound in weight in a sector were located, their positions recorded using coordinates based on the near centerline corner of the sector, and their weights estimated. Larger ejecta were weighed in a sling-and-spring-scale device. Figure 2.7 shows this procedure.

The outer fringes of the ejecta distribution were sampled by means of a plane-table survey in order to determine maximum missile range. The area surveyed was a 110-degree arc southwest of GZ as shown in Figure 2.5. As in the counting sectors, the survey was restricted to missiles at least 1 pound in weight. The remainder of the ejecta-distribution periphery was inspected visually to insure that the maximum-range missile was found.

2.4.3 Ejecta-Dust Sampling. Fine-grain ejecta dust (sand size and smaller) falling beyond the crater lip was sampled with metal collector pads like that shown in Figure 2.8. Larger particles which were found on the pads were included in the sampling; these

were found mostly on the close-in rings. Primarily, however, photography was relied upon for obtaining data on the larger particles, while the pads provided data on the fine material. The pads were arranged in a circular pattern around GZ as shown in Figure 2.9. This pattern consisted of concentric rings in a geometric progression from GZ with stations at 100, 140, 190, 270, 370, 520, 720, and 1,000 feet. The inner five rings contained 16 pads each spaced every 22.5 degrees, while the outer three rings had 32 pads each spaced every 11.25 degrees. The array contained 176 pads, of which 174 were actually placed before shot MINE ORE (satisfactory locations for two pads could not be found). Each pad was a 3- by 2.5-foot sheet of No. 20 gauge steel. The leading edge of each pad was turned down in order to anchor it more firmly into the soil overburden. Most pads were held down by 8-inch gutter spikes driven into the overburden. Some pads, located on bare rock, were held down with rock studs. The pads on the inner three rings had their leading edges anchored in grout to prevent displacement by the airblast. After the detonation, the deposited material was collected from the pads with whisk brooms and dust pans and sealed in paint cans (Figure 2.10). After an initial weighing of each sample, they were sent to the U. S. Army Engineer Waterways Experiment Station for sieve analysis.

2.5 MISSILE-TRAJECTORY EXPERIMENTS

This section describes the experiments performed to obtain data on missile-trajectory parameters such as ejection angle, initial velocity, impact angle, impact velocity, and range. Three experiments were performed involving: (1) colored-grout columns, (2) artificial missiles, and (3) styrofoam missile traps.

2.5.1 Colored-Grout Columns. An array of 8-inch boreholes was drilled in the vicinity of the MINE ORE GZ as part of the Crater Investigations Subtask (Reference 11) to aid in defining the true crater boundary and to measure residual ground displacement. One borehole was drilled at GZ, and others were drilled along radials to the south and west at 5-foot intervals. These were filled with colored grout designed to match as closely as possible the density of the granite at the test site. Portions of the columns falling within the expected area of the true crater were also divided into 1-foot sections by the addition of colored plastic beads to the grout mixture. Table 2.1 gives the coding for the colored-grout columns. After the detonation, a search was made for ejected grout particles; those located provided initial and final positions for individual pieces of crater ejecta. This provided information necessary for studying the mechanics of crater formation as well as missile trajectory.

2.5.2 Artificial Missiles. A second missile study involved

placing a large number of artificial missiles near the MINE ORE GZ. As with the grout columns, initial and final positions of the ejected material were known; however, with the artificial missiles, shape and weight were also known. This information provides a basis for studying drag forces and ballistic coefficients of discrete ejecta particles.

Two types of artificial missiles were used--cylinders and spheres. Table 2.2 lists the number of missiles placed along with their physical properties. The cylinders were made of aluminum with a 2.5-inch diameter (Figure 2.11). Each cylinder was subdivided into a 4-inch cylinder, a 2-inch cylinder, a 1-inch cylinder, and a 1-inch cylinder divided into half and quarter wedges (see Table 2.2). The cylinders were emplaced in NX holes (3-inch diameter) at 2.5 and 7.5 feet from GZ along the south and west radials. The spherical missiles were made of three metals: aluminum, steel, and lead (Figure 2.12). They varied from 1 to 6 inches in diameter. The missiles were number-coded and placed in the two NX holes and in the top 3 feet of the first five grout holes (excluding GZ) along the south radial. Figure 2.13 shows the preshot positions of the artificial missiles. Density-matching grout was used to backfill around the missiles.

Seven large aluminum missiles were also used in an attempt to evaluate initial trajectory conditions of ejecta. It was planned

that with their brightly polished or painted surfaces they would be detected by the test photography, giving early velocity data (ejection angle and speed).

2.5.3 Styrofoam Missile Traps. Styrofoam missile traps were used to evaluate terminal trajectory parameters. The traps were 8- by 4-foot styrofoam pads (125-psi compressive strength), 4 inches thick. Six such pads were used along a radial to the south of GZ (Figure 2.9) at distances of 400, 500, 600, 700, 800, and 900 feet. Each pad was positioned so that its top surface was flush with the ground surface. After the detonation, the pads were examined for missile hits from which impact angles and depths of penetration could be measured. From these values it is anticipated that the impact velocities of the missile can be inferred by calibration experiments relating penetration and impact velocity.

TABLE 2.1 GROUT-COLUMN COLOR AND BEAD CODING, EVENT MINE ORE

Material above dashed line was dissociated and/or ejected. Holes R1-1 through R1-5 also contained artificial missiles (see Figure 2.13). Key to bead colors: R, red; Y, yellow; T, turquoise; A, amber; Bl, black; O, orange; G, green.

Column→	GZ	R1-1	R1-2	R1-3	R1-4	R1-5	R1-6	R1-7	R1-8	R1-9
Grout Color→	Red	Brown	Green	Black	Yellow	Orange	Brown	Green	Red	Yellow
Range, feet→	0	5	10	15	20	25	30	35	40	45
Depth	Bead Color(s)									
feet										
South Radial (Azimuth = 195 degrees):										
0-1	R	T	Y	R	R,Y	O	R	T	T	T
1-2	G	Y	A	O	G	Bl	Y	Y	Y	G
2-3	T	O	G	G	T	A	O	O	O	A
3-4	Y	Bl	R	T	Y	T	Bl	G	Bl	R
4-5	T	A	T,Y	A	O	R	T	R	--	Bl
5-6	A	R,G	T,O	Bl,T	A	R,T	G	A	--	--
6-7	Bl	R,T	T,Bl	R,G	R,G	T,A	--	--	--	--
7-8	R,G	R,Y	--	R,A	R,T	Bl,T	--	--	--	--
8-9	R,T	R,O	--	--	R	--	--	--	--	--
9-10	R,Y	R,Bl	--	--	--	--	--	--	--	--
10-11	R,O	R,A	--	--	--	--	--	--	--	--
11-12	R,Bl	--	--	--	--	--	--	--	--	--
12-13	R,A	--	--	--	--	--	--	--	--	--

Column→	R3-1	R3-2	R3-3	R3-4	R3-5	R3-6	R3-7	R3-8	R3-9
Grout Color→	Black	Orange	Yellow	Green	Black	Brown	Red	Yellow	Black
Range, feet→	5	10	15	20	25	30	35	40	45
Depth	Bead Color(s)								
feet									
West Radial (Azimuth = 279 degrees):									
0-1	T	A	T	R	T	R	A	T	A
1-2	R	R	Y	G	G	G	R	Y	R
2-3	G	T	G,A	T	Y	O	T	C	Y
3-4	Y	G	Bl	Y	O	T	G	G	G
4-5	Bl	Y	O	O	Bl	Bl	--	--	--
5-6	O	Bl	A	Bl	A	A	--	--	--
6-7	A	O	G	A	G	--	--	--	--
7-8	T,R	R,A	R	R,G	R	--	--	--	--
8-9	T,G	R,O	R,A	R,T	T,Y	--	--	--	--
9-10	T,Y	R,Bl	T,A	--	O,Bl	--	--	--	--
10-11	T,Bl	R,Y	Bl,A	--	--	--	--	--	--
11-12	T,O	R,G	--	--	--	--	--	--	--
12-13	T,A	R,T	--	--	--	--	--	--	--

TABLE 2.2 ARTIFICIAL MISSILES, EVENT MINE ORE

Missile Type	Material	Size		Weight	Number Emplaced
		Length	Diameter		
		inches	inches	pounds	
Cylinder	Aluminum	4	2.5	1.82	39
Cylinder	Aluminum	2	2.5	0.91	39
Cylinder	Aluminum	1	2.5	0.46	39
Cylinder	Aluminum	1[a]	--	0.23	39
Cylinder	Aluminum	1[b]	--	0.12	78
Sphere	Aluminum	--	6.0	10.50	5
Sphere	Aluminum	--	5.5	8.10	2
Sphere	Aluminum	--	2.5	0.76	26
Sphere	Aluminum	--	1.0	0.05	114
Sphere	Lead	--	2.5	3.37	24
Sphere	Steel	--	2.0	1.17	8
Sphere	Steel	--	1.0	0.15	10
				Total	423

[a] Cylinder divided into half wedges.
[b] Cylinder divided into quarter wedges.

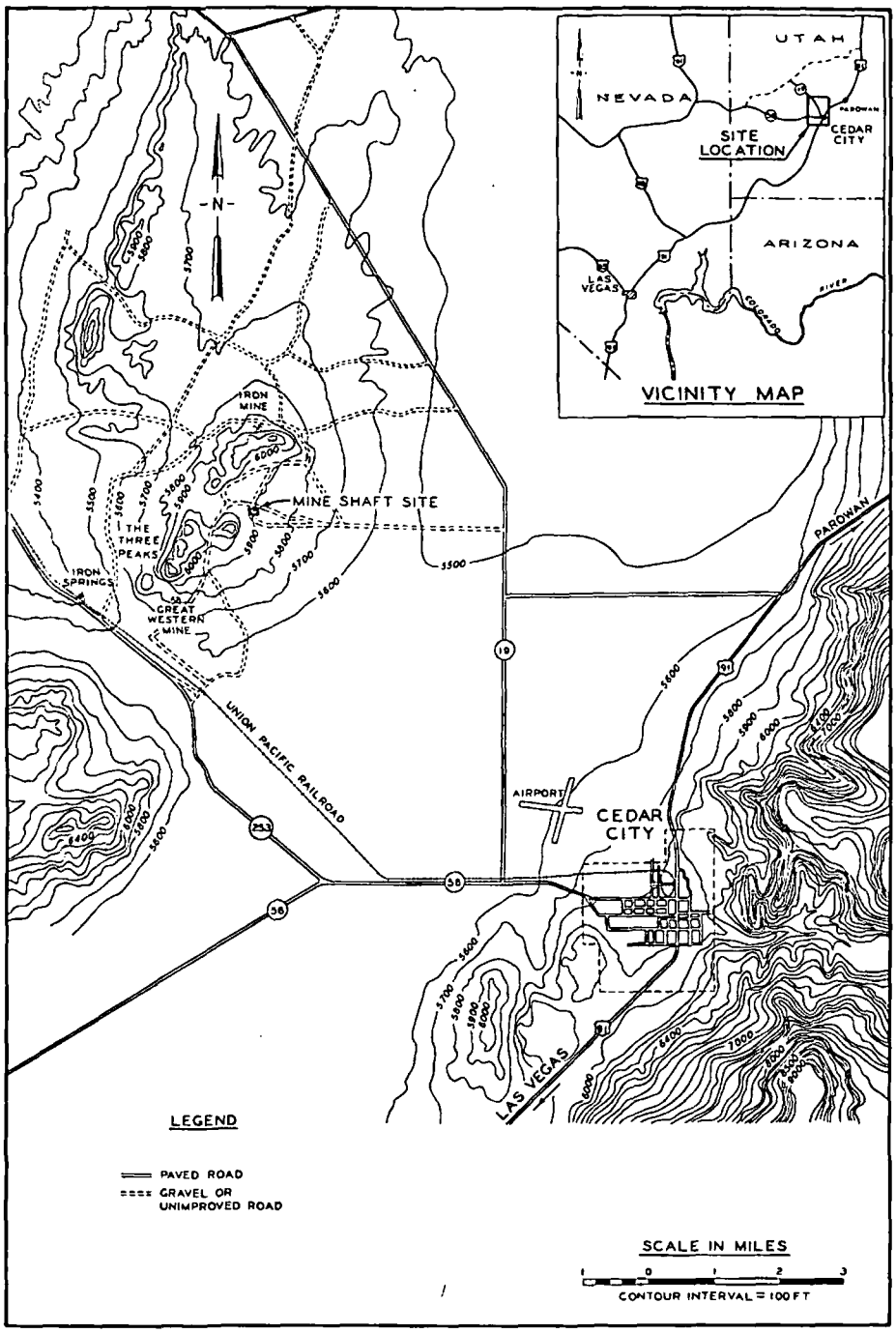

Figure 2.1 Location and vicinity maps for MINE SHAFT. Contours are in feet above mean sea level (msl).

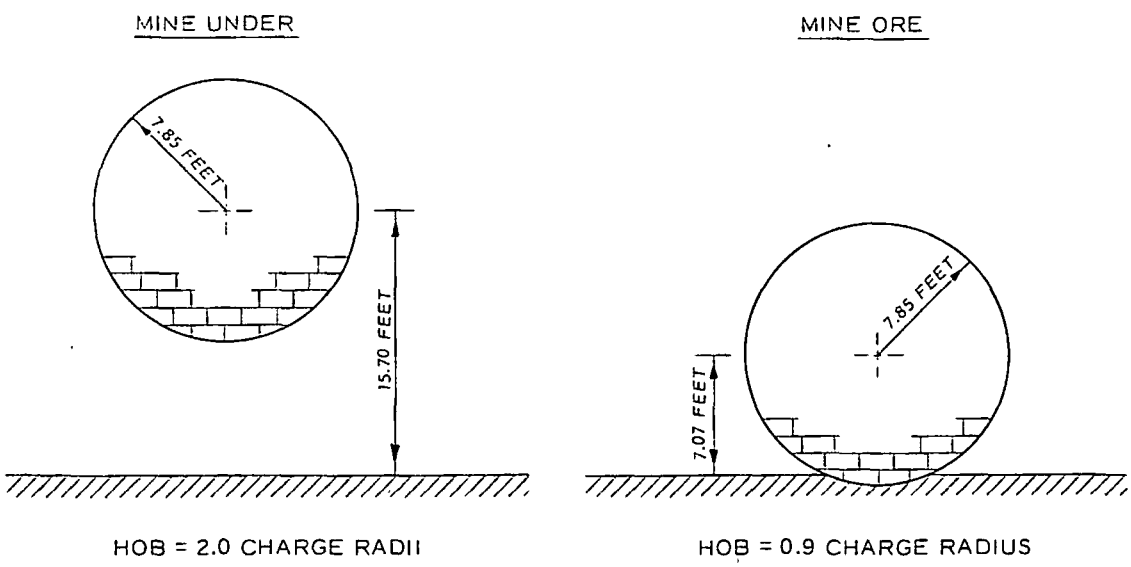

Figure 2.2 Charge geometries for Events MINE UNDER and MINE ORE.

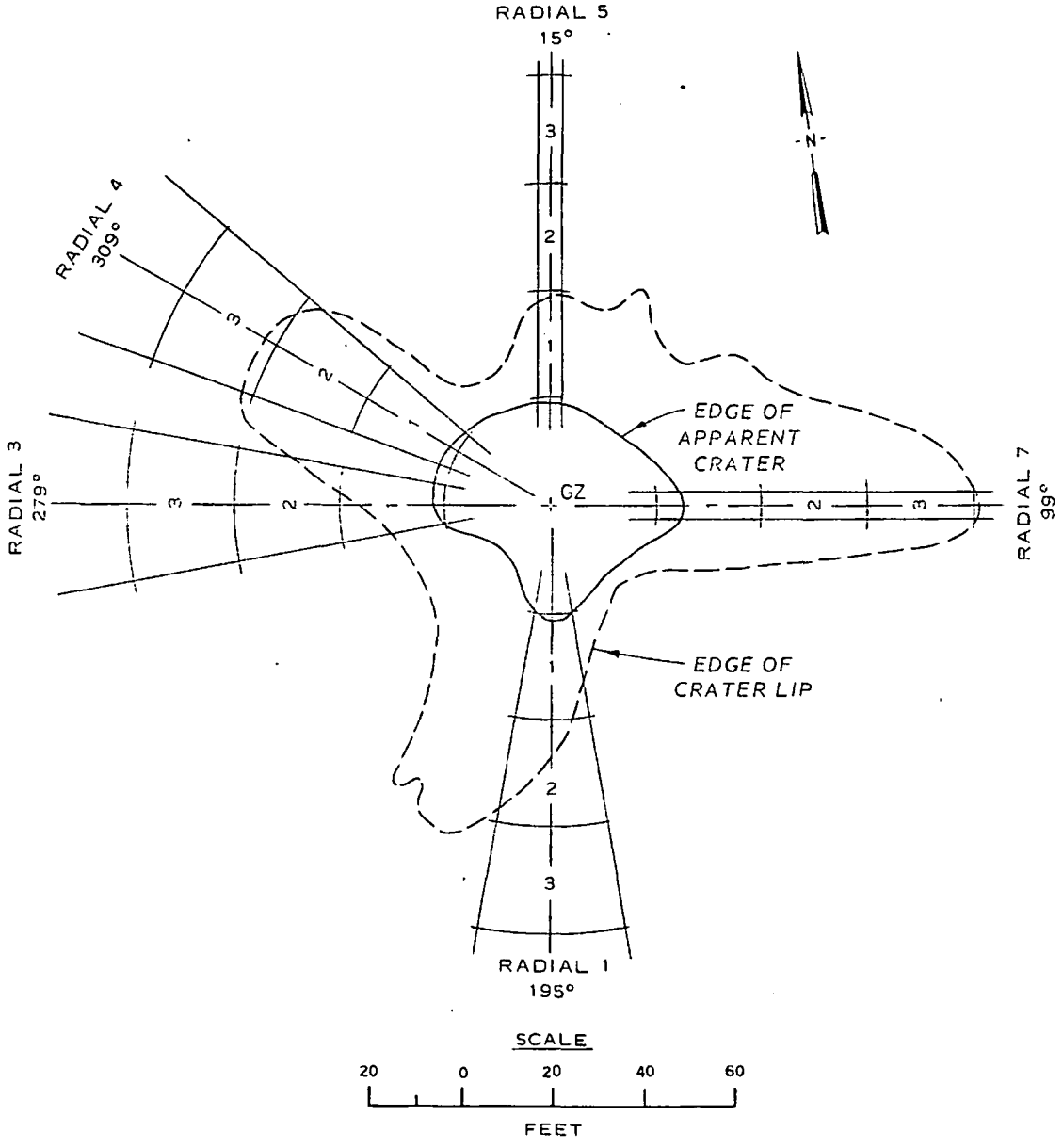

Figure 2.3 Excavation trenches through the crater lip, MINE ORE. Radial numbering system corresponds with that of Crater Investigations Study (Subtask N121). Arrow indicates true north.

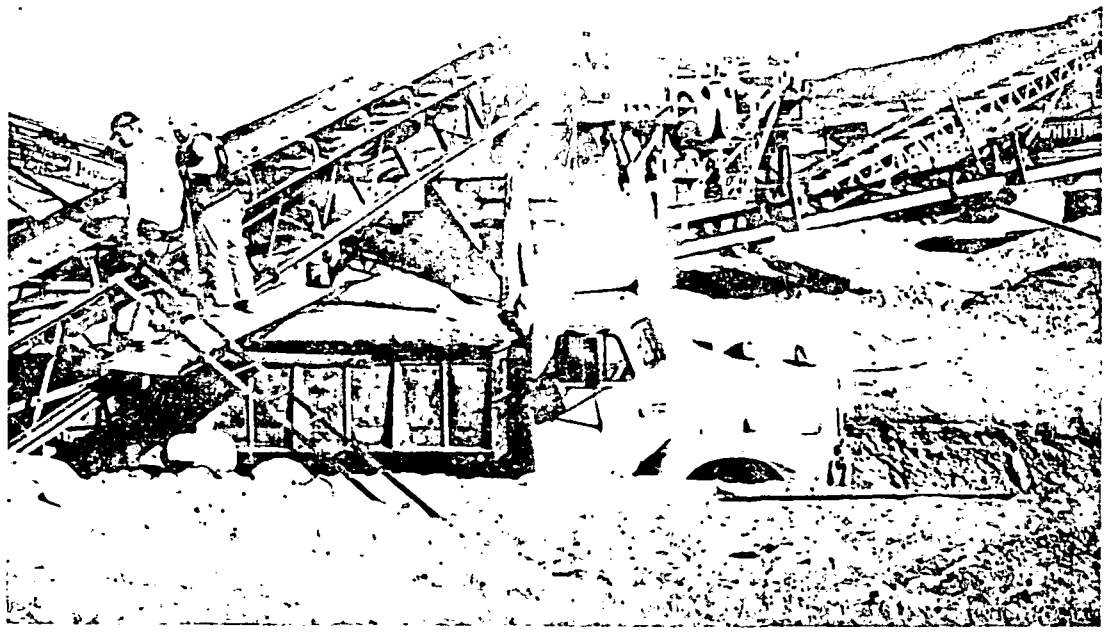

Figure 2.4 Sieving of ejecta from the crater lip of MINE ORE at rock-crushing plant (Western Rock Products Corp., Cedar City, Utah).

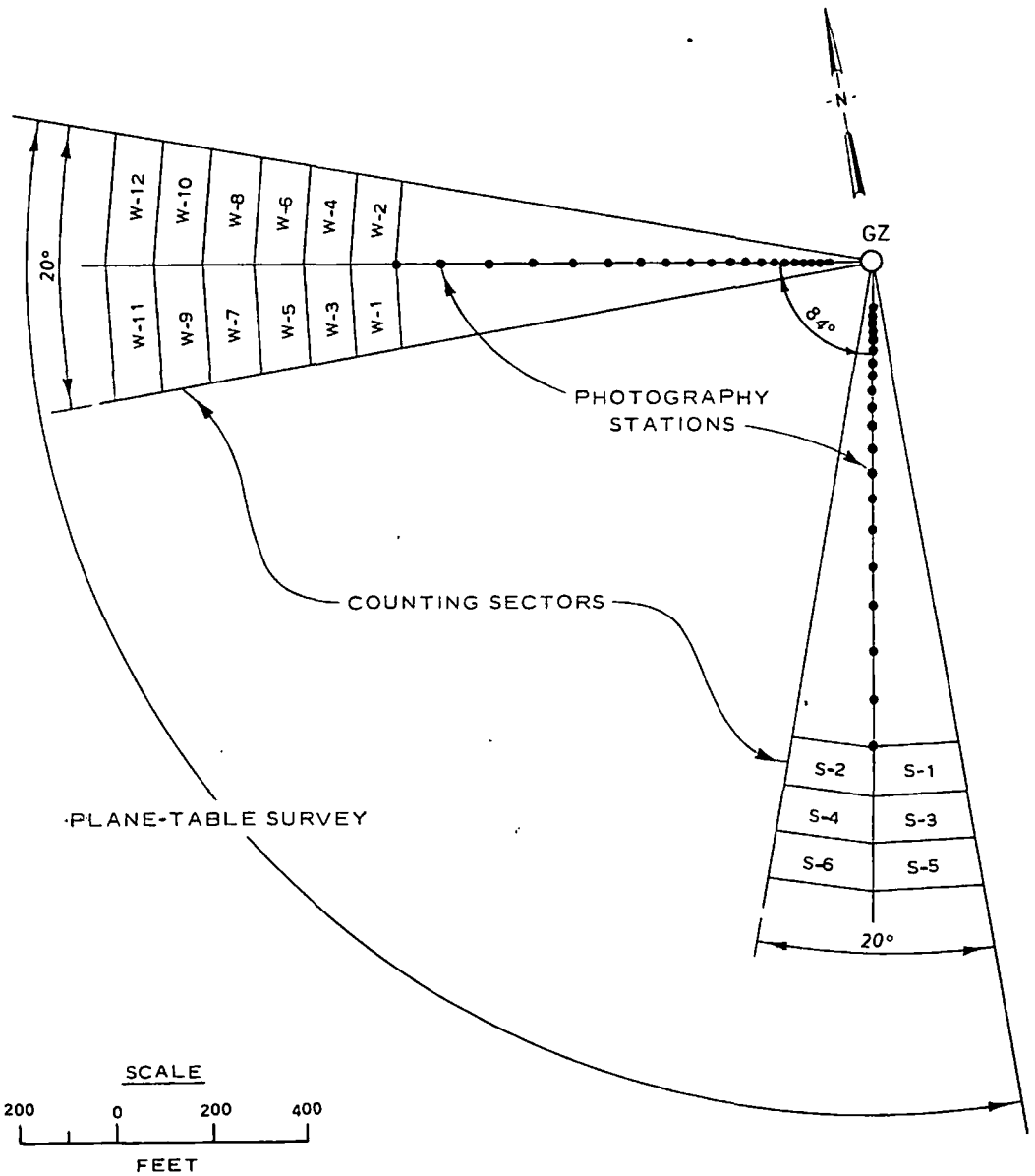

Figure 2.5 Ejecta sampling zones in areas beyond the crater lip, Event MINE ORE.

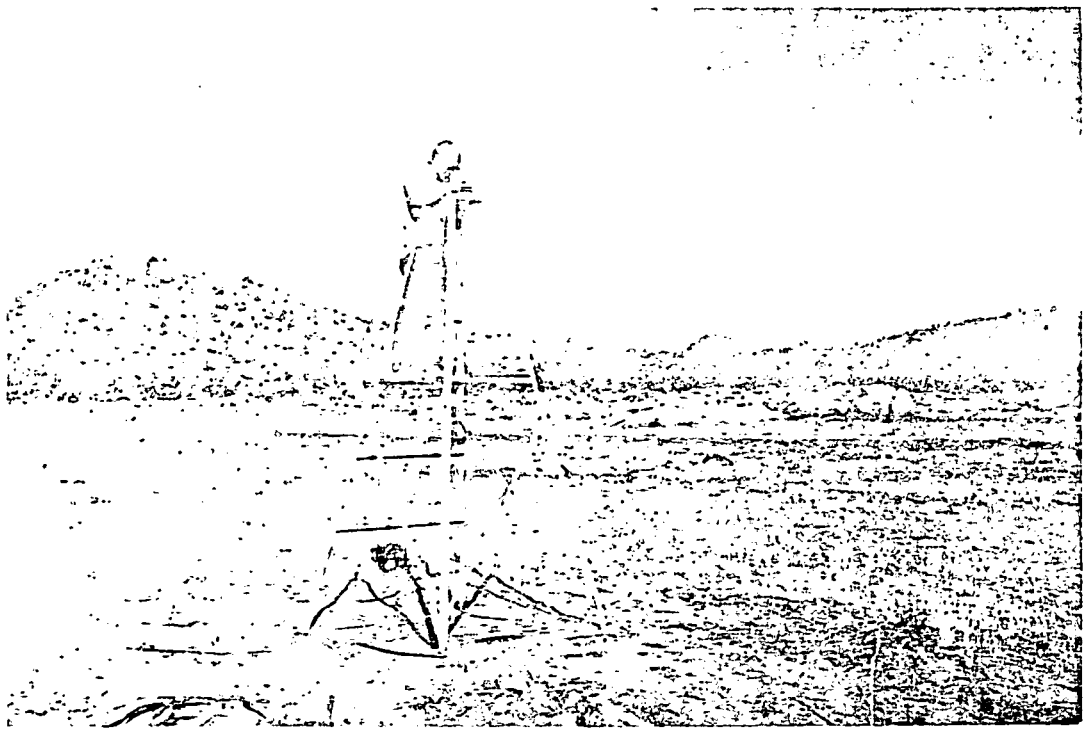

Figure 2.6 Camera grid and mount for photographing ejecta beyond the crater lip, Event MINE ORE.

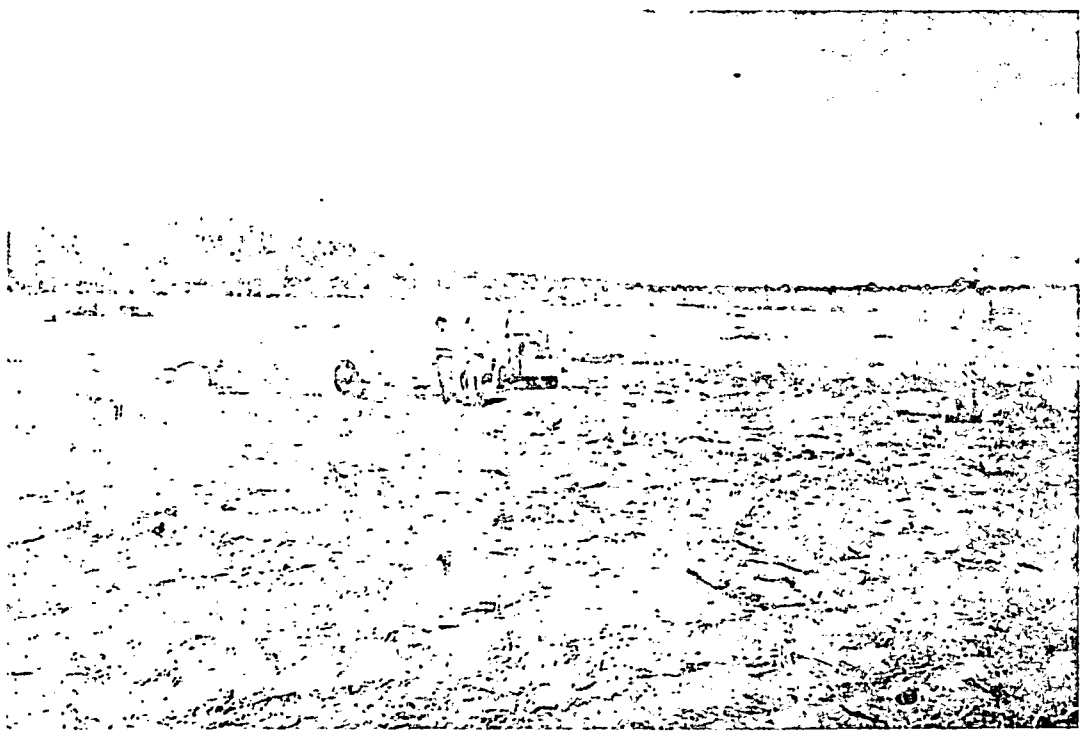

Figure 2.7 Sampling ejecta in the counting and weighing sectors, Event MINE ORE. GZ is in the background at left. Spring scale can be seen near truck.

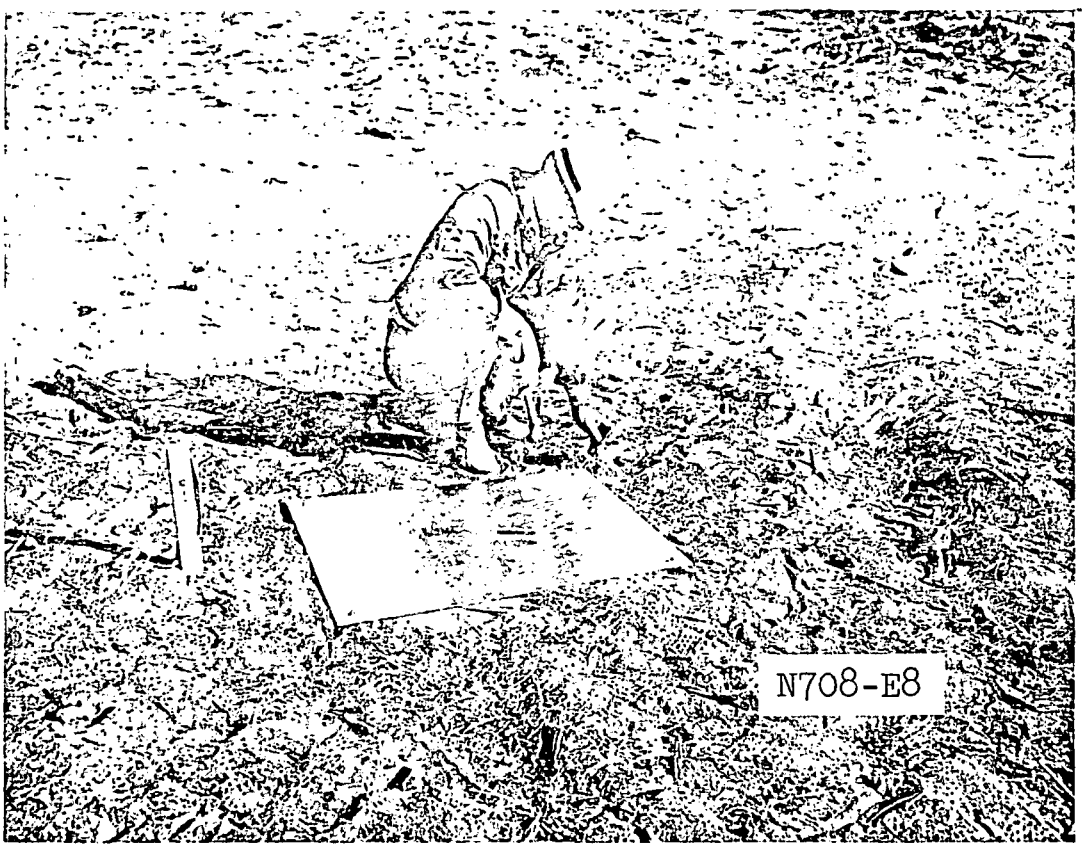

Figure 2.8 Ejecta dust-collector pad.

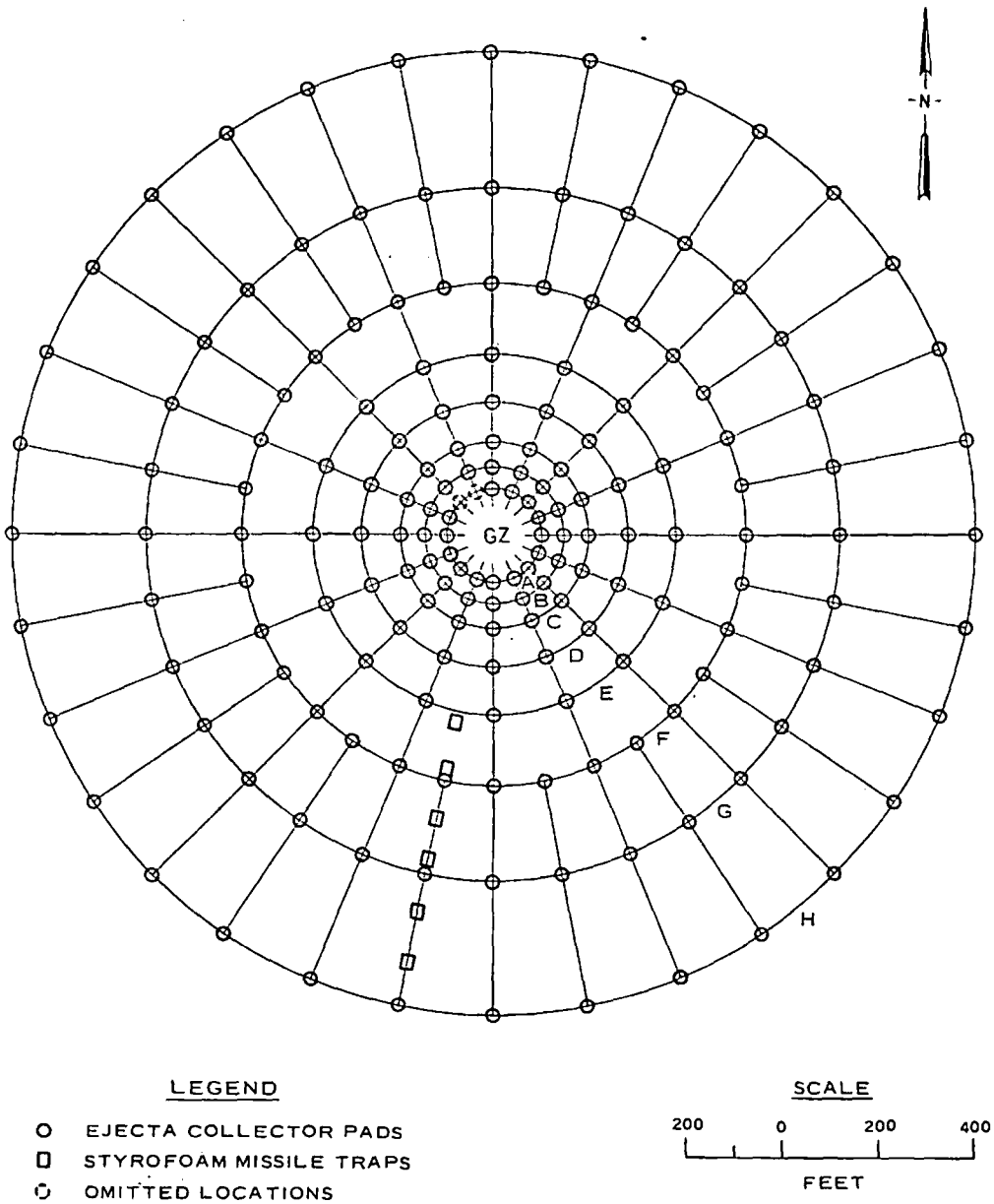

Figure 2.9 Ejecta dust-collector pad layout for MINE ORE, showing sampling stations and ring designations.

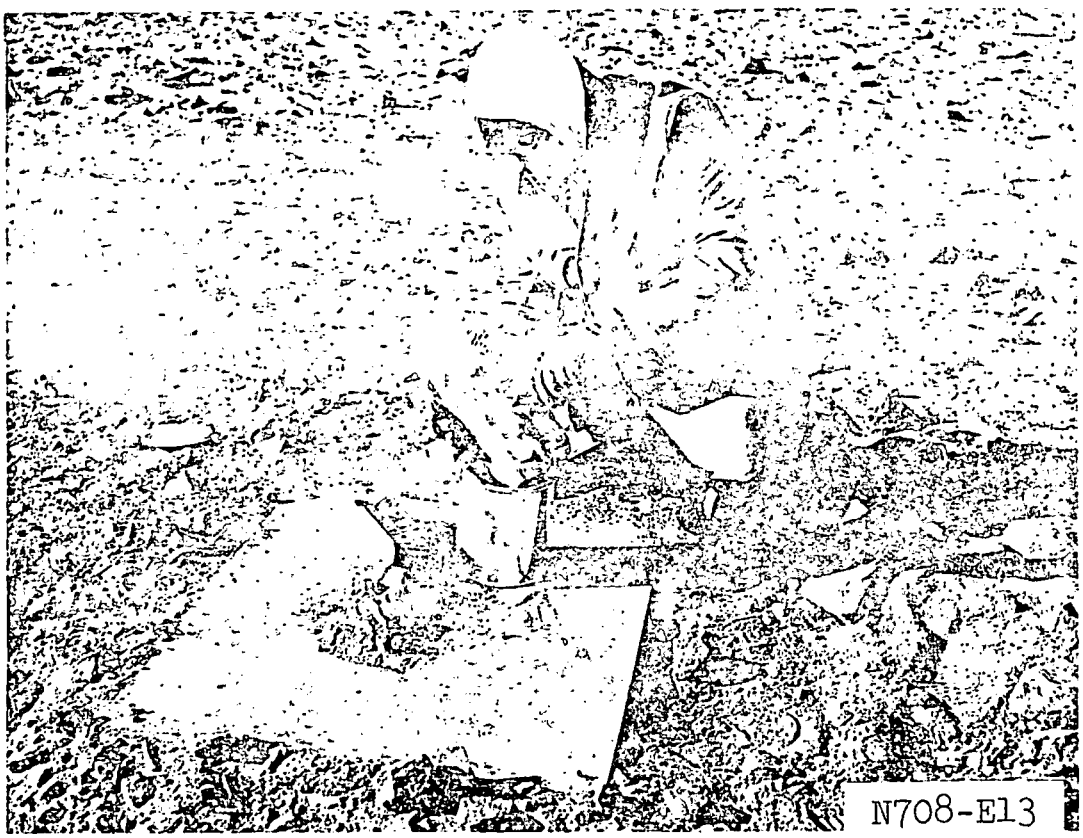

Figure 2.10 Recovery of samples from ejecta dust-collector pad.

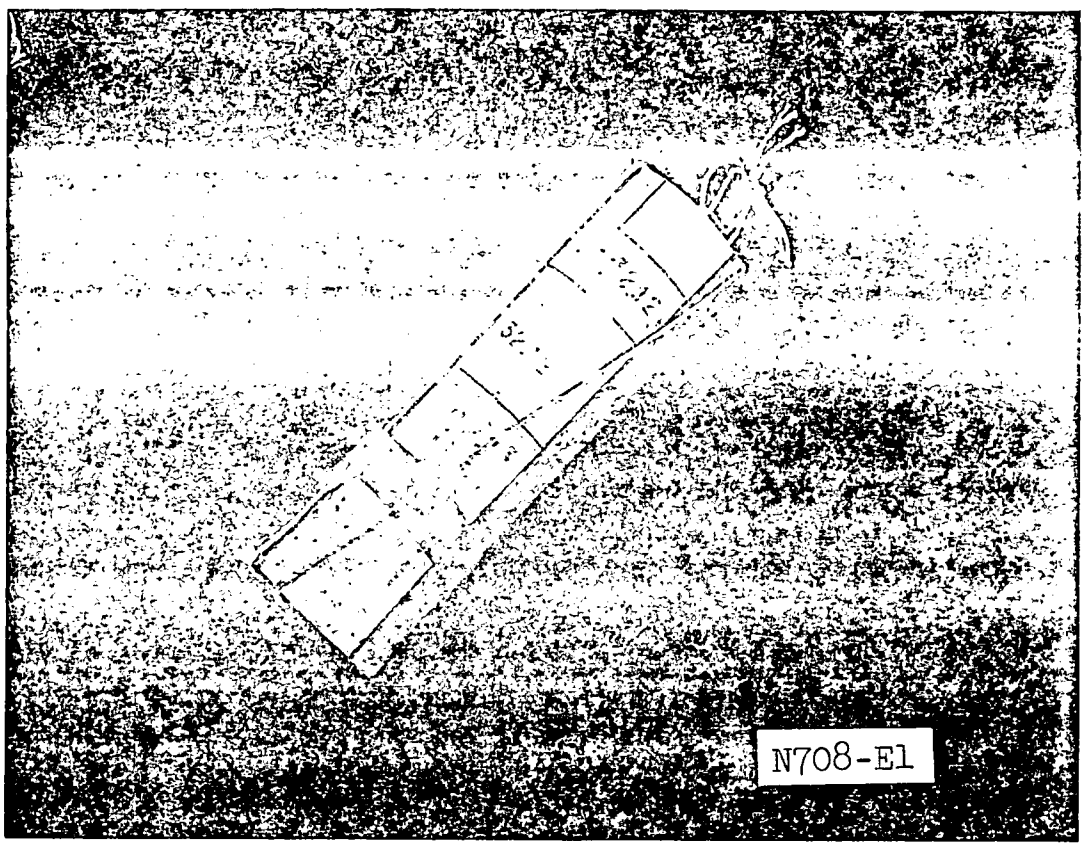

Figure 2.11 Cylindrical artificial missile used in MINE ORE.

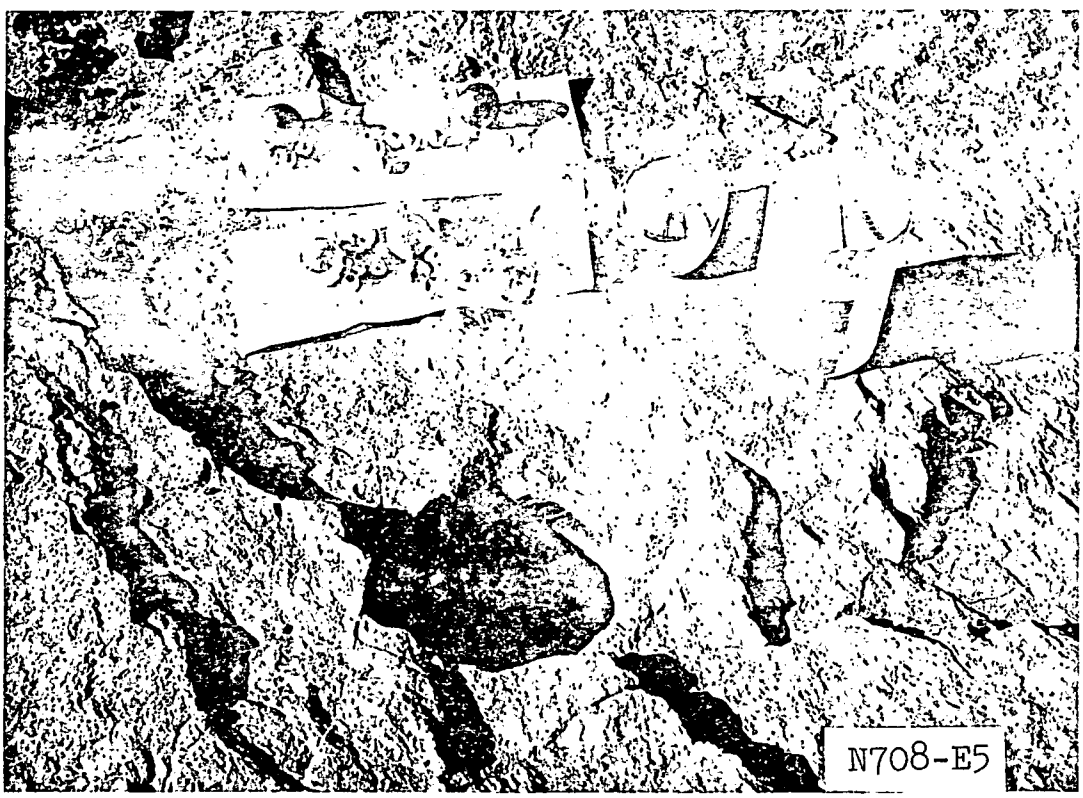

Figure 2.12 Spherical artificial missiles used in MINE ORE. Missile at right is encased in plaster of paris.

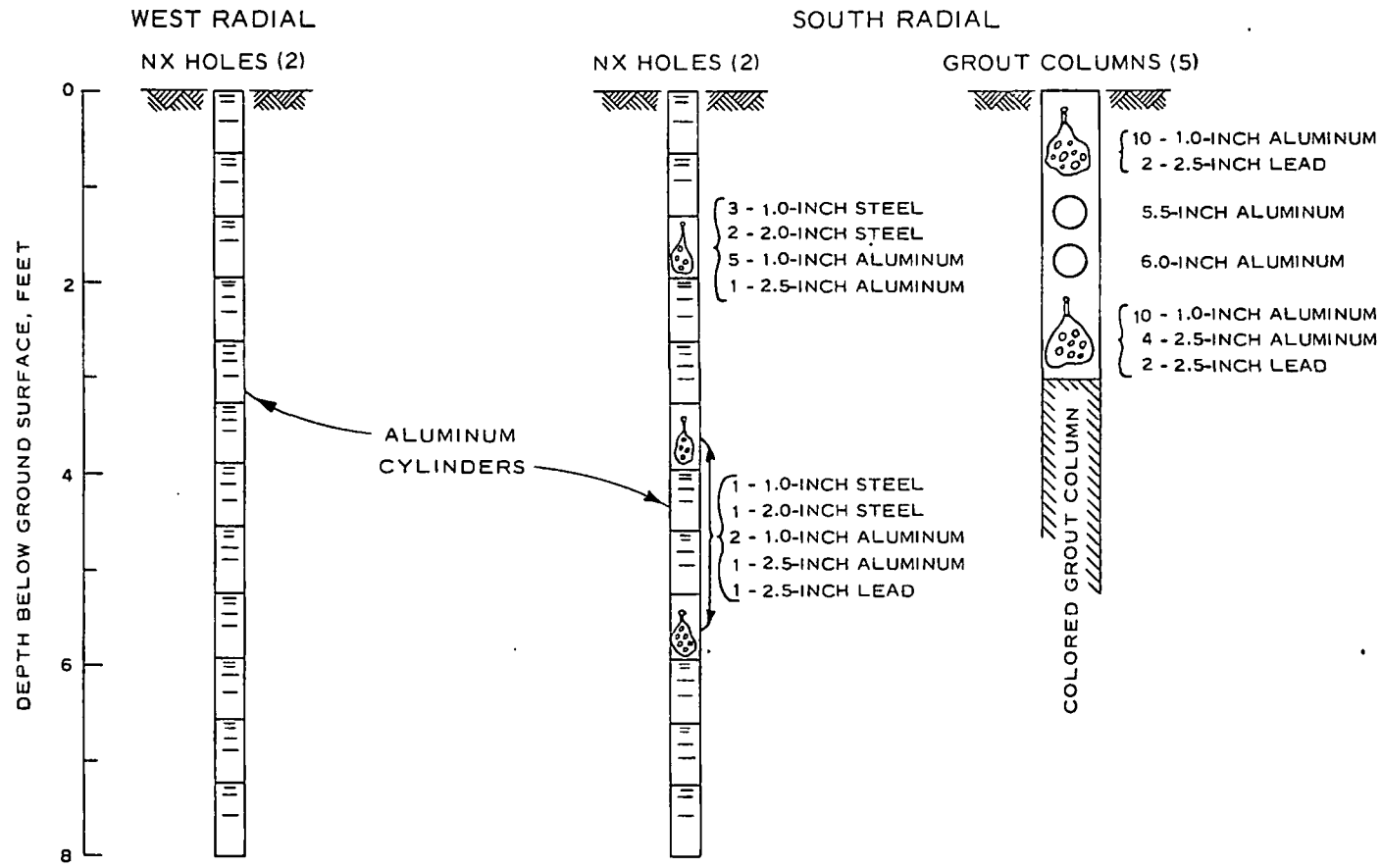

Figure 2.13 Preshot positions of artificial missiles, Event MINE ORE.

CHAPTER 3

PRESENTATION OF RESULTS

3.1 EJECTA DISTRIBUTION

Figure 3.1 is a postshot aerial photograph of the MINE ORE site showing the ejecta distribution pattern. Several distinct ejecta rays are visible, extending northwest, south-southwest, south, and east. The formation of these rays appeared to be controlled by the vertical joint faces found in the rock mass in the vicinity of GZ (Reference 11), the joint faces tending to deflect and channel a large portion of the ejecta along these rays. Between rays, distribution of discrete ejecta appeared to be random and less dense. The northwest ejecta ray was taken as typical and examined in some detail. It was found to be approximately 950 feet long. The numerical density of the missiles remained fairly constant at 10 to 12 missiles per square foot. However, the average size of the missiles (and thus the mass density) decreased with increasing distance from GZ. A few large missiles, greater than 1 foot in diameter, were found in the ray. Again, the frequency decreased with increased distance from GZ.

Although the jointing pattern of the rock was probably the single most important factor in the ejecta distribution (apart from test conditions of yield, medium, and geometry), other topographical and

vegetal features of the test site were also influential. The site sloped gently to the south and east at about 2 degrees, with missile ranges being greater in the downhill direction. A large hill was located approximately 1,800 feet west-southwest of GZ, restricting somewhat missile ranges in that direction. To the south of GZ, juniper and pine trees were removed to a distance of only 1,000 feet from GZ. Since missile ejection angles were small due to the high center of gravity of the charge geometry and there was evidence of considerable bounce and roll with accompanying comminution, these trees had a screening effect which reduced the range of missiles because of their flat trajectories.

Ambient wind conditions had no visible effect on the distribution of the discrete ejecta. The only part of the experiment subject to weather disturbance was the dust samples on the metal collector pads. However, the majority of these samples were collected immediately after the shot (within 6 hours), before they could be disturbed significantly by wind. The weather in the 2-week data collection period following the shot was cool but fair.

Maximum significant missile range for MINE ORE was 2,120 feet for a 1-pound missile lying south-southeast of GZ. A few smaller particles were noted 100 to 200 feet farther from GZ, giving a maximum range of about 2,300 feet. Figure 3.2 is a plane-table map of the long-range natural missiles in the southwest quadrant. The

maximum-range missiles were found downslope of GZ and roughly parallel to the main north-south jointing pattern of the rock. In other directions, the approximate periphery of missile distribution was as follows: north--1,600 feet; east--1,800 feet.

3.2 EJECTA MASS DENSITY, MINE ORE

3.2.1 Within the Crater Lip. Table 3.1 gives the size distribution and mass densities for the ejected material excavated from the MINE ORE crater lip. Examination of these data and Figure 2.3 shows that the ejecta was not evenly distributed around the crater, but was thickest to the east, south, and northwest. As with the missile-ejecta distribution, this distribution was probably controlled by the rock jointing system near GZ.

3.2.2 Beyond the Crater Lip. Tables 3.2 through 3.4 give the ejecta mass density beyond the crater lip. Table 3.2 contains the data from the photography stations which were used between the edge of the crater lip (100 feet from GZ) and 1,000 feet from GZ. The data include sample area, number of missiles, total ejecta weight in the area, and mass density. Table 3.3 gives the same information for the counting and weighing sectors used beyond 1,000 feet. Finally, Table 3.4 summarizes ejecta mass density, exclusive of pad samples, as a function of radial distance for the south and west radials.

The ejecta-dust density data from the metal collector pads are given in Tables 3.5 and 3.6. Samples were recovered from 152 (87 percent) of the pads. In Table 3.5, the average mass density for each ring is shown. Table 3.6 gives the average grain-size distribution for the ejecta on each ring, while Figure 3.3 presents grain-size distribution curves. The plots show that the material was mostly a uniformly graded, sand-sized alluvium. The curves for Rings A, B, and F show the influence of ejected rock missiles which landed randomly on pads in these rings.

3.3 MISSILE-TRAJECTORY EXPERIMENTS, MINE ORE

The results of the experiments designed to evaluate missile-trajectory parameters are discussed below. The tests included the artificial missiles, colored-grout column ejecta, and styrofoam missile traps.

3.3.1 Artificial Missiles. Table 3.7 presents the results of the artificial missile experiment, including only those missiles located and identified postshot. A total of 423 artificial missiles (cylinders and spheres) were emplaced preshot. Eighty-one, or 19 percent, were recovered, identified, and mapped postshot. Several other missiles were found, but they were badly deformed or too scarred to be identifiable. In Table 3.7, the identification number of each missile gives its initial position. For the cylinders, the

first digit identifies the radial on which the missile was located, the second digit gives the borehole number, and the third digit, on the right of the decimal, denotes the relative depth of that missile in the borehole. For example, Cylinder No. 31.5 was originally placed on Radial 3 (279 degrees azimuth), Borehole No. 1 (2.5 feet from GZ), and was the fifth missile down from the ground surface. Since all spheres were placed along the south radial, their identification numbers give only hole number (first digit) and nominal depth in feet (second digit). Thus, Sphere 43 was originally emplaced in Hole 4 (20 feet from GZ) at a depth of approximately 3 feet. The seven large spheres were identified by color or by a single number indicating borehole location. Figure 3.4 is a plane-table map of the postshot positions of the artificial missiles.

Most artificial missiles found had traveled less than 200 feet. Only three long-range artificial missiles were located: a 2-inch cylinder (32.2) located 1,662 feet along the west radial, an unidentified 1-inch quarter cylinder at 1,412 feet along the west radial, and a 1-inch cylinder (12.4) at 1,051 feet along the south radial. The maximum range for a sphere was 209 feet for a 1-inch aluminum sphere (41) originally located 20 feet from GZ at a depth of 0.98 foot. The large polished or painted aluminum spheres which were located traveled less than 210 feet and were not detected by the test photography.

3.3.2 Colored-Grout Ejecta. Figure 3.5 shows the postshot positions of the colored-grout ejecta. The maximum range for a piece of grout ejecta was 1,250 feet to the west of GZ. Average weight of the grout missiles was about 2 pounds. The majority of the colored-grout ejecta followed two of the ejecta rays, to the northwest and south-southwest. An analysis of initial position and range of the colored-grout ejecta in the study of crater formation is found in Reference 11.

3.3.3 Styrofoam Missile Traps. The measurements of terminal trajectory parameters obtained from the styrofoam missile traps are given in Table 3.8. The missile traps were placed too far from GZ to obtain a good sample of natural missiles. Those collected were very small, most of them being approximately 1 cm in diameter and weighing less than 1 gram. It was also noted that most had impact angles greater than 90 degrees, indicating that at the time of impact they were traveling toward GZ, evidently as a result of the negative-pressure phase and accompanying afterwinds.

3.4 EJECTA TRAP

An ejecta collector trap, installed at the request of the Boeing Company, was located about 75 feet northeast of GZ. This consisted of a 4-foot-square wooden box, placed in a natural depression in the overall rock formation. Although the depth varied

slightly across the bottom of the cavity, the average depth was about 38 inches. Sufficient grout was poured outside the box to bring the surrounding surface up to the top of the box.

The cavity was severely deformed by the blast, with only the west corner remaining intact. The east and west corners were filled with ejecta to ground level, while the north and south corners were filled to within 1.80 and 1.20 feet of ground level, respectively. The average thickness of deposition in the cavity was 2.5 feet. Since the trap was located beyond the edge of the crater lip in an area occupied only by discrete ejecta particles, this deposition indicates that a considerable amount of the material deposited had arrived by the process of rolling and bouncing along the ground surface rather than by direct missile trajectory.

3.5 MINE UNDER EJECTA

Although no crater or ejecta was expected from Event MINE UNDER, a rubble mound and some ejected material were observed after the blast. Presumably, this was the result of shallow spallation of the rock surface (possibly enhanced by pile-driving action by the wooden legs of the charge support platform) and elastic rebound. The ejecta field consisted of rock fragments thrown out in an irregular pattern around GZ. A plane-table map (Figure 3.6) was made of the larger ejecta missiles and the outer fringes of the ejecta distribution,

where the survey was restricted to missiles at least 1 pound in weight. The maximum missile range observed was 695 feet for a 1-pound missile lying northwest of GZ. The major concentration of ejecta, an oval-shaped cluster, lay approximately 250 feet southwest of GZ. Smaller concentrations were found to the southeast and north. The southeast and southwest concentrations were roughly perpendicular to a main north-south joint in the rock on the west side of GZ. These concentrations followed smaller east-west joints. The small northern concentration paralleled the main joint. However, the effect of the rock jointing on the ejecta distribution was not as evident here as it was for MINE ORE. This is presumably due to the fact that the spallation process involved only the top few inches of the rock surface and the ejecta was not subject to deflection and channeling by vertical joints as was the ejecta from MINE ORE.

TABLE 3.1 EJECTA SIZE DISTRIBUTION AND MASS DENSITY WITHIN AND ADJACENT TO THE CRATER LIP, MINE ORE

Radial	Section	Weight of Ejecta of Indicated Sizes, inches				Total Weight of Ejecta	Areal Mass Density
		>12	6-12	3-6	<3		
		pounds	pounds	pounds	pounds	pounds	lb/ft^2
1	1	16,970	4,960	7,460	7,040	36,430	132
	2, 3	4,788	1,310	4,330	4,670	15,098	14
3	1	--	--	--	--	--	--
	2	488	587	268	487	1,830	4
	3	105	205	318	546	1,174	2
4	1	--	--	--	--	--	--
	2, 3	25,360	5,300	9,190	16,220	56,070	52
5	1	5,980	1,370	2,720	3,060	13,130	95
	2	630	660	180	1,260	2,703	20
	3	150	125	109	75	459	3
7	1, 2, 3	36,470	5,710	9,620	17,860	69,660	168

TABLE 3.2 EJECTA MASS DENSITY FROM 1.2 [illegible] STATIONS, MINE SRN

Distance[a] from GZ	Station[b] Area	[illegible] Missiles	Calculated Ejecta Weight	Areal Mass Density
feet	ft^2		pounds	lb/ft^2
West Radial:				
100	20	18	22.11	1.11
115	20	47	31.16	1.56
130	20	3[illegible]	1[illegible]	$\times 10^{-1}$
145	20	[illegible]	6.30	3.15×10^{-1}
160	20	[illegible]	4.77	2.39×10^{-1}
185	20	33	[illegible].13	4.57×10^{-1}
210	20	14	1.05	5.25×10^{-2}
235	20	10	1.41	7.05×10^{-2}
[illegible]	72	11	[illegible]	1.11×10^{-1}
[illegible]	72	[illegible]	[illegible]	7.99×10^{-1}
[illegible]	72	[illegible]	[illegible]	7.31×10^{-1}
[illegible]	72	[illegible]	[illegible]	1.17×10^{-2}
[illegible]	72	[illegible]	[illegible]	7.21×10^{-3}
[illegible]	272	11	[illegible]	$[illegible] \times 10^{-2}$
[illegible]	272	[illegible]	[illegible]	3.40×10^{-2}
710	272	11	16.19	$[illegible] \times 10^{-2}$
805	272	11	7.89	2.90×10^{-2}
905	272	3	1.69	6.25×10^{-3}
1,000	272	5	2.09	7.68×10^{-3}
South Radial:				
100	20	44	127.20	6.36
115	20	49	131.[illegible]	6.58
130	20	33	13[illegible]	6.78
145	20	28	123.82	6.19
165	20	49	145.55	7.28
185	20	43	49.55	2.48
210	20	38	131.62	6.58
235	20	22	16.63	8.32×10^{-1}
270	72	15	28.27	3.93×10^{-1}
385	72	6	13.72	1.91×10^{-1}
435	72	6	8.14	1.13×10^{-1}
490	72	2	10.35	1.44×10^{-1}
555	272	16	8.83	3.25×10^{-2}
630	272	24	12.12	4.46×10^{-2}
710	272	21	25.50	9.38×10^{-2}
805	272	16	9.64	3.54×10^{-2}
905	272	9	6.51	2.39×10^{-2}
1,000	272	23	23.65	8.69×10^{-2}

[a] Stations 300 and 340 on the south radial and 340 on the west radial fell within access road.

[b] Station areas reduced from actual grid size due to trimming and overlapping of photographs.

TABLE 3.3 EJECTA MASS DENSITY IN COUNTING AND WEIGHING SECTORS, MINE ORE

Sector	Distance from GZ[a]	Sector Area	No. of Missiles	Ejecta Weight	Areal Mass Density
	feet	ft^2		pounds	lb/ft^2
S-1	1,050	18,300	13	18	9.84×10^{-4}
S-2	1,050	18,300	70	162	9.40×10^{-3}
S-3	1,150	20,000	13	65	3.25×10^{-3}
S-4	1,150	20,000	29	49	2.45×10^{-3}
S-5	1,250	21,850	1	1	4.58×10^{-5}
S-6	1,250	21,850	6	12	5.49×10^{-4}
W-1	1,050	18,300	44	96	5.25×10^{-3}
W-2	1,050	15,600	6	7	4.49×10^{-4}
W-3	1,150	20,000	24	37	1.85×10^{-3}
W-4	1,150	17,450	6	7	4.01×10^{-4}
W-5	1,250	21,850	16	17	7.78×10^{-4}
W-6	1,250	19,150	5	5	2.61×10^{-4}
W-7	1,350	23,450	11	12	5.12×10^{-4}
W-8	1,350	20,850	6	7	3.36×10^{-4}
W-9	1,450	25,250	3	3	1.19×10^{-4}
W-10	1,450	22,700	5	6	2.64×10^{-4}
W-11	1,550	26,450	9	15	5.67×10^{-4}
W-12	1,550	25,550	4	6	2.35×10^{-4}

[a] To center of sector.

TABLE 3.4 EJECTA MASS DENSITY AS A FUNCTION OF RADIAL DISTANCE FROM GZ, MINE ORE

Distance from GZ	Areal Mass Density	
	West Radial	South Radial
feet	lb/ft^2	lb/ft^2
100	1.11	6.36
115	1.56	6.58
130	9.28×10^{-1}	6.78
145	3.15×10^{-1}	6.19
165	2.39×10^{-1}	7.28
185	4.57×10^{-1}	2.48
210	5.25×10^{-2}	6.58
235	7.05×10^{-2}	8.32×10^{-1}
270	5.11×10^{-2}	3.93×10^{-1}
300	7.22×10^{-1}	--
340	--	--
385	7.31×10^{-1}	1.91×10^{-1}
435	1.17×10^{-2}	1.13×10^{-1}
490	7.01×10^{-2}	1.44×10^{-1}
555	5.44×10^{-2}	3.25×10^{-2}
630	9.40×10^{-2}	4.46×10^{-2}
710	5.95×10^{-2}	9.38×10^{-2}
805	2.90×10^{-2}	3.54×10^{-2}
905	6.95×10^{-3}	2.39×10^{-2}
1,000	7.68×10^{-3}	8.69×10^{-2}
1,050	2.85×10^{-3}	5.19×10^{-3}
1,150	1.13×10^{-3}	2.85×10^{-3}
1,250	5.20×10^{-4}	2.97×10^{-4}
1,350	4.24×10^{-4}	--
1,450	1.92×10^{-4}	--
1,550	4.01×10^{-4}	--

TABLE 3.5 AVERAGE EJECTA-DUST DENSITY

Ring	Distance from GZ	Average Weight of Ejecta per Pad	Areal Mass Density
	feet	pounds	lb/ft^2
A	100	15.92	2.27
B	140	31.02	4.42
C	190	18.29	2.61
D	270	5.93	0.84
E	370	2.32	0.33
F	520	2.40	0.34
G	720	0.72	0.10
H	1,000	0.11	0.02

TABLE 3.6 AVERAGE GRAIN-SIZE DISTRIBUTION FOR EJECTA DUST

Ring	Weight of Material Retained on and Percentage of Material Finer than Indicated Sieve										
	1-inch		1/2-inch		No. 4		No. 16		No. 200		Pan
	Retained	Passing	Retained	Passing	Retained	Passing	Retained	Passing	Retained	Passing	Retained
	pounds	percent	pounds	percent	pounds	percent	pounds	percent	pounds	percent	pounds
A	5.76	63	0.58	59	0.67	55	4.09	29	3.04	10	1.60
B	8.02	73	1.19	69	1.50	64	3.08	54	11.39	15	4.30
C	2.29	87	0.30	85	0.49	82	1.84	72	9.13	21	3.79
D	0.77	88	0.15	86	0.23	82	0.81	69	3.33	16	1.05
E	0.27	88	0.05	86	0.06	83	0.27	71	1.31	15	0.37
F	1.05	52	0.02	51	0.04	49	0.19	40	0.63	11	0.27
G	0.15	80	0.01	79	0.02	76	0.09	64	0.35	17	0.12
H	0.02	80	Negli-gible	80	0.01	70	0.01	60	0.04	20	0.02

TABLE 3.7 ARTIFICIAL MISSILE DATA

Missile No.	Cylinder Length or Sphere Diameter	Initial Position			Final Position		Distance Traveled
		Radial Azimuth	Distance from GZ	Depth from Surface	Radial Azimuth	Distance from GZ	
	inches	degrees	feet	feet	degrees	feet	feet
Aluminum Cylinders, 2.5-inch Diameter:							
11.5	1[a]	195	2.5	0.60	211	19	17
11.5	1[b]	195	2.5	0.60	271	53	53
11.5	1	195	2.5	0.69	249	11	11
11.11	2	195	2.5	6.69	195	3	1
11.11	4	195	2.5	6.94	195	3	1
12.4	1	195	7.5	0.27	200	1,051	1,043
12.5	1[a]	195	7.5	0.91	213	222	215
12.5	1	195	7.5	1.00	205	257	249
12.5	2	195	7.5	1.12	194	195	237
12.5	4	195	7.5	1.37	211	57	49
12.6	1	195	7.5	2.23	215	72	65
12.6	2	195	7.5	2.35	211	74	66
12.6	4	195	7.5	2.60	203	58	55
31.2	4	279	2.5	0.78	163	42	44
31.5	4	279	2.5	2.64	208	16	16
32.2	2	279	7.5	0.39	284	1,662	1,654
32.6	2	279	7.5	3.15	269	67	59
32.6	4	279	7.5	3.40	255	90	83
32.7	1	279	7.5	3.79	256	50	43
32.8 (2)	1[a]	279	7.5	4.34	279	12	5
32.8	1[b]	279	7.5	4.34	279	12	5
32.8	1	279	7.5	4.43	279	12	5
32.9	1	279	7.5	4.96	254	10	2
Spheres:							
1	6 A[c]	195	5.0	2.13	179	33	28
3	6 A	195	15.0	1.66	194	216	201
4	6 A	195	20.0	1.24	203	132	112
5	6 A	195	25.0	1.62	192	147	122
Orange	5-1/2 A	195	15.0	2.06	193	200	185
Red	5-1/2 A	195	25.0	2.12	200	35	10
23	2-1/2 A	195	10.0	3.42	192	135	125
23	2-1/2 A	195	10.0	3.42	192	135	125
23	2-1/2 A	195	10.0	3.42	205	145	135
33	2-1/2 A	195	15.0	2.70	199	195	180
33	2-1/2 A	195	15.0	2.70	196	174	159
33	2-1/2 A	195	15.0	2.70	195	159	144
33	2-1/2 A	195	15.0	2.70	198	156	141

(Continued)

[a] Cylinder divided into quarter wedges.
[b] Cylinder divided into half wedges.
[c] A denotes aluminum; L denotes lead.

TABLE 3.7 ARTIFICIAL MISSILE DATA (CONCLUDED)

Missile No.	Cylinder Length or Sphere Diameter	Initial Position			Final Position		Distance Traveled
		Radial Azimuth	Distance from GZ	Depth from Surface	Radial Azimuth	Distance from GZ	
	inches	degrees	feet	feet	degrees	feet	feet
Spheres (Continued):							
43	2-1/2 A	195	20.0	1.61	202	134	114
43	2-1/2 A	195	20.0	1.61	207	121	102
43	2-1/2 A	195	20.0	1.61	208	92	73
53	2-1/2 A	195	25.0	4.87	202	31	6
53	2-1/2 A	195	25.0	4.87	202	31	6
53	2-1/2 A	195	25.0	4.87	202	31	6
53	2-1/2 A	195	25.0	4.87	215	37	16
21	1 A	195	10.0	2.67	193	197	187
23	1 A	195	10.0	3.42	195	133	123
23	1 A	195	10.0	3.42	193	106	96
23	1 A	195	10.0	3.42	194	170	160
31	1 A	195	15.0	1.29	195	219	204
31	1 A	195	15.0	1.29	200	206	192
31	1 A	195	15.0	1.29	193	193	182
31	1 A	195	15.0	1.29	194	187	172
33	1 A	195	15.0	2.70	199	191	176
33	1 A	195	15.0	2.70	198	178	163
33	1 A	195	15.0	2.70	194	115	100
33	1 A	195	15.0	2.70	201	114	99
33	1 A	195	15.0	2.70	199	191	176
33	1 A	195	15.0	2.70	200	152	137
41	1 A	195	20.0	0.98	199	223	203
41	1 A	195	20.0	0.98	197	229	209
41	1 A	195	20.0	0.98	197	224	204
41	1 A	195	20.0	0.98	197	224	204
41	1 A	195	20.0	0.98	201	181	161
41	1 A	195	20.0	0.98	197	165	145
41	1 A	195	20.0	0.98	197	173	153
43	1 A	195	20.0	1.61	201	103	83
43	1 A	195	20.0	1.61	208	110	90
43	1 A	195	20.0	1.61	208	110	90
53	1 A	195	25.0	4.87	215	37	16
53	1 A	195	25.0	4.87	215	37	16
53	1 A	195	25.0	4.87	215	37	16
53	1 A	195	25.0	4.87	215	37	16
53	1 A	195	25.0	4.87	215	37	16
53	1 A	195	25.0	4.87	215	37	16
53	1 A	195	25.0	4.87	215	37	16
53	1 A	195	25.0	4.87	215	37	16
31	2-1/2 L	195	15.0	1.29	193	192	177
41	2-1/2 L	195	20.0	0.98	200	184	164
43	2-1/2 L	195	20.0	1.61	207	85	65
43	2-1/2 L	195	20.0	1.61	201	102	82
53	2-1/2 L	195	25.0	4.87	215	37	16

TABLE 3.8 MISSILE IMPACT DATA FROM STYROFOAM MISSILE TRAPS

Missile No.	Distance from GZ	Missile Weight	Impact Angle[a]	Depth of Penetration
	feet	grams	degrees	feet
1	400	1.07	98.0	0.082
2	400	0.51	96.0	0.140
3	400	0.09	91.5	0.059
4	400	0.35	89.0	0.205
5	400	4.29	109.5	0.090
6	400	0.15	88.0	0.132
7	400	0.09	92.5	0.063
8	400	0.21	92.0	0.078
9	500	0.40	100.5	0.165
10	500	0.35	108.5	0.100
11	500	0.30	99.0	0.067
12	500	0.09	87.5	0.081
13	500	0.92	112.0	0.036
14	500	0.21	78.0	0.036
15	600	0.10	92.0	0.045
16	600	2.80	90.5	0.069
17	800	2.96	~100	0.070

[a] Sketch illustrating impact angle:

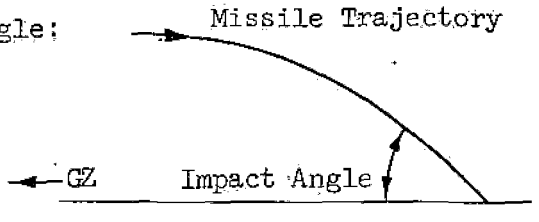

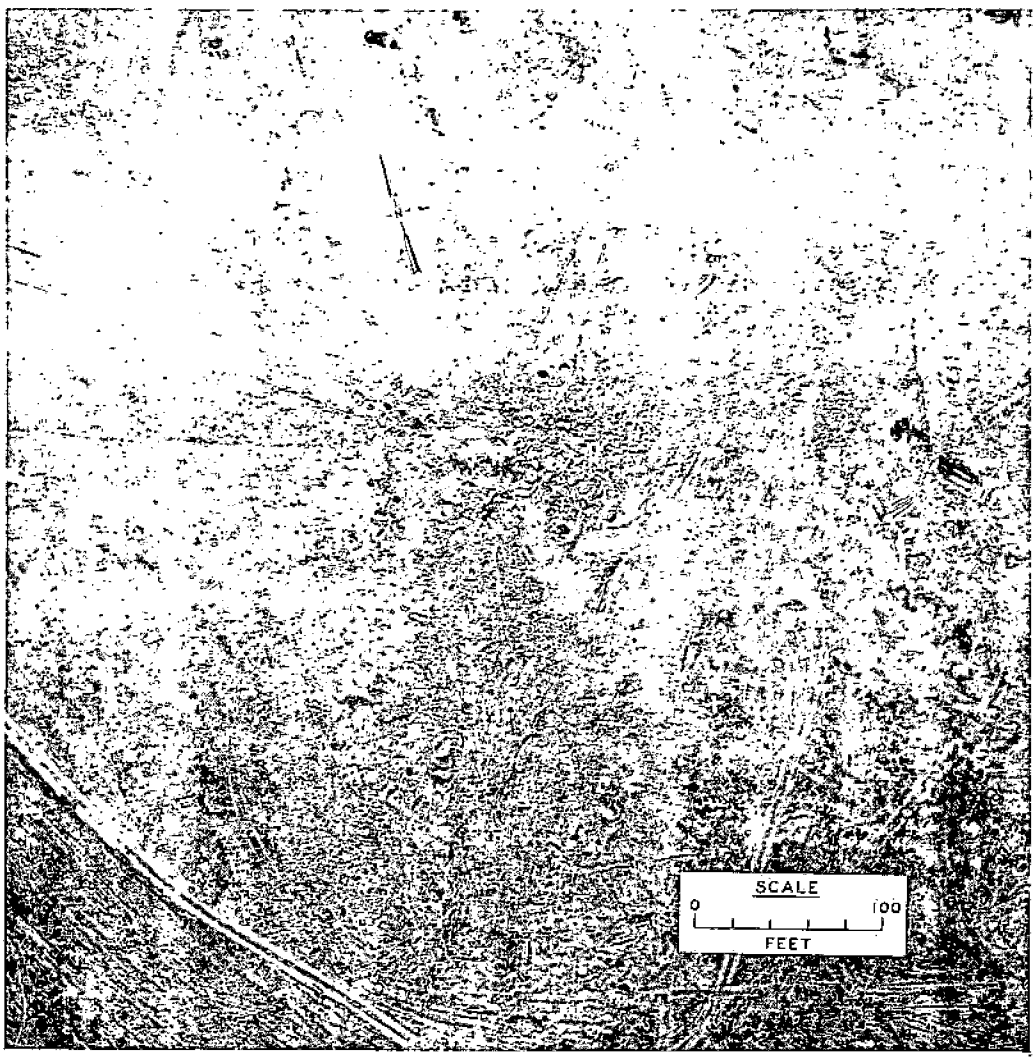

Figure 3.1 Ejecta distribution for the MINE ORE Event.

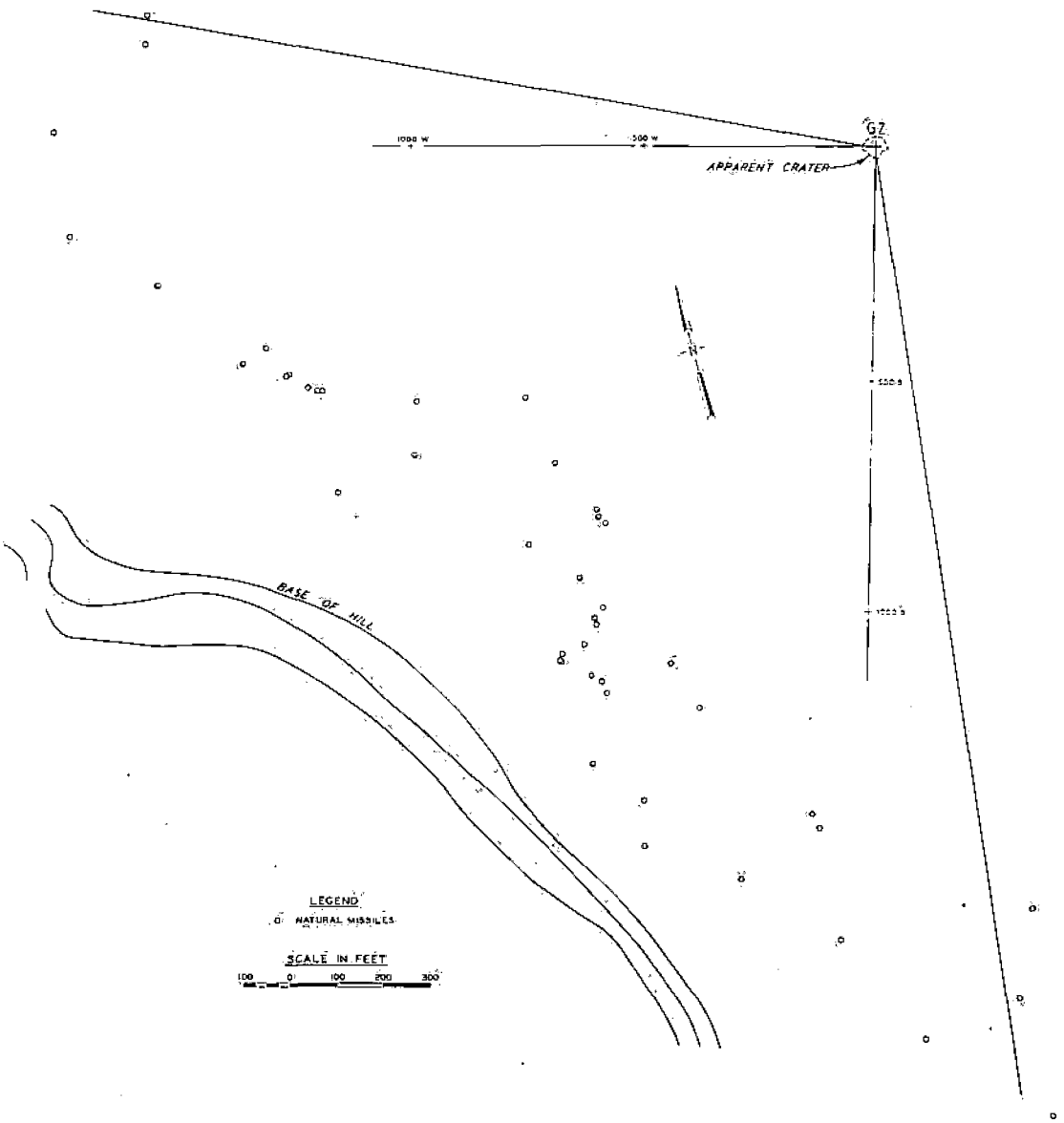

Figure 3.2 Outer limit of ejecta distribution, approximate southwest quadrant of MINE ORE.

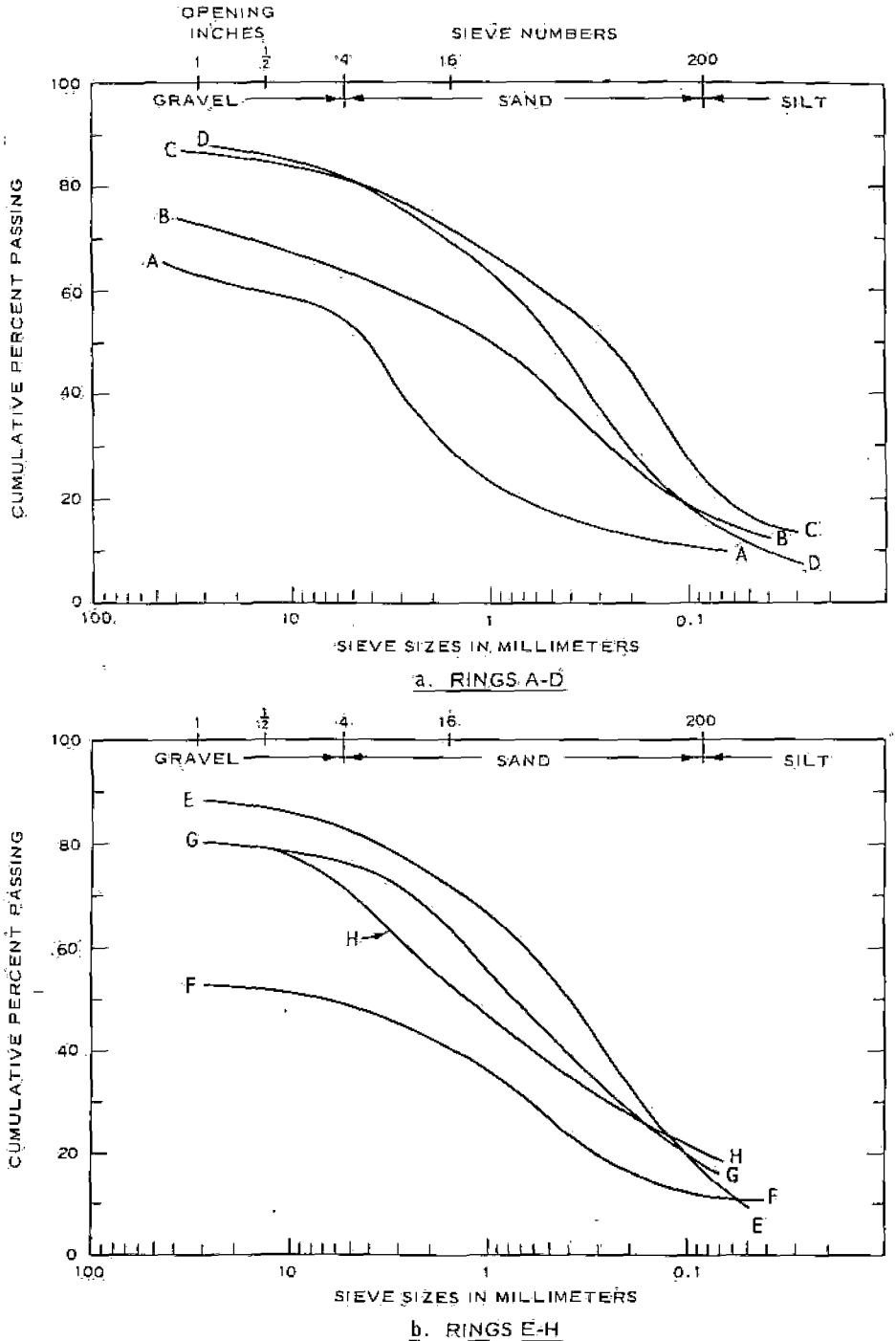

Figure 3.3 Grain-size distribution of ejecta dust, Rings A-H, MINE ORE.

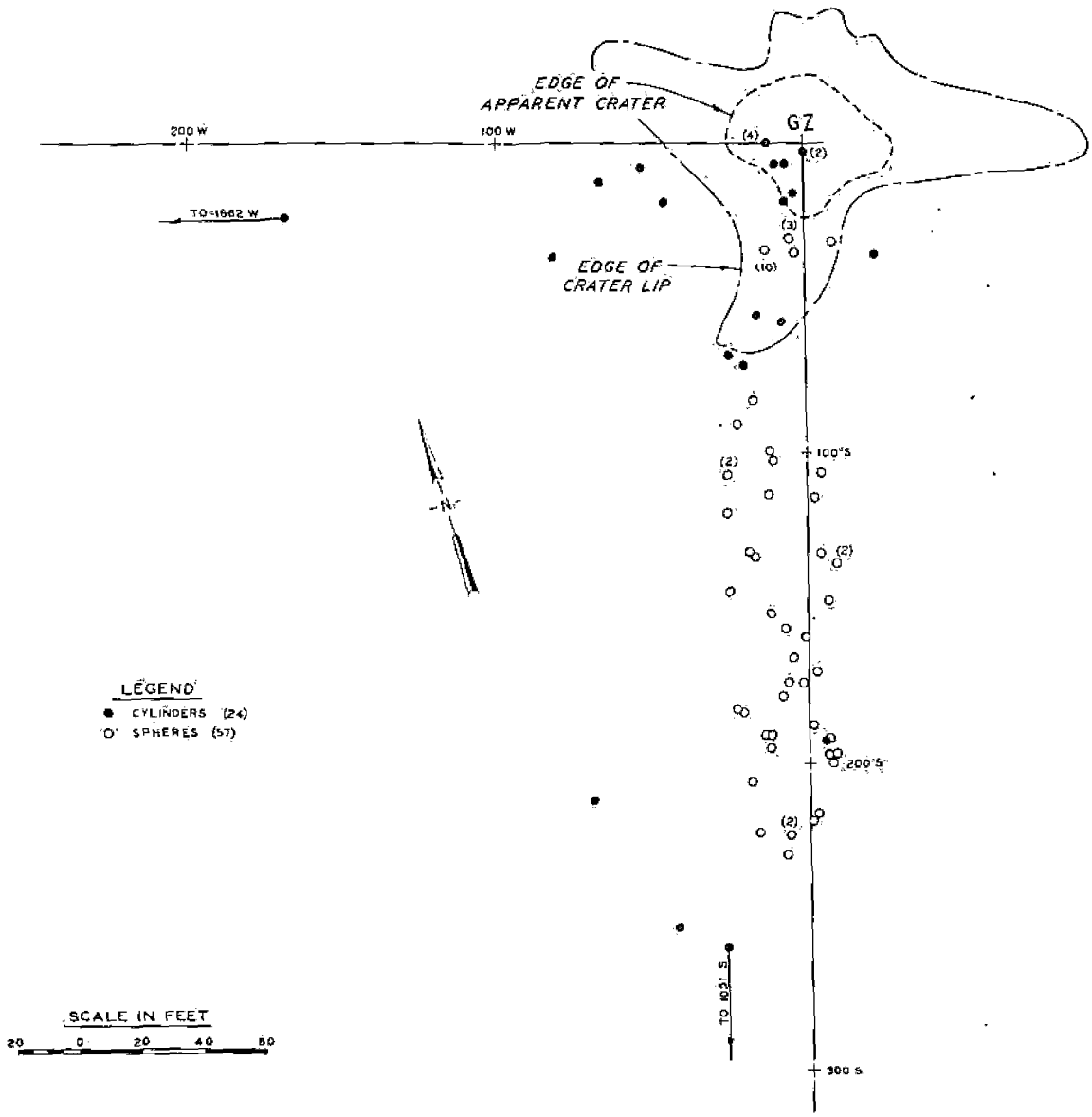

Figure 3.4 Postshot positions of artificial missiles, MINE ORE.

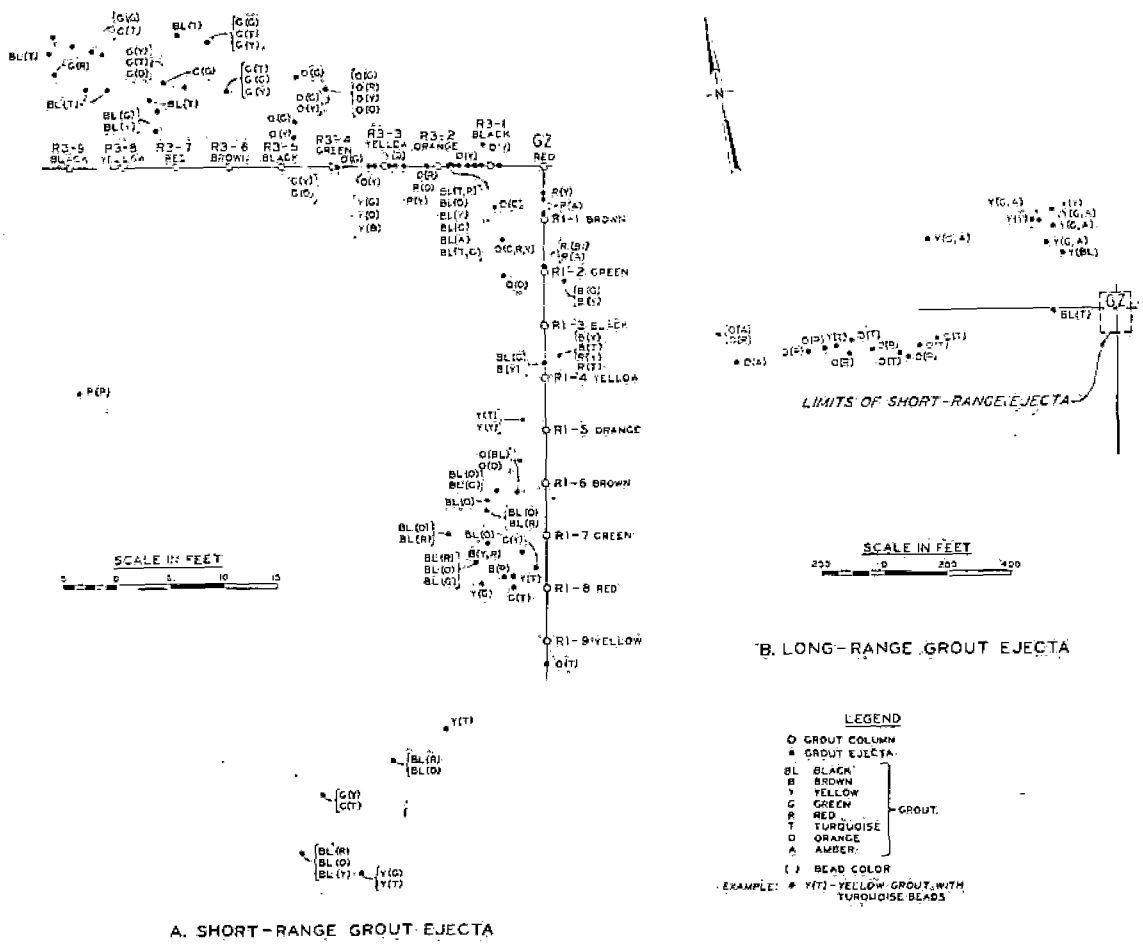

Figure 3.5 Postshot positions of colored-grout ejecta, MINE ORE.

Figure 3.6 MINE UNDER ejecta distribution, showing a partial plane-table survey of the larger (diameter ≥1 foot) natural missiles and the outer periphery of missiles at least 1 pound in weight.

CHAPTER 4

DISCUSSION OF RESULTS, MINE ORE EVENT

4.1 EJECTA MASS DENSITY, VOLUME, AND AZIMUTHAL DISTRIBUTION

The primary objective of this study was to obtain data on ejecta mass density and azimuthal distribution. The test procedures used to fulfill this objective (collector pads; camera, mount, and grid; counting sectors) provided good information on the larger particles, but were of doubtful value with regard to the finer particles (say 1/2 inch or less), especially beyond the C or D rings.

Figure 4.1 shows graphically the areal mass density plotted as a function of radial distance from GZ. The density data in this plot include those obtained from the lip excavation, photographic techniques, and the counting sectors. Data for the crater lip and south and west radials have been fitted to straight lines on logarithmic paper by the method of least squares. Additionally, an average, overall fit of the data is presented. It compares favorably with the distribution observed in other explosion tests in rock or cohesive-type materials (References 5, 12, and 13), especially when differences in shot geometry are taken into consideration. From the equation for average areal distribution, the total weight of ejected material E_w can be calculated as follows:

$$E_w = 2\pi \int_{r_a}^{\infty} \delta R \, dR \qquad (4.1)$$

(for notation, see Figures 1.1 and 4.1). The lower limit is taken to correspond with the average crater radius, although the distance r_h is theoretically correct. For crater and lip shapes like those of the MINE ORE Event, the error thus incurred is considered negligible. Similarly, experience has shown that the integration may be carried to infinity without significantly affecting results. Substituting,

$$E_W = 6.28 \int_{23}^{\infty} \left(3.90 \times 10^6 \, R^{-2.95}\right) R \, dR$$

$$= 1.32 \times 10^6 \text{ pounds}$$

The volume of ejecta, based upon the assumption of granitic density of 162 pcf and making no allowances for bulking, is found to be approximately 300 yards^3, probably significant to only the first integer.

An examination of the ejecta data from the photographic stations and counting sectors showed no clear relation between mean ejecta size and radial distance. However, these covered a small fraction of the total area, and an overall, visual survey showed a decrease in both size and missile numbers with increasing radial distance. This was particularly evident in the ejecta rays. The mean equivalent diameter for a piece of ejecta beyond the crater lip was about 3 inches. The average size in the sampled area of the crater lip (Figure 2.3) was between 6 and 12 inches, based upon the sieve-analysis

data in Table 3.1. The maximum-size particle ejected beyond the crater lip had an equivalent diameter of about 3 feet. It was located approximately 260 feet northwest of GZ. The largest particle in the crater lip was about 5 by 4 by 2-1/2 feet (about 3,100 pounds) located in Sector 3 of Radial 4 (Figure 2.3).

The most striking feature of the azimuthal distribution in this experiment was the pronounced ejecta rays, both in the crater lip and beyond (Figure 3.1). These rays indicate the strong dependence of ejecta distribution in rock on the site geology. The most influential factor in this distribution was the jointing pattern of the rock; comparison of ejecta-ray orientation and direction of major rock jointing in the crater (Figure 4.2) showed that the rays were very nearly parallel to major rock-joint faces. A specific example was the scarcity of ejecta directly north of GZ. A large vertical joint face north of GZ apparently deflected practically all of the ejecta originally traveling in a northerly direction into the northwest and east rays. All of the major ejecta rays can thus be traced to parallel joint faces within the crater area (Reference 11). Azimuthal distribution is illustrated graphically in Figure 4.3. For this purpose, data from close-in (Rings A-D) collector pads have been included with those from other sources.

4.2 EJECTA MISSILE RANGES

The range of maximum ejecta distances which might be expected

from the calculations in Chapter 1 is around 1,000 to 4,000 feet. This wide variation reflects the uncertainty concerning the origin of the ejection process. Calculations based upon a scouring action by the shock front provide the lower limit of maximum-distance predictions. The most promising approach to determination of ejecta ranges would appear to be by scaling according to charge yields, but here the choice of scaling exponents produces a wide variation of results. In addition to the factors discussed in Chapter 1, there were a number of physical characteristics of the site which may have affected scaling relations between the calibration series and MINE ORE, such as joint pattern, rock competence, and the various topographical features. Further, more detailed data will probably be necessary to establish a workable scaling exponent for this particular geometry; based upon the MINE SHAFT data now available, it appears certainly to lie in the range of $W^{1/4}$ to $W^{1/3}$, and at this point conforms very well with $W^{0.3}$.

The range within which 90 percent of ejected material falls is a useful figure, since it denotes the limit of an area within which the missile population is relatively dense. Based on weight, the 90 percent ejecta limit (or any desired limit) may be calculated from Equation 4.1. Again using the average curve from Figure 4.1,

$$E_{W_{90}} = 6.28 \int_{23}^{R_{90}} \left(3.90 \times 10^{6} R^{-2.95}\right) R \, dR$$

where

$E_{w_{90}}$ = 90 percent of the total weight of ejecta and

R_{90} = the 90 percent limit of ejected material

Thus

$$(0.90)(1.32 \times 10^6) = 2.45 \times 10^7 \left[\frac{R_{90}^{-0.95}}{-0.95} - \frac{(23)^{-0.95}}{-0.95} \right]$$

and

$$R_{90} = 263 \text{ feet}$$

Similar calculations can be made for debris falling beyond the crater lip. This was done for the south and west radials, using a lower limit of integration = 100 feet, and the results indicate that, on the average, 90 percent of the ejected material falling beyond the crater lip is contained within a radius of 1,375 feet.

4.3 SECONDARY EXPERIMENTAL OBJECTIVES

Between the grout-column and artificial-missile data, sufficient information was obtained to permit certain conclusions on the mechanics of the MINE ORE crater formation. This analysis is contained in Reference 11.

The definition of ejecta trajectories is largely dependent upon correlation of artificial-missile data with test photography. Additional time will be required to accomplish this secondary objective. Analysis of the test photography (Reference 14) has, however, provided

valuable data for this purpose. Ejecta speeds on the order of 600 ft/sec were observed upon emergence from the fireball. It is interesting to note that the velocity values reported in Reference 14 also indicate a scaling factor of approximately $W^{0.3}$. Ejection angles (with the horizontal) were very close to that assumed in Chapter 1. Unfortunately, camera failure precluded observation of much of the ejecta after about 2 seconds following detonation. Projections of the observed portions of these trajectories (in Reference 14) generally result in greater ranges than actually occurred, especially when the probable bounce and roll of the individual particles are considered. Although the middle and terminal portions of ejecta trajectories are still incompletely understood, it appears that an analysis of the photography and artificial-missile data, taking into consideration such external forces as afterwinds, may contribute to a solution of the problem.

The evaluation of natural missile hazards will also require more time than has been available for preparation of this report. The establishment of a usable scaling exponent for ejecta range is an important step in the realization of this objective, which must also include a statistical study of areal distribution for various particle sizes at various ranges.

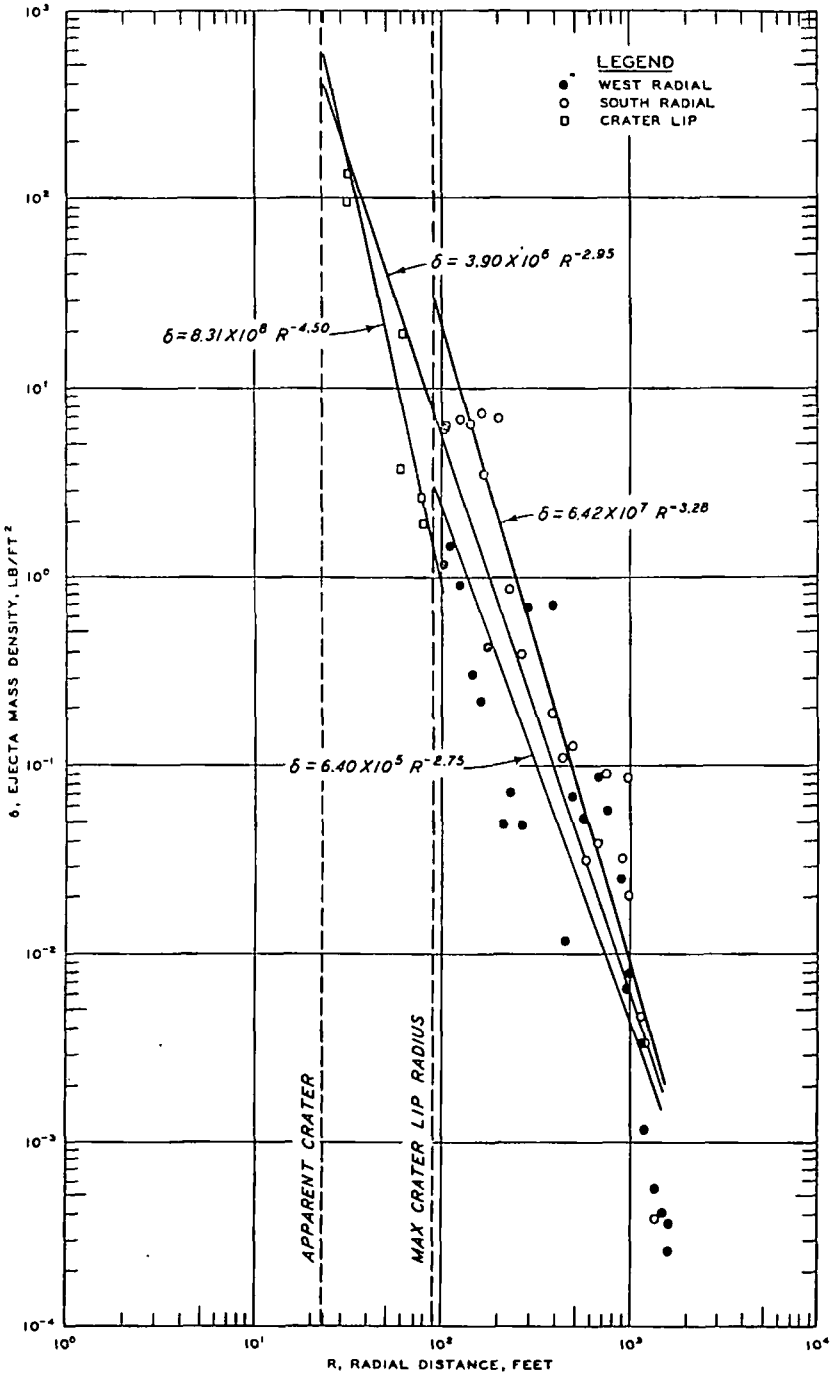

Figure 4.1 Areal mass density of ejecta as a function of distance from GZ, Event MINE ORE.

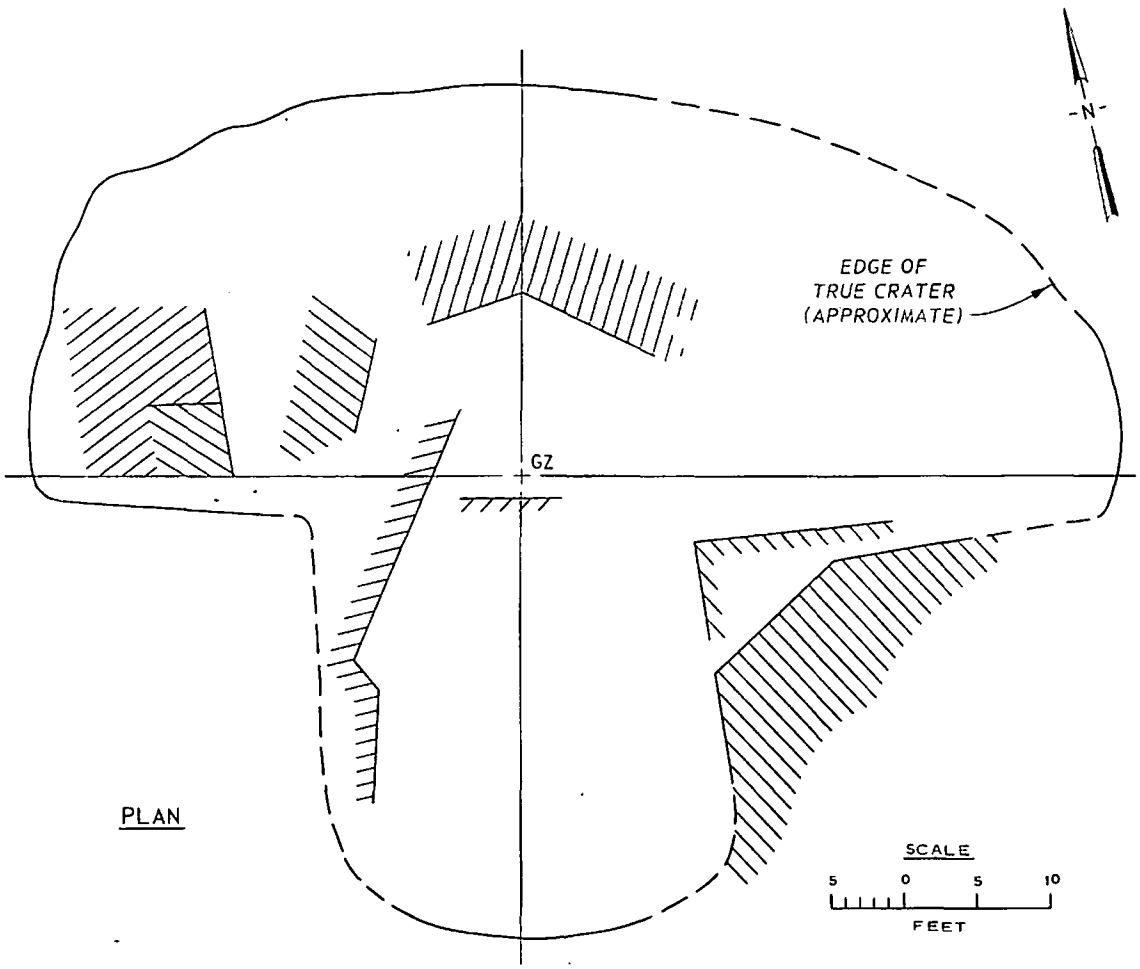

Figure 4.2 Rock-joint faces which affected MINE ORE ejecta distribution (Reference 11).

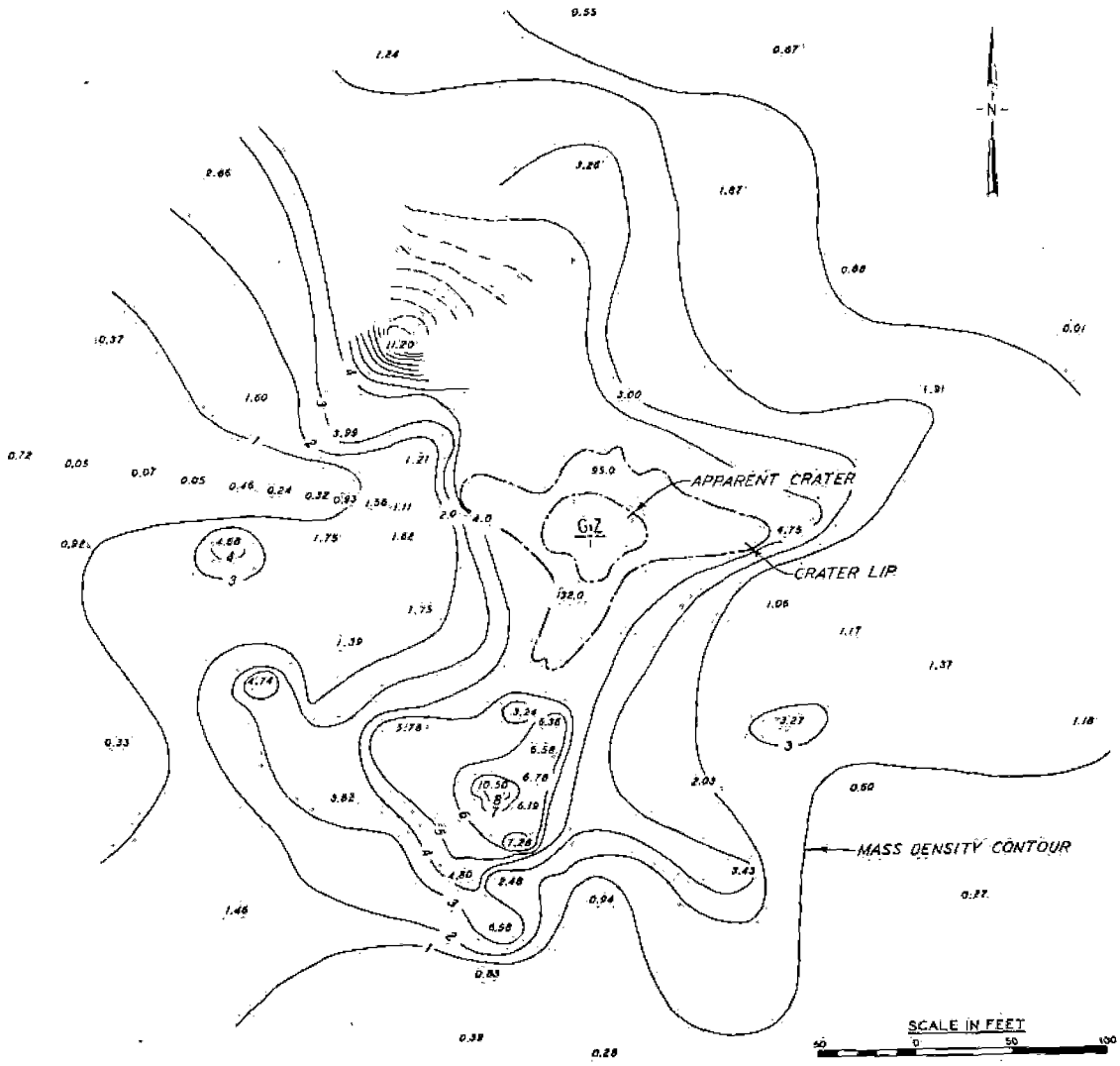

Figure 4.3 Isodensity contours, MINE ORE. Contours and data points represent areal densities of ejecta in pounds per square foot.

CHAPTER 5

TENTATIVE CONCLUSIONS AND RECOMMENDATIONS

5.1 TENTATIVE CONCLUSIONS

In view of the possibility of a second experiment in the MINE SHAFT Series essentially duplicating the MINE ORE Event,[1] firm conclusions regarding the ejecta studies should be delayed to include, if possible, considerations on the reproducibility of the data. Certain tentative conclusions can, however, be drawn on the basis of MINE ORE as follows:

1. Ejecta distribution from a surface or very near-surface burst in rock is highly dependent upon the joint pattern of the medium. The average azimuthal distribution as a function of range, however, does not differ markedly from those observed for other large explosions in rock or cohesive material and at deeper depths of burial (DOB's). It does differ from the distribution observed at or near optimum DOB (Reference 15).

2. Ejecta ranges for this experimental geometry scale according

---

[1] Memorandum from the Technical Director, MINE SHAFT Series, U. S. Army Engineer Waterways Experiment Station, Vicksburg, Mississippi; Subject: "Follow-On Events of the MINE SHAFT Series"; 19 November 1968; Unclassified.

to an exponent which is significantly larger than that indicated by theory. Lacking better data, this exponent may be taken as approximately $W^{0.3}$.

3. For the MINE ORE Shot, the missile hazard to exposed personnel would have extended to a maximum distance of around 2,200 to 2,400 feet. At this range, the hazard would have consisted mostly of small (less than 1 pound) ejecta particles bouncing along the ground, and in most cases breaking up on impact. For 1-pound particles, capable of doing considerable damage, the maximum danger range was slightly over 2,100 feet. Ejecta population was quite sparse at these ranges, however, and the hazard, in terms of the probability of a given spot being struck, was small.

5.2 RECOMMENDATIONS

5.2.1 Procedural Changes. The general approach to this experiment appears sound, and the authors recommend that it be repeated in essentially the same form on future events for which ejecta is expected. Several recommendations seem in order, however, as follows:

1. Increased "seeding" of the crater area with artificial missiles seems desirable, with the object of increasing the numbers of different sizes, shapes, and densities of those missiles which can be located postshot. Particular attention should be paid to the region

between the edge of the charge and two or three charge radii from GZ, as it appears that the greatest ranges may be realized by ejecta originating in this general area.

2. An increased effort to obtain early photography of ejected material is highly desirable, although the technical problems which this imposes are recognized. Further, it is recommended that an effort be made to photographically follow entire missile trajectories. There is evidence that debris which is ejected from a position near the charge has a high initial speed but slows to a much lower speed early in its trajectory (Reference 1). Further, it appears that afterwinds exert a varying drag force upon the longer range particles. More complete information on typical trajectory histories will probably be necessary to an understanding of observed ranges and size distributions.

3. Photographic sampling of ejecta was quite successful, and this procedure should be expanded to include more and larger samples.

4. The use of collector pads should be reduced or eliminated. This is one of the most time-consuming aspects of an experiment of this type, and one which yields probably the least usable data. In and near the crater lip, where deposition of fine particulate may be significant, prepared surfaces (e.g., asphalt) are recommended to replace the pads. Farther out, if dust-density data are required, a better sampling technique is needed. There appear to be two

possibilities--dust-cloud opacity measurements and aboveground vacuum samplers. It is recommended that both of these techniques be investigated for future experiments.

5.2.2 Postseries Analysis. Rigorous analysis of gathered ejecta data was not within the scope of the ejecta project as concerns the first two events of the MINE SHAFT Series.[2] Time has not permitted such a detailed study. It might rather be appropriate for such an analysis to await the completion of all ejecta-producing MINE SHAFT events. It is most important, however, that the experimenter be afforded the opportunity to completely analyze, correlate, and document an experiment before it is considered closed. This will provide the maximum in descriptive detail to the later user of the experimental input, with the least likelihood of misinterpretation or the necessity for laborious correlative effort in assessing the ejecta phenomena.

---

[2] See Paragraph 5.5, Reference 10.

REFERENCES

1. E. B. Ahlers and C. A. Miller; "Ferris Wheel Series, FLAT TOP Event, Project 1.5a, Crater Ejecta Studies"; POR-3006 (WT-3006), November 1966; Defense Atomic Support Agency, Washington, D. C.; Report prepared by Illinois Institute of Technology Research Institute, Chicago, Illinois; Unclassified.

2. J. Wisotski; "Photographic Data from Calibration MINE SHAFT Series, Interim Report Part I"; 3884-6806-I, June 1968; Denver Research Institute, University of Denver, Denver, Colorado; Unclassified.

3. A. D. Rooke and L. K. Davis; "Ferris Wheel Series, FLAT TOP Event, Project 1.9, Crater Measurements"; POR-3008 (WT-3008), August 1966; Defense Atomic Support Agency, Washington, D. C.; Report prepared by U. S. Army Engineer Waterways Experiment Station, CE, Vicksburg, Mississippi, and published as its Miscellaneous Paper No. 1-896; Unclassified.

4. A. E. Sherwood; "The Effect of Air Drag on Particles Ejected During Explosive Cratering"; UCRL-14974, June 1966; Lawrence Radiation Laboratory, Livermore, California; Unclassified.

5. A. D. Rooke, Jr., G. B. Clark, and J. N. Strange; "Operation

SUN BEAM, Shot JOHNIE BOY, Project 1.5, Mass Distribution Measurements (U)"; POR-2282 (WT-2282), 25 February 1965; Defense Atomic Support Agency, Washington, D. C.; Confidential.

6. G. P. Ganong and W. A. Roberts; "The Effect of the Nuclear Environment on Crater Ejecta Trajectories for Surface Bursts"; Technical Report No. AFWL-TR-68-125, October 1968; Air Force Weapons Laboratory, Kirtland Air Force Base, New Mexico; Unclassified.

7. L. K. Davis; "MINE SHAFT Series, Subtask N123, Calibration Cratering Events" (in preparation); U. S. Army Engineer Waterways Experiment Station, CE, Vicksburg, Mississippi; Unclassified.

8. A. J. Chabai; "Scaling Dimensions of Craters Produced by Buried Explosions"; SC-RR-65-70, February 1965; Sandia Corporation, Albuquerque, New Mexico; Unclassified.

9. L. J. Vortman; "Maximum Missile Ranges from Surface and Buried Explosions"; SC-RR-67-616, September 1967; Sandia Corporation, Albuquerque, New Mexico; Unclassified.

10. "MINE SHAFT Series, Events MINE UNDER and MINE ORE, Technical, Administrative, and Operational Plan"; DASIAC Special Report 77-1, 1 October 1968; Headquarters, Defense Atomic Support Agency, DASA Information and Analysis Center, General Electric Company,

TEMPO, Santa Barbara, California; Unclassified.

11. L. K. Davis; "MINE SHAFT Series, Events MINE ORE and MINE UNDER, Subtask N121, Crater Investigations" (in preparation); U. S. Army Engineer Waterways Experiment Station, CE, Vicksburg, Mississippi; Unclassified.

12. M. V. Anthony, T. P. Day, and C. R. Wauchope; "FERRIS WHEEL Series, FLAT TOP Event, Project 1.5b, Ejecta Distribution from FLAT TOP I Event"; POR-3007 (WT-3007), 18 October 1965; Defense Atomic Support Agency, Washington, D. C.; Report prepared by the Boeing Company, Seattle, Washington; Unclassified.

13. A. D. Rooke, Jr., and T. D. Chew; "Crater and Ejecta Measurements for a Full-Scale Missile Detonation in an Underground Cell"; Miscellaneous Paper No. 1-853, November 1966; U. S. Army Engineer Waterways Experiment Station, CE, Vicksburg, Mississippi; For Official Use Only.

14. J. Wisotski; "Technical Photography from MINE UNDER and MINE ORE Events of the MINE SHAFT Series"; 3884-6902-F, February 1969; Denver Research Institute, University of Denver, Denver, Colorado; Unclassified.

15. L. K. Davis and A. D. Rooke, Jr.; "DANNY BOY Event,

Project 1.6: Mass Distribution Measurements of Crater Ejecta and Dust; POR 1815 (WT), Appendix B, Volumetric Equalities of the Crater"; Miscellaneous Paper No. 1-754, December 1965; U. S. Army Engineer Waterways Experiment Station, CE, Vicksburg, Mississippi; Unclassified.

DISTRIBUTION LIST

Address	No. of Copies
DOD	
Director, Defense Atomic Support Agency, Washington, D. C. 20305 ATTN: Technical Library (APTL); STSP; OAOP (OPQR)	5
Commander, Field Command, Defense Atomic Support Agency, Sandia Base, Albuquerque, N. Mex. 87115 ATTN: Technical Library (FCTG-5; FCDV-1)	3
Commander, Test Command, Defense Atomic Support Agency, Sandia Base, Albuquerque, N. Mex. 87115 ATTN: Document Control	2
Administrator, Defense Documentation Center, Cameron Station, Bldg. 5, Alexandria, Va. 22314 ATTN: Document Control	20
Director, Defense Intelligence Agency, Washington, D. C. 20301 ATTN: DIAAP-8B; DIAST-3	2
Assistant to the Secretary of Defense (Atomic Energy), Washington, D. C. 20315 ATTN: Class Rec. Library	1
Director of Defense Research and Engineering, Washington, D. C. 20301 ATTN: Asst. Director (Strategic Weapons); Asst. Director (Nuclear Programs)	2
Director, Weapons Systems Evaluation Group, Washington, D. C. 20305 ATTN: Document Control	1
Joint Strategic Target Planning Staff, Offutt AFB, Nebr. 68113	1
Army	
Chief of Engineers, Department of the Army, Bldg. T-7, Gravelly Point, Washington, D. C. 20315 ATTN: ENGMC-EM; ENGME; Director of Military Construction	4
Chief of Research and Development, Department of the Army, Washington, D. C. 20310 ATTN: Nuclear, Chemical-Biological Division	1
Commanding General, Army Engineer Center, Ft. Belvoir, Va. 22060 ATTN: Asst. Commandant Engineer School	1
Commanding Officer, Army Combat Developments Command, Institute of Nuclear Studies, Ft. Bliss, Tex. 79916 ATTN: Document Control	1
Commanding Officer, Army Engineer Nuclear Cratering Group, Lawrence Radiation Laboratory, P. O. Box 808, Livermore, Calif. 94550 ATTN: Document Control	1
Division Engineer, Army Engineer Division, Ohio River, P. O. Box 1159, Cincinnati, Ohio 45201 ATTN: Document Control	1
Division Engineer, Army Engineer Division, Huntsville, Box 1600 West Station, Huntsville, Ala. 35807 ATTN: Mr. H. L. Solomonson; Mr. M. Dembo	2
District Engineer, Army Engineer District, Omaha, 215 N. 17th Street, Omaha, Nebr. 68102 ATTN: Document Control	1

Address	No. of Copies
Army (Continued)	
Commanding General, Army Materiel Command, Bldg. T-7, Gravelly Point, Washington, D. C. 20315 ATTN: AMCRD-BN	2
Commanding Officer, Army Ballistic Research Laboratories, Aberdeen Proving Ground, Md. 21005 ATTN: Document Control for Mr. John Keefer	2
Navy	
Chief of Naval Operations, Navy Department, Washington, D. C. 20350 ATTN: OP-03EG; OP-75	3
Chief of Naval Research, Navy Department, Washington, D. C. 20360 ATTN: Code 811	1
Commander, Naval Facilities Engineering Command, Headquarters, Washington, D. C. 20390 ATTN: Code 04; Code 03	2
Commander, Naval Ship Engineering Center, Washington, D. C. 20360 ATTN: Document Control	1
Director, Strategic Systems Projects Office, Navy Department, Washington, D. C. 20360 ATTN: NSP-272	1
Commanding Officer and Director, Naval Civil Engineering Laboratory, Port Hueneme, Calif. 93041 ATTN: Document Control	1
Commander, Naval Ordnance Laboratory, Silver Springs, Md. 20910 ATTN: EA; EU; E	3
Superintendent, Naval Postgraduate School, Monterey, Calif. 93940 ATTN: Technical Library	1
Commanding Officer, Naval School, Civil Engineer Corps Officers, Naval Construction Battalion Center, Port Hueneme, Calif. 93041 ATTN: Document Control	1
Commanding Officer and Director, Naval Ship Research and Development Center, Washington, D. C. 20007 ATTN: Technical Library	1
Air Force	
Headquarters, USAF, Washington, D. C. 20330 ATTN: AFNINDE (Dissemination Req. Res. Br.); AFOCE (Dir. of Civil Eng.); AFRDQSN (Strat. and Def. Forces, Nuc Ord. Div.); AFRDDF (Missile Sys. Div., Dir. of Dev.)	4
Headquarters, Air Force Systems Command, Andrews AFB, Washington, D. C. 20331 ATTN: SCS-7 (COL W. P. Wood); SCTSW	2
Strategic Air Command, Offutt AFB, Nebr. 68113 ATTN: OAI (Stinfo Section); DPLBIC (LTC J. B. Tye)	2
AFSC STLO (SCTL-10), Air Force UPO, Los Angeles, Calif. 90045 ATTN: RTSAL	1

Address	No. of Copies
Air Force (Continued)	
Air Force Weapons Laboratory, AFSC, Kirtland AFB, N. Mex. 87117 ATTN: WLIL, Technical Library; WLDC; WLPM; Dr. E. Zwoyer	4
Aerospace Defense Command, Ent AFB, Color 80912 ATTN: ADLDC (DCS OF Plans); ADLMD-W (Missile and Space Weapons Div.)	4
Space and Missile Systems Organization, AFSC, Air Force Unit Post Office, Los Angeles, Calif. 90045 ATTN: SMNP; SAFSP-6	4
Space and Missile Systems Organization, AFSC, Norton AFB, Calif. 92409 ATTN: SMQHF; SMQN (MINUTEMAN Engineering Div.); SMTSM-1; SMY	7
AEC	
Sandia Corporation, P. O. Box 5800, Albuquerque, N. Mex. 87116 ATTN: Document Control for: Dr. M. L. Merritt, Mr. W. R. Perrett	3
Other	
Bureau of Mines, Bldg. 20, Denver Federal Center, Denver, Colo. 80225 ATTN: Science Advisor, Mining Research, Dr. L. A. Obert	1
Civilian Contractors	
Aerospace Corporation, P. O. Box 95085, Los Angeles, Calif. 90045 ATTN: Technical Information Services	2
Aerospace Corporation, 1111 East Mill Street, P. O. Box 1308, San Bernardino, Calif. 92402 ATTN: Mr. Mason Watson; Mr. W. Pferrerle; Mr. Craig Smith; Dr. William Brown	4
Agbabian-Jacobsen Associates, 8939 South Sepulveda Blvd., Los Angeles, Calif. 90045 ATTN: Document Control	1
Analytical Services, Inc., 5613 Leesburg Pike, Falls Church, Va. 22041 ATTN: George Hesselbacher	1
Applied Theory, Inc., 1728 Olympic Blvd., Santa Monica, Calif. 90404 ATTN: Security Officer	1
Battelle Memorial Institute, 505 King Avenue, Columbus, Ohio 43201 ATTN: Mr. R. W. Klingesmith	1
The Boeing Company, P. O. Box 3707, Seattle, Wash. 98124 ATTN: Mr. John Blaylock	1
EG&G, Inc., P. O. Box 227, Bedford, Mass. 01730 ATTN: Document Control Center for D. W. Hansen	1
Engineering Physics Company, 12721 Twinbrook Parkway, Rockville, Md. 28052 ATTN: Mr. Vincent J. Cushing	1
Environmental Research Corporation, 813 N. Royal Street, Alexandria, Va. 22314 ATTN: Mr. O. A. Israelson	1

Address	No. of Copies
Civilian Contractors (Continued)	
General American Research Division, General American Transportation Corp., 7449 N. Natchez Avenue, Niles, Ill. 60648 ATTN: Dr. Neidhardt	1
General Electric Company, Tempo-Center for Advanced Studies, 816 State Street, Santa Barbara, Calif. 93102 ATTN: DASA Information and Analysis Center, W. Chan	2
General Motors Corporation, Manufacturing Development, Manufacturing Staff, 12 Mile and Mound Roads, Warren, Mich. 48092 ATTN: Mr. W. Isbell; Dr. C. Maiden	2
General Research Corporation, P. O. Box 3587, Santa Barbara, Calif. 93105 ATTN: Dr. Benjamin Alexander	1
General Research Corporation, 1501 Wilson Blvd., Arlington, Va. 22209 ATTN: Dr. W. Layson	1
Gulf General Atomic, Inc., P. O. Box 1111, San Diego, Calif. 92112 ATTN: Chief, Tech. Information Services for: H. Kratz	1
IIT Research Institute, 10 West 35th Street, Chicago, Ill. 60616 ATTN: Technical Library; Dr. E. Sevin	2
Institute for Defense Analyses, 400 Army-Navy Drive, Arlington, Va. 22202 ATTN: Technical Information Office	2
Kaman Sciences Corporation, Kaman Nuclear Division, Garden of the Gods Road, Colorado Springs, Colo. 80907 ATTN: Mr. Paul Ellis	1
Dr. Nathan M. Newmark, 1114 Civil Engineering Bldg., University of Illinois, Urbana, Ill. 61801 ATTN: Professor D. V. Deere; Professor A. J. Hendron	2
Physics International Company, 2700 Merced Street, San Leandro, Calif. 94577 ATTN: Dr. Charles Gadfrey	1
The Rand Corporation, 1700 Main Street, Santa Monica, Calif. 90406 ATTN: Library; Dr. A. L. Latter; Dr. H. Brode; Mr. W. B. Wright; Dr. Olen A. Nance; Dr. C. C. Mow	6
Research Analysis Corporation, McLean, Va. 22101 ATTN: Documents Library	1
Stanford Research Institute, 333 Ravenswood Avenue, Menlo Park, Calif. 94025	1
Systems, Science, and Software, Inc., P. O. Box 1620, La Jolla, Calif. 92037 ATTN: Document Control	1
TRW Systems Group, San Bernardino Operations, P. O. Box 1310, 600 East Mill Street, San Bernardino, Calif. 92402 ATTN: J. L. Merritt, Mgr. HARD ROCK SILO OFF.; Mr. Fred Pieper	2
TRW Systems Group, One Space Park, Redondo Beach, Calif. 90278 ATTN: Mr. J. Carpenter	1

Address	No. of Copies
Civilian Contractors (Continued)	
URS Corporation, 1811 Trousdale Drive, Burlingame, Calif. 94011 ATTN: Mr. Harold Mason	1
Paul Weidlinger, Consulting Engineer, 777 Third Avenue, New York, N. Y. 10017 ATTN: Dr. M. Baron	1
U. S. Geological Survey, Flagstaff, Ariz. 86001 ATTN: Dr. Roddy	1
Defence Research Establishment, Suffield, Ralston, Alberta, Canada ATTN: Mr. A. P. R. Lambert	1
Denver Research Institute, University of Denver, University Park, Denver, Colo. 80210 ATTN: Mr. John Wisotski	1

Unclassified
Security Classification

DOCUMENT CONTROL DATA - R & D

(Security classification of title, body of abstract and indexing annotation must be entered when the overall report is classified)

1. ORIGINATING ACTIVITY (Corporate author)
U. S. Army Engineer Waterways Experiment Station
Vicksburg, Mississippi

2a. REPORT SECURITY CLASSIFICATION
Unclassified

2b. GROUP

3. REPORT TITLE
MINE SHAFT SERIES: EVENTS MINE UNDER AND MINE ORE, EJECTA STUDIES

4. DESCRIPTIVE NOTES (Type of report and inclusive dates)
Final report

5. AUTHOR(S) (First name, middle initial, last name)
John W. Meyer
Allen D. Rooke, Jr.

6. REPORT DATE	7a. TOTAL NO. OF PAGES	7b. NO. OF REFS
September 1969	91	16

8a. CONTRACT OR GRANT NO.	9a. ORIGINATOR'S REPORT NUMBER(S)
b. PROJECT NO.	Miscellaneous Paper N-69-2
c.	9b. OTHER REPORT NO(S) (Any other numbers that may be assigned this report)
d.	

10. DISTRIBUTION STATEMENT
Each transmittal of this document outside the Department of Defense must have prior approval of Defense Atomic Support Agency.

11. SUPPLEMENTARY NOTES	12. SPONSORING MILITARY ACTIVITY
	Defense Atomic Support Agency Washington, D. C.

13. ABSTRACT

The MINE SHAFT Series is a program of high-explosive tests primarily concerned with ground-shock and cratering effects from explosions at or near the surface of a rock medium. The series is sponsored by the Defense Atomic Support Agency (DASA) as a follow-on to similar tests in soil (SNOW BALL, DISTANT PLAIN, PRAIRIE FLAT). The two major events of MINE SHAFT during 1968 were MINE UNDER and MINE ORE; both were explosions of 100-ton TNT spheres detonated in near-surface geometries and in/over a granite medium. Studies of the crater ejecta were conducted on MINE ORE (buried one-tenth of the charge radius) with the objectives of determining the spoil density and distribution from this event, examining the role of the ejection mechanism in crater formation for this medium, and obtaining additional information on natural missile trajectories. MINE UNDER, an above-surface event, produced a spalled rubble mound and a small field of debris; this was also recorded as part of the study. MINE ORE produced a low, irregular crater lip which extended to an average range of 47 feet from ground zero (GZ) with a maximum of roughly 90 feet. Beyond this, discrete ejecta particle size and distribution frequency decreased with increasing distance from GZ. The maximum observed range was 2,120 feet for a 1-pound natural missile with smaller fragments found out to about 2,300 feet from GZ. Maximum ejecta ranges were observed downhill from and parallel to the main joints. Missile ranges scaled approximately as $W^{0.3}$. The jointing system of the rock appeared to be the single most influential element in concentrating debris along certain radials, as well as in the overall distribution of debris.

DD FORM 1 NOV 1473 REPLACES DD FORM 1473, 1 JAN 64, WHICH IS OBSOLETE FOR ARMY USE.

Unclassified
Security Classification

14. KEY WORDS	LINK A		LINK B		LINK C	
	ROLE	WT	ROLE	WT	ROLE	WT
Cratering						
Crater ejecta						
Ejection						
Explosions						
Ground shock						
Mine Ore (Event)						
Mine Shaft (Series)						
Mine Under (Event)						

and the muds from its leaching. The considerable range of reflections shows that it is well crystallised. The Mg-Fe-chlorite is characterterised by a small number of diffractions, which indicates poor crystallisation.

On the DTA and DTG curves (figs. 3 and 4) there is an endothermic effect at 600-650°C, corresponding to release of the first portion of structural water from the brucite-like layer, and a small endothermic effect at 750-800°C, which characterises release of the second portion of structural water from the mica-like layer. The endothermic effect passes directly into a well defined exothermic effect with a maximum at 820°C (fig. 3) corresponding to recrystallisation of an olive structure.

The derivatogram of the red mud from the leaching of the Belgorod bauxites (fig. 5) as a whole is characterised by the presence of the same effects as the derivatograms of the muds given in figs. 3 and 4. Consequently, the muds from the leaching of Fe and Mg-Fe-chlorites are represented by undecomposed chlorites. Hydrated sodium aluminosilicate was not found in the muds, and this confirmed the thermodynamic calculations.

Thus, the chlorites are not decomposed during the autoclave leaching, and their presence in the bauxites from some deposits is reflected in the technology of the extraction of alumina by the Bayer method. For example, the incomplete extraction of the Al_2O_3 from the hydrargillite bauxites of the Belgorod KMA deposit in the Bayer process is due to the fact that about 10% of the alumina contained in the bauxites and practically all the silica are present in the composition of high-iron chlorite, which does not decompose during autoclave leaching of bauxites.

Conclusions

1. The decomposition reactions of various types of chlorites in alkaline aluminate solutions are thermodynamically impossible.
2. The results from the thermodynamic calculations were confirmed by various methods of physico-chemical analysis of the muds after the leaching of chlorites and KMA bauxites.

References

1) M F Kompaniets: Tsvetnye Metally 1958, (8).
2) L P Khodak et alia: Tr. Khim. Metallurg. In-ta Vol. 7 Nauka, Alma-Ata 1969.
3) A S Povarennykh: Crystal-chemical classification of mineral forms: Naukova Dumka, Kiev 1966.
4) P Cottrell: The strength of chemical bonds (translated into Russian) Moscow IL 1956.
5) N A Landiya: Calculation of high-temperature heat capacities of inorganic materials from standard entropies: Tbilisi, Akad. Nauk Gr SSR 1962.
6) V I Babushkin et alia: Thermodynamics of silicates Stroizdat Moscow 1965.
7) M Kh Karapet'yants: Introduction to the theory of chemical processes: Moscow 1970.

SUBJ
MNG
NAA

800. Non-fe
1975 v-3 N2

UNIVERSITY OF UTAH
RESEARCH INSTITUTE
EARTH SCIENCE L...

UDC 669.712

Nitric acid autoclave recovery of products from concentration of high-silica bauxites

Yu E Sutyrin and L V Zverev (VIMS)

Recently researches into the mechanical concentration of bauxites have been widely developed in the USSR. Usually, the concentration of low-grade bauxites leads to the production of two products i.e., a concentrate distinguished from the initial rock by an increased silica ratio and a second product, which contains a considerable amount of alumina in the form of kaolinite or other aluminosilicates and is not waste material. The mechanical concentration could become most effective if the bauxite concentrate were treated by the Bayer process and the low-ratio product, which contains an increased amount of silica, were treated by the acid method.

Investigations carried out in the USSR and abroad show that it is possible to use autoclave treatment for the extraction of alumina from clays and kaolins. According to calculations made in recent years[1], the nitric acid method is the most economical of the acid methods for the production of alumina from clays. It seemed expedient to investigate the use of this method for the treatment of high-silica bauxites and kaolinite products from their mechanical concentration, which differ from clays by the presence of bauxite minerals and a higher content of alumina.

Earlier[2] we studied the behaviour of the principal alumina-contai ing minerals in the breakdown of the products from concentration with nitric acid. The conditions for transfer of aluminium into solution and separation of aluminium from iron directly during nitric acid treatment of the boehmite-kaolinite product isolated during the concentration of high-silica bauxites of the North-Onega deposit are examined in the present work.

The starting material is characterised by a particle size of -44 μ and by the following contents of the principal components (wt.%): 47.5 Al_2O_3, 22.5 SiO_2, 7.6 Fe_2O_3, and 16.1 calcination loss. The alumina-containing minerals are represented by kaolinite, boehmite, and hydrargillite and, in smaller amounts, diaspore and hydromica; the iron-containing minerals are goethite and haematite.

Treatment of the boehmite-kaolinite product with nitric acid under atmospheric pressure conditions does not secure satisfactory extraction of alumina. Thus, treatment of the raw product with 40% nitric acid only extracts about 5% of the alumina into solution, while treatment of the roasted product does not extract more than 50%. Treatment at increased temperatures in an autoclave possesses advantages, among which the high degree of decomposition, the reduction in the acid consumption, and the production of solutions less contaminated with iron should be noted primarily.

The experimental part of the work was carried out in autoclave bombs made of Kh18N9T steel. Samples of the initial product were roasted in a muffle furnace at 600°C for 2h (the optimum roasting conditions for the given product) and loaded into bombs with a specified amount of 40% HNO_3, with filling factors of 0.6-0.7. The bombs were placed in an air thermostat with an electric heater and automatic temperature control. Agitation of the pulp was realised by rotation of the bombs through the "head". The degree of breakdown of the initial product was determined from the Al_2O_3 and Fe_2O_3 contents in the insoluble residue, and in addition the solutions were analysed for iron and aluminium content.

The effect of the acid consumption and the length and temperature of the process on the breakdown of the previously roasted boehmite-kaolinite product was investigated. In the first stage of the investigations a 100% consumption of nitric acid on the stoichiometric amount for the formation of $Al(NO_3)_3$ was used. The initial concentration of the acid amounted to 40%; it is not advisable to use stronger acid, since 50% HNO_3 gives a thick pulp, which must then be diluted considerably with water.

Fig.1 shows the effect of the length of autoclave treatment of the boehmite-kaolinite product with nitric acid at 140, 160, and 180°C on the extraction of aluminium (curves 1-3).

and iron (curves 4-6) into solution. With short treatment (1h) the increase in temperature has a significant effect on the degree of extraction of aluminium. However, the longer the process, the smaller the effect of temperature. Maximum extraction of aluminium, corresponding to 94-95%, was obtained after 1h at 180°C, 1.5h at 160°C, and 2h at 140°C. The strong effect of temperature on the decomposition rate of the alumina-containing minerals makes it possible to suppose that the process is controlled by a kinetic stage under the conditions adopted.

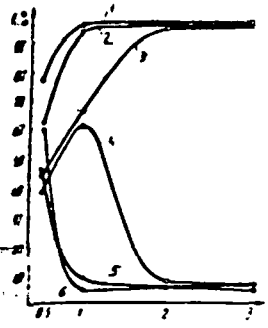

Fig.1

Extraction of aluminium (1-3) and iron (4-6) into solution as a function of the length of the process of breakdown of the initial product at various temperatures (°C): 180 (1,6), 160 (2,5); 140 (3,4).

The insoluble residues after nitric acid treatment, filtration, and washing (satisfactory filtration) were analysed by IR spectroscopy. In those cases where extraction of aluminium close to the maximum value was obtained the Al_2O_3 was detected in the residue mainly in the form of hydromica. The content of this mineral is clearly explained by the incomplete extraction of aluminium into solution.

The behaviour of iron during nitric acid treatment of the product investigated is interesting. Curves 4-6 (fig.1) show that two processes take place simultaneously during treatment of the product in the autoclave, i.e., dissolution of iron and its precipitation as a result of hydrolysis, and the curves for the extraction of iron with time therefore have a maximum. At 140°C (curve 4) this maximum is clearly defined, and at higher temperatures (curves 5 and 6) it lies to the left of the first experimental points. As a result of hydrolysis the concentration of iron in the solution decreases to 0.9-1.1 g/l, and the iron ratio of the solution (μ_{Fe} = Al_2O_3/Fe_2O_3) increases to 100.

The hydrolysis of aluminium under the adopted conditions does not go further than the formation of soluble basic salts since the concentration of aluminium in the solution does not decrease.

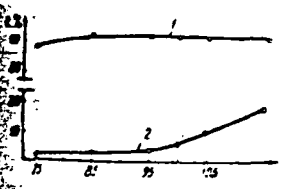

Fig.2

Extraction of aluminium (1) and iron (2) into solution as a function of the acid consumption.

The effect of the acid consumption on the extraction of aluminium and iron into solution is shown in fig.2. The extraction of alumina does not increase when the acid consumption exceeds the stoichiometric amount for the formation of $Al(NO_3)_3$. The hydromicas still remain unopened. Even with an acid consumption of 85-95% of the stoichiometric perfectly acceptable extraction of alumina (93-94%) is obtained, and 0.4-0.5 g/l of Fe_2O_3 is retained in the main solution, which has pH = 1.2-1.4, and this amounts to ~2.5% of the amount of iron present in the raw material. The solutions contain about 0.02 g/l of SiO_2 and less than 0.01 g/l of TiO_2. The aluminium content in these solutions corresponds to 100-110 g/l, and after combination with the wash waters it decreases to 85 g/l.

The obtained solutions have an iron ratio approaching 300. The insoluble residues contain (wt.%): 5.5-6.0 Al_2O_3, 53-54 SiO_2, 19-20 Fe_2O_3.

Consequently, considerable removal of iron from the solution of aluminium nitrate is achieved directly during nitric acid autoclave treatment of the boehmite-kaolinite product containing 7.6% Fe_2O_3. However, this degree of removal of iron is not the maximum; further higher purification of the solution can be realised after removal of the solid phase. This is demonstrated by investigations of the high-temperature hydrolysis of iron from nitrate solutions, realised both on synthetic solutions and on solutions obtained during the bleaching of clay[3,4]).

Conclusions

1. The low-ratio kaolinite products obtained during concentration of bauxites can be subjected to a nitric acid autoclave treatment in order to transfer the aluminium selectively into solution.

2. For the case of a boehmite-kaolinite product containing iron it was shown that under conditions of nitric acid autoclave treatment it is possible almost completely to transfer the aluminium into solution and to separate it from the bulk of the iron, silicon, and titanium.

References

1) Ekspress-informatsiya: Tsvetnaya Metallurgiya 1971, (5), 11.

2) Yu E Sutyrin and L V Zverov: Izv Vuz Tsvetnaya Metallurgiya 1974, (3).

3) V S Makarova, D M Chizhikov and Yu A Lainer: Investigation of processes in the metallurgy of nonferrous and rare metals. Nauka, Moscow, 1969, p.195.

4) Kh R Ismatov and R Z Karimov: Byul. Tsvetnaya Metallurgiya 1968, (18).

UDC 669.71.533.15

Diffusion and activity of hydrogen in the aluminium-copper system

K I Vashchenko, D F Chernega, D F Ivanchuk, O M Vyalik, and G A Remizov (Kiev Polytechnical Institute. Department of Machines and Technology in Casting Production)

The interest in the study of the liquid state in metals is due to successes in the theory of the liquid state and the increasing possibilities for practical utilisation of laboratory experimental data. The study of the diffusion of hydrogen in liquid metals is of theoretical and practical interest.

Of the three main links in the interaction of gases with liquid metals (absorption, diffusion, dissolution) the least investigated is diffusion. The setting up of experiments on the determination of the diffusion of hydrogen in molten metals involves procedural difficulties, i.e., convective flows in the melt and the difficulty of their suppression

SUBJ
MNG
NACP

UNIVERSITY OF UTAH
RESEARCH INSTITUTE
EARTH SCIENCE LAB.

Natural Acidity and Copper Precipitation

A record of practical experiences of copper leaching operations.

Frank Cloke

The author considers it may be of interest to place on record two instances, within his own knowledge and experience, in which insufficient knowledge of the effect of natural acidity on copper precipitation gave rise to very considerable losses in cash and metallic copper values.

In 1913, when engaged in the leaching and precipitation of the copper in about 135,000 tons of burnt arsenical-copper ore on an abandoned mine, he had his first experience of the kind.

In digging trenches to intercept the pregnant water passed through the dump a drain was met carrying about 400 g.p.m. of water. This was assayed and proved to contain several ounces of Cu per ton of water. A plant was promptly constructed large enough to treat it, but without success. There was a notable suspension of hydrated oxides of iron and alumina, which quickly coated the iron and steel lathe turnings used and precipitation, if at all, was very sluggish indeed.

The late Dr. Alfred C. Fryer, in the usual course of his duties, went over the plant. His attention was called to the stream and its failure to respond to the usual treatment. He suggested acidifying it and recommended "nitre-cake"—a waste-product in the manufacture of sulphuric acid—for the purpose. This was tried at once, with complete success. Very considerable losses had, of course, taken place already.

The second instance of this phenomenon took place during the author's last stay in the United States, from 1924 to 1933. He was surveying for eight years of that period, but was the assistant to the chief chemist for one year. While engaged on a 7-mile surface triangulation survey which passed through a very large adjoining mine the writer noticed many thousands of tons of overburden dumps, on both properties, which showed small pieces of copper carbonate throughout. At the base of a dump of about 500,000 tons there was a small derelict precipitation plant. On the top of the same dump a number of bays had been thrown up, showing that an attempt had previously been made to leach out and precipitate the copper.

The author was then transferred, on loan, from the surveying to the assaying laboratory. Upon proper acquaintance he expressed his surprise to the chief chemist that no attempt was being made to leach that 500,000-ton dump, but was then told that a well-known expert had carried out experiments for about a year with a view to leaching and recovering the great amount of copper values in it. In his report the expert had stated that the copper was amenable to sulphuric acid leaching, but upon passing the leach liquor through the test plant no precipitation took place at all. In an endeavour to ascertain the cause of the failure a number of experiments were carried out in the laboratory. The results of these led to the belief that the abundance of aluminous clay in the material was almost entirely responsible for the failure of precipitation.

This was naturally a reminder of the experience in 1913. While readily accepting the verdict of the expert he felt that it was, in all probability, a matter of acid condition. He decided to pursue the matter to its logical conclusion, if able, and being employed in the laboratory had all that he required for the purpose. Knowing the importance of working with pure solutions a few crystals of copper sulphate were taken and dissolved in distilled water. It was expected, the salt being a chemical union between an acid much more powerful than the base, that the solution would perhaps

1947

UNIVERSITY OF UTAH

give an acid reaction. A leaf of blue litmus paper shaken in the solution turned red quickly. The next step was to clean the blade of the pocket-knife and dip it into the liquid; at once the usual deposition of copper was obtained.

He next wondered what would happen if the acid reaction were neutralized. Accordingly a suitably-diluted solution of pure ammonia was made up and cautiously added drop by drop with thorough mixing between each drop until the solution gave no visible colour change with either blue litmus or red. Again the knife blade was cleaned and shaken vigorously in the solution for at least a minute; not the least sign of copper appeared on the blade.

The next question was: Would re-acidification of the solution again restore the precipitation reaction? Suitably diluted pure sulphuric acid solution was added a drop at a time, with mixing, until, approximately, the original acidity was reached. Upon dipping the cleaned knife blade in the solution the precipitation took place at once, as at first.

This clearly proves, of course, that acidity is essential to the precipitating reaction. The acidity may be greater than the natural acidity of a solution of pure sulphate of copper in distilled water, but in view of the fact that precipitation is completely arrested upon neutralization, it necessarily follows that immediately the acidity falls below the natural level the speed of the precipitation falls very rapidly and soon comes to rest.

It is clear, at any rate, that the phenomenon may yet prove of use to anyone contemplating leaching operations on dumps of low-grade cupriferous material.

Aluminium Industry for Australia

A brief outline of plans to create an aluminium industry in Tasmania.

Kura East

Introduction

War-time experience showed Australians that a self-contained aluminium industry was essential to defence. In 1939 imports of aluminium were only 1,320 tons; with the war they skyrocketed to a maximum of 10,440 tons in 1944. The annual consumption during 1943 and 1944 was about 5,000 tons. In December, 1944, the Federal Parliament passed the Australian Aluminium Industry Act and so gave parliamentary sanction to plans developed in the early stages of the war for the manufacture of aluminium ingot in Australia. In 1945 the Australian Aluminium Production Commission was set up.

The aluminium ingot industry can be divided into three major operations—mining of the ore, chemical treatment to obtain alumina, and electrolytic reduction of alumina to metal. The three processes may be separated if an integrated plant to carry out all three functions in the same area is not practicable. Before sites for each section can be fixed, however, an examination must be made of the quantity and quality of available bauxite; of water, coal, or limestone supplies; of the use of direct or alternating current for power, and of transport costs of raw, semi-finished, or finished material. A supply of cheap power from hydro-electric resources led Tasmania to be chosen as the most suitable place for the Australian industry. In 1944 an agreement was made between the Commonwealth and the Tasmanian State Government for the joint establishment of the industry.

Its careful investigations completed, the Commission informed the Premier of Tasmania in February, 1946, that a convenient site in the Launceston area in the north of the State had been fixed for the site of the aluminium industry, subject to a final

SUBJ
MNG
NAPF

UNIVERSITY OF UTAH
RESEARCH INSTITUTE
EARTH SCIENCE LAB.

NEW APPROACHES TO PROBLEMS OF FLUID FLOW IN FRACTURED ROCK MASSES

Paul A. Witherspoon, Yvonne W. Tsang,
Jane C. S. Long, and Jahandar Noorishad

Lawrence Berkeley laboratory,
University of California
Berkeley, California 94720

Proceedings of the 22nd U.S. Symposium on Rock Mechanics: Rock Mechanics from Research to Application held at Mass. Inst. of Tech., June 28-July 2, 1981 compiled by H.H. Einstein

INTRODUCTION

Investigations on the factors that control the movement of fluids in the underground inevitably become involved with fractured rock masses. In the petroleum industry, it was recognized long ago that the presence of fractures, either natural or man made, is crucial to the economics of the recovery methods to be employed in many oil fields. The development of groundwater resources is likewise often dependent on the presence of fractures to provide a drainage system in low permeability rocks. Geotechnical engineers have been faced with difficult problems when designing and constructing large engineering works in fractured rocks; catastrophic failures of large dams provide evidence of the magnitude of their problems. The leakage problems that have resulted when natural fractures were not detected in developing projects for underground storage of petroleum hydrocarbons are still another kind of evidence of the importance of fracture systems. The current problem of evaluating migration of aqueous solutions of radionuclides through crystalline rock masses where the movement will be controlled by the discontinuities is a critical issue in the design of nuclear waste repositories. These examples simply serve to illustrate the fact that the fractures play a key role in understanding the flow behavior of rock systems.

Despite the importance of this problem and the great amount of investigation by many workers, much remains to be done in developing a complete understanding of the factors that control fluid movement through fractured rocks. The range of subject matter covered by the papers presented in Topic Area 1 of this symposium gives a good indication of the complex problems that face earth scientists.

We shall address three different aspects of this problem in an effort to describe some investigations currently underway in this laboratory. The first part of this paper is an attempt to develop an expression for fluid flow in a deformable fracture. Our approach to this problem of the hydromechanical behavior of a deformable fracture differs from that of Gangi (1978) although we both have a common starting point, the roughness of the fracture surface. The second part has to do with the problem of how to treat flow through networks of fractures. It is customary to consider a discontinuous rock mass by some equivalent porous medium but this raises some important questions that will be discussed. The third part will present the most recent results by our group to develop a fully coupled finite element code for flow through fractured porous media subject to thermal, hydraulic and mechanical stresses.

HYDROMECHANICS OF FLOW IN A SINGLE FRACTURE

We have developed a simple physical model to understand the effect of normal stress on flow through a single rough walled fracture. In order to gain a fundamental understanding of the problem, we have focussed on the physical mechanisms and have excluded the use of arbitrary fitting parameters. A single fracture is considered to be composed of a collection of voids, and the closure of the fracture under stress to result from the deformation of these voids. From such a model, the macroscopic measurable quantities, such as the normal stress and corresponding normal fracture displacements, can be correlated to the geometrical characterization of a rough walled fracture. The effect of roughness is incorporated into the usual parallel plate model of a fracture, and the flow rate as a function of normal stress is predicted and validated against laboratory data on granite and basalt.

Solutions of the Navier Stokes equation show (Boussinesq, 1868; Bear, 1972) that steady, laminar flow through two smooth parallel plates separated by a constant distance b obeys the cubic law, that is, the flow rate is proportional to b^3. The cubic law has been shown to hold down to apertures of 0.2 μm in open fractures made of optically smooth glass (Romm, 1966). We have shown (Tsang and Witherspoon, 1981) that an equivalent cubic law may be used for a rough walled fracture if the constant value for the aperture is replaced by a statistical average. This implies that the hydrological property of a rough walled fracture may be suitably modeled by a mathematical aperture distribution function.

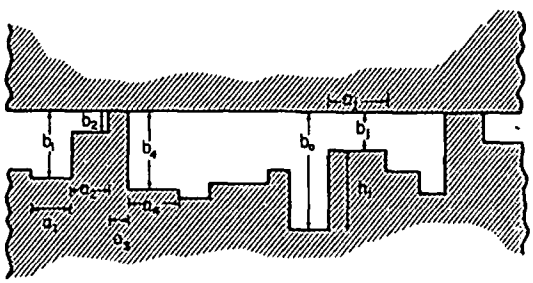

Fig. 1 Schematic representation of a fracture by an asperity model.

Fig. 1 shows such a schematic representation for a fracture, which consists of a smooth top slab and a rough bottom slab with asperities of different heights (h_j). The configuration of asperities gives rise to a fracture with variable aperture b_j. The problem is then to develop an asperity function that is a correct mathematical expression for the variability of the real, physical fracture.

Theoretical Development

Geometrically, a single rough walled fracture may be envisioned either as a collection of voids or as an array of asperities (Fig. 2). Under increasing

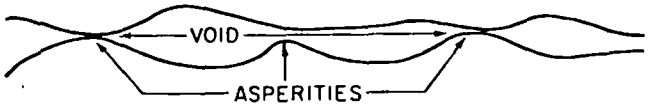

Fig. 2 Schematic representation of a fracture by either the asperity or the void model.

normal stress, more asperities come in contact and the average distance between points of contact decreases. Though an asperity description for a fracture seems to be a natural candidate for the study of flow through fractures, we find that the void description is better suited to the interpretation of the mechanical property of a single fracture under stress. By considering the closure of a single fracture as resulting from the shortening of the average crack length of the voids, we were able to arrive at an asperity function consistent with mechanical measurements of fracture displacement and applied normal stress.

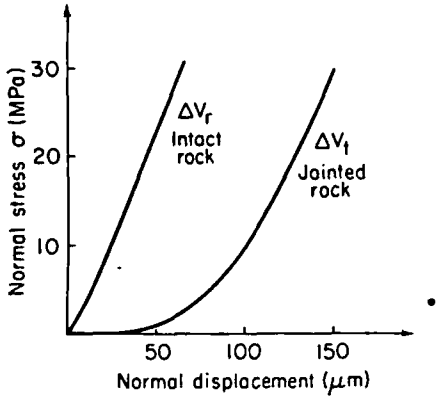

Fig. 3 Typical normal stress-displacement behavior for intact and jointed rock.

Given measurements of normal stress displacement for both intact and jointed rock such as those shown in Fig. 3, we may define both the intrinsic Young's modulus, E, for the intact rock and the effective Young's modulus, E_{eff}, for the jointed rock from the respective slopes of the stress-displacement curves:

$$E(\sigma,\Delta V_r) = \frac{1}{\ell}\frac{d\sigma}{d\Delta V_r} \qquad (1)$$

$$E_{eff}(\sigma,\Delta V_t) = \frac{1}{\ell}\frac{d\sigma}{d\Delta V_t} \qquad (2)$$

At low stresses, the effective Young's modulus E_{eff} of the jointed rock is much smaller than that of the solid rock. As stress is increased, E_{eff} approaches the value of E for the solid rock.

Consider first the geometry of one elliptic flat crack of length 2d enclosed in a rock volume of $u = \Delta x\Delta y\Delta z$. Following closely the formulation of Walsh (1965), one can show that for a rock with a collection of voids, all with the same orientation as the one shown in Fig. 4, the effective modulus E_{eff}

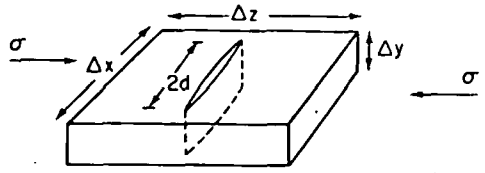

Fig. 4 Geometry of a flat elliptic crack in in rock block under stress.

of the rock with voids is related to the intrinsic rock modulus E by:

$$\frac{1}{E_{eff}} = \frac{1}{E} + \frac{4\pi\langle d^3\rangle}{E\langle u\rangle}, \qquad (3)$$

where both the half-crack length cubed and the volume enclosing each void have been averaged over all the voids in the sample. This expression is not sensitive to the actual shape of the void. The second term on the right-hand side of (3) arises from the strain energy associated with the cracks. Since (3) applies to a physical situation of sparse voids, the effect of the voids on the elastic modulus is expected to be small. Then the property of the rock medium in which the voids are situated may be described by Young's modulus for the intact rock, and therefore the same modulus E appears in the strain energy term associated with the cracks.

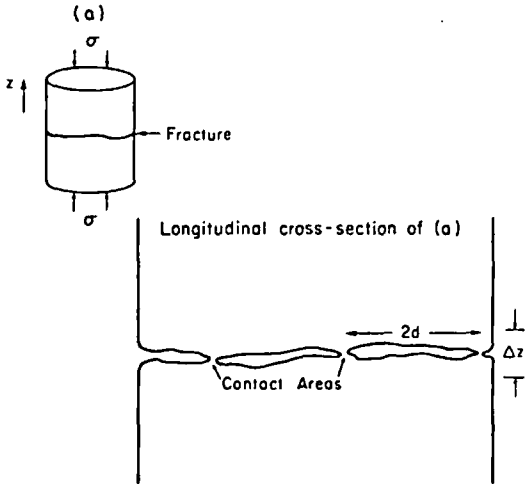

Fig. 5 Representation of single horizontal fracture by an array of voids.

If we were to consider one single horizontal fracture as a collection of voids, the physical situation will be as shown in Fig. 5. Here the voids are dense and the void ratio is large. Only a small fraction of the total fracture area is in contact. To describe the effective modulus E_{eff} of the fractured rock in the vicinity of the fracture, (3) may be modified to:

$$\frac{1}{E_{eff}} = \frac{1}{E} + \frac{4\pi\langle d^3\rangle}{E_{eff}\langle u\rangle}, \qquad (4)$$

where (4) now includes E_{eff} in the last term. When the voids are large in number and close in proximity, the void-void interaction is no longer negligible as is assumed in the derivation of (3). Since it is difficult if not impossible to account for this interaction in the calculation of strain energies, we make a plausibility argument to lump the effect of the interaction by introducing E_{eff} in the last term of (4). The argument being that due to the high void ratio, the property of the rock medium is better represented by the effective modulus of the fractured rock than by the modulus of the intact rock.

Suppose there are M_v voids in the fracture with a total cross sectional area A. then the average volume enclosing each crack may be written as:

$$\langle u \rangle = \frac{A\,\Delta z}{M_v} \tag{5}$$

where Δz is a thickness around the fracture within which E_{eff} is applicable (see Fig. 5). Since the rock fracture is represented by a collection of voids, one expects the contact area of the fracture walls to be small such that the total void area is almost identical to the total fracture cross section area A. Therefore:

$$\langle (2d)^2 \rangle\, M_v \approx A \ . \tag{6}$$

In addition, for a spatially random collection of M_v voids, $\langle d^3 \rangle \approx \langle d^2 \rangle \langle d \rangle$ and (4) may now be written approximately as:

$$\frac{E_{eff}}{E} \approx 1 - \frac{\pi \langle d \rangle}{\Delta z} \tag{7}$$

Equation 7 gives a useful relationship between the two moduli and the average half-crack length $\langle d \rangle$ which characterizes the rough fracture at different levels of stress.

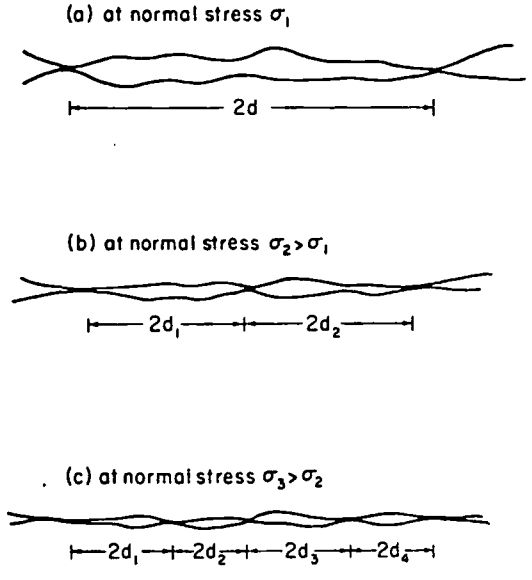

Fig. 6 Deformation of voids in a sequence of increasing normal stresses.

The physical picture implied by (7) is illustrated schematically in Fig. 6, which is an attempt to portray a portion of fracture shown in Fig. 5 at different stages of normal stress. The crack length 2d is defined as the distance between two adjacent areas where the two fracture surfaces come into contact. These areas of contact are simply the asperities as shown in Fig. 2. Under increasing load, the deformation of the voids causes more asperities to come in contact, and leads to a decrease in the average crack length. This process results in a gradual increase of the effective modulus with increasing normal stress according to (7). The average crack length $2\langle d \rangle$ continues to decrease as the voids deform until the term $\langle d \rangle / \Delta z$ becomes negligibly small compared to 1, at which point the jointed rock will exhibit an effective modulus identical to that of the intrinsic modulus.

We therefore attribute the "softness" of a jointed rock to an average crack length that initially is relatively long and the stiffening of the jointed rock under compression to the shortening of this average crack length. This differs from Gangi's (1978) "bed of nails" model, in which he ascribes the closure of a fracture to the elastic compression of the "nails" or "asperities". In Gangi's model, the "softness" of the fracture is said to result from the small number of asperities that are in contact. These areas therefore sustain much higher stresses than that measured by the total load divided by the total fracture area. As a result, the strain of these asperities in contact is expected to be larger than the strain in an intact rock under the same load.

However, when we apply such an asperity model to both the flow data and stress-strain measurements in a granite fracture [Iwai, 1976], we found that in order to obtain a result that is quantitatively compatible with the data, we had to assume that the total area of all the asperities that are in contact with the top slab (Fig. 1) took on a value of less than .001 of the total fracture area at an applied stress level of 20 Mpa. The experimental measurement [Iwai, 1976] gives a value between .1 to .2 for the contact area of the fracture at the same stress level. The discrepancy of two orders of magnitude between a parameter in the theory and measurement implies that the physical fracture system appears to be much "softer" than that described by the asperity model. On the other hand, the alternate mechanism proposed above, where the closure of the fracture under normal stress is ascribed to the deformation of voids, does predict a very soft elastic property at low stress. It also predicts a gradual increase of Young's modulus with stress, and a correct contact area in accordance with the laboratory measurment.

It is clear from Fig. 6 that one may view the sequence (a) (b) (c) either as a decrease in the average crack length $2\langle d \rangle$ or as an increase in the number N_c of areas in contact under increasing load. For a rough-walled fracture, we shall describe the former process as a "void model" and the latter process as an "asperity model." For a spatially random distribution of voids or asperities, N_c varies inversely with $\langle d \rangle$. Given elastic stress measurements, it is evident from (7) that the relative average crack length $2\langle d \rangle$ as a function of stress or fracture displacement can be calculated, and therefore, N_c may be deduced.

The number of contact areas, N_c, is the key to aperture distribution. Fig. 1 represents a rough-

walled fracture as an array of asperities of varying heights h_j. At zero applied stress, the maximum possible aperture is b_o, which corresponds to an asperity of zero height. With applied axial stress, the fracture closure ΔV results in a downward displacement of the top slab. At nonzero stresses, the aperture which corresponds to each asperity of height h is:

$$b = \begin{cases} (b_o - \Delta V - h) & h < (b_o - \Delta V) \\ o & h \geq (b_o - \Delta V) \end{cases} \quad (8)$$

Let n(h) denote the asperity height frequency distribution function which characterizes the fracture prior to loading. Then N_c, the total number of asperities in contact at any stress, is:

$$N_c(\Delta V) = \int_{b_o - \Delta V}^{b_o} n(h)\, dh. \quad (9)$$

It is clear from (9) that the asperity height distribution function, n(h), can be obtained from the derivative of N_c. For a given set of stress displacement measurements, it is possible only to deduce the change in $\langle d \rangle / \Delta z$ relative to its value at zero applied stress from (7). This implies that N_c and in turn n(h) can only be determined to within some constant multiplier, because the value of b_o is not known. If the contact area as a fraction of the total fracture area is known to be ω at a specified deformation ΔV, then:

$$\omega = \frac{N_c(\Delta V)}{N_c(b_o)} \quad (10)$$

and b_o is readily determined if a functional form exists for $N_c(\Delta V)$.

We have shown (Tsang and Witherspoon, 1981) that if the aperture variation of the fracture is spatially random, the equivalent cubic law for flow through a rough walled fracture may be written as:

$$\frac{Q}{\Delta \phi} = C \langle b^3 \rangle \quad (11)$$

where C is a proportionality constant that depends on the macroscopic fracture dimensions and properties of the fluid. The statistical average for the variation in aperture may therefore be computed from:

$$\langle b^3(\Delta V, \sigma) \rangle = \frac{\int_0^{b_o - \Delta V} (b_o - \Delta V - h)^3 n(h)\, dh}{\int_0^{b_o} n(h)\, dh} \quad (12)$$

Once the normal stress displacement measurements and an estimated contact area of the fracture at any stress are known, flow through the rough fracture may be calculated from (12).

Application to Laboratory Data

We used results from Iwai's (1976) laboratory investigations on the mechanical and hydrological properties of tension fractures in samples of basalt and granite to test the validity of our physical theory. Iwai measured normal displacements for both intact and jointed rock at normal stresses up to 20MPa, and he also estimated the contact area within the fracture to be 10 to 20% of the total fracture area at maximum stress. Figure 7 shows how his results for radial flow of water through a single fracture in basalt decreased with increasing normal stress during the first loading cycle. Based on his fracture displacements, we used (12) to determine average apertures and then computed flow rates from (11) for fractional contact areas of 10, 15, and 20%. The smooth curves on Figure 7 show how the theoretical results compare with Iwai's experimental data.

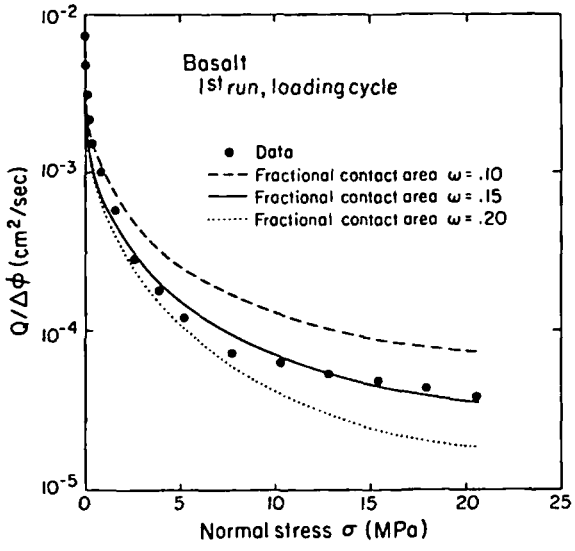

Fig. 7 Experimental and theoretical flow as a function of normal stress in basalt.

In analyzing Iwai's (1976) data for radial flow in a granite fracture, we used his results for both the loading and unloading cycles. Fig. 8 shows the

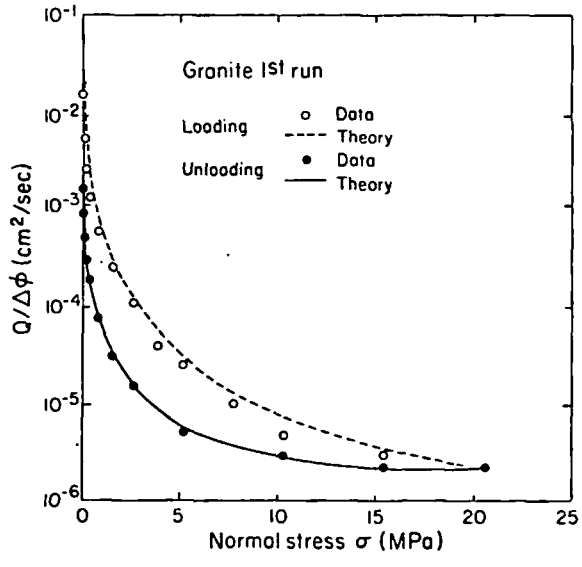

Fig. 8 Experimental and theoretical flow as a function of normal stress in the first loading and unloading cycles in granite.

hysteresis that he observed as a result of a permanent set in the fracture. We assumed a maximum fractional contact area of 15% at maximum applied stress and the smooth curves indicate how our theory compares with his experimental data. Since no curve fitting is involved in handling the flow data, we believe our theory probably contains the essential physics that is relevant to the coupling between stress and flow in a deforming fracture.

Summmary

Both a "void" and an "asperity" description of the fractures are used in this theory. The former is suited to the mechanical property, and the latter, to the hydrological property of the rough-walled fracture. The physical picture that emerges from such a model is that at zero applied stress, the fracture is propped open by only a few tall asperities, giving rise to very long average "crack" lengths. Therefore, the elastic property of the jointed rock appears to be extremely soft at low applied stresses. At higher stresses, the number of asperities in contact increases rapidly, causing a rapid decrease in the average crack length. Thus, the Young's modulus of the jointed rock approaches that of the intact rock.

The fact that the fractional contact area of the fracture at the maximum applied stress of 20 MPa is on the order of 0.15 is of considerable interest. While the stress-displacement measurements indicate that the Young's modulus of the jointed rock becomes almost identical to that of the intact rock at this stress level, the fracture is far from being "closed"; in fact, only about 15% of the fracture surfaces is in contact. The mechanical property of the fracture becomes indistinguishable from that of the intact rock, not because the fracture is "closed," but because the average crack length under increased load has shortened sufficiently, causing the voids in the fracture to deform from elongated shapes (Figs. 4 and 5) to voids more like spheroids. Thus, with respect to its elastic behavior, the fracture is very much like an intact rock; but with respect to its hydraulic behavior, the fracture is definitely "open" to allow fluid transport. Our observation therefore indicates that unless there are very high normal stresses, a fracture probably cannot be "closed" sufficiently to completely prevent hydraulic flow. This seems to be consistent with the observation of Kranz et al. (1979) from their measurement of permeability from pulse decay data. Kranz et al. deduced indirectly from their data that the difference in the flow rate between a jointed and an unjointed rock does not vanish until the effective pressure is at least 200-300 MPa.

POROUS MEDIA EQUIVALENT FOR A NETWORK OF DISCONTINUOUS FRACTURES

One of the important questions that arises when considering the flow of fluids through a discontinuous rock mass is whether or not the fracture network behaves like porous media. In other words, can one model the system by an equivalent permeability tensor and proceed to determine the movement of fluids under the application of known boundary and initial conditions?

Work that has been done to determine the equivalent permeability of fractured rocks from information on fracture geometry (assuming an impermeable matrix) can be classified into two categories. Most of the work that has been done falls into the first category where fractures are assumed to be of infinite extent (continuous or extensive fractures). Very little work has been done in the second category, taking into account the finite or nonextensive nature of fracture size.

Mathematical studies of extensive fracture systems were made by Snow (1965). Snow developed a mathematical expression for the permeability tensor of a single fracture of arbitrary orientation and aperture relative to a fixed coordinate system. The permeability tensor for a network of fractures is therefore the tensor formed by adding the respective components of the permeability tensors for each individual fracture.

It can be seen in the field that fractures are clearly of finite dimensions. The fact that fractures are finite means that each fracture can contribute to the permeability of the rock only insofar as it intersects other conducting fractures. In the extreme, an isolated fracture which does not intersect any other fracture effectively contributes nothing to the permeability of the total rock mass. This means that flow in any given fracture is not independent of flow in every other fracture.

Two approaches have been taken to account for the finite nature of real fractures. Parsons (1966) and Caldwell (1971, 1972) have used analogue models to study finite fractures. Rocha and Franciss (1977) have proposed a field method for finding a correction factor to Snow's (1965) analysis.

A significant result of Parson's work was that doubling the permeability of all fracture elements in the x direction increased the permeability in the y direction. This effect would not be seen in continuous fractures, but with discontinuous fractures the net flow in the y direction must proceed through some fractures oriented in the x direction. Also, for a similar reason, permeability in the x direction is less than doubled. This is a significant property of fracture systems that must be kept in mind.

Homogeneous Anistropic Permeability

In order to determine when a fractured medium behaves as a homogeneous, anistropic medium, one must determine if a symmetric permeability tensor exists. The only way to show this is to actually measure the directional permeability. Darcy's law:

$$q_i = K_{ij} \frac{\partial \phi_i}{\partial x_j} \qquad (13)$$

can be used to examine the theory of directional permeability measurement. The fact that flow and gradient are not necessarily in the same direction can be seen from inspection of the above Darcy equation. Only when flow and gradient coincide with one of the principle axes of permeability will flow and gradient be in the same direction.

Marcus and Evanson (1961), Marcus (1962), and Bear (1972) give both the expression for permeability in the direction of flow and permeability in the direction of gradient. Both show how the results of

directional permeability measurement can be plotted as ellipsoids. For K_f, the permeability measured in the direction of flux, $\sqrt{K_f}$ plotted versus α, the direction of measurement, on polar coordinate paper will be an ellipsoid given by:

$$1 = \frac{x^2}{K_1} + \frac{y^2}{K_2} + \frac{z^2}{K_3} \tag{14}$$

Likewise for K_g, the permeability in the direction of the gradient, $1/\sqrt{K_g}$ plotted versus α will be an ellipsoid given by:

$$1 = \frac{x^2}{1/K_1} + \frac{y^2}{1/K_2} + \frac{z^2}{1/K_3} \tag{15}$$

For permeability measured in the direction of flux, the major axis of the ellipsoid is in the direction of maximum permeability. For permeability measured in the direction of the gradient, the major axis of the ellipsoid is in the direction of minimum permeability.

Another basic problem is that of establishing homogeneity. Homogeneity has been discussed by Hubbert (1956), Fara and Scheidigger (1961), Toth (1967), Bear (1972), and Freeze (1975). Freeze points out that there is really no such thing as a truly homogeneous medium in geology. However, in order to have a tractable analysis of flow, a scale of measurement (the macroscopic scale) must be found for which the porous medium is seen as a continuum (Hubbert, 1956). On this scale the medium is said to be homogeneous. The scale at which analysis is possible is commonly illustrated with a diagram such as Figure 9. The volume at which the parameter

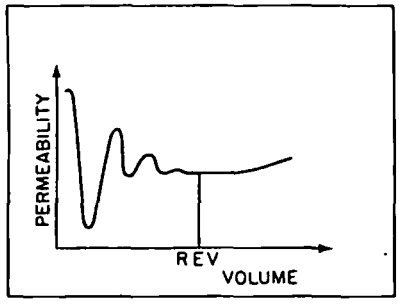

Fig. 9 Change in value of measured permeability with size of sample.

of interest, in this case permeability, ceases to vary is defined as the representative elementary volume (REV). With respect to permeability, the REV of a medium can be sought by measuring the average permeability of increasing volumes of rock until the value does not change significantly with the addition or subtraction of a small volume of rock.

There is no guarantee that such an REV exists for every permeable system. Indeed, Snow's (1969) theoretical and experimental work shows the permeability of fractured rock may continue to increase with the volume tested. This implies that the statistical sample continues to change with the size of the sample. A further problem has been studied by Freeze (1975), Smith and Freeze (1979a, 1979b), and Smith (1978). They have concluded that for some problems it may not always be possible to define equivalent homogeneous properties for inherently heterogeneous systems.

The difficulty in identifying equivalent permeability is that, (a) the equivalent permeability tensor that works for one set of boundary conditions will not necessarily predict the correct flux for another set of boundary conditions, and (b) an equivalent permeability which is correct in terms of flux may not predict the correct average head distribution. The first difficulty arises because, in general, different boundary conditions induce different gradients in different parts of the flow field. The permeability in one part of the field which has a higher gradient will have more effect on the total flux than the permeability in another part of the field which has a lower gradient. When the boundary conditions change, the emphasis changes. Therefore, a given equivalent permeability tensor will only apply absolutely to kinematically similar flow systems.

If the gradient within the internally heterogeneous REV remains approximately constant, each part of the element will have equal emphasis, and it may be possible to define a unique equivalent permeability tensor which will be correct for approximately linear flow in any direction. However, if the isopotentials and flow lines are curved relative to the dimensions of the statistically determined REV, then the value of the equivalent permeability of the REV will depend on the particular kinematics of the flow system. In this case, analysis of the flow system would depend on the knowledge of the equivalent permeability and the value of the equivalent permeability would depend on the flow system. So a unique solution to the flow problem is not guaranteed. If, on the other hand, the gradient is constant and the average flow lines are linear within the statistically determined REV, then there may exist a single permeability tensor which can be used to correctly predict flow in any direction. However, even under the constraints of a constant gradient, there is still no guarantee that a unique, symmetric permeability tensor will exist for every medium on any scale.

Given a flow system such as seepage under a dam, the size of the appropriate REV must be small enough to have approximately a constant gradient throughout and therefore linear average flow lines. However, it must also be large enough to contain a representative sample of the heterogeneities. In some cases, it may be that a statistically defined REV is too large to have linear average flow lines. In this case, either a smaller REV must be found as the basis for analysis or a non-continuum analysis must be used.

The above discussion leads to several conclusions central to this investigation. First, it only makes sense to look for REVs in fractured rocks using flow systems which would produce a constant gradient and linear flow lines in a truly homogeneous, anisotropic medium. Boundary conditions which produce such a flow system will be described below. Second, the following criteria must be met in order to replace a heterogeneous system of given dimensions with an equivalent homogeneous system for the purposes of analysis:

(1) there is an insignificant change in the value of the equivalent permeability with a small addition or subtraction to the flow volume;

(2) an equivalent symmetric permeability tensor exists which predicts the correct flux when the direction of gradient is changed.

Point (1) implies that the size of the sample under consideration is a good statistical sample of the heterogeneities. Point (2) implies that the boundary conditions are applied to the sample which would produce a constant gradient throughout a truly homogeneous anisotropic sample. The actual gradient within the heterogeneous sample does not have to be exactly constant for (2) to be satisfied.

Statistics of Fracture Geometry

Under a given set of boundary conditions, the hydraulic behavior of a fractured rock mass with an impermeable matrix is determined entirely by the geometry of the fracture system. Real fractures have complex surfaces and variable apertures, but for the purposes of this study and most other studies of fracture systems, the geometric description is simplified. The assumption is made that individual fractures lie in a single plane and have a constant hydraulic aperture. Characterization of a fracture system is considered complete when each fracture is described in terms of: (1) hydraulic or effective aperture, (2) orientation, (3) location, and (4) size.

As has been discussed in the first part of this review, the hydraulic behavior of fractures has been shown to be a function of their aperture (equation 11). Characterization of the permeability of a fracture requires determining the hydraulic aperture. Unfortunately, it is very difficult to perform hydraulic tests on isolated fractures in the field. For example, Gale (1975) isolated a limited number of horizontal fractures with packers and performed injection tests to determine their apertures. Gale's data, however, is not extensive enough to make significant analysis of the relationship between hydraulic and apparent apertures.

Because of the difficulty involved in hydraulically isolating a single fracture underground, what we know of fracture aperture distributions is limited to apparent apertures that have been observed directly in cores or well logs. The distribution of apertures measured by Bianchi and Snow (1968) was found to be very close to lognormal. It may be reasonable to expect the distribution of true hydraulic apertures to also be distributed lognormally.

The statistics of fracture orientation are perhaps the best understood of all the geometric properties of fractures. Orientation is easily measured in cores or in outcrops with simple tools. For instance, Mahtab (1972) developed a computerized method for analyzing clusters of orientation data. Once clusters had been identified they were compared to Arnold's hemispherical normal distribution.

The mathematical description of fracture locations and fracture dimensions are interrelated. Fracture traces can be observed in outcrops or in excavations. The location of the intersections of fractures within a borehole can also be determined. What we know about the location of fractures in space and their shape and dimensions comes from this trace length and intersection data.

Robertson (1970), Priest and Hudson (1976), Hudson and Priest (1979), and Baecher (1978) have studied length and spacing distributions for fractures. Baecher et al. (1977) have reviewed this literature on spacing and length distribution. Spacing and length have both been reported to vary exponentially and lognormally. Baecher (1978) developed a conceptual joint geometry model. Joint trace lengths are assumed to be lognormally distributed and spacings are assumed to be exponentially distributed. The authors infer that joints are circular disks randomly distributed in space. Joint radii are shown to be lognormally distributed.

Numerical Method of Analysis

A numerical code has been developed to generate sample fracture systems in two dimensions using the geometric properties described above and to determine the permeability of such systems. The computer program has been used to study samples of both extensive and nonextensive fracture networks.

The two-dimensional mesh generator produces random realizations of a population of fractures. Input to the generator includes specification of the distributions that describe the fracture population. The mesh generator can randomly choose fractures for the sample according to these distributions. Details of the scheme for mesh generation are given by Long et al. (1981). A finite element analysis can then be used to calculate Q_g, the component of flow through the pattern in the direction of the gradient. Using Darcy's law, the hydraulic conductivity in the direction of the gradient of the sample fracture pattern is calculated from:

$$K_g = \frac{Q_g}{A \nabla \phi} \tag{16}$$

where A is the gross area perpendicular to flow. The analysis of permeability is independent of the type of fracture model generated. This generator produces models similar to Baecher's (1978) but another fracture model, such as that proposed by Veneziano (1979) could just as easily have been used.

The effect of sample size on conductivity measurement can be studied with this program. First a large fracture pattern is generated. A small piece of this sample can be numerically removed and subjected to the numerical conductivity test described above (equation 16). Succeedingly larger pieces can be tested and the results compared.

The program can also be used to study the variation in conductivity between different realizations of a statistically described fracture system. This Monte Carlo type analysis could also be used to analyze statistical data collected in the field. An expected value and standard deviation of equivalent porous media conductivity would be obtained in this way.

As previously discussed, a method which obtains conductivity in the direction of the gradient must be used. Gradient can be approximately linear throughout a heterogeneous region in steady flow if the region is an REV. The direction of flow, however, is controlled by the direction of the fractures. The boundary conditions necessary to produce a constant gradient in a rectangular, anisotropic flow region are illustrated in Fig. 10. It consists of two constant-head boundaries (sides 2 and 4) and two boundaries (sides 1 and 3) with the same linear

variation in head from $\phi_2 = 1.0$ to $\phi_4 = 0$. An example of the configuration used in these analyses is shown in Fig. 10. Conductivity is measured in the direction perpendicular to sides 2 and 4.

The linearly varying boundary conditions on sides 1 and 3 are necessary because, in general, the medium in the flow region is anisotropic. Without these boundaries the lines of constant head would be distorted near sides 2 and 4.

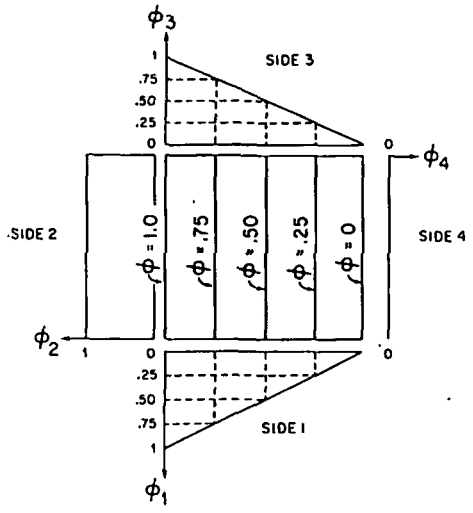

Fig. 10 Boundary conditions necessary to produce constant gradient in a homogeneous anisotropic flow region.

For the boundary conditions shown in Fig. 10, $\partial\phi/\partial y$ is zero. K_{xx} can be calculated from:

$$K_{xx} = \frac{\frac{Q_x}{(\phi_2 - \phi_4)L}}{L} = \frac{Q_x}{\phi_2 - \phi_4}. \qquad (17)$$

where Q_x is the total flux per unit thickness in the x direction. For $\phi_2 = 1$ and $\phi_4 = 0$, and consistent units, K_{xx} is numerically equal to Q_x. Also, since Q_y, the total flux per unit thickness in the y direction, is known, K_{xy} can be calculated from:

$$K_{xy} = \frac{\frac{Q_y}{(\phi_2 - \phi_4)L}}{L} = \frac{Q_y}{\phi_2 - \phi_4} \qquad (18)$$

For $\phi_2 = 1$ and $\phi_4 = 0$, as above, $K_{xy} = Q_y$.

Flow through the fracture system is computed using a finite-element program developed by Wilson and Witherspoon (1970) for fracture flow. Fractures are represented as line elements with flux related to aperture by the cubic law. The rock matrix is assumed to be impermeable. Only the steady state flow rate is calculated.

In general, the fracture pattern results in an anisotropic medium. Conductivity in such a fracture pattern can be measured in any direction chosen. For homogeneous anisotropic media, $1/\sqrt{K_{xx}}$ versus α, the angle of rotation, is an ellipse when plotted in polar coordinates. However, for inhomogeneous fractured media, $1/\sqrt{K_{xx}}$ may not plot as a smooth ellipse. In fact, the shape of a plot using measured values of K_{xx} for a given area of rock may be quite erratic. This plot can be used as a test of whether or not the given area can be approximated as a homogeneous porous medium. If $1/\sqrt{K_{xx}}$ does not plot at least approximately as an ellipse, then no single symmetric conductivity tensor can be written to describe the medium. If there is no conductivity tensor then flow through the medium cannot be analyzed by existing continuum techniques.

Validation of Numerical Method

The following two examples will illustrate the use of this numerical method of analyzing flow in two-dimensional networks of fractures. The first example is a fracture system of known conductivity and was used to verify the numerical method of permeability measurement. The conductivity of fracture systems with infinitely long fractures is known from the theory developed by Snow (1965) and others. Because of the physical basis of this fracture model, we could only examine finite pieces of such fracture systems. The infinite fractures are seen in a finite model as fractures which transect the entire model. An arbitrary extensive fracture system with two sets of parallel, evenly spaced, equal aperture fractures was tested. To provide an anisotropic case, the two sets were placed 30° apart. The numerical code was used to determine K_g for variations of α ranging from 0° to 105° as measured from one of the two fracture sets. Theoretically, this fracture network should produce an ellipse for $1/\sqrt{K_g}$ as shown by the solid line on the polar plot in Fig. 11. The plotted points represent the results

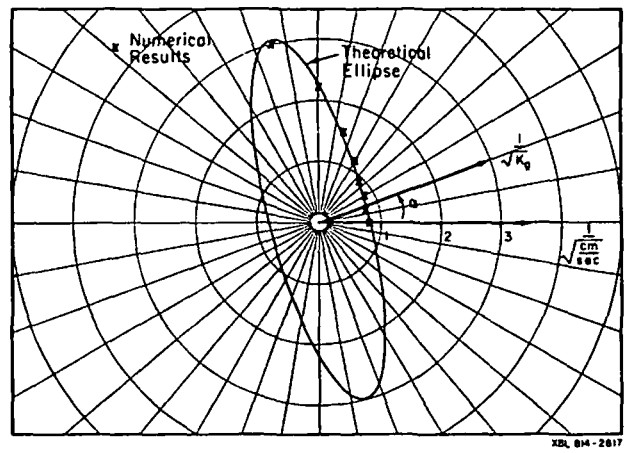

Fig. 11 Polar plot of numerical results for $1/\sqrt{K_g}$ compared to theoretical ellipse. Extensive fracture system composed of two sets of parallel, evenly spaced, equal aperture fractures placed 30° apart.

from the numerical analysis as the direction of the hydraulic gradient was changed in increments of 15°. The small differences between theoretical and numerical results can be attributed to the finite nature of the numerical model. Obviously, a fracture network with these properties could be replaced by an equivalent porous media.

The second example is a nonextensive fracture system that was developed at random using the mesh generation scheme described by Long et al. (1981).

Table 1 gives the statistics used to generate the fractures. The generation region was 110cm x 110cm.

Table 1. Input parameters for random network of fractures.

Parameters		Set 1	Set 2
Density	Number of Fractures	49	100
Orientation	Normal distribution m, s^2 (deg)	30, 5	60, 10
Length	Lognormal distribution m, s^2 (cm)	40, 10	30, 7.5
Aperture	Lognormal distribution m, s^2 (cm)	.001, .005	.005, .0001

To determine what variations might be expected from a repetitive generation of networks having the same parameters listed in Table 1, three different fracture systems were examined. Flow regions 75cm x 75cm oriented with $\alpha = 0°$ were investigated in each network. The three regions had network characteristics as given in Table 2.

Table 2. Characteristics of three random fracture networks.

Network	Number of Fractures	Number of Fracture Intersections	Number of Nodes	Number of Elements
1	81	123	285	327
2	86	110	282	306
3	90	139	319	368

Boundary conditions were applied to these three flow regions such that conductivity in the same direction could be measured. That is, sides 1 and 3 were given a linearly varying head distribution, side 2 had a constant head of 1, side 4 had a constant head of 0 (see Fig. 10). Table 3 gives the total fluxes in cm^3/s from each side for each flow region. A positive sign indicates flow into the region and a negative sign indicates flow out of the region.

Table 3. Total fluxes for three random fracture networks.

Network	Side 1 cm^3/s	Side 2 cm^3/s	Side 3 cm^3/s	Side 4 cm^3/s
1	0.13402E-19	4.41796E-7	-4.41384E-7	-4.11388E-10
2	0.39260E-10	2.00821E-5	-2.00809E-5	-8.67380E-10
3	0.42390E-10	1.01927E-4	-1.01927E-4	-8.97845E-11

Examination of Table 3 leads to several conclusions. First, there is a great deal of variation between the three networks generated using the same statistical fracture population. As shown in Table 2, the number of fractures in each flow region varies. Thus some of the variation in flow rate is due to nonergotic sampling. Recall that under the boundary conditions used, for an ideal porous medium the flux in the x direction, i.e. from side 2 to side 4, is numerically equal to the conductivity. However, examination of Table 3 shows that the flux into side 2 does not equal the flux out of side 4. The sum of the fluxes through all sides, however, is zero as expected. These samples are clearly not behaving like porous media. In anisotropic porous media under the chosen boundary conditions the flux on opposite sides would be equal.

To investigate the problem of directional permeability, Network 3 was selected for further analysis. Flow regions 75cm x 75cm in size were rotated at intervals of 15° so that α could be varied from 0° to 180°. Fig. 12A shows the fracture network of the

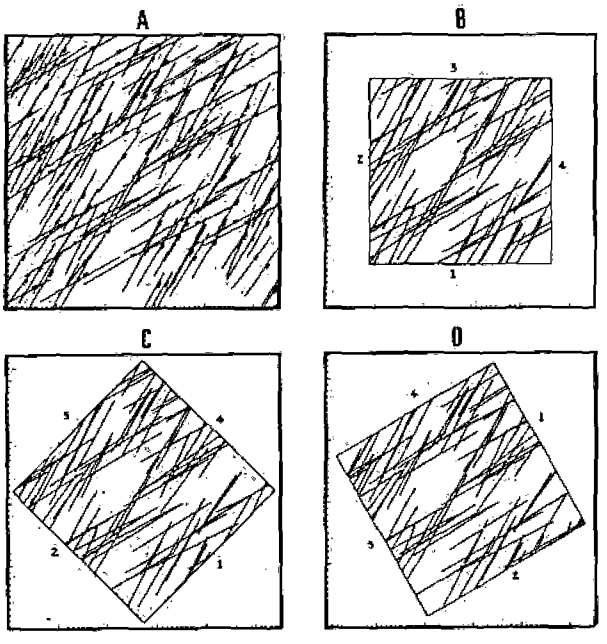

Fig. 12 Nonextensive random fracture system showing original generation region (A), and flow regions investigated when $\alpha = 0°$ (B), $\alpha = 45°$ (C), and $\alpha = 120°$ (D).

original generation region and Figs. 12B-C-D illustrate how different flow regions were created simply by rotating the boundaries while the network remained fixed.

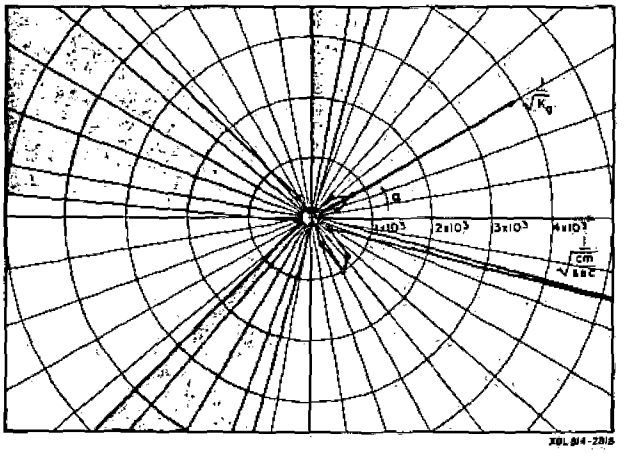

Fig. 13 Polar plot of numerical results for $1/\sqrt{K_g}$ for a nonextensive random fracture system.

Figure 13 shows the values of $1/\sqrt{K_g}$ plotted on polar coordinate paper where K_g is defined in terms of flux across side 2. The fact that inflow does not equal outflow on opposite sides leads to a problem in defining conductivity. If conductivity is arbitrarily defined as numerically equal to the inflow into side 2, no information is lost. Side 2 for any angle α becomes side 4 for $\alpha + 180°$, etc.

The results on Fig. 13 clearly do not plot as an ellipse; nor are they symmetric. For certain angles of rotation (e.g., 75°, 90°) the value of $1/\sqrt{K_g}$ becomes very large and goes off the scale of the graph. For these angles, K_g is very small because there is practically no hydraulic connection between sides 2 and any other side. This cannot be completely confirmed visually from the plots of these flow regions because aperture has not been included in the figures. Although isopotentials have not been plotted for these samples, it is fairly certain they will not be linear. If we define K_{yx} as numerically equal to the flow into or out of side 3, then K_{xy} is the flow into or out of side 1 when the flow mesh is rotated 90°. K_{xy} should equal K_{yx} if K_{ij} is symmetric. For this example, computed values of K_{yx} did not equal computed values of K_{xy} for any angle of rotation. This further demonstrates the nonsymmetric nature of the permeability.

The tests described above show clearly that the sample chosen does not have a symmetric conductivity tensor and cannot be represented by an equivalent porous medium. As further proof of the nonhomogeneous nature of Network 3, flow regions of different sizes were extracted and tested. The particular orientation shown on Fig. 12 for $\alpha = 0°$ was selected, and the flow region was reduced from 75cm x 75cm to 25cm x 25cm, while remaining centrally located in the original generation region. The results revealed order of magnitude changes in hydraulic conductivity from sample to sample and further illustrated the marked differences between the fluid flow behavior of this random fracture network and that of homogeneous porous media.

Summary

A numerical model has been developed to produce random networks of fractures. A computer program for fluid-flow analysis then measures the directional conductivity of these samples.

To determine if the fractured rock samples behave like porous media, the samples must be subjected to boundary conditions which would produce a constant gradient in homogeneous anisotropic media. If the medium has an equivalent porous medium permeability, these directional conductivity measurements should plot as an ellipse when $1/\sqrt{K_g}$ is plotted versus direction α on polar coordinate paper. Also, inflow will equal outflow on opposite sides of the rectangular volume element tested, and measured values of K_{xy} will equal measured values of K_{yx}. Average isopotentials within the element will probably be linear, but this is not a necessary criterion for behavior as an equivalent porous medium. If the volume of the element tested is changed slightly, the measured values of K_{ij} should not change significantly.

It is possible to find a fractured rock population for which no equivalent homogeneous porous medium permeability exists. This can occur for one of two reasons. First, the size of the REV may exceed the volume of rock that exists. Secondly, for the case of an impermeable matrix, the fractures may not be dense enough to behave as a medium with a symmetric permeability tensor. Non-"tensorial" behavior would result from insufficient interconnections between fractures. In this case, the volume of fractured rock may be large enough to be a good sample of the fracture population, but the nature of the fractures is such that they will not behave hydraulically as a porous medium on any scale.

The numerical techniques described here will be used to find fractured rock systems that do behave like anisotropic porous media. Fracture systems with specified geometries (spacing, aperture, length, and orientation) will be investigated. If the total number of fractures is held constant, the density of the fractures will be increased until systems are found which behave more like porous media. For a given population and a given total number of fractures, we should be able to identify minimum fracture densities which produce homogeneous anisotropic behavior. The effect of each distributed parameter on the size of the REV and the value of the resulting conductivity can then be determined.

Systems for which no REV exists will also be sought. This can be done by examining systems that are not dense enough to act like porous media. By holding this density constant and increasing the area of investigation, we can see if the behavior of the system becomes more like that of porous media or remains erratic.

Methods for quantifying the porous media nature of fracture systems are under development. One method currently being investigated is to quantify how well the permeability data plot as an ellipse. Such an approach should lead to an understanding of the errors that can result from assuming a porous medium equivalent for a fractured rock mass when no such equivalence exists. Ultimately, our goal is to be able to analyze field data on fracture systems to determine when it is appropriate to make the simplifying assumption of a porous medium equivalent. This, of course, will require an understanding of the need to extend the technique to three dimensions.

COUPLED THERMAL-HYDRAULIC-MECHANICAL FINITE ELEMENT MODEL FOR SATURATED FRACTURED POROUS MEDIA

In the usual treatment of fluid flow in porous media, the rock deformation has been considered through the concept of the coefficient of specific storage. This approach, although by no means precise, is adequate to represent most fluid flow problems. A more realistic treatment of the fluid flow behavior of deformable porous media came about after the introduction of the well-known theory of consolidation by Terzaghi (1925). With the advent of computers, numerical solution techniques for coupled one-dimensional equations of consolidation and multidimensional equations of fluid flow provided an approximate means of analyzing general fluid flow problems in deformable porous media (Helm, 1974, Narasimhan and Witherspoon 1977). Biot (1940) introduced the general theory of consolidation which makes possible a more realistic treatment of the hydromechanical behavior of saturated porous rocks. In an attempt to develop a method for the solution of general consolidation problems, Sandhu and Wilson (1969) applied the variational finite element method

to the problem of fluid flow through saturated porous elastic solids. This method was extended by Ghaboussi and Wilson (1971) in considering effects of fluid compressibility.

The theories of mixtures (Green and Naghdi, 1965), Crochet and Naghdi (1966), which have a sound thermodynamical basis and a general associated constitutive theory, can be reduced to a special case of a theory for flow of fluids through porous elastic solids which is equivalent to Biot's work. The basic assumption of this approach leads to certain conceptual difficulties in the physical interpretation of partial stresses.

Recently Safai and Pinder (1979), in a Galerkin finite element method of analysis for fluid flow through deformable porous media, made an attempt to consider the entire saturated-unsaturated flow regime. The proper constitutive stress-strain relationship for the extension of Biot's (1940) theory to the entire flow regime was later provided by Noorishad et al (1981a).

Consideration of fracture deformability along with its hydromechanical behavior has appeared in the literature mainly since 1965. Davis and Moore (1965) measured one of the first direct evidences of fracture deformations of the order of microns caused by earth tides. Snow (1968) reported strains of 10^{-7} to 10^{-8} at a distance of about 300 ft from a water well in metamorphic rocks subjected to a significant drawdown. To handle this behavior, the early hydraulic and hydromechanical analysis of fractures was achieved using an equivalent porous medium approach. Theoretical and numerical studies of fluid flow in a rock mass taking into account the deformable nature of fractures in a discrete manner was first carried out by Noorishad et al. (1971). This work was based on earlier studies of discrete fracture behavior from a load-deformation point of view by Goodman et al. (1968) and a fluid flow point of view by Wilson and Witherspoon (1970).

Numerical studies on deformable fractured rocks have been carried out by Rodatz and Wittke (1972) and Gale (1975). Iwai (1976) made a detailed series of laboratory tests on flow through a single fracture under load. The laboratory and field tests by Gale (1975) provided strong evidence of a nonlinear fracture deformability induced by fluid pressure changes and also verified the capability of the numerical solution technique. The static approach of Noorishad et al (1971) was later extended by Hilber et al. (1979) into the dynamic range where stick-slip phenomena due to injection of an incompressible fluid in a nonporous fractured rock was studied.

A two-medium statistical-numerical model was presented by Duguid (1973) who extended the method introduced by Barenblatt et al (1960) to fissured elastic porous media using a finite element numerical procedure. A deterministic solution for transient flow of fluids in deformable fractured porous rocks was recently achieved using an enumerative approach (Ayatollahi, 1978). This variational finite element technique is based on a generalization of Biot's (1940) constitutive stress-strain equation and uses a Gurtin (1964) type variational principal. An extension of this work by Noorishad et al. (1981b) provides a general two-dimensional, finite element solution technique for the investigation of the deformation, stress distribution, fluid storage, and fluid flow properties of a fractured porous medium under the influence of hydraulic and structural boundary conditions. At present, several groups are investigating a host of numerical hydromechanical models which are at different stages of development. Baca (1980) and Tsang (1980) have summarized the capabilities of some of these new models.

The presence of heat in fluid flow regimes brings about a chain of coupled effects which shall be referred to here as thermal-hydraulic-mechanical phenomena. The coupled phenomena for fluid and heat flow, usually known as hydrothermal flow, have been the subject of several detailed studies. A complete account of the state-of-the-art can be found in Pinder (1979) and Wang et al (1980). However, it should be pointed out that hydrothermal investigation of discontinuous rock masses is a problem that needs much more investigation.

Studies of thermal effects on linear and nonlinear materials, known as thermoelasticity, are thoroughly covered in the physics and engineering disciplines and need not be considered here. As far as rock mechanics usage is concerned, thermoelasticity lies mostly within the confines of continuum applications. An account of the status and needs of the thermomechanical modeling techniques for continuous and discontinuous media is given by Hocking (1979). More recent reports (Bacca, 1980; Tsang, 1980) indicate that a number of the new, developing models either have provisions for incorporating fractures or actually have the capability of modeling the discontinuities in a discrete manner.

A natural outgrowth of hydromechanical, hydrothermal, and thermomechanical modeling techniques is the development of a general model incorporating all of the above techniques. Baca (1980) and Wang et al. (1980) have reported that a number of research organizations are engaged in the development of such general modeling techniques but to our knowledge, the details have not yet been published. Various rock-water interaction studies have been underway in this laboratory for some years, and the development of an approach to the thermal-hydraulic-mechanical behavior (or hydrothermoelasticity) of fractured rocks is part of an ongoing effort (Noorishad and Witherspoon, 1981). The essential features of this coupled finite element method of analyzing fractured porous rocks will be presented below.

Field Equations

Using τ_{ij} for the components of the bulk stress tensor, P for fluid pressure, and T for temperature, Noorishad and Witherspoon (1981) have shown that the stress-strain relationship for an elastic isotropic porous medium can be written:

$$\tau_{ij} = 2\mu e_{ij} + \lambda\delta_{ij}\,\delta_{k\ell}e_{k\ell} - \beta\delta_{ij}T + \alpha\delta_{ij}P \qquad (19)$$

$$\xi = \frac{\rho_\ell}{\rho_o}\,\alpha\delta_{ij}e_{ij} + \frac{1}{M}\,P + \frac{1}{M_T}\,T$$

In the above equations the dependent variables e, T, and P are incremental in value and represent deviations from the zero state (stress-free state). Also, contact equilibrium between the fluid and the solid is assumed.

The governing equation for the fluid flow is written as:

$$\frac{\partial \xi}{\partial t} = \nabla \cdot \left[\frac{\rho_\ell \underline{k}_f}{\rho_o} (\nabla p + \rho_\ell g \nabla z) \right] \tag{20}$$

and ρ_ℓ and ρ_o are related through the equation of state for the fluid:

$$\rho_\ell = \rho_o \left[1 + \beta_T T + \beta_p P \right] \tag{21}$$

Note that internal or boundary source terms are absent in (20), a restriction which is later easily relaxed.

The law governing the static equilibrium is given as:

$$\frac{\partial \tau_{ij}}{\partial x_j} + \rho_s f_i = 0 \tag{22}$$

Finally the law for conservation of energy is represented in the following form:

$$\frac{\partial}{\partial t}[(\rho C)_M T + T_o \beta \delta_{ij} e_{ij}] + \varepsilon \rho_\ell C_{v\ell} \underline{q} \cdot \nabla T = \nabla \cdot \underline{K}_M \nabla T \tag{23}$$

where:

$$(\rho C)_M = \varepsilon \rho_\ell C_{v\ell} + (1 - \varepsilon) \rho_s C_{vs}$$

$$\underline{K}_M = \varepsilon \underline{K}_\ell + (1 - \varepsilon) \underline{K}_s$$

The Darcy fluid velocity $\underline{q}$ is given as:

$$\underline{q} = - \frac{\underline{k}_f}{\eta_\ell} (\nabla p + \rho_\ell g \nabla z) \tag{24}$$

The quantity T_o represents the absolute temperature in the stress-free state. In deriving the governing equation for heat flow (23), the following assumptions are made:

(i) thermal contact equilibrium between the fluid and the solid
(ii) energy associated with the fluid dilatation is negligible
(iii) fluid shearing stresses are absent in macroscopic sense
(iv) internal source terms and boundary source terms are absent.

The last assumption is later removed in the numerical algorithm.

The fundamental laws governing static equilibrium, fluid flow, and heat flow are coupled through the dependent variables of the solid displacement vector, fluid pressure, and macroscopic medium temperature. These laws, presented in equations 20, 22, and 23, in conjunction with constitutive equations 19 and 21 provide the complete mathematics of the coupled quasi-linear, thermal-hydraulic-mechanical phenomena in saturated porous elastic media. Extension of the above development to the nonlinear range is no major task and has already been accomplished. For the sake of simplicity, the extended development for the nonlinear fractured media will not be presented here. The above equations with proper initial and boundary conditions (see Appendix) define the mixed initial-boundary-value problem for thermal-hydraulic-mechanical phenomena in porous media.

Method of Solution

The complexity of the hydrothermoelasticity equations is such that an analytic (mathematical) solution for even simple initial and boundary value problems is not likely to be found. However, numerical solutions to the most general problems can easily be sought. Various numerical schemes using well-known numerical techniques, such as finite element and finite difference, can be utilized. In this work a finite element technique, was given strong preference because of earlier experience with this approach to linear and nonlinear problems of hydroelasticity (Ayatollahi, 1978; Noorishad et al., 1981b). A mixed variational and Galerkin finite element method forms the basis of this approach. As a result, the following set of matrix equations is obtained:

$$\underline{K}\,\underline{U} + \underline{C}_{UP}\underline{P} + \underline{C}_{UT}\underline{T} = \underline{F} \tag{25}$$

$$\underline{C}_{PU}\underline{U} + (\underline{E}_f + 1^*\underline{H}_f)\underline{P} + \underline{C}_{PT}\underline{T} = -1^*\underline{Q}_\ell \tag{26}$$

$$\underline{C}_{TU}\underline{U} + [\underline{E}_h + 1^*(\underline{H}_{hf} + \underline{H}_h)]\underline{T} = -1^*\underline{Q}_h \tag{27}$$

where 1^* represents time integration. Details of the method of solution and the complete expressions for the matrix coefficients are given in the Appendix.

To handle discretization in the time domain, two different schemes of time integration are used to integrate matrix equations 25, 26, and 27. A predictor-corrector scheme (Taylor, 1974) is used for the integration of the first two implicitly coupled equations (Ayatollahi et al., 1981). The energy equation uses a Crank-Nicholson step-by-step procedure with the solution of each time step being sought in the middle of the interval.

The coupling of (27) to (26) is nonlinear and is implicitly expressed in $\underline{H}_{hf}$, the nonsymmetric convective thermal conductivity matrix. The large time constant for the energy equation as compared to that of the flow equation suggests that the above formulation is easily adapted to an interlacing scheme of solutions such as used by Sorey (1975). This interlacing scheme uses the fluid velocities obtained from a direct solution of (25) and (26) and feeds back the temperature resulting from a solution of (27). This approach of explicitly solving the coupled equations is enhanced by the low sensitivity of the dependent variables P and U within some ranges of temperature in different problems. Therefore, the energy equation in these ranges can march through time using large time steps compared to the small time steps required to solve the other two equations. A further advantage is gained in situations where the mass transfer contribution to temperature distribution is negligible. In these cases a single solution for the energy equation provides the needed temperature information for the stepwise solution of the other two equations.

Three types of elements are used in this coupled technique: (a) two-dimensional isoparametric elements for solid fluid mixtures, (b) one-dimensional elements representing fracture segments from the flow point of view, and (c) one-dimensional joint elements to represent fracture segments for structural considerations. Natural coordinates are used for discretization of the displacement, pressure, and temperature

fields within the quadrilateral element. This leads to a parametric formulation for the corresponding integrals in terms of coordinate parameters for the porous solid-fluid mixture elements. Numerical integration is performed using the Gauss quadrature formula. The isoparametric bilinear function used for discretization and the parametric details can be found in finite element texts (Zienkiewicz, 1971]. For the structural joint element and the flow-line element, discretization of the displacement and pressure fields, is written in terms of local coordinates. Where necessary, the results are transformed to the global coordinate system. The assumption of uniform aperture within each fracture was used throughout the derivation of the matrices involving fracture volume integrals.

Validation of Numerical Scheme

The complexity of the coupled phenomena under consideration makes it possible to present only a partial verification of the method of analysis presented here. In the following discussion, we shall include results of the application of the method to hydromechanical, thermomechanical, and hydrothermal problems. These examples do not fully reveal the power of this approach.

In choosing an example of a hydromechanical problem, we examined a fracture flow problem for which an analytical solution exists (Raghavan et al., 1976). Since this problem does not require coupling between fluid flow and rock deformation, the coupling coefficient α was set to zero and 1/M was changed to S_s in equation 19.

The problem is that of a single vertical fracture intersecting a well of zero radius in a rectangular porous medium. The fracture is assumed to be rigid and of very high conductivity. The material properties of the fluid and rock are given in Table 4. Fig. 14 shows the finite element mesh used and Fig. 15 shows how the numerical results compare with the analytical solution (Raghavan et al., 1976). For the case $X_D = 1$, there is excellent agreement over the whole time span. In the case $X_D = 3$, the differences noted on Fig. 15 between numerical and analytical solutions is attributed to the coarseness of the finite element mesh. The half slope of the curve for P_D versus t_D at early time is often used as evidence in the petroleum literature for the presence of a fractured system (Gringarten et al., 1975).

This problem was also solved in a coupled manner where deformability in both the fracture and the matrix were introduced (Table 4). The fracture was also given a specific aperture (10^{-4}m) so that it had a finite permeability. The effect of treating

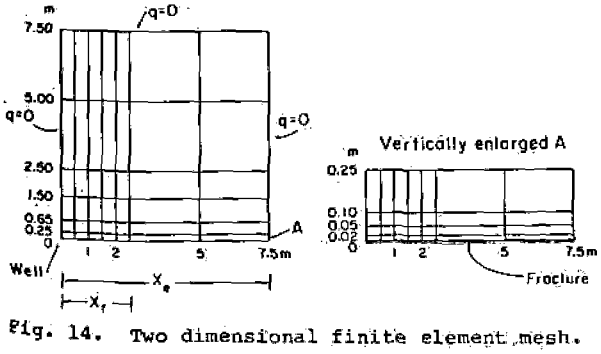

Fig. 14. Two dimensional finite element mesh.

Table 4. Material properties for hydromechanical analysis of fractured rock mass.

Material	Property	Value
Fluid	Mass density, ρ_ℓ	9.80×10^2 kg/m^3
	Compressibility, β_p	5.13×10^{-1} GPa^{-1}
	Dynamic viscosity, η_ℓ	2.80×10^{-4} N sec/m^2
Rock	Young's modulus, E_s	2.45 GPa
	Poisson's ratio, ν_s	0.25
	Mass density, ρ_s	2.5×10^3 kg/m^3
	Porosity, ϵ	0.15
	Intrinsic Permeability, k_f	10^{-12} m^2
	Biot's constant, M	1.47GPa, 14.0 GPa*
	Biot's coupling constant, α	1.0, 0.0*
Fractures	Initial normal stiffness, K_{fn}	1.60 GPa/m
	Initial tangential stiffness, K_{fs}	0.50 GPa/m
	Cohesion, C_o	0.0
	Friction angle, δ	30°
	Initial aperture, b	10^{-3}m, 10^{-4}m
	Porosity, ϵ	0.15
	Biot's constant, M	1.47 GPa, 14.0 GPa*
	Biot's constant, α	1.0,0.0*

*Used in the uncoupled case.

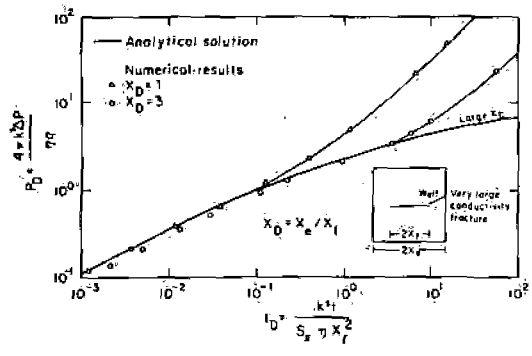

Fig. 15 P_D versus t_D for single vertical fracture of very large conductivity in porous medium. Analytical solution after Raghavan et al. (1976).

the system in this fashion is to change the pressure drawdowns significantly. For example, Fig. 16 shows how pressures decrease from the wellbore to the end of the vertical fracture. It will be noted that the pressure drop at the end of the fracture is about half that at the wellbore. For comparison, the problem was rerun in a decoupled mode and the pressure differences are far less (see curve labeled "fluid flow analysis" on Fig. 16).

Fig. 17 shows a plot of P_D versus t_D for this finite conductivity fracture problem to demonstrate the differences from the case of a very high conductivity fracture (Fig. 15). Note that at early time, the half slope relationship no longer holds. Note also the separation between the two curves that increases with time revealing the importance of fracture deformability and the need for coupled analysis.

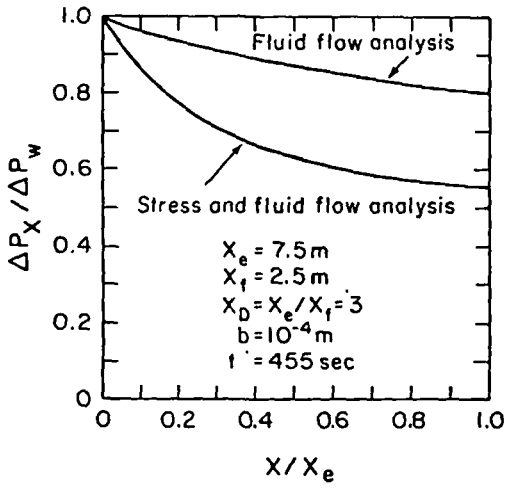

Fig. 16 Pressure drops along vertical fracture of finite conductivity in porous medium showing differences between analyses based only on fluid or on coupled stress and fluid flow.

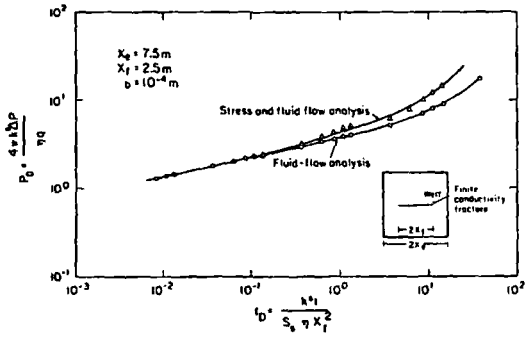

Fig. 17 P_D versus t_D for single fracture of finite conductivity in porous medium showing differences between analyses based only on fluid flow or on coupled stress and fluid flow.

In choosing a problem for a thermomechanical investigation, we first carried out some preliminary validation studies using both SAP4 and the present code. Solutions to two linear-elastic problems involving: (1) a finite line source in an infinite medium, and (2) a semi-infinite space subject to a constant temperature boundary condition were obtained. The results from the two approaches were in excellent agreement.

To demonstrate the ability of the code to handle non-linearities, a simple thermomechanical problem

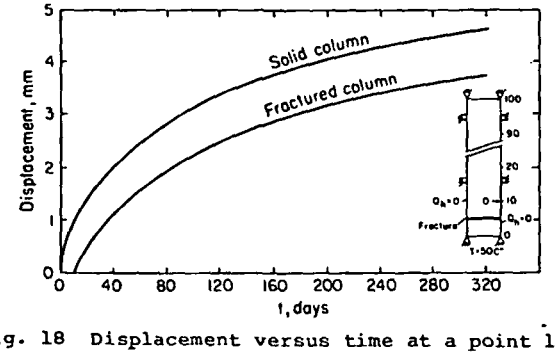

Fig. 18 Displacement versus time at a point 10m above base of rock column showing effect of fracture in reducing movement.

consisting of a long column of rock intersected near its base by a fracture was chosen (see inset on Fig. 18). Initially, the column temperature is 0°C, and after a step increase of 50° at the base, the problem is to determine the time variation of displacements above the fracture at a height of 10m. The material properties of the rock are given in Table 5. Fig. 18 shows the highly non-linear mechanical behavior of the fractured column and illustrates the ability of this finite element method to model discontinuous rock systems.

Table 5. Material properties for thermomechanical analysis of fractured rock column.

Property	Value
Mass density, ρ_s	2.5×10^3 kg/m^3
Specific heat capacity, C_{vs}	2.1×10^{-1} Kcal/kg °C
Thermal conductivity, K_s	7.65×10^{-4} Kcal/m sec °C
Thermal expansion coefficient, γ	1.11×10^{-5} °C^{-1}
Initial normal stiffness, K_{fn}	2.5×10^{-3} Pa/m
Young's modulus, E_s	5.13 MPa
Poisson's ratio, ν_s	0.25

An interesting problem that demonstrates only part of the hydrothermal capabilities of this code is the simulation of a saturated porous medium that is given a momentary thermal front. The onset of convective motion due to buoyancy is to be determined. The physical system consists of two porous reservoirs that initially are kept at temperatures T_o and T_1, as illustrated by the inset on Fig. 19. Initially, a thermal barrier separates the two reservoirs, both of which are horizontally semi-infinite and insulated top and bottom. At t = 0, the barrier is removed, and the problem is to determine the instantaneous horizontal velocity profile along the thermal front. An analytical solution for this problem has been published by Cleasson (1979).

This particular problem is very sensitive to the finite element mesh that is selected, and some effort was required to achieve the optimum grid for a specific number of nodal points. The problem was solved with a network of 252 elements requiring 286 nodal points. The material properties of the fluid and porous medium are given in Table 6.

Table 6. Material properties for hydrothermal analysis of thermal front problem.

Property	Value
Downstream temperature, T_o	20°C
Downstream mass density, ρ_o	9.98×10^2 kg/m^3
Downstream dynamic viscosity, η_o	9.89×10^{-4} kg/m sec
Upstream temperature, T_1	90°C
Upstream mass density, ρ_1	9.66×10^2 kg/m^3
Upstream dynamic viscosity, η_1	2.17×10^{-4} kg/m sec
Fluid thermal expansion coefficient, β_T	-4.46×10^{-4} °C^{-1}
Intrinsic permeability, k_f	10^{-12} m^2
Gravity acceleration, g	9.80 m/sec^2
$\frac{k_f(\rho_o-\rho_1)g}{\eta_o+\eta_1}$, q_o	2.42×10^{-7} m/sec
Finite element mesh width, W	900 m
Finite element mesh height, H	20 m

Fig. 19 shows a comparison of the numerical results for the instantaneous normal (horizontal)

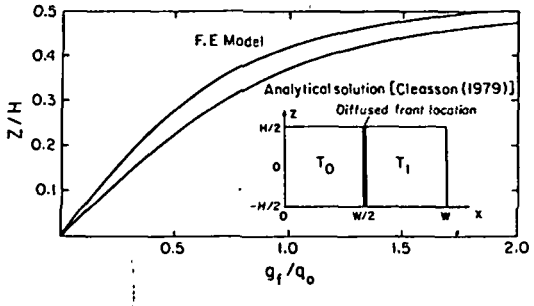

Fig. 19 Profile of instantaneous horizontal velocities due to buoyancy effects at location of thermal front in saturated porous media.

velocities compared with those of the analytical solution of Cleasson (1979). Considering the fact that in the numerical approach, the thermal front must be modelled by a zone of finite width, which in our case was 0.4m, the agreement is quite good. Further mesh refinement would undoubtedly lead to closer agreement with the analytical solution.

Summary

An extension of Biot's (1940) theory of consolidation is proposed here to provide a new technique for a realistic method of investigating the thermal-hydraulic-mechanical behavior of fractured porous media. A direct solution process has been developed that involves a variational formulation and a Galerkin integral to produce a set of three matrix equations. In this approach the equations of static equilibrium and fluid flow appear in an implicitly coupled form and the energy equation is explicitly coupled to these equations. Finite element descretization, along with two schemes for time descretization, yield the final form of the matrix equations which are then soved in a two-step procedure, referred to as an interlacing scheme.

A partial validation of this new technique is presented by considering applications to hydromechanical, thermomechanical, and hydrothermal problems. The hydromechanical problem involves the calculation of pressure drops in a vertical fracture that intersects a well and acts as a drain for the surrounding porous medium. The results reveal the errors that can occur when the interaction between hydraulic and mechanical stresses is ignored. The thermomechanical problem involves the calculation of the expansion of a rock column with a heat source placed at one end. When a fracture exists between the location of the heat source and a point where one is attempting to predict the magnitude of thermally induced displacements, a highly non-linear behavior results that will not be predicted if one ignores the existence of the discontinuity. The hydrothermal problem involves a saturated porous medium that is given a momentary thermal front. The difficulty in predicting the onset of a natural convective motion can be handled by this new technique when the appropriate finite element mesh is selected. Complete validation of this new thermal-hydraulic-mechanical finite element model for saturated fracturd porous media will require much more work.

ACKNOWLEDGEMENTS

This work was supported by the Director, Office of Energy Research, Office of Basic Energy Sciences, Division of Engineering, Mathematics, and Geosciences; and by the Assistant Secretary for Nuclear Energy, Office of Waste Isolation of the U. S. Department of Energy under Contract No. W-7405-ENG-48.

NOMENCLATURE

a	typical asperity size
A	fracture cross sectional area
A_1, A_2	structural boundaries where displacements and surface tractions are prescribed
b	fracture aperture
b_o	maximum fracture aperture
B_1, B_2 & C_1, C_2	fluid flow and heat flow boundary parts where Dirichlet or Neuman boundary conditions are prescribed
$\underline{C}$	elasticity matrix
C_{ijkl}	components of elasticity tensor for solid phase
C_o	fracture cohesion
$\underline{C}_{PT}$	pressure-temperature coupling matrix
$\underline{C}_{UP}$	displacement-pressure coupling matrix
$\underline{C}_{UT}$	displacement-temperature coupling matrix
C_{vl}	specific heat capacity of liquid at constant volume
C_{vs}	specific heat capacity of solid at constant volume
d	half-crack length
D/D^St	comoving time derivative following solid
e_{ij}	components of strain tensor for solid phase
E, E_s	Young's modulus for rock
E_{eff}	Effective Young's modulus for jointed rock
$\underline{E}_f$	fluid storativity matrix
$\underline{E}_h$	heat capacity matrix
f_i	components of body force vector
$\underline{F}$	force vector
g	gravitational acceleration
$\underline{G}$	traction vector on A_2 boundary
h	asperity height in fracture
$\underline{H}_f$	fluid conductivity matrix
$\underline{H}_h$	heat conductivity matrix
$\underline{H}_{hf}$	mass transfer conductivity matrix
$\underline{k}_f$	intrinsic permeability tensor
$\underline{K}$	stiffness matrix
K_{fn}	normal stiffness
K_{fs}	tangential stiffness
K_{ij}	permeability tensor components
K_f	permeability measured in the direction of flux
K_g	permeability measured in the direction of hydraulic gradient

$\underline{K}_\ell$	liquid thermal conductivity tensor
$\underline{K}_M$	solid-fluid mixture thermal conductivity tensor
$\underline{K}_s$	solid thermal conductivity tensor
$\underline{\ell}$	length of cylindrical rock sample
L	length of the boundary
m	distribution mean
M	Biot's constant for $1/\varepsilon\beta_p$
M_T	Biot's constant for $1/\varepsilon\beta_T$
M_v	number of voids in schematic representation of fracture
N	total number of elements in finite element idealization
$\underline{n}$	outward normal direction cosine vector
n_i	indices used to designate number of elements, i = 1, 2, 3
n(h)	asperity height distribution function
$N_c(\Delta V)$	number of areas of contact in fracture
P	pressure
$\hat{P}$	pressure assigned on B_1 boundary
$\underline{P}$	pressure vector
$\underline{P}_t$	pressure vector at preceding time step
ΔP_w	pressure drop
$\underline{q}$	fluid flow vector
q_i	components of fluid flow vector and the
q_f	horizontal component of fluid flow vector
q	rate of fluid discharge from well
Q	flow per unit width
Q_g	flow per unit width in direction of hydraulic gradient
$\underline{Q}_h$	heat flow vector
$\hat{Q}_h$	normal heat outflow from C_2 boundary
$\underline{Q}_\ell$	fluid flow vector
$\hat{Q}_\ell$	normal fluid outflow from B_2 boundary
s	distribution variance
S_s	specific storage coefficient of saturated porous elastic solid
T	temperature
$\underline{T}$	temperature vector
$\underline{T}_t$	temperature vector at preceding time step
u	volume enclosing one crack
$\underline{U}$	solid element displacement vector
V	space occupied by fluid-solid mixture
V^n	region of space occupied by fluid-solid mixture of an element n
ΔV	fracture deformation
ΔV_r	rock deformation
ΔV_t	total jointed rock deformation
x_i or x,y,z	Cartesian coordinates, i = 1,2,3
α	Biot's hydroelastic coupling coefficient or angle of orientation of hydraulic gradient
β	Thermoelastic coupling coefficient equal to $(2\mu+3\lambda)\gamma$
β_p	fluid compressibility
β_T	fluid thermal expansion coefficient
γ	solid thermal expansion coefficient
δ_{ij}	Kronecker delta function
δ	friction angle
ε	porosity
η_ℓ, η	liquid dynamic viscosity
λ	Lamé's elasticity constant
μ	Lamé's elasticity constant
ν	functional perturbation parameter
ν_s	Poisson's ratio
ξ	fluid volume strain
ρ_ℓ, $\hat{\rho}_\ell$	liquid mass density and average liquid mass density
ρ_s, $\hat{\rho}_s$	solid mass density and average solid mass density of porous space
ρ_M	solid-fluid mixture mass density
$(\rho C)_M$	solid-fluid heat capacity
$\underline{\tau}, \tau_{ij}$	stress tensor and components
$\underline{\tau}_T, \tau_{Tij}$	thermal stress tensor and components
τ, σ	stress normal to fracture
ϕ	hydraulic potential
$\underline{\Phi}_u$	displacement interpolation function matrix
$\underline{\Phi}_e$	strain-nodal displacement transformation matrix
$\underline{\Psi}$	pressure and temperature interpolation function matrix
$\underline{\Phi}_\theta$	transformation matrix for pressure or temperature gradients
ω	fractional fracture contact area

REFERENCES

AYATOLLAHI, M.S., 1978, Stress and Flow in Fractured Porous Media, Ph.D. Thesis, University of California, Berkeley.

AYATOLLAHI, M.S., J. NOORISHAD AND P. A. WITHERSPOON, 1981, A finite-element method for stress and fluid flow analysis in fractured rock masses, submitted to Journal of Engineering Mechanics Div., ASCE.

BACA, R.G., 1980, Coupled geomechanical/hydrological modeling: An overview of BWIP studies, in Proceedings ONWI Workshop on Thermomechanical-Hydrochemical Modeling for a Hard Rock Waste Repository, Berkeley, California, Lawrence Berkeley Laboratory Report LBL-11204, ONWI-164.

BAECHER, G.B., N.A. LANNEY AND H.H. EINSTEIN, 1977, Statistical descriptions of rock properties and sampling, Proceedings 18th U.S. Symposium on Rock Mechanics.

BAECHER, G.B., 1978, Trace length biases in joint surveys, Proceedings 19th U.S. Symposium on Rock Mechanics.

BARENBLATT, G., U.P. ZHELTOV AND G.H. KOCHINA, 1960, Basic concepts in the theory of seepage of homogeneous liquids in fractured rocks, in Prikladnaya Matem, i Mekh., v. 24, pp. 852-864, (in Russian).

BEAR, J., 1972, Dynamics of Fluids in Porous Media, American Elsevier Co., New York, London, Amsterdam.

BIANCHI, L. AND D.T. SNOW, 1968, Permeability of crystalline rock interpreted from measured orientations and apertures of fractures. Annals of the Arid Zone, v. 8, no. 2, pp. 231-245.

BIOT, M.A., 1940, General theory of three-dimensional consolidation, Journal Applied Physics, v. 12, pp. 155-164.

BOUSSINESQ, J., 1868, Journal de Liouville, v. 13, pp. 377-424.

CALDWELL, J.A., 1971, The Theoretical Determination of the Fluid Potential Distribution in Jointed Rocks, M.Sc. Thesis, University of Witwatersrand, Johannesburg, South Africa.

CALDWELL, J.A., 1972, The theoretical determination of the permeability tensor for jointed rock, Proceedings of Symposium on Percolation Through Fissured Rock, Stuttgart, 1972, Int'l. Soc. for Rock Mech. and Int'l Assoc. of Engineering Geology.

CLEASSON, J., 1979, Notes on Ground Water Thermohydraulics, Report, Dept. of Mathematical Physics, Lund, Sweden.

CROCHET, M.J. AND P.M. NAGHDI, 1966, On constitutive equations for flow of fluid through an elastic solid, International Journal of Engineering Science, v. 4, pp. 383-401.

DAVIS, S.N. AND G.W. MOORE, 1965, Semidiurnal movement along a bedrock joint in Wool Hollow Cave, California, National Speological Society Bulletin, v. 27, no. 4, pp. 133-142.

DUGUID, J.O., 1973, Flow in Fractured Porous Media, Ph.D. Thesis, Princeton University.

FARA, H.D. AND A.E. SCHEIDEGGER, 1961, Statistical geometry of porous media, Journal Geophysical Research. v. 66, pp. 3279-3284.

FREEZE, R.A., 1975, A stochastic-conceptual analysis of one-dimensional groundwater flow in nonuniform homogeneous media, Water Resources Research, v. 11 no. 5, pp. 725-741.

GALE, J.E., 1975, A Numerical Field and Laboratory Study of Flow in Rocks with Deformable Fractures, Ph.D. Thesis, University of California, Berkeley.

GANGI, A.F., 1978, Variation of whole and fractured porous rock permeability with confining pressure, International Journal of Rock Mechanics and Mining Sciences, v. 15, pp. 249-257.

GHABOUSSI, J. AND E.L. WILSON, 1971, Flow of Compressible Fluids in Porous Media, SESM Report No. 72-12, University of California, Berkeley.

GOODMAN, R.E., R.L. TAYLOR AND T. BREKKE, 1968, A model for the mechanics of jointed rock, Journal of Soil Mechanics and Foundation Division, ASCE, v. 94, no. SM3.

GREEN, A.E. AND P.M. NAGHDI, 1965, A dynamical theory of interacting continua, International Journal of Engineering Sciences, v. 3, pp. 231-241.

GRINGARTEN, A.C., H.J. RAMEY JR. AND R. RAGHAVAN, 1975, Applied pressure analysis for fractured wells, Journal Petroleum Technology, Transactions AIME, v. 259, pp. 887-892.

GURTIN, M., 1964, Variational principles for linear initial-value problems, Quarterly of Applied Mathematics, v. 22, no. 3, p. 252.

HELM, D.C., 1974, Evaluation of Stress-Dependent Aquitard Parameters by Simulating Observed Compaction from Known Stress History, Ph.D. Thesis, University of California, Berkeley.

HILBER, H.M., R.L. TAYLOR AND P.A. WITHERSPOON, 1979, Transient response of fractured rock systems to fluid injection: A finite element study, Proceedings of the Third International Conference on Numerical Methods in Geomechanics, Aachen.

HOCKING, G., 1979, Thermomechanical modeling for hardrock: Status and needs, in Proceedings Workshop on Thermomechanical Modeling for a Hardrock Waste Repository, Berkeley, California, Lawrence Livermore Laboratory Report UCAR-10043; ONWI-98, Livermore.

HUBBERT, M.K., 1956, Darcy's law and the field equations of the flow of underground fluids. Petroleum Transactions, AIME, v. 207, pp. 222-239.

HUDSON, J.A. AND S.D. PRIEST, 1979, Discontinuities and rock mass geometry, International Journal of Rock Mechanics and Mining Sciences, v. 16, pp. 339-363.

IWAI, K., 1976, Fundamental Studies of Fluid Flow Through a Single Fracture, Ph.D. Thesis, University of California, Berkeley.

KRANZ, R.L., A.D. FRANKEL, T. ENGELDER AND C. H. SCHOLZ, 1979, The permeability of whole and jointed Barre granite, International Journal of Rock Mechanics and Mining Sciences, v. 16, pp. 225-234.

LONG, J.C.S., J. REMER, C. WILSON AND P.A. WITHERSPOON, 1981, Porous media equivalent for a network of discontinuous fractures, submitted to Water Resources Research.

MAHTAB, M.A., D.D. BOLSTED AND J.R. ALLDREDGE, 1972, Analysis of Fracture Orientations for Input to Structure Models of Discontinuous Rock, U.S. Dept. of Interior, Bureau of Mines Report, Invest. N7669.

MARCUS, H. AND D. EVANSON, 1961, Directional Permeability in Anisotropic Porous Media, Water Resources Center Contribution No. 31, University of California, Berkeley.

MARCUS, H., 1962, Permeability of an anistropic porous medium, Journal of Geophysical Research, v. 67, p. 525.

NARASIMHAN, T.N., AND P. A. WITHERSPOON, 1977, Numerical model for saturated-unsaturated flow in deformable porous media, 1. Theory, Water Resources Research, v. 13, no. 3, pp. 657-664.

NOORISHAD, J., P.A. WITHERSPOON AND T.L. BREKKE, 1971, A Method For Coupled Stress and Flow Analysis of Fractured Rock Masses, Geotechnical Engineering Publication No. 71-6, University of California, Berkeley.

NOORISHAD, J, M. MEHRAN AND T.N. NARASIMHAN, 1981a, On the formulation of saturated-unsaturated fluid flow in deformable porous media, Advances in Water Resources (in press).

NOORISHAD, J. AND P.A. WITHERSPOON, 1981, Hydrothermoelasticity Part 1: Fundamentals and Analysis Approach, Lawrence Berkeley Laboratory Report LBL-12354, Berkeley.

NOORISHAD, J., P.A. WITHERSPOON AND M.S. AYATOLLAHI, 1981b, Coupled stress and fluid flow analysis of fractured rocks, submitted to International Journal of Rock Mechanics and Mining Sciences.

PARSONS, R.W., 1966, Permeability of idealized fractured rock, Society of Petroleum Engineers Journal, v. 6, pp. 126-136.

PINDER, G.F., 1979, State-of-the-Art Review of Geothermal Reservoir Modeling, Lawrence Berkeley Laboratory Report LBL-9093, Berkeley.

PRIEST, S.D. AND J. HUDSON, 1976, Discontinuity spacings in rock, International Journal of Rock Mechanics and Mining Sciences, v. 13, pp. 135-148.

RAGHAVAN, R., A. URAIET AND G. W. THOMAS, 1976, Vertical Fracture Height: Effect on Transient Flow Behavior, paper presented at 51st SPE-AIME meeting, New Orleans, October 3-6.

ROBERTSON, A, 1970, The interpretation of geological factors for use in slope stability, Proceedings Symposium on the Theoretical Background to the Planning of Open Pit Mines with Special Reference to Slope Stability, pp. 55-71.

ROCHA, M. AND F. FRANCISS, 1977, Determination of permeability in anisotropic rock masses from integral samples, In Structural and Geotechnical Mechanics, W. J. Hall (ed.), Prentice-Hall, Inc., New Jersey.

RODATZ, W. AND W. WITTKE, 1972, Wechselwirkung Zwischen Deformation und Durchströmung in Klüftigen, Anisotropen Gebirge, Proceedings of Symposium on Percolation Through Fissured Rock, Stuttgart, 1972, p. T2-1.

ROMM, E.S., 1966, Flow Characteristics of Fractured Rocks, Nedra, Moscow (in Russian).

SAFAI, N.M. AND G. F. PINDER, 1979, Vertical and horizontal land deformation in a desaturating porous medium, Advances in Water Resources, v. 2, pp. 19-25.

SANDHU, R.S. AND E.L. WILSON, 1969, Finite-element analysis of seepage in elastic media, Journal of Engineering Mechanics, Division ASCE, v. 95, no. EM3, p. 641-652.

SMITH, L., 1978, Stochastic Analysis of Steady State Groundwater Flow in a Bounded Domain, Ph.D. Thesis, University of British Columbia, Vancouver.

SMITH, L. AND R.A. FREEZE, 1979a, Stochastic analysis of steady state groundwater flow in a bounded domain, 1: One-dimensional simulations, Water Resources Research, v. 15, no. 3, pp. 521-528.

SMITH, L. AND R.A. FREEZE, 1979b, Stochastic analysis of steady groundwater flow in a bounded domain, 2: Two-dimensional simulations, Water Resources Research, v. 15, no. 6, pp. 1543-1559.

SNOW, D.T., 1965, A Parallel Plate Model of Fractured Permeable Media, Ph.D. Thesis, University of California, Berkeley.

SNOW, D.T., 1968, Fracture deformation and changes of permeability and storage upon changes of fluid pressure, Quartlery Colorado School of Mines, v. 63, no. 1, pp. 201.

SNOW, D.T., 1969, Anistropic permeability of fractured media, Water Resources Research, v. 5, no. 6, p. 1273.

SOREY, M.L, 1975, Numerical Modeling of Liquid Geothermal Systems, Ph.D. Thesis, University of California, Berkeley.

TAYLOR, R.L., 1974, Analysis of Flow of Compressible or Incompressible Fluids in Porous Elastic Solids, Consulting report to the Naval Civil Engineering Laboratory, Port Hueneme, California.

TERZAGHI, K., 1925, Erdbaumechanik auf Bodenphsikalischer Grundlage, Leipzig, F. Deuticke.

TOTH, J, 1967, Groundwater in sedimentary (clastic rocks), Proceedings of the National Symposium on Groundwater Hydrology, San Francisco, California, November 6-8.

TSANG, C.F., 1980, A review of the state-of-the-art of thermomechanical-hydrochemical modeling of a hardrock waste repository, Proceedings ONWI Workshop on Thermomechanical-Hydrochemical Modeling for a Hardrock Waste Repository, Berkeley, California, Lawrence Berkeley Laboratory Report LBL-11204, ONWI-164, Berkeley.

TSANG, Y.W. AND P.A. WITHERSPOON, 1981, Hydromechanical behavior of a deformable rock fracture subject to normal stress, submitted to Journal of Geophysical Research.

VENEZIANO, D., 1979, Probabilistic Model of Joints in Rock, Civil Engineering Department, Massachusetts Institute of Technology, Boston, 47 pp.

WALSH, J.B., 1965, The effect of cracks on the uniaxial elastic compression of rocks, Journal Geophysical Research, v. 70, pp. 399-411.

WANG, J.S Y., R. STERBENTZ AND C. F. TSANG, 1980, The State-of-the-Art of Numerical Modeling of Thermo-hydrologic Flow in Fractured Rock Masses, Lawrence Berkeley Laboratory Report LBL-10524, Berkeley.

WILSON, C.R. AND P.A. WITHERSPOON, 1970, An Investigation of Laminar Flow in Fractured Rocks, Geotechnical Report No.70-6, University of California, Berkeley.

ZIENKIEWICZ, O.C., 1971, The Finite Element Method in Engineering Science, McGraw-Hill, London.

APPENDIX

Initial and Boundary Conditions

The equations governing fluid flow (20), static equilibrium (22), and conservation of energy (23) in conjunction with the constitutive equations for the stress-strain relationships (19) and the equation of state for the fluid (21) have previously been discussed. These equations with the proper initial and boundary conditions define the problem to be solved. The initial and boundary conditions for the saturated porous elastic medium are:

$$\underline{U}(\underline{x}, t) = \hat{\underline{U}}(\underline{x}, t) \qquad \text{on } A_1 x[0, \infty)$$

$$\underline{\tau}(\underline{x}, t) \cdot \underline{n}(\underline{x}) = \hat{\underline{G}}(\underline{x}, t) \qquad \text{on } A_2 x[0, \infty)$$

$$P(\underline{x}, t) = \hat{P}(\underline{x}, t) \qquad \text{on } B_1 x[0, \infty)$$

$$\frac{\underline{k}_f}{\eta_\ell} \nabla(P + \rho_\ell g z) \cdot \underline{n}(\underline{x}) = \hat{Q}_\ell(\underline{x}, t) \qquad \text{on } B_2 x[0, \infty) \tag{A1}$$

$$T(\underline{x}, t) = \hat{T}(\underline{x}, t) \qquad \text{on } C_1 x[0, \infty)$$

$$K_M \nabla T \cdot \underline{n}(\underline{x}) = \hat{Q}_h(\underline{x}, t) \qquad \text{on } C_2 x[0, \infty)$$

$$\underline{U}(\underline{x}, 0) = 0 \qquad \text{on } V$$

$$\underline{\tau}(\underline{x}, 0) = 0 \qquad \text{on } V$$

$$P(\underline{x}, 0) = 0 \qquad \text{on } V \qquad \text{(A1)}$$

$$T(x, 0) = T_o \qquad \text{on } V$$

A, B, C represent parts of the boundary for stress-displacement, pressure-fluid flow, and temperature-heat flux considerations. V represents the volume under consideration. As mentioned earlier, the dependent variables $\underline{U}$, P and T represent incremental deviations from the strain-free state assumed by the above choice of initial conditions. Consideration of a different set of values for the initial conditions will necessitate replacement of $\underline{U}$, P, and T by $(U - U_o)$, $(P - P_o)$, and $(T - T_o)$ in all corresponding equations. Also τ has to change to $(\underline{\tau} - \underline{\tau}_o)$. However, to cause less manipulation, it is preferable that the displacement vector $\underline{U}$ be kept incremental in nature and left unchanged which will not affect the results of the analysis.

Variational Formulation

The variational method is used to formulate the hydroelastic [Ayatollahi, 1978] part of the hydrothermoelastic phenomena. Let $R = \underline{U}, P$ be an admissible state in J defined in $V \times [0, \infty)$ and let the functions $\underline{U}$ and P possess the appropriate continuity and differentiability conditions. J is the set of all admissible states and V is the region of space occupied by the fluid-porous solid mixture. A function $\Omega_t(R)$ over J for each time $t \in [0, \infty)$ is defined as:

$$\Omega_t(R) = \int_V (e_{ij} * C_{ijk\ell} e_{k\ell} - 2T * \beta\delta_{ij} e_{ij}$$

$$- 2\rho_s f_i * U_i + 2P * \frac{\alpha\rho_\ell}{\rho_o}\delta_{ij} e_{ij}$$

$$- 1 * \nabla P * \frac{k_f}{\eta_\ell}\nabla P - P * \frac{1}{M} P - P * \frac{1}{M_T} T$$

$$+ 2 * \rho_\ell g \nabla z * \nabla P) dv - 2\int_{A_2} \hat{G}_i * U_i ds$$

$$- 2\int_{B_2} 1 * \hat{Q}_\ell * P ds \qquad \text{(A2)}$$

It can be shown that

$$\delta_R \Omega(R) = \frac{d}{d\nu}\Omega(R + \nu\bar{R})\Big|_{\nu=0} = 0 \qquad \text{(A3)}$$

for every $R \in J$ if, and only if, R is a solution state of the mixed boundary-value problem. The presence of temperature terms in the variational principle is justified physically, besides the mathematical soundness of the formulation, by the fact that thermal effects act in the form of initial strains (Zienkiewicz, 1971).

Galerkin formulation

The Galerkin method is used to obtain a numerical formulation for the energy equation. Choosing approximating functions of the form $T = \underline{\Phi}\underline{T}$, where Φ_i represents the basis functions and T_i signifies the discrete temperature values to be determined, the Galerkin procedure requires the following:

$$\int_V \Big\{ (\rho C)_M \Phi_i \frac{\partial T}{\partial t} + \beta T_o \Phi_i \frac{\partial}{\partial t}(\delta_{ij} e_{ij})$$

$$+ \rho_\ell C_{v\ell} \Phi_i \underline{q} \cdot \nabla T + \nabla\Phi_i \cdot K_M \nabla T \Big\} dv$$

$$- \int_{C_2} \Phi_i \hat{Q}_h ds = 0 \qquad \text{(A4)}$$

where the volume integral in equation (A4) represents a global restatement of (23), and the surface integral indicates the global satisfaction of the heat flux boundary condition.

Finite-Element Discretization

The field variables for the displacement vector, the pressure, and the temperature can be discretized as follows:

$$\underline{U} = \underline{\Phi}_U^{T_r}\underline{U}$$

$$P = \underline{\Phi}^{T_r}\underline{P} \qquad \text{(A5)}$$

$$T = \underline{\Phi}^{T_r}\underline{T}$$

where the Φ_i are piecewise continuous polynomial functions which are used in conjunction with the mixed isoparametric quadrilateral elements. Proper substitution of equation (A5) and related derivatives of $\underline{\Phi}_u$ and $\underline{\Phi}$ represented by $\underline{\Phi}_e$ and $\underline{\Phi}_\theta$ in the Galerkin integral and the functional, after proper differentiation, yields the following matrix finite element formulation:

$$\underline{K}\,\underline{U} + \underline{C}_{UP}\underline{P} + \underline{C}_{UT}\underline{T} = \underline{F} \qquad \text{(A6)}$$

$$\underline{C}_{PU}\underline{U} + (\underline{E}_f + 1^*\underline{H}_f)\underline{P} + \underline{C}_{PT}\underline{T} = -1^*\underline{Q}_\ell \qquad \text{(A7)}$$

$$\underline{C}_{TU}\underline{U} + [\underline{E}_h + 1^*(\underline{H}_{hf} + \underline{H}_h)]\underline{T} = -1^*\underline{Q}_h \qquad \text{(A8)}$$

where 1^* represents time integration. The matrix coefficients in the above formulation are defined by the following:

$$\underline{K} = \sum_{n=1}^{N} \int_{v^n} \underline{\Phi}_e^{n} \underline{C}^{n} \underline{\Phi}_e^{n\,T_r} dv^n$$

$$\underline{C}_{PU} = \underline{C}_{UP}^{T_r} = \sum_{n=1}^{N} \int_{v^n} \underline{\Phi}^n \frac{\alpha^n \rho_\ell^n}{\rho_o} \hat{1}\, \underline{\Phi}_e^{n\,T_r} dv^n$$

$$\underline{C}_{UT} = \sum_{n=1}^{N} \int_{v^n} \underline{\Phi}^n \beta \hat{\underline{1}} \, \underline{\Phi}_e^{n\,T_r} dv^n$$

$$\underline{C}_{TU} = \frac{1}{T_o} \underline{C}_{UT}^{T_r}$$

$$\underline{E}_f = \sum_{n=1}^{N} \int_{v^n} \underline{\Phi}^n \frac{1}{M^n} \underline{\Phi}^{n\,T_r} dv^n$$

$$\underline{H}_f = \sum_{n=1}^{N} \int_{v^n} \underline{\Phi}_\theta \frac{\underline{k}_f^n}{\eta_\ell} \underline{\Phi}_\theta^{T_r} dv^n$$

$$\underline{C}_{PT} = \sum_{n=1}^{N} \int_{v^n} \underline{\Phi}^n \frac{1}{M_T^n} \underline{\Phi}^{n\,T_r} dv^n$$

$$\underline{E}_h = \sum_{n=1}^{N} \int_{v^n} \underline{\Phi}^n (\rho C)_M^n \underline{\Phi}^{n\,T_r} dv^n$$

$$\underline{H}_{hf} = \sum_{n=1}^{N} \int_{v^n} \underline{\Phi}^n (\varepsilon \rho_\ell \, C_{v\ell})^n \underline{q} \, \underline{\Phi}_\theta^{n\,T_r} dv^n$$

$$\underline{H}_h = \sum_{n=1}^{N} \int_{v^n} \underline{\Phi}_\theta^n \underline{K}_M^n \underline{\Phi}_\theta^{T_r} dv^n$$

$$\underline{Q}_\ell = \sum_{n=1}^{n_1} \int_{B_2^n} \underline{\Phi}^n \underline{\Phi}^{n\,T_r} \hat{Q}_f^n ds^n$$

$$+ \sum_{n=1}^{N} \int_{v^n} \underline{\Phi}_\theta \frac{\underline{k}_f^n}{\eta_\ell} \rho_\ell g \hat{\underline{1}}_z dv^n$$

$$\underline{Q}_h = \sum_{n=1}^{n_2} \int_{C_2^n} \underline{\Phi}^n \underline{\Phi}^{n\,T_r} \hat{Q}_h ds^n$$

$$\underline{F} = \sum_{n=1}^{n_3} \int_{A_2^n} \underline{\Phi}_u^n \underline{\Phi}_u^{n\,T_r} \hat{\underline{G}} \, ds^n$$

$$+ \sum_{n=1}^{N} \int_{v^n} \underline{\Phi}_u \rho_s^n g \, \hat{\underline{1}}_z dv^n$$

where $\hat{\underline{1}} = \begin{Bmatrix} 1 \\ 1 \\ 1 \\ 0 \\ 0 \\ 0 \end{Bmatrix}$ and $\hat{\underline{1}}_z = \begin{Bmatrix} 0 \\ 0 \\ 1 \end{Bmatrix}$

The superscript T_r stands for matrix transposition operation.

SUBJ
MNG
NCRG

Presented at
82nd Northwestern Mining Assoc
Conv. — Dec 6, 1980
Spokane, WA

NEW CONCEPTS OF REGIONAL GEOLOGY AND URANIUM EXPLORATION IN NORTHEASTERN WASHINGTON

CHENEY, Eric S., Department of Geological Sciences, AJ-20, University of Washington, Seattle, Washington 98195

UNIVERSITY OF UTAH
RESEARCH INSTITUTE
EARTH SCIENCE LAB.

ABSTRACT

Many uranium showings plus one future and two operating mines occur in northeastern Washington. The regional geology is generally considered to consist of Mesozoic (Shuswap) gneiss domes and Mesozoic to Tertiary plutons that are cut by Tertiary grabens that were basins of deposition for local formations. I (1980b) have suggested that the sillimanite-grade rocks are not gneiss domes but pre-Beltian(?) cores of Tertiary anticlines and that regionally extensive Tertiary rocks are preseved in fault-bounded synclines adjacent to the anticlines = metamorphic core complexes.

Accordingly, stratigraphic or sandstone-type uranium deposits probably are localized by regionally extensive facies changes, not by facies changes in local basins. The recognition of regional unconformities and facies changes is, therefore, critical to exploration. Deposits of probable supergene origin, such as the Midnite deposit, may be related to a specific Tertiary regional unconformity (which could be post-Eocene) or to multiple regional unconfomrities. Unfortunately the regional facies of the Tertiary strata, the location of Tertiary unconformities, and their ages with respect to ages of known uranium deposits are still only poorly known.

Most pegmatitic deposits in the metamorphic rocks are too small or low grade to be commercial Rössing-type deposits. However, the uranium from such pegmatites may have been reconcentrated in Tertiary strata, below Tertiary unconformities, or in the cataclastic zones peripheral to the core complexes. Structurally controlled deposits in the cataclastic zones may have formed in a manner similar to the unconformity-vein deposits of Saskatchewan or in zones of hydrothermal alteration. Thus, the margins of the core complexes deserve to be intensively prospected.

References

Cheney, E. S., 1980a, New concepts of regional geology and uranium exploration in northeastern Washington (abs.): Geol. Soc. Amer. Abstracts with Programs, v. 12, p. 102.

Cheney, E. S., 1980b, Kettle Dome and related structures of northeastern Washington: Geol. Soc. Amer. Memoir 153, p. 463-483.

Rhodes, B. P., 1980, The low-angle Kettle River fault: the eastern contact of Kettle dome, northeastern Washington (abs.): Geol. Soc. Amer. Abstracts with Programs, v. 12, p. 508.

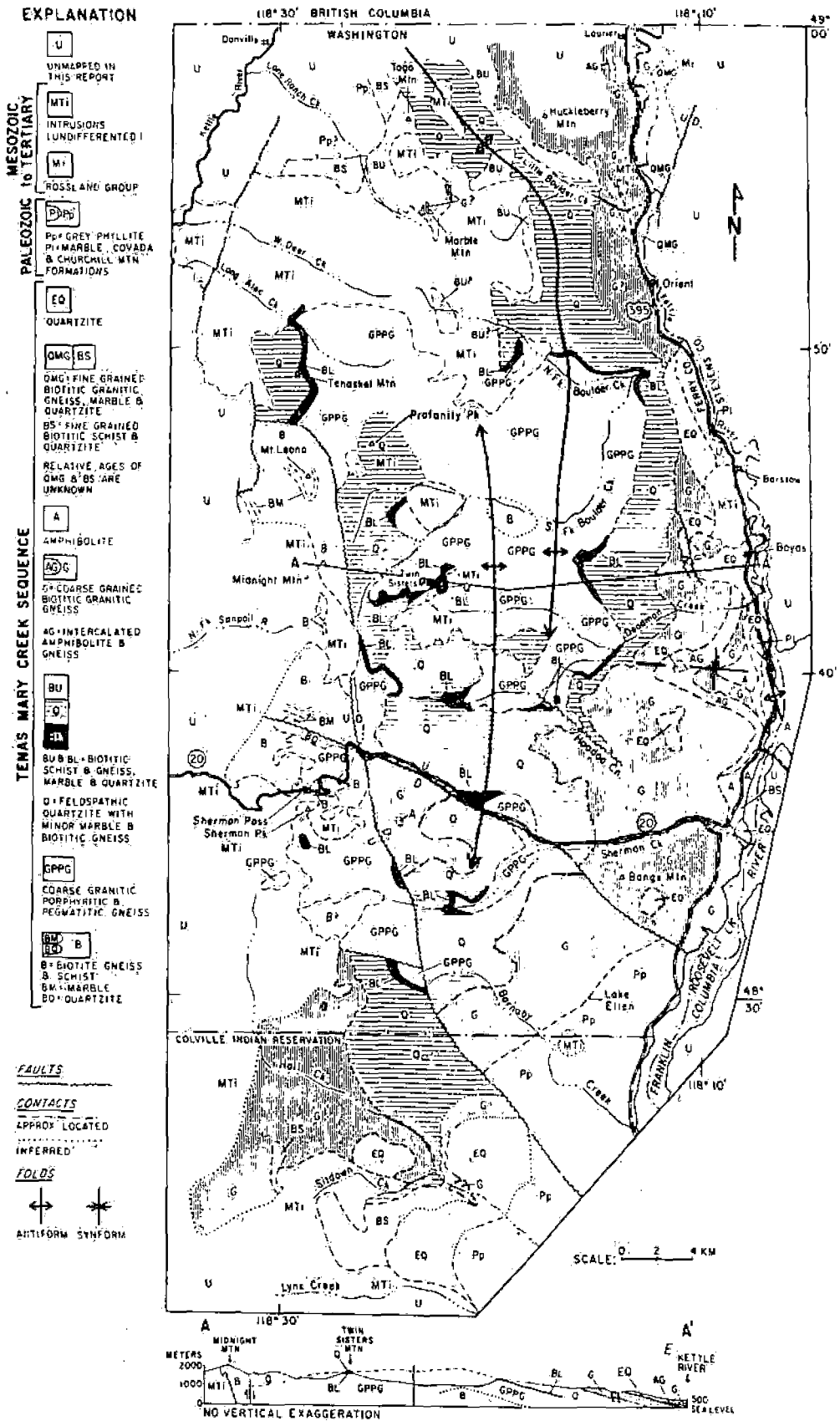

Figure 2. Preliminary geologic map of the Kettle dome, Ferry County, Washington.

TABLE 1. CRITERIA FOR DISTINGUISHING BETWEEN INTERVALS DOMINATED BY BIOTITIC SCHIST AND GNEISS IN THE KETTLE DOME

Map unit*	Approximate thickness (m)	Apparent geographic restriction	Distinctive lithologies and mineralogies	Thickness of marble and quartzite (m)	Amount of pegmatite
BS	200 to 600	Northeast quarter of Togo Mountain and north half of Twin Lakes quadrangle	Fine-grained biotitic schist, calc-silicate schist, minor amphibolite, no sillimanite	No marble ~30	None
QMG	>600	Southwest third of Laurier quadrangle	Fine-grained biotitic gneiss, calc-silicate gneiss	<15	None?
BU	0 to 300	North half of Togo Mountain quadrangle	Medium-grained biotitic, sillimanite-bearing schist and gneiss, phlogopitic marble, quartzite	<60	Little
BL	100 to 150	Sherman Peak and south third of Togo Mountain quadrangle	Medium-grained biotitic, sillimanite-bearing schist and gneiss, phlogopitic marble, quartzite	<15	Common
B	800(?)	Mount Leona to Sherman Pass	Medium-grained, biotitic, sillimanite-bearing schist and gneiss, phlogopitic marble, quartzite	<60	Very common

*These map units are shown in Figure 2.

Granitic, Porphyritic, Pegmatitic Gneiss. The lowest widespread unit is a granitic, porphyritic, pegmatitic gneiss (GPPG in Fig. 2, hereafter "pegmatitic gneiss") that commonly has no compositional layering. The megacrysts are potassium feldspar. The pegmatitic portions are dikelets <1 m thick and irregular clots about a metre in diameter that grade outward into nonpegmatitic gneiss. Some of the irregular clots are remnants of dikelets that were disrupted along foliation planes or dismembered by folding. The foliation is sufficiently weak that some previous investigators included the pegmatitic gneiss in adjacent intrusions. This gneiss is one of the thickest (>850 m) and most extensive of all of the Tenas Mary Creek units, extending from the crest of the range on the west to the valley bottoms on the east. Small outcrops of biotitic gneiss and marble along the North Fork of Deadman Creek suggest that the lower contact of the pegmatite gneiss may be exposed. This interpretation is shown in the cross section of Figure 2.

The stratiform map pattern of the thin unit of biotitic schist, gneiss, and rather pure marble in the quartzite-dominated sequence above the pegmatite gneiss led Parker and Calkins (1964) to suggest that the pegmatite gneiss itself is a metasedimentary unit. However, Pearson (1967) was impressed by the lack of compositional layering and suggested that it is an orthogneiss and that the unit of biotitic schist and gneiss and marble was nonconformably deposited upon it.

An alternative interpretation is that the protolith of the pegmatite gneiss originally was a prekinematic or synkinematic pluton intruded into the pelitic rocks. Indeed, near the mouth of the South Fork of Boulder Creek large outcrops of quartzite and of biotitic schist occur within the pegmatitic gneiss. Furthermore, well-foliated, 1- to 2-m-thick concordant bodies of orthogneiss are ubiquitous in the overlying metasedimentary rocks; these orthogneisses are compositionally similar to the pegmatitic gneiss but lack the augen of feldspar and the pegmatitic bodies. Similar concordant bodies occur in the Grand Forks area (Preto, 1970) and in the Curlew area, where they are as much as 12 m thick (Parker and Calkins, 1964). In addition, the biotitic schist and gneiss that overlie the pegmatitic gneiss are so similar to the biotitic schist and gneiss below the pegmatitic gneiss (Table 1) that they may be the same unit. In the Grand Forks area (Table 2), the apparent absence of pegmatitic gneiss plus the presence of 2,000 m of biotitic and associated metasedimentary rocks underlying the quartzite also support the interpretation that the protolith of the pegmatitic gneiss was intrusive into the pelitic rocks.

Preto (1970) correlated Daly's Cascade gneiss (1912) with the pegmatitic gneiss of the Curlew area. However, the Cascade gneiss in the Grand Forks area consists of several bodies only a few square

TABLE 2. CORRELATION AND THICKNESS OF THE TENAS MARY CREEK SEQUENCE AND PALEOZOIC UNITS IN NORTHERN WASHINGTON AND ADJACENT BRITISH COLUMBIA

Kettle Dome (this paper)	Curlew quadrangle (Parker and Calkins, 1964)	Bodie Mountain quadrangle (Pearson, 1967)	Grand Forks, British Columbia (Preto, 1970)	Republic and Aeneas quadrangles (Muessig, 1967)	Bald Knob quadrangle (Staatz, 1964)	Buckhorn Mountain district (McMillan, 1979)
Covada and Churchill Mountain formations	Phyllite assigned to rocks of Tenas Mary Creek	Metamorphic rocks of Buckhorn Mountain; phyllite and marble assigned to the metamorphic rocks in the southwest corner of quadrangle	3	Rocks near Sheep Mountain	Graywacke, phyllite, black shale, and probably, quartzite of Permian or Triassic rocks	Anarchist group
Eastern quartzite, <300 m	Absent	Absent	Absent	Absent	Quartzite within Permian or Triassic rocks?	Absent
Fine-grained biotite schist, 600 m	Schist in rocks of Tenas Mary Creek, 2,750 m	Metamorphic rocks in southwest corner of quadrangle	Part of V(?), >200 m?; IV	Metamorphic rocks near Golden Harvest Creek	Phyllitic quartzite, 1850 m; schist in Permian or Triassic rocks	Goat Ranch metamorphic complex
Amphibolite, 200 m	Hornblende schist in rocks of Tenas Mary Creek?	Amphibolite in rocks of Tenas Mary Creek	IV?, <1,100 m; V?	Absent	Absent	Absent
Eastern granite gneiss, >800 m	Quartz-plagioclase gneiss in rocks of Tenas Mary Creek, 500 to 1,000 m	Quartz-feldspar gneiss in rocks of Tenas Mary Creek	IX	Absent	Absent	Absent
Biotitic schist and gneiss with minor quartzite and marble, <300 m	Absent	Metamorphic rocks of Tonata Creek	III, <1200 m	Absent	Absent	Absent
Feldspathic quartzite with minor biotitic schist and marble, >650 m	Quartzite in rocks of Tenas Mary Creek and of St. Peter Creek, 970 m	Quartzite in rocks of Tenas Mary Creek	II, <430 m	Absent	Absent	Absent
Biotitic schist and gneiss with minor quartzite and marble, <150 m	Marble and associated rocks in rocks of Tenas Mary Creek, 3 to 240 m	Marble in rocks of Tenas Mary Creek	I	Absent	Absent	Absent
Granitic, porphyritic, pegmatic gneiss, >850 m	Orthoclase-quartz-oligoclase gneiss in rocks of Tenas Mary Creek, >1,100 m	Granitic gneiss in rocks of Tenas Mary Creek	VII?	Assigned to quartz monzonite east of Sherman fault	Absent	Absent
Biotitic schist and gneiss with minor quartzite and marble, >700 m	Quartz-biotite schist, calc-schist, and quartzite of rocks of St. Peter Creek	Absent	I, 2,000 m	Metamorphic rocks east of Sherman fault	Absent	Absent

kilometres in area. The body about 7 km east of Grand Forks, the only one I have examined, lacks the feldspar megacrysts and pegmatitic patches representative of pegmatitic gneiss. Perhaps the Cascade gneiss and the smaller concordant bodies of gneiss above the pegmatitic gneiss in the Kettle dome were satellitic stocks, sills, and dikes of the pluton from which the pegmatitic gneiss formed.

Quartzite-dominated Sequence. Overlying the pegmatitic gneiss are heterogeneous units (sillimanitic biotitic schists and gneiss with minor quartzite and marble) above and below >650 m of feldspathic quartzite (Table 1). The lower heterogeneous unit is so thin that it was not always encountered during reconnaissance mapping; thus, it is not shown as a continuous unit in Figure 2. It is present in the Tenas Mary Creek and Grand Forks areas (Table 2), and more detailed mapping (Pearson, 1977) shows that it is continuous in the southern part of the Togo Mountain quadrangle.

Rusty- to white-weathering quartzite >650 m thick overlies the lower heterogeneous unit. The quartzite has 5% to 10% white-weathering feldspar 1 to 5 mm in diameter. The feldspar is more commonly orthoclase than plagioclase (Parker and Calkins, 1964; Preto, 1970). The quartzite generally is nonmicaceous, but does contain intercalated biotitic schists and gneisses >20 m thick. On the southern side of Profanity Peak, coarse white marble 30 to 60 m thick occurs within the quartzite. The heterogeneous unit above the quartzite appears to be restricted to the northern part of the Togo Mountain quadrangle and the Grand Forks area.

Eastern Granitic Gneiss. Above the quartzite-dominated sequence on the eastern limb of the dome are >800 m of coarse-grained, very well foliated, unlayered to indistinctly layered, granodioritic orthogneiss. The gneiss generally is not pegmatitic but does have some plagioclase megacrysts as much as 1 cm long. The basal part of this gneiss commonly is more leucocratic and has inclusions of feldspathic quartzite similar to those in the underlying rocks. Amphibolites and thin quartzites along U.S. Route 395 in the Laurier quadrangle are of uncertain origin; they may have been either xenoliths or intercalated sediments. In the Curlew quadrangle (Parker and Calkins, 1964) and in the Boyds quadrangle on the eastern limb of the Kettle dome, the upper part of the gneiss contains stratiform amphibolites. The regionally discordant contacts of this gneiss shown in Figure 2 may indicate the intrusive origin of its protolith.

This unit has caused considerable confusion. Pardee (1918) and Campbell (1938, 1946) included it within the Colville batholith. Still more confusing is the similarity of this unit to the pegmatitic gneiss, especially in the few places where the latter is not particularly pegmatitic or the eastern gneiss has 1-cm plagioclase megacrysts. In these places the >650-m quartzite above or below a gneissic unit is diagnostic. Judging from the description of Parker and Calkins (1964) and Pearson (1967), the pegmatitic gneiss contains more potassium feldspar and less hornblende than the eastern gneiss. Bowman (1950), Campbell and Thorsen (1966), Lyons (1967), and Pearson (1977) lumped the two gneisses as a single unit. Bowman (1950) correlated the eastern orthogneiss at Laurier on the Canadian border with the Cascade gneiss. However, the Cascade gneiss 7 km east of Grand Forks is neither as hornblende-rich nor as well foliated as the eastern gneiss.

The remarkable areal extents of the eastern granitic gneiss and the pegmatitic gneiss deserve comment. Both gneisses occur throughout the Kettle dome (Fig. 2). Both also are present as far northwest as the bend in the Kettle River in the Curlew quadrangle (Parker and Calkins, 1964), and both probably occur in the Grand Forks area of British Columbia mapped by Preto (1970). Thus the pegmatitic gneiss has a minimum distance of outcrop of 50 km and the eastern gneiss a minimum of 70 km. Because both gneisses are overlain or intruded by other units, their total length could be greater. How much of their present form was caused by attenuation of the original plutons during metamorphism is not known.

Amphibolite. On the eastern limb of the dome, a 200-m thick, black amphibolite overlies the eastern granitic gneiss; similar stratiform amphibolites occur within the gneiss. On the basis of elemental ratios, Preto (1970) concluded that similar amphibolites of the Grand Forks area originally were mafic

intrusions, but Donnelly (1978) noted that metasomatism may make these results inconclusive. The presence of blue-green hornblende accompanied by oligoclase or andesine suggests that the amphibolite is not of sillimanite grade (Donnelly, 1978).

Fine-Grained Biotitic Rocks. Fine-grained, biotitic, granitic gneiss with intercalated calc-silicate units, quartzite, and amphibolite overlie the eastern granitic gneiss in the Laurier quadrangle; these are labeled QMG in Figure 2. Compositionally similar rocks (labeled BS) in the northwestern and southeastern margins of the dome are schistose to almost phyllitic instead of gneissic (Table 1). Correlation of QMG with BS cannot be demonstrated because the two belts of outcrop cannot be traced into each other. Because neither unit crops out near Boyds, their position relative to the 200-m-thick amphibolite is not known.

The schistose rocks are similar to the fine-grained biotitic schist and biotitic quartzite with intercalated fine-grained amphibolite and calc-silicate schist mapped by Staatz (1964), Muessig (1967), and McMillen (1979) in the Okanogan dome (Table 2). The fine-grained schist does not seem to be sillimanite-bearing (Parker and Calkins, 1964; Staatz, 1964; Muessig, 1967; Preto, 1970; McMillen, 1979), except adjacent to plutons in the Okanogan dome.

Eastern Quartzite. A slabby, slightly rusty weathering, fine-grained quartzite with micaceous partings occurs along the southeastern margin of the Kettle dome. Muscovite and minor biotite on the partings and the presence of isoclinal recumbent folds (outlined by the micaceous partings) suggest that metamorphism of the rocks in the Kettle dome is younger than this quartzite. Sillimanite has yet to be found in this quartzite, even in the schistose partings (Donnelly, 1978). Because the quartzite overlies the 200-m amphibolite, the eastern gneiss, and the fine-grained biotite schists (Fig. 2), the basal contact of the quartzite may be a major unconformity.

Because this quartzite occurs on both sides of the Columbia River near the bridge at Kettle Falls, it must be >200 m thick. Along U.S. Route 395 in the unmapped area between Boyds and Orient, where calc-silicate gneisses of unknown affinity appear to overlie the quartzite, the quartzite appears to be about 300 m thick.

I have suggested (Cheney, 1977) that the eastern quartzite might be equivalent to the 580 to 910 m of thin platy quartzite with sericitic partings near the top of the basal Cambrian Gypsy quartzite described by Park and Cannon (1943) in northeasternmost Washington. However, the eastern quartzite, which seems to have a higher metamorphic grade than all known examples of the Gypsy, could equally well not be Gypsy.

Because the >650-m quartzite within the dome contains intercalated units of biotitic gneiss and marble as much as 60 m thick but the eastern quartzite does not, these two quartzites probably are not correlative. All known examples of Beltian Revett Quartzite in Stevens County are gray and occur in lower grade rocks, so that this correlation may not be likely. Because Donnelly (1978) observed that the eastern quartzite has the same recumbent and other folds as the underlying amphibolite and the other rocks of Tenas Mary Creek described by Lyons (1967), the eastern quartzite is provisionally included within the Tenas Mary Creek sequence.

Paleozoic and Younger Rocks

Black argillite, gray phyllite, dark limestone, and white marble of late Paleozoic age, together with greenstone of reputed Triassic age, overlie the high-grade metamorphic rocks of the dome. In the Orient district, Bowman (1950) called these the Churchill formation; in the Colville Indian Reservation, Pardee (1918) used the name Covada group. Table 2 and Figure 3 indicate tht similar rocks have been described elsewhere. These formations may not be strictly correlative, but all are inferred to be Pennsylvanian to Triassic in age. The next youngest unit is the Jurassic Rossland Group of volcanic rocks. The Tertiary rocks are described later.

Although the fine-grained biotitic schist is compositionally similar to the late Paleozoic phyllitic rocks, the two probably are not the same unit subjected to different grades of regional metamorphism. For example, the late Paleozoic phyllitic rocks contain thick pods of quite pure limestone and marble, whereas fine-grained biotitic schists have only thin calc-silicate schists. Furthermore, the eastern quartzite occurs between the fine-grained schists and the phyllites on the southeastern limb of the dome, and the fine-grained biotitic schist is locally absent along margins of the dome that are overlain by phyllite. Parker and Calkins (1964) suggested that in the Curlew quadrangle an unconformity exists between fine-grained biotitic schist and the overlying phyllites. Such an unconformity would explain the relationships seen in the Kettle dome.

Age and Correlation of the Rocks of the Tenas Mary Creek Sequence

Bowman (1950) applied the name Boulder Creek Formation to the metamorphic rocks in the small part of the Kettle dome that he mapped. However, the sequence is better exposed and described as several mappable units in the area of the Tenas Mary Creek. Hence, the name Tenas Mary Creek sequence proposed by Parker and Calkins (1964) is preferred. However, the basal heterogeneous unit of biotitic gneiss, marble, and quartzite does not crop out in the type area. Furthermore, Parker and Calkins included phyllite in the top part of the Tenas Mary Creek sequence. Because the phyllite has a much lower metamorphic grade (greenschist) and may be unconformable on the rocks of the Tenas Mary Creek, I believe it should be excluded. Until more extensive stratigraphic and petrographic studies are available, the fine-grained biotitic schists, amphibolite, and the eastern quartzite are provisionally included in the Tenas Mary Creek sequence.

The age and regional correlation of the rocks of Tenas Mary Creek are poorly known. Engels and others (1976) listed K-Ar dates on individual minerals of 50 and 67 m.y. for amphibolites. R. L. Armstrong (1977, personal commun.) has obtained preliminary whole-rock Rb-Sr dates of 600 to 1,200 m.y. B.P. on the pegmatitic gneiss and the eastern gneiss of the Kettle dome. He regards the dates as typical of the Shuswap terrane.

Parker and Calkins (1964), Pearson (1967), Preto (1970), and Donnelly (1978) correlated the rocks of Tenas Mary Creek with the Shuswap terrane of southern British Columbia. The mantling metasedimentary rocks in the Shuswap have been regarded as probably mostly Precambrian and Paleozoic but with some as young as Triassic-Jurassic (Wanless and Ressor, 1975; Okulitch and others, 1977). The thick quartzites in the Shuswap terrane were regarded as possibly Lower Cambrian (Okulitch and others, 1977); thus, by analogy, the >650-m quartzite in the Tenas Mary Creek or the eastern quartzite in the Kettle dome might be Lower Cambrian. However, the Shuswap now appears to include metasedimentary rocks as much as 3,000 m.y. old that were intruded by 1,960-m.y.-old granitic rocks and then metamorphosed 935 m.y. ago (Duncan, 1978).

If the rocks of Tenas Mary Creek are Precambrian, they could be equivalent to Windermere, Beltian, or pre-Beltian rocks. The Beltian rocks closest to the Kettle dome are in southeastern Stevens County and have been described by Miller and Clark (1975). These and other known examples of Beltian rocks in Washington and adjacent Idaho are of much lower metamorphic grade (the pelitic rocks are still black argillites). Furthermore, the 950-m Beltian Revett Quartzite weathers gray and is not as feldspathic as quartzite of the Tenas Mary Creek, and marbles of the Tenas Mary Creek rocks do not resemble the carbonate rocks of the Belt. These same arguments could be applied to the Windermere–Deer Trail rocks which, in addition, have thick greenstones that have no analogues, except possibly the amphibolites, in the rocks of the Tenas Mary Creek.

Lithologically and structurally, the most probable correlatives of the Tenas Mary Creek sequence are sillimanite-grade rocks in the Spokane area (Fig. 3). These rocks include the cataclastic Newman

Lake orthogneiss with 5-cm potassium feldspar megacrysts (Miller, 1974d; Weissenborn and Weis, 1976) and a feldspathic quartzite near Freeman (Weis, 1968) that appears to be at least as thick as the quartzite of Tenas Mary Creek. Furthermore, Griggs (1973) showed that these rocks define a flat-topped dome, herein called the Spokane dome. The northeasternmost rocks of this terrane in Idaho also are domal and yield ages of about 1,500 m.y. (Clark, 1973). The Pb-α ages of 1,150 m.y. for the Hauser Gneiss (Weis, 1968) are, of course, suspect but are suggestive of a correlation with the Tenas Mary Creek.

Most workers (Griggs, 1973; Clark, 1973; Miller, 1974b; Miller and Clark, 1975; Weissenborn and Weis, 1976) have suggested that the rocks of the Spokane dome are high-grade portions of the Belt Supergroup. However, Armstrong (1975) suggested that paragneiss, quartzite, marble, schist, amphibolite, and orthogneiss in central Idaho and the Spokane dome are part of a pre-Beltian metamorphic terrane. Because Griggs (1973) and Miller and Clark (1975) showed that on a regional scale the Spokane dome is conformably surrounded on the southern and western sides by Beltian strata, the abrupt change in metamorphic grade could be due to an unrecognized, gently domed sub-Beltian unconformity or low-angle fault. I prefer this alternative and believe that the high-grade rocks of the Spokane dome probably are pre-Beltian.

Initial strontium isotopic ratios of Mesozoic plutons in northern Washington also suggest that the rocks of the Tenas Mary Creek may be Precambrian. Plutons as far west as long. 121°W have initial ratios >0.704, which implies that the magmas were contaminated by radiogenic strontium from a Precambrian basement (Armstrong and others, 1977). Thus, the rocks of the Tenas Mary Creek could be part of such a basement. If so, the lithologic similarity of the rocks of the Tenas Mary Creek to those in the Spokane dome would support the suggestion of Armstrong and others (1977) that on the basis of these initial strontium isotopic ratios, the Precambrian basement of pre-Mesozoic North America extended westward into northern Washington.

In summary, meager stratigraphic and radiometric evidence, including a comparison with the Shuswap rocks, favor but do not prove a Precambrian age for the rocks of the Tenas Mary Creek in the Kettle dome. Regional structural interpretations, in turn, favor a pre-Beltian age for the high-grade metamorphic rocks in the Spokane dome and, by analogy, the rocks of the Tenas Mary Creek in the Kettle dome. However, because the Spokane dome is east of the Kootenay arc and Kettle dome is west of it, such a correlation is, admittedly, unconventional.

Plutons

A number of Mesozoic and Tertiary granitic plutons intrude the Tenas Mary Creek, Paleozoic, and Mesozoic rocks. The plutons vary from biotite dominated to hornblende dominated, from fine and medium grained to coarse grained, and from foliated to unfoliated phases. At present it is not known how many discrete plutons there are. All are shown as a single unit in Figure 2.

STRUCTURE OF KETTLE DOME

Kettle Dome

The antiformal nature of the rocks underlying the Kettle River Range was first recognized by Campbell (1946). He noted that near and south of State Route 20 the foliation forms a dome "12 miles wide" elongated to the northeast. He also realized that the cataclasis of the rocks is similar to that of the Okanogan dome.

The antiformal pattern of the Kettle dome is best shown by the map pattern of the >650-m quartzite

(Fig. 2) and by the antiformal dips of this quartzite. Rocks of the Tenas Mary Creek sequence on the eastern and southeastern limbs of the dome form prominent dip slopes near Orient, Kettle Falls, and Lake Ellen. The best-preserved dip slope on rocks of the Tenas Mary Creek sequence defining the western limb of the dome is Tenasket Mountain.

The dome is >65 km long north-south and 27 km wide. The structural relief is only about 3 km (Fig. 2). The northern end of the dome is a northwest-trending antiform, defined by opposing dips in the >650-m quartzite and biotitic rocks on Huckleberry Mountain and on Togo and Marble Mountains.

The dips of bedding and of foliation within the Tenas Mary Creek units crudely define two en echelon north-trending, gently antiformal axes within the dome. Dips generally are <25°, and locally foliation and bedding are nearly horizontal, forming flat-topped ridges in the center of the dome. However, contacts are unusually steep to vertical along the northwesternmost margin of the dome and near Profanity Peak along the north-trending fault on the western side of the dome.

The simple domal structure could be part of a larger, more complex structure. For example, detailed mapping might show that the domal structure is the upper limb of a large recumbent fold similar to the small folds commonly seen in outcrops. Furthermore, if the eastern quartzite could be shown to be correlative with, or older than, the >650-m quartzite within the dome, the structure is more complex than shown in Figure 2. When the reconnaissance nature of the mapping is considered, such possibilities should not be ignored.

Structures within the Dome

Folds larger than those in outcrops but with map patterns smaller than several kilometres are difficult to recognize in reconnaissance mapping. A gently eastward-plunging synform may exist in the eastern gneiss and amphibolites south of Deadman Creek in the Boyds quadrangle. The amphibolite north of the mouth of Sherman Creek in the Bangs Mountain quadrangle may mark a similar synform. An east-trending antiform brings the lowest units of Tenas Mary Creek to the surface along the Kettle River in Canada (Preto, 1970), and this fold could account for the east-trending salient of the eastern gneiss at the Canadian border near Laurier in Figure 2. Gentle northwest-trending folds in the eastern quartzite along the eastern margin of the dome may be minor folds associated with formation of the dome.

A north-trending fault in the western part of the Sherman Peak and Togo Mountain quadrangles juxtaposes structurally higher rocks on the east against structurally lower rocks on the west. The ≥2-km vertical separation on this fault shown on the cross section in Figure 2 could produce the 10 km of apparent left-lateral separation shown on the map in Figure 2. The fault does not seem to offset the hornblende quartz dioritic pluton in the valley of the North Fork of Sherman Creek.

A west-northwest–trending fault with the northeast side up occurs in Hoodoo Canyon. A similar fault in the Sherman Peak and Bangs Mountain quadrangles may offset the north-trending fault mentioned above. Such a northwest-trending fault would explain why marble and quartzite in the biotitic unit north of Sherman Pass dip toward each other. It would also explain the apparent juxtaposition of the eastern gneiss and pegmatitic gneiss along State Route 20 northeast of Sherman Pass. The same fault would account for the northward termination of the upper Paleozoic phyllites along the southeastern edge of the dome, as well as the straight courses of Sherman Creek and of Donaldson Draw on Bangs Mountain. Smaller faults within Tenas Mary Creek rocks probably are more numerous than reconnaissance mapping can resolve. Small northwest-trending faults do cut the eastern quartzite and eastern gneiss in the Boyds quadrangle.

The maps of Parker and Calkins (1964) and Muessig (1967) indicate that neither of the large faults offset the faults that bound Tertiary rocks to the west of the dome. Thus, the large faults within the

Kettle dome probably are pre-Tertiary. On the eastern side of the Kettle River in the Orient quadrangle, pyroxenites and other mafic rocks mark the contact between the rocks of the Tenas Mary Creek and upper Paleozoic phyllites and Tertiary rocks (Bowman, 1950). Perhaps this is a postdome fault (like the serpentinite-bearing Sherman fault west of the dome, shown in Fig. 3).

The contact between the rocks of the Tenas Mary Creek sequence and the overlying low-grade rocks along the eastern margin of the dome appears to be tectonic. Campbell (1938, 1946) described cataclasis in the eastern gneiss on the southeastern limb of the dome. Locally, chloritic fractures and brecciation are well developed along the northeastern margin of the dome (Bowman, 1950; Lyons, 1967; Donnelly, 1978), especially in the small plutons near Orient (Bowman, 1950). Cataclasis (microshears and microbrecciation) in the metasedimentary rocks is parallel to but later than the foliation that outlines the recumbent folds (Lyons, 1967; Donnelly, 1978). Furthermore, unmetamorphosed nonrecrystallized, but brecciated limestone (presumably of late Paleozoic age) overlies rocks of Tenas Mary Creek in three places: just west of the confluence of the Kettle and Columbia Rivers, on the Kettle River 3.3 km northwest of Barstow, and on U.S. Route 395 2 km northwest of Barstow. The granitic gneisses of the Tenas Mary Creek below the limestone of the Kettle River locality are extensively chloritized. It seems likely that detailed mapping would show that the limestone in the Orient and Boyds quadrangles overlies a gently eastward-dipping tectonic zone.

REGIONAL GEOLOGY

Terranes Equivalent to the Kettle Dome

The cataclastic and domal nature of the gneisses between the Republic area and the Okanogan River have been described by Waters and Krauskopf (1941), Snook (1965), and Fox and others (1976, 1977). Although this dome is structurally similar to the Kettle dome, it is predominantly composed of Mesozoic(?) orthogneiss and granitic plutons.

The dioritic gneisses in the western part of the Okanogan dome were regarded as paragneisses by Snook (1965). Fox and others (1976) proposed that Snook's name of Tonasket Gneiss be applied to all such rocks (Fig. 3). My preliminary mapping suggests that virtually all of the Tonasket Gneiss in the central part of the dome is derived from a pluton grading inward from diorite to quartz diorite to porphyritic granodiorite.

The age of the Tonasket Gneiss is not too well known. On the southeastern margin of the dome, upper Paleozoic hornfelsic phyllite occurs adjacent to an orthogneiss that is similar to the interior porphyritic granodioritic phase of the Tonasket Gneiss. Fox and others (1976) reported U-Pb ages of 87 and 100 m.y. and a Th-Pb age of 94 m.y. from a euhedral zircon from hornblende-rich Tonasket Gneiss.

The eastern part of the Okanogan dome is dominated by biotitic quartz monzonitic to granodioritic plutons that intrude the Tonasket Gneiss and the late Paleozoic phyllitic rocks. Portions of these plutons have been described by Waters and Krauskopf (1941), Parker and Calkins (1964), Staatz (1964), Muessig (1967), and Pearson (1967). In general, the plutons are texturally zoned, becoming coarser grained and more porphyritic inward, weakly to moderately foliated, and locally cataclastic. The western contacts of the westernmost plutons that I have mapped in the dome commonly dip $\leq 25°$ eastward. Pardee (1918) named various crystalline rocks, including such plutons at the southern ends of both the Kettle and Okanogan domes, the Colville batholith. The term "Colville batholith" probably should be reserved for these variably foliated, leucocratic quartz monzonitic to granodioritic Mesozoic plutons as Staatz (1964) suggested.

Studies of the Okanogan dome have led to three theories of origin that might be applicable to the other domes as well. Waters and Krauskopf (1941) considered the cataclasis of the Tonasket Gneiss to

be the protoclastic border, or carapace, of the Colville batholith. Snook (1965) demonstrated the metamorphic nature of the Tonasket Gneiss and pointed out that cataclasis postdates the mylonitization that cuts the foliation within the Tonasket Gneiss. He concluded that the increasingly cataclastic nature of the gneiss adjacent to the border of the dome could be attributed to later folding of an originally flat thrust in the gneisses, rather than to batholithic emplacement. The presumed paragneissic origin of the Tonasket Gneiss and 66- to 46-m.y. ages determined by K-Ar and fission-track measurments led Fox and others (1976, 1977) to suggest that the rocks were emplaced as an Upper Cretaceous gneiss dome that cooled through the Eocene.

As noted above, rocks similar to those in the Kettle dome occur in the Spokane dome. At present, cataclasis (Fig. 3) has been reported only in the coarse Newman Lake Orthogneiss and the Mesozoic Loon Lake batholith (Weissenborn and Weis, 1976; Miller, 1974d). Mylonitic rocks are known at two localities on the eastern edge of the dome between Coeur d'Alene and lat 48°N (Miller and Engels, 1975, p. 524).

Regional Extent of Tertiary Formations and Folding

An understanding of the regional geology (Fig. 3) is helpful in determining the origin and the age of the Kettle dome. The maps of Parker and Calkins (1964), Muessig (1967), and Staatz (1964) demonstrate that a syncline occurs west of the Kettle dome. This fold was recognized by Wright (1949) and named the "Sanpoil syncline" by Muessig. In the center of the fold is the Eocene Klondike Mountain Formation; successively outward (down the section) are the Eocene Sanpoil volcanic rocks, the Eocene O'Brien Creek Formation, and the upper Paleozoic to Triassic rocks. The synclinal map pattern is discernible on Figure 3.

Another north-trending synclinal inlier of the same three Eocene formations occurs near Orient on the northeastern margin of the dome (Fig. 3). Dips as great as 50° occur in the lower part of the Klondike Mountain Formation (Pearson and Obradovich, 1977).

Discordant K-Ar dates similar to those reported by Fox and others (1976, 1977) in the Okanogan dome are common in northeastern Washington and adjacent British Columbia (Miller and Engels, 1975; Armstrong and others, 1977). An alternative explanation to a cooling gneiss dome is that these dates were caused by Eocene volcanism and plutonism (Armstrong and others, 1977). As noted below, the Eocene volcanic rocks (Sanpoil Volcanics and Klondike Mountain Formation) were of regional extent, and Eocene plutons are common; the quartz monzonite of Long Alec Creek (K-Ar age of 51.7 ± 1.6 m.y., according to Engels and others, 1976) in the northern end of the Kettle Dome (Figs. 2, 3) even has batholithic dimensions.

Because the Kettle dome is bounded on the west and the northeast by Tertiary synclines, its present antiformal structure also is most likely Tertiary (Cheney, 1976, 1977). Furthermore, the length, trend, and structural relief of the Sanpoil syncline are similar to those of the dome. The axis of the Kettle dome is not parallel to the axis of the Sanpoil syncline, but this difference may be due to the combined effect of Tertiary folding and older structures within the rocks of the Tenas Mary Creek sequence. The high-grade metamorphism and related folding within the Tenas Mary Creek probably is pre-Tertiary (and probably pre-Beltian), and much of the uplift of the Tenas Mary Creek from the depths at which sillimanite forms probably was pre-Tertiary.

The regional extent of Tertiary folding is best appreciated after recognition of the regional extent of the Tertiary formations. Pearson and Obradovich (1977) have shown that the Eocene O'Brien Creek Formation, the dacites of the Sanpoil Volcanics, and the volcanic and volcaniclastic rocks of the Klondike Mountain Formation in the Republic area (Meussig, 1967) extend across northeastern Washington. The regional presence of the same three unconformity-bounded Tertiary formations suggests that they were not deposited in local basins as most authors—including Parker and Calkins

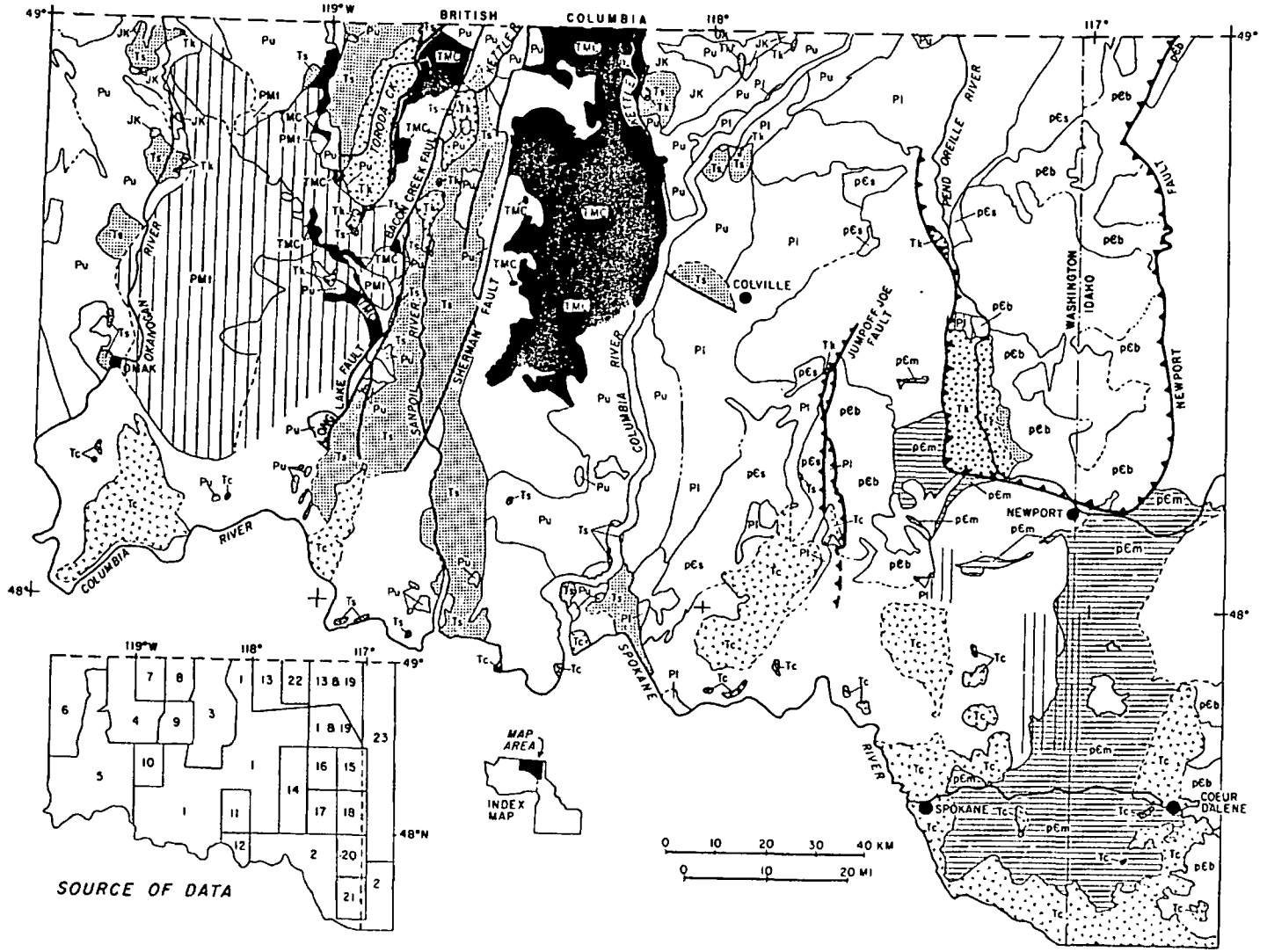
BRITISH COLUMBIA
119°W
118°
117°
49°
48°
COLVILLE
NEWPORT
SPOKANE
COEUR D'ALENE
WASHINGTON
IDAHO
COLUMBIA RIVER
OKANOGAN RIVER
SANPOIL RIVER
KETTLE RIVER
PEND OREILLE RIVER
SPOKANE RIVER
SHERMAN FAULT
BACON CREEK FAULT
LONG LAKE FAULT
JUMPOFF JOE FAULT
NEWPORT FAULT
TORODA CK.
ONAK
MAP AREA
INDEX MAP
SOURCE OF DATA
0 10 20 30 40 KM
0 10 20 MI

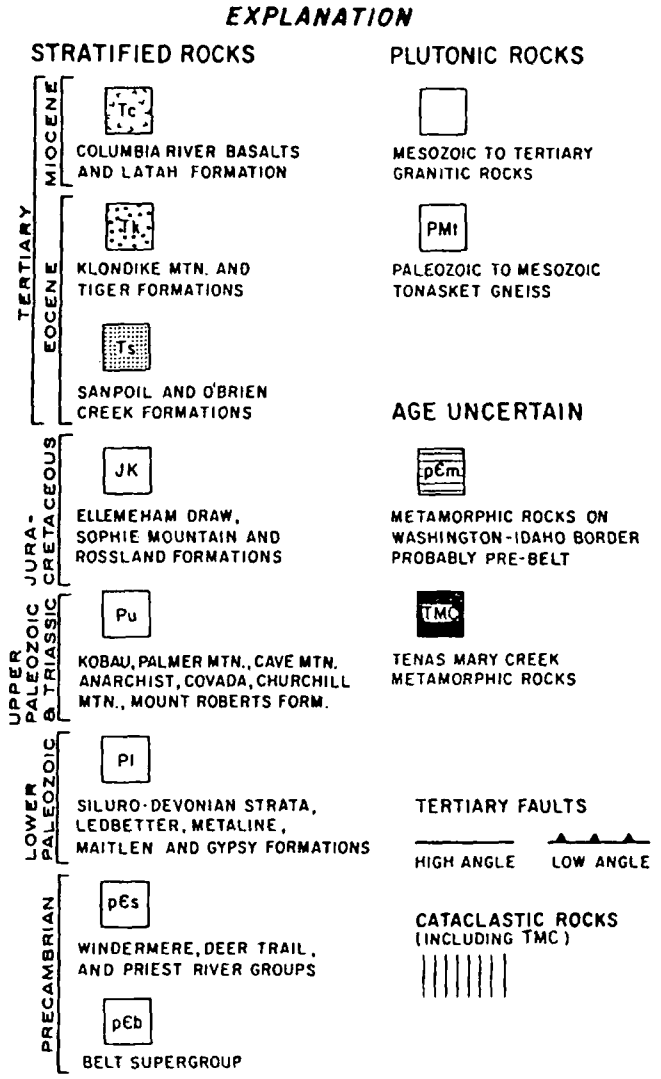

Figure 3. Geologic map of northeastern Washington and adjacent Idaho. For cartographic clarity, small stocks and the letter designations of Tertiary and Mesozoic plutons have been omitted from the map. Data sources are (1) Huntting and others (1961); (2) Griggs (1973); (3) Cheney (this paper); (4) Cheney (unpub. mapping); (5) Fox and others (1977); (6) Rinehart and Fox (1972); (7) Pearson (1967); (8) Parker and Calkins (1964); (9) Muessig (1967); (10) Staatz (1964); (11) Campbell and Raup (1964); (12) Becraft and Weis (1963); (13) Yates (1971); (14) Miller and Clark (1975); (15) Miller (1974a); (16) Miller (1974b); (17) Miller (1974c); (18) Miller (1974d); (19) Miller and Engels (1975); (20) Weissenborn and Weis (1976); (21) Weis (1968); (22) Yates (1964); (23) Bond (1978).

(1964), Muessig (1967), and Pearson and Obradovich (1977)—suppose.

The Klondike Mountain Formation as shown in Figure 3 is more extensive than shown by Pearson and Obradovich (1977). The map of Fox (1970) suggests that the Klondike Mountain Formation may exist in the Okanogan Valley. East of the Columbia River the mafic, olivine-bearing flows that locally lie above the Sanpoil immediately east of long. 118°W (Yates, 1971) might correlate with Muessig's (1967) basaltic upper member of the Klondike Mountain Formation. Pearson and Obradovich (1977) gave the following minimum ages: O'Brien Creek, 53 m.y.; Sanpoil, 50 m.y.; and Klondike Mountain, 41 m.y.

For simplicity, the conglomerates and sandstones of the Tiger Formation that unconformably overlie Sanpoil lavas in the Pend Oreille Valley (Pearson and Obradovich, 1977) are shown in the same pattern in Figure 3 as the Klondike Mountain Formation. However, no evidence presently exists as to whether these formations are correlative or not. Indeed, because the Tiger Formation varies greatly in provenance and appearance, it may have been deposited in more than one epoch of the Tertiary (Miller, 1971, 1974b). Additionally, although some parts of the Tiger appear to dip westward into the Newport fault, Miller (1971) pointed out that other parts of the Tiger appear to overlie the fault and no part of the formation is known to show the effects of proximity to such a major fault as the Newport fault. Thus, at least part of the Tiger may be correlative with at least one of the two unconformity-bounded epiclastic units described by Muessig (1967) and Pearson and Obradovich (1977) in the lower part of the Klondike Mountain Formation.

The Sanpoil syncline and the syncline near Orient already have been noted. The regional map of Rinehart and Fox (1972) shows two synclinal remnants of the Eocene formations along the western border of the Okanogan dome near Tonasket. The inliers of Eocene rocks just east of the Columbia River are partly synclinal and partly fault bounded (Yates, 1971; Pearson and Obradovich, 1977) and are aligned along a north-northeast trend. Perhaps the inliers west of the Okanogan dome and east of the Columbia River are remnants of formerly more extensive north-northeast–trending synclinal belts of Tertiary rocks similar to the Sanpoil syncline.

The inlier of Eocene formations on the Canadian border northwest of the Sanpoil syncline has been named the "Toroda Creek graben" by Pearson and Obradovich (1977). This inlier may also be synclinal, but, admittedly, the number of westward-dipping flow structures in the eastern edge of the Klondike Mountain Formation are few (Pearson, 1967), unconformities obscure a synclinal map pattern in the Tertiary rocks, and the eastern edge of the Klondike Mountain Formation is faulted (Pearson, 1967).

Tertiary Faults and Cataclasis

The synformal Newport fault zone in northeastern Washington and northwestern Idaho (Fig. 3) may cut the Tertiary Tiger Formation (Miller, 1974b) and does cut a 45- to 51-m.y.-old pluton (Miller and Engels, 1975). The fault separates structurally lower muscovite-biotite schist, micaceous quartzite, gneiss, and batholithic rocks from Tertiary rocks and only mildly metamorphosed Paleozoic and Beltian rocks (Miller, 1971, 1974b, 1974c, 1974d). The fault is a gently northward-plunging, synformal, cataclastic zone 300 m wide. Figure 3 shows areas of cataclasis beyond the fault described by Miller (1974b, 1974c, 1974d); detailed petrographic studies might enlarge these areas. K-Ar dates of plutons peripheral to the fault are typically 45 to 51 m.y. B.P. (Miller and Engels, 1975). Miller and Engels suggested that the preservation of much older K-Ar dates (typically 93 to 101 m.y. B.P.) in the plutonic rocks 8 to 25 km from the fault and in the upper plate of the fault indicates lateral displacement of 70 to 100 km.

A smaller Newport-type fault may bound the belt of Tertiary rocks of the so-called Toroda Creek graben. Along the northeastern margin of this belt, between the Canadian border and the Kettle River,

Parker and Calkins (1964) described a fault with a 400-m-wide zone of sheared breccia; this fault separates rocks of the Tenas Mary Creek in their type area from the Tertiary rocks to the west. Along this contact southwest of the Kettle River, Pearson (1967) described westward-dipping sheets of breccia as much as 30 m (locally 300 m) thick below and within the Klondike Mountain Formation. Although he suggested that these breccias were debris flows, Pearson also interpreted the eastern contact of the Tertiary rocks as a fault dipping 20° to 30° westward. Pearson and Obradovich (1977) extended this fault southward toward Granite Creek in the Aeneas quadrangle. In the valley of Granite Creek, a very poorly sorted and poorly stratified breccia consisting mostly of granitic fragments in an arkosic matrix occurs beneath the Klondike Mountain volcanic rocks. Muessig (1967) and Pearson and Obradovich (1977) regarded these breccias as sedimentary, but my mapping indicates that (1) locally some of the clasts are "smeared out" in a well-foliated matrix; (2) matrix-filled fractures down to hairline width extend into a few clasts, and (3) the underlying granites have mylonitic seams. Thus, the breccia may be tectonic. If, like the Newport fault, a western limb of this fault does exist, it may explain the juxtaposition of low-grade upper Paleozoic strata against garnet-staurolite mica schist at Wauconda Summit in the northwestern corner of the Aeneas quadrangle. This fault would be on strike with the fault that Pearson (1967) mapped just to the north and would separate the Tertiary volcanic rocks to the east from schist, phyllite, amphibolite, and marble to the west. Because additional mapping is necessary to determine whether these faults are segments of a single system analogous to the Newport fault, a single fault is not shown on Figure 3.

Although the faults on the western side of the Sanpoil syncline (Fig. 3) clearly are regarded as the western boundary faults of the Republic graben (Parker and Calkins, 1964; Muessig, 1967; Staatz, 1964), a number of anomalies exist (Cheney, 1979). Firstly, the traces of these faults are more sinuous than can be shown on Figure 3. Secondly, Wright (1949) concluded that most of the epithermal gold ore in the Sanpoil Volcanics in the Republic district adjacent to the Bacon Creek fault is in thrust faults that dip 55° to 65° eastward. He illustrated (1949, Figs. 3, 4b, 7) the Bacon Creek fault as a major break along which an anticline involving the Sanpoil and Klondike Mountain units was thrust westward over Colville granitic rocks. Furthermore, highly sheared and veined phyllite with concordant rhombic tectonic clasts of limestone dips 20° eastward in an adit in sec. 32, T. 37 N., R. 32 E., where Muessig (1967) interpreted the junction of the Bacon Creek and Scatter Creek faults; the location is virtually on strike with Wright's (1949) cross section showing the Bacon Creek fault.

On Figure 3, the Scatter Creek fault is the unlabeled segment between the Bacon Creek and Long Lake faults. Muessig noted (1967) that in one adit the Scatter Creek fault is horizontal. Two of the three western boundary faults in the Bald Knob quadrangle to the southwest dip gently eastward (Staatz, 1964). In Figure 3, the King Creek and Nespelem River faults are the first and second faults, respectively, east of the Long Lake fault. Staatz showed the King Creek fault as a thrust and only assumed normal movement on the Long Lake fault. He also showed the high-angle Nespelem River fault as up on the eastern side (not the western side as one might expect for a western-bounding fault of a graben).

Another thrust exists at least locally on the eastern limb of the Sanpoil syncline. Muessig (1967) mapped a "major thrust fault," the Lambert Creek thrust, cutting Sanpoil flows and the younger quartz monzonite of Herron Creek. Parker and Calkins (1964) did not recognize such a fault in the neighboring Curlew quadrangle, but the sinuous St. Peter fault, which is cut by the Sherman fault, is a likely candidate. The Sherman fault east of the Sanpoil syncline does appear to be a high-angle fault (Staatz, 1964; Meussig, 1967).

In summary, the so-called Toroda Creek and Republic grabens may be synclinely folded allochthons rather than grabens. Alternatively, if they are bounded only on one side by thrusts, they are only half-grabens. In any case they are not grabens in which the Tertiary rocks were deposited.

Available mapping (Campbell, 1938, 1946; Waters and Krauskopf, 1941; Snook, 1965; Petro, 1970;

Weissenborn and Weis, 1976) indicates that cataclasis within the crystalline rocks of the three domes increases in intensity toward the margins of each dome. Furthermore, the intensely cataclastic marginal zones, including the previously discussed northeastern margin of the Kettle dome, have sinuous traces suggestive of low dips. Snook (1965) has already suggested that the cataclastic zone along the western margin of the Okanogan dome is due to folding of an originally flat thrust and that erosion has removed the cataclastic zone from the crest of the dome.

Although cataclasis is easier to detect in coarse-grained crystalline rocks, the greatest shearing probably occurred in the incompetent rocks (such as the upper Paleozoic argillites) above the crystalline rocks. The Osoyoos and Whiskey Mountain plutons within upper Paleozoic strata peripheral to the northwestern margin of the Okanogan dome do become more cataclastic toward the dome (Fox and others, 1976; Rinehart and Fox, 1972). An intensely shattered and hydrothermally altered pluton occurs in phyllitic rocks south of Lake Ellen on the southeastern margin of the Kettle dome, and Campbell (1938) described cataclastic sills and quartzite in the Paleozoic phyllites in this area. In fact, Campbell (1938) probably was the first to suggest that intense shearing in the phyllitic rocks and the intense cataclasis in the adjacent gneiss were similar to the effects of major thrust faults, but he discarded this idea in favor of a protoclastic border of what he inferred was the Colville batholith.

If these cataclastic zones are antiformal analogues of the synformal Newport fault, a westward-dipping fault zone should occur between the Newport fault and the Kettle dome. A possible candidate is the gently westward-dipping Jumpoff Joe fault in the Chewelah area. Miller and Clark (1975) suggested that thrusting on the Jumpoff Joe fault might be extensive enough to explain the structural and stratigraphic contrasts between the Deer Trail group west of the fault and the Belt rocks to the east. Where the fault cuts 100-m.y.-old plutons, Miller and Clark reported that it forms a cataclastic zone as much as 150 m wide; south of Chewelah, upper Miocene Columbia River Basalt overlies the fault (Miller and Clark, 1975). Miller and Clark also suggested that northeast-striking faults that pass a few kilometres northwest of Chewelah might be the major structures in the area.

If the Jumpoff Joe fault and the imbricate zone beneath it that involves lower Paleozoic strata are equivalent to the Newport fault, the lower Paleozoic and the Precambrian Deer Trail–Windermere–Priest River strata are restricted to the upper plate. Units of the Belt Supergroup in the Chewelah area (Miller and Clark, 1975) would be in the lower plate, but east of the Pend Oreille River (Miller, 1974a), such units are in the upper plate of the Newport fault.

The Newport fault, the low-angle faulting in the Toroda Creek area, the faults bordering the western limb of the Sanpoil syncline, and the Lambert Creek fault may be similar in age. All cut Eocene rocks. The Newport fault cuts a 45- to 51-m.y.-old pluton (Miller and Engels, 1975). The Lambert Creek thrust cuts the quartz monzonite of Herron Creek, which is similar to the Long Alec Creek batholith that has been dated at 53 m.y. B.P. (Pearson and Obradovich, 1977). Furthermore, the 48- to 49-m.y.-old Swimptkin Creek and Coyote Creek plutons in the Okanogan dome are slightly cataclastic (Fox and others, 1977). Whether these faults are portions of a single regional fault, a series of related faults, or merely local zones of decoupling is not yet known.

TIMING OF STRUCTURAL EVENTS

Mylonites and brecciated rocks have been described in the crystalline rocks of each of the three domes. Snook (1965) stressed that, although both commonly occur in the same rocks on the western margin of the Okanogan dome, the directionless microbreccias formed later than the schistose mylonites and that in most mylonites the biotite did not change to chlorite, whereas, chlorite, epidote, and zeolites are prominent in the microbreccias. The same relationships occur on the northern margin of the Okanogan dome in the contact metamorphic aureole of the Mount Bonaparte pluton

(one of the Colville plutons) and as discrete sericitic phyllonite zones within the Cretaceous(?) Buckhorn Mountain pluton a few kilometres north of the dome (McMillen, 1979). As McMillen (1979) has stresed, the petrographic descriptions of Campbell (1938), Parker and Calkins (1964), Lyons (1964), and Donnelly (1978) suggest that mylonitization and later brecciation accompanied by retrograde metamorphism also are common on the margins of the Kettle dome.

Thus, although the mylonites and the cataclastic zones characterized by brecciated rocks commonly are coincident, they differ in age. Mylonitization is Cretaceous(?) or younger (McMillen, 1979) but has not been observed in Eocene rocks; whereas, cataclasis is Eocene or younger. Thus, mylonitization in the crystalline rocks of the domes is not related to the Tertiary faults and cataclasis described above. If the Jumpoff Joe fault near Chewelah, which is overlain by Columbia River basalt, is related to the other low-angle faults marked by cataclastic zones, these faults are pre-late Miocene. A study of that part of the Tiger Formation that appears to overlie the Newport fault might provide a better age for the faulting.

The antiformal nature of the cataclastic zones around the margins of the domes indicates that the cataclastic zones have been folded. The age of this folding is not well known. The map and cross section C–C′ of Weissenborn and Weis (1976) suggest that the erosion surface beneath the Columbia River Basalt and the interlayered Latah formation dips southwesterly off the Spokane dome; thus, at least part of the doming may be older than the basalt. However, because the greater structural relief of the larger north-trending Cascade arch to the west is younger than the Columbia River Basalt (McKee, 1972), it is tempting to speculate that the present structural relief of the north-trending Spokane, Kettle, and Okanogan domes also may be due to folding younger than the basalt.

CONCLUSIONS

In summary, northeastern Washington is characterized by north-northeast–trending Tertiary folds tens of kilometres long but with amplitudes of only a few kilometres. The synclines are marked by remnants of Tertiary strata that once were regionally extensive. Instead of being diapiric gneiss domes, I believe that the Okanogan dome, the Kettle dome, the Paleozoic and Precambrian rocks near Chewelah between the Pend Oreille and Columbia Rivers, and the Spokane dome are the anticlines. The cores of the Kettle and Spokane domes consist of high-grade metamorphic rocks that probably are pre-Beltian in age. The high-grade rocks near Chewelah probably are pre-Beltian also. Mylonites within the domes probably are Cretaceous in age.

At present, any relationship between the Newport, the Jumpoff Joe, and other low-angle faults must be regarded as speculative, and no unequivocal physical evidence exists for significant displacement along any of them or on the cataclastic zones rimming the domes. Until physical evidence of significant displacement is available and until the ages of most of the cataclastic zones are known, the cataclastic zones should be regarded as local zones of Tertiary decoupling between the crystalline batholithic and metamorphic basement and the stratified cover rocks. Only additional investigations can determine whether the low-angle faults and cataclastic zones are a major folded Tertiary thrust, a series of thrusts, or purely local phenomena. The folding that caused the present distribution of faults and the present structural relief of the domes may be Miocene or younger.

ACKNOWLEDGMENTS

I thank Urangesellshaft, Chevron Resources, and Wold Nuclear for supporting the field work that made this paper possible. I am particularly grateful to D. S. Cowan, S. J. Reynolds, and A. V. Okulitch for very critical reviews of an earlier version of the manuscript and for attempting to moderate some of its more controversial aspects.

REFERENCES CITED

Armstrong, R. L., 1975, Precambrian (1500 m.y. old) rocks of central Idaho; The Salmon River arch and its role in Cordilleran sedimentation and tectonics: American Journal of Science, v. 275-A, p. 437–467.

Armstrong, R. L., Taubeneck, W. H., and Hales, P. O., 1977, Rb-Sr and K-Ar geochronometry of Mesozoic granitic rocks and their Sr isotope composition, Oregon, Washington, and Idaho: Geological Society of America Bulletin, v. 88, p. 397–411.

Becraft, G. E., and Weis, P. L., 1963, Geology and mineral deposits of the Turtle Lake quadrangle, Washington: U.S. Geological Survey Bulletin 1131, 73 p.

Bond, J. G., compiler, 1978, Geologic map of Idaho: Idaho Bureau of Mines and Geology, scale 1:500,000.

Bowman, E. C., 1950, Stratigraphy and structure of the Orient area, Washington [Ph.D. dissert.]: Cambridge, Mass., Harvard University, 149 p.

Campbell, A. B., and Raup, O. B., 1964, Preliminary geological map of the Hunters quadrangle, Stevens and Ferry Counties, Washington: U.S. Geological Survey Map MF-276, scale 1:48,000.

Campbell, C. D., 1938, An unusually wide zone of crushing in the rocks near Kettle Falls, Washington: Northwest Science, v. 12, p. 92–94.

——1946, Structure in the east border of the Colville batholith, Washington [abs.]: Geological Society of America Bulletin, v. 57, p. 1184–1185.

Campbell, C. D., and Thorsen, G. W., 1966, Compilation of geological mapping from 1935 to 1966 in the Sherman Peak and Kettle Falls quadrangles: Washington Division of Geology and Earth Resources Open-File Maps, scale 1:62,500.

Cheney, E. S., 1976, Kettle Dome, Okanogan Highlands, Ferry County, Washington: Geological Society of America Abstracts with Programs, v. 8, p. 360.

——1977, The Kettle dome: The southern extension of the Shuswap terrane into Washington: Geological Society of America Abstracts with Programs, v. 9, p. 926.

——1979, Tertiary decollement in northeastern Washington?: Geological Society of America Abstracts with Programs, v. 11, p. 72.

Clark, S.H.B., 1973, Interpretation of a high-grade Precambrian terrane in northern Idaho: Geological Society of America Bulletin, v. 84, p. 1999–2004.

Daly, R. A., 1912, Geology of the North American Cordillera at the forty-ninth parallel: Canadian Geological Survey Memoir 38, Part 1, 546 p.

Davis, G. H., and Coney, P. J., 1979, Geologic development of the Cordilleran metamorphic core complexes: Geology, v. 7, p. 120–124.

Donnelly, B. J., 1978, Structural geology of the Nancy Creek area, east flank of the Kettle dome, Ferry County, Washington [M.S. thesis]: Pullman, Washington State University, 251 p.

Duncan, I. J., 1978, Rb/Sr whole rock evidence for three Precambrian events in the Shuswap complex, southeast British Columbia: Geological Society of America Abstracts with Programs, v. 10, p. 392–393.

Engels, J. C., and others, 1976, Summary of K-Ar, Rb-Sr, U-Pb, Pb-α, and fission-track ages of rocks from Washington State prior to 1975 (exclusive of Columbia Plateau basalts): U.S. Geological Survey Miscellaneous Field Studies Map MF-70 (two sheets).

Fox, K. F., Jr., 1970, Geologic map of the Oroville quadrangle, Okanogan County, Washington: U.S. Geological Survey Open-File Map, scale 1:48,000.

Fox, K. F., Rinehart, C. D., and Engels, J. C., 1977, Plutonism and orogeny in north-central Washington—Timing and regional context: U.S. Geological Survey Professional Paper 989, 27 p.

Fox, K. F., Jr., and others, 1976, Age of emplacement of the Okanogan gneiss dome, north-central Washington: Geological Society of America Bulletin, v. 87, p. 1217–1224.

Griggs, A. B., 1973, Geologic map of the Spokane quadrangle, Washington, Idaho, and Montana: U.S. Geological Survey Map I-768, scale 1:250,000.

Huntting, M. T., and others, 1961, Geologic map of Washington: Washington Division of Mines and Geology, scale 1:500,000.

Lyons, D. J., 1967, Structural geology of the Boulder Creek metamorphic terrane, Ferry County, Washington [Ph.D. dissert.]: Pullman, Washington State University, 115 p.

McKee, B., 1972, Cascadia: The geologic evolution of the Pacific Northwest: New York, McGraw-Hill Book Company, 394 p.

McMillen, D. D., 1979, The structure and economic geology of Buckhorn Mountain, Okanogan County, Washington [M.S. thesis]: Seattle, University of Washington, 68 p.

Miller, F. K., 1971, The Newport fault and associated mylonites, northeastern Washington: U.S. Geological Survey Professional Paper 750-D, p. D77–D79.

——1974a, Preliminary geologic map of the Newport Number 1 quadrangle, Pend Oreille County, Washington, and Bonner County, Idaho: Washington Division of Geology and Earth Resources Map GM-7, scale 1:62,500.

——1974b, Preliminary geologic map of the Newport Number 2 quadrangle, Pend Oreille and Stevens

Counties, Washington: Washington Division of Geology and Earth Resources Map GM-8, scale 1:62,500.

——1974c, Preliminary geologic map of the Newport Number 3 quadrangle, Pend Oreille, Stevens, and Spokane Counties, Washington: Washington Division of Geology and Earth Resources Map GM-9, scale 1:62,500.

——1974d, Preliminary geologic map of the Newport Number 4 quadrangle, Spokane and Pend Oreille Counties, Washington, and Bonner County, Idaho: Washington Division of Geology and Earth Resources Map GM-10, scale 1:62,500.

Miller, F. K., and Clark, L. D., 1975, Geology of the Chewelah-Loon Lake area, Stevens and Spokane Counties, Washington: U.S. Geological Survey Professional Paper 806, 74 p.

Miller, F. K., and Engels, J. C., 1975, Distribution and trends of discordant ages of the plutonic rocks of northeastern Washington and northern Idaho: Geological Society of America Bulletin, v. 86, p. 517–528.

Muessig, S., 1967, Geology of the Republic quadrangle and a part of the Aeneas quadrangle, Ferry County, Washington: U.S. Geological Survey Bulletin 1216, 135 p.

Okulitch, A. V., Price, R. A., and Richards, T. A., editors, 1977, Geology of the southern Canadian Cordillera—Calgary to Vancouver: Geological Association of Canada Guidebook to Field Trip 8, 135 p.

Pardee, J. T., 1918, Geology and mineral deposits of the Colville Indian Reservation, Washington: U.S. Geological Survey Bulletin 677, 186 p.

Park, C. F., Jr., and Cannon, R. S., Jr., 1943, Geology and ore deposits of the Metalline quadrangle, Washington: U.S. Geological Survey Professional Paper 202, 81 p.

Parker, R. L., and Calkins, J. A., 1964, Geology of the Curlew quadrangle, Ferry County, Washington: U.S. Geological Survey Bulletin 1169, 95 p.

Pearson, R. C., 1967, Geologic map of the Bodie Mountain quadrangle, Ferry and Okanogan Counties, Washington: U.S. Geological Survey Map GQ-636, scale 1:62,500.

——1977, Preliminary geological map of the Togo Mountain quadrangle, Ferry County, Washington: U.S. Geological Survey Open-File Report 77-371, scale 1:62,500.

Pearson, R. C., and Obradovich, J. D., 1977, Eocene rocks in northeast Washington—Radiometric ages and correlation: U.S. Geological Survey Bulletin 1433, 41 p.

Preto, V. A., 1970, Structure and petrology of the Grand Forks group, British Columbia: Geological Survey of Canada Paper 69-22, 80 p.

Rinehart, C. D., and Fox, K. F., Jr., 1972, Geology and mineral deposits of the Loomis quadrangle, Okanogan County, Washington: Washington Division of Mines and Geology Bulletin 64, 124 p.

Snook, J. R., 1965, Metamorphic and structural history of the "Colville batholith" gneisses, north-central jWashington: Geological Society of America Bulletin, v. 76, p. 759–776.

Staatz, M. H., 1964, Geology of the Bald Knob quadrangle, Ferry and Okanogan Counties, Washington: U.S. Geological Survey Bulletin 1161-F, 79 p.

Wanless, R. K., and Reesor, J. E., 1975, Precambrian zircon age of orthogneiss in the Shuswap metamorphic complex, British Columbia: Canadian Journal of Earth Science, v. 12, p. 326–334.

Waters, A. C., and Krauskopf, K., 1941, Protoclastic border of the Colville batholith: Geological Society of America Bulletin, v. 52, p. 1355–1417.

Weis, P. L., 1968, Geologic map of the Greenacres quadrangle, Washington and Idaho: U.S. Geological Survey Map GQ-734, scale 1:62,500.

Weissenborn, A. E., and Weis, P. L., 1976, Geologic map of the Mount Spokane quadrangle, Spokane County, Washington, and Kootenai and Bonner Counties, Idaho: U.S. Geological Survey Map GQ-1336, scale 1:62,500.

Wright, L. B., 1949, Geologic relations and new ore bodies of the Republic district, Washington: American Institute of Mining and Metallurgical Engineers Transactions, v. 178, p. 264–282.

Yates, R. G., 1964, Geologic map and sections of the Deep Creek area, Stevens and Pend Oreille Counties, Washington: U.S. Geological Survey Map I-412, scale 1:31,680.

——1971, Geologic map of the Northport quadrangle, Washington: U.S. Geological Survey Map I-603, scale 1:31,680.

MANUSCRIPT RECEIVED BY THE SOCIETY JUNE 21, 1979

MANUSCRIPT ACCEPTED AUGUST 7, 1979